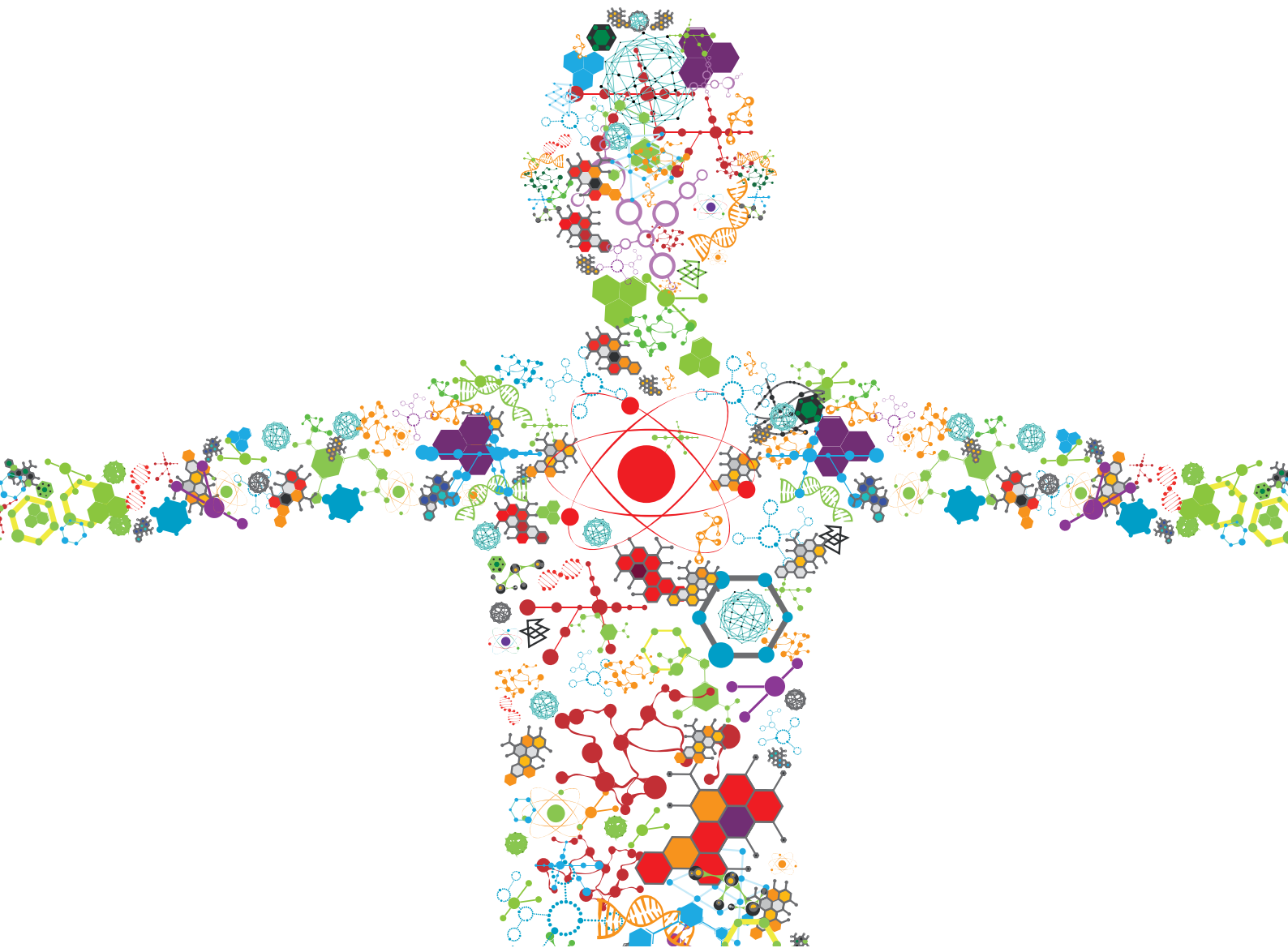


ADVANCES IN BRAIN MECHANICS

EDITED BY: Silvia Budday, Philip Bayly and Gerhard A. Holzapfel
PUBLISHED IN: Frontiers in Bioengineering and Biotechnology and
Frontiers in Mechanical Engineering





frontiers

Frontiers eBook Copyright Statement

The copyright in the text of individual articles in this eBook is the property of their respective authors or their respective institutions or funders. The copyright in graphics and images within each article may be subject to copyright of other parties. In both cases this is subject to a license granted to Frontiers.

The compilation of articles constituting this eBook is the property of Frontiers.

Each article within this eBook, and the eBook itself, are published under the most recent version of the Creative Commons CC-BY licence.

The version current at the date of publication of this eBook is CC-BY 4.0. If the CC-BY licence is updated, the licence granted by Frontiers is automatically updated to the new version.

When exercising any right under the CC-BY licence, Frontiers must be attributed as the original publisher of the article or eBook, as applicable.

Authors have the responsibility of ensuring that any graphics or other materials which are the property of others may be included in the CC-BY licence, but this should be checked before relying on the CC-BY licence to reproduce those materials. Any copyright notices relating to those materials must be complied with.

Copyright and source acknowledgement notices may not be removed and must be displayed in any copy, derivative work or partial copy which includes the elements in question.

All copyright, and all rights therein, are protected by national and international copyright laws. The above represents a summary only. For further information please read Frontiers' Conditions for Website Use and Copyright Statement, and the applicable CC-BY licence.

ISSN 1664-8714

ISBN 978-2-88974-279-0

DOI 10.3389/978-2-88974-279-0

About Frontiers

Frontiers is more than just an open-access publisher of scholarly articles: it is a pioneering approach to the world of academia, radically improving the way scholarly research is managed. The grand vision of Frontiers is a world where all people have an equal opportunity to seek, share and generate knowledge. Frontiers provides immediate and permanent online open access to all its publications, but this alone is not enough to realize our grand goals.

Frontiers Journal Series

The Frontiers Journal Series is a multi-tier and interdisciplinary set of open-access, online journals, promising a paradigm shift from the current review, selection and dissemination processes in academic publishing. All Frontiers journals are driven by researchers for researchers; therefore, they constitute a service to the scholarly community. At the same time, the Frontiers Journal Series operates on a revolutionary invention, the tiered publishing system, initially addressing specific communities of scholars, and gradually climbing up to broader public understanding, thus serving the interests of the lay society, too.

Dedication to Quality

Each Frontiers article is a landmark of the highest quality, thanks to genuinely collaborative interactions between authors and review editors, who include some of the world's best academicians. Research must be certified by peers before entering a stream of knowledge that may eventually reach the public - and shape society; therefore, Frontiers only applies the most rigorous and unbiased reviews.

Frontiers revolutionizes research publishing by freely delivering the most outstanding research, evaluated with no bias from both the academic and social point of view. By applying the most advanced information technologies, Frontiers is catapulting scholarly publishing into a new generation.

What are Frontiers Research Topics?

Frontiers Research Topics are very popular trademarks of the Frontiers Journals Series: they are collections of at least ten articles, all centered on a particular subject. With their unique mix of varied contributions from Original Research to Review Articles, Frontiers Research Topics unify the most influential researchers, the latest key findings and historical advances in a hot research area! Find out more on how to host your own Frontiers Research Topic or contribute to one as an author by contacting the Frontiers Editorial Office: frontiersin.org/about/contact

ADVANCES IN BRAIN MECHANICS

Topic Editors:

Silvia Budday, University of Erlangen Nuremberg, Germany

Philip Bayly, Washington University in St. Louis, United States

Gerhard A. Holzapfel, Graz University of Technology, Austria

Citation: Budday, S., Bayly, P., Holzapfel, G. A., eds. (2022). Advances in Brain Mechanics. Lausanne: Frontiers Media SA. doi: 10.3389/978-2-88974-279-0

Table of Contents

- 04 Editorial: Advances in Brain Mechanics**
Silvia Budday, Philip V. Bayly and Gerhard A. Holzapfel
- 07 A Machine Learning Enhanced Mechanistic Simulation Framework for Functional Deficit Prediction in TBI**
Anna Schroder, Tim Lawrence, Natalie Voets, Daniel Garcia-Gonzalez, Mike Jones, Jose-Maria Peña and Antoine Jerusalem
- 26 Calibration of a Heterogeneous Brain Model Using a Subject-Specific Inverse Finite Element Approach**
J. Sebastian Giudice, Ahmed Alshareef, Taotao Wu, Andrew K. Knutsen, Lucy V. Hiscox, Curtis L. Johnson and Matthew B. Panzer
- 43 Real-Time Multifrequency MR Elastography of the Human Brain Reveals Rapid Changes in Viscoelasticity in Response to the Valsalva Maneuver**
Helge Herthum, Mehrgan Shahryari, Heiko Tzschätzsch, Felix Schrank, Carsten Warmuth, Steffen Görner, Stefan Hetzer, Hennes Neubauer, Josef Pfeuffer, Jürgen Braun and Ingolf Sack
- 55 A Methodology to Compare Biomechanical Simulations With Clinical Brain Imaging Analysis Utilizing Two Blunt Impact Cases**
X. Gary Tan, Venkata Siva Sai Sujith Sajja, Maria M. D'Souza, Raj K. Gupta, Joseph B. Long, Ajay K. Singh and Amit Bagchi
- 72 Brain Shape Changes Associated With Cerebral Atrophy in Healthy Aging and Alzheimer's Disease**
Yana Blinkouskaya and Johannes Weickenmeier
- 89 Poro-Viscoelastic Effects During Biomechanical Testing of Human Brain Tissue**
Alexander Greiner, Nina Reiter, Friedrich Paulsen, Gerhard A. Holzapfel, Paul Steinmann, Ester Comellas and Silvia Budday
- 107 Unraveling the Local Relation Between Tissue Composition and Human Brain Mechanics Through Machine Learning**
Kevin Linka, Nina Reiter, Jasmin Würges, Martin Schicht, Lars Bräuer, Christian J. Cyron, Friedrich Paulsen and Silvia Budday
- 124 An Overview of the Effectiveness of Bicycle Helmet Designs in Impact Testing**
Javid Abderezaei, Fargol Rezayaraghi, Brigit Kain, Andrea Menichetti and Mehmet Kurt
- 137 A Machine Learning Approach to Investigate the Uncertainty of Tissue-Level Injury Metrics for Cerebral Contusion**
Andrea Menichetti, Laura Bartsoen, Bart Depreitere, Jos Vander Sloten and Nele Famaey
- 154 A Nitric Oxide-Modulated Variable-Order Fractional Maxwell Viscoelastic Model of Cerebral Vascular Walls**
Corina S. Drapaca
- 167 Subject-Specific Head Model Generation by Mesh Morphing: A Personalization Framework and Its Applications**
Xiaogai Li



Editorial: Advances in Brain Mechanics

Silvia Budday^{1*}, Philip V. Bayly² and Gerhard A. Holzapfel³

¹Friedrich Alexander University Erlangen-Nürnberg, Erlangen, Germany, ²Washington University in St. Louis, St. Louis, MO, United States, ³Graz University of Technology, Austria and Norwegian University of Science and Technology (NTNU), Trondheim, Norway

Keywords: Brain mechanics, data-driven modeling, finite element method, nonlinear continuum mechanics, personalized simulations, traumatic brain injury, multiphysics modeling

Editorial on the Research Topic

Advances in Brain Mechanics

Increasing evidence confirms that mechanics plays a critical role in brain function and dysfunction. In recent years, computational mechanics has become a powerful tool for studying and predicting the behavior of the human brain under both physiological and pathological conditions. Yet, important challenges that have hindered realistic and reliable numerical predictions remain unresolved. This Frontiers Research Topic covers recent advances, current challenges, and perspectives in brain mechanics modeling. It encompasses novel experimental and modeling approaches, including computational solid and fluid mechanics as well as data-driven modeling, which ultimately target at personalized simulations that add value to clinicians.

The mechanical response of brain tissue is highly complex: it is ultra-soft with a shear modulus on the order of 1kPa, biphasic, and heterogeneous; different brain regions show different mechanical behavior, for example in gray matter versus white matter. Therefore, the measured properties strongly depend on the length and time scale of the specific experimental setup. Common techniques include large-strain compression, tension, and shear experiments, which are typically performed *ex vivo*, as well as indentation measurements and magnetic resonance elastography, which can be performed *in vivo*. In addition to the loading and boundary conditions, assumptions made when analyzing the corresponding data can affect the reported values for properties like stiffness and viscosity. These difficulties have led to apparently contradicting experimental results in the literature. What may seem like inconsistencies at first glance, however, can often be brought together by nonlinear continuum mechanics modeling and finite element simulations, providing material models that capture the behavior of brain tissue across different time scales and loading conditions. Greiner et al. demonstrate, for example, that a poro-viscoelastic model can explain why indentation experiments suggest that white matter tissue in the human brain is stiffer than gray matter tissue, while large-strain compression experiments show the opposite trend. This study highlights the potential of mechanical modeling and simulation to standardize and help interpret experimental observations in the future.

Well-designed mechanical experiments are critical to properly calibrate models for finite element simulations of brain mechanics. So far, mechanical *ex vivo* testing techniques have mainly been used to identify material parameters. However, in order to achieve the goal of establishing personalized finite element models of the human brain, the *in vivo* characterization of human brain tissue properties becomes important. The latest developments in this direction enable the live assessment of mechanical properties using multi-modal magnetic resonance elastography (MRE), as presented in Herthum et al. While this technique is currently limited to small deformations and relatively high frequencies, which has limited its suitability for calibrating nonlinear material models at large strains, Giudice et al. are now introducing a multi-stage inverse finite element approach to calibrate

OPEN ACCESS

Edited and reviewed by:

Juergen Brugger,
Swiss Federal Institute of Technology
Lausanne, Switzerland

*Correspondence:

Silvia Budday
silvia.budday@fau.de

Specialty section:

This article was submitted to
Micro- and Nanoelectromechanical
Systems,
a section of the journal
Frontiers in Mechanical Engineering

Received: 27 October 2021

Accepted: 22 November 2021

Published: 17 December 2021

Citation:

Budday S, Bayly PV and Holzapfel GA
(2021) Editorial: Advances in
Brain Mechanics.
Front. Mech. Eng 7:803151.
doi: 10.3389/fmech.2021.803151

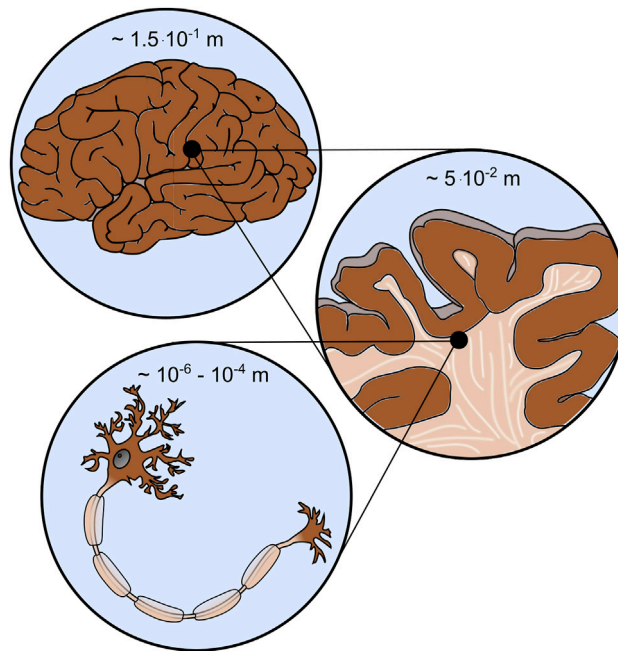


FIGURE 1 | Brain mechanics involves different scales, e.g., the cell (**bottom**), tissue (**middle**), and organ (**top**) scale.

heterogeneous subject-specific material parameters for injury prediction from MRE data. The parameters define the underlying nonlinear deviatoric response by minimizing the error between model-predicted brain displacements and experimental displacement data. In the future, such MRE-based, heterogeneous, subject-specific material properties can serve as a basis for improving the biofidelity of finite element brain models and enhance their potential as a tool for predicting injuries, assisting the diagnosis of diseases and further developing current treatment strategies.

To provide personalized predictions, subject-specific head models are also required. Xiaogai Li presents a methodology for personalizing a baseline model through hierarchical imaging registrations with multiple features and multiple modalities, mesh morphing, and mesh grouping. The efficient generation of subject-specific finite element head models will be an important step for personalized simulations aimed at addressing clinical questions.

The complex mechanical properties of brain tissue are closely coupled to biochemical and biological processes. Therefore, multiphysics modeling has proven to be a valuable tool for predictively understanding phenomena related to development, aging and disease. Blinkouskaya et al., for example, present a model that couples tissue atrophy, the shrinking of our brain and biomarker progression in Alzheimer's disease. Their ultimate goal is to develop a diagnostic tool able of distinguishing between healthy aging and accelerated aging typically seen in Alzheimer's disease and related dementias. In this regard, the proposed approach based on continuum mechanics could allow earlier and more effective interventions. Another example of a coupled problem in the brain involves the smaller blood vessels, which, due to the

pulsating blood flow, experience not only oscillatory forces, but also structural and morphological changes that are controlled by the surrounding brain cells. Corina S. Drapaca introduces a variable-order, fractional viscoelastic model to predict how the mechanical deformation of the cerebral artery wall is caused by pulsating blood flow and the dynamics of the neuronal nitric oxide. The model could prove to be a valuable tool to better understand the dynamic interaction between nitric oxide and brain microvessels related to neurometabolism in healthy and diseased states.

Another promising way to advance brain mechanics modeling in the future is to complement physics-based models with machine learning techniques. In Schroder et al. a machine learning layer is integrated into a mechanical damage model in order to accelerate the prediction of functional deficits after traumatic brain injury. The machine learning prediction closely matches the full simulation results and opens the door to live predictions of changes in the functional activity of the brain or to reverse engineering the mechanisms of an accident. Similarly, Menichetti et al. present an artificial neural network as a computationally efficient surrogate of a finite element porcine brain model to predict the localized brain strain and strain rate resulting from experiments with controlled cortical influence. The model is used to create tissue-level injury metrics and corresponding thresholds for cerebral contusion. Finally, in Linka et al. a "constitutive artificial neural network" is being established to predict the viscoelastic stress-strain response of brain tissue solely on the basis of microstructural data. The network then enables the modeler to assess the relevance of certain features such as cellular and extracellular tissue components for the macroscopic large-strain mechanical response and thus gain

new insights into the microstructure-mechanics relationships in the brain. These studies highlight how the combination of physics-based modeling and machine learning techniques can advance the field of brain mechanics.

In general, the integration of both mechanical data and modeling, as well as imaging or medical data, will be key to bringing computational brain mechanics models closer to their use in clinical practice. Tan et al. present, for example, a methodology to combine computational simulations with clinical data for the interpretation of blunt traumatic brain injury. This study demonstrates how the integration of techniques from computational biomechanics and medical data assessed in the clinic (e.g., magnetic resonance imaging) can help predict injuries, support early medical diagnosis, or evaluate the effectiveness of personal protective equipment. This approach can lead to improved bicycle helmet designs that are effective in preventing traumatic brain injury (TBI), as discussed in Abderezaei et al.

By gathering these recent advances in the rapidly evolving field of brain mechanics, we aim to foster further synergies between various experimental and modeling approaches that will help overcome remaining challenges and frontiers. Together, these advances are moving the field towards its goal of generating high-fidelity models that can provide novel insights into brain injuries

and disease and ultimately improve strategies for their diagnosis and treatment.

AUTHOR CONTRIBUTIONS

SB wrote the original draft, PB and GH carefully revised the article. All authors approved the final version.

Conflict of Interest: The authors declare that the research was conducted in the absence of any commercial or financial relationships that could be construed as a potential conflict of interest.

Publisher's Note: All claims expressed in this article are solely those of the authors and do not necessarily represent those of their affiliated organizations, or those of the publisher, the editors and the reviewers. Any product that may be evaluated in this article, or claim that may be made by its manufacturer, is not guaranteed or endorsed by the publisher.

Copyright © 2021 Budday, Bayly and Holzapfel. This is an open-access article distributed under the terms of the Creative Commons Attribution License (CC BY). The use, distribution or reproduction in other forums is permitted, provided the original author(s) and the copyright owner(s) are credited and that the original publication in this journal is cited, in accordance with accepted academic practice. No use, distribution or reproduction is permitted which does not comply with these terms.



A Machine Learning Enhanced Mechanistic Simulation Framework for Functional Deficit Prediction in TBI

OPEN ACCESS

Edited by:

Philip Bayly,
Washington University in St. Louis,
United States

Reviewed by:

Kenneth L. Monson,
The University of Utah, United States
Pamela J. VandeVord,
Virginia Tech, United States

*Correspondence:

Natalie Voets
natalie.voets@ndcn.ox.ac.uk
Jose-Maria Peña
jm.pena@lurtis.com
Antoine Jerusalem
antoine.jerusalem@eng.ox.ac.uk

†Present address:

Anna Schroder,
Department of Medical Physics and
Biomedical Engineering, University
College London, London,
United Kingdom
Daniel Garcia-Gonzalez,
Department of Continuum Mechanics
and Structural Analysis, Universidad
Carlos III de Madrid, Leganes, Spain

Specialty section:

This article was submitted to
Biomechanics,
a section of the journal
Frontiers in Bioengineering and
Biotechnology

Received: 24 July 2020

Accepted: 18 January 2021

Published: 03 March 2021

Citation:

Schroder A, Lawrence T, Voets N,
Garcia-Gonzalez D, Jones M,
Peña J-M and Jerusalem A (2021) A
Machine Learning Enhanced
Mechanistic Simulation Framework for
Functional Deficit Prediction in TBI.
Front. Bioeng. Biotechnol. 9:587082.
doi: 10.3389/fbioe.2021.587082

Anna Schroder^{1†}, Tim Lawrence², Natalie Voets^{2*}, Daniel Garcia-Gonzalez^{1†}, Mike Jones³, Jose-Maria Peña^{4*} and Antoine Jerusalem^{1*}

¹ Department of Engineering Science, University of Oxford, Oxford, United Kingdom, ² Nuffield Department of Clinical Neurosciences, University of Oxford, Oxford, United Kingdom, ³ Institute of Medical Engineering and Medical Physics, Cardiff University, Cardiff, United Kingdom, ⁴ Lurtis Ltd., Oxford, United Kingdom

Resting state functional magnetic resonance imaging (rsfMRI), and the underlying brain networks identified with it, have recently appeared as a promising avenue for the evaluation of functional deficits without the need for active patient participation. We hypothesize here that such alteration can be inferred from tissue damage within the network. From an engineering perspective, the numerical prediction of tissue mechanical damage following an impact remains computationally expensive. To this end, we propose a numerical framework aimed at predicting resting state network disruption for an arbitrary head impact, as described by the head velocity, location and angle of impact, and impactor shape. The proposed method uses a library of precalculated cases leveraged by a machine learning layer for efficient and quick prediction. The accuracy of the machine learning layer is illustrated with a dummy fall case, where the machine learning prediction is shown to closely match the full simulation results. The resulting framework is finally tested against the rsfMRI data of nine TBI patients scanned within 24 h of injury, for which paramedical information was used to reconstruct *in silico* the accident. While more clinical data are required for full validation, this approach opens the door to (i) on-the-fly prediction of rsfMRI alterations, readily measurable on clinical premises from paramedical data, and (ii) reverse-engineered accident reconstruction through rsfMRI measurements.

Keywords: traumatic brain injury, resting state functional magnetic resonance imaging, default mode network, finite element simulation, machine learning

1. INTRODUCTION

Traumatic brain injury (TBI) is one of the leading causes of death in people under the age of 45 years (Maas et al., 2008). In the EU, it is estimated that 2.5 million people suffer annually from TBI (Maas et al., 2015). While they can also result from non-impact conditions such as blast waves arising from an explosion, most TBIs occur as a consequence of head impacts, e.g., during falls, road traffic accidents, assaults, and sport injuries. The impact conditions can be very diverse, as expected from the large parameter space characterizing the boundary conditions of the contact (location, impact velocity, angle of impact, impactor shape, impactor material properties, etc.), as well as the

high sensitivity associated to some of these (Fahlstedt et al., 2012). Despite improvements in care, functional outcomes are equally variable, even among those with apparently minor early injury severity. The limited predictive power of current clinical head injury scales raises a prominent need for tools better able to anticipate the long-term effects of TBI.

To understand better the effects of these impact conditions, computational models, and, in particular, finite element head models (FEHMs), have been used to predict mechanical deformation and stress levels on brain tissue (Raul et al., 2008; Dixit and Liu, 2017). This approach has typically been leveraged to correlate mechanistic measures (e.g., pressure, von Mises stress, principal strains, etc.) with different degrees of tissue damage. Historically, FEHMs have successfully been utilized for the prediction of structural events such as skull fracture (Garcia-Gonzalez et al., 2017). However, as local mechanical disturbances in the brain can lead to time-dependent systemic biological and multiphysics responses, these models are intrinsically unable to mechanistically predict functional alterations or cognitive deficits. Barring a few exceptions (Garcia-Gonzalez et al., 2018b), very little work has focussed on correlating functional deficits, tissue damage, and mechanical features in a fully validated framework, e.g., with clinical or animal data. Even then, in most of the cases, the high cost (both in man-hour and computational) to develop, run, and analyze the underlying FEHM remains extremely impractical and not fit for direct clinical use. While coupling mechanistic approaches to machine learning (ML) methods has been recently highlighted as a potential avenue for alleviating these restrictions (Baker et al., 2018), very little has been done in this field.

At the clinical end of the spectrum, the diagnosis and prognosis of TBI rely heavily on the clinician's experience. Indeed, while a lot of effort has focused on outcome prediction—outcome being often defined in relatively broad terms, e.g., “mortality” or “unfavorable outcome” (Roozenbeek et al., 2012)—, these prognostic models are not directly usable for individual patients (Menon and Harrison, 2008). Instead, head injury assessment by healthcare professionals still relies on general guidance built around a set of recommendations such as the ones provided by the National Institute for Health and Care Excellence (National Institute for Health and Care Excellence, 2019). Even then, the immediate cognitive evaluation of the sufferer is generally based on the Glasgow Coma Scale (GCS) originally defined in mid 70s (Royal College of Physicians and Surgeons of Glasgow, 1974), and solely focused on symptoms as opposed to cause identification.

The recent development in magnetic resonance imaging (MRI) has allowed for the identification of new candidates for direct functional evaluation of the brain. In particular, resting state functional MRI (rsfMRI) is a technique that identifies correlated networks in the absence of specific tasks (Fox and Raichle, 2007), offering insight into network function among unconscious patients unable to engage in active cognitive tasks (Kondziella et al., 2016). Among the common findings in patients with TBI is the alteration to the default mode network (DMN) (Sharp et al., 2014). While rsfMRI could hold the key to a more direct and straightforward diagnosis of eventual cognitive deficits

in TBI, a prognostic/diagnostic tool to link network alteration and tissue damage still remains elusive.

To this end, this work proposes a new method aimed at predicting rsfMRI network deficit directly from trauma data by means of a ML layer taking as inputs a combination of impact conditions, namely: location, velocity of impact, angle of impact (represented by a binary input indicating whether the impact is perpendicular or not), and shape of the impactor (represented by their radii of curvature). The ML layer predicts the extent of tissue damage after being trained by a library of pre-simulated impact loaded FEHMs for which a shear energy rate threshold is used to estimate the percentage of tissue damage in the DMN. Our results show that it is able to capture very well the proportion of brain damage sustained mechanically, and thus alleviate significantly the computational time experienced by direct FEHM simulations. In parallel to this, a functional criterion defined as the proportion of brain voxels statistically decoupled from the neurologically normal DMN is proposed to quantify the functional damage to the DMN. Both mechanistic and functional criteria are then evaluated for nine TBI patients with clinical and rsfMRI data available in the hyper-acute phase (first few hours) after trauma, for whom the accident is reproduced *in silico* from paramedical data. Despite a very wide variability in the extent of the predicted DMN tissue damage, the mechanical damage values are generally aligned in trend with the “ground truth” functional damage observed in these patients as quantified by the functional criterion. Assuming a direct relationship between the two criteria, the proposed framework is ultimately used to estimate the real velocity of impact experienced by the nine patients.

While future validation work is needed to extend these model predictions to an even more comprehensive range of head injuries, we propose that this virtual prediction framework offers avenues for realistic estimation of either brain functional deficit when knowing the accident conditions, or the accident conditions when having access to the functional evaluation. Such estimations have direct clinical utility in the general clinical setting where very rare hyper-acute MRI scans, used to validate model predictions here, are not obtainable. Once fully validated on a larger cohort, this approach could find a direct use in clinical and forensic environments.

2. MATERIALS AND METHODS

2.1. Clinical Data

2.1.1. Participants

Adult patients (aged 18 years and over) were prospectively recruited from the Emergency Department at the Oxford University Hospitals NHS Foundation Trust as early as possible following traumatic head injury. Eighteen patients in total were recruited, among which nine patients (mean age: 55.8 range: 22–83) were selected for this study based on having a single defined mechanism of injury suited to modeling. Patients underwent a CT scan as part of standard trauma care. Once immediately life-threatening conditions were identified and treated, patients were recruited for a research MRI scan within 24 h of injury

(the “hyper-acute” phase). Patients who were intubated and ventilated at the time of recruitment were transferred to MRI by a dedicated neuro-intensive care team consisting of a consultant neuro-anaesthetist, neuro-intensive care nurse, MRI research nurse, and consultant neurosurgeon. The same team managed the patient throughout the scan before transferring to intensive care. Patients were excluded from the study if they had contraindications to MRI, injuries requiring urgent surgery, or were medically unstable so that scanning would not be safe. Patients were followed throughout their hospital stay and returned at 6–9 months following injury for repeat assessments. Initial severity of injury was assessed using post-resuscitation GCS at presentation. Severity, at 1 week/short term outcome, was assessed using both the GCS and location of the patient (in hospital or discharged). Patients with a GCS of 12 or less were considered moderate-severe. Patients with a GCS 13–15 were considered mild. All patients still in hospital with a GCS 12 or less and/or still in hospital (due to TBI) at 7 days were considered moderate-severe at this point. A neurological examination and Glasgow Outcome Scale (extended)—GOSe—questionnaire were completed at 6–9 months by the patients or their relatives/carers if they were unable. The mechanism of injury for every patient was ascertained from medical notes recorded at the scene or in discussion with the patient/witnesses. Patient demographics and clinical data are presented in **Table 1**.

Eighteen healthy controls, age and sex-matched to the patients, were recruited for normative data. Exclusion criteria for controls included contraindications to MRI and any current or historical neurological or psychiatric conditions. Healthy controls provided informed written consent. All patients with capacity at the time of initial recruitment gave written informed consent. For patients lacking capacity, the lead clinician, in consultation with the family, signed a declaration form to confirm agreement for the patient to be recruited into the study. Explicit patient consent was sought as soon as possible upon recovery. The study was approved by the South Central-Berkshire Research Ethics Committee.

2.1.2. MRI Data Acquisition

MRI data were acquired on a 3T Siemens Magnetom Verio scanner at the Oxford Acute Vascular Imaging Centre (AVIC). The scanning protocol included T1-weighted MPRAGE and resting fMRI, acquired using an echo-planar T2*-weighted imaging sequence. The resting fMRI sequence parameters were: voxel size of $3 \times 3 \times 3 \text{ mm}^3$, multiband acceleration factor: 2, repetition time: 1,640 ms, echo time: 30 ms, acquisition time: 05:35 min. Field maps were acquired to allow for correction of field inhomogeneity-induced geometric distortions in the fMRI data.

2.1.3. rsfMRI Data Pre-processing

The rsfMRI data were analyzed using dedicated tools in the FMRIB Software Library (FSL) (<http://fsl.fmrib.ox.ac.uk/fsl>). First, standard pre-processing was performed, including brain extraction, motion correction, distortion correction using field maps, spatial smoothing (full-width at half maximum of 5 mm), and high-pass temporal filtering (100 s). To enable

between-subject comparisons, individual subjects' functional scans were linearly registered to their respective high resolution structural (T1) scans and then nonlinearly aligned to the Montreal Neurological Institute (MNI) standard template brain, accounting for any gross brain pathology (such as contusions, haematoma).

Next, in order to objectively extract the DMN from each individual participant's resting fMRI data, we performed a dual-regression analysis, as previously described (Khalili-Mahani et al., 2012; Voets et al., 2012). For this analysis, we obtained a template set of 10 well-validated resting state networks (including the DMN) identified in healthy adults (Smith et al., 2009). A two-stage (temporal and spatial) regression was then performed. Each template resting network has a characteristic time-course. Therefore, in the first stage, each of the template networks was regressed against the rsfMRI time-series acquired in our individual subjects to identify time-courses corresponding to each template component (Voets et al., 2012). The second stage then identified brain voxels that shared this time course, for each of the 10 networks separately, from which we selected the DMN for further analysis. In this way, we obtained z-normalized single subject spatial maps, representing for every voxel in the brain the strength of its functional connectivity with the DMN in our nine patients and eighteen healthy controls (see **Figure 1**).

2.1.4. Resting State Network Based Damage

Finally, we performed single-subject case-control statistical analyses. The objective of these analyses was to generate a DMN “damage load” index for every TBI patient by calculating the number of voxels in each patient's DMN whose connectivity was altered when compared to healthy controls. Since distributions in small samples may violate the assumptions underlying single case *t*-test analyses, for this analysis, we performed inference testing using Permutation Analysis of Linear Models (PALM) with signal flipping (Winkler et al., 2014), as described previously (Voets et al., 2017). These analyses were constrained to cortical voxels by constructing a group mean gray matter mask from automatic tissue segmentations of each subject's T1-weighted anatomical scan obtained using FSL-FAST (Zhang et al., 2001). For each patient, we compared the whole-brain DMN connectivity map to the distribution of connectivity maps generated from our 18 healthy controls using the general linear model framework. Two groups were created (corresponding to $n = 18$ healthy control and $n = 1$ patient, substituting the data for each of the nine patients in turn) and a single contrast (controls > patient, testing for voxels with lower DMN functional connectivity in the patient compared with controls). We performed 5,000 permutations for each case-control analysis and report permutation *p*-values for significant voxels using the thresholding method Cluster Free Threshold Enhancement (TFCE). TFCE offers a simple approach for calculating cluster-like voxel-wise statistics, providing sensitivity both to local maxima and spatial extent of signal without the need to define an arbitrary hard initial cluster-forming threshold (Smith and Nichols, 2009).

To obtain the individual patient DMN “damage load” metric, the resulting *t*-statistic maps (not corrected for multiple comparisons) were thresholded at a *p*-value of 0.05 to

TABLE 1 | GCS, Glasgow Coma Scale; GOSe, Glasgow Outcome Score (extended).

Case	Age	Sex	Mechanism of injury	Severity at presentation	GCS (15-point scale), at 7–9 days	GOSe at 6–9 months (8-point scale)
1	83	M	Fall from a 2-story house, injuries suggestive of hip and left frontal head impact	Severe	Intubated and sedated	3
2	22	M	Closed hand hit to the face, fell backwards	Moderate	15	7
3	70	F	Kicked by a horse in the abdomen and head, fell backwards	Mild	15	8
4	30	M	Pedestrian, hit by van traveling at 20–30 mph. Hit head on wing mirror and knocked to the floor	Mild	15	8
5	61	F	Pedestrian, hit by cyclist. Impact to right side of the head behind ear	Moderate	15	4
6	52	F	Pedestrian, hit by car traveling at approx. 30 mph. Impact to right orbital/frontal region of the head	Moderate	15	8
7	41	M	Fall from 3-story roof. Impact to left temporal and frontal head regions. Additional right wrist fracture, cervical, and thoracic transverse spinous process fractures	Severe	Intubated and sedated	5
8	62	M	Charge by bull running out of a cattle truck. Thrown back against a metal fence and onto concrete. Landed on back of head	Moderate	15	6
9	72	M	Cyclist, knocked off bike, landed on head. Impact to left parietal head region and left shoulder.	Severe	Intubated and sedated	3

The GOSe provides a numeric measure corresponding to the degree of disability a patient is left with after a head injury (Weir et al., 2012); lower scores indicate worse outcomes. GOSe differs from the GCS which is a 15-point measure of a patient’s degree of consciousness, typically used as a marker of severity following injury (lower scores indicate more severe injury). The scale is intended for use after discharge from hospital, and in particular, moderate disability and good recovery are not assessable until after discharge. Assessment beyond 6 months is considered to provide a reasonable marker of the long-term cognitive effects attributable to the TBI (Dikmen et al., 2009).

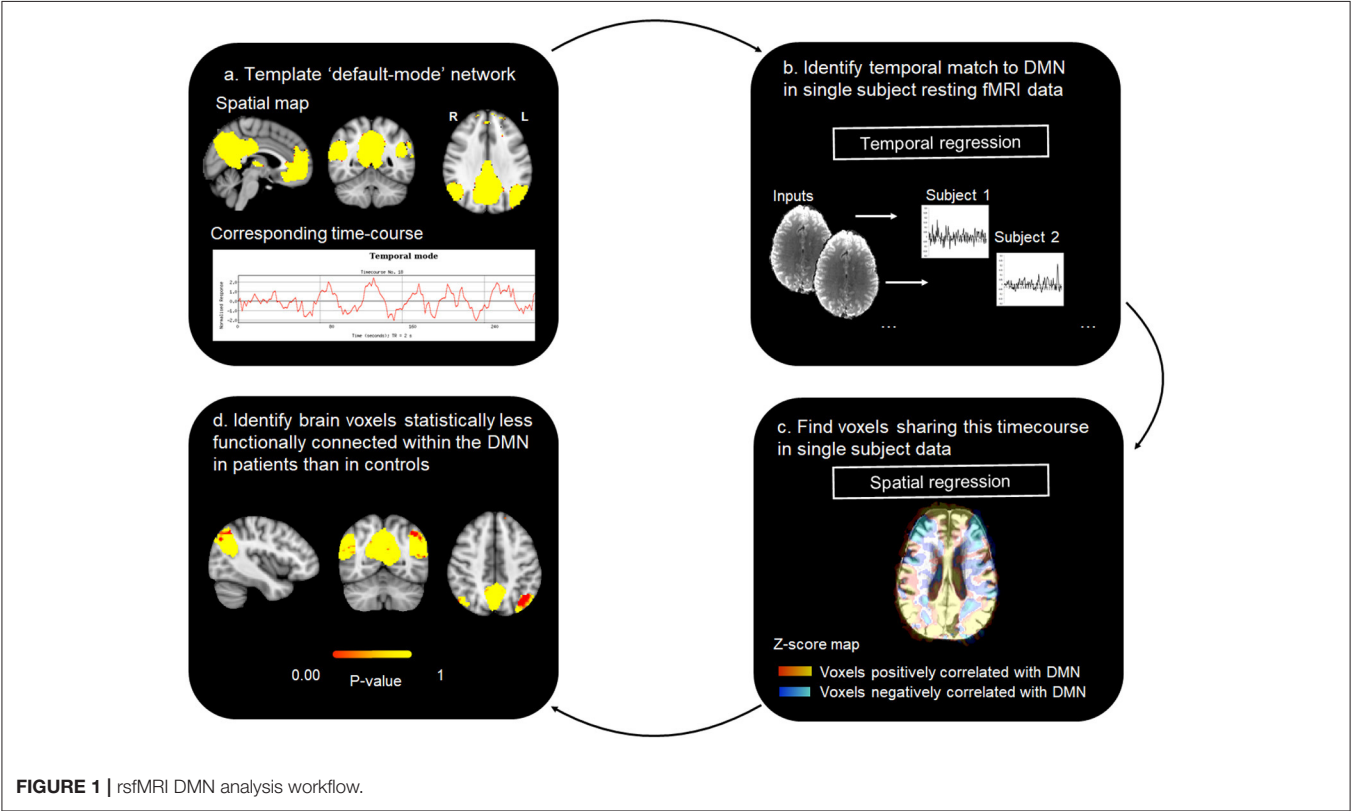


FIGURE 1 | rsfMRI DMN analysis workflow.

calculate the number of statistically “disconnected” voxels. Finally, the number of “disconnected” voxels was expressed as a percentage of the total DMN mask. The latter was calculated by generating a binary mask of the DMN, by

thresholding the template DMN mask (Smith and Nichols, 2009) at z-score of 3.1 (corresponding to a p-value of 0.05) and binarizing the resulting spatial map to extract its volume.

2.1.5. Impact Velocity and Location Estimations

The data gathered in **Table 1** were analyzed to estimate the impact location and velocity in a fashion consistent with medico-legal expertise. Additional data were made available by neurosurgeon and paramedic.

- **Case 1:** An unwitnessed fall from a 2-story house roof, the victim sustained abrasions to the left forehead and face, a fracture to the left zygoma and a left intratrochanteric hip fracture, suggesting that the left frontal region made contact with the ground; the hip fracture suggests that the head was unlikely to have contacted the ground first. That forehead and facial grazes were in evidence, suggests a concomitant or subsequent involvement of the maxilla and/or temporal bones and thus, a more diffuse, focal loading. The general description of the grazes suggests some tangential motion of the head, relative to a primary contact between the lower limb and the ground. This potentially was a result of angular motion of the trunk and upper body, relative to the contact of the lower limb. The provision of greater detail of the grazes may have informed the directionality and mechanics of the relationship between the head and contact surface further. The site and limited severity of the zygomatic fracture suggests that the head impact was relatively low energy, certainly compared to the potential for injury posed by a fall height through the distance presented in this case and that the surface was flat and firm, rather than irregular. Whether the surface was unyielding is unknown, however, given the overall low level of injury, the surface was probably not hard, i.e., neither concrete nor tarmac. The first point of contact was logically likely to have absorbed/dissipated a significant proportion of the impact energy. If it had been the head, a greater degree of injury severity might have been expected. However, a glancing head contact and subsequent lateral upper leg impact cannot be excluded. The fall height can be assumed to have been in the region of 5.7 m (typical height to the gutter of a 2-story house), the height of the gutter approximately 0.1 m, the assumed standing height of the accident victim, assumed 50th percentile male = 1.76 m, minus the 0.1 m distance from the top of the head to the likely point of contact around the “hat brim region.” Therefore, a total minimum fall height of 7.3 m is assumed, since by default, the assumption is that the male was standing at the lower edge of the roof, with no initial velocity and simply pitched forwards. Therefore, a simple fall is assumed, with no initial velocity or arc of rotation considered, through 7.3 m from which a maximum impact velocity is calculated to be 12 m/s. Forces which exceed the fracture tolerance limit in the literature are in the region of 5.35 kN (1,200 lbf), assuming an adult head mass of 6.82 kg (15 lb) and an acceleration of 80 g (Pappachan and Alexander, 2012). The fracture tolerance of the zygoma is in the order of 0.89–2.00 kN (200–450 lbf) (Pappachan and Alexander, 2012). Thus, the minimum velocity to produce fracture would be in the order of 2.24–5.02 m/s (5–11.25 mph). **The left frontal region is suspected to have made first contact with ground between 2.24 and 12 m/s.**
- **Case 2:** Involved a typical “sucker punch” (or “king hit”) assault case (Patton and McIntosh, 2017). The male victim was punched to the face, which resulted in him falling backwards and striking his occiput on a rigid surface. The resulting head injuries may have been due to the punch, the fall, or a combination of both. A spectrum of punch response outcomes is possible, for example, if the punch had been delivered, such that little momentum (push) was transferred, producing a sudden loss of consciousness and no reflexive actions, then victim could have simply collapsed downwards and backwards, or downwards into sitting position and backwards. Alternatively, if the victim had been struck squarely, then momentum transfer would have produced an angular (arcing) motion of the upper body relative to his fixed feet, acting as a fulcrum. This would have resulted either in a relatively pure angular velocity about the fixed feet, if the legs had stiffened as a result of the blow, or alternatively, produced a combined linear and angular velocity if the legs had given way. Thus, a higher velocity and impact energy would have been produced. The worst case would be for a punch with significant transference of momentum such that the victim’s straight body is submitted to translational velocity of 6.75 ± 0.27 m/s. The best case would be for the victim’s body being slightly bent at waist with a translational velocity of 4.85 ± 1.33 m/s (Patton and McIntosh, 2017). **The victim is estimated to have hit his occiput on the ground with a velocity between 4.85 and 6.75 m/s.**
- **Case 3:** The victim was reported to have been kicked by a horse both to the abdomen and head and to have fallen backwards, prior to striking her head against the ground. Thus, the areas of impact were to the front, as a result of contact with the kick to the abdomen and head and back of the head (occipital region), due to the fall backwards. This was accompanied by a loss of consciousness for a brief period. Although the sequence was not specified, one could assume that the abdominal kick was first, since a kick to the head would have likely caused the victim to have initially fallen backwards away from any subsequent kick. With respect to the occipital impact, the velocity range is reported as being between a straight body translational velocity of 4.80 ± 0.22 m/s and a slightly bent at waist translational velocity of 3.78 ± 0.53 m/s (Patton and McIntosh, 2017). **In light of all the unknowns, an occipital impact velocity is estimated to have been between 3.2 and 4.8 m/s.**
- **Case 4:** The victim was a pedestrian hit by a van traveling at an estimated 20–30 mph. The head was reported to have contacted with the wing mirror before the victim was knocked to the ground. Frontal and occipital scalp degloving and significant arm and soft tissue injuries were produced. The primary impact velocity of the van cannot be directly attributed to the subsequent occipital contact with the ground, which can be assumed to be a result of a secondary impact, from momentum transfer producing a kinematic pedestrian response. If one were to consider just the vertical velocity of falling, one might consider the impact scenario similar

to a crouched fall from standing, i.e., a slightly bent at waist translational velocity of 4.85 ± 1.33 m/s (Patton and McIntosh, 2017), though the degloving does suggest a more complex tangential component. If the head impact had been with a non-yielding part of the van, the fact that serious extra- and intracranial injury is absent would indicate an impact velocity to the front or rear of the head below 20 km/h (12 mph) (AL-Graitti et al., 2017). This is probably not the case here, since significant arm and soft tissue injuries were also reported. **Considering all these results in combination and comparing with other reported cases, the occipital region was probably impacted at velocity of between 4.17 and 9.72 m/s (15 and 35 km/h) (AL-Graitti et al., 2017).**

- **Case 5:** The victim was a pedestrian hit by a cyclist. Subsequent to a brief loss of consciousness, the victim had no recollection of the events prior to the accident. The right side of the head behind the ear impacted with the ground. A right posterior fossa epidural hematoma accumulated between the skull and dura, a consequence of skull fracture tearing an underlying blood vessel. This is frequently caused by a lateral force over the mastoid. Threshold velocity for impact related fracture data is of the order of 5 m/s (Gurdjian and Lissner, 1947; McIntosh et al., 1996; Yoganandan and Pintar, 2004). **As such, the impact is assumed to be on the right side of the head behind the ear at a velocity of 5 m/s.**
- **Case 6:** The victim was a pedestrian hit by a car traveling at approximately 30 mph. The right orbital/frontal region was impacted and fractured. This was followed by a loss of consciousness at the scene for at least 5 min. Fracture tolerance data does not exist for the facial fractures in evidence in this case. The mechanism of fracture is often associated with a “blow out,” a sudden increase in pressure in the orbit of the eye. This is attributed to an impact or impactor, which is larger than the orbital rim. The bones of the orbit are very fragile and no reliable fracture tolerance data exists. Whilst the fracture tolerance of the orbital rim is unknown, the frontal bone is the strongest bone of the face/head and since no fracture has occurred in this area, this suggests that a sub fracture level of loading has occurred. Force to the face is associated in the literature, assuming a head mass of 6.82 kg (15 lb) and an acceleration of 80 g [easily obtainable in a 13.4 m/s (30 mph) impact], with 5.35 kN (1,200 lbf), which exceeds the fracture limit of most of the facial bones (Pappachan and Alexander, 2012). The fracture tolerance of the frontal bones is in the order of 3.57–7.13 kN (800–1,600 lbf) corresponding to minimum impact velocities in the order of 8.9–17.88 m/s (20–40 mph) (Pappachan and Alexander, 2012). Thus, an absence of frontal bone fracture suggests impact velocities below this level. Since significantly lower average strength has been found for the female bone structure during impact experiments, the lowest values are considered. **As a consequence, an impact on the right orbital/frontal region at a velocity of 9 m/s is assumed.**
- **Case 7** The victim fell from a 3-story roof. The left temporal and frontal regions are reported to have made contact with the ground and a right wrist fracture, cervical and thoracic transverse spinous process fractures were also observed. The hand fracture, multiple rib and transverse process fractures suggest an impact to the back or side of the torso (no details provided about location), and a sacrifice related injury to the hand. As a result of a lack of detail, one can assume a superficial contact to the front/side of the head. That these injuries are as superficial as they are, given that cervical and thoracic transverse process fractures are in evidence, suggests that either the head made contact with a pliant surface, such as sand or soil, or that the significant impact energy was dissipated during an impact with the right hand and subsequently the side or back. The fall height can be assumed to be approximately 8.3 m (height to the gutter of a 3-story house), plus the height of the gutter approximately 0.1 m, plus the assumed standing height of the accident victim, assumed 50th percentile male = 1.76 m, minus the 0.1 m distance from the top of the head to the likely point of contact around the “hat brim region.” Therefore, a minimum fall height of 10.1 m is assumed, since again by default, the assumption is that the male was standing at the lower edge of the roof. Therefore, a simple fall with no initial velocity is assumed and no arc or rotation considered, with a height of 10.1 m producing an impact velocity of 14.1 m/s. **This analysis demonstrates that an impact to the left temporal and frontal region at a peak velocity of 14.1 m/s could have occurred, however, a lower velocity could be expected.**
- **Case 8:** The victim was charged by a bull running out of a cattle truck and thrown backwards against a metal fence and onto concrete, impacting his head, (occiput mainly), rendering him unconscious for a few minutes. Reverse engineering of a bull’s velocity from the account provided, would require an appreciation of the bull’s acceleration and velocity at the point of contact, which is not possible here. However, it is reasonable to assume that the victim’s secondary impact velocity had to be at least as great as a simple fall backwards from standing, i.e., a straight body translational from standing velocity of 6.75 ± 0.27 m/s (Patton and McIntosh, 2017). Since there are facial fractures in evidence, and that the fracture tolerance of the frontal bones is 3.57–7.13 kN (800–1,600 lbf), corresponding minimum impact velocities are of the order of 8.94–17.88 m/s (20–40 mph) (Pappachan and Alexander, 2012). **As a consequence, an impact velocity at the occiput between 6.75 and 8.94 m/s is assumed.**
- **Case 9:** The victim was a cyclist knocked off a bicycle and reported to have landed on his head, such that his left parietal region made contact with the ground. This was accompanied by a left shoulder injury and multiple skin abrasions. Bitemporal contusions, traumatic subarachnoid hemorrhage and frontal and left parietal fractures were reported. A similar case was simulated and reported in

the literature (Fahlstedt et al., 2012) with a resultant linear velocity of 5.3 m/s and a vertical velocity between 4 and 5.4 m/s. **As a consequence, an impact velocity of between 4 and 5.4 m/s on the left parietal region is assumed here.**

While some of these estimations are probably relatively accurate, an important proportion of these are extremely difficult to evaluate, due to an insufficiency of detail, and may be subject to very large variations. Those (e.g., case 7) were left anyway for the sake of discussion.

2.2. Mechanistic Simulations

The mechanistic simulations consisted of a FEHM submitted to different loading scenarios defined by predefined sets of impact boundary conditions. For each simulation, a mechanistic criterion was defined by the maximum shear energy rate each gray matter element of the head model experiences throughout the duration of the impact. This simulation was repeated with a range of loading scenarios to provide a library of pre-calculated damages.

2.2.1. Finite Element Head Model

The FEHM is adapted from a previous version proposed earlier by Garcia-Gonzalez et al. (2018b), where it was validated for cranial impacts. It accounts for the gray matter, white matter with axonal anisotropy captured from diffusion tensor imaging (DTI), cerebrospinal fluid (CSF), skull, falx, scalp, and ventricles and consists of 2,354,594 tetrahedral elements. For each simulation, the boundary conditions were specified as described below, and a dynamic explicit simulation was run for 8 ms on Abaqus (ABAQUS Inc.). The mechanical behavior of each skull and gray matter element was tracked throughout each simulation. The von Mises stress was calculated in the skull elements and the shear energy rate was calculated in the gray matter elements. The maximum value experienced by each element throughout each simulation was recorded. A total of 445 simulations was run, of which 407 did not result in a fractured skull (see section 2.2.4).

One important assumption of this model is that only the inertia of the head contributes to the impact, and the rest of the body is left unmodeled. While this assumption has implications on the evaluation of the brain damage, the additional modeling of the body would be hampered by a lack of paramedical information. As such, this assumption is kept as a first approximation. Moreover, it is worth emphasizing that, under this assumption, the FEHM was validated against experimental data by means of acceleration-time curves for three impact conditions representative of real accidents and falls (see Garcia-Gonzalez et al., 2017 for more details): fall of a person from a bed; bike accident reconstruction; and experimental impact of human heads from cadavers against a rigid plate.

2.2.2. Material Models

The constitutive framework originally developed by Garcia-Gonzalez et al. (2018a), and further extended for blast TBI simulations by Garcia-Gonzalez et al. (2018b), is taken as a

basis. In this regard, the mechanical response of each tissue is decomposed into volumetric and shear components, leading to the definition of the Cauchy stress tensor as:

$$\boldsymbol{\sigma} = \boldsymbol{\sigma}_{vol} + \boldsymbol{\sigma}_{iso} \quad (1)$$

where $\boldsymbol{\sigma}_{vol}$ and $\boldsymbol{\sigma}_{iso}$ are the volumetric and isochoric Cauchy stress tensor components, respectively. This decomposition is also adopted to describe the total deformation gradient \mathbf{F} as:

$$\mathbf{F} = J^{1/3} \mathbf{F}^* \quad (2)$$

where $J = \det(\mathbf{F})$ is the Jacobian and \mathbf{F}^* is the distortional part of the deformation gradient.

In this work, the skull, falx, CSF, and ventricles are modeled as proposed by Garcia-Gonzalez et al. (2017) for similar impact conditions: skull and falx as elasto-plastic materials with their corresponding material properties at the mean strain rate observed in the impact conditions tested ($\approx 1 \text{ s}^{-1}$); CSF and ventricles by the Mie-Grüneisen equation of state and a dynamic viscosity. Regarding the scalp, white and gray matter, these tissues are modeled by Garcia-Gonzalez et al. (2018b) by more sophisticated approaches based on hyperelastic theories to accurately describe nonlinearities. While the scalp tissue is defined in the exact same manner by a neo-Hookean model, the constitutive law for white and gray matter is modified to provide a more efficient solution for the specific impact simulations conducted here (the aforementioned work dealt with blast scenarios rather than head impact). The modified formulation for the total Cauchy stress contribution reads as:

$$\begin{aligned} \boldsymbol{\sigma} = & \frac{\mu_m}{J} \frac{1}{1 - \frac{I_1^* - 3}{j_m}} \text{dev}(\mathbf{B}^*) \\ & + \frac{2k_1}{J} (I_4^* - 1) \exp \left[k_2 (I_4^* - 1)^2 \right] \text{dev}(\mathbf{F}^* \mathbf{A}_o \mathbf{F}^{*T}) \\ & - \frac{K_o}{\Lambda_o + 1} \left[\left(\frac{\rho}{\rho_o} \right)^{\Lambda_o + 1} - 1 \right] \mathbf{I} \end{aligned} \quad (3)$$

where $\mathbf{B}^* = \mathbf{F}^* \mathbf{F}^{*T}$, $I_1^* = \text{tr}(\mathbf{F}^{*T} \mathbf{F}^*)$, $I_4^* = \text{tr}(\mathbf{A}_o \mathbf{F}^{*T} \mathbf{F}^*)$, \mathbf{A}_o is the structural tensor providing axonal orientation within the white matter (see Garcia-Gonzalez et al., 2018b for more details), ρ is the current density and \mathbf{I} is the second order unit tensor. Moreover, μ_m , j_m , k_1 , k_2 , K_o , Λ_o , and ρ_o are material parameters, whose values are provided for white and gray matter in Tables 2, 3. The calibration of the isochoric response of both white and gray matter was consistently performed accounting for the mean strain rate observed in the simulations. Note that this formulation, for the strain rate conditions observed in the simulations, is equivalent to the full original formulation published by Garcia-Gonzalez et al. (2018b).

2.2.3. Impact Boundary Conditions

Simulations were defined by a set of inputs for velocity, location of incidence, angle of incidence, and impactor geometry. The

TABLE 2 | Constitutive parameters for white matter used in the simulations.

Volumetric response			
ρ_o (kg/m ³)	K_o (GPa)	Λ_o (–)	
1,140	2.19	6.15	
Isochoric response			
μ_m (kPa)	j_m (–)	k_1 (kPa)	k_2 (kPa)
550	1.1	2.14	0

TABLE 3 | Constitutive parameters for gray matter used in the simulations.

Volumetric response			
ρ_o (kg/m ³)	K_o (GPa)	Λ_o (—)	
1,140	2.19	6.15	
Isochoric response			
μ_m (kPa)	j_m (—)	k_1 (kPa)	k_2 (kPa)
450	1.4	—	—

TABLE 4 | Impact boundary conditions.

Boundary condition feature	Range
Velocity	1 m/s < V < 16 m/s
Locations of impact	(a) lateral fronto-parietal (b) fronto-polar (c) vertex (d) occipital (e) temporal
Angle of impact (from perpendicular)	–45° < θ < 45°
Indenter geometry	(i) blunt corner (ii) round (iii) flat (iv) sharp corner

range of these boundary conditions were chosen so as to encompass the vast majority of impact cases, while avoiding velocities either *a priori* too small or too high to avoid extreme cases, e.g., no trauma or death on impact (see **Table 4**). All impactors were modeled as rigid, with a friction coefficient of 0.4 (Garcia-Gonzalez et al., 2017). For the “round” impactor, a cylindrical shape with a radius of curvature of 3.6 cm was used, while the “blunt corner” impactor was made of a right angle analytical surface smoothed along the edge with a 1 cm radius of curvature quarter of a cylinder, and the “sharp corner” impactor was made of an right angle smoothed with an edge of 0.3 cm. This determined the range of inputs for the library of pre-calculated FEHM simulations (see **Figure 2**).

2.2.4. Mechanical Damage

All cases which resulted in a fractured skull were removed from the database. The skull was assumed to be fractured if more than 4% of all skull elements in the head model (4% corresponds to the percentage of skull elements spanning the maximum thickness of the skull) underwent a maximum von Mises stress exceeding the ultimate strength of bone (92.72 MPa; Wood, 1971).

A binary mask of the DMN mask was created by thresholding the template DMN mask from Smith and Nichols (2009) at a z-score of 3.1 (corresponding to a *p*-value of 0.05) and binarizing the resulting spatial map. The coordinate system of the finite element mesh was aligned with that of the fMRI images. The binary mask of the DMN (see section 2.1.4) was applied and all mesh nodes with coordinates within the DMN mask were extracted. Finally, all elements connected to these nodes were extracted to provide a DMN element set, and hence a mapping from the MRI domain to the element mesh. Damage to each gray matter element was determined by a material damage criterion. Previous studies of blast induced TBI suggested that a shear energy rate damage criterion of 100 MJ/m³s in the gray matter provides a good correspondence to regions with oxidative stress in rat brains (Garcia-Gonzalez et al., 2018b). As both loading conditions and damage pathways are different (blast injuries and impact injuries have very different injury signatures), other thresholds were evaluated to match the functional criterion (see section 3). A final value of ≈ 1 MJ/m³s was eventually chosen maximizing the correlation between mechanical and functional criteria. **Figure 3** shows the isosurface of the damaged region of the brain for a blunt corner impact, perpendicular velocity of 8 m/s, lateral fronto-parietal location at 1.6 ms after initial contact (note that this case resulted in a damage of 50.22% to the DMN).

For each simulation in which the skull was not fractured, when the shear energy rate exceeded this criterion during the simulation, the element was assumed to be damaged. The percentage of damaged elements in the DMN was then calculated. This provided a library of pre-calculated loading scenarios on which the ML model could be trained and evaluated.

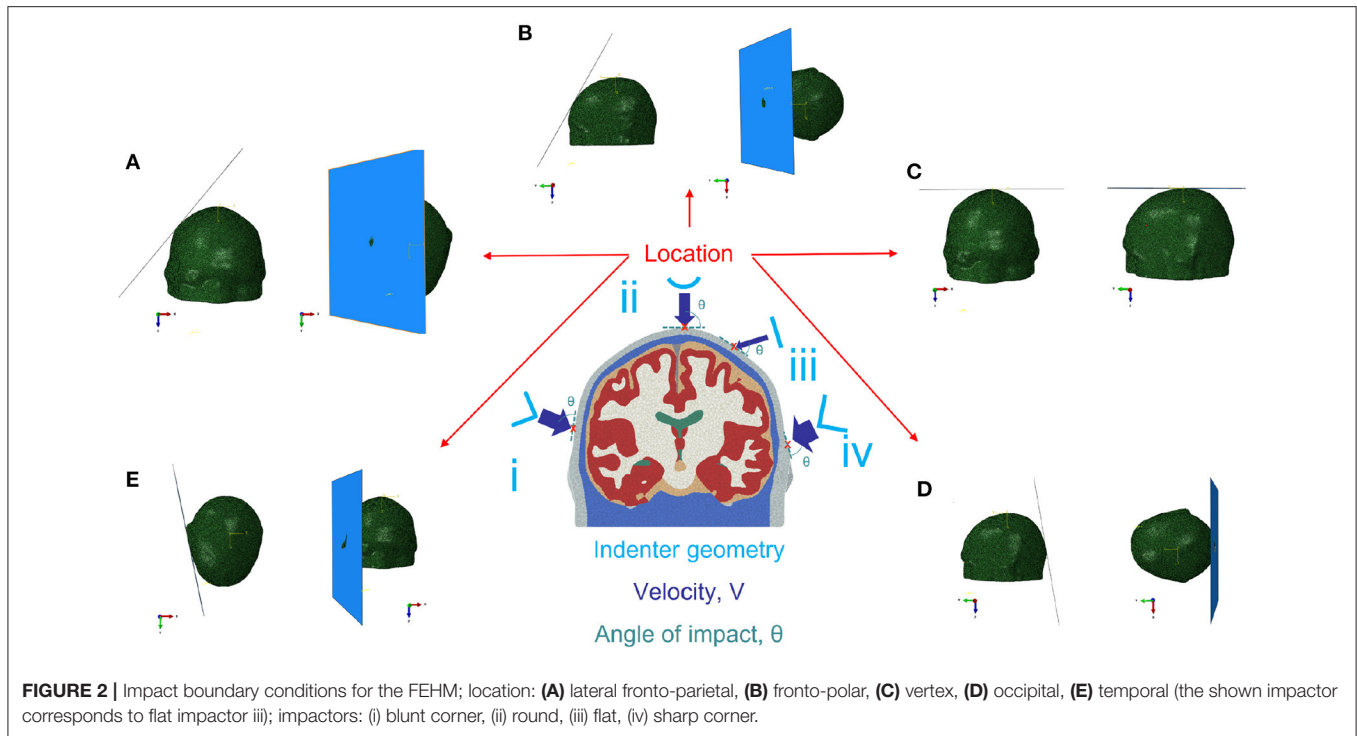
2.3. Machine Learning Layer

A ML layer was created to avoid the need to reproduce the FEHM simulations for each single scenario. To this end, the model was trained with 407 FEHM simulations for a range of combinations listed in **Table 4**. The overall approach and validation is explained below (see **Figure 4**).

2.3.1. Machine Learning Algorithm

A ML layer was trained on binary outcome data to predict the probability that the extent of network damage exceeds a given threshold during an impact. In order to do this, a separate model was trained for each proposed threshold of network damage. The inputs used in the layer correspond to the inputs defined in section 2.2.3. Note that the shape of the impactor was represented by the radius of curvature of the impactor (the flat one was given a radius of 1 m). From these inputs and the FEHM, two additional features were extracted to be included in the ML layer inputs: distance from the point of impact to the closest element of the DMN; and angle between trajectory to the closest DMN node and trajectory of impact. To define the binary outcome, the DMN was considered damaged if the percentage of damaged gray matter elements exceeded the given network damage threshold.

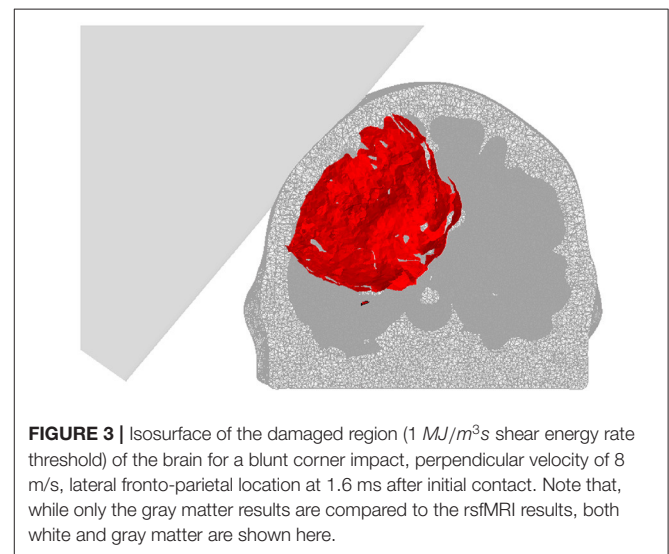
The predictive ability of two ML approaches were compared in this paper. Logistic regression (Pregibon et al., 1981) was compared to a bagging ensemble method (Breiman, 1996). Although several other algorithms have been used to analyze



TBI-related data (Siddiqui et al., 2015; Mitra et al., 2016; Minaee et al., 2019), logistic regression has previously been shown to outperform more complex models in TBI clinical outcome prediction (Steyerberg et al., 2008). The bagging method involves training a model with each of the following ML techniques: logistic regression (Pregibon et al., 1981), gaussian discriminant analysis (Fisher, 1936), k-nearest neighbor (Cover and Hart, 1967), Naïve Bayes classifier (Hand and Yu, 2001), and support vector machines (Boser et al., 1992). Given a test point, the ensemble method calculates the mean probability of damage from each of these trained models. This approach reduces the risk of incorrect classification and has been shown to outperform single algorithms (Dietterich, 2000).

A greedy forward feature selection approach was used to select statistically relevant input variables for each model; all other variables were excluded from the model. This was implemented with 5-fold cross validation and a fast algorithm (logistic regression) to reduce computational costs (Zhang, 2009). Feature selection was performed for each model independently. This resulted in a range of input variable sets dependent on the network damage threshold considered in each model.

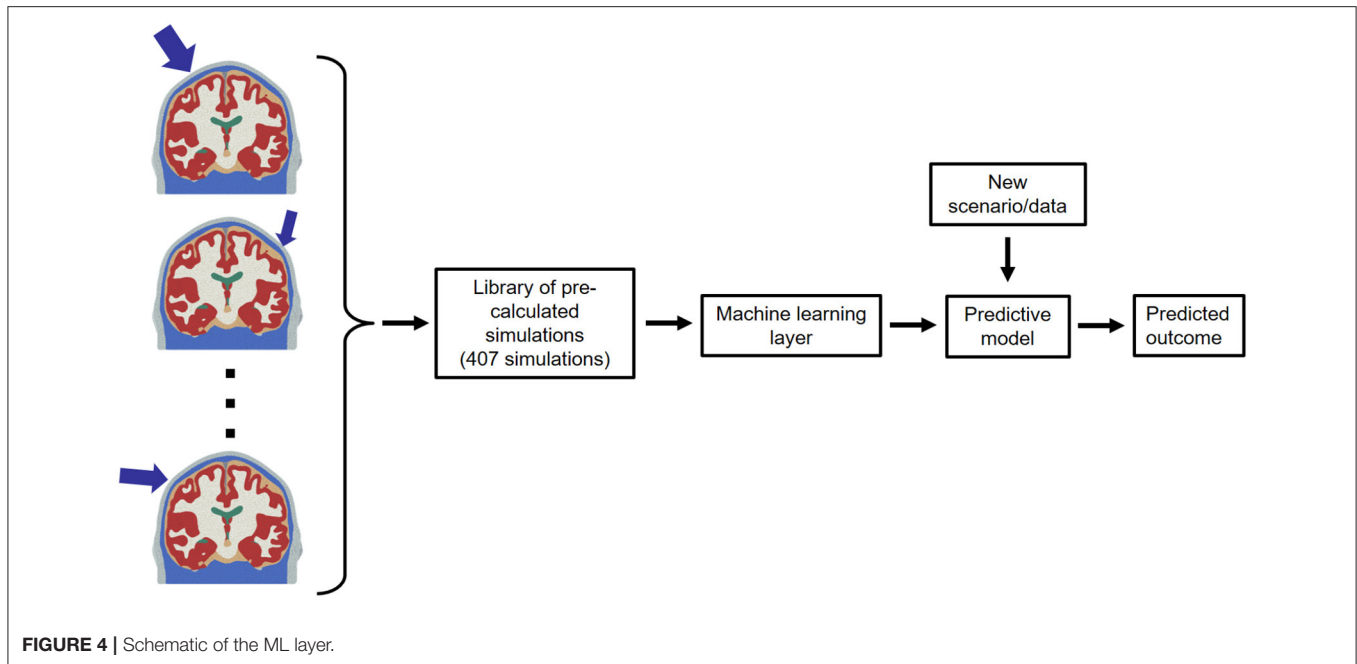
In order to validate the ML pipeline and ensure robustness, the network damage threshold was set to a range of values (10, 30, 50, 70, 90%), and the model performance was assessed for each threshold. Performance was evaluated by leave-one-out validation (Wong, 2015). The area under the curve (AUC), sensitivity, and specificity were calculated for each model. When validating the model against the dummy and clinical datasets, the network damage threshold was set to the FEHM estimated network damage, and the clinically estimated network damage, respectively. This allowed the ML layer to predict the



probability that at least the given proportion of the network was damaged.

Given the trained model and model inputs from nine clinical cases, the probability that mechanical damage exceeded the FEHM network damage estimation was predicted. In seven of the nine cases, there was a degree of uncertainty in the accident reconstruction, resulting in a range of mechanical damage predictions.

Finally, the ML models were used to predict the velocity at which the proportion of network damage is reached. For this



analysis, the input velocity of each scenario was varied between 1 and 15 m/s whilst all other inputs remained constant. The predicted probability of reaching the network damage proportion was calculated for each velocity. This was plotted on a graph of probability against velocity. Because the ML model predicts only the probability that *at least* a given proportion of the DMN is damaged, the velocity at which the DMN is damaged by *exactly* this proportion can be understood as the velocity at which this plateau is *first* reached. This is assumed to be at $\approx 95\%$ of the final plateau region.

2.3.2. Dummy Validation

A series of experiments were carried out to simulate real-world accident scenarios to illustrate the comparison between direct FEHM and ML predictions of mechanical damage. These experiments provide a range of realistic inputs to the models.

The experiments involved a dummy falling down a set of stairs in a range of motions: forwards and backwards. Each fall was captured with video and motion capture software in Audiomotion Studios (Oxford, UK). The motion capture enabled accurate measurement of the velocity of impact, whilst video footage provided the location and angle of head impact and the impactor geometry. The dummy used in these experiments weighed 65 kg and was approximately 1.7 m tall, whilst the full height of the staircase was 2.07 m.

From these experiments, two scenarios were extracted, one fall forwards and one backwards, see **Supplementary Videos 1, 2**, respectively. In each of these scenarios, the stairs were the first point of contact for the head. In the forward fall, the head of the dummy impacted the (blunt) corner of the stairs in the fronto-polar region with a perpendicular impact velocity of 7.12 m/s. In the backwards fall the occipital region impacted the corner of the stairs with a perpendicular velocity of 7.69 m/s.

The FEHM, which simulated the impact, and the ML model were both used to predict damage to the DMN. These damage estimates were carried out independently from one another and the FEHM results were not used to train the ML layer. These damage estimates provided a means of comparing the FEHM outputs to those of the ML layer in a scenario used by the police and medico-legal community.

3. RESULTS

3.1. DMN Functional Damage

The DMN resting brain network was successfully identified from MRI scans conducted in the hyper-acute phase through dual regression in each of nine TBI patients and all 18 healthy controls. The “disconnectivity” within the DMN, i.e., the proposed functional damage parameter, varied substantially across the nine patients (see **Figure 5**), ranging from 1.5 to 19.4% (see **Table 5**).

3.2. Numerical Model Performance

3.2.1. Machine Learning Layer Performance

Tables 6, 7 provide a comparison of model performance when implementing a bagging ensemble method and logistic regression, respectively. These models were validated over a range of network damaged proportion thresholds. All models provide good discrimination, with AUC values consistently >0.975 across all damage thresholds. The bagging method outperformed the use of logistic regression alone. The average AUC across all network damaged proportion thresholds was 0.985 for the bagging method, and 0.981 for logistic regression.

Dataset balance identifies the proportion of simulations which resulted in damage to the brain’s network. In most metrics, results were unbiased by the dataset balance, with AUC and Brier’s scores remaining relatively constant. However, the dataset balance had

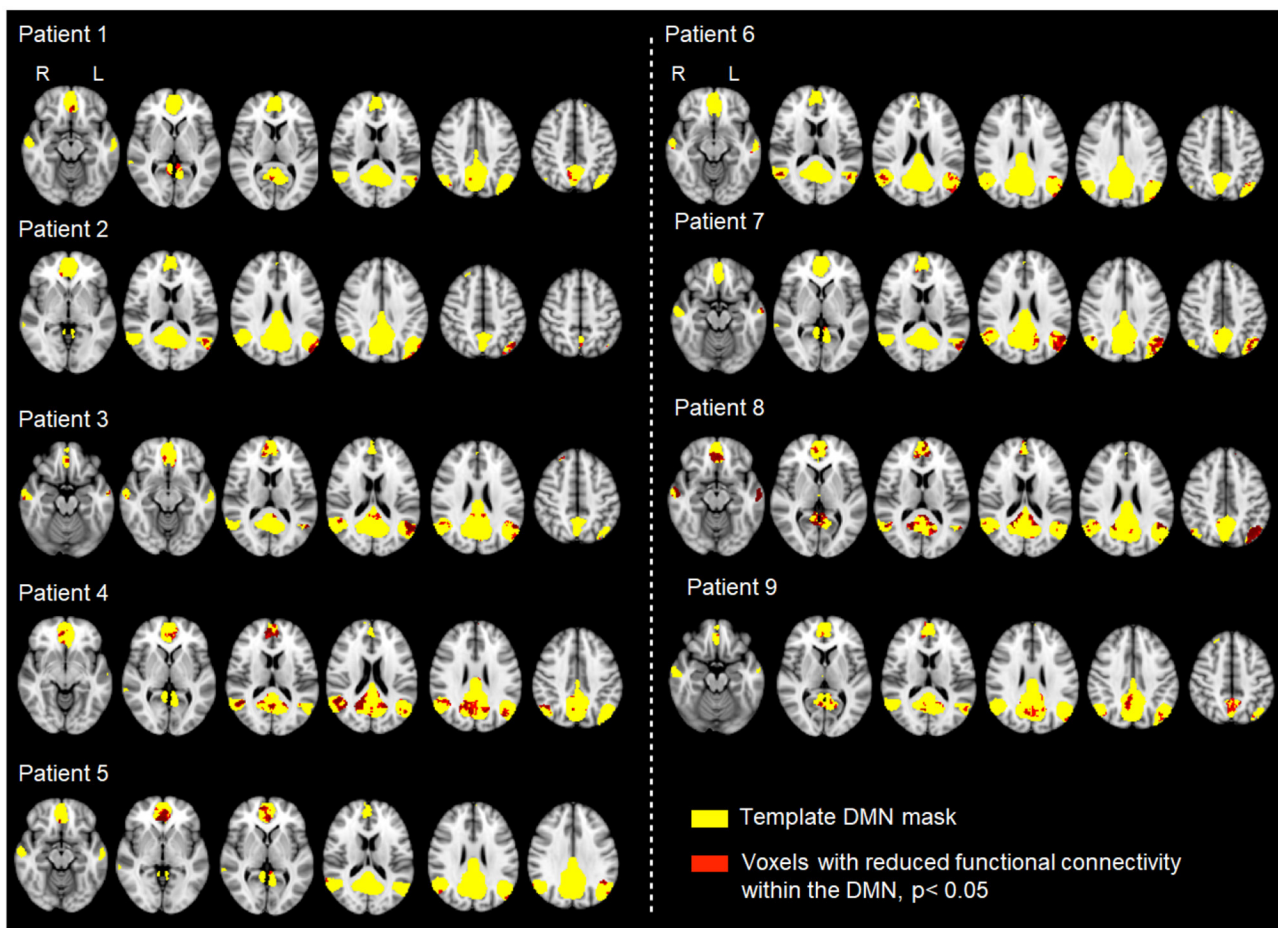


FIGURE 5 | Analysis of functional connectivity (rsfMRI signal correlation) within the DMN across nine patients with varying degrees of TBI and different mechanisms of injury. Individual patient resting data were compared to 18 controls using permutation testing. Each map shows the patient-specific threshold-free cluster-enhancement t-statistic images, depicting all voxels with significantly lower functional connectivity ($p < 0.05$) than the corresponding values in healthy controls.

TABLE 5 | Proportion of functional damage in the DMN as evaluated from functional correlation disruption.

Cases	1	2	3	4	5	6	7	8	9
Damaged DMN (%)	1.48	3.2	5.17	14.67	4	2.53	8.93	19.43	6.17

an impact on the model's sensitivity, its ability to predict the cases that resulted in damage to the DMN. On average, the bagging method provided improved AUC to that of logistic regression, and was thus used subsequently.

3.2.2. Dummy Validation

In the two dummy fall scenarios, damage to the DMN was predicted by both full FEHM simulations and the ML model. **Table 8** shows the resulting damage and velocity predictions from these two approaches. The predictions of 64.1 and 24.9% are the proportions of elements in the DMN region having reached the threshold of shear energy rate of $1\text{MJ}/\text{m}^3\text{s}$ in the direct FEHM simulations

TABLE 6 | Bagging method performance for a range of network damaged proportion thresholds.

	DMN damaged proportion threshold (%)				
	10	30	50	70	90
AUC	0.987	0.986	0.986	0.989	0.976
Brier's score	0.052	0.046	0.034	0.027	0.030
Sensitivity	0.752	0.702	0.790	0.829	0.731
Specificity	0.983	0.988	0.988	0.981	0.976
Accuracy	0.921	0.958	0.958	0.966	0.961
Dataset balance	0.268	0.206	0.1523	0.101	0.064

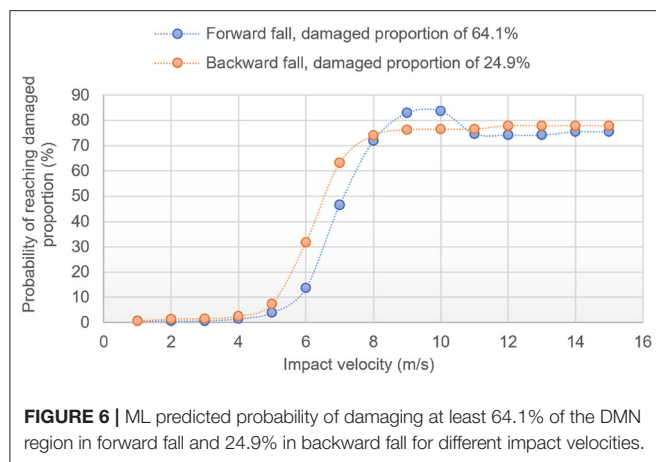
for the forward and backward impacts, respectively. The ML probabilities correspond to the predicted probability that the two impact scenarios would lead to, at least, those proportions, i.e., the ML layer predicts that there is 50.6 and 72.7% of chance that the impact damages at least 64.1 and

TABLE 7 | Logistic regression method performance for a range of network damaged proportion thresholds.

	DMN damaged proportion threshold (%)				
	10	30	50	70	90
AUC	0.979	0.981	0.978	0.988	0.979
Brier's score	0.056	0.048	0.034	0.027	0.028
Sensitivity	0.817	0.762	0.823	0.829	0.615
Specificity	0.956	0.966	0.986	0.986	0.987
Accuracy	0.919	0.924	0.961	0.971	0.963
Dataset balance	0.268	0.206	0.1523	0.101	0.064

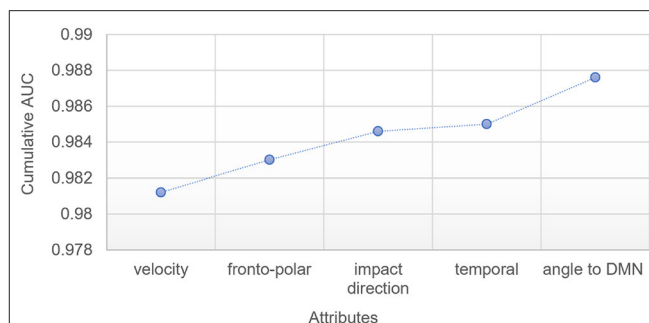
TABLE 8 | A comparison of FEHM and ML mechanical damage prediction for two dummy fall scenarios: "FEHM prediction" is the proportion of the DMN region damaged according to the finite element simulation, "ML probability" is the ML-predicted probability that "at least that much DMN region is damaged," "ML velocity" is the ML-predicted velocity at which there is 95% chance that the FEHM-predicted damaged proportion is reached.

Fall motion (impact velocity)	FEHM prediction (%)	ML probability (%)	ML velocity (m/s)
Forwards (7.12 m/s)	64.1	50.6	≈8.6
Backwards (7.69 m/s)	24.9	72.7	≈7.9



24.9% of the DMN region, for the forward and backward impacts, respectively.

Figure 6 offers another way to use the ML model by showing the probabilities that these proportions are reached for a range of potential impact velocities, for both scenarios. Both curves are sigmoids with plateau regions of ≈83% (≈75% if considering the last portion of the plateau) and ≈76.5%. Assuming that the plateau is first reached at ≈95% of the plateau value, the ML model predicts that reaching 64.1 and 24.9% a damaged proportion would occur at ≈8.6 m/s (≈8 m/s if considering the last portion of the plateau) and ≈7.9 m/s for the forward and backward falls, respectively (see **Table 8**). In this graph, the sigmoid never reaches 100% probability. This is due to nature of

**FIGURE 7** | Improvement in ML model AUC with each additional attribute, for ML model trained at a 50% threshold.

the ML methods, which are unlikely to estimate 100% probability that the given network damage threshold has been reached.

While an overall good match is confirmed between the FEHM and the ML model in this "real life" scenario, it is worth emphasizing that, because of the nature of the sigmoid shapes, velocity predictions for a given proportion of damaged DMN are less subject to noise error than the probability predictions for a given impact velocity. Another point is that the ML layer is bound to struggle at high velocities/high proportions because of the smallest population of training data having such large damage; this explains why the sigmoid curves might oscillate in the upper plateau region.

3.3. In silico Model Prediction

3.3.1. Input Sensitivity

A feature selection algorithm was implemented to identify the most predictive model inputs. **Figure 7** highlights the improvement in model performance with each additional input when the model is trained at a 50% threshold. Velocity was selected as the most predictive attribute, providing an AUC of 0.985 when used alone to predict network damage. Whether the fronto-polar region was impacted, whether the impact was perpendicular to the head, and whether the temporal region was impacted, best improved the prediction in this order, with the angle between impact location to closest DMN node, and impact direction finally allowing the AUC to reach a value of ≈0.988.

3.3.2. Clinical Validation

In this section, the conditions established in section 2.1.5 were used as inputs for the ML model. The same methodology described in section 3.2.2 was used, but instead of taking as input the DMN damaged proportion as predicted from FEHM simulations, the proportion of damaged DMN calculated from the proposed functional criterion (see section 2.1.4) was used instead. **Table 9** shows the ML predicted probabilities that the clinically predicted damaged DMN proportion (see **Table 5**) was reached for the velocity ranges evaluated in section 2.1.5 for all nine patients.

As highlighted in section 2.3.2, the impact velocity prediction for a given damaged DMN proportion is prone to greater error than the damaged DMN proportion prediction for a given impact

TABLE 9 | Proportion of functional damage in the DMN as evaluated from correlation disruption, ML predicted probabilities that at least this proportion is reached for the manually estimated range of impact velocities, and ML predicted impact velocities at which 95% of the final plateau probability P_f is reached for the clinical DMN damaged proportion, for the nine patients (see section 2.1.5 and Figure 2).

Cases (conditions)	Functionally damaged DMN (%)	ML predicted probability (P) range for impact velocity (V) range evaluation	ML predicted velocity at 95% P_f (m/s)
1 (b-iii)	1.48	$5.2\% < P < 91.1\%$ (2.24 m/s $< V < 12$ m/s)	≈ 6
2 (d-iii)	3.2	$17.5\% < P < 70.7\%$ (4.85 m/s $< V < 6.75$ m/s)	≈ 7.5
3 (d-iii)	5.17	$6.0\% < P < 30.5\%$ (3.25 m/s $< V < 4.8$ m/s)	≈ 7.4
4 (d-iii)	14.67	$2.6\% < P < 97.0\%$ (3.52 m/s $< V < 9.72$ m/s)	≈ 7.1
5 (a-iii)	4	$P \approx 36.0\%$ ($V \approx 5$ m/s)	≈ 6.9
6 (b-iii)	2.53	$P \approx 95.3\%$ ($V \approx 9$ m/s)	≈ 5.9
7 (e-iii)	8.93	$P < 76.5\%$ ($V < 14.1$ m/s)	≈ 7
8 (d-iii)	19.43	$56.0\% < P < 77.0\%$ (6.75 m/s $< V < 8.94$ m/s)	≈ 7.9
9 (a-iii)	6.17	$18.0\% < P < 71.4\%$ (4 m/s $< V < 5.4$ m/s)	≈ 6.9

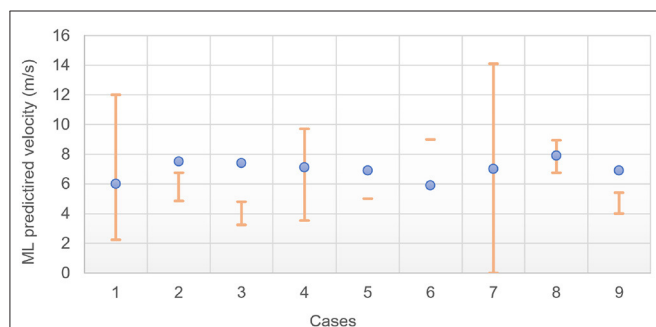


FIGURE 8 | ML predicted impact velocities at which 95% of the final plateau probability P_f is reached for the clinical DMN damaged proportion; orange bars are the velocity range estimates from the analysis of section 2.1.5.

velocity. In addition, the probability refers to the fact that *at least* a given proportion of DMN is damaged. As such, while case 1's results point toward a velocity of impact most likely to be toward the end of the range (12 m/s), it is not clear whether the probability of 91.1% for 12 m/s sits in the plateau region of the sigmoid, i.e., if a lower velocity would also reach such high proportion. To avoid this difficulty in the interpretation of the results, the sigmoid curves of the ML predicted probabilities of reaching the clinically evaluated damaged DMN against different impact velocities were plotted for all nine cases (not shown here).

For each one of them, the velocity at which 95% of the plateau probability is reached was extracted. This value corresponds to the velocity at which the clinically evaluated damaged DMN proportion is first reached according to the ML model. The results are compared against the “manually” estimated range of velocity of section 2.1.5 in Figure 8 and Table 9.

4. DISCUSSION

4.1. Model Limitations

4.1.1. Head Model Dependence

The FEHM used here was originally developed from high resolution anatomical T1 and T2-weighted MRI images of a subject available from the Human Connectome Project (HCP Subject ID: 100307) (Essen et al., 2013; Garcia-Gonzalez et al., 2018b). Ideally, one would use a dedicated FEHM for each individual to offer a more tailored solution to the damage prediction by accounting for morphological differences between patients. Because of the time it would take to develop such models (on-the-fly in the context of clinical admission), and despite some recent advances in this direction (Li et al., 2020), such a solution remains impractical. Additionally, due to the very nature of the ML layer, which first requires training on a library of FEHM simulations, doing so would not allow for ML prediction. It is also worth mentioning that having a morphologically correct head model scanned before injury for any TBI patient is unrealistic. An alternative would be to create a finite library of population-wide representative head morphologies, which would constitute one of the inputs of the ML layer. This would however require much larger libraries for the training of the layer, if one were to account for sex, age, etc. A direct comparison between three different head models has shown significant disparities in the brain mechanical response in nearly all brain regions of the models (with the caveat that these head models were all idealized and not constructed from imaging) (Ji et al., 2014). More recently, the study of more realistic head models for different morphologies has reached similar conclusions (Li et al., 2020). However, in the former study, the models showed similar trends in the relationship between mechanical response and kinematic response, indicating that a given model can be used independently of the others for a given set of impact conditions as long as it is used consistently. While not excluding the possibility to include more flexibility in the morphological variations between patients in some future work by using, e.g., novel morphing approaches (Li et al., 2020), the approach consisting of using only one model thus seems justified as a first approximation, while allowing for faster ML predictions.

Each FEHM requires a set of constitutive models for the different regions identified within the head (typically, gray and white matter, skull, CSF as a minimum). Those need to be chosen carefully depending on the level of detail (e.g., homogenized brain vs. independent white and gray matter) but also loading conditions. For instance, blast loading conditions would typically require equations of state to adequately capture the volumetric response under shock waves and the viscous-relaxation processes can *a priori* be ignored for very short time-scales (Moore et al., 2009), while slow loading scenarios, such as in the second stage of labor, when the head of the fetus

is being compressed in the vaginal canal, would ideally require viscoelastic laws to capture the fetal head molding of the infant head (Ami et al., 2019). Any intermediate situation, such as the ones considered here, would need to balance the need for time-dependent models against the timescales involved, along with other features more or less relevant depending on the leading deformation mechanisms: whether viscoelastic models are required, whether tissue damage and/or fracture should be accounted for, whether tissue anisotropy is relevant, etc. Here, a careful analysis of the most salient features was carried out, and each region of the used FEHM was assigned a constitutive model with parameters identified for the range of loading considered in this work. While more work is required to ensure that each chosen constitutive model and its associated material parameters are indeed optimum, the proposed setup is believed to constitute a first good approximation. It must finally be noted that as better models and material parameters are identified, the overall framework function remains the same and those new changes would be trivial to incorporate.

4.1.2. Kinematics

In the approach followed here, the kinematic behavior immediately after impact is assumed to be solely driven by the inertia of the head, i.e., the contribution of the rest of the body, and in particular, the neck is not accounted for. This approach has been proven to be deficient in some cases (Wang et al., 2020). While it could be argued that it could still be considered as valid in cases where the inertia of the body does not contribute to the impact (e.g., if one falls sideways, and/or is hit directly at the head), or when the neck does not hamper the movement of the head (e.g., during and immediately after the impact of an unaware or unconscious individual), it remains an inaccurate representation of the real-life impact. An ideal simulation would couple a multibody dynamics simulation to the proposed FEHM to ensure that the kinematic behavior of the head is more accurately modeled. It must, however, be emphasized that the more complex the underlying mechanistic model is, the more inputs a given ML layer would have to incorporate. Therefore, while having a set of impact conditions on the head, as done here, can easily be incorporated in the ML layer, incorporating inputs related to the entire body based on clinical information from the scene is realistically currently unworkable.

4.1.3. Skull Fracture

A final limitation of the FEHM is that, while the onset of skull fracture was predicted, its mechanical deformation post-fracture was not modeled. As such, the choice was made to train the ML layer exclusively on simulations which did not result in skull fracture. However, five out of the nine patients studied in this work experienced skull fracture (cases 1, 6, 7, 8, and 9), and, while those were not judged to be important enough to influence significantly the brain deformation in those cases (e.g., left zygoma fracture for case 1), it is clear that better predictions would be expected with additional fracture mechanistic features embedded in the FEHM for a more general applicability.

4.2. Predictive Accuracy

The ML layer has been shown to be very effective in the prediction of the simulation behavior (with AUC values all above 0.97 in the worst case), especially considering the reduced number of simulation scenarios. This prediction could be enough for some preliminary clinical assessment. An eventual high-fidelity ML prediction with additional inputs could be leading to some overfitting, owing to the relatively general nature of the mechanistic model. The proposed approach is a trade-off between the descriptive power of the simulation and the granularity of the ML predictions. According to this, the number of features and the feature selection procedure are tailored to the overall complexity of the ML tasks (in number of instances and features). As seen in section 3.3.1, a single feature already provides a reasonable high accuracy level. Additionally, the characteristics of the data also constrain the use of a given ML algorithm. More advanced techniques, such as neural networks (e.g., deep learning as an extreme case) are designed for two or more higher orders of magnitude in the number of simulations to analyze.

Another interesting aspect is the stability of the results independently of the DMN damage proportion threshold (see **Tables 6, 7**). Indeed, from 10% threshold up to 90% threshold, there is a $\times 4$ factor in the ratio of the minority class (0.064–0.268 for 90 and 10%, respectively). In all cases, neither the AUC nor the sensitivity or the specificity are compromised.

The stability of the sensitivity and specificity is of particular importance in the clinical setting. Sensitivity would be crucial to enable identification of network damage within the DMN in the acute or hyper acute phase following injury. Specificity would allow clinicians to rule out the possibility of injury enabling decisions regarding discontinuation of neuro protective interventions. **Tables 6, 7** show that the specificity consistently performs higher than the sensitivity for both models. Future ML models could be tuned to ensure that the specificity is not maximized at the expense of the sensitivity.

In the future, both the mechanistic simulations and the ML layer should become more detailed. This also means that the number of required simulations should become larger but also the number of descriptive features (now constrained to the primary characteristics: velocity, location, and angle). In addition, other derived indicators shall be obtained and other topological and spatial considerations shall be included.

4.3. Clinical Data

One of the main limitations of this work is the relative scarcity of clinical data. However, the data were acquired within the first 24 h of head trauma, including severe injuries. This quick-paced availability requires a specialist center, able to acquire data in patients who are ventilated and intubated. For logistical reasons such data are therefore exceptionally difficult to acquire in large volumes. While our sample size is limited for this reason, the type of data presented here is precisely what is required to make realistic predictions in a clinically meaningful (“hyper-acute”) time period. As such, balancing data quality and data quantity was a necessary challenge in this work. By providing here a novel framework with proactively gathered (albeit limited) data,

the goal of this work is to emphasize the need for established widespread protocols for data curation in a proactive model driven fashion, as opposed to models making use of limited data available after their independent retrieval, usually from much later time-periods after injury, and likely brain recovery processes, have occurred.

It is finally worth emphasizing that our patients were followed for 6–9 months, which could offer further development to the model predictions in future work.

4.4. Resting State Network Relevance for TBI Prediction

Despite advances in the care of patients suffering TBI, long-term clinical and neuropsychological outcomes are often poor, irrespective of apparent injury severity (Brooks et al., 2013; Stocchetti and Zanier, 2016). MRI studies performed in the days, weeks, and months following TBI have uncovered a crucial role played by diffuse axonal injury (DAI) in the long term clinical, functional and neuropsychological outcome (Tong et al., 2004; Li and Feng, 2009; Skandsen et al., 2010). Midline structures, including the corpus callosum and cingulum bundle are particularly susceptible to the shearing forces causing DAI (Yount et al., 2002; Chan et al., 2003). Since high level cognitive functions such as memory, attention and executive function require the integration of information processing across spatially distinct brain regions, it has been proposed that DAI induces cognitive impairment by disconnecting distributed brain networks (Inglese et al., 2005; Niogi et al., 2008; Kinnunen et al., 2010; Bonnelle et al., 2011).

rsfMRI is not, *per se*, optimum to measure functional activity, given that one cannot be certain of what function is being measured (this applies especially in the context of the DMN, which “shuts off” during tasks). However, this remains to date the only method available for use in severely head injured patients, many of whom were intubated and ventilated during scanning. rsfMRI allows measurement of slow neuronal signal fluctuations without the need for a task, enabling the study of functionally relevant brain networks in TBI patients regardless of the severity of injury. In this way, the use of rsfMRI enabled us to measure functional brain networks in patients among our cohort who were intubated and ventilated during MRI scanning. Among brain networks known to be disrupted following TBI (Stevens et al., 2012), the DMN has received particular interest due to its proposed role in the development of attentional deficits (Raichle, 2010; Bonnelle et al., 2011; Sharp et al., 2011) which often follow DAI (Scheid et al., 2003; Povlishock and Katz, 2005). The brain regions that make up the DMN (Raichle et al., 2001) are particularly susceptible to DAI, including notably the midline posterior cingulate cortex, precuneus, and ventromedial prefrontal cortex alongside the inferior parietal lobe, lateral temporal cortex, and hippocampal formation. Crucially, the regions of the DMN show highly correlated brain activity at rest.

Previous studies report differing DMN functional connectivity according to severity of injury and timing of imaging (Zhou et al., 2012; van der Horn et al., 2017). Here, we show that DMN disruption can be identified within the first 24 h following

trauma, using an objective statistical metric sensitive to network disruption at the single patient level. We propose that our damage load metric offers advantages over typical group-based studies in understanding and predicting the effects of trauma. Group-based or population average studies, by definition, aim to identify features that are common across patients. Such approaches consequently discard the fundamental heterogeneity in head injury mechanisms and their downstream network impact that likely account for vast differences in outcomes among individuals.

4.5. *In silico* TBI Prediction

4.5.1. Coupling of Causality and Correlation

Figure 7 shows the five more important attributes in the ML layer per increased order of contribution to the prediction of the layer when used at a 50% threshold. Unsurprisingly, the velocity of impact is the most important factor. Whether or not the impact location is in the fronto-polar region or the temporal region are the second and fourth most important attributes, with the third being whether the impact was perpendicular to the head. Finally, the angle between impact location to closest DMN node and impact direction allows for a slight increase in the predictive ability.

From a geometrical perspective with respect to the DMN nodes, an impact location in the fronto-polar should indeed *a priori* have a stronger influence on the DMN than a temporal impact. The relative importance of the angle to DMN (by 0.3%) is slightly more surprising, especially considering the fact that the binary attribute indicating whether the impact is perpendicular or not was already selected as the third most important attribute. This particular trait demonstrates the advantage to couple mechanistic simulations with ML. In this case, the mechanistic FEHM simulations incorporate indirectly information related to the angle between impact direction with respect to the closest DMN node. A ML layer on its own would not be able to incorporate information of this kind without additional preprocessing of the head morphologies and mechanical features of stress wave propagation with respect to impact direction. Such complementarity of causality (through the mechanistic simulations) and correlation (through the ML layer) has already been advocated as an ideal way to incorporate physical mechanisms in a scalable fashion (Baker et al., 2018). This work demonstrates that additional information driven by a mechanistic understanding of the physical processes at play during tissue damage can indeed allow for additional predictive power in the ML layer.

It is worth noticing that, for each given damaged DMN proportion, a new training session is needed. This means that, while **Figure 7** only shows the results for a 50% threshold, each new threshold, and thus each curve in **Figure 6**, will select a new set of attributes to work with. For two of the nine patients of this study, training did not use the angle to DMN but selected the fact that the impactor is or is not perpendicular (results not shown here). In all cases however, the velocity of impact was the main attribute followed by either the shape of the impactor or the angle to DMN.

Overall, this dynamic feature selection offers an individualized prediction of the impact on brain function based on a given head injury. These predictions shed light onto the nature and extent of likely associated tissue disruption in an individual patient that is not captured by current clinical assessments. In this way, models able to predict down-stream functional outcomes from early paraclinical metrics offer potential to optimize treatment at a time when crucial clinical decisions need to be made.

4.5.2. Predictive Performance

The method proposed here postulates a direct relationship between mechanical damage and functional damage. It can be used in two ways: (i) it can assess the probability that the DMN has been damaged to the extent measured clinically for a given impact, (ii) or it can predict a velocity at which such extent of damage can be reached, assuming one knows the remaining boundary condition attributes (impact location, angle, etc.). This approach was tested for nine patients whose impact conditions were estimated from paramedical and clinical notes in a manner consistent with medico-legal methodology.

The shear energy rate damage criterion was taken to be at $\approx 1 \text{ MJ/m}^3\text{s}$ (see section 2.2.4). The quantitative evaluation of DMN damage proposed here is a novel approach whose correlation with mechanical damage has never been attempted. Garcia-Gonzalez et al. (2018b) successfully observed a correlation with oxidative stress in the context of blast injury for a much larger value of the shear energy rate damage criterion, but as loading conditions and damage pathways are different (blast injuries and impact injuries have very different injury signatures), another value needed to be estimated. The proposed threshold of $\approx 1 \text{ MJ/m}^3\text{s}$ is interestingly close to the axonal deformation energy rate threshold of $1.5 \text{ MJ/m}^3\text{s}$ for oxidative stress in blasted white matter (Garcia-Gonzalez et al., 2018b). While white matter damage was not predicted here for lack of experimental comparison (rsfMRI measures gray matter activity), indirect damage of white matter might also directly influence the rsfMRI results, and the proposed model could be benchmarked in future work against DTI data to assess damage in the white matter tracts. This could also be done indirectly by measuring the correlation (or lack thereof) of the DMN with the rest of the brain. It is finally important to note that the results obtained here intrinsically depend on this threshold calibration. However, to confirm with sufficient significance that the value chosen here is indeed the right one, a much larger dataset of patients would be needed. Future work shall focus on gathering such data.

The two predictions made by the ML method are assessed in **Table 9** and **Figure 8**. Firstly, the model should be able to assess the probability that the DMN exceeds a given threshold. When the threshold of the model was set to the clinically observed network damage, an ideal model should provide a high probability that the network is damaged for the given scenario. In **Table 9**, seven out of nine cases produce a probability of damage over 70%, however some probabilities of damage range from small to large values, for example in cases 2 and 4. This reflects the difficulties faced in estimating the impact scenarios from parametric data, which often resulted in a large range of possible impact velocities.

The model also provides an estimate of the velocity at which the clinically observed network damage was met. As shown in **Table 9** and **Figure 8**, four out of nine patients' ML predicted velocity is within the range manually estimated. As indicated earlier, a few of these cases did not have enough information to allow for a confident estimation; very rough values were still proposed in the interest of discussion. All patients presented significant TBI and the model predicts that the range of velocity expected to lead to such TBI is much narrower than manually evaluated. In particular, values of impact velocity between 6 and 8 m/s for all nine patients are expected, while the manual estimation of the range was six-fold larger. Note, however, that different ML training designs could be used to better estimate velocities. In particular, a backward estimator (from the damage to the characteristics of the impact) could be used instead of the forward model proposed here (from the features to the predicted damage).

4.5.3. Forensic Relevance

Establishing whether a traumatic head injury is a result of an accidental or non-accidental cause is a fundamental question in forensic investigations. Often, practitioners are provided with only a brief third-party description of a causal event and struggle to establish a sufficiently detailed understanding of a cause and effect relationship with which to make a differentiation. Current medical understanding, acquired by training, anecdote, and experience is supplemented with scientific evidence, drawn from specialties such as pathology, radiology, and population-based epidemiology. The head and central nervous system may be injured by many different mechanisms; therefore, developing a necessary understanding of the cause from practical experience and epidemiology alone is a significant challenge, since there are very many biomechanical variables that require consideration.

A retrospective biomechanical engineering analysis can assist a forensic investigation by providing cause and effect understanding with regard to a stated or inferred injury-causing event. This can be undertaken by characterizing the biomechanical loading environment during the event in question, quantifying the physical loading conditions and evaluating their potential to produce injury by, where possible, drawing comparisons with injury tolerance and/or epidemiological data.

Given the wide range of velocities, locations, angles, and materials associated with head injury mechanics, it is unrealistic to anticipate that a single injury risk metric can exist for every possible scenario. Specific to the head, one primary reason is the very many different motions that can occur when a head is struck with an object, or when a head strikes a surface and/or is whiplashed, since the complex variety of potential responses makes each injury-causing event potentially unique.

General characterization of the biomechanical loading environment can, however, assist in developing a better understanding of the mechanisms of injury in question. In particular, the approach proposed here has a direct forensic value in the analysis of image based evidence, e.g., CCTV video footage, from which more accurate measures of velocity, location, and angle of impact might be obtained.

DATA AVAILABILITY STATEMENT

The datasets generated during and/or analyzed during the current study are not publicly available due to restrictions stipulated by the ethical approval for the study in order to protect patient confidentiality. The FEHM model used in this work is available on <http://jerugroup.eng.ox.ac.uk/fehm.html> and on the Oxford University Innovation Software Store <https://process.innovation.ox.ac.uk/software>. The ML pipeline is available under academic license on <http://jerugroup.eng.ox.ac.uk/mltbi.html> and on the Oxford University Innovation Software Store. Requests to access the datasets should be directed to antoine.jerusalem@eng.ox.ac.uk.

ETHICS STATEMENT

The studies involving human participants were reviewed and approved by South central—Berkshire Research Ethics Committee. The patients/participants provided their written informed consent to participate in this study.

AUTHOR CONTRIBUTIONS

AS, NV, DG-G, MJ, J-MP, and AJ wrote the article. TL and NV designed the clinical programme. TL produced the

clinical data. NV produced the functional clinical criterion and post-processed the clinical data. MJ produced the forensic analysis. DG-G produced the constitutive models. AS implemented the model and performed the simulations. J-MP and AJ designed the overall computational study. All authors contributed to the article and approved the submitted version.

FUNDING

AS, J-MP, and AJ acknowledge funding from the University of Oxford University Challenge Seed Fund. DG-G and AJ also acknowledge funding from the EPSRC Healthcare Technologies Challenge Award No. EP/N020987/1. Finally, TL acknowledge funding from the NIHR Oxford Biomedical Research Centre and NV, from the University of Oxford Wellcome Centre for Integrative Neuroimaging.

SUPPLEMENTARY MATERIAL

The Supplementary Material for this article can be found online at: <https://www.frontiersin.org/articles/10.3389/fbioe.2021.587082/full#supplementary-material>

REFERENCES

- AL-Graitti, A., Khalid, G., Berthelson, P., Mason-Jones, A., Prabhu, R., and Jones, M. (2017). Auto rickshaw impacts with pedestrians - a computational analysis of post-collision kinematics and injury mechanics. *Int. J. Biomed. Biol. Eng.* 11, 568–587.
- Ami, O., Maran, J. C., Gabor, P., Whitacre, E. B., Musset, D., Dubray, C., et al. (2019). Three-dimensional magnetic resonance imaging of fetal head molding and brain shape changes during the second stage of labor. *PLoS ONE* 14:e215721. doi: 10.1371/journal.pone.0215721
- Baker, R. E., Pea, J.-M., Jayamohan, J., and Jerusalem, A. (2018). Mechanistic models versus machine learning, a fight worth fighting for the biological community? *Biol. Lett.* 14:20170660. doi: 10.1098/rsbl.2017.0660
- Bonnelle, V., Leech, R., Kinnunen, K. M., Ham, T. E., Beckmann, C. F., De Boissezon, X., et al. (2011). Default mode network connectivity predicts sustained attention deficits after traumatic brain injury. *J. Neurosci.* 31, 13442–13451. doi: 10.1523/JNEUROSCI.1163-11.2011
- Boser, B. E., Guyon, I. M., and Vapnik, V. N. (1992). "A training algorithm for optimal margin classifiers," in *Proceedings of the Fifth Annual Workshop on Computational Learning Theory* (New York, NY), 144–152. doi: 10.1145/130385.130401
- Breiman, L. (1996). Bagging predictors. *Mach. Learn.* 24, 123–140. doi: 10.1007/BF00058655
- Brooks, J., Strauss, D., Shavelle, R., Paculdo, D., Hammond, F., and Harrison-Felix, C. (2013). Long-term disability and survival in traumatic brain injury: results from the national institute on disability and rehabilitation research model systems. *Arch. Phys. Med. Rehabil.* 94, 2203–2209. doi: 10.1016/j.apmr.2013.07.005
- Chan, J., Tsui, E., Peh, W., Fong, D., Fok, K., Leung, K., et al. (2003). Diffuse axonal injury: detection of changes in anisotropy of water diffusion by diffusion-weighted imaging. *Neuroradiology* 45, 34–38. doi: 10.1007/s00234-002-0891-y
- Cover, T., and Hart, P. (1967). Nearest neighbor pattern classification. *IEEE Trans. Inform. Theory* 13, 21–27. doi: 10.1109/TIT.1967.1053964
- Dietterich, T. G. (2000). *Ensemble Methods in Machine Learning*. Lecture Notes in Computer Science (including subseries Lecture Notes in Artificial Intelligence and Lecture Notes in Bioinformatics), Vol. 1857. Berlin; Heidelberg: Springer. doi: 10.1007/3-540-45014-9_1
- Dikmen, S. S., Corrigan, J. D., Levin, H. S., Machamer, J., Stiers, W., and Weisskopf, M. G. (2009). Cognitive outcome following traumatic brain injury. *J. Head Trauma Rehabil.* 24. doi: 10.1097/HTR.0b013e3181c133e9
- Dixit, P., and Liu, G. R. (2017). A review on recent development of finite element models for head injury simulations. *Arch. Comput. Methods Eng.* 24, 979–1031. doi: 10.1007/s11831-016-9196-x
- Essen, D. C. V., Smith, S. M., Barch, D. M., Behrens, T. E., Yacoub, E., and Ugurbil, K. (2013). The WU-minn human connectome project: an overview. *NeuroImage* 80, 62–79. doi: 10.1016/j.neuroimage.2013.05.041
- Fahlstedt, M., Halldin, P., Vander Sloten, J., Goffin, J., Depreitere, B., and Kleiven, S. (2012). "Influence of impact velocity and angle in a detailed reconstruction of a bicycle accident," in *IRCOBI Proceedings* (Dublin), 787–799.
- Fisher, R. A. (1936). The use of multiple measurements in taxonomic problems. *Ann. Eugen.* 7, 179–188. doi: 10.1111/j.1469-1809.1936.tb02137.x
- Fox, M. D., and Raichle, M. E. (2007). Spontaneous fluctuations in brain activity observed with functional magnetic resonance imaging. *Nat. Rev. Neurosci.* 8, 700–711. doi: 10.1038/nrn2201
- Garcia-Gonzalez, D., Jayamohan, J., Sotiropoulos, S., Yoon, S.-H., Cook, J., Siviour, C., et al. (2017). On the mechanical behaviour of PEEK and HA cranial implants under impact loading. *J. Mech. Behav. Biomed. Mater.* 69, 342–354. doi: 10.1016/j.jmbm.2017.01.012
- Garcia-Gonzalez, D., Jerusalem, A., Garzon-Hernandez, S., Zaera, R., and Arias, A. (2018a). A continuum mechanics constitutive framework for transverse isotropic soft tissues. *J. Mech. Phys. Solids* 112, 209–224. doi: 10.1016/j.jmps.2017.12.001
- Garcia-Gonzalez, D., Race, N. S., Voets, N. L., Jenkins, D. R., Sotiropoulos, S. N., Acosta, G., et al. (2018b). Cognition based bTBI mechanistic criteria: A tool for preventive and therapeutic innovations. *Sci. Rep.* 8:10273. doi: 10.1038/s41598-018-28271-7

- Gurdjian, E., and Lissner, H. (1947). Deformations of the skull in head injury as studied by the "stresscoat" technic. *Am. J. Surg.* 73, 269–281. doi: 10.1016/0002-9610(47)90321-8
- Hand, D. J., and Yu, K. (2001). Idiot's Bayes-not so stupid after all? *Int. Stat. Rev.* 69, 385–398. doi: 10.1111/j.1751-5823.2001.tb00465.x
- Inglese, M., Makani, S., Johnson, G., Cohen, B. A., Silver, J. A., Gonen, O., et al. (2005). Diffuse axonal injury in mild traumatic brain injury: a diffusion tensor imaging study. *J. Neurosurg.* 103, 298–303. doi: 10.3171/jns.2005.103.2.0298
- Ji, S., Ghadyani, H., Bolander, R. P., Beckwith, J. G., Ford, J. C., McAllister, T. W., et al. (2014). Parametric comparisons of intracranial mechanical responses from three validated finite element models of the human head. *Ann. Biomed. Eng.* 42, 11–24. doi: 10.1007/s10439-013-0907-2
- Khalili-Mahani, N., Zoethout, R. M., Beckmann, C. F., Baerends, E., de Kam, M. L., Soeter, R. P., et al. (2012). Effects of morphine and alcohol on functional brain connectivity during "resting state": a placebo-controlled crossover study in healthy young men. *Hum. Brain Mapp.* 33, 1003–1018. doi: 10.1002/hbm.21265
- Kinnunen, K. M., Greenwood, R., Powell, J. H., Leech, R., Hawkins, P. C., Bonnelle, V., et al. (2010). White matter damage and cognitive impairment after traumatic brain injury. *Brain* 134, 449–463. doi: 10.1093/brain/awq347
- Kondziella, D., Friberg, C. K., Frokjaer, V. G., Fabricius, M., and Möller, K. (2016). Preserved consciousness in vegetative and minimal conscious states: systematic review and meta-analysis. *J. Neurol. Neurosurg. Psychiatry* 87, 485–492. doi: 10.1136/jnnp-2015-310958
- Li, X., Zhou, Z., and Kleiven, S. (2020). An anatomically detailed and personalizable head injury model: significance of brain and white matter tract morphological variability on strain. *Biomech. Model. Mechanobiol.* 1–29. doi: 10.1007/s10237-020-01391-8
- Li, X.-Y., and Feng, D.-F. (2009). Diffuse axonal injury: Novel insights into detection and treatment. *J. Clin. Neurosci.* 16, 614–619. doi: 10.1016/j.jocn.2008.08.005
- Maas, A. I., Menon, D. K., Steyerberg, E. W., Citerio, G., Lecky, F., Manley, G. T., et al. (2015). Collaborative European neurotrauma effectiveness research in traumatic brain injury (CENTER-TBI): a prospective longitudinal observational study. *Neurosurgery* 76, 67–80. doi: 10.1227/NEU.0000000000000575
- Maas, A. I., Stocchetti, N., and Bullock, R. (2008). Moderate and severe traumatic brain injury in adults. *Lancet Neurol.* 7, 728–741. doi: 10.1016/S1474-4422(08)70164-9
- McIntosh, A., Svensson, N., Kallieris, D., Mattern, R., Krabbel, G., and Ikels, K. (1996). "Head impact tolerance in side impacts," in *Proceedings of the Fifteenth International Technical Conference on the Enhanced Safety of Vehicles*, Vol. 2 (Melbourne), 1273–1280.
- Menon, D., and Harrison, D. (2008). Prognostic modelling in traumatic brain injury. *BMJ* 336, 397–398. doi: 10.1136/bmj.39461.616991.80
- Minaee, S., Wang, Y., Aygar, A., Chung, S., Wang, X., Lui, Y. W., et al. (2019). MTBI identification from diffusion MR images using bag of adversarial visual features. *IEEE Trans. Med. Imag.* 38, 2545–2555. doi: 10.1109/TMI.2019.2905917
- Mitra, J., Shen, K.-K., Ghose, S., Bourgeat, P., Fripp, J., Salvado, O., et al. (2016). Statistical machine learning to identify traumatic brain injury (TBI) from structural disconnections of white matter networks. *NeuroImage* 129, 247–259. doi: 10.1016/j.neuroimage.2016.01.056
- Moore, D. F., Jérusalem, A., Nyein, M., Noels, L., Jaffee, M. S., and Radovitzky, R. A. (2009). Computational biology-modeling of primary blast effects on the central nervous system. *NeuroImage* 47, T10–T20. doi: 10.1016/j.neuroimage.2009.02.019
- National Institute for Health and Care Excellence (2019). *Head Injury: Assessment and Early Management, Clinical Guideline [CG176]*. Available online at: <https://www.nice.org.uk> (accessed February 1, 2021).
- Niogi, S., Mukherjee, P., Ghajar, J., Johnson, C., Kolster, R., Sarkar, R., et al. (2008). Extent of microstructural white matter injury in postconcussive syndrome correlates with impaired cognitive reaction time: a 3t diffusion tensor imaging study of mild traumatic brain injury. *Am. J. Neuroradiol.* 29, 967–973. doi: 10.3174/ajnr.A0970
- Pappachan, B., and Alexander, M. (2012). Biomechanics of cranio-maxillofacial trauma. *J. Maxillofac. Oral Surg.* 11, 224–230. doi: 10.1007/s12663-011-0289-7
- Patton, D. A., and McIntosh, A. S. (2017). *Head Impact Biomechanics of "King Hit" Assaults*. Cham: Springer International Publishing. doi: 10.1007/978-3-319-30808-1_185-1
- Povlishock, J. T., and Katz, D. I. (2005). Update of neuropathology and neurological recovery after traumatic brain injury. *J. Head Trauma Rehabil.* 20, 76–94. doi: 10.1097/00001199-200501000-00008
- Pregibon, D., et al. (1981). Logistic regression diagnostics. *Ann. Stat.* 9, 705–724. doi: 10.1214/aos/1176345513
- Raichle, M. E. (2010). Two views of brain function. *Trends Cogn. Sci.* 14, 180–190. doi: 10.1016/j.tics.2010.01.008
- Raichle, M. E., MacLeod, A. M., Snyder, A. Z., Powers, W. J., Gusnard, D. A., and Shulman, G. L. (2001). A default mode of brain function. *Proc. Natl. Acad. Sci. U.S.A.* 98, 676–682. doi: 10.1073/pnas.98.2.676
- Raul, J.-S., Deck, C., Willinger, R., and Ludes, B. (2008). Finite-element models of the human head and their applications in forensic practice. *Int. J. Legal Med.* 122, 359–366. doi: 10.1007/s00414-008-0248-0
- Rozenbeek, B., Lingsma, H. F., Lecky, F. E., Lu, J., Weir, J., Butcher, I., et al. (2012). Prediction of outcome after moderate and severe traumatic brain injury: external validation of the international mission on prognosis and analysis of clinical trials (IMPACT) and corticoid randomisation after significant head injury (CRASH) prognostic models. *Crit. Care Med.* 40, 1609–1617. doi: 10.1097/CCM.0b013e31824519ce
- Royal College of Physicians and Surgeons of Glasgow (1974). *The Glasgow Structured Approach to Assessment of the Glasgow Coma Scale*. Available online at: <https://www.glasgowcomascale.org/what-is-gcs/> (accessed February 1, 2021).
- Scheid, R., Preul, C., Gruber, O., Wiggins, C., and von Cramon, D. Y. (2003). Diffuse axonal injury associated with chronic traumatic brain injury: evidence from t2*-weighted gradient-echo imaging at 3 t. *Am. J. Neuroradiol.* 24, 1049–1056.
- Sharp, D. J., Beckmann, C. F., Greenwood, R., Kinnunen, K. M., Bonnelle, V., De Boissezon, X., et al. (2011). Default mode network functional and structural connectivity after traumatic brain injury. *Brain* 134, 2233–2247. doi: 10.1093/brain/awr175
- Sharp, D. J., Scott, G., and Leech, R. (2014). Network dysfunction after traumatic brain injury. *Nat. Rev. Neurol.* 10, 156–166. doi: 10.1038/nrneurol.2014.15
- Siddiqui, Z. F., Krempel, G., Spiliopoulou, M., Pe na, J. M., Paul, N., and Maestu, F. (2015). Predicting the post-treatment recovery of patients suffering from traumatic brain injury (TBI). *Brain Informatics* 2, 33–44. doi: 10.1007/s40708-015-0010-6
- Skandsen, T., Kvistad, K. A., Solheim, O., Strand, I. H., Folvik, M., and Vik, A. (2010). Prevalence and impact of diffuse axonal injury in patients with moderate and severe head injury: a cohort study of early magnetic resonance imaging findings and 1-year outcome. *J. Neurosurg.* 113, 556–563. doi: 10.3171/2009.9.JNS09626
- Smith, S. M., Fox, P. T., Miller, K. L., Glahn, D. C., Fox, P. M., Mackay, C. E., et al. (2009). Correspondence of the brain's functional architecture during activation and rest. *Proc. Natl. Acad. Sci. U.S.A.* 106, 13040–13045. doi: 10.1073/pnas.0905267106
- Smith, S. M., and Nichols, T. E. (2009). Threshold-free cluster enhancement: addressing problems of smoothing, threshold dependence and localisation in cluster inference. *NeuroImage* 44, 83–98. doi: 10.1016/j.neuroimage.2008.03.061
- Stevens, M. C., Lovejoy, D., Kim, J., Oakes, H., Kureshi, I., and Witt, S. T. (2012). Multiple resting state network functional connectivity abnormalities in mild traumatic brain injury. *Brain Imag. Behav.* 6, 293–318. doi: 10.1007/s11682-012-9157-4
- Steyerberg, E. W., Mushkudiani, N., Perel, P., Butcher, I., Lu, J., McHugh, G. S., et al. (2008). Predicting outcome after traumatic brain injury: Development and international validation of prognostic scores based on admission characteristics. *PLoS Med.* 5:e50165. doi: 10.1371/journal.pmed.0050165
- Stocchetti, N., and Zanier, E. (2016). Chronic impact of traumatic brain injury on outcome and quality of life: a narrative review. *Crit. Care* 20:148. doi: 10.1186/s13054-016-1318-1
- Tong, K. A., Ashwal, S., Holshouser, B. A., Nickerson, J. P., Wall, C. J., Shutter, L. A., et al. (2004). Diffuse axonal injury in children: clinical

- correlation with hemorrhagic lesions. *Ann. Neurol.* 56, 36–50. doi: 10.1002/ana.20123
- van der Horn, H. J., Scheenen, M. E., de Koning, M. E., Liemburg, E. J., Spikman, J. M., and van der Naalt, J. (2017). The default mode network as a biomarker of persistent complaints after mild traumatic brain injury: a longitudinal functional magnetic resonance imaging study. *J. Neurotrauma* 34, 3262–3269. doi: 10.1089/neu.2017.5185
- Voets, N. L., Beckmann, C. F., Cole, D. M., Hong, S., Bernasconi, A., and Bernasconi, N. (2012). Structural substrates for resting network disruption in temporal lobe epilepsy. *Brain* 135, 2350–2357. doi: 10.1093/brain/awt137
- Voets, N. L., Hodgetts, C. J., Sen, A., Adcock, J. E., and Emir, U. (2017). Hippocampal MRS and subfield volumetry at 7t detects dysfunction not specific to seizure focus. *Sci. Rep.* 7:16138. doi: 10.1038/s41598-017-16046-5
- Wang, F., Yu, C., Wang, B., Li, G., Miller, K., and Witterk, K. (2020). Prediction of pedestrian brain injury due to vehicle impact using computational biomechanics models: are head-only models sufficient? *Traff. Injury Prevent.* 21, 102–107. doi: 10.1080/15389588.2019.1680837
- Weir, J., Steyerberg, E. W., Butcher, I., Lu, J., Lingsma, H. F., McHugh, G. S., et al. (2012). Does the extended glasgow outcome scale add value to the conventional glasgow outcome scale? *J. Neurotrauma* 29, 53–58. doi: 10.1089/neu.2011.2137
- Winkler, A. M., Ridgway, G. R., Webster, M. A., Smith, S. M., and Nichols, T. E. (2014). Permutation inference for the general linear model. *NeuroImage* 92, 381–397. doi: 10.1016/j.neuroimage.2014.01.060
- Wong, T.-T. (2015). Performance evaluation of classification algorithms by k-fold and leave-one-out cross validation. *Pattern Recogn.* 48, 2839–2846. doi: 10.1016/j.patcog.2015.03.009
- Wood, J. L. (1971). Dynamic response of human cranial bone. *J. Biomech.* 4. doi: 10.1016/0021-9290(71)90010-8
- Yoganandan, N., and Pintar, F. A. (2004). Biomechanics of temporo-parietal skull fracture. *Clin. Biomech.* 19, 225–239. doi: 10.1016/j.clinbiomech.2003.12.014
- Yount, R., Raschke, K. A., Biru, M., Tate, D. F., Miller, M. J., Abildskov, T., et al. (2002). Traumatic brain injury and atrophy of the cingulate gyrus. *J. Neuropsychiatry Clin. Neurosci.* 14, 416–423. doi: 10.1176/jnp.14.4.416
- Zhang, T. (2009). On the consistency of feature selection using greedy least squares regression. *J. Mach. Learn. Res.* 10, 555–568.
- Zhang, Y., Brady, M., and Smith, S. (2001). Segmentation of brain MR images through a hidden Markov random field model and the expectation-maximization algorithm. *IEEE Trans. Med. Imag.* 20, 45–57. doi: 10.1109/42.906424
- Zhou, Y., Milham, M. P., Lui, Y. W., Miles, L., Reaume, J., Sodickson, D. K., et al. (2012). Default-mode network disruption in mild traumatic brain injury. *Radiology* 265, 882–892. doi: 10.1148/radiol.12120748

Conflict of Interest: JM-P was employed by the company Lurtis, Ltd.

The remaining authors declare that the research was conducted in the absence of any commercial or financial relationships that could be construed as a potential conflict of interest.

Copyright © 2021 Schroder, Lawrence, Voets, Garcia-Gonzalez, Jones, Peña and Jerusalem. This is an open-access article distributed under the terms of the Creative Commons Attribution License (CC BY). The use, distribution or reproduction in other forums is permitted, provided the original author(s) and the copyright owner(s) are credited and that the original publication in this journal is cited, in accordance with accepted academic practice. No use, distribution or reproduction is permitted which does not comply with these terms.



Calibration of a Heterogeneous Brain Model Using a Subject-Specific Inverse Finite Element Approach

J. Sebastian Giudice¹, Ahmed Alshareef², Taotao Wu¹, Andrew K. Knutsen³, Lucy V. Hiscox⁴, Curtis L. Johnson⁴ and Matthew B. Panzer^{1*}

¹ Center for Applied Biomechanics, University of Virginia, Charlottesville, VA, United States, ² Department of Electrical and Computer Engineering, Johns Hopkins University, Baltimore, MD, United States, ³ Center for Neuroscience and Regenerative Medicine, The Henry M. Jackson Foundation for the Advancement of Military Medicine, Bethesda, MD, United States, ⁴ Department of Biomedical Engineering, University of Delaware, Newark, DE, United States

OPEN ACCESS

Edited by:

Silvia Budday,
University of Erlangen Nuremberg,
Germany

Reviewed by:

Johannes Weickenmeier,
Stevens Institute of Technology,
United States
Ingolf Sack,
Charité – Universitätsmedizin
StateBerlin, Germany

*Correspondence:

Matthew B. Panzer
panzer@virginia.edu

Specialty section:

This article was submitted to
Biomechanics,
a section of the journal
Frontiers in Bioengineering and
Biotechnology

Received: 04 February 2021

Accepted: 12 April 2021

Published: 04 May 2021

Citation:

Giudice JS, Alshareef A, Wu T, Knutsen AK, Hiscox LV, Johnson CL and Panzer MB (2021) Calibration of a Heterogeneous Brain Model Using a Subject-Specific Inverse Finite Element Approach. *Front. Bioeng. Biotechnol.* 9:664268. doi: 10.3389/fbioe.2021.664268

Central to the investigation of the biomechanics of traumatic brain injury (TBI) and the assessment of injury risk from head impact are finite element (FE) models of the human brain. However, many existing FE human brain models have been developed with simplified representations of the parenchyma, which may limit their applicability as an injury prediction tool. Recent advances in neuroimaging techniques and brain biomechanics provide new and necessary experimental data that can improve the biofidelity of FE brain models. In this study, the CAB-20MSym template model was developed, calibrated, and extensively verified. To implement material heterogeneity, a magnetic resonance elastography (MRE) template image was leveraged to define the relative stiffness gradient of the brain model. A multi-stage inverse FE (iFE) approach was used to calibrate the material parameters that defined the underlying non-linear deviatoric response by minimizing the error between model-predicted brain displacements and experimental displacement data. This process involved calibrating the infinitesimal shear modulus of the material using low-severity, low-deformation impact cases and the material non-linearity using high-severity, high-deformation cases from a dataset of *in situ* brain displacements obtained from cadaveric specimens. To minimize the geometric discrepancy between the FE models used in the iFE calibration and the cadaveric specimens from which the experimental data were obtained, subject-specific models of these cadaveric brain specimens were developed and used in the calibration process. Finally, the calibrated material parameters were extensively verified using independent brain displacement data from 33 rotational head impacts, spanning multiple loading directions (sagittal, coronal, axial), magnitudes (20–40 rad/s), durations (30–60 ms), and severity. Overall, the heterogeneous CAB-20MSym template model demonstrated good biofidelity with a mean overall CORA score of 0.63 ± 0.06 when compared to *in situ* brain displacement data. Strains predicted by the calibrated model under non-injurious rotational impacts in human volunteers ($N = 6$) also demonstrated similar biofidelity compared to *in vivo* measurements obtained from tagged magnetic resonance imaging studies. In addition to serving as an anatomically accurate model for

further investigations of TBI biomechanics, the MRE-based framework for implementing material heterogeneity could serve as a foundation for incorporating subject-specific material properties in future models.

Keywords: traumatic brain injury, material properties, magnetic resonance elastography, image registration, morphing

INTRODUCTION

Traumatic brain injury (TBI) is a significant source of injury, disability, and death. Recent epidemiological studies have estimated that TBIs account for approximately one-third of all injury-related deaths in the United States (Faul and Coronado, 2015). In 2010, the Centers for Disease Control (CDC) estimated that TBIs resulted in 2.5 million emergency department (ED) visits (87%), hospitalizations (11%), and deaths (2%) (Centers for Disease Control and Prevention, 2015). Finite element (FE) models of the brain have rapidly become indispensable tools for investigating TBI mechanisms, assessing new protective technology, and developing injury risk criteria (Kleiven and von Holst, 2002; Giordano and Kleiven, 2014; Gabler et al., 2018). FE models of the brain are typically used to investigate the dynamic 3D deformation of the human brain under simulated head impacts relevant to sports, automotive crashes, and falls. While FE models have been instrumental to furthering our understanding of TBI biomechanics, many FE brain models have been developed to represent the brain as a simplified physical system, both in their representation of the anatomy and material properties, thus limiting their accuracy and utility in predicting deformations experienced due to head impacts.

Perhaps the most significant differences across brain models in the field relate to the constitutive laws and material parameters chosen to represent the material behavior of the simulated brain tissue (Jin et al., 2013; Dixit and Liu, 2017; Fahlstedt et al., 2021). At the simplest level, the brain is modeled as a single isotropic and homogeneous material (Kleiven and von Holst, 2002; Takhounts et al., 2008; Ji et al., 2015). However, unique material properties can be assigned to different parts of the brain, which typically represent tissue types with different cellular composition or segmented anatomical labels, and many FE models include differences in material properties between white and gray matter (Horga and Gilchrist, 2003; Kimpara et al., 2006; McAllister et al., 2012; Panzer et al., 2012; Mao et al., 2013; Miller et al., 2016, 2017). At the most complex level, the brain has been modeled as an anisotropic, heterogeneous structure by explicitly modeling axonal fiber tracts by embedding 1D elements in the brain mesh (Garimella et al., 2019; Hajiaghdammar et al., 2019; Wu et al., 2019). While the embedded axon approach provides a more biofidelic structural representation of the axonal tissue, which is known to exhibit anisotropy and regional variations in tissue material properties (Jin et al., 2013; Budday et al., 2015, 2017a, 2019; Weickenmeier et al., 2016), the embedding of 1D axonal tract elements can significantly increase computational cost. A potential alternative for modeling brain heterogeneity is to model the brain with material stiffness varying throughout the

brain regardless of the tissue classification of each element, which can be obtained using magnetic resonance elastography (MRE).

Recently, MRE has been utilized to non-invasively measure *in vivo* material properties of the human brain in healthy volunteers (Weaver et al., 2012; Johnson et al., 2013a,b; Hiscox et al., 2016). In MRE, an external transducer (commonly a head pillow) mechanically vibrates the head (10–100 Hz) to induce micron-level displacements in the brain that can be measured and used to estimate elastic and viscous material properties throughout the brain with high spatial resolution (Hiscox et al., 2016). To date, MRE has been used to investigate global brain material properties with voxel-level resolution, regional variations in tissue stiffness, and material properties associated with brain pathology (Hiscox et al., 2016; Johnson and Telzer, 2018; Murphy et al., 2019). While stiffness measurements vary, most studies agree that the measured brain stiffness is dependent on the actuation frequency (due to viscoelasticity), and that white matter regions are stiffer than gray matter regions (Hiscox et al., 2016). However, since the measured properties are dependent on the actuation frequency and obtained from micron-level displacements of the brain, additional work is needed to apply the MRE-derived stiffness maps to a FE brain model.

The goal of this study is to calibrate and verify a heterogeneous FE brain model by leveraging experimental datasets reporting (1) MRE-derived material properties (Hiscox et al., 2020), (2) high rate, *in situ*, brain displacements measured from human cadaveric specimens using sonomicrometry (Alshareef et al., 2020a), and (3) low rate, *in vivo*, brain strain measured from human volunteers using tagged magnetic resonance imaging (tMRI; Knutsen et al., 2020). Material parameters for the model were developed in three phases. First, stiffness data from an MRE template image (average of 134 subjects; Hiscox et al., 2020) was used to define the relative stiffness gradient throughout the brain model. Second, the linear stiffness parameter was calibrated using low-displacement cases from the Alshareef et al. (2020a) dataset and verified using brain strain data from the *in vivo* tMRI dataset. Finally, the non-linear stiffness parameter was calibrated using high-deformation cases from the Alshareef et al. (2020a) dataset. To verify that the calibrated material parameters were physically reasonable, a comprehensive verification was performed using the remaining rotational cases from these datasets that were not used for calibration. The response of the calibrated material used in the model was also compared to experimental *in vitro* material test data available in the literature (Jin et al., 2013) to ensure that the median stiffness response was within the range of experimental data. In addition to serving as a model for investigating TBI biomechanics, the technique for implementing MRE-derived heterogeneous material properties can be adapted to

implement subject-specific material properties in future subject-specific brain models.

MATERIALS AND METHODS

Development of CAB-20MSym Template Model

The mesh of the CAB-20MSym template model was chosen to represent the anatomy of the CAB-20MSym template image developed by Giudice et al. (2020). This template was constructed from T1-weighted MRI scans obtained from 20 young, healthy adult males (22 ± 3 years). Details regarding these images are provided elsewhere (Giudice et al., 2020; Reynier et al., 2020).

The CAB-20MSym template image was segmented to identify the brain parenchyma, peripheral cerebrospinal fluid (CSF), internal CSF, and ventricles. To generate the template model mesh, each 1 mm isotropic voxel in the segmentation image was directly converted into a cubic hexahedral (i.e., voxel) element and assigned to a part based on its segmentation label. This approach was selected as voxel meshes have the accuracy and stability benefits of hexahedral elements and can capture complex anatomical features at the native spatial resolution (in this case, 1 mm) of the MRI images used to construct them (Miller et al., 2016; Ghajari et al., 2017). To include the sagittal sinus, falx cerebri, and tentorium cerebelli, the voxels surrounding these regions were manually delineated and two-dimensional shell elements were generated at the corresponding mid-surfaces. Finally, a layer of rigid shell elements surrounding the outermost surface of the peripheral CSF part was generated to represent the dura, which was assumed to be rigidly connected to the inner surface of the skull (Miller et al., 2016). The selection of the numerical implementation approach was informed by an analytical review of the numerical methods utilized by the TBI modeling community performed by Giudice et al. (2019b) and is summarized in the **Supplementary Material**. All interfaces were continuous and connected through shared nodes.

The material properties for the CSF (peripheral and internal), ventricles, skull, sagittal sinus, falx, and tentorium were adapted from previous brain models (Takhounts et al., 2008; Mao et al., 2013; Miller et al., 2016). To account for the nominal stiffness provided by the trabeculae and bridging vessels located within the subarachnoid space, the peripheral CSF was modeled using a linear viscoelastic material with very low stiffness ($G_0 = 0.5$ kPa; $G_\infty = 0.1$ kPa). As these properties do not exist for CSF, an elastic fluid (bulk modulus, $K = 2.1$ GPa) was assigned to the ventricle and internal CSF parts. The sagittal sinus, falx, and tentorium were modeled as elastic materials (Young's modulus, $E = 31.5$ MPa; Poisson's ratio, $\nu = 0.45$). Finally, the skull was modeled as rigid to allow the implementation of 6 degree-of-freedom head kinematic boundary conditions for all analyses (Gabler et al., 2016). Further details regarding these material properties are available in the **Supplementary Material**. The material implementation of the brain parenchyma is described in Sections "Implementation of Brain Heterogeneity" and "Constitutive Modeling of Brain Parenchyma."

Implementation of Brain Heterogeneity

The implementation of brain material heterogeneity in the CAB-20MSym template model was derived from the MRE134 template image (Hiscox et al., 2020). This template was constructed using MRE data from 134 healthy, young adults (18–35 years, 78F/56M) using common MRE acquisition and data processing protocols (Hiscox et al., 2020). To adapt the MRE134 template, originally defined in MNI152 space with 2 mm isotropic voxels, it was first non-linearly registered to the CAB-20MSym template space using ANTs non-linear registration (Avants et al., 2008). To eliminate stiffness measurements potentially influenced by numerical artifacts or edge effects, stiffness values beyond the 98th percentile were excluded. In the CAB-20MSym template model, CSF spaces were modeled using CSF-specific constitutive models, however, in the MRE134 template image, CSF spaces were not differentiated from the brain tissue. Therefore, stiffness values below the 15th percentile, which corresponded to the approximate stiffness in the MRE134 template in CSF areas (approximately 0–1.5 kPa; Hiscox et al., 2020), were excluded. From this truncated distribution, the stiffness value of each voxel was normalized by the median stiffness and binned into 10 groups. Voxels that had original stiffnesses below the 15th and above the 98th percentile were assigned to the lowest and largest normalized stiffness bins, respectively. This process yielded a normalized stiffness label image where voxels were categorized by their relative stiffness, and not according to an anatomical segmentation label. In doing so, this approach accounts for stiffness variations present within tissue groups, such as white and gray matter. Normal variations in the material properties of various tissue groups are reported in the literature (Hiscox et al., 2020).

Constitutive Modeling of Brain Parenchyma

The 10 parts comprising the brain parenchyma, using the binned groups from the previous section, were modeled using a quasi-linear viscoelastic (QLV) model (Fung, 1993). In Fung's QLV theory, it is assumed that the response of a material can be separated into a normalized function of time only, $g(t)$, and an elastic function of strain only, $T^e(\epsilon)$ (Fung, 1993). For a QLV model, the stress relaxation function, $R(\epsilon, t)$, is:

$$R(\epsilon, t) = g(t) \cdot T^e(\epsilon)$$

In this study, the instantaneous elastic response function, $T^e(\epsilon)$, was derived from an Ogden strain energy density (Ogden and Hill, 1972).

$$W(\lambda_1, \lambda_2, \lambda_3) = \frac{\mu}{\alpha} (\lambda_1^\alpha + \lambda_2^\alpha + \lambda_3^\alpha - 3)$$

Where λ_j are the three principal stretches, μ is the shear modulus, and α is a unitless non-linearity coefficient. The infinitesimal shear modulus (i.e., initial slope of the non-linear shear stress-strain curve), μ_0 , can be obtained as a function of the material parameters.

$$\mu_0 = \frac{1}{2} \mu \alpha$$

Finally, four Prony terms ($N = 4$) were included in the reduced relaxation function.

$$g(t) = g_{\infty} + \sum_{i=1}^N g_i e^{-\beta_i t}$$

$$\beta_i = \frac{1}{\tau_i}$$

$$g_{\infty} + \sum_{i=1}^N g_i = 1$$

Where, g_{∞} and g_i are normalized coefficients associated with the long-term response and each time constant, τ_i . The density, ρ , and Poisson's ratio, ν , of the brain parenchyma material were 1.123×10^{-6} kg/mm³ (Miller et al., 2016) and 0.499999, respectively.

The reduced relaxation function was fit to experimental $\tan(\delta)$ data obtained from studies that characterized the viscoelastic properties of brain tissue over wide ranges of input frequencies (Fallenstein et al., 1969; Shuck and Advani, 1972; Arbogast et al., 1997; Bilston et al., 1997, 2001; Arbogast and Margulies, 1998; Brands, 2000; Darvish and Crandall, 2001; Lippert et al., 2004; Nicolle et al., 2004; Hrapko et al., 2006; Shen et al., 2006; Garo et al., 2007). The $\tan(\delta)$ response represents material damping as a function of frequency, and is independent of the material stiffness, making it suitable for calibrating the reduced relaxation function. Optimization of g_i and τ_i was performed using a least squares optimization. The Ogden parameters defining the median deviatoric response of the brain, to which the brain parenchyma heterogeneity was applied relative to, was calibrated using an iFE calibration scheme and is described in the following sections.

Calibration Objective and Approach

To reduce the number of optimized parameters and simplify the calibration process, it was assumed that the damping of the brain and hyperelastic non-linearity were homogeneous throughout the brain. As such, the reduced relaxation function parameters were assigned to all brain parenchyma parts. Therefore, the objective of this inverse FE approach was to calibrate two parameters:

1. The median stiffness of the brain, μ_{med} , that defined the material heterogeneity.
2. The non-linearity coefficient, α , that defined the hyperelastic non-linearity.

Material parameters were calibrated using an iFE approach in which parameters were optimized to minimize the error between model and experimental results. In this case, a subset of the impact cases in the *in situ* brain displacement dataset (Alshareef et al., 2018, 2020a,b) were simulated using subject-specific models and the error between nodal displacements and the corresponding experimental displacements were minimized. In this dataset, *in situ* brain deformation was measured at discrete locations using sonomicrometry sensors (i.e., “receivers”),

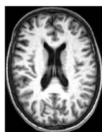
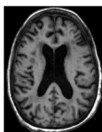
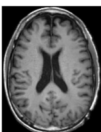
distributed throughout the brain parenchyma of cadaveric head-neck specimens. Three subject-specific models were generated to represent the anatomies of subjects SONO-896, SONO-900, and SONO-904 (Table 1; Alshareef et al., 2020a). Further details regarding this experimental dataset and the corresponding model setup are provided in the **Supplementary Materials**.

To minimize the likelihood of obtaining a non-unique solution, μ_{med} and α were optimized independently by leveraging specific cases in the *in situ* brain displacement database. To optimize μ_{med} a low severity case (Axial 20 rad/s, 60 ms) was used to optimize the median infinitesimal quasi-static shear stiffness (a function of μ_{med}). This case was selected as preliminary simulations indicated that the deformations induced in this case were not sensitive to the material non-linearity coefficient. A higher severity case (Coronal 40 rad/s, 30 ms) was used to optimize α while maintaining the optimized infinitesimal quasi-static shear stiffness. This coronal rotation case was selected as preliminary simulations indicated that the deformations predicted in this case were sensitive to the material non-linearity coefficient and avoided calibrating the material parameters under a single loading direction. Finally, the calibrated heterogeneous material parameters were verified using the remaining cases in the *in situ* brain deformation database, as well as low severity *in vivo* brain strain data obtained using the *in vivo* tMRI database (Knutsen et al., 2020). This final verification included 39 simulations; 11 simulations for each SONO subject-specific model (not including case used for calibration) and 6 simulations for the tMRI cases. Details regarding these experimental datasets and the respective model setups are provided in the **Supplementary Materials**. As a final check, the material response was assessed in tension, compression, and simple shear loading over strain rates of 0.5, 5, and 30 1/s and compared to experimental data (Jin et al., 2013).

The material calibration process is summarized below:

1. Optimize μ_{med} under low severity rotational impacts.
2. Intermediate verification to assess calibrated μ_{med} under independent low severity cases.
3. Optimize α under higher severity rotational impacts.
4. Comprehensive verification of calibrated material parameters

TABLE 1 | Specimen information for subjects used to assess deformation response (Alshareef et al., 2020a).

Specimen	SONO-896	SONO-900	SONO-904
Axial MRI			
Sex	Female	Female	Male
Age (yrs)	57	66	67
Height (cm)	163	165	177
Body Mass (kg)	31.1	56.2	54.9
ICV (cm ³)	1300	1406	1545

All models used in this study were subject-specific, constructed to represent the anatomies of the subjects from which the experimental data were collected. As such, the deformation response of each subject-specific model was compared to the experimental data obtained from that subject only. This was crucial to eliminate geometric effects from the calibration and verification processes, ensuring that discrepancies between simulation and experimental results, for each subject, were due to variations in material parameters only. All subject-specific models were generated using registration-based morphing (RBM), which is a non-linear morphing technique that was developed specifically for generating subject-specific models of the brain by leveraging image registration transformations (Giudice et al., 2020). Metrics of morphing accuracy and element quality for all subject-specific models generated in this study are provided in the **Supplementary Materials**.

Objective Rating and Optimization Strategy

CORrelation and Analysis (CORA) scores were used to quantify the error between the nodal displacements in the model and the receiver displacements in the experimental dataset. Since experimental displacements were 3D (i.e., x , y , and z displacement time-histories for each receiver), a composite score (cCORA) was calculated to obtain a single objective rating for each receiver. cCORA was computed as the weighted average of the CORA scores in each orthogonal direction, weighted by the relative magnitude of the experimental signal in each direction (Giudice et al., 2019a). Finally, the overall score for each rotational case was computed as the weighted average of all receiver cCORA scores, weighted by the experimental maximum resultant displacement for each receiver (wcCORA). In this study, the default CORA parameters were used (Gehre et al., 2009).

$$wcCORA = \sum_i^N \alpha_i \times cCORA_i$$

$$\alpha_i = \frac{\beta_i}{\sum_i^N \beta_i}$$

Where, β_i is the experimental maximum resultant displacement for the i^{th} receiver and N is the number of receivers for each rotation case. For the calibration of the Ogden material parameters, wcCORA was used to quantify the error between the nodal displacements and the experimental receiver displacements for each rotation simulation. To obtain a set of parameters that best represented the overall response of the three subjects used for calibration, a joint optimization was performed where the goal was to maximize the mean wcCORA score for subjects SONO-896, SONO-900, and SONO-904.

$$f(x) = \frac{wcCORA_{896} + wcCORA_{900} + wcCORA_{904}}{3}$$

A golden ratio search algorithm was used to identify the maximum mean overall wcCORA as a function of the material parameter being optimized. In the first iteration, a series of

simulations were run to identify the bounds for the golden search algorithm. For example, when calibrating α , three simulations with $\alpha = 2, 6$, and 10 were run to determine the bounds for calibration. The parameters investigated in each subsequent iteration, i ($x_{i,1}$ and $x_{i,2}$) were determined by the golden ratio search algorithm.

$$x_{i,1} = a_i + (1 - \varphi)(b_i - a)$$

$$x_{i,2} = a_i + \varphi(b_i - a)$$

$$\varphi = \frac{\sqrt{5} - 1}{2}$$

Where a_i and b_i are the lower and upper bounds for iteration, i . The bounds were updated based on the mean wcCORA score for each parameter investigated [$f(x_1)$ and $f(x_2)$] in the previous iteration ($i - 1$).

If $f(x_1) > f(x_2)$ then $a_i = a_{(i-1)}$ and $b_i = x_{(i-1),2}$

If $f(x_1) < f(x_2)$ then $a_i = x_{(i-1),1}$ and $b_i = b_{(i-1)}$

This process was repeated until the termination criteria was satisfied. The parameter that had the greatest mean wcCORA was selected as the calibrated value. The first iteration and termination criteria for the calibration of μ_{med} and α are shown in **Table 2**. These values were selected based on parameters reported in the literature for human brain tissue (Miller and Chinzei, 2002; Nicolle et al., 2004; Franceschini et al., 2006; Kleiven, 2007; Kaster et al., 2011; Moran et al., 2014; Budday et al., 2017a).

Calibration and Verification of Median Shear Modulus

In the first step of the material calibration process, μ_{med} was optimized by simulating the Axial 20 rad/s, 60 ms case (Z: 20–60). All simulations were run for 200 ms. Pilot simulations indicated that the predicted deformations in this loading case were not sensitive to material non-linearity that is governed by α . Therefore, in this optimization the shear response of the material was constrained to the linear response of a Neo-Hookean solid ($\alpha = 2$), where the shear modulus defined in the Ogden model is identical to the infinitesimal shear modulus of the material (μ_0).

Since the model incorporates material heterogeneity relative to the median stiffness of the brain, the stiffness of each of the 10

TABLE 2 | First iteration parameters and termination criteria for calibrated material parameters.

Parameter	1st Iteration	Termination Criteria
μ_{med}	$\mu_{med} = 0.25, 0.7, 1.15, 1.6, 2.05, 2.6$ kPa	$b_{(i+1)} - a_{(i+1)} < 0.1$ kPa
α	$\alpha = 2, 6, 10$	$b_{(i+1)} - a_{(i+1)} < 0.2$

parts was defined relative to the median stiffness defined for any given optimization iteration.

$$\mu_i = \gamma_i \mu_{med} = \gamma_i \mu_{0,med}$$

Where γ_i is the relative stiffness of the i th part and varies between 0.53 and 1.53. All stiffness values reported in this study refer to quasi-static parameters (i.e., μ_{med} and α represent the quasi-static response of the material).

To verify the calibrated median shear stiffness ($\mu_{0,med} = \mu_{med}$) the remaining 20 rad/s, 60 ms cases in the coronal (X: 20–60) and sagittal (Y: 20–60) directions were simulated and compared to each specimen's experimental data using wcCORA. Verification of the strain response was performed by simulating *in vivo* brain strain experiments (Knutsen et al., 2020). In this dataset, three subjects (tM-3978, tM-4838, and tM-6176) were subjected to sagittal rotations ($\omega_{max} = 1.4$ – 1.6 rad/s) and three subjects (tM-3978, tM-7126, and tM-9475) were subjected to axial rotations ($\omega_{max} = 4$ – 5.4 rad/s) of the head. This verification step was performed to ensure that the calibrated $\mu_{0,med}$ was physically meaningful and resulted in biofidelic deformation predictions under independent low-deformation test cases. This also provided reassurance that the final set of calibrated material parameters were unique, given the model's sensitivity to both μ and α .

To compare the predicted strain response of each subject-specific model, the maximum principal strain (MPS) of each element was computed and mapped to the corresponding voxel in the subject image. As a global metric of strain, the 95th percentile MPS value (MPS-95) predicted by the model was compared to the equivalent experimental measures. In addition, the volume fraction of elements exceeding 2% strain was compared between the model and experimental data. These volume fractions were computed globally, as well as regionally for the cerebral gray and white matter and the cerebellum. These regions were identified using a segmentation image provided in the tMRI database. MPS-95 was also computed for the elements/voxels located in these regions.

Calibration and Verification of Non-linear Coefficient

In the previous steps, the median shear stiffness, which was equivalent to the median infinitesimal shear modulus ($\mu_{0,med} = \mu_{med}$) since the shear response was assumed to be linear ($\alpha = 2$), was determined and verified. In this step, the non-linear coefficient (α) was calibrated by simulating the Coronal 40 rad/s, 30 ms rotation case. All simulations were run for 200 ms. To preserve the previously calibrated $\mu_{0,med}$, μ_{med} was also adjusted such that $\mu_{0,med}$ was equivalent to the value determined in the first step of the optimization procedure. Therefore, for the i^{th} part in the heterogeneous CAB-20MSym template model the shear modulus in the Ogden constitutive model, μ_i , was defined as a function of μ_{med} , α , and γ_i .

$$\mu_i = \frac{2\gamma_i \mu_{0,med}}{\alpha}$$

To verify the calibrated heterogeneous material, the remaining 11 rotation cases for each subject were simulated (36 total

simulations including case used for calibration), and the nodal displacements of the calibrated subject-specific models were compared to the corresponding experimental brain displacement data using wcCORA. To assess the calibrated model performance relative to other state-of-the-art and widely used FE brain models, wcCORA values obtained in this study were compared to those reported for the Global Human Body Models Consortium (GHBM) brain model (Mao et al., 2013) and the UVA embedded axon model (UVA-EAM) (Wu et al., 2019, 2020, 2021). These models were morphed to the anatomy of the three subjects using surface-based morphing (Wu et al., 2019) and simulated under identical boundary conditions, resulting in 36 simulations per model.

The set of tMRI simulations used to verify the calibrated median infinitesimal shear stiffness were also simulated using the final calibrated heterogeneous model to ensure that the incorporation of material non-linearity did not influence the model predictions. Since the brain strains in these simulations were low (less than 6% MPS), material non-linearity was not expected to influence the model results.

Finally, the calibrated Ogden material response was compared to experimental material test data. To verify the optimized parameters, the complex modulus of the derived model was compared to the complex moduli reported in the rheological characterization dataset. Furthermore, a series of single element (1 mm × 1 mm × 1 mm) simulations were run with the fit material parameters to verify the response of the constitutive model as well as the Ogden QLV implementation in LS-Dyna. These single element simulations were run in tension, compression, and simple shear at loading rates of 0.5, 5, and 30 1/s to 50% engineering strain and the results were compared to average response corridors constructed from the material characterization data in the literature (Jin et al., 2013).

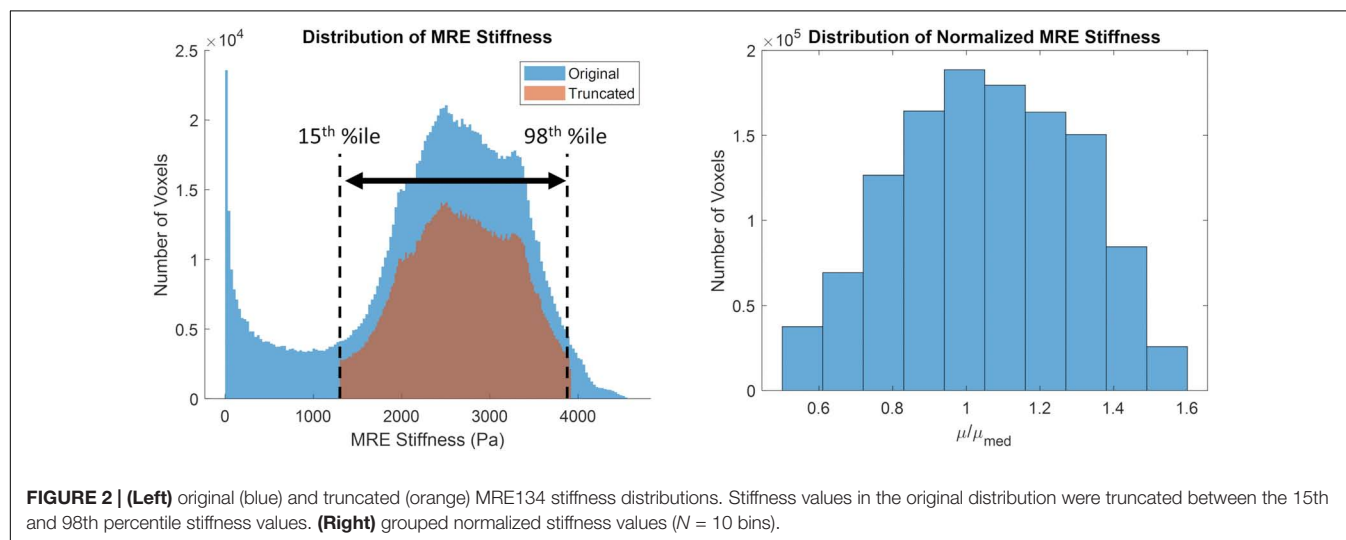
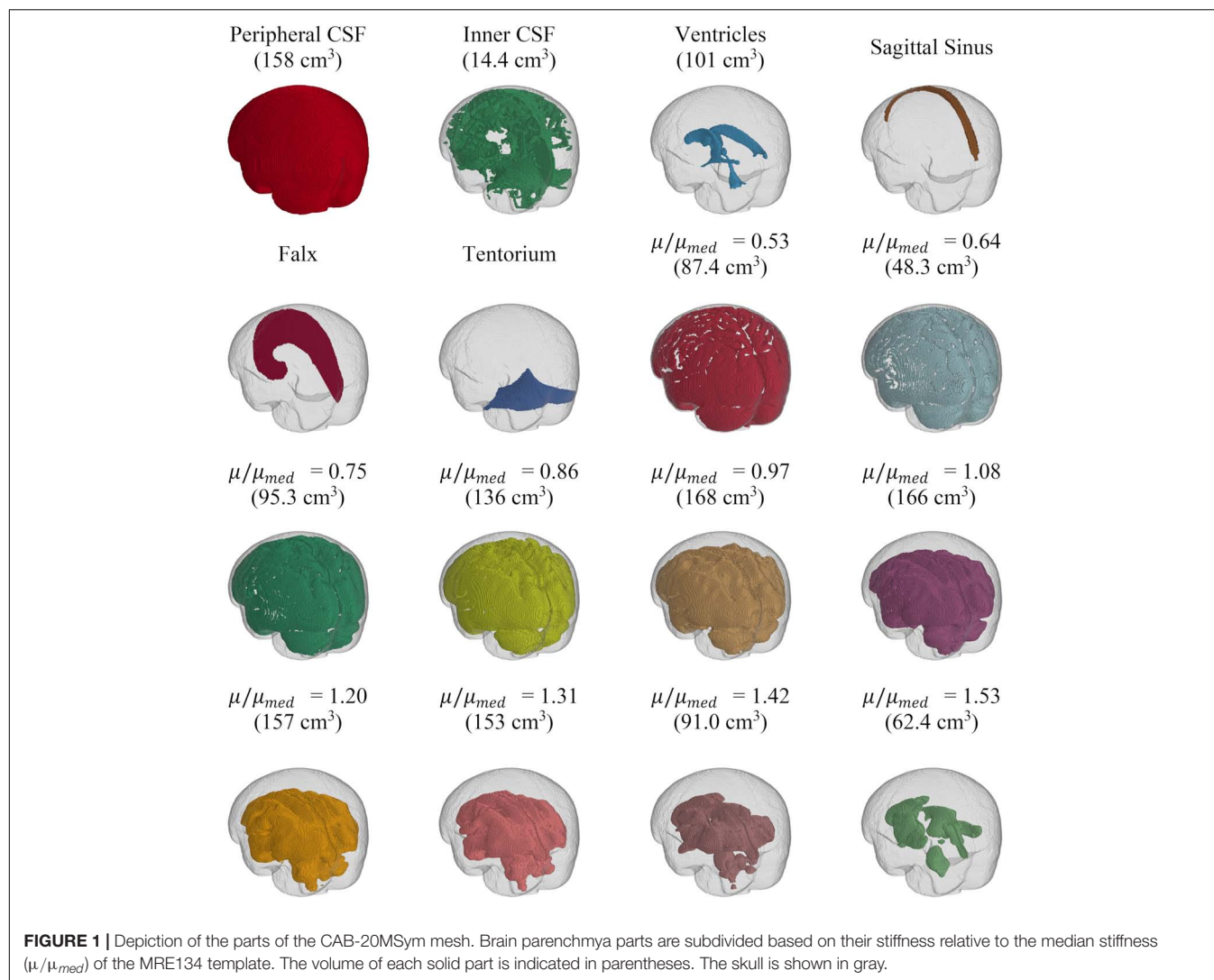
RESULTS

Development of CAB-20MSym Template Model

The CAB-20MSym template model had an intracranial volume of 1439 cm³ and approximately 1.6 million elements, 1.5 million nodes, and 16 parts (Figure 1). Note that Figure 1 depicts the external surfaces of each of these parts and is not representative of the entire volume of each part. All interfaces (e.g., falx-brain) were continuous and defined using shared nodes.

Implementation of Brain Heterogeneity

The original and truncated stiffness distributions from the MRE134 template, mapped to CAB-20MSym space, are shown in Figure 2. In the truncated distribution, the median stiffness was 2.53 kPa and the mean ± standard deviation was 2.37 ± 0.99 kPa. To convert the MRE134 template image into the CAB-20MSym template model, the truncated distribution was grouped into 10 bins, which were used to classify the normalized stiffness of each voxel in the CAB-20MSym model. The 10 relative stiffness groups were 0.53, 0.64, 0.75, 0.86, 0.97, 1.08, 1.20, 1.31, 1.42, and 1.53,



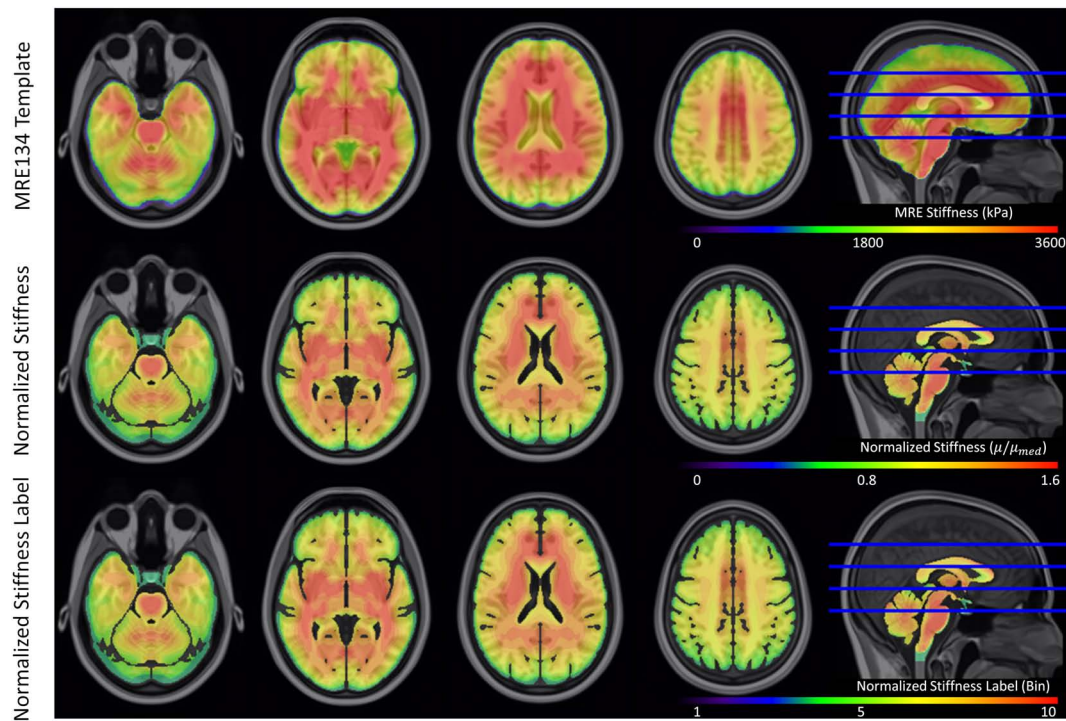


FIGURE 3 | Magnetic resonance elastography template (MRE134), normalized stiffness image, and normalized stiffness label image (used to construct CAB-20MSym template model). Each of the 10 bins in the normalized stiffness label corresponded to an individual part in the template model.

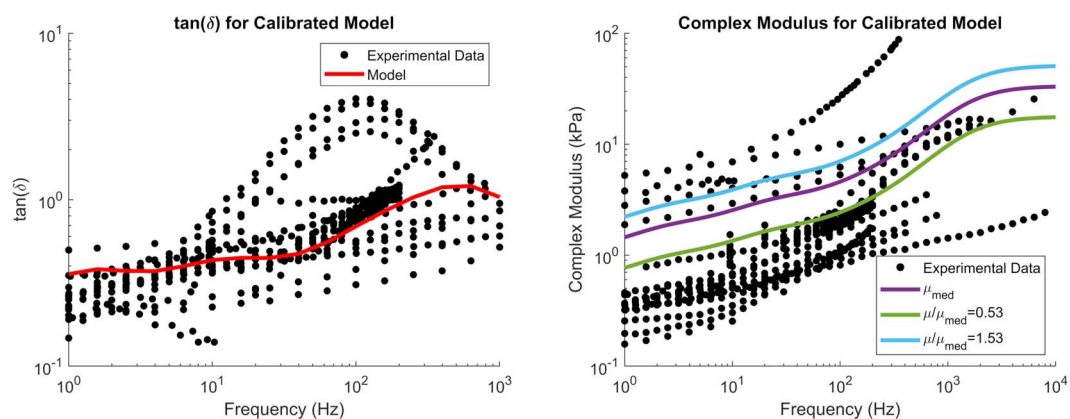


FIGURE 4 | $\tan(\delta)$ (left) and complex modulus (right) of the calibrated material parameters, demonstrating the median complex modulus of the brain (purple) as well as the complex modulus for the softest (green) and stiffest (blue) relative stiffness parts. Note that $\tan(\delta)$ is a function of damping only and not tissue stiffness. Experimental data were obtained from the literature (see Section “Constitutive Modeling of Brain Parenchyma” for list of references).

which corresponded to the bin centers (Figure 2). The MRE134 template, normalized stiffness image, and normalized stiffness label image are shown in Figure 3.

Constitutive Modeling of the Brain Parenchyma

The reduced relaxation function parameters were obtained by fitting g_i and β_i ($i = 4$) to match experimental $\tan(\delta)$ data (Figure 4). The fit reduced relaxation parameters are

shown in Table 3. These viscoelastic parameters were applied homogeneously throughout the entire brain model.

Calibration and Verification of Median Shear Modulus

The median shear stiffness of the material was calibrated using the axial 20 rad/s, 60 ms rotation case in the *in situ* brain displacement database. The calibrated value of μ_{med} was 1.125 kPa. Since this initial constitutive model constrained

TABLE 3 | Prony series parameters for the brain parenchyma.

Material Parameters	
$g_1 = 0.8619$	$\beta_1 = 10 \text{ ms}$
$g_2 = 0.0383$	$\beta_2 = 1 \text{ ms}$
$g_3 = 0.0412$	$\beta_3 = 0.1 \text{ ms}$
$g_4 = 0.0249$	$\beta_4 = 0.01 \text{ ms}$
$g_\infty = 0.0337$	

the non-linear coefficient to 2 (representing a Neo-Hookean solid), μ_{med} was equivalent to the infinitesimal quasi-static shear modulus, $\mu_{0,med}$. Six iterations (12 simulations) were required to satisfy the termination criteria specified in **Table 2**, resulting in an optimal mean wcCORA of 0.62 (**Figure 5**). The calibrated value was within the range of other Ogden rubber infinitesimal quasi-static shear moduli reported in the literature for the brain (Miller and Chinzei, 2002; Nicolle et al., 2004; Franceschini et al., 2006; Kleiven, 2007; Kaster et al., 2011; Moran et al., 2014; Budday et al., 2017a), which varied from 0.27 to 1.49 (mean \pm standard deviation = 0.92 ± 0.38).

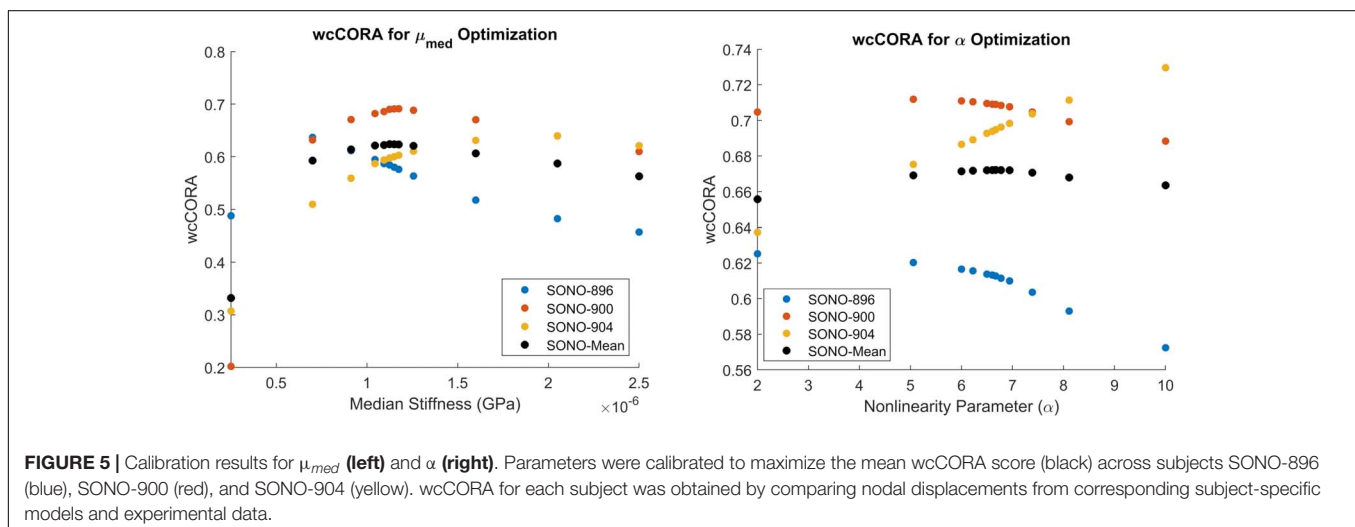
Using the jointly calibrated $\mu_{med} = \mu_{0,med}$ value, the Coronal and Sagittal 20 rad/s, 60 ms cases for the same specimens were simulated to verify the subject-specific model responses. The wcCORA scores for the coronal, sagittal, and axial simulations were between 0.66–0.72, 0.50–0.67, and 0.58–0.69, respectively (**Table 4**). In general, wcCORA scores were greatest in the coronal rotation, and across the three subjects, the SONO-900 model yielded the highest wcCORA scores using the jointly calibrated μ_{med} value.

A series of tMRI experiments were simulated using subject-specific models to verify the calibrated value of $\mu_{med} = \mu_{0,med}$. The strain response of subject tM-9475 during the axial rotation is shown in **Figure 6**. Qualitatively, the tM-9475 subject-specific model demonstrated a similar deformation pattern compared to the experimental data. In general, MPS was largest in the cortex and smallest in the cerebellum (**Figure 6**). Additionally,

in both simulation and experiment, larger strains were observed at the apexes of the ventricles (i.e., frontal and occipital horns) which propagated through the cerebrum. This can be seen in slices $z = 20$ –40 in **Figure 6**. However, in the experimental data cortical strain was consistently asymmetric, with the largest strains observed in the right hemisphere of the brain, whereas in the simulation the MPS distribution was relatively symmetric. These trends were similar for all subjects tested in the axial rotation protocol.

These trends were salient in the MPS-95 and strain volume fraction metrics used to quantify brain deformation globally and regionally. For subject tM-9475, global and regional MPS-95 values were similar to the experimental data, with absolute differences between 0.0025 and 0.0084 strain. However, while regional MPS-95 values were similar between the model and experiment, larger differences in the volume fraction of voxels that exceeded 2% strain was observed, particularly in the cerebellum (simulation: 0.15; experiment: 0.33) and gray matter (simulation: 0.34; experiment: 0.61). Figures showing MPS-95 and volume fraction results for the axial and sagittal tMRI cases are included in the **Supplementary Materials**.

The strain response of subject tM-4838 during the sagittal rotation is shown in **Figure 6**. Qualitatively, the tM-4838 subject-specific model demonstrated a similar MPS pattern compared to the experimental data with the largest MPS values observed at the periphery of the brain, including the cortex, base of the cerebrum, and anterior surface of the brainstem, and lowest in the midbrain (**Figure 6**). However, strains in the cerebellum and brainstem were larger in the experimental data than predicted by the simulation. This is particularly evident in slices $x = -15$ –5 in **Figure 6**. In general, global and regional MPS-95 metrics were similar between the subject-specific model and experimental data with absolute differences in MPS-95 between 0.0003 and 0.0067 for subject tM-4838. The volume fraction of voxels that exceeded 2% strain was also similar, except for the cerebellum, where the experimental volume fraction was 0.16 compared to only 0.06 in the simulation. These trends were similar for all subjects tested in the sagittal rotation protocol.



Calibration and Verification of Non-linear Coefficient

The non-linearity parameter of the Ogden constitutive model, α , was calibrated using the Coronal 40 rad/s, 30 ms rotation case in the *in situ* brain deformation database. The calibrated value of α was 6.67, which yielded a mean wcCORA of 0.67 across subjects SONO-896, SONO-900, and SONO-904 (Figure 5). Eight iterations (12 simulations) were required to satisfy the termination criteria specified in Table 2. The final calibrated material parameters for each brain parenchyma part (grouped by stiffness relative to the median stiffness) are shown in Table 5. The viscoelastic parameters for the brain parts are shown in Table 3.

To verify the calibrated material parameters, all 12 impact cases for subjects SONO-896, SONO-900, and SONO-904 were simulated and assessed using wcCORA. The three subject-specific models demonstrated good biofidelity with a mean wcCORA of 0.63 ± 0.06 for all 36 simulations (range: 0.50–0.74). Across the three subjects, SONO-900 demonstrated the highest wcCORA scores (0.68 ± 0.03) and wcCORA was similar for SONO-896 (0.61 ± 0.07) and SONO-904 (0.61 ± 0.06). In general, wcCORA scores were highest in the coronal impacts (0.68 ± 0.04) and similar in the sagittal (0.61 ± 0.06) and axial (0.61 ± 0.06) impacts. A summary of the wcCORA scores for all three subjects is shown in Figure 7. Exemplary nodal displacement-time histories for subject SONO-904 in the 40 rad/s, 60 ms cases are shown in the **Supplementary Materials**.

The tMRI simulations were run with the final calibrated material model to ensure that the addition of material non-linearity did not influence the strain prediction. As expected, the brain strain response in these simulations was dominated by the infinitesimal shear stiffness, which was optimized in the first stage of material calibration. The incorporation of material non-linearity had negligible effect on the MPS distribution since this second optimization was performed while maintaining the infinitesimal shear modulus previously calibrated.

The complex modulus, as a function of frequency, for the median stiffness response and softest ($\mu/\mu_{med} = 0.53$) and stiffest ($\mu/\mu_{med} = 1.53$) relative stiffness parts are shown in Figure 4. All three responses were within the range of experimental data. Finally, the median, softest ($\mu/\mu_{med} = 0.53$), and stiffest ($\mu/\mu_{med} = 1.53$) material responses were assessed in tension, compression, and simple shear loading at strain rates of 0.5, 5,

and 30 1/s and compared to experimental data (Figure 8; Jin et al., 2013). At the highest strain rate (30 1/s) and intermediate (5 1/s), the three material responses were like the experimental corridors for all three loading modes, simultaneously. At the lowest strain rate (0.5 1/s), the three material responses were similar to the experimental in compression but were stiffer in tension and shear.

DISCUSSION

In this study the heterogeneous CAB-20MSym template model was developed, calibrated, and extensively evaluated using a comprehensive set of experimental data that included measurements of material properties using *in vivo* MRE experiments (Hiscox et al., 2020), *in situ* brain displacement measured using sonomicrometry (Alshareef et al., 2020a), *in vivo* brain strain measured using tagged MRI (Knutsen et al., 2020), and *in vitro* material response (Jin et al., 2013; Meaney et al., 2014). In all assessments of model biofidelity, the CAB-20MSym template model demonstrated a high fidelity to the experimental data which represented a spectrum of TBI severity, ranging from non-injurious (tMRI cases) to moderate-to-severe TBI (sonomicrometry cases).

Our approach to implement heterogeneity using MRE data was selected for several reasons. This technique implemented material heterogeneity without significantly increasing the computational cost. Other studies have implemented heterogeneity using embedded beam elements to explicitly model the structural contributions of axonal fiber tracts (Garimella and Kraft, 2017; Garimella et al., 2019; Wu et al., 2019). However, this technique has been reported to increase the computational cost by a factor of 2.4. For the models developed to calibrate the material parameters, this would have increased the computational time for each simulation from approximately 15 to 36 h (simulating 200 ms of response). As such, the computational time required to run the battery of the 36 *in situ* brain deformation simulations (Alshareef et al., 2020a) would have increased from approximately 540 to 1300 h.

The relative stiffness approach was also chosen with consideration of effects specific to the MRE data. The MRE stiffness measurements we used were determined at a single frequency of 50 Hz, though brain tissue properties from MRE have been shown to be dependent on the actuation frequency due to the viscoelasticity of the brain (Sack et al., 2013). Thus, the specific shear stiffness values recovered at this frequency may not be most relevant for a TBI model. Furthermore, MRE measures tissue stiffness under micron-level displacements. Since the brain is a highly non-linear material, these stiffness results may not be applicable at the finite levels of deformation associated with TBI. Using relative stiffness minimizes any contributions these factors may have had on the absolute stiffness measurements.

There are also several limitations associated with the MRE-based approach. Firstly, although brain heterogeneity was represented as a function of tissue stiffness and not tissue type, the implementation was still isotropic as brain MRE measurements typically assume material isotropy, though methods for

TABLE 4 | wcCORA scores for $\mu_{0,med}$ joint optimization and verification.

Subject	wcCORA		
	X: 20–60	Y: 20–60	Z: 20–60*
SONO-896	0.67	0.67	0.58
SONO-900	0.72	0.63	0.69
SONO-904	0.66	0.50	0.60
SONO-Mean	0.68 ± 0.03	0.60 ± 0.09	0.62 ± 0.06

*Axial 20 rad/s, 60 ms (Z: 20–60) case used for calibration.

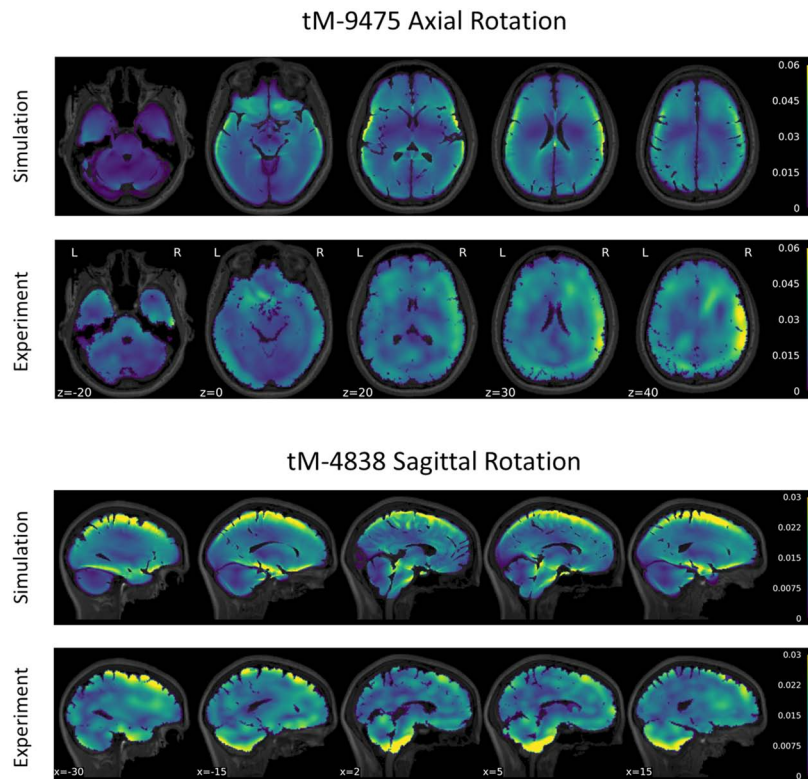


FIGURE 6 | Comparison of maximum principal strain distribution for subject tM-9475 under axial rotation (top) and tM-4838 under sagittal rotation (bottom).

extracting anisotropic properties are being developed (Romano et al., 2012; Tweten et al., 2015; McGarry et al., 2020; Smith et al., 2020). Secondly, it was assumed that the relative stiffnesses obtained from the micron-level displacements used in MRE were linear with strain, and that the heterogeneity observed in MRE was applicable for higher levels of deformation. While the validity of these assumptions is unclear, the verification of the brain response with these material parameters over a wide range of rotational loading conditions minimizes their significance.

An inverse FE approach was used to calibrate the material parameters of the heterogeneous CAB-20MSym template model using subject-specific models. However, three challenges faced by any iFE calibration problem are overfitting, obtaining a unique solution, and computational cost. The likelihood of overfitting and obtaining non-unique solutions in an optimization problem is typically increased by using an excessively complicated model (i.e., optimizing many material parameters) and an imbalance between the amount of data used to fit the model and the data used to validate the model (i.e., excessive training data). Furthermore, since one simulation is required for each test case, the computational cost of calibrating a material model increases significantly with the number of parameters included. Given that each simulation in this study took approximately 15 h to run, a robust and efficient approach to material calibration was required.

In the heterogeneous CAB-20MSym template model, each brain parenchyma material requires two parameters to describe

bulk properties (density, ρ and Poisson's ratio, ν), two parameters to describe deviatoric elastic properties (μ and α), and eight parameters to describe viscoelastic properties (g_1 – g_4 and β_1 – β_4), for a total of 12 parameters per material. Without further reduction, a full material calibration would require optimizing 120 parameters, which would likely result in non-unique solutions and the computational cost would be prohibitive. In this study, several assumptions were made to reduce the

TABLE 5 | Calibrated Ogden material parameters for each brain parenchyma part, grouped by stiffness relative to the median value.

Relative Stiffness	μ (kPa)	α
μ_{med}^a	0.337	6.67
$\mu/\mu_{med} = 0.53$	0.179	
$\mu/\mu_{med} = 0.64$	0.216	
$\mu/\mu_{med} = 0.75$	0.254	
$\mu/\mu_{med} = 0.86$	0.291	
$\mu/\mu_{med} = 0.97$	0.328	
$\mu/\mu_{med} = 1.08$	0.366	
$\mu/\mu_{med} = 1.20$	0.403	
$\mu/\mu_{med} = 1.31$	0.441	
$\mu/\mu_{med} = 1.42$	0.478	
$\mu/\mu_{med} = 1.53$	0.515	

^aNot physically represented in model.

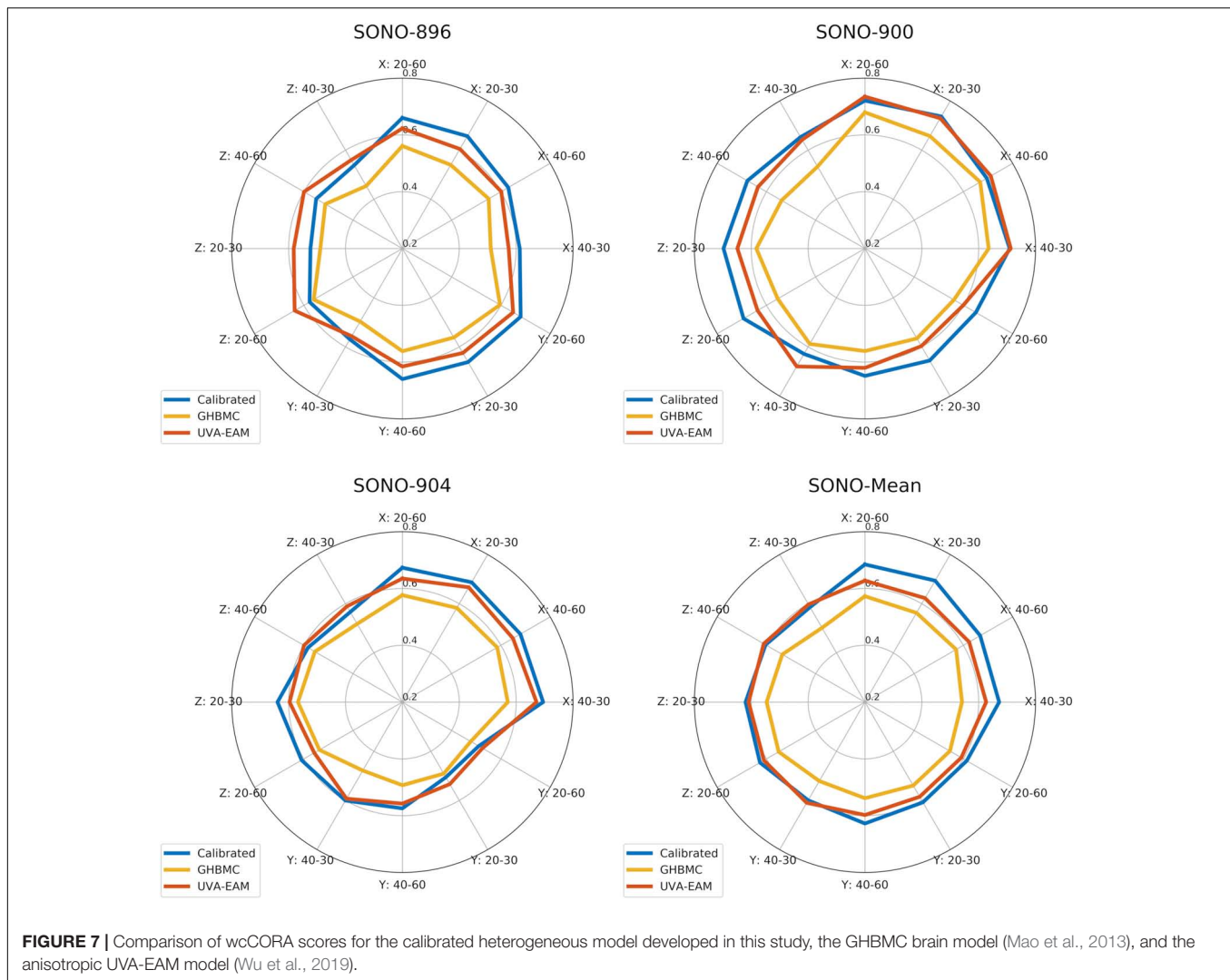
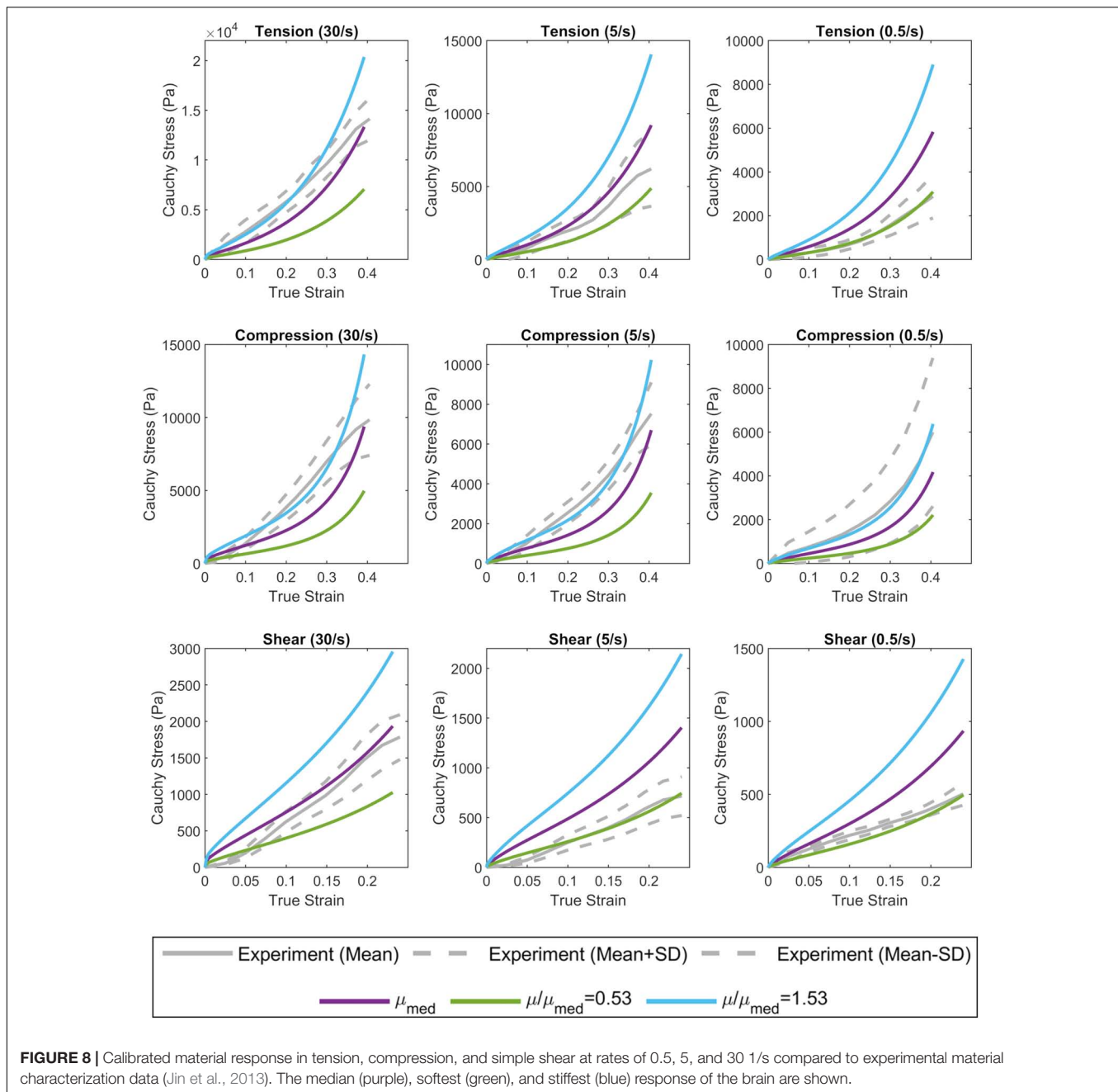


FIGURE 7 | Comparison of wCCORA scores for the calibrated heterogeneous model developed in this study, the GHBM brain model (Mao et al., 2013), and the anisotropic UVA-EAM model (Wu et al., 2019).

number of material parameters included in the optimization problem. First, all brain tissues were assumed to have the same density and Poisson's ratio, which is consistent with the TBI biomechanics literature and is common practice in FE brain modeling (Takhounts et al., 2008; Mao et al., 2013; Wu et al., 2019; Alshareef et al., 2020a). This reduced the number of material parameters from 120 to 100. By assuming homogeneous damping and non-linearity, the total number of variables calibrated in this study was reduced to 11 (μ for each material, and a single non-linearity coefficient, α). For the stiffness variables, each material was defined relative to the median value using experimental MRE data, further reducing the total number of calibrated parameters to 2 (μ_{med} and α). While non-linearity and viscoelastic properties of the brain have been shown to vary spatially throughout the brain (Johnson et al., 2016; Budday et al., 2017a,b, 2019; Hiscox et al., 2018), these are more challenging measurements and the extent to which viscoelasticity and elastic non-linearity vary remains an open question. These disparities are likely attributed to differences in experimental protocols, including tissue harvest sites, tissue hydration, and loading conditions

(Budday et al., 2019). The membranes implemented in the model (falx and tentorium) and CSF parts were not included in the optimization, as a preliminary sensitivity study indicated that the influences of the stiffness and damping of these structures on the deformation response was negligible, compared to the brain parenchyma parts.

We used a combined optimization to calibrate the median shear stiffness and non-linear coefficient, as opposed to an individual calibration for each of the three subjects. The objective of the study was to obtain a singular set of optimal material parameters to be used in the CAB-20MSym template model. Subject-specific material properties could have been combined (e.g., averaged), however, due to the highly non-linear nature of this optimization problem this may not have yielded an optimal solution for the CAB-20MSym template model. Nonetheless, the calibration process indicated that the three subjects likely had different underlying material properties (Figure 5). For example, the estimated optimal median shear moduli for subjects SONO-896, SONO-900, and SONO-904 were approximately 0.70, 1.18, and 2.05 kPa, respectively. A simple average of these values



would have resulted in an “optimal” shear modulus of 1.31 kPa, compared to 1.13 kPa determined by the optimization which maximized wcCORA. An important limitation was that only three elderly (57–67 years), cadaveric subjects were used in the optimization process due to the availability of experimental brain deformation data. However, the calibrated model demonstrated a biofidelic response when verified using the *in vivo* tMRI dataset, which included younger, living subjects between 21 and 42 years of age (Knutsen et al., 2020). Nonetheless, the calibrated material parameters may not be representative of the general population and this calibration should be repeated once brain deformation data for more specimens is available. It should also

be noted that since these material parameters were obtained using an inverse FE process, they are model specific and cannot be arbitrarily applied to other models (Giudice et al., 2019b). However, given that the calibrated materials have been verified using experimental material characterization data, it is very likely that they represent the underlying material response, and not the contributions of the numerical implementation. Nonetheless, if implemented in another model, the deformation response should be thoroughly investigated prior to model deployment.

The final calibrated material model was verified by its response to experimental tissue data from multiple sources. The complex modulus of the calibrated materials and the response in tension,

compression, and simple shear were compared to experimental material characterization data for cortical tissue. In both assessments, the median, softest, and stiffest material responses in the calibrated CAB-20MSym template model were similar to the experimental data, verifying that the material parameters obtained from the iFE calibration were physically meaningful and representative of the underlying tissue. In these comparisons, the full range of material response was compared to the experimental data to account for the fact that the experimental data may not necessarily represent the median response of the brain.

The biofidelity of the calibrated CAB-20MSym template model was assessed using brain deformation data from the experiments conducted by Alshareef et al. (2018, 2020a) and Knutsen et al. (2020). Collectively, these datasets encapsulated various magnitudes (2.5–40 rad/s), durations (30–60 ms), and directions of rotational loading (coronal, sagittal, axial). The model demonstrated biofidelic responses under the test conditions used by Alshareef et al. Interestingly, differences in wcCORA scores across subjects reflected the subject-specific relationships between material properties and wcCORA scores in the optimization process. For example, wcCORA scores for SONO-900 were generally greater than those for SONO-896. In the material calibration process, the estimated optimal material properties for SONO-900 were similar to the joint optimal value ($\mu_{0,med} = 1.18$ kPa), whereas the estimated optimal material properties for SONO-896 were softer ($\mu_{0,med} \approx 0.7$ kPa). The opposite was true for SONO-904 ($\mu_{0,med} \approx 2.0$ kPa). These differences in calibrated parameters likely reflect variability in material properties between these specimens. While variation in material parameters is to be expected, future work is required to quantify this variability across larger populations. This may be an important factor as subject-specific models of the brain become more prominent in research and clinical applications. Moving forward, the MRE-based framework used to implement material heterogeneity in this study will be adapted to incorporate subject-specific material properties in future models that consider the entire subject-specific brain structure. While the CAB-20MSym template model demonstrated a biofidelic response under the loading conditions investigated in this study, additional verification is required if the model is exercised under loading conditions that deviate from those used in the current study (e.g., blast loading or micron-level harmonic displacements).

While a high-resolution measurement of brain strain at injurious loading conditions is not available, assessing the biofidelity of a brain model's strain prediction using low severity, non-injurious loading conditions can improve the confidence of a model's strain response. In general, the CAB-20MSym demonstrated good biofidelity under the axial and sagittal tMRI cases compared to the experimental data. However, there were some discrepancies between the model and experimental results, particularly in the volume fraction exceeding 2% strain. These differences could have been attributed to several factors. Firstly, in the experimental tMRI data set, only resultant head cradle kinematics were recorded. Therefore, to simulate these experiments it was assumed that the head was perfectly coupled to the head cradle and that the applied rotational head kinematics

were perfectly uniaxial (either axial or sagittal). While the head was tightly coupled to the head cradle, it is possible that there were slight discrepancies between the head kinematics in the experiments and simulations. Secondly, the brain-skull interface was implemented by modeling the CSF layer between the brain and skull. While many approaches have been investigated to model this interface (Wang et al., 2018), the relative motion between the brain and skull is not well characterized and there is no consensus on best modeling practices for this interface. Therefore, discrepancies between the relative skull-brain motion in the simulations and experiments could have contributed to the observed differences in volume fraction and deformation fields, especially in these low deformation impacts. Furthermore, the brainstem of the CAB-20MSym template model was truncated at the foramen magnum due to a lack of MRE data in the inferior portions of the brainstem and superior portions of the spinal cord. This may have attributed to some of the observed differences, especially in the inferior regions of the brain. However, since the deformations induced in these experiments were small, it is possible that these factors had an exaggerated effect on the predicted strains, and it is not clear how these effects translate to larger deformation cases. Finally, while tMRI is a well-established imaging technique, it can be susceptible to experimental error (approximately 0.7% strain, introduced during filtering or interpolation), which could affect these low strain measurements and the resulting 2% strain volume fractions (Gomez et al., 2019). Nonetheless, the overall biofidelity of the CAB-20MSym template model's strain prediction under these low severity loading conditions was satisfactory.

Summary

In this study, the CAB-20MSym template model was developed, calibrated, and extensively verified over a wide range of rotational head kinematic loading conditions. This model utilized a computationally efficient approach for incorporating material heterogeneity that leveraged data from a MRE template image that represented the average brain stiffness of 134 healthy adult subjects. Overall, the developed model demonstrated a biofidelic response for both nodal displacement and element strain metrics. Moving forward this template model will serve as the foundation of the registration-based morphing pipeline developed by Giudice et al. (2020) and can serve as an anatomically accurate model for further investigations of TBI mechanisms and to aid the development of novel protective equipment and safety countermeasures. Furthermore, the framework for implementing material heterogeneity using MRE data can be adapted to incorporate subject-specific material properties in future models of the brain.

DATA AVAILABILITY STATEMENT

Publicly available datasets were analyzed in this study. This data can be found here: NKI-RS:

http://fcon_1000.projects.nitrc.org/indi/enhanced/; MRE-134 Template: <https://github.com/mechneurolab/mre134>; *In Situ Brain Deformation*: <https://www.nhtsa.gov/research-data/databases-and-software>.

AUTHOR CONTRIBUTIONS

All authors contributed to the conception, design, and interpretation of results presented in this study and are accountable for all aspects of this work.

REFERENCES

- Alshareef, A., Giudice, J. S., Forman, J., Salzar, R. S., and Panzer, M. B. (2018). A novel method for quantifying human in situ whole brain deformation under rotational loading using sonomicrometry. *J. Neurotrauma* 35, 780–789. doi: 10.1089/neu.2017.5362
- Alshareef, A., Giudice, J. S., Forman, J., Shedd, D. F., Reynier, K. A., Wu, T., et al. (2020a). Biomechanics of the human brain during dynamic rotation of the head. *J. Neurotrauma* 37, 1546–1555. doi: 10.1089/neu.2019.6847
- Alshareef, A., Giudice, J. S., Forman, J., Shedd, D. F., Wu, T., Reynier, K. A., et al. (2020b). Application of trilateration and Kalman filtering algorithms to track dynamic brain deformation using sonomicrometry. *Biomed. Signal Process. Control* 56:10. doi: 10.1016/j.bspc.2019.101691
- Arbogast, K. B., and Margulies, S. S. (1998). Material characterization of the brainstem from oscillatory shear tests. *J. Biomech.* 31, 801–807. doi: 10.1016/S0021-9290(98)00068-2
- Arbogast, K. B., Thibault, K. L., Pinheiro, B. S., Winey, K. I., and Margulies, S. S. (1997). A high-frequency shear device for testing soft biological tissues. *J. Biomech.* 30, 757–759. doi: 10.1016/s0021-9290(97)00023-7
- Avants, B., Epstein, C., Grossman, M., and Gee, J. (2008). Symmetric diffeomorphic image registration with cross-correlation: evaluating automated labeling of elderly and neurodegenerative brain. *Med. Image Anal.* 12, 26–41. doi: 10.1016/j.media.2007.06.004
- Bilston, L. E., Liu, Z., and Phan-Thien, N. (1997). Linear viscoelastic properties of bovine brain tissue in shear. *Biorheology* 34, 377–385. doi: 10.1016/s0006-355x(98)00022-5
- Bilston, L. E., Liu, Z., and Phan-Thien, N. (2001). Large strain behaviour of brain tissue in shear: some experimental data and differential constitutive model. *Biorheology* 38, 335–345.
- Brands, D. A. (2000). The large shear strain dynamic behavior of in-vitro porcine brain tissue and a silicone gel model material. *Stapp Car Crash J.* 44, 249–260.
- Budday, S., Nay, R., de Rooij, R., Steinmann, P., Wyrobek, T., Ovaert, T. C., et al. (2015). Mechanical properties of gray and white matter brain tissue by indentation. *J. Mech. Behav. Biomed. Mater.* 46, 318–330. doi: 10.1016/j.jmbbm.2015.02.024
- Budday, S., Ovaert, T. C., Holzapfel, G. A., Steinmann, P., and Kuhl, E. (2019). Fifty shades of brain: a review on the mechanical testing and modeling of brain tissue. *Arch. Comput. Methods Eng.* 27, 1187–1230. doi: 10.1007/s11831-019-09352-w
- Budday, S., Sommer, G., Birk, C., Langkammer, C., Haybaeck, J., Kohnert, J., et al. (2017a). Mechanical characterization of human brain tissue. *Acta Biomater.* 48, 319–340. doi: 10.1016/j.actbio.2016.10.036
- Budday, S., Sommer, G., Haybaeck, J., Steinmann, P., Holzapfel, G. A., and Kuhl, E. (2017b). Rheological characterization of human brain tissue. *Acta Biomater.* 60, 315–329. doi: 10.1016/j.actbio.2017.06.024
- Centers for Disease Control and Prevention (2015). “Report to congress on traumatic brain injury in the united states: epidemiology and rehabilitation,” in *National Center for Injury Prevention and Control. Presented at the Division of Unintentional Injury Prevention*, (Atlanta, GA: Centers for Disease Control and Prevention), 1–72. Available online at: https://www.cdc.gov/traumaticbraininjury/pdf/TBI_Report_to_Congress_Epi_and_Rehab-a.pdf

ACKNOWLEDGMENTS

The authors gratefully acknowledge the Achievement Rewards for Collegiate Scientists (ARCS) Foundation and the UVA Brain Institute for supporting this research.

SUPPLEMENTARY MATERIAL

The Supplementary Material for this article can be found online at: <https://www.frontiersin.org/articles/10.3389/fbioe.2021.664268/full#supplementary-material>

- Darvish, K. K., and Crandall, J. R. (2001). Nonlinear viscoelastic effects in oscillatory shear deformation of brain tissue. *Med. Eng. Phys.* 23, 633–645. doi: 10.1016/S1350-4533(01)00101-1
- Dixit, P., and Liu, G. R. (2017). A review on recent development of finite element models for head injury simulations. *Arch. Comput. Methods Eng.* 24, 979–1031. doi: 10.1007/s11831-016-9196-x
- Fahlstedt, M., Abayazid, F., Panzer, M. B., Trotta, A., Zhao, W., Ghajari, M., et al. (2021). Ranking and rating bicycle helmet safety performance in oblique impacts using eight different brain injury models. *Ann. Biomed. Eng.* 49, 1097–1109. doi: 10.1007/s10439-020-02703-w
- Fallenstein, G. T., Hulse, V. D., and Melvin, J. W. (1969). Dynamic mechanical properties of human brain tissue. *J. Biomechan.* 2, 217–226. doi: 10.1016/0021-9290(69)90079-7
- Faul, M., and Coronado, V. (2015). *Epidemiology of Traumatic Brain Injury*, in: *Handbook of Clinical Neurology*. Amsterdam: Elsevier, 3–13.
- Franceschini, G., Bigoni, D., Regitnig, P., and Holzapfel, G. A. (2006). Brain tissue deforms similarly to filled elastomers and follows consolidation theory. *J. Mech. Phys. Solids* 54, 2592–2620. doi: 10.1016/j.jmps.2006.05.004
- Fung, Y. (1993). *Biomechanics: Mechanical Properties of Living Tissues*. Berlin: Springer Science & Business Media.
- Gabler, L. F., Crandall, J. R., and Panzer, M. B. (2016). Assessment of kinematic brain injury metrics for predicting strain responses in diverse automotive impact conditions. *Ann. Biomed. Eng.* 44, 3705–3718. doi: 10.1007/s10439-016-1697-0
- Gabler, L. F., Crandall, J. R., and Panzer, M. B. (2018). Development of a second-order system for rapid estimation of maximum brain strain. *Ann. Biomed. Eng.* 47, 1971–1981. doi: 10.1007/s10439-018-02179-9
- Garimella, H. T., and Kraft, R. H. (2017). Modeling the mechanics of axonal fiber tracts using the embedded finite element method: axonal fiber mechanics using the embedded element method. *Int. J. Numer. Methods Biomed. Eng.* 33:e2823. doi: 10.1002/cnm.2823
- Garimella, H. T., Menghani, R. R., Gerber, J. I., Sridhar, S., and Kraft, R. H. (2019). Embedded finite elements for modeling axonal injury. *Ann. Biomed. Eng.* 47, 1889–1907. doi: 10.1007/s10439-018-02166-0
- Garo, A., Hrapko, M., Van Dommelen, J. A. W., and Peters, G. W. M. (2007). Towards a reliable characterisation of the mechanical behaviour of brain tissue: the effects of post-mortem time and sample preparation. *Biorheology* 44, 51–58.
- Gehre, C., Gades, H., and Wernicke, P. (2009). “Objective rating of signals using test and simulation responses,” in *Proceedings of the 21st International Technical Conference on the Enhanced Safety of Vehicles*, (Stuttgart).
- Ghajari, M., Hellyer, P. J., and Sharp, D. J. (2017). Computational modelling of traumatic brain injury predicts the location of chronic traumatic encephalopathy pathology. *Brain* 140, 333–343. doi: 10.1093/brain/aww317
- Giordano, C., and Kleiven, S. (2014). Evaluation of axonal strain as a predictor for mild traumatic brain injuries using finite element modeling. *Stapp. Car Crash J.* 58:29.
- Giudice, J. S., Alshareef, A., Wu, T., Gancayco, C. A., Reynier, K. A., Tustison, N. J., et al. (2020). An image registration-based morphing technique for generating subject-specific brain finite element models. *Ann. Biomed. Eng.* 48, 2412–2424. doi: 10.1007/s10439-020-02584-z

- Giudice, J. S., Park, G., Kong, K., Bailey, A., Kent, R., and Panzer, M. B. (2019a). Development of open-source dummy and impactor models for the assessment of american football helmet finite element models. *Ann. Biomed. Eng.* 47, 464–474. doi: 10.1007/s10439-018-02155-3
- Giudice, J. S., Zeng, W., Wu, T., Alshareef, A., Shedd, D. F., and Panzer, M. B. (2019b). An analytical review of the numerical methods used for finite element modeling of traumatic brain injury. *Ann. Biomed. Eng.* 47, 1855–1872. doi: 10.1007/s10439-018-02161-5
- Gomez, A. D., Knutsen, A. K., Xing, F., Lu, Y.-C., Chan, D., Pham, D. L., et al. (2019). 3-D measurements of acceleration-induced brain deformation via harmonic phase analysis and finite-element models. *IEEE Trans. Biomed. Eng.* 66, 1456–1467. doi: 10.1109/TBME.2018.2874591
- Hajjaghammar, M., Wu, T., Panzer, M. B., and Margulies, S. S. (2019). Embedded axonal fiber tracts improve finite element model predictions of traumatic brain injury. *Biomech. Model. Mechanobiol.* 19, 1109–1130. doi: 10.1007/s10237-019-01273-8
- Hiscox, L. V., Johnson, C. L., McGarry, M. D. J., Perrins, M., Littlejohn, A., van Beek, E. J. R., et al. (2018). High-resolution magnetic resonance elastography reveals differences in subcortical gray matter viscoelasticity between young and healthy older adults. *Neurobiol. Aging* 65, 158–167. doi: 10.1016/j.neurobiolaging.2018.01.010
- Hiscox, L. V., McGarry, M. D., Schwarb, H., Van Houten, E. E., Pohlig, R. T., Roberts, N., et al. (2020). Standard-space atlas of the viscoelastic properties of the human brain. *Hum. Brain Mapp.* 41, 5282–5300. doi: 10.1002/hbm.25192
- Hiscox, L. V., Johnson, C. L., Barnhill, E., McGarry, M. D., Huston, J. III, Van Beek, E. J., et al. (2016). MRE of the human brain: technique, findings and clinical applications. *Phys. Med. Biol.* 61:R401.
- Horgan, T. J., and Gilchrist, M. D. (2003). The creation of three-dimensional finite element models for simulating head impact biomechanics. *Int. J. Crashworthiness* 8, 353–366. doi: 10.1533/ijcr.2003.0243
- Hrapko, M., Van Dommelen, J. A. W., Peters, G. W. M., and Wismans, J. (2006). The mechanical behaviour of brain tissue: large strain response and constitutive modelling. *Biorheology* 43, 623–636.
- Ji, S., Zhao, W., Ford, J. C., Beckwith, J. G., Bolander, R. P., Greenwald, R. M., et al. (2015). Group-Wise evaluation and comparison of white matter fiber strain and maximum principal strain in sports-related concussion. *J. Neurotrauma* 32, 441–454. doi: 10.1089/neu.2013.3268
- Jin, X., Zhu, F., Mao, H., Shen, M., and Yang, K. H. (2013). A comprehensive experimental study on material properties of human brain tissue. *J. Biomech.* 46, 2795–2801. doi: 10.1016/j.jbiomech.2013.09.001
- Johnson, C. L., McGarry, M. D., Gharibans, A. A., Weaver, J. B., Paulsen, K. D., Wang, H., et al. (2013a). Local mechanical properties of white matter structures in the human brain. *Neuroimage* 79, 145–152. doi: 10.1016/j.neuroimage.2013.04.089
- Johnson, C. L., McGarry, M. D., Van Houten, E. E., Weaver, J. B., Paulsen, K. D., Sutton, B. P., et al. (2013b). Magnetic resonance elastography of the brain using multishot spiral readouts with self-navigated motion correction. *Magn. Reson. Med.* 70, 404–412. doi: 10.1002/mrm.24473
- Johnson, C. L., Schwarb, H., McGarry, M. D. J., Anderson, A. T., Huesmann, G. R., Sutton, B. P., et al. (2016). Viscoelasticity of subcortical gray matter structures. *Hum. Brain Mapp.* 37, 4221–4233. doi: 10.1002/hbm.23314
- Johnson, C. L., and Telzer, E. H. (2018). Magnetic resonance elastography for examining developmental changes in the mechanical properties of the brain. *Dev. Cogn. Neurosci.* 33, 176–181. doi: 10.1016/j.dcn.2017.08.010
- Kaster, T., Sack, I., and Samani, A. (2011). Measurement of the hyperelastic properties of ex vivo brain tissue slices. *J. Biomech.* 44, 1158–1163. doi: 10.1016/j.jbiomech.2011.01.019
- Kimpara, H., Nakahira, Y., Iwamoto, M., Miki, K., Ichihara, K., and Kawano, S. (2006). Investigation of anteroposterior head-neck responses during severe frontal impacts using a brain-spinal cord complex FE model. *Stapp. Car Crash J.* 50:509.
- Kleiven, S. (2007). Predictors for traumatic brain injuries evaluated through accident reconstructions. *Stapp. Car Crash J.* 51, 81–114.
- Kleiven, S., and von Holst, H. (2002). Consequences of head size following trauma to the human head. *J. Biomech.* 35, 153–160. doi: 10.1016/s0021-9290(01)00202-0
- Knutsen, A. K., Gomez, A. D., Gangolli, M., Wang, W.-T., Chan, D., Lu, Y.-C., et al. (2020). In vivo estimates of axonal stretch and 3D brain deformation during mild head impact. *Brain Multiphysics* 1:100015. doi: 10.1016/j.brain.2020.100015
- Lippert, S. A., Rang, E. M., and Grimm, M. J. (2004). The high frequency properties of brain tissue. *Biorheology* 41, 681–691.
- Mao, H., Zhang, L., Jiang, B., Genthikatti, V. V., Jin, X., Zhu, F., et al. (2013). Development of a finite element human head model partially validated with thirty five experimental cases. *J. Biomech. Eng.* 135:111002. doi: 10.1115/1.4025101
- McAllister, T. W., Ford, J. C., Ji, S., Beckwith, J. G., Flashman, L. A., Paulsen, K., et al. (2012). Maximum principal strain and strain rate associated with concussion diagnosis correlates with changes in corpus callosum white matter indices. *Ann. Biomed. Eng.* 40, 127–140. doi: 10.1007/s10439-011-0402-6
- McGarry, M. D., Van Houten, E., Guertler, C., Okamoto, R. J., Smith, D. R., Sowinski, D. R., et al. (2020). A heterogeneous, time harmonic, nearly incompressible transverse isotropic finite element brain simulation platform for MR elastography. *Phys. Med. Biol.* doi: 10.1088/1361-6560/ab9a84 [Epub ahead of print].
- Meaney, D. F., Morrison, B., and Bass, C. D. (2014). The mechanics of traumatic brain injury: a review of what we know and what we need to know for reducing its societal burden. *J. Biomech. Eng.* 136:021008.
- Miller, K., and Chinzei, K. (2002). Mechanical properties of brain tissue in tension. *J. Biomech.* 35, 483–490. doi: 10.1016/S0021-9290(01)00234-2
- Miller, L. E., Urban, J. E., and Stitzel, J. D. (2016). Development and validation of an atlas-based finite element brain model. *Biomech. Model. Mechanobiol.* 15, 1201–1214. doi: 10.1007/s10237-015-0754-1
- Miller, L. E., Urban, J. E., and Stitzel, J. D. (2017). Validation performance comparison for finite element models of the human brain. *Comput. Methods Biomech. Biomed. Eng.* 20, 1273–1288. doi: 10.1080/10255842.2017.1340462
- Moran, R., Smith, J. H., and García, J. J. (2014). Fitted hyperelastic parameters for human brain tissue from reported tension, compression, and shear tests. *J. Biomech.* 47, 3762–3766. doi: 10.1016/j.jbiomech.2014.09.030
- Murphy, M. C., Huston, J. III, and Ehman, R. L. (2019). MR elastography of the brain and its application in neurological diseases. *NeuroImage* 187, 176–183. doi: 10.1016/j.neuroimage.2017.10.008
- Nicolle, S., Lounis, M., and Willinger, R. (2004). Shear properties of brain tissue over a frequency range relevant for automotive impact situations: new experimental results. *Stapp. Car Crash J.* 48, 239–258.
- Ogden, R. W., and Hill, R. (1972). Large deformation isotropic elasticity – on the correlation of theory and experiment for incompressible rubberlike solids. *Proc. R. Soc. Lond. Math. Phys. Sci.* 326, 565–584. doi: 10.1098/rspa.1972.0026
- Panzer, M. B., Myers, B. S., Capehart, B. P., and Bass, C. R. (2012). Development of a finite element model for blast brain injury and the effects of CSF cavitation. *Ann. Biomed. Eng.* 40, 1530–1544. doi: 10.1007/s10439-012-0519-2
- Reynier, K. A., Alshareef, A., Sanchez, E. J., Shedd, D. F., Walton, S. R., Erdman, N. K., et al. (2020). The effect of muscle activation on head kinematics during non-injurious head impacts in human subjects. *Ann. Biomed. Eng.* 48, 2751–2762. doi: 10.1007/s10439-020-02609-7
- Romano, A., Scheel, M., Hirsch, S., Braun, J., and Sack, I. (2012). In vivo waveguide elastography of white matter tracts in the human brain. *Magn. Reson. Med.* 68, 1410–1422. doi: 10.1002/mrm.24141
- Sack, I., Jöhrens, K., Würfel, J., and Braun, J. (2013). Structure-sensitive elastography: on the viscoelastic powerlaw behavior of in vivo human tissue in health and disease. *Soft. Matter* 9, 5672–5680. doi: 10.1039/c3sm50552a
- Shen, F., Tay, T. E., Li, J. Z., Nigen, S., Lee, P. V. S., and Chan, H. K. (2006). Modified Bilston nonlinear viscoelastic model for finite element head injury studies. *J. Biomech. Eng.* 128, 797–801. doi: 10.1115/1.2264393
- Shuck, L. Z., and Advani, S. H. (1972). Rheological response of human brain tissue in shear. *J. Basic Eng.* 94, 905–911. doi: 10.1115/1.3425588
- Smith, D. R., Guertler, C. A., Okamoto, R. J., Romano, A. J., Bayly, P. V., and Johnson, C. L. (2020). Multi-Excitation magnetic resonance elastography of the brain: wave propagation in anisotropic white matter. *J. Biomech. Eng.* 142:071005.
- Takhounts, E. G., Ridella, S. A., Hasija, V., Tannous, R. E., Campbell, J. Q., Malone, D., et al. (2008). Investigation of traumatic brain injuries using the next generation of simulated injury monitor (SIMon) finite element head model. *Stapp. Car Crash J.* 52, 1–31. doi: 10.1155/2015/837585

- Tweten, D. J., Okamoto, R. J., Schmidt, J. L., Garbow, J. R., and Bayly, P. V. (2015). Estimation of material parameters from slow and fast shear waves in an incompressible, transversely isotropic material. *J. Biomech.* 48, 4002–4009. doi: 10.1016/j.jbiomech.2015.09.009
- Wang, F., Han, Y., Wang, B., Peng, Q., Huang, X., Miller, K., et al. (2018). Prediction of brain deformations and risk of traumatic brain injury due to closed-head impact: quantitative analysis of the effects of boundary conditions and brain tissue constitutive model. *Biomechan. Model. Mechanobiol.* 17, 1165–1185. doi: 10.1007/s10237-018-1021-z
- Weaver, J. B., Pattison, A. J., McGarry, M. D., Perreard, I. M., Swienckowski, J. G., Eskey, C. J., et al. (2012). Brain mechanical property measurement using MRE with intrinsic activation. *Phys. Med. Biol.* 57:7275. doi: 10.1088/0031-9155/57/22/7275
- Weickenmeier, J., de Rooij, R., Budday, S., Steinmann, P., Ovaert, T. C., and Kuhl, E. (2016). Brain stiffness increases with myelin content. *Acta Biomater.* 42, 265–272. doi: 10.1016/j.actbio.2016.07.040
- Wu, T., Alshareef, A., Giudice, J. S., and Panzer, M. B. (2019). Explicit modeling of white matter axonal fiber tracts in a finite element brain model. *Ann. Biomed. Eng.* 47, 1908–1922. doi: 10.1007/s10439-019-02239-8
- Wu, T., Antona-Makoshi, J., Alshareef, A., Giudice, J. S., and Panzer, M. B. (2020). Investigation of cross-species scaling methods for traumatic brain injury using finite element analysis. *J. Neurotrauma* 37, 410–422. doi: 10.1089/neu.2019.6576
- Wu, T., Hajiaghameh, M., Giudice, J. S., Alshareef, A., Margulies, S., and Panzer, M. B. (2021). Evaluation of tissue-level brain injury metrics using species-specific simulations. *J. Neurotrauma Neu.* 2020:7445. doi: 10.1089/neu.2020.7445

Conflict of Interest: The authors declare that the research was conducted in the absence of any commercial or financial relationships that could be construed as a potential conflict of interest.

Copyright © 2021 Giudice, Alshareef, Wu, Knutsen, Hiscox, Johnson and Panzer. This is an open-access article distributed under the terms of the Creative Commons Attribution License (CC BY). The use, distribution or reproduction in other forums is permitted, provided the original author(s) and the copyright owner(s) are credited and that the original publication in this journal is cited, in accordance with accepted academic practice. No use, distribution or reproduction is permitted which does not comply with these terms.



Real-Time Multifrequency MR Elastography of the Human Brain Reveals Rapid Changes in Viscoelasticity in Response to the Valsalva Maneuver

Helge Herthum¹, Mehrgan Shahryari², Heiko Tzschätzsch², Felix Schrank², Carsten Warmuth², Steffen Görner², Stefan Hetzer³, Hennes Neubauer², Josef Pfeuffer⁴, Jürgen Braun¹ and Ingolf Sack^{2*}

¹ Institute of Medical Informatics, Charité – Universitätsmedizin Berlin, Corporate Member of Freie Universität Berlin, Humboldt-Universität zu Berlin, and Berlin Institute of Health, Berlin, Germany, ² Department of Radiology, Charité – Universitätsmedizin Berlin, Corporate Member of Freie Universität Berlin, Humboldt-Universität zu Berlin, and Berlin Institute of Health, Berlin, Germany, ³ Berlin Center for Advanced Neuroimaging (BCAN), Berlin, Germany, ⁴ Application Development, Siemens Healthcare GmbH, Erlangen, Germany

OPEN ACCESS

Edited by:

Silvia Budday,
University of Erlangen Nuremberg,
Germany

Reviewed by:

Mehmet Kurt,
Stevens Institute of Technology,
United States
Lucy Hiscox,
University of Delaware, United States

*Correspondence:

Ingolf Sack
ingolf.sack@charite.de

Specialty section:

This article was submitted to
Biomechanics,
a section of the journal
Frontiers in Bioengineering and
Biotechnology

Received: 10 February 2021

Accepted: 07 April 2021

Published: 05 May 2021

Citation:

Herthum H, Shahryari M,
Tzschätzsch H, Schrank F,
Warmuth C, Görner S, Hetzer S,
Neubauer H, Pfeuffer J, Braun J and
Sack I (2021) Real-Time
Multifrequency MR Elastography
of the Human Brain Reveals Rapid
Changes in Viscoelasticity
in Response to the Valsalva
Maneuver.
Front. Bioeng. Biotechnol. 9:666456.
doi: 10.3389/fbioe.2021.666456

Modulation of cerebral blood flow and vascular compliance plays an important role in the regulation of intracranial pressure (ICP) and also influences the viscoelastic properties of brain tissue. Therefore, magnetic resonance elastography (MRE), the gold standard for measuring *in vivo* viscoelasticity of brain tissue, is potentially sensitive to cerebral autoregulation. In this study, we developed a multifrequency MMRE technique that provides serial maps of viscoelasticity at a frame rate of nearly 6 Hz without gating, i.e., in quasi-real time (rt-MMRE). This novel method was used to monitor rapid changes in the viscoelastic properties of the brains of 17 volunteers performing the Valsalva maneuver (VM). rt-MMRE continuously sampled externally induced vibrations comprising three frequencies of 30.03, 30.91, and 31.8 Hz were over 90 s using a steady-state, spiral-readout gradient-echo sequence. Data were processed by multifrequency dual elasto-visco (MDEV) inversion to generate maps of magnitude shear modulus $|G^*|$ (stiffness) and loss angle φ at a frame rate of 5.4 Hz. As controls, the volunteers were examined to study the effects of breath-hold following deep inspiration and breath-hold following expiration. We observed that $|G^*|$ increased while φ decreased due to VM and, less markedly, due to breath-hold in inspiration. Group mean VM values showed an early overshoot of $|G^*|$ 2.4 ± 1.2 s after the onset of the maneuver with peak values of 6.7 ± 4.1 % above baseline, followed by a continuous increase in stiffness during VM. A second overshoot of $|G^*|$ occurred 5.5 ± 2.0 s after the end of VM with peak values of 7.4 ± 2.8 % above baseline, followed by 25-s sustained recovery until the end of image acquisition. φ was constantly reduced by approximately 2% during the entire VM without noticeable peak values. This is the first report of viscoelasticity changes in brain tissue induced by physiological maneuvers known to alter ICP and detected by clinically applicable rt-MMRE. Our results show that apnea and VM slightly alter brain properties toward a more rigid-solid behavior. Overshooting stiffening reactions seconds after onset and end of VM reveal rapid autoregulatory processes of brain tissue viscoelasticity.

Keywords: real-time multifrequency MRE, cerebral autoregulation, Valsalva maneuver, stiffness, viscoelasticity

INTRODUCTION

A balance of intracranial mechanical properties is of crucial importance for normal brain function (Linninger et al., 2005; Guyton and Hall, 2006; Wagshul et al., 2006; Schmid Daners et al., 2012). Shear modulus and bulk modulus of brain tissue influence cerebrovascular compliance and pulsatility as well as intracranial pressure (ICP) (Giulioni et al., 1988; Greitz et al., 1992; Wagshul et al., 2011; Parker, 2017). While shear modulus can be measured non-invasively by magnetic resonance elastography (MRE) (Hirsch et al., 2017), there is currently no method for direct ICP measurement without an intervention or without making model assumptions (Guyton and Hall, 2006). In complex multiphasic mechanical systems such as the brain, shear modulus and pressure are linked through poroelastic interactions between the fluid and solid spaces (Bilston, 2002; Tully and Ventikos, 2011; Parker, 2014). Thus, it is likely that regulation of ICP, which is one of the most important vital functions of intracranial mechanics, also affects shear viscoelasticity (Perrinez et al., 2009; McGarry et al., 2015; Lilaj et al., 2020). However, this mechanical component of cerebral autoregulation is largely unstudied due to a lack of imaging techniques that can measure cerebral shear modulus *in vivo* with high spatial and temporal resolution.

In the past, cerebral MRE was used to study a wide variety of physiological effects or diseases which affect the *in vivo* shear modulus of brain tissue (Hiscox et al., 2016; Yin et al., 2018). It has been shown that the brain becomes softer during normal aging (Sack et al., 2009; Arani et al., 2015) or pathophysiological processes such as neuroinflammation (Riek et al., 2012; Wang et al., 2019), demyelination (Schregel et al., 2012), or neurodegeneration (Murphy et al., 2012; Munder et al., 2018). In patients, brain softening has been observed in a wide set of neuronal disorders including multiple sclerosis (Wuerfel et al., 2010; Fehlnner et al., 2016), Alzheimer's disease (Murphy et al., 2011; Murphy et al., 2016; Gerischer et al., 2018), Parkinson's disease (Lipp et al., 2013, 2018) and normal pressure hydrocephalus (Streitberger et al., 2011; Juge et al., 2016; Murphy et al., 2020). Brain tumors can be either softer or stiffer than normal tissue (Simon et al., 2013; Jamin et al., 2015; Reiss-Zimmermann et al., 2015), while malignant tumors have reduced viscosity (Streitberger et al., 2014; Schregel et al., 2018; Streitberger et al., 2020). A higher stiffness of neural tissue has been associated with increased perfusion pressure (Chatelin et al., 2015; Hetzer et al., 2018, 2019; Bertalan et al., 2019a), ICP (Hatt et al., 2015; Arani et al., 2018), formation of cytotoxic edema in dying animals (Weickenmeier et al., 2018; Bertalan et al., 2020), proliferation of neurons (Klein et al., 2014), neuronal activity (Patz et al., 2019; Lan et al., 2020), and brain maturation (Guo et al., 2019). All of these studies have revealed that brain viscoelasticity can change within minutes (perfusion alterations), weeks (brain maturation in mice), or years (aging, disease progression). However, requiring several minutes of data acquisition, conventional MRE is limited in resolving non-periodic rapid processes such as cerebral autoregulation and ICP alterations which cannot be consistently repeated in volunteers.

Faster techniques including time-harmonic ultrasound elastography (Tzschatzsch et al., 2018; Kreft et al., 2020) and real-time MRE (rt-MRE) (Schrack et al., 2020a) have been

introduced recently. While cerebral ultrasound elastography is limited by acoustic windows and cannot generate detailed maps, rt-MRE has the potential to map viscoelasticity with both high spatial resolution and high frame rates. However, feasibility of rt-MRE has as yet only been demonstrated with a small field of view in the lower extremities (Schrack et al., 2020a) and has never been tested in the brain.

Therefore, we here introduce real-time multifrequency MRE (rt-MMRE) for applications in the human brain. Multifrequency extension of rt-MRE was motivated by previous work on multifrequency wavefield inversion promising higher stability and consistency of parameter maps than single-frequency direct inversion (Papazoglou et al., 2012; Hirsch et al., 2014). Moreover, rt-MRE builds on continuous stroboscopic sampling of harmonic vibrations (Schrack et al., 2020b), which can be spectrally decomposed into multifrequency vibrations without extra scan time. As such, rt-MMRE is a natural extension of rt-MRE that yields, at no extra cost, consistent viscoelasticity maps at relatively high frame rates in the order of 6 Hz depending on the repetition time (TR). Since rt-MRE does not require gating and provides multiple viscoelasticity maps per second, we consider this method as a real-time imaging technique.

Using rt-MMRE, we investigate rapid viscoelastic changes during cerebral autoregulation associated with the Valsalva maneuver (VM). The VM is a standard maneuver to voluntarily increase ICP by forceful breathing against the closed airway with abdominal muscle contraction at the same time. VM will be compared with normal breath-holds in inspiration (BH-in) and expiration (BH-ex). To address frequency dispersion and to test the overall consistency of the values measured in association with the VM, the experiment is repeated with a second set of drive frequencies.

Overall, this study has two aims: first, we introduce rt-MMRE based on three simultaneous excitation frequencies to acquire hundreds of viscoelasticity maps within less than 1 min of scan time. Second, we explore cerebral autoregulation with the unprecedentedly high spatiotemporal resolution offered by rt-MMRE.

MATERIALS AND METHODS

Subjects

rt-MMRE was performed in 17 healthy volunteers without a history of neurological diseases (5 females, 36 ± 13 years, age range: 25–81 years, randomly selected). The study was approved by the ethics committee of Charité – Universitätsmedizin Berlin in accordance with the Ethical Principles for Medical Research Involving Human Subjects of the World Medical Association Declaration of Helsinki. Every participant gave written informed consent. Participant characteristics are summarized in **Table 1**. Group mean time curves of heart rate are given in **Inline Supplementary Figure 1**.

Experimental Setup

All experiments were performed in a 3T MRI scanner (Siemens MAGNETOM Prisma, Erlangen) using a 32-channel head coil. Triple-harmonic vibrations in a narrowband frequency regimen

TABLE 1 | Participant characteristics with abbreviations: body mass index (BMI), systolic blood pressure (BPsys), diastolic blood pressure (BPdia), and heart rate (HR).

ID	Sex	Age in years	BMI in kg/m ²	BPsys in mmHg	BPdia in mmHg	HR in bpm
1	f	37	17.5	97	56	69
2	m	29	24.2	130	77	80
3	m	43	23.6	150	88	88
4	m	46	26.3	134	85	62
5	m	34	22.7	124	68	76
6	m	25	20.8	120	70	70
7	m	27	21.6	118	70	64
8	m	30	26.3	126	78	78
9	f	28	20.7	131	85	62
10	m	36	19.9	77	50	54
11	m	26	20.2	121	75	80
12	f	26	20.5	113	60	55
13	f	29	25.7	114	72	73
14	m	51	20.7	130	85	62
15	m	37	26.2	122	72	70
16	f	27	31.6	140	78	90
17	m	81	22.5	125	80	70
Mean (SD)	–	36 (13)	23 (3)	122 (16)	74 (10)	71 (10)

were synchronously induced by four pressurized air drivers attached to a transmission plate and placed underneath the head. The applied frequencies were: 30.03, 30.91, and 31.8 Hz

(hereinafter referred to as 31-Hz regimen). The two outmost drivers were operated at the highest frequencies with alternated phases relative to each other. The two inner drivers were operated with the same frequency, again with alternated phases. This way each frequency induced mainly lateral-rotational head motion with minimized compression components. The setup is shown in **Figure 1**.

Vibrations and radiofrequency (RF) excitation started 5 s before data acquisition to ensure establishment of steady states of time-harmonic oscillations and magnetization before start of each experiment. The following rt-MMRE experiments were performed:

- i Valsalva maneuver (VM)
- ii deep inspiration and breath-hold (BH-in)
- iii expiration and breath-hold (BH-ex)

The VM experiment included four consecutive phases: 30 s baseline, 5 s breath-hold in inspiration, 20 s VM and 35 s recovery (total scan time: 90 s). Prior to the experiment, subjects were trained to perform a moderate Valsalva maneuver that could be easily sustained for 20 s to prevent involuntary movement after deep breathing. This experiment was repeated with a second narrowband frequency regimen comprising 40.77, 41.67, and 42.55 Hz (hereinafter referred to as 42-Hz regimen) in order to check the overall consistency of MRE during VM and if there is a noticeable influence of frequency.

BH-in and BH-ex experiments consisted of 30-s baseline acquisition with the volunteer breathing normally, followed by

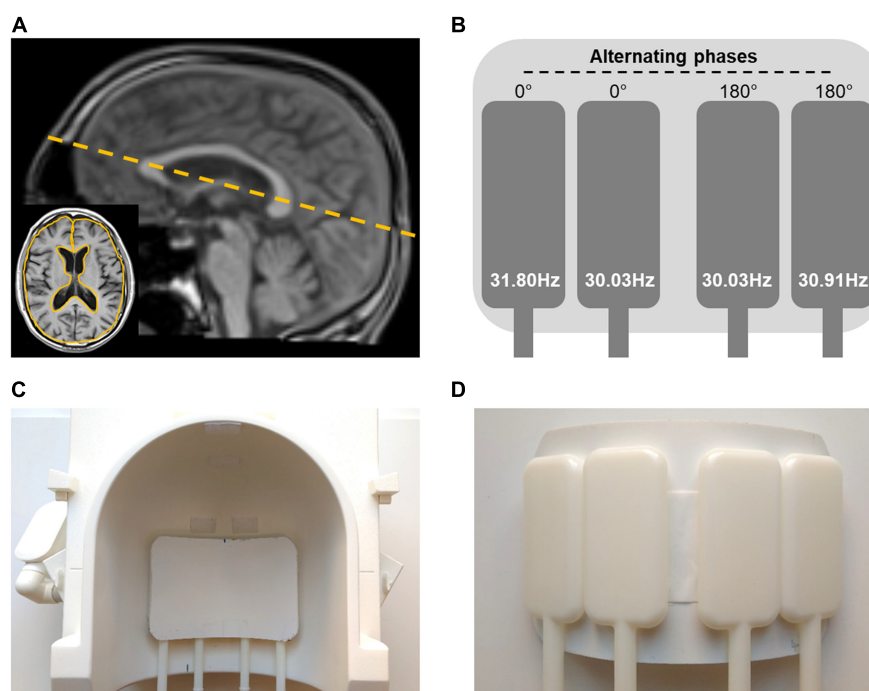


FIGURE 1 | Experimental setup. **(A)** Image slice position (dashed yellow line) and region of interest (ROI) based on anatomical image (yellow solid line in the insert) for rt-MMRE of the brain. **(B)** Diagram of the four flask drivers with vibration frequencies and 180°-phase alterations between the drivers. **(C)** Top view of positioning of actuator setup in the 32-channel head coil. **(D)** Bottom view of driver setup.

a 25-s breath-hold in inspiration or expiration, and a final 35 s recovery phase (total scan time: 90 s).

A resting period of at least 30 s was observed between the experiments. Start and stop commands were given as visual signals to the volunteers. The finger pulse was continuously recorded to track changes in heart rate.

Additionally, anatomical images were acquired using a T1-weighted, turbo-spin echo (TSE) sequence.

rt-MMRE Pulse Sequence

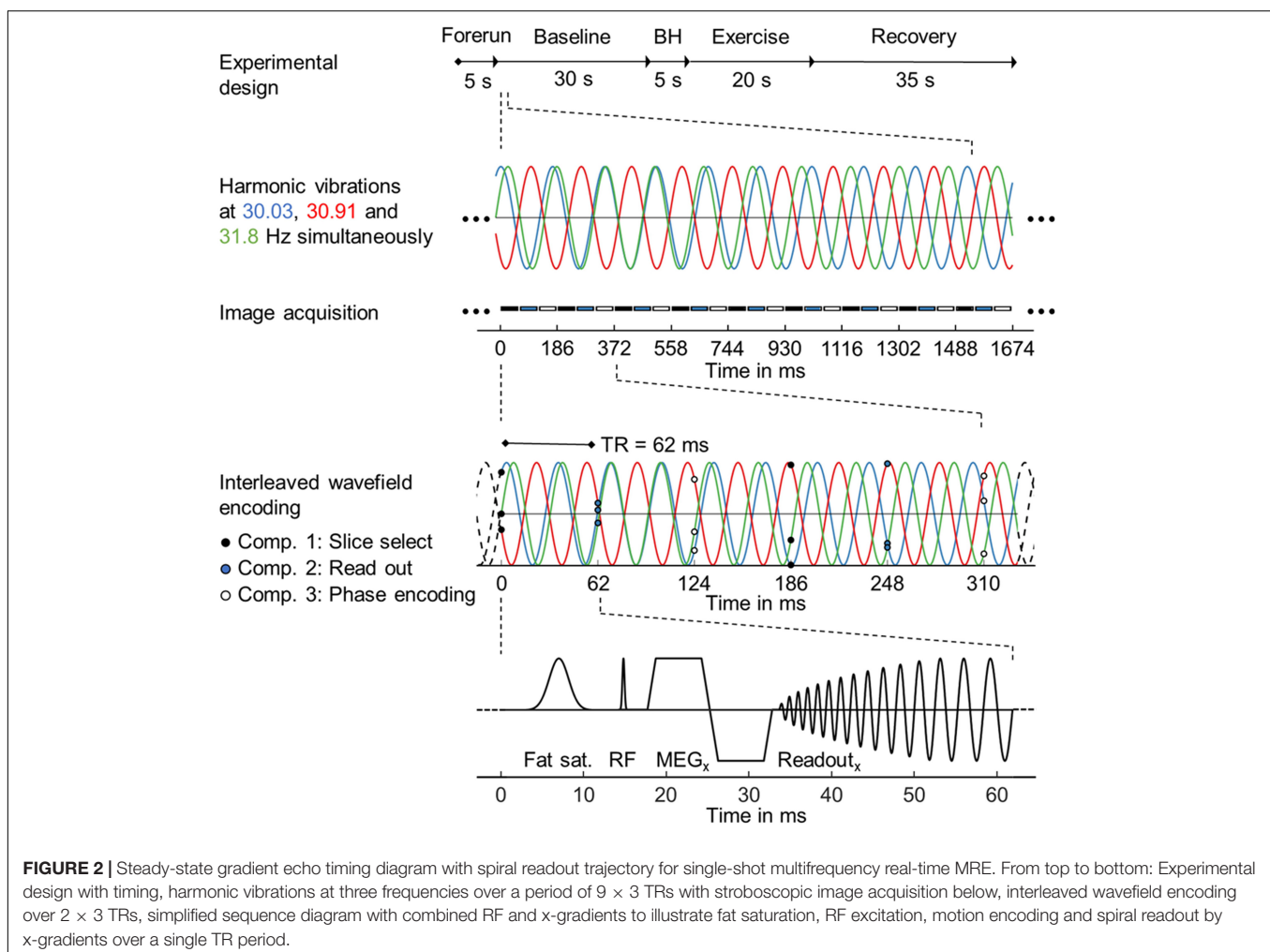
Single-frequency rt-MRE using a 2D single-shot gradient echo MRE pulse sequence with spiral readout was recently introduced for directly mapping skeletal muscle function (Schrack et al., 2020a). For rt-MMRE we used a similar prototype—a single-shot, gradient-echo sequence with dual-density spiral readout, which samples multifrequency vibrations in a stroboscopic fashion as illustrated in **Figure 2**. TR was 62 ms including RF excitation with 20° flip angle, 20 ms TE, 28 ms readout length, signal spoiling and fat suppression. For motion encoding, a single-cycle, bipolar motion-encoding gradient of 17.5-ms duration (57 Hz) and 40-mT/m amplitude was deployed within each TR according to the principle of fractional encoding (Rump et al., 2007). Images

were reconstructed using the SPIRiT non-Cartesian parallel imaging technique (Lustig and Pauly, 2010). Three Cartesian motion components were encoded in an interleaved fashion within the series of consecutive TRs, yielding a sequence of 1,458 wave images. Collapsing these three components into a single viscoelasticity map resulted in a total MRE frame rate of $3 \times \text{TR} = 186$ ms, or approximately 5.4 Hz.

Data were acquired in a single transverse image slice with a field of view (FoV) of $192 \times 192 \text{ mm}^2$ and $2 \times 2 \times 5 \text{ mm}^3$ voxel size. The slice was automatically positioned using the localizer-based auto-align function at the level of the basal nuclei along the largest diameter of the lateral ventricles in the sagittal plane as shown in **Figure 1**.

Parameter Reconstruction

The 1,458 raw, complex-valued MR images were smoothed with a Gaussian filter ($\sigma = 0.65$ px) and subsequently unwrapped using gradient unwrapping (Hirsch et al., 2017). The three vibration frequencies were decomposed by temporal Fourier transformation. Due to stroboscopic undersampling of vibrations in rt-MMRE, the frequencies appeared at aliased positions in the spectrum (see **Figure 3A**). The frequencies were selected



by three Gaussian bandpass filters ($\sigma = 0.1$ Hz) each of which centered at the expected (aliased) frequency of the fundamental drive frequency. These filters were used for inverse Hilbert transformation to compute complex-valued wave fields (wave images) for each vibration frequency, separately yielding 4,374 ($1,458 \times 3$ vibration frequencies) time-resolved wave images (Schrank et al., 2020b). Nine wave images of three Cartesian field components and three vibration frequencies (see **Figure 3B**) were fed into multifrequency dual elasto-visco inversion (Papazoglou et al., 2012), yielding 486 ($4,374/3$ encoding components/ 3 vibration frequencies) consecutive maps of stiffness ($|G^*|$) and

loss angle (φ) with 5.4-Hz frame rate over the entire examination time. While $|G^*|$ is a measure of stiffness, φ describes the ratio of elastic to viscous tissue properties indicating fluid properties as explained in Streithberger et al. (2020) $|G^*|$ and φ maps from the beginning and end of the series were discarded within 5-s margins to minimize transient effects introduced by periodic boundary conditions of the Hilbert transform. Consequently, the final observation window was 80 s. All data processing was done in MATLAB (version 2020a). The inversion pipeline is publicly available at [https://bioic-\\$-apps.charite.de](https://bioic-$-apps.charite.de) (Meyer et al., 2019). Main results are given in **Table 1**, **Table 2** and in

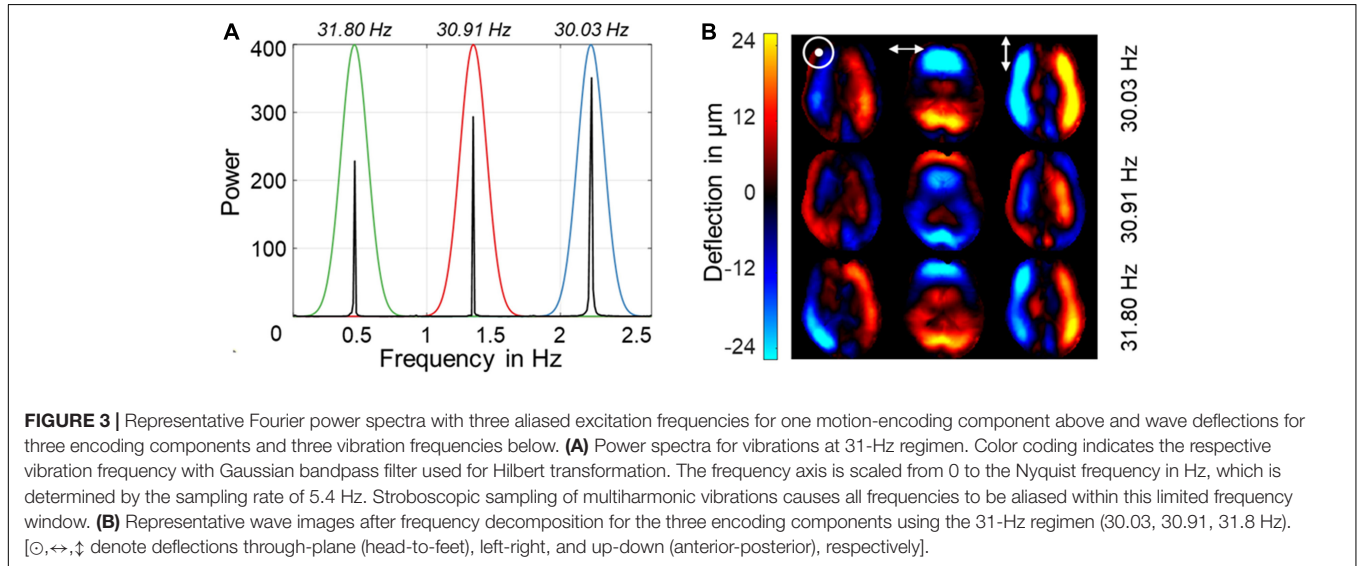


TABLE 2 | Mean $|G^*|$ (SD) in Pa and mean φ (SD) in rad for each phase and participant in the Valsalva maneuver experiments using the 31-Hz regimen (30.03, 30.91, 31.8 Hz).

ID	Mean $ G^* $ (SD) in Pa				Mean φ (SD) in rad			
	BSL	ESM	LRM	REC	BSL	ESM	LRM	REC
1	1290(6)	1323(17)	1313(5)	12902 (8)	0.841(0.001)	0.831(0.001)	0.849(0.001)	0.840(0.001)
2	1243(16)	1340(17)	1327(10)	1237(11)	0.816(0.007)	0.798(0.003)	0.799(0.003)	0.817(0.001)
3	1351(11)	1415(14)	1409(5)	1336(9)	0.783(0.001)	0.769(0.003)	0.791(0.005)	0.783(0.002)
4	1490(12)	1530(29)	1525(6)	1495(8)	0.87(0.002)	0.853(0.001)	0.87(0.003)	0.868(0.004)
5	1441(6)	1484(24)	1566(14)	1456(10)	0.799(0.003)	0.777(0.005)	0.811(0.009)	0.794(0.004)
6	1502(4)	1536(7)	1609(3)	1511(7)	0.795(0.001)	0.789(0.004)	0.799(0.002)	0.795(0.002)
7	1321(8)	1363(17)	1395(14)	1301(11)	0.818(0.004)	0.815(0.006)	0.83(0.002)	0.829(0.002)
8	1495(6)	1519(20)	1655(8)	1534(16)	0.791(0.002)	0.763(0.004)	0.796(0.008)	0.79(0.004)
9	1515(7)	1620(9)	1617(6)	1549(1)	0.809(0.003)	0.765(0.008)	0.778(0.006)	0.792(0.001)
10	1395(4)	1431(8)	1473(8)	1401(8)	0.78(0.002)	0.776(0.004)	0.779(0.003)	0.778(0.001)
11	1237(12)	1238(11)	1312(15)	1242(9)	0.807(0.004)	0.806(0.003)	0.81(0.005)	0.804(0.001)
12	1312(11)	1350(7)	1416(11)	1310(11)	0.758(0.003)	0.742(0.004)	0.755(0.001)	0.754(0.003)
13	1509(4)	1510(15)	1572(2)	1509(5)	0.809(0.001)	0.807(0.001)	0.804(0.001)	0.8(0.001)
14	1373(8)	1407(14)	1392(3)	1353(4)	0.792(0.002)	0.777(0.002)	0.787(0.002)	0.786(0)
15	1295(8)	1421(35)	1407(13)	1325(15)	0.784(0.005)	0.741(0.018)	0.796(0.002)	0.781(0.003)
16	1356(7)	1391(19)	1422(2)	1330(18)	0.813(0.003)	0.795(0.004)	0.805(0.002)	0.805(0.003)
17	1157(3)	1192(9)	1175(12)	1212(6)	0.733(0.003)	0.725(0.002)	0.722(0.002)	0.728(0.001)
Mean(SD)	1370(106)	1416(108)	1446(126)	1376(108)	0.800(0.030)	0.784(0.032)	0.799(0.032)	0.797(0.031)

BSL, Baseline; ESM, established maneuver; LRM, late response maneuver; REC, recovery.

Supplementary Tables 1a–c. Raw data can be made available upon request without restrictions.

Parameter Analysis and Statistical Tests

For every time frame, $|G^*|$ and φ were quantified by averaging values over the same region of interest (ROI). ROIs were manually drawn based on anatomical T1-weighted images, as shown in **Figure 1A**. Furthermore, these ROIs were refined by empirical thresholds of 10 (time-averaged MRE signal magnitude) and of 950 Pa (time-averaged $|G^*|$ map) to remove ventricles and larger sulci similar to Shahryari et al. (2020) (see **Figure 4**).

The same ROI was also used to determine magnetization signal-to-noise ratio (SNR) and wave displacement SNR (WSNR) for every time frame. WSNR was derived using the blind noise estimation method proposed by Donoho et al. (1995) as outlined and previously applied to MRE data in Bertalan et al. (2019b) and Schrank et al. (2020a). This noise estimation method is suited for wave image analysis since the spatial frequencies of MRE waves and noise are well separated in the wavelet domain (Selesnick et al., 2005; Barnhill et al., 2017).

To test if multifrequency inversion yields more stable values than single-frequency inversion we determined the coefficient of

variation (CV) during the baseline phase prior to VM, BH-in and BH-ex for both $|G^*|$ and φ in all volunteers. The same raw data was used, but for the single-frequency inversion only one frequency from the temporal Fourier spectrum was selected.

We further analyzed difference $|G^*|$ and φ values relative to mean baseline values given as $\Delta|G^*| = |G^*|_{(t)} - |G^*|_{(\text{baseline})}$ (correspondingly for $\Delta\varphi$) in order to quantify individual parameter changes. In addition, peak viscoelasticity values and their temporal delays relative to the onset and end of VM were identified and tabulated for each volunteer.

Finally, group statistics was applied to the absolute values of $|G^*|$ and φ , after temporal averaging over the following experimental phases for each participant:

- (1) Baseline (BSL): 2.5–22.5 s
- (2) Established maneuver (ESM): 32.5–47.5 s
- (3) Late response maneuver (LRM): 52.5–57.5 s
- (4) Recovery (REC): 70–80 s.

Of note, these time intervals were given by the aforementioned study design (30–25–35 s. for baseline-breathhold/VM-recovery) minus 2.5 s transition phases at the beginnings and ends of these phases including an additional late-response phase. The transition phases were discarded from our analysis in order to minimize transients resulted by the frequency bandpass filter. Also, 5 s BH (25–30 s) and 10 s of post-VM (60–70 s) were considered as transition phases and henceforth not included in our group statistical analysis. All phases are demarcated in **Figure 5**.

To test possible deformations of lateral ventricles due to VM as reported previously (Ertl-Wagner et al., 2001), we applied automatic segmentation of cerebral spinal fluid (CSF) to the temporal averaged MRE magnitude images of the different experimental phases using SPM12 (Penny et al., 2011; see **Figure 4**). CSF probability maps were thresholded at 0.5 to generate logical CSF-associated voxel masks. A linear mixed-effects model with varying intercept was employed. CSF volume was used as dependent variable and the individual phases as independent variables. Participants were assigned as random effect, and P -values were calculated using Tukey's *post hoc* test with Bonferroni correction for multiple comparisons. To test for significant changes in $|G^*|$ and φ between phases (1)–(4), a linear mixed-effects model with varying intercept was employed. $|G^*|$ and φ were used as dependent variables and the individual phases as independent variables. Participants were assigned as random effect, and P -values were calculated using Tukey's *post hoc* test with Bonferroni correction for multiple comparisons. This test does not account for inter-individual slope variations of $|G^*|$ and φ but analyzes the significance of temporal changes of these parameters. SNR and viscoelastic parameters were correlated using a linear mixed model with $|G^*|$ and φ as dependent variables and SNR or WSNR as fixed effects with subjects as random factor. All statistical analysis was done in R (version 3.6.2). Unless otherwise stated, errors are given as standard deviation (SD). Correlations between viscoelastic baseline values as well as individual peak responses and participant characteristics (see **Table 1**) were analyzed

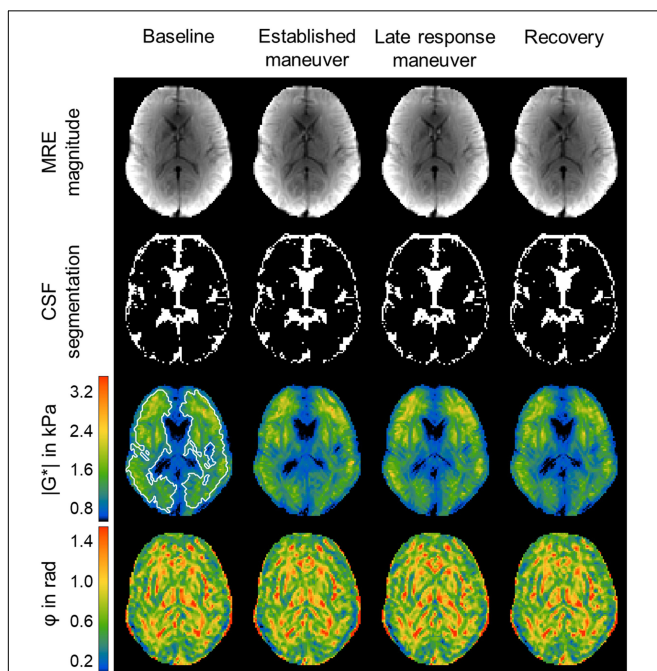
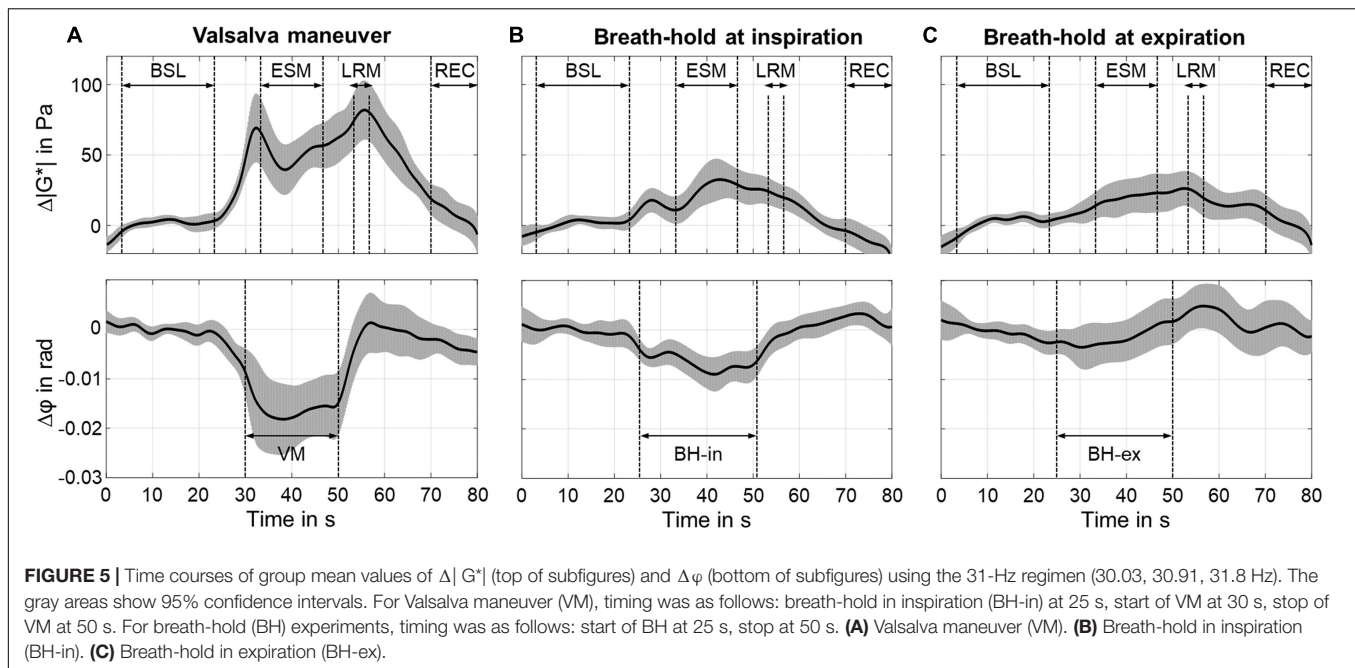


FIGURE 4 | Representative rt-MRE MRE magnitude, CSF masks, $|G^*|$ and φ maps of the *in vivo* human brain. Time-averaged MRE magnitude, derived CSF masks, $|G^*|$ and φ maps of one volunteer over the four phases [baseline (BSL), established maneuver (ESM), late response maneuver (LRM) and recovery (REC)] of the VM experiment using the 31-Hz regimen (30.03, 30.91, 31.8 Hz). The number of CSF associated voxels for each phase was BSL: 1079, ESM: 1128, LRM: 1069, REC: 1074. The $|G^*|$ maps show slightly elevated values throughout the slice. The region of interest (ROI) is indicated by white lines. The same ROI was used for all phases and for the φ maps as well.



using Pearson's correlation coefficient. P -values below 0.05 were considered statistically significant.

RESULTS

Variation in baseline $|G^*|$ and φ was smaller when using multifrequency inversion ($CV = 0.74\%$, 0.51%) than single frequencies ($CV = 0.99\%$, 0.77% , $P < 0.001$).

Figure 4 shows representative time-averaged MRE magnitude images, automatically segmented CSF masks, as well as $|G^*|$ and φ maps acquired during the four phases of the experiment. A slight increase in $|G^*|$ was visible in the late VM response, whereas no response of φ was apparent in individual maps. Group statistics revealed no significant change of CSF-associated voxels between the different states of the maneuver. A descriptive statistic for the individual phases of the VM experiment in the 31-Hz regimen and for each participant is given in **Supplementary Table 2**.

Relative $|G^*|$ and φ Changes

Individual analysis of $|G^*|$ showed an increase ($6.7 \pm 4.1\%$, $P < 0.001$) at approximately 2.4 ± 1.2 s after start of VM and 5.5 ± 2.0 s after end of VM ($7.4 \pm 2.8\%$, $P < 0.001$). φ decreased during ESM ($-2.1 \pm 1.4\%$, $P < 0.001$). Averaged time courses of $\Delta|G^*|$ and $\Delta\varphi$ are presented in **Figure 5**. An early peak of $\Delta|G^*|$ showed a difference of 69 ± 50 Pa ($P < 0.001$) from baseline values. After a short drop, $\Delta|G^*|$ steadily increased during ESM. The second overshoot differed from baseline by 82 ± 42 Pa ($P < 0.01$). $\Delta|G^*|$ recovered toward baseline values once the volunteers returned to normal breathing. $\Delta\varphi$ was constantly decreased during ESM (-0.018 ± 0.012 rad, $P < 0.01$).

The BH-in experiment showed an increase in $\Delta|G^*|$ after 3.0 ± 1.0 s (18 ± 16 Pa, $P < 0.001$) with a maximum at 17.0 ± 2.0 s

after start of BH-in (32 ± 29 Pa, $P < 0.001$). $\Delta\varphi$ decreased during ESM (-0.006 ± 0.004 rad, $P < 0.001$) reaching a minimum at 17 ± 2 s after start of BH-in (-0.009 ± 0.007 rad, $P < 0.001$).

The BH-ex experiment showed no clear peak, neither in $\Delta|G^*|$ nor $\Delta\varphi$. $|G^*|$ increased continuously with onset of BH-ex and reached a maximum 2.5 ± 1.5 s after the end of BH-ex (26 ± 23 Pa, $P < 0.001$).

Absolute $|G^*|$ and φ Changes

Figure 6 shows boxplots with median effects for different states of the maneuver for $|G^*|$ and φ . The significance levels, indicated by asterisks, were determined from a linear mixed model analysis with varying intercept and participants as random effect. For the VM, different individual effect sizes were observed; however, all subjects showed an increase in $|G^*|$ and a decrease in φ due to the maneuver. Averaged $|G^*|$ values changed between all phases of the experiment (range: 1,370–1,446 Pa) with significance levels indicated in the figure. Averaged φ values changed both from BSL to ESM and again from ESM to LRM (range: 0.784–0.800 rad).

By contrast, $|G^*|$ only changed at the start and end of the maneuver in BH-in (range: 1,338–1,372 Pa), whereas φ changed between BSL and ESM as well as between ESM and LRM (range: 0.783–0.792 rad). In the BH-ex experiment, $|G^*|$ changed between LRM and REC (range: 1,348–1,371 Pa) while φ changed between ESM and LRM (range: 0.786–0.791 rad).

Results of the second VM experiment performed using the 42-Hz regimen are presented in **Supplementary Material**. No significant differences in viscoelastic responses between the 31-Hz and 42-Hz regimen were observed ($P = 0.24$).

Descriptive statistics of $|G^*|$ in Pa and φ in rad for the individual phases of the VM experiment and for each participant are summarized in **Table 2A**. Correspondingly, statistical results

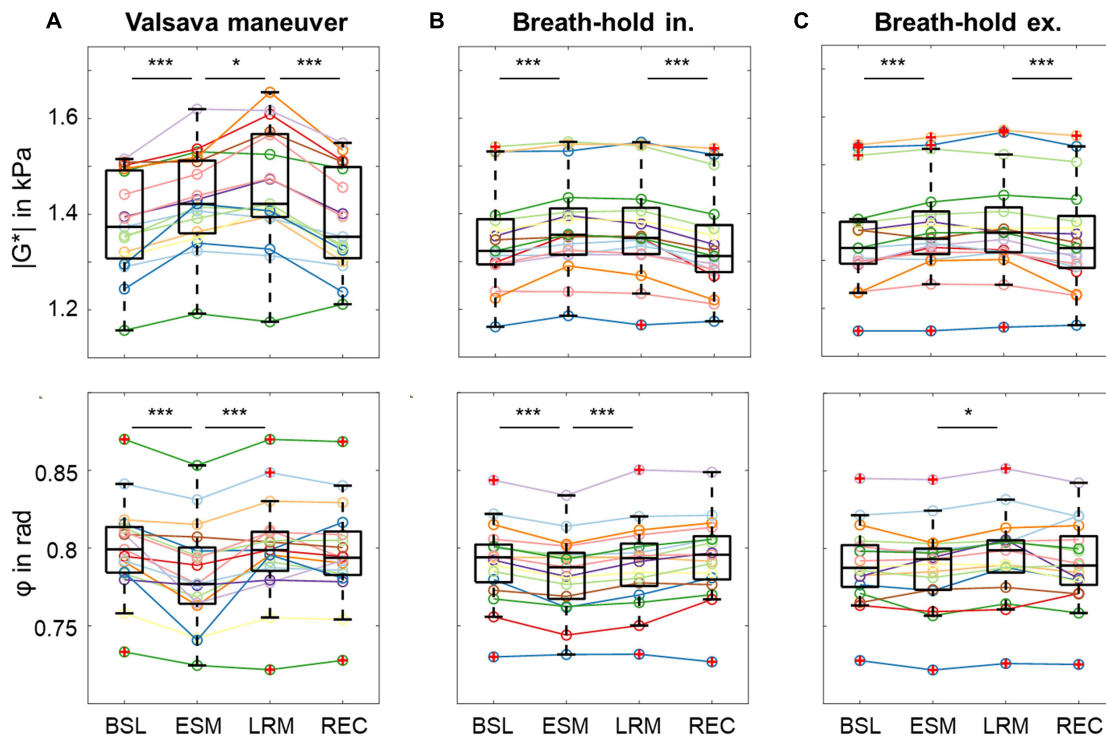


FIGURE 6 | Group values as boxplots for the absolute values of $|G^*|$ (top) and ϕ (bottom) in each phase illustrate the changes in viscoelastic properties induced by the different maneuvers using the 31-Hz regimen for each phase [baseline (BSL), established maneuver (ESM), late response maneuver (LRM), recovery (REC)]. **(A)** Valsalva maneuver (VM). **(B)** Breath-hold in inspiration (BH-in). **(C)** Breath-hold in expiration (BH-ex). Asterisks at the top demarcate significant changes in $|G^*|$ and ϕ which were determined from a linear mixed-effects model with varying intercept. $|G^*|$ and ϕ assigned dependent variables and the individual phases as independent variables. Participants were assigned as random effect, and P -values were calculated using Tukey's *post hoc* test with Bonferroni correction for multiple comparisons. (* $P < 0.05$, *** $P < 0.001$).

for the breath-hold and VM experiments performed with the 42-Hz regimen are presented in **Supplementary Tables 1a–c**. Participant characteristics did not correlate with $|G^*|$ or ϕ .

SNR Analysis

Time-averaged SNR and WSNR values did not change significantly across volunteers and over time ($P = 0.43$). Mean SNR was 29 ± 2 dB across all volunteers with minor and insignificant variations of ± 0.5 dB over the course of the experiment. Mean WSNR was 36 ± 2 dB with minor and insignificant variations of ± 1 dB over the course of the experiment. Significant correlation between group mean $|G^*|$ and ϕ was observed (31-Hz regimen: $R = -0.4$, $P < 0.001$, 42-Hz regimen: $R = -0.5$, $P < 0.001$).

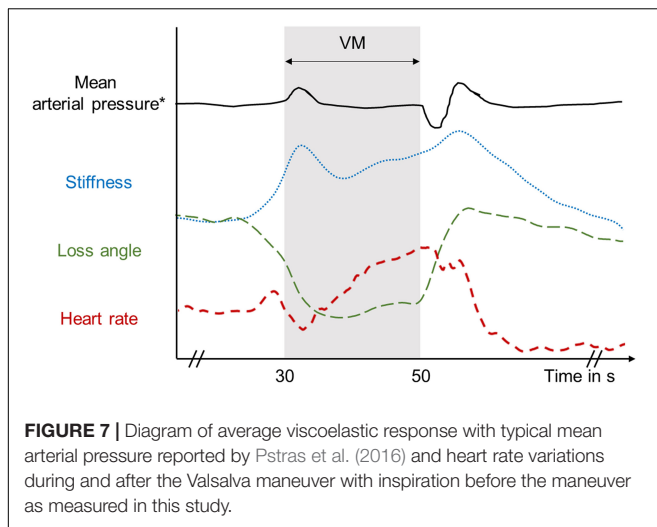
DISCUSSION

This paper presents a novel rt-MMRE technique for the *in vivo* measurement of rapid and non-periodic changes in brain viscoelasticity in humans. MRE exploiting stroboscopic sampling of multifrequency harmonic vibrations revealed the viscoelastic response of brain tissue to the Valsalva maneuver. Overall, the extension of rt-MRE to rt-MMRE by simultaneous excitation of multifrequency oscillations has increased the consistency of our

measurements without adding scanning time. Probably for this reason, all subjects consistently showed an increase in $|G^*|$ and a decrease in ϕ with VM, resulting in high statistical significance. This basic finding is remarkable, since the VM is known to induce variability by subjective pressure generation. To further discuss our results we start by briefly reviewing the basic effects of VM on cerebral perfusion and ICP.

Physiological Effects of VM on Cerebral Blood Flow, ICP and MRE

In this study, elevation of intrathoracic pressure during VM was induced by deep inspiration following and increased abdominal pressure similar to the maneuver used in Ipek-Ugay et al. (2017). With onset of VM and elevated intrathoracic pressure, arterial blood pressure (ABP) increases (Elisberg, 1963; Smith et al., 1987). Intrathoracic pressure is communicated through the vascular tree into the cranial cavity, leading to a transient increase in ICP and obstruction of venous outflow from the brain with, thus, increased venous pressure (Prabhakar et al., 2007). Reduced venous return to the heart causes ABP to decrease. Hence, cerebral perfusion pressure is reduced, leading to a reduction in cerebral blood flow (CBF). Cerebral autoregulation is a mechanism to maintain constant CBF. For this reason, cerebral autoregulation, after the decrease in CBF, immediately



responds to reduce vascular resistance by dilating the cerebral arteries in order to facilitate blood flow and maintain stable CBF. At the same time, the heart rate is increased through the baroreflex (Eckberg, 1980; Looga, 1997), which restores normal ABP and accumulation of blood in the brain, since venous return is still diminished. Constant influx of blood with reduced outflow steadily increases ICP. With release of intrathoracic pressure, there is a significant drop of ABP (Stone et al., 1965), and ICP returns to normal. As a result, normal venous return is restored and more blood flows back into the heart, leading to a transient increase in cardiac output and overshoot in ABP. Since vascular resistance is still low, CBF overshoots as well.

The time curves of MRE parameters presented in **Figure 7** suggest that stiffness ($|G^*|$) correlates with ICP while viscosity-related φ correlates with reduced venous outflow or cerebral perfusion pressure. Perfusion pressure is proportional to CBF normalized by mean vascular diameter (Hetzer et al., 2019) and, thus, decreases upon vasodilation with constant CBF. The ramp-up of $|G^*|$ during the continuing VM phase seems to reflect the increasing heart rate and steady accumulation of blood in the brain, which drives ICP. By contrast, φ remains low throughout the VM phase as if viscous damping in brain tissue is lower when perfusion pressure is reduced. It is an intriguing result that possible ICP changes during VM can be indirectly monitored using rt-MMRE since non-invasive ICP measurement are still an unsolved problem. These findings could help to relate pathologically increased ICP to overall brain stiffness for clinical applications.

In previous work we observed an increase in φ of the brain due to hypercapnia (2% increase) (Hetzer et al., 2019) and arterial pulsation (0.5% increase) (Schränk et al., 2020b). In both studies, there was an increase in CBF with a concomitant increase in perfusion pressure while, as explained above, CBF in VM is, due to cerebral autoregulation, associated with a fairly constant CBF and reduced perfusion pressure. Together, the two rt-MMRE parameters, $|G^*|$ and φ , provide complementary information on the concert of physical parameters involved in ICP autoregulation.

Overall, our baseline parameters of brain viscoelasticity are in good agreement with previously reported values acquired in similar frequency ranges (Hetzer et al., 2018, 2019; Schränk et al., 2020b). We observed no significant differences in the responses of rt-MMRE parameters to VM between the 31 and 42 Hz regimens. This consistency of multifrequency data further validates the technique of rt-MMRE. Furthermore, this observation indicates that the poroelastic response of brain tissue (Lilaj et al., 2020) is similar at 30 and 40 Hz (McGarry et al., 2015). Additional validation of rt-MMRE was obtained by reference experiments performed during breath-holds but without sustained VM. BH-in induced a similar increase in stiffness and decrease in φ as observed during VM. Thus, from an MRE perspective, deep inspiration followed by breath-holding induces effects similar to a *light* VM. Otherwise, no such changes were observed in BH-ex, rendering this maneuver neutral with regard to ICP. Nevertheless, even BH-ex had some small effect on MRE parameters, which, notably, were not correlated to changes in either SNR or WSNR. Also, analysis of CSF volume and ventricle size did not reveal any significant correlation with VM. Previous work by us and others showed that total brain volume increases due to VM by approximately 3% while ventricle volume shrinks by 20% (Ertl-Wagner et al., 2001; Mousavi et al., 2014). In contrast to these studies, our subjects were instructed to perform a moderate Valsalva maneuver to minimize variations in thoracic pressure, muscle strain, and head position.

In our previous work we used ultrasound time-harmonic elastography in a temporal bone window to acquire VM-induced rapid changes in shear wave speed in the temporal lobes of healthy volunteers (Tzschatzsch et al., 2018). Effect sizes in that region were higher ($10.8 \pm 2.5\%$) than revealed by MRE in the full brain tissue slice. It should be noted that the regions covered by our current study do not correspond to the medial temporal gyrus addressed by transtemporal time-harmonic elastography, which makes a direct comparison of effect sizes between the two studies difficult. To analyze the spatial representation of viscoelasticity changes we performed automatic image segmentation using MNI-based registration as well as voxel-wise correlation analysis based on a boxcar function. No significant patterns of viscoelasticity changes could be detected. A more detailed analysis of the spatiotemporal representation of brain viscoelasticity in response to the VM is warranted.

Our study has limitations. The nature of stroboscopic sampling of vibrations by steady-state single-shot acquisitions limited our technique to 2D wave field sampling including three encoding components. This intrinsic limitation of rt-MMRE can currently not be overcome by a multishot variant because VM is a non-periodic event and cannot be repeated with enough temporal reliability. Consequently, our multi-frequency inversion technique was entirely 2D, which may have led to variability due to different slice positioning and oblique intersection of 3D shear wavefields rendering our values as effective viscoelasticity parameters. Nevertheless, our conclusions are drawn from group values in two different frequency regimens. The fact that these values changed with statistical significance

in VM, while neither SNR nor anatomy changed, emphasizes the robustness of the observed MRE effects. Furthermore, our data could be used for suppression of bulk waves based on the in-plane curl component. However, this curl-analysis did not provide more consistent values than our standard MDEV inversion with respect to confidence intervals and statistical power. Finally, 2D brain MRE has a long tradition in disease detection (Wuerfel et al., 2010; Streitberger et al., 2012, 2017, 2020; Lipp et al., 2013, 2018; Fehlnner et al., 2016; Gerischer et al., 2018) as well as in the study of brain physiology (Sack et al., 2009, 2011; Schrank et al., 2020b; Herthum et al., 2021). It remains to be determined whether single-frequency 3D MRE can provide similarly consistent clinical and physiological brain data. Instead, as shown herein, unintentional breath-holds may affect 3D MRE due to long scan times. Generally, current MRE techniques cannot account for poroelasticity, heterogeneity, hyperelasticity, anisotropy and temporal variations of brain tissue at the same time. Therefore, to date *all* values measured by brain MRE should be considered as effective parameters.

In summary, we studied the viscoelastic response of the human brain to breathing and the Valsalva maneuver using a novel real-time multifrequency MRE technique. Significant increases in brain stiffness and decreases in φ due to VM were observed with use of two different frequency regimens. Control experiments showed that breath-holds after inhalation induce a response similar to VM but with a smaller effect size. By contrast, breath-holds after exhalation had the smallest effects on cerebral MRE parameters. The time courses we report here provide a reference for the VM response in healthy subjects and might be of value for studying dysfunctional autoregulation as associated with various neurological diseases. rt-MMRE is a fast technique which can provide consistent imaging markers of brain viscoelasticity within a fraction of a minute.

DATA AVAILABILITY STATEMENT

The original contributions presented in the study are included in the article/**Supplementary Material**, further inquiries can be directed to the corresponding author/s.

REFERENCES

- Arani, A., Min, H. K., Fattahi, N., Wetjen, N. M., Trzasko, J. D., Manduca, A., et al. (2018). Acute pressure changes in the brain are correlated with MR elastography stiffness measurements: initial feasibility in an in vivo large animal model. *Magn. Reson. Med.* 79, 1043–1051. doi: 10.1002/mrm.26738
- Arani, A., Murphy, M. C., Glaser, K. J., Manduca, A., Lake, D. S., Kruse, S. A., et al. (2015). Measuring the effects of aging and sex on regional brain stiffness with MR elastography in healthy older adults. *Neuroimage* 111, 59–64.
- Barnhill, E., Hollis, L., Sack, I., Braun, J., Hoskins, P. R., Pankaj, P., et al. (2017). Nonlinear multiscale regularisation in MR elastography: towards fine feature mapping. *Med. Image Anal.* 35, 133–145. doi: 10.1016/j.media.2016.05.012
- Bertalan, G., Boehm-Sturm, P., Schreyer, S., Morr, A. S., Steiner, B., Tzschatzsch, H., et al. (2019a). The influence of body temperature on tissue stiffness, blood perfusion, and water diffusion in the mouse brain. *Acta Biomater.* 96, 412–420. doi: 10.1016/j.actbio.2019.06.034

ETHICS STATEMENT

The studies involving human participants were reviewed and approved by the Ethics committee of Charité – Universitätsmedizin Berlin in accordance with the Ethical Principles for Medical Research Involving Human Subjects of the World Medical Association Declaration of Helsinki. The patients/participants provided their written informed consent to participate in this study.

AUTHOR CONTRIBUTIONS

HH carried out all experiments and contributed to all parts of the manuscript. MS assisted in interpreting the results with regard to physiological changes and statistical analysis. FS, HT, and SH helped to carry out the data processing and verified the results. CW and JP carried out the MRI sequence implementation and image reconstruction. SG and HN contributed to the experimental setup. JB helped supervise the project and constructed the actuation system. IS designed and directed the project and aided in interpreting the results. All authors provided critical feedback and helped shape the research and manuscript.

FUNDING

Funding from the German Research Foundation (GRK 2260 BIOQIC, SFB1340 Matrix in Vision, Neuro-MRE Sa901/17-2) and from the European Union's Horizon 2020 Program (ID 668039, EU FORCE – Imaging the Force of Cancer) is gratefully acknowledged.

SUPPLEMENTARY MATERIAL

The Supplementary Material for this article can be found online at: <https://www.frontiersin.org/articles/10.3389/fbioe.2021.666456/full#supplementary-material>

- Bertalan, G., Guo, J., Tzschatzsch, H., Klein, C., Barnhill, E., Sack, I., et al. (2019b). Fast tomoelastography of the mouse brain by multifrequency single-shot MR elastography. *Magn. Reson. Med.* 81, 2676–2687. doi: 10.1002/mrm.27586
- Bertalan, G., Klein, C., Schreyer, S., Steiner, B., Kreft, B., Tzschatzsch, H., et al. (2020). Biomechanical properties of the hypoxic and dying brain quantified by magnetic resonance elastography. *Acta Biomater.* 101, 395–402. doi: 10.1016/j.actbio.2019.11.011
- Bilston, L. E. (2002). The effect of perfusion on soft tissue mechanical properties: a computational model. *Comput. Methods Biomech. Biomed. Eng.* 5, 283–290. doi: 10.1080/10255840290032658
- Chatelin, S., Humbert-Claude, M., Garteiser, P., Ricobaraza, A., Vilgrain, V., Van Beers, B. E., et al. (2015). Cannabinoid receptor activation in the juvenile rat brain results in rapid biomechanical alterations: neurovascular mechanism as a putative confounding factor. *J. Cereb. Blood Flow Metab.* 36:954–964. doi: 10.1177/0271678x15606923
- Donoho, D. L., Johnstone, I. M., Kerkycharian, G., and Picard, D. (1995). Wavelet shrinkage: asymptopia? *J. R. Statist. Soc. Ser. B (Methodological)* 57, 301–337. doi: 10.1111/j.2517-6161.1995.tb02032.x

- Eckberg, D. L. (1980). Parasympathetic cardiovascular control in human disease: a critical review of methods and results. *Am. J. Physiol.* 239, H581–H593.
- Elisberg, E. I. (1963). Heart rate response to the Valsalva maneuver as a test of circulatory integrity. *JAMA* 186, 200–205. doi: 10.1001/jama.1963.03710030040006
- Ertl-Wagner, B. B., Lienemann, A., Reith, W., and Reiser, M. F. (2001). Demonstration of periventricular brain motion during a Valsalva maneuver: description of technique, evaluation in healthy volunteers and first results in hydrocephalic patients. *Eur. Radiol.* 11, 1998–2003.
- Fehlner, A., Behrens, J. R., Streiberger, K. J., Papazoglou, S., Braun, J., Bellmann-Strobl, J., et al. (2016). Higher-resolution MR elastography reveals early mechanical signatures of neuroinflammation in patients with clinically isolated syndrome. *J. Magn. Reson. Imag.* 44, 51–58.
- Gerischer, L. M., Fehlner, A., Kobe, T., Prehn, K., Antonenko, D., Grittner, U., et al. (2018). Combining viscoelasticity, diffusivity and volume of the hippocampus for the diagnosis of Alzheimer's disease based on magnetic resonance imaging. *Neuroimage Clin.* 18, 485–493.
- Giulioni, M., Ursino, M., and Alvisi, C. (1988). Correlations among intracranial pulsatility, intracranial hemodynamics, and transcranial doppler wave form: literature review and hypothesis for future studies. *Neurosurgery* 22, 807–812. doi: 10.1227/00006123-198805000-00001
- Greitz, D., Wirestam, R., Franck, A., Nordell, B., Thomsen, C. & Stahlberg, F. (1992). Pulsatile brain movement and associated hydrodynamics studied by magnetic resonance phase imaging. the monro-Kellie doctrine revisited. *Neuroradiology* 34, 370–380. doi: 10.1007/bf00596493
- Guo, J., Bertalan, G., Meierhofer, D., Klein, C., Schreyer, S., Steiner, B., et al. (2019). Brain maturation is associated with increasing tissue stiffness and decreasing tissue fluidity. *Acta Biomater.* 99, 433–442. doi: 10.1016/j.actbio.2019.08.036
- Guyton, A., and Hall, J. (2006). *Textbook of Medical Physiology*, 11th ed. Elsevier Inc., Amsterdam.
- Hatt, A., Cheng, S., Tan, K., Sinkus, R., and Bilston, L. E. (2015). MR elastography can be used to measure brain stiffness changes as a result of altered cranial venous drainage during jugular compression. *AJNR Am. J. Neuroradiol.* 36, 1971–1977. doi: 10.3174/ajnr.a4361
- Herthum, H., Dempsey, S. C. H., Samani, A., Schrank, F., Shahryari, M., Warmuth, C., et al. (2021). Supraviscous properties of the in vivo brain at large scales. *Acta Biomater.* 121, 393–404. doi: 10.1016/j.actbio.2020.12.027
- Hetzer, S., Birr, P., Fehlner, A., Hirsch, S., Dittmann, F., Barnhill, E., et al. (2018). Perfusion alters stiffness of deep gray matter. *J. Cereb. Blood Flow Metab.* 38, 116–125.
- Hetzer, S., Dittmann, F., Bormann, K., Hirsch, S., Lipp, A., Wang, D. J., et al. (2019). Hypercapnia increases brain viscoelasticity. *J. Cereb. Blood Flow Metab.* 39, 2445–2455.
- Hirsch, S., Braun, J., and Sack, I. (2017). *Magnetic Resonance Elastography: Physical Background and Medical Applications*. Wiley-VCH: Weinheim.
- Hirsch, S., Guo, J., Reiter, R., Papazoglou, S., Kroenke, T., Braun, J., et al. (2014). MR elastography of the liver and the spleen using a piezoelectric driver, single-shot wave-field acquisition, and multifrequency dual parameter reconstruction. *Magn. Reson. Med.* 71, 267–277. doi: 10.1002/mrm.24674
- Hiscox, L. V., Johnson, C. L., Barnhill, E., McGarry, M. D. J., Huston, J., van Beek, E. J. R., et al. (2016). Magnetic resonance elastography (MRE) of the human brain: technique, findings and clinical applications. *Phys. Med. Biol.* 61, R401–R437.
- Ipek-Ugay, S., Tzschatzsch, H., Fischer, T., Braun, J., and Sack, I. (2017). Physiological reduction of hepatic venous blood flow by Valsalva maneuver decreases liver stiffness. *J. Ultrasound Med.* 36, 1305–1311.
- Jamin, Y., Boulton, J. K. R., Li, J., Popov, S., Garteiser, P., Ulloa, J. L., et al. (2015). Exploring the biomechanical properties of brain malignancies and their pathologic determinants in vivo with magnetic resonance elastography. *Cancer Res.* 75, 1216–1224. doi: 10.1158/0008-5472.can-14-1997
- Juge, L., Pong, A. C., Bongers, A., Sinkus, R., Bilston, L. E., and Cheng, S. (2016). Changes in rat brain tissue microstructure and stiffness during the development of experimental obstructive hydrocephalus. *PLoS One* 11:e0148652. doi: 10.1371/journal.pone.0148652
- Klein, C., Hain, E. G., Braun, J., Riek, K., Mueller, S., Steiner, B., et al. (2014). Enhanced adult neurogenesis increases brain stiffness: in vivo magnetic resonance elastography in a mouse model of dopamine depletion. *PLoS One* 9:e92582. doi: 10.1371/journal.pone.0092582
- Kreft, B., Tzschatzsch, H., Schrank, F., Bergs, J., Streiberger, K. J., Waldchen, S., et al. (2020). Time-Resolved response of cerebral stiffness to hypercapnia in humans. *Ultrasound Med. Biol.* 46, 936–943. doi: 10.1016/j.ultrasmedbio.2019.12.019
- Lan, P. S., Glaser, K. J., Ehman, R. L., and Glover, G. H. (2020). Imaging brain function with simultaneous BOLD and viscoelasticity contrast: fMRI/fMRE. *Neuroimage* 211:116592. doi: 10.1016/j.neuroimage.2020.116592
- Lilaj, L., Fischer, T., Guo, J., Braun, J., Sack, I., and Hirsch, S. (2020). Separation of fluid and solid shear wave fields and quantification of coupling density by magnetic resonance poroelastography. *Magn. Reson. Med.* 85, 1655–1668. doi: 10.1002/mrm.28507
- Linninger, A. A., Tsakiris, C., Zhu, D. C., Xenos, M., Roycewicz, P., Danziger, Z., et al. (2005). Pulsatile cerebrospinal fluid dynamics in the human brain. *IEEE Trans. Biomed. Eng.* 52, 557–565. doi: 10.1109/tbme.2005.844021
- Lipp, A., Skowronek, C., Fehlner, A., Streiberger, K. J., Braun, J., and Sack, I. (2018). Progressive supranuclear palsy and idiopathic Parkinson's disease are associated with local reduction of in vivo brain viscoelasticity. *Eur. Radiol.* 28, 3347–3354. doi: 10.1007/s00330-017-5269-y
- Lipp, A., Trbojevic, R., Paul, F., Fehlner, A., Hirsch, S., Scheel, M., et al. (2013). Cerebral magnetic resonance elastography in supranuclear palsy and idiopathic Parkinson's disease. *Neuroimage Clin.* 3, 381–387. doi: 10.1016/j.nicl.2013.09.006
- Looga, R. (1997). Reflex cardiovascular responses to lung inflation: a review. *Respir Physiol.* 109, 95–106. doi: 10.1016/s0034-5687(97)00049-2
- Lustig, M., and Pauly, J. M. (2010). SPIRiT: Iterative self-consistent parallel imaging reconstruction from arbitrary k-space. *Magn. Reson. Med.* 64, 457–471. doi: 10.1002/mrm.22428
- McGarry, M. D., Johnson, C. L., Sutton, B. P., Georgiadis, J. G., Van Houten, E. E., Pattison, A. J., et al. (2015). Suitability of poroelastic and viscoelastic mechanical models for high and low frequency MR elastography. *Med. Phys.* 42, 947–957. doi: 10.1118/1.4905048
- Meyer, T., Tzschatzsch, H., Braun, J., Kalra, P., Kolipaka, A., and Sack, I. (2019). "Online platform for extendable server-based processing of magnetic resonance elastography data," in *Proceedings of the 27th Annual Meeting of ISMRM* (Montreal, QC, Canada), 3966.
- Mousavi, S. R., Fehlner, A., Streiberger, K. J., Braun, J., Samani, A., and Sack, I. (2014). Measurement of in vivo cerebral volumetric strain induced by the Valsalva maneuver. *J. Biomech.* 47, 1652–1657. doi: 10.1016/j.jbiomech.2014.02.038
- Munder, T., Pfeffer, A., Schreyer, S., Guo, J., Braun, J., Sack, I., et al. (2018). MR elastography detection of early viscoelastic response of the murine hippocampus to amyloid β accumulation and neuronal cell loss due to Alzheimer's disease. *J. Magn. Reson. Imag.* 47, 105–114. doi: 10.1002/jmri.25741
- Murphy, M. C., Cogswell, P. M., Trzasko, J. D., Manduca, A., Senjem, M. L., Meyer, F. B., et al. (2020). Identification of normal pressure hydrocephalus by disease-specific patterns of brain stiffness and damping ratio. *Invest. Radiol.* 55, 200–208. doi: 10.1097/rli.0000000000000630
- Murphy, M. C., Curran, G. L., Glaser, K. J., Rossmann, P. J., Huston, J., 3rd, Poduslo, J. F., et al. (2012). Magnetic resonance elastography of the brain in a mouse model of Alzheimer's disease: initial results. *Magn. Reson. Imag.* 30, 535–539. doi: 10.1016/j.mri.2011.12.019
- Murphy, M. C., Huston, J., 3rd, Jack, C. R., Jr., Glaser, K. J., Manduca, A., et al. (2011). Decreased brain stiffness in Alzheimer's disease determined by magnetic resonance elastography. *J. Magn. Reson. Imag.* 34, 494–498. doi: 10.1002/jmri.22707
- Murphy, M. C., Jones, D. T., Jack, C. R., Jr., Glaser, K. J., Senjem, M. L., et al. (2016). Regional brain stiffness changes across the Alzheimer's disease spectrum. *Neuroimage Clin.* 10, 283–290. doi: 10.1016/j.nicl.2015.12.007
- Papazoglou, S., Hirsch, S., Braun, J., and Sack, I. (2012). Multifrequency inversion in magnetic resonance elastography. *Phys. Med. Biol.* 57, 2329–2346. doi: 10.1088/0031-9155/57/8/2329
- Parker, K. J. (2014). A microchannel flow model for soft tissue elasticity. *Phys. Med. Biol.* 59, 4443–4457. doi: 10.1088/0031-9155/59/15/4443
- Parker, K. J. (2017). Are rapid changes in brain elasticity possible? *Phys. Med. Biol.* 62, 7425–7439. doi: 10.1088/1361-6560/aa8380

- Patz, S., Fovargue, D., Schregel, K., Nazari, N., Palotai, M., Barbone, P. E., et al. (2019). Imaging localized neuronal activity at fast time scales through biomechanics. *Sci. Adv.* 5:eaav3816. doi: 10.1126/sciadv.aav3816
- Penny, W. D., Friston, K. J., Ashburner, J. T., Kiebel, S. J., and Nichols, T. E. (2011). *Statistical Parametric Mapping: the Analysis of Functional Brain Images*. Elsevier: Amsterdam.
- Perrinez, P. R., Kennedy, F. E., Van Houten, E. E., Weaver, J. B., and Paulsen, K. D. (2009). Modeling of soft poroelastic tissue in time-harmonic MR elastography. *IEEE Trans. Biomed. Eng.* 56, 598–608. doi: 10.1109/tbme.2008.2009928
- Prabhakar, H., Bithal, P. K., Suri, A., Rath, G. P., and Dash, H. H. (2007). Intracranial pressure changes during Valsalva manoeuvre in patients undergoing a neuroendoscopic procedure. *Minim. Invasive Neurosurg.* 50, 98–101. doi: 10.1055/s-2007-982505
- Pstras, L., Thomaseth, K., Waniewski, J., Balzani, I., and Bellavere, F. (2016). The Valsalva manoeuvre: physiology and clinical examples. *Acta Physiol. (Oxf)* 217, 103–119. doi: 10.1111/apha.12639
- Reiss-Zimmermann, M., Streitberger, K. J., Sack, I., Braun, J., Arlt, F., Fritzsche, D., et al. (2015). High resolution imaging of viscoelastic properties of intracranial tumours by multi-frequency magnetic resonance elastography. *Clin. Neuroradiol.* 25, 371–378. doi: 10.1007/s00062-014-0311-9
- Riek, K., Millward, J. M., Hamann, I., Mueller, S., Pfueller, C. F., Paul, F., et al. (2012). Magnetic resonance elastography reveals altered brain viscoelasticity in experimental autoimmune encephalomyelitis. *Neuroimage Clin.* 1, 81–90. doi: 10.1016/j.nicl.2012.09.003
- Rump, J., Klatt, D., Braun, J., Warmuth, C., and Sack, I. (2007). Fractional encoding of harmonic motions in MR elastography. *Magn. Reson. Med.* 57, 388–395. doi: 10.1002/mrm.21152
- Sack, I., Beierbach, B., Wuerfel, J., Klatt, D., Hamhaber, U., Papazoglou, S., et al. (2009). The impact of aging and gender on brain viscoelasticity. *Neuroimage* 46, 652–657. doi: 10.1016/j.neuroimage.2009.02.040
- Sack, I., Streitberger, K. J., Krefling, D., Paul, F., and Braun, J. (2011). The influence of physiological aging and atrophy on brain viscoelastic properties in humans. *PLoS One* 6:e23451. doi: 10.1371/journal.pone.0023451
- Schmid Daners, M., Knobloch, V., Soellinger, M., Boesiger, P., Seifert, B., Guzzella, L., et al. (2012). Age-specific characteristics and coupling of cerebral arterial inflow and cerebrospinal fluid dynamics. *PLoS One* 7:e37502. doi: 10.1371/journal.pone.0037502
- Schrank, F., Warmuth, C., Gorner, S., Meyer, T., Tzschätzsch, H., Guo, J., et al. (2020a). Real-time MR elastography for viscoelasticity quantification in skeletal muscle during dynamic exercises. *Magn. Reson. Med.* 84, 103–114. doi: 10.1002/mrm.28095
- Schrank, F., Warmuth, C., Tzschätzsch, H., Krefl, B., Hirsch, S., Braun, J., et al. (2020b). Cardiac-gated steady-state multifrequency magnetic resonance elastography of the brain: effect of cerebral arterial pulsation on brain viscoelasticity. *J. Cereb. Blood Flow Metab.* 40, 991–1001. doi: 10.1177/0271678x19850936
- Schregel, K., Nazari, N., Nowicki, M. O., Palotai, M., Lawler, S. E., Sinkus, R., et al. (2018). Characterization of glioblastoma in an orthotopic mouse model with magnetic resonance elastography. *NMR Biomed.* 31:e3840. doi: 10.1002/nbm.3840
- Schregel, K., Wuerfel, E., Garteiser, P., Gemeinhardt, I., Prozorovski, T., Aktas, O., et al. (2012). Demyelination reduces brain parenchymal stiffness quantified in vivo by magnetic resonance elastography. *Proc. Natl. Acad. Sci. U.S.A.* 109, 6650–6655. doi: 10.1073/pnas.1200151109
- Selesnick, I. W., Baraniuk, R. G., and Kingsbury, N. G. (2005). The dual-tree complex wavelet transform. *IEEE Signal Process. Magazine* 22, 123–151.
- Shahryari, M., Meyer, T., Warmuth, C., Herthum, H., Bertalan, G., Tzschätzsch, H., et al. (2020). Reduction of breathing artifacts in multifrequency magnetic resonance elastography of the abdomen. *Magn. Reson. Med.* 85:1962–1973. doi: 10.1002/mrm.28558
- Simon, M., Guo, J., Papazoglou, S., Scholand-Engler, H., Erdmann, C., Melchert, U., et al. (2013). Non-invasive characterization of intracranial tumors by MR-Elastography. *N. J. Phys.* 15:085024. doi: 10.1088/1367-2630/15/8/085024
- Smith, S. A., Salih, M. M., and Littler, W. A. (1987). Assessment of beat to beat changes in cardiac output during the Valsalva manoeuvre using electrical bioimpedance cardiography. *Clin. Sci. (Lond)* 72, 423–428. doi: 10.1042/cs0720423
- Stone, D. J., Lyon, A. F., and Teirstein, A. S. (1965). A reappraisal of the circulatory effects of the Valsalva maneuver. *Am. J. Med.* 39, 923–933. doi: 10.1016/0002-9343(65)90114-2
- Streitberger, K. J., Fehner, A., Pache, F., Lacheta, A., Papazoglou, S., Bellmann-Strobl, J., et al. (2017). Multifrequency magnetic resonance elastography of the brain reveals tissue degeneration in neuromyelitis optica spectrum disorder. *Eur. Radiol.* 27, 2206–2215. doi: 10.1007/s00330-016-4561-6
- Streitberger, K. J., Lilaj, L., Schrank, F., Braun, J., Hoffmann, K. T., Reiss-Zimmermann, M., et al. (2020). How tissue fluidity influences brain tumor progression. *Proc. Natl. Acad. Sci. U.S.A.* 117, 128–134. doi: 10.1073/pnas.1913511116
- Streitberger, K. J., Reiss-Zimmermann, M., Freimann, F. B., Bayerl, S., Guo, J., Arlt, F., et al. (2014). High-resolution mechanical imaging of glioblastoma by multifrequency magnetic resonance elastography. *PLoS One* 9:e110588. doi: 10.1371/journal.pone.0110588
- Streitberger, K. J., Sack, I., Krefling, D., Pfuller, C., Braun, J., Paul, F., et al. (2012). Brain viscoelasticity alteration in chronic-progressive multiple sclerosis. *PLoS One* 7:e29888. doi: 10.1371/journal.pone.0029888
- Streitberger, K. J., Wiener, E., Hoffmann, J., Freimann, F. B., Klatt, D., Braun, J., et al. (2011). In vivo viscoelastic properties of the brain in normal pressure hydrocephalus. *NMR Biomed.* 24, 385–392.
- Tully, B., and Ventikos, Y. (2011). Cerebral water transport using multiple-network poroelastic theory: application to normal pressure hydrocephalus. *J. Fluid Mech.* 667, 188–215. doi: 10.1017/s0022112010004428
- Tzschätzsch, H., Krefl, B., Schrank, F., Bergs, J., Braun, J., & Sack, I. (2018). In vivo time-harmonic ultrasound elastography of the human brain detects acute cerebral stiffness changes induced by intracranial pressure variations. *Sci. Rep.* 8:17888.
- Wagshul, M. E., Chen, J. J., Egnor, M. R., McCormack, E. J., and Roche, P. E. (2006). Amplitude and phase of cerebrospinal fluid pulsations: experimental studies and review of the literature. *J. Neurosurg.* 104, 810–819. doi: 10.3171/jns.2006.104.5.810
- Wagshul, M. E., Eide, P. K., and Madsen, J. R. (2011). The pulsating brain: a review of experimental and clinical studies of intracranial pulsatility. *Fluids Barriers CNS* 8:5.
- Wang, J., Shan, Q., Liu, Y., Yang, H., Kuang, S., He, B., et al. (2019). 3D MR elastography of hepatocellular carcinomas as a potential biomarker for predicting tumor recurrence. *J. Magn. Reson. Imag.* 49, 719–730. doi: 10.1002/jmri.26250
- Weickenmeier, J., Kurt, M., Ozkaya, E., de Rooij, R., Ovaert, T. C., Ehman, R. L., et al. (2018). Brain stiffens post mortem. *J. Mech. Behav. Biomed. Mater.* 84, 88–98. doi: 10.1016/j.jmbbm.2018.04.009
- Wuerfel, J., Paul, F., Beierbach, B., Hamhaber, U., Klatt, D., Papazoglou, S., et al. (2010). MR-elastography reveals degradation of tissue integrity in multiple sclerosis. *Neuroimage* 49, 2520–2525. doi: 10.1016/j.neuroimage.2009.06.018
- Yin, Z., Romano, A. J., Manduca, A., Ehman, R. L. and Huston, J. 3rd. (2018). Stiffness and beyond: what MR elastography can tell us about brain structure and function under physiologic and pathologic conditions. *Top Magn. Reson. Imag.* 27, 305–318. doi: 10.1097/rmr.000000000000178

Conflict of Interest: JP was employed by company Siemens Healthcare GmbH, Erlangen, Germany.

The remaining authors declare that the research was conducted in the absence of any commercial or financial relationships that could be construed as a potential conflict of interest.

Copyright © 2021 Herthum, Shahryari, Tzschätzsch, Schrank, Warmuth, Görner, Hetzer, Neubauer, Pfeuffer, Braun and Sack. This is an open-access article distributed under the terms of the Creative Commons Attribution License (CC BY). The use, distribution or reproduction in other forums is permitted, provided the original author(s) and the copyright owner(s) are credited and that the original publication in this journal is cited, in accordance with accepted academic practice. No use, distribution or reproduction is permitted which does not comply with these terms.



A Methodology to Compare Biomechanical Simulations With Clinical Brain Imaging Analysis Utilizing Two Blunt Impact Cases

X. Gary Tan^{1*}, Venkata Siva Sai Sujith Sajja², Maria M. D'Souza³, Raj K. Gupta⁴, Joseph B. Long², Ajay K. Singh⁵ and Amit Bagchi¹

¹ U.S. Naval Research Laboratory, Washington, DC, United States, ² Walter Reed Army Institute of Research, Silver Spring, MD, United States, ³ Institute of Nuclear Medicine and Allied Sciences, New Delhi, India, ⁴ U.S. Army Medical Research and Development Command, Fort Detrick, MD, United States, ⁵ Life Sciences Directorate, Defence Research and Development Organisation (DRDO), New Delhi, India

OPEN ACCESS

Edited by:

Gerhard A. Holzapfel,
Graz University of Technology, Austria

Reviewed by:

Xiaogai Li,
Royal Institute of Technology, Sweden
Jingwen Hu,
University of Michigan, United States

*Correspondence:

X. Gary Tan
gary.tan@nrl.navy.mil

Specialty section:

This article was submitted to
Biomechanics,
a section of the journal
Frontiers in Bioengineering and
Biotechnology

Received: 17 January 2021

Accepted: 06 April 2021

Published: 01 July 2021

Citation:

Tan XG, Sajja VSSS,
D'Souza MM, Gupta RK, Long JB,
Singh AK and Bagchi A (2021) A
Methodology to Compare
Biomechanical Simulations With
Clinical Brain Imaging Analysis
Utilizing Two Blunt Impact Cases.
Front. Bioeng. Biotechnol. 9:654677.
doi: 10.3389/fbioe.2021.654677

According to the US Defense and Veterans Brain Injury Center (DVBIC) and Centers for Disease Control and Prevention (CDC), mild traumatic brain injury (mTBI) is a common form of head injury. Medical imaging data provides clinical insight into tissue damage/injury and injury severity, and helps medical diagnosis. Computational modeling and simulation can predict the biomechanical characteristics of such injury, and are useful for development of protective equipment. Integration of techniques from computational biomechanics with medical data assessment modalities (e.g., magnetic resonance imaging or MRI) has not yet been used to predict injury, support early medical diagnosis, or assess effectiveness of personal protective equipment. This paper presents a methodology to map computational simulations with clinical data for interpreting blunt impact TBI utilizing two clinically different head injury case studies. MRI modalities, such as T1, T2, diffusion-weighted imaging (DWI) and apparent diffusion coefficient (ADC), were used for simulation comparisons. The two clinical cases have been reconstructed using finite element analysis to predict head biomechanics based on medical reports documented by a clinician. The findings are mapped to simulation results using image-based clinical analyses of head impact injuries, and modalities that could capture simulation results have been identified. In case 1, the MRI results showed lesions in the brain with skull indentation, while case 2 had lesions in both coup and contrecoup sides with no skull deformation. Simulation data analyses show that different biomechanical measures and thresholds are needed to explain different blunt impact injury modalities; specifically, strain rate threshold corresponds well with brain injury with skull indentation, while minimum pressure threshold corresponds well with coup–contrecoup injury; and DWI has been found to be the most appropriate modality for MRI data interpretation. As the findings from these two cases are substantiated

with additional clinical studies, this methodology can be broadly applied as a tool to support injury assessment in head trauma events and to improve countermeasures (e.g., diagnostics and protective equipment design) to mitigate these injuries.

Keywords: traumatic brain injury (TBI), computational, modeling and prediction, traffic accidents, magnetic resonance imaging (MRI), diffusion weighted imaging (DWI), apparent diffusion coefficient (ADC), injury assessment

INTRODUCTION

Traumatic brain injury (TBI) has become a growing health concern worldwide, leading to a wide range of problems from mild memory deficits to persistent vegetative states (Florence et al., 2018). According to the 2014 Centers for Disease Control and Prevention (CDC) statistics, over 2.8 million cases of TBI are diagnosed in the United States alone (CDC, 2020). The majority of cases are often the result of motor vehicle accidents, contact sports, and falls. The Glasgow Coma Scale (GCS), based on visual, verbal, and motor response, has been used as the standard diagnostic tool to assess head injuries, which are categorized as mild (GCS score: 13–15), moderate (GCS score: 9–12), and severe (GCS score: 8 or less). Depending upon the extent of the insult and the intensity of the impact, injuries can result in combinations of skull fractures, brain hemorrhage, contusions, subdural hematoma, and diffuse axonal injuries, which can be diagnosed from mild to severe range depending on GCS scores (Post et al., 2015). GCS score based diagnosis can be compromised by clinician-to-clinician variability despite attempts to adhere to the guidelines of the American College of Emergency Physicians criteria (Holdgate et al., 2006). Categorically similar GCS scores can be assigned to vastly different brain injuries ranging from localized lesions with/without skull fractures to coup and contrecoup without any presentation of outward signs of injury. Further variation in diagnoses stems from differences in clinical training, available clinical tools, and also the country of training. Despite the engineering perception that bigger impacts worsen the condition, it was found that skull fractures have not consistently correlated with worsened clinical prognosis. Some TBI patients with skull fracture may have mild symptoms from brain injury, while others with no skull fractures can have sustained severe brain injury (Goldsmith, 2001). While moderate to severe injuries are frequently and easily diagnosed based upon impairments that are clinically obvious, mild injuries have been much harder to diagnose, and distinguishing the extent of the injury based upon clinical presentation with GCS scores is typically challenging.

Neuroimaging tools, such as computed tomography (CT) and magnetic resonance imaging (MRI), play a critical role in clinical evaluation of patients with TBI, specifically with mild TBI, and help characterize the types of injury in addition to GCS scores. Acute TBI could lead to both extra-axial and intra-axial injuries. The former manifests as extradural, subdural, and sub-arachnoid lesions. The latter is seen as contusions and parenchymal hematomas, diffuse axonal injury, and vascular injury (Kazam and Tsiouris, 2015). In contrast to CT, MRI can depict the exquisite details of brain parenchymal changes in mild TBI (Wu et al., 2016). Subtleties in some cases of

mild TBI with various macrostructural and microstructural changes, including disrupted neuronal tracts and blood-related products in the brain, have been revealed with novel and unconventional magnetic resonance (MR) techniques including three-dimensional MRI, susceptibility-weighted imaging (SWI), echo-planar imaging-based diffusion-weighted imaging (DWI) and apparent diffusion coefficient (ADC) maps, and higher-order diffusion imaging (Van Boven et al., 2009; Hunter et al., 2012; Lu et al., 2014). However, these modalities are infrequently used in the clinical setting due to either lack of high-resolution MR capabilities or a limited number of specialized personnel required to process the data. One of the goals of this study is to understand if these imaging modalities can help provide information for injury prediction from computational biomechanics and correspondence.

Over the years, numerous studies on impact head trauma have been conducted to understand biological and biomechanical mechanisms of traumatic brain injury. Translational and rotational forces from rapid acceleration/deceleration of head (coup and contrecoup injury), blows to the head/falls (local lesions), and combinations of these loading conditions have been shown to cause TBI. Pre-clinical models have been a great resource to understand controlled intracranial injury outcomes, but bridging the gap between the species to translate the data into humans has been a challenge (Cernak et al., 2017). Moreover, the biomechanical parameters that correspond with injury are currently unclear as also are the intracranial manifestations of the insult. Post-mortem human subjects have provided important biomechanical data (Hardy et al., 2007), but the introduction of sensors and other instrumentation alters the tissue response. The data collected in the laboratory setting (e.g., cadaveric studies or controlled experimental impact loading) often do not translate to “real-world” scenario due to the variety of actual loading conditions and the clinical presentation. Computational biomechanics provides an alternative approach to sidestep these confounding issues (Ji et al., 2014). The validated head model, such as in Refs. (Mao et al., 2013; Giudice et al., 2019; Zhou et al., 2019; Budday et al., 2020; Li et al., 2020), can establish full relationships between the impact loading on the head and the internal biomechanical response for actual loading conditions that may not be practical to recreate experimentally. The severity of injury from these biomechanical measures, such as pressures, strains, stress, and their time variances, can be represented using established injury criteria (Zhang et al., 2003, 2004; Fernandes and Alves de Sousa, 2015) and applying such criteria for each element of the model.

Our group has developed a multi-fidelity computational model to represent the dynamics of a pedestrian fall and subsequent structural response of the human head due to an

impact (Tan et al., 2020). The developed high-fidelity finite element (FE) model accurately reproduces the complex internal and external structures of the head (Cotton et al., 2015) and has been validated using data from human cadaver tests (Saunders et al., 2018; Tan et al., 2020). This hybrid (biodynamics and biomechanics analyses) approach has simplified the simulation and provided the effect of human body kinematics in calculating stress and strain distributions in the brain. The biomechanical results have been compared with MRI readouts from a case of a motor vehicle accident involving a fall to show the qualitative correspondence between the biomechanical outcomes and the assessed injury (Tan et al., 2020).

A key question from qualitative assessments in our previous research (Tan et al., 2020) was if the clinical data from MR images and their analyses can be quantitatively compared with biomechanical simulation results of real-world blunt impact incidents. The application of different MRI modalities to cross-correlate clinical injury assessment with biomechanical simulations of reconstructing an incident is a missing link. In this work, we aim to develop a method that can map the clinical findings onto quantitative biomechanical results, and create a link between the clinical and biomechanics research on brain injury models and mechanisms due to blunt impact. We analyze two clinical cases of blunt impact, one with coup injury and skull indentation, and the other with coup–contrecoup injury and no skull indentation. The head finite element (FE) model is used to reconstruct the high-fidelity biomechanical response of the skull and brain to blunt impact in a fall based on eyewitness reports and clinical assessment. Different mechanical measures such as pressure, shear stress, principal strain, strain rate, product of strain and strain rate, and strain energy are analyzed to identify possible correspondence between their field values and *in vivo* MRI data. The thresholds of such biomechanical measures for injury severity are determined based on the neuroimaging modality that quantifies the injury. We found that an unconventional MRI modality, such as DWI, is a useful diagnostic tool that can inform computational biomechanics, irrespective of injury type. A methodological implementation of this approach to map computational biomechanical simulation results with clinical image-based data is discussed.

METHODS

Ethics of Data Collection

A written informed consent was obtained from the individuals for the publication of any potentially identifiable images or data included in this article. The institutional Ethics Committee for the Institute of Nuclear Medicine and Allied Sciences (INMAS) approved the study.

Clinical Data Collection

Two clinical cases of blunt impact were considered. Both cases had sustained blunt injury to the cranium, but through different mechanisms. While one individual had a motor vehicle accident, the other sustained a fall from a height. Both suffered from a

concussion with transient loss of consciousness, corresponding to mild traumatic brain injury.

Imaging modalities like CT and MRI are widely used to assess the extent of damage to the skull and brain parenchyma. Among these modalities, MRI is acclaimed as the most sensitive to detect and delineate brain injury (Amyot et al., 2015). MRI data was collected on a Siemens Skyra 3.0T scanner using a 20-channel phased array head coil and a 45 mT/m actively shielded gradient system. The MR protocol used in this study consisted of the following:

1. Three-plane localizer imaging with TR = 8.6 ms and TE = 4.0 ms;
2. T1 weighted axial images with TR = 2,110 ms, TE = 12.0 ms, TI = 898 ms, slice thickness = 5 mm, field of view = 179×220 mm;
3. T2 weighted axial images with TR = 6,000 ms, TE = 100 ms, slice thickness = 5 mm, field of view = 179×220 mm, image matrix = 175×320 ;
4. Fluid attenuation inversion recovery (FLAIR) axial images with TI = 2,500 ms, TR = 9,000 ms, TE = 81.0 ms, field of view = 172×220 mm, slice thickness = 5 mm, image matrix = 175×320 ;
5. FLAIR coronal images with TI = 2,500 ms, TR = 9,000 ms, TE = 81.0 ms, field of view = 172×220 mm, slice thickness = 4.5 mm, image matrix = 175×320 ;
6. T2 weighted sagittal images with TR = 4,550 ms, TE = 87 ms, slice thickness = 4 mm, field of view = 220×220 mm, image matrix = 285×384 ;
7. Magnetization-prepared rapid acquisition gradient echo (MPRAGE) with 160 sagittal slices, slice thickness = 0.9 mm, field of view = 240 mm, TR = 1,900 ms, TE = 2.49 ms;
8. Susceptibility-weighted imaging (SWI) with TR = 28 ms, TE = 20 ms and 3D MPRAGE images using TI = 900 ms, TR = 1,900 ms, TE = 2.4 ms, slice thickness = 0.9 mm, field of view = 240×240 mm, and image matrix = 218×256 ;
9. Echo-planar imaging (EPI) sequence for generation of DWI and subsequent ADC maps with TR = 8,800 ms, TE = 95 ms, slice thickness = 3 mm, field of view = 230×230 mm, and image matrix = 128×128 .

Each of the above sequences highlights a particular aspect of the tissue, and the integrated use of these sequences provides a holistic understanding of the organ being imaged as well as its underlying pathology. T1-weighted sequences are best for producing the most “anatomical” representation, resulting in images that most closely approximate the macroscopic anatomy of tissues (Mangrum et al., 2012). T2-weighted images are excellent for highlighting pathology as they are very sensitive to changes in water content (Mangrum et al., 2012). FLAIR images are especially useful in the brain, and enable detection of parenchymal edema without the glaring high signal from cerebrospinal fluid (CSF) (Vaswani et al., 2014). SWI images, with their superior sensitivity for paramagnetic deoxygenated blood products enable the detection of hemorrhagic foci in the parenchyma (Tong et al., 2008). Some of the abovementioned

sequences are acquired in all three planes of axial, coronal, and sagittal so as to better visualize the details. The MPRAGE sequence is a three-dimensional T1-weighted sequence, which provides a whole brain coverage in a short scan time with isotropic images that can be viewed in multiple planes (Nelson et al., 2008).

DWI exploits the random motion of water molecules in tissue and thereby gives insight into cellularity, cell swelling, and edema (Hagmann et al., 2006). This random motion can be quantitatively assessed using the ADC value, which is displayed as a parametric map that reflects the degree of diffusion of water molecules through different tissues. The normal ADC value ranges from 700 to $1,000 \times 10^{-6} \text{ mm}^2/\text{s}$ for gray matter, from 670 to $800 \times 10^{-6} \text{ mm}^2/\text{s}$ for white matter, and from $3,000$ to $4,000 \times 10^{-6} \text{ mm}^2/\text{s}$ for CSF (Sener, 2001). Injury to any part of the brain would alter the ADC value, thus providing an objective quantitative assessment of injury severity. Currently available evidence suggests the ADC change is more sensitive in the detection of sustained brain tissue injury than other available imaging modalities and is better correlated with symptoms (Goetz et al., 2004; Moen et al., 2014).

ADC image data were extracted from 45 transverse slices, 4 mm apart, using ImageJ (Schneider et al., 2012) software, and the data results were saved for further analysis. For 3D reconstruction, the ADC data were mapped to a rectangular box with a $128 \times 128 \times 45$ grid. The resulting ADC model can be viewed in any post-processing application, such as Paraview (Ahrens et al., 2005), and used to compare with biomechanical measures such as pressure, shear stress, strain rate, product of strain and strain rate, and strain energy for the correlation.

Biomechanics Modeling and Simulation

A multi-fidelity, two-step modeling approach has been used for simulating the brain injury biomechanics in the reconstructed accident. The first step simulates the biodynamics of a whole-body model by the external loading on the body, representing a pedestrian fall. The second step applies the initial condition and effective boundary condition from the biodynamic simulation to the head to determine stresses and strains in the head and brain using FE-based biomechanics analysis. The explicit finite element solver CoBi-FEM (Tan et al., 2017) was chosen for such impact analysis. The solver has been verified in many biomechanics-related projects (Teferra et al., 2018; Saunders et al., 2019; Tan et al., 2020; Tan and Matic, 2020).

To simulate the kinematics of pedestrian fall, an articulated human biodynamic model developed by Tan and Przekwas (2011) was used. This articulated human body model is partitioned into 16 major body components, such as head, neck, chest, and abdomen. Fifteen joints connect these body components to represent the pedestrian. The fast-running biodynamics simulation provides the proper initial and loading conditions for the high-fidelity head FE model, including translational and rotational velocities of the head, and forces and moments at the base of the neck before the head impact. The

details of the biodynamic modeling of an articulated human body fall can be found in Tan and Przekwas (2011).

To simulate the biomechanics of blunt impact to the pedestrian due to the fall, the US Naval Research Laboratory high-fidelity human head FE model, developed based upon high-resolution MRI scans of 50th percentile adult male, was used. This model uses 4.5 million tetrahedral elements to discretize the complicated head geometry that includes 29 anatomic tissue components (Cotton et al., 2015). The average characteristic element size is less than 2 mm, which is suitable for capturing impact-induced stress wave propagation in the head. The material properties of the tissue components in the head are based on literature findings (Brewick et al., 2017) that are used to calibrate the material models. The gray matter and white matter are modeled as hyper-viscoelastic materials. The cortical and cancellous bones are modeled as elastoplastic materials to account for large permanent deformation at the impact region. The CSF in ventricles and subarachnoid space surrounding the brain and the spinal cord is modeled as a hyperelastic material with the same speed of sound as water and a very low shear modulus. Average nodal pressure (ANP) linear tetrahedral elements (Bonet et al., 2001) are used to circumvent the locking problem associated with the nearly incompressible biological tissues. Furthermore, this element does not have hourglass instability issue and, thus, provides robust performance in modeling of the large localized deformation in the head (Tan et al., 2020). We have validated the current head model with the experimental results of a cadaveric head (Nahum et al., 1977; Trosseille et al., 1992; Hardy et al., 2007) in both the intracranial pressure (ICP) and brain motion (Saunders et al., 2018; Tan et al., 2020). To produce a typical 20 ms of response time, the simulation required 24 h of computational time using 96 cores on a high-performance computing (HPC) cluster. The cluster is an HPE SGI 8600 system with 48 cores per node, where each node has 192 GB of shared memory, and each core includes an Intel Xeon Platinum 8168/2.7 GHz processor.

From the FE simulation, we obtain various biomechanical variables including the indentation of skull and brain, pressure, principal strain, effective strain, shear stress, von Mises stress, strain rate, product of strain and strain rate, dilatational strain energy density, and distortional strain energy density as listed in **Table 1**. The strains are based on the Green-Lagrangian strain tensor E since the simulations involve large strain. The stresses are based on the Cauchy stress tensor. The strain rate is the symmetrized velocity gradient. The effective strain is defined as $\sqrt{\frac{3}{2} E^d : E^d}$ where E^d is the deviatoric strain of E . Similarly, we can define the von Mises stress and the effective strain rate. The internal energy can be split into the dilatational energy and distortional energy. The dilatational energy is the integration of the product of pressure and local volume change over the entire volume, while the distortional energy is the integration of the product of deviatoric stress and deviatoric strain tensors over the volume. Their maximum or minimum values in the simulation are used to identify the possible correspondence with the *in vivo* MRI injury data. For the 3D spatial dataset, different cross sections of the head are used for both the qualitative

and quantitative comparison between MRI data and simulation results. More details on how to make the comparison specifically for individual cases will be described in the results.

RESULTS

Clinical Interpretation of Brain Injury Due to Fall

Table 2 shows the two cases used in this study. High-resolution image data of case 1 was obtained from an MRI scan of a young South Asian adult, who had sustained head injury from a road traffic accident, a few days prior to the scan. The hospital report indicated that the individual was a pedestrian who was hit by a speeding motor vehicle from the front, sustained a concussion due to the backward fall on the ground, and suffered from loss of consciousness for a period of approximately 20 min. The GCS score at the time of hospital admission, in less than 1 h from the blunt impact, was 13, which is attributed to a mild brain injury. A depressed fracture of the skull with underlying hemorrhagic changes was observed in CT imaging. The MRI data revealed a depressed fracture of the right parietal bone of the skull with a hemorrhagic contusion in the underlying brain parenchyma and associated subdural hematoma in the first row of **Figure 1**. The maximum skull indentation at the impacted region measured from the MRI image is found to be approximately 9 mm. No contrecoup injury was observed in the actual medical images (second row of **Figure 1**).

Case 2 was a middle-aged South Asian adult, who accidentally fell to the ground from a height, according to the hospital report. The individual hit his head in the occipital region and sustained a head injury with a transient loss of consciousness for approximately 15 min. At the time of admission to the hospital, the patient had regained consciousness and had a GCS score of 15. CT scan revealed hemorrhagic contusions in the right cerebellar and left frontal regions, but no skull fracture or visible skull deformation was observed. He underwent an MRI scan several days after injury. This, too, revealed hemorrhagic contusions in the right cerebellar and left frontal regions with a fine extra-axial subdural fluid collection in the left fronto-temporo-parietal regions suggestive of a coup–contrecoup injury (last two rows of **Figure 1**). The complete set of FLAIR images for both cases can be found in **Supplementary Figures 1, 2** which show the gross injury patterns well.

Correspondence Between Clinical Images and Biomechanics

Conditions of Biomechanical Simulations

The biodynamics of the fall was modeled using the case reports documented by the hospital, as well as clinicians' assessment of the most likely trajectory of the fall and the impact (**Figure 2A**). For the cases simulated here, the assumptions were: (i) The head was rotating backward around the first thoracic vertebra (T1) before hitting the ground (**Figure 2B**). (ii) The head impacted a solid hemispherical object on the ground. The distance between T1 and the center of the mass of the head was approximately 0.2 m. For case 1, the biodynamic simulation of the fall suggested

a 30 rad/s angular velocity of the head around joint T1 when impacting a 15-mm radius solid object (**Figure 2C**) to generate a comparable skull indentation as in the MRI image. For case 2, the simulation suggested a 15 rad/s angular velocity of the head around joint T1 when impacting a 60-mm radius solid object (**Figure 2D**) without creating a visible skull deformation at the impact region. The size of the solid object for each case was determined based on the information from the emergency room (ER) documentation and clinical report. The forces on the head due to the impact were the boundary conditions used to simulate the biomechanics of the blunt impact to the head. Both simulations were carried out for a total duration of 20 ms from the point of contact between the head and the hemispherical object.

Kinetics of Simulated Blunt Impacts

From the biomechanical simulations, the time histories of contact force components for case 1 and case 2 are shown in **Figure 3**. The force components rise faster and last a much shorter duration (approximately 5 ms) in case 1 compared with that in case 2 (time for the force to return to zero is approximately 8 ms). The displacements of the head at the center of gravity are shown in **Figure 4**, which show that the head initially moves toward the impactor and then rebounds around 2.5 ms for both cases.

The change in kinetic energy from the impact of the pedestrian's head with the solid object is shown in **Figure 5A** for case 1 and **Figure 5B** for case 2. **Figures 5A,B** also show the energy absorbed by the skull due to elastic and/or plastic deformation during the impact. The kinetic energy is maximum at the onset of the impact, at approximately 80 J. Over time, i.e., during the contact, this energy is partly absorbed by the skull to cause elastic and plastic (permanent) deformation of the skull, and partly transmitted into the brain. **Figure 5A** shows that for case 1, the maximum energy absorbed by the skull is approximately 50 J, which causes skull indentation (**Figure 3A**). This energy is responsible for large local strains and pressure build-up in the coup region of the brain in case 1. The concentration of the strains in the brain at the point of impact perhaps reflects the higher energy being absorbed by the brain in this region. The change in energy distribution for case 2, shown in **Figure 5B**, on the other hand, shows a different pattern. The total kinetic energy due to the impact is approximately 20 J, but a smaller proportion of this energy (approximately 8 J) is absorbed by the skull, and most of it, we assume, contributes to an elastic deformation of the skull. The energy transmitted into the brain is distributed more evenly in the coup region, causing the coup–contrecoup phenomenon in the brain.

The global response in cases 1 and 2 can also be represented through head accelerations over time, shown in **Figure 6**. Although both acceleration profiles are similar, case 1 has a higher peak (270 g) than case 2 (150 g); on the other hand, case 1 has a shorter period of contact (approximately 4.5 ms) than case 2 (approximately 6.7 ms). These differences suggest that both the impact energy and impactor can affect the head acceleration. While the acceleration profile can suggest a measurable parameter, the limited data set here is not adequate to relate acceleration to any of the region-specific clinically identified brain injuries for these cases. For reference, the

TABLE 1 | Biomechanical variables used to compare with clinical data.

Biomechanical measures	Variables
Deformation	Indentation of skull and brain
Strain related	First principal strain, effective strain First principal strain rate, effective strain rate, shear strain rate Product of effective strain and effective strain rate
Stress	Pressure, maximum shear stress, von Mises stress
Energy	Dilatational strain energy density, distortional strain energy density

TABLE 2 | Clinical assessment of brain injury due to fall accidents.

Case number	Cause of blunt impact	GCS score at emergency room	Injury assessment
1	Road traffic accident; backward fall	13	Skull indentation; coup injury
2	Fall from height; occipital collision	15	Coup and contrecoup injury

US Army aircrew helmet requirements use an average peak acceleration of 150 g with a maximum of 300 g, for the blunt impact pass-fail criteria (McEntire and Whitley, 2005).

Computational Biomechanical Outcomes

In the following paragraph, we present the results related to the observed injury in the brain for these two cases. The contour of maximum effective strain rate on the brain during 20 ms of biomechanical simulation for case 1 is shown in the first row of **Figure 7**. Among the three types of strain rates commonly used, the peak value of the maximum shear strain rate is the largest, the effective strain rate is slightly smaller, and the maximum principal strain rate is about one-half of the maximum shear strain rate or effective strain rate. When comparing the contour pattern of strain rate in the brain, these three strain rates are similar in their respective value ranges in both cases (shown in **Supplementary Figure 3**). In this paper, we use the effective strain rate for the comparison. Due to the local skull indentation of case 1, the brain is in compression, and the minimum pressure shown in **Figure 7** is small. Similar to observations from clinical imaging of case 1, the skull deformation is observed at the impact region with anatomical accuracy. The large value of maximum effective strain rate mainly appears near the indented area, similar to the injury locations seen in **Figure 1** and **Supplementary Figure 1**. In contrast to case 1, the skull in case 2 has no observable deformation, and the strain rate is relatively small and distributed around the brain, as shown in the third row of **Figure 7**. The contour of minimum pressure on the brain during 20 ms of computational simulation for case 2 is also shown in **Figure 7**. The minimum pressure around -100 kPa was found at both coup and contrecoup regions, similar to the injury locations as observed in case 2 of **Figure 1** and **Supplementary Figure 2**.

Unlike the effective strain rate, the large values of first principal strain, maximum shear stress, and the product of effective strain and effective strain rate in **Figure 7** are seen in the area beyond the indented region in case 1. In case 2, the maximum shear stress, effective strain rate, and the product of effective strain and effective strain rate are relatively small and again distributed around the brain in **Figure 7**. In both cases, the von Mises stress contours are similar to those of maximum shear

stress, while the contours of strain energy density are similar to those of the product of effective strain and effective strain rate and, thus not shown here.

Different cross sections of the 3D head can be used for comparison between MRI data and simulation results. From the MRI images, the most injured regions are near the impact site and/or along the impact direction. Compared with other planar views such as sagittal, transverse and coronal planes, the plane passing through a line joining the impact location and its diametrically opposite point on the skull is more representative for visualization of the injury in the brain. Such a vertical plane, shown by the red lines in the left column of **Figure 7**, was chosen to represent the transitions in the ADC values from the MRI as well as the simulated biomechanical measures. Details of the computed maximum pressure, minimum pressure, maximum first principal strain, maximum shear stress and maximum effective strain rates for the two cases are elaborated in the second and fourth rows of **Figure 7**. For case 1 with the coup injury, only the maximum effective strain rate in the second row of **Figure 7** shows a large value in the coup region and smaller values in other areas. For case 2, with the coup–contrecoup injury, only the minimum pressure in the fourth row of **Figure 7** shows the large value at both coup and contrecoup regions. Other variables do not show correspondence with the clinically identified extent of injury. Note that the maximum pressure is large in the entire brain in case 1, while it is large only at the coup region in case 2. The time to reach the maximum for all biomechanical variables in the brain shown in **Figure 7** during the impact events is in **Table 3**.

Comparison of Magnetic Resonance Imaging-Apparent Diffusion Coefficient Data With Computational Biomechanics

The ADC maps for the two cases considered here are compared with the biomechanical measures in **Figures 8, 9**. We identified the location of the center of impact region of the head from the MRI data, and the point on the diametrically opposite surface of the cranium, and termed them as the coup and contrecoup points, respectively. We compare below, the injury assessment of ADC data with biomechanical measures along the

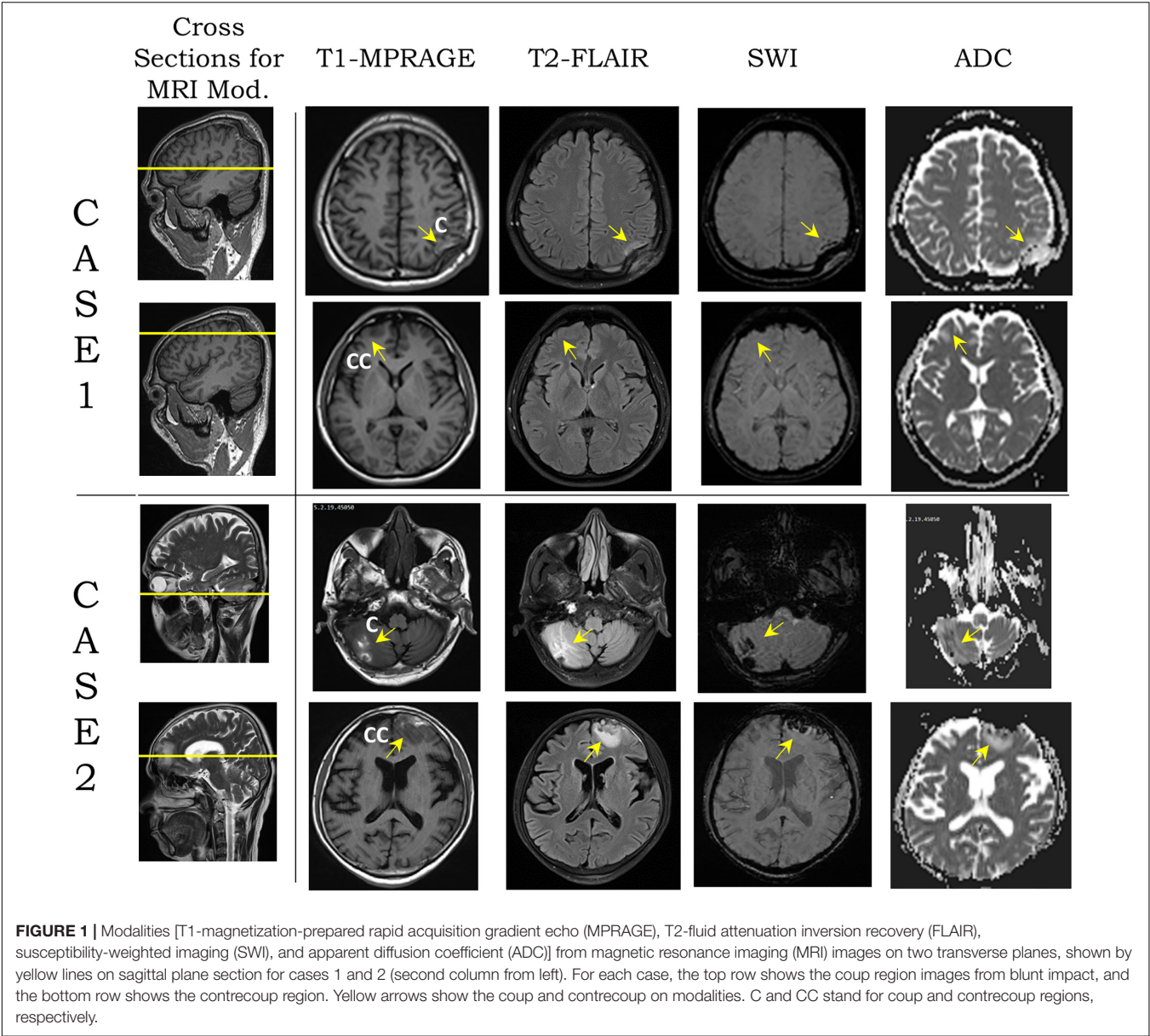


TABLE 3 | The time to reach the maximum of different variables in the brain (ms).

Case number	Compressive pressure	Tensile pressure	First principal strain	Maximum shear stress	Effective strain rate	(Effective strain) × (Effective strain rate)
1	2.9	0.4	4.3	4.1	1.9	4.7
2	15.1	13.7	9.7	13.5	17.1	11.4

coup–contrecoup line, as a representative way to identify the correspondence between clinical analysis and simulation results. **Figures 8, 9** show the ADC contour maps on the left and the corresponding ADC values along the coup–contrecoup line on the right in the top row, and maximum effective strain rate and minimum pressure contour maps and the corresponding distributions along the same line in the bottom row, respectively,

for cases 1 and 2. All ADC values are compared with respect to an approximate mean value of $750 \times 10^{-6} \text{ mm}^2/\text{s}$ of gray matter and white matter, which is displayed by the dotted lines in **Figures 8B, 9B**. For case 1, in the brain injury region (i.e., the coup region), the relative change in ADC from the mean normal value ranges from -450 to $1,150 \times 10^{-6} \text{ mm}^2/\text{s}$ (**Figure 8B**), and this significant

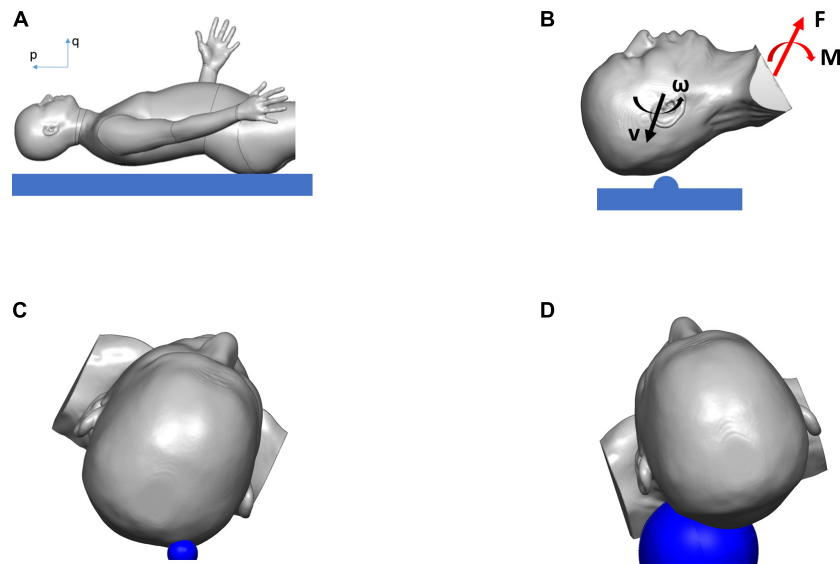


FIGURE 2 | Simulation results showing the biodynamics of the fall, resulting in blunt impact to the head: **(A)** head position just before hitting the ground, **(B)** head with initial velocities hitting hemispherical object and rotating about T1, and producing the forces and the moments applied to the head and neck, **(C)** head hitting hemispherical object of radius 15 mm (in blue) in case 1, **(D)** head hitting hemispherical object of radius 60 mm (in blue) in case 2.

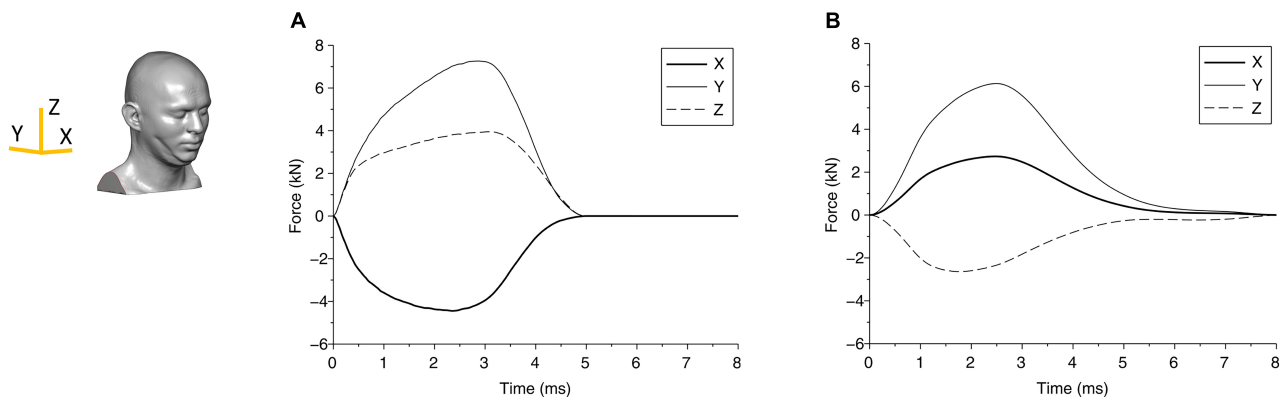


FIGURE 3 | The force components due to the blunt impact between the head and the impactor are shown for **(A)** case 1 and **(B)** case 2. The axes are shown in the head finite element (FE) model.

change is observed up to a depth of approximately 10 mm from the cerebral cortex. In the same region, i.e., at the same depth from the brain cortex, computational simulation shows the maximum effective strain rates to be from 250 to 950 s^{-1} . In the contrecoup region, there is no observable change in ADC values from the baseline, while the effective strain rate increases up to 150 s^{-1} . This suggests that smaller strain rates may represent correspondingly small or no noticeable ADC changes in injured brain tissue.

For case 2, a comparison of ADC map with simulated minimum pressure at the coup–contrecoup cross section is shown in **Figure 9**. At the end of the 20-ms contact–rebound simulation period, the large minimum/tensile pressure appears at both the coup and contrecoup regions. However, when

compared with the coup region, the contrecoup exhibits larger tensile pressures in the superficial cortical structures. In the coup region of the brain injury, the relative change in ADC shows a clearly identifiable range from -750 to $950 \times 10^{-6} \text{ mm}^2/\text{s}$, and this higher value is observed up to a depth of approximately 30 mm from the cerebral cortex. In the contrecoup region of the brain injury, the ADC change increases to $1,100 \times 10^{-6} \text{ mm}^2/\text{s}$, and this higher value is observed up to a depth of approximately 20 mm from the cerebral cortex. In the same coup region at the same depth, computational simulation shows minimum pressure from -90 to -100 kPa . In the contrecoup region at the same depth, computational simulation shows a minimum pressure from -90 to -110 kPa . **Table 4** summarizes the ADC changes from the mean value in the coup

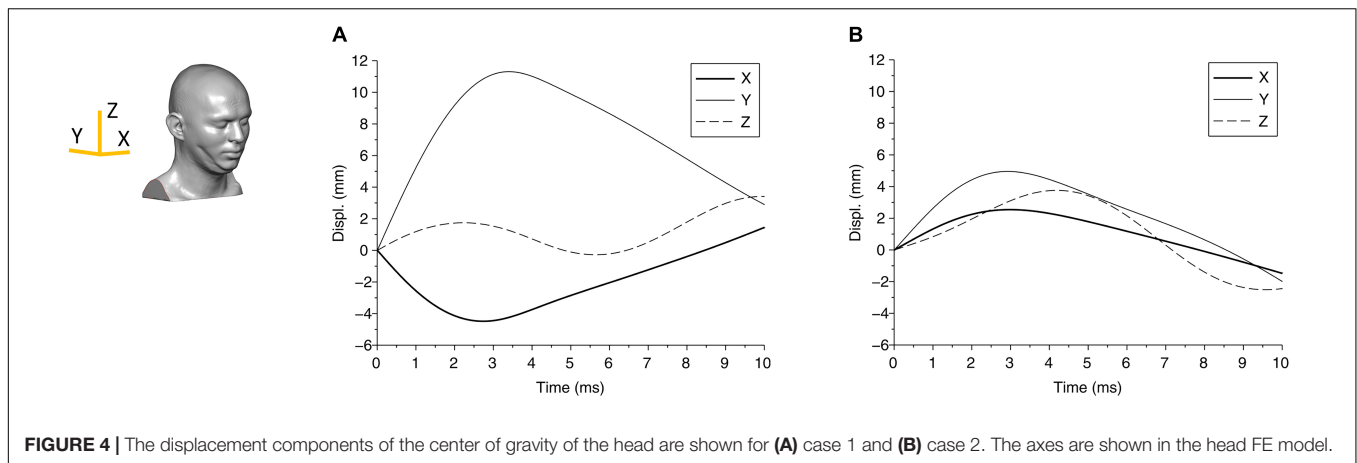


FIGURE 4 | The displacement components of the center of gravity of the head are shown for (A) case 1 and (B) case 2. The axes are shown in the head FE model.

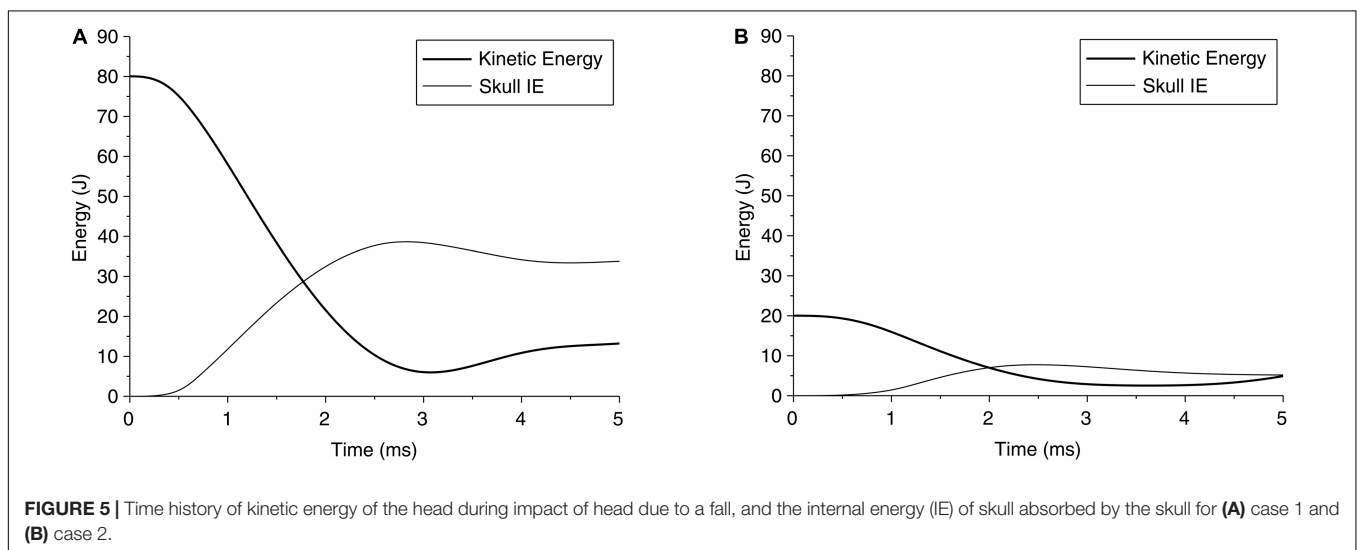


FIGURE 5 | Time history of kinetic energy of the head during impact of head due to a fall, and the internal energy (IE) of skull absorbed by the skull for (A) case 1 and (B) case 2.

and contrecoup regions and biomechanical parameters and the influence of depth for the two cases. Additional comparison between ADC data and simulation results in the transverse plane showing similar outcomes for the two cases can be found in **Supplementary Figures 4, 5**.

Comparison of Injury Types in Case 1 (Skull Indentation) and Case 2 (Coup and Contrecoup Injury)

At the impact location (i.e., coup region), the maximum ADC change for case 1 is around $1,150 \times 10^{-6} \text{ mm}^2/\text{s}$, which is larger than that for case 2 (around $950 \times 10^{-6} \text{ mm}^2/\text{s}$). When the deformation of the tissue from brain surface is considered, the depth of ADC change is relatively smaller in case 1 (approximately 10 mm) when compared with case 2 (approximately 30 mm). For case 2, the maximum ADC change in the coup region (around $950 \times 10^{-6} \text{ mm}^2/\text{s}$) is smaller compared with that at the contrecoup region (around $1,100 \times 10^{-6} \text{ mm}^2/\text{s}$). The region of the brain normal to the interior surface of the skull shows noticeable ADC change at

the coup region (approximately 30 mm) compared with that at the contrecoup (approximately 20 mm). In comparison, for case 1, the maximum effective strain rate is above 250 s^{-1} up to a depth of 10 mm in the coup region but less than 150 s^{-1} in the contrecoup region. For case 2, the minimum pressure below -90 kPa is 30 mm into the brain tissue in the coup region and 20 mm in the contrecoup region. In addition, the minimum pressure in the coup region (-100 kPa) is less than that in the contrecoup region (-110 kPa). The similarity of both the ADC change and simulated minimum pressure appears to be that the contrecoup injury is more severe than the coup injury but affects a smaller depth in the brain.

Sensitivity of Simulation Results Related to Impact Conditions

Sensitivity analysis was carried out with computational simulations by assessing the effect of impact condition on the injury outcome from the clinical analysis. A number of simulations were performed by changing the angular velocity of the head in case 1 and case 2. As shown in **Table 5**, for

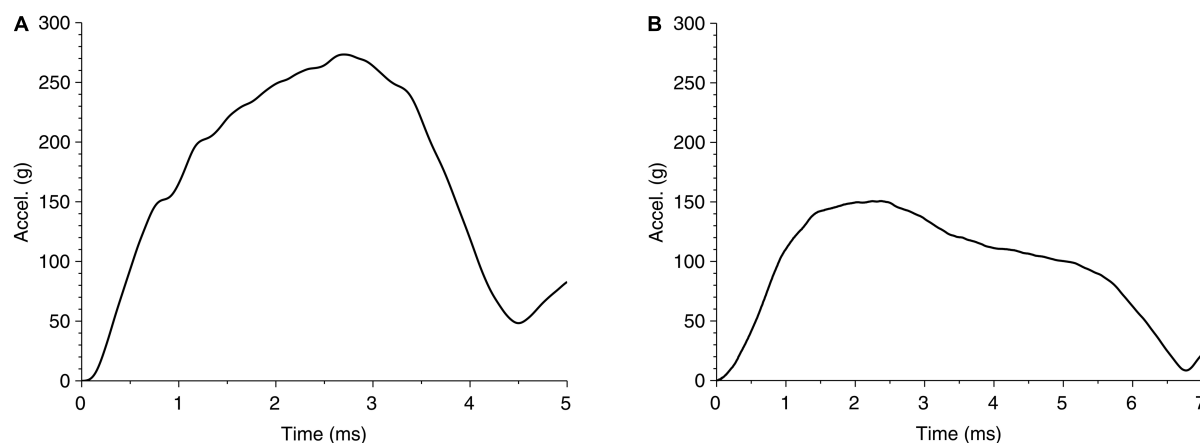


FIGURE 6 | Time history of head acceleration during impact of head due to fall for (A) case 1 and (B) case 2.

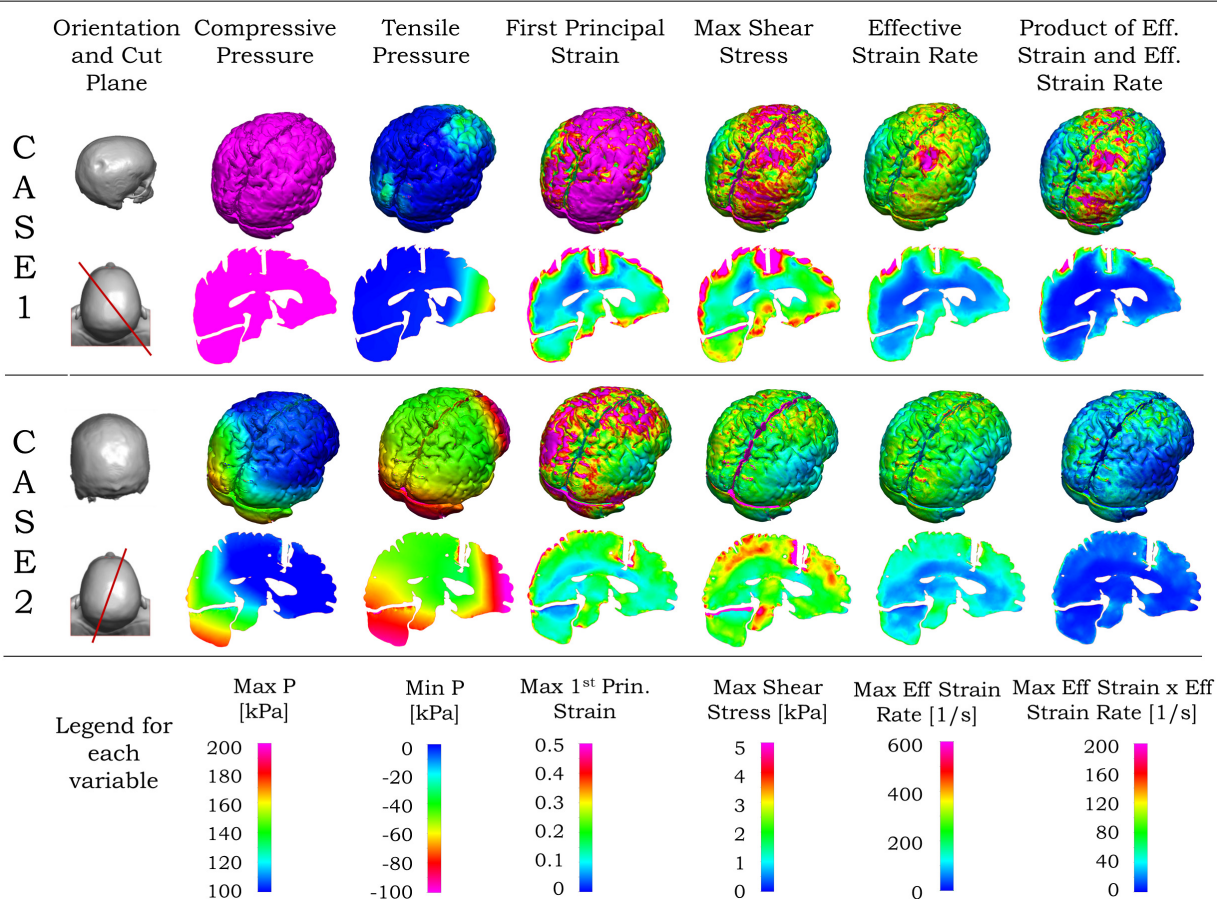


FIGURE 7 | Simulated blunt impact biomechanical responses for cases 1 and 2. For both cases, the second column from left shows the head (top), and vertical plane through the coup–contrecoup line (bottom). For each case, the upper row shows the biomechanical contours for the brain, and the bottom row the contours on the vertical plane passing through the coup–contrecoup line. The last row shows the legends for the maximum of each biomechanical variable specified on the top row. Only data for cerebrum, cerebellum, and brainstem regions are shown.

case 1, when the angular velocity is varied between 28 and 32 rad/s, the skull indentation changes from 8.6 to 9.5 mm and the head acceleration from 245 to 290 g. The region of

the brain that exceeds the effective strain rate of 250 s^{-1} also varies, in which the depth of this region from the brain outer surface along the coup–contrecoup line changes from

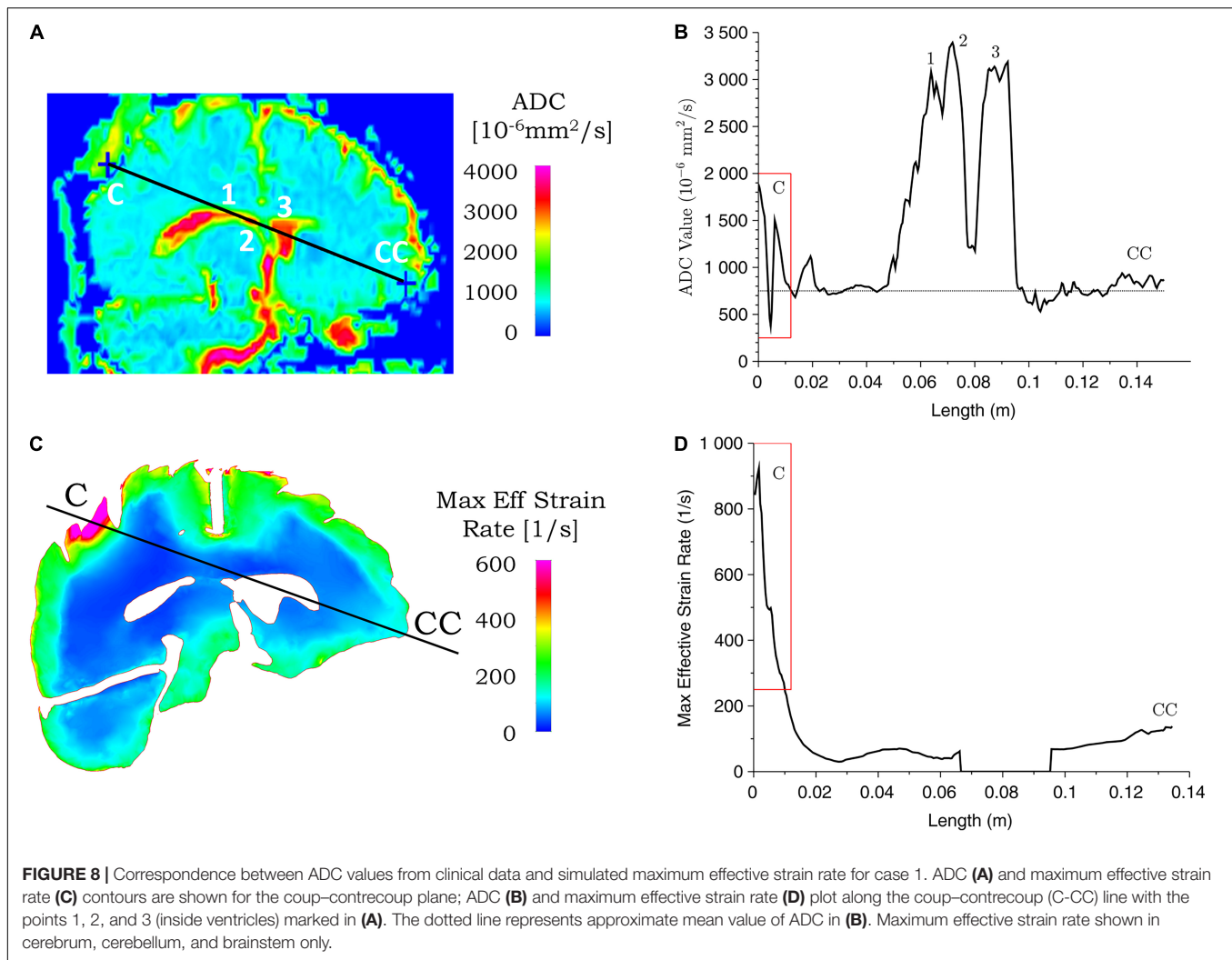


TABLE 4 | Comparison between the change in ADC and biomechanical measures for the two cases.

Case number	Range of ADC change and depth in the coup region	Range of ADC change and depth in the contrecoup region	Depth of effective strain rate ($>250 \text{ s}^{-1}$) in the coup region	Depth of pressure ($<-90 \text{ kPa}$) in the coup region	Depth of pressure ($<-90 \text{ kPa}$) in the contrecoup region
1	(-450,1,150), ~10 mm	—	~10 mm	—	—
2	(-750,950), ~30 mm	(0,1,100), ~20 mm	—	~30 mm	~20 mm

8.8 to 10.2 mm (see **Figure 8** for the coup–contrecoup line and the plot of strain rate contour for angular velocity of 30 rad/s). At angular velocities lower than 28 rad/s or higher than 32 rad/s, both the skull indentation and injury depth in brain become increasingly different from those measured from the MRI data. This suggests that an angular velocity close to 30 rad/s reasonably represents the actual accident condition being modeled.

In case 2, as shown in **Table 5**, when the angular velocity is varied between 12 and 15 rad/s, the head acceleration changed from 125 to 150 g with no visible deformation on the skull.

The region of the brain with a maximum tensile pressure in the coup and contrecoup regions below -90 kPa also changes. On the coup side, the depth of this region (i.e., with a tensile pressure below -90 kPa) ranges from 15 to 30 mm. On the contrecoup side, the depth of this region is increased from 17 to 20 mm (see **Figure 9** for the coup–contrecoup line and the plot of minimum pressure contour for angular velocity of 15 rad/s). With angular velocities smaller than 12 rad/s, little or no injury is seen at the coup or contrecoup regions based on the given pressure criterion. At angular velocities greater than 15 rad/s, at the coup region, the skull deforms plastically,

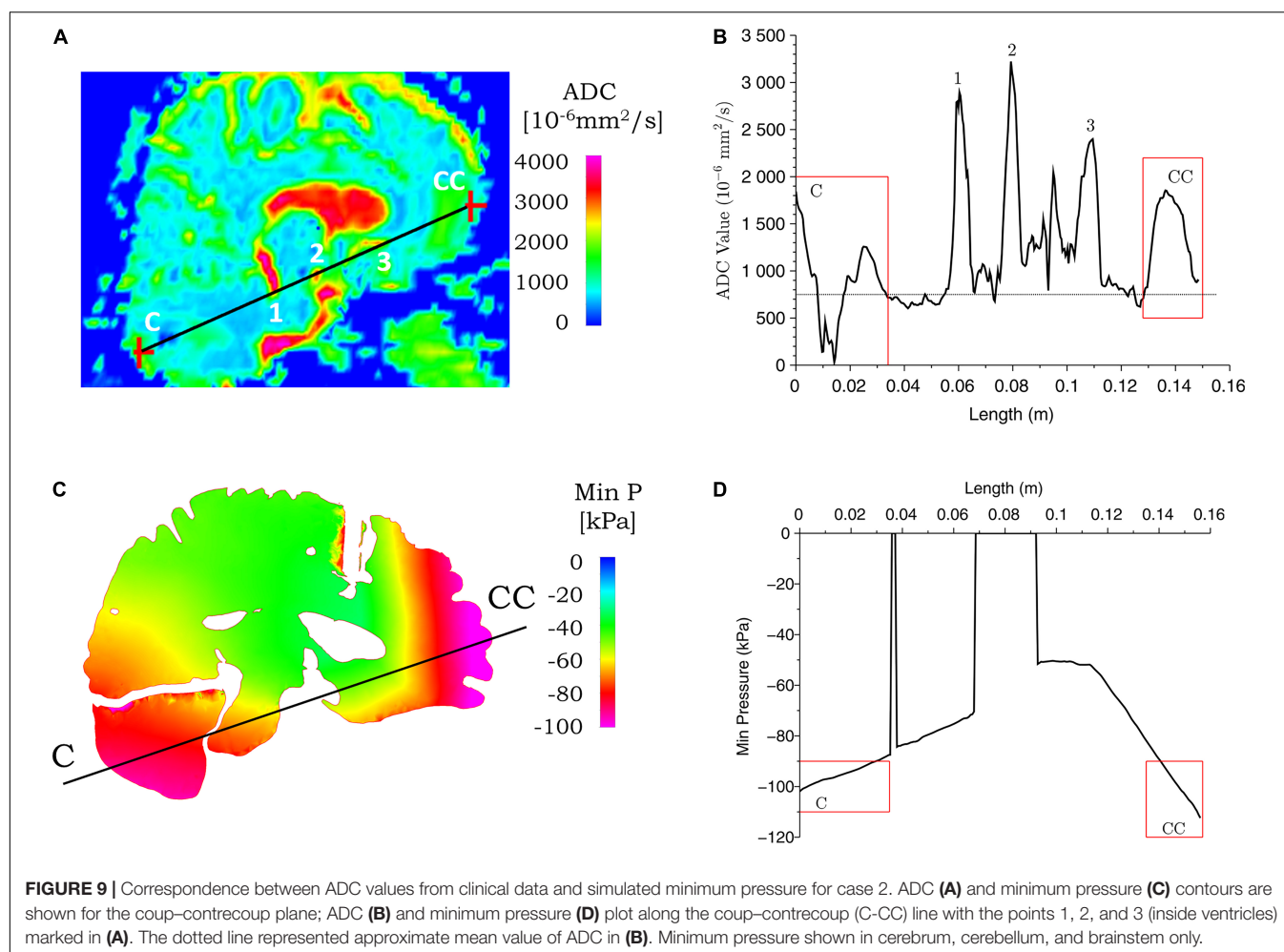


TABLE 5 | Sensitivity of simulation results for the two cases.

Case number	Impact angular velocity (rad/s)	Head acceleration (g)	Depth of indentation (mm)	Normal depth into brain (mm)	
				Strain rate ($>250 \text{ s}^{-1}$)	Pressure ($<-90 \text{ kPa}$)
1	28	245	8.6	Coup: 8.8	None
	30	270	9.1	Coup: 9.8	None
	32	290	9.5	Coup: 10.2	None
2	12	125	None	None	Coup: 15 Contrecoup: 17
	15	150	None	None	Coup: 30 Contrecoup: 20

the tensile pressure disappears, and the strain rate gradually increased to over 250 s^{-1} . This suggests that the angular velocity of 15 rad/s is a realistic value to be used in the modeling of case 2.

The effect of the impactor size is also examined by using the same impact velocity for these two cases. When an impactor with a large radius of curvature is used, a significantly higher angular velocity is needed to indent the skull to the same depth seen with an impactor with a small radius. For example, if the same angular velocity of 15 rad/s is used, case 1 shows an approximately 3 mm skull indentation and a small focal injury at the coup, while case 2 of relatively large impactor

shows no visible skull deformation, but a coup–contrecoup injury is apparent.

DISCUSSION

Clinical Observation of Injury Patterns

The present study, based upon MRI findings, has considered two cases from subjects who sustained blunt trauma to the head with characteristically two different types of injury that were diagnosed as mild TBI. Both cases had GCS scores of 13–15 (mild TBI) at the time of diagnosis by the attending physician. Based

on eyewitness report and emergency room medical assessment documentation, the way the injuries were sustained due to the falls are different. In the first case, a young adult male sustained a road traffic accident, fell backward, hit an object with a small radius of curvature, and had a depressed fracture of the skull at the site of impact. The underlying brain parenchyma showed evidence of a hemorrhagic contusion. Notably, no contrecoup lesion was visualized as reported in the clinical assessment documentation. Since the underlying hemorrhagic contusion was limited to a site of the injury in the brain parenchyma, adjacent to the depressed skull, certain changes in ADC values were not demonstrated appreciably due to the potential infiltration of blood and meningeal encroachment into the brain parenchyma, but a significant lesion site is visibly identifiable. In addition, magnetic susceptibility artifacts generated by the overlying skull bone could have contributed to those ADC values. No other change was observed in the range of ADC values specific to tissue/region in any other parts of the brain parenchyma.

In the second case, a middle-aged male had an accidental fall from a height, sustained a hemorrhagic contusion in the left cerebellar hemisphere and right frontal lobe corresponding to a coup and contrecoup lesion, respectively, with no skull fractures. The lesions reported in the clinical assessment documentation and seen in the images in this paper were larger than those in the previous case, likely owing to the impact condition and the intact skull during impact. These changes were mirrored in the ADC maps. The hemorrhagic areas showed restricted diffusion corresponding to reduced ADC values at the coup, a well-known phenomenon due to blood at the lesion site (Kang et al., 2001; Shah et al., 2004). These areas were surrounded by edema, which corresponded to an area of increased ADC at both sites (coup and contrecoup). This is owing to the relatively unrestricted diffusion in areas with increased interstitial fluid.

Both of these cases were diagnosed similarly as mild TBI from the GCS scores, but the clinical presentation with skull indentation with a localized lesion in case 1 is significantly different from case 2 with no visible skull fractures but presented with coup–contrecoup lesions when observed through MRI. The nature of the injuries imparts different biomechanical loading on the head, producing characteristically different injury patterns albeit with a similar diagnosis. These injuries in the real-world scenario with mild TBI are not necessarily diagnosed using MRI unless enrolled in a clinical study to understand the intricacies of case-to-case differences. Thus, reconstructing the incident from medical reports can provide objective information on possible real-time injury patterns and diagnosis decisions at the site of injury or in the emergency room.

Possible Injury Mechanisms and Injury Criteria

Comparing the simulation results and ADC data for case 1, the maximum effective strain rate above 250 s^{-1} is found to correspond with significant ADC changes in the coup side of the brain. High strain and stress values are seen not only in the coup but also in other regions of the brain that do not show observable ADC changes. This suggests that if a stress-

or strain-based injury criterion is used to evaluate the brain tissue damage, the threshold for injury cannot be constant and needs to depend inversely on the strain rate. For impact loading at a lower strain rate, the stress or strain threshold is higher, while at a higher strain rate, it becomes lower. In other words, the brain tissue, like other materials, may become more brittle at a higher strain rate (Yang and Zhang, 2019). This is probably because micromechanically, there is not enough time for dispersion of the linear momentum into other regions of the brain, and the localized deformation is manifested through skull indentation and coup injury. Conversely, *in vitro* tissue experiments showed that for the same strain magnitude, the extent of injury and pathophysiology can be influenced by strain rate (Bar-Kochba et al., 2016) and high water content in the brain tissue (Prabhu et al., 2019).

On the other hand, for case 2, the minimum peak pressure below -90 kPa seems to be the biomechanical parameter that best represents the ADC change associated with the coup–contrecoup injury. There can be several possible mechanisms for coup–contrecoup injury. One possibility is a mismatch between brain and skull motions causing the coup and contrecoup injury. To evaluate this as a possible mechanism, the brain motion relative to the skull was examined for the duration of the simulation, and no direct skull–brain contact was found during the impact. A longer duration simulation may reveal this information, which will be considered in future studies. Another possible mechanism is the stress wave inside the cranium. In the current simulation for this case, we found a stress wave originating and propagating from the impact site on the skull, and being reflected from the free surface from the skull on the contrecoup side that appears to create the tensile/negative pressure in the brain. Since materials like brain tissue are weaker in tension than compression, we conjecture that the excessively large tensile pressure and possibly some cavitation could contribute to brain injury at the contrecoup site as shown in the MRI and ADC data. Experimental and simulation data from impact loading to tissue and gel samples (Kang and Raphael, 2018) showed rapidly increasing tension, which contributed to cavitation and may cause extensive damage to the surrounding tissue. We surmise that while stress wave propagation in the head may be a mechanism for blunt impact injury, current understanding of possible brain cavitation in the brain tissue is limited.

For case 1, the higher kinetic energy seems to localize the effect by indenting the skull and creating large deformation in the coup region in the brain, with little or no effect on the contrecoup side of the brain. We see increased pressure throughout the brain, which may have prevented any clinically identifiable contrecoup injury, perhaps due to an absence of tensile pressure in this region. In case 2, on the contrary, a lower kinetic energy is distributed over a larger area of the skull and the brain, resulting in a characteristic coup–contrecoup effect, which may be attributed to how energy and acceleration change over time (Figures 5, 6). We conjecture that the rapid transition from kinetic energy to internal energy in case 1 compared with the gradual transition in case 2 may explain the different deformation mechanisms in the brain between the two cases. The peak acceleration in case 1 is higher than that in case

2, which corresponds to that of clinically reported GCS score severity. It also appears that flattening the head acceleration curve with a longer duration and lower peak could reduce brain injury severity when comparing the accelerations between case 2 and case 1. This principle based upon the rate of energy and acceleration increments can be applied to study various injury types due to mechanical trauma (e.g., blunt impact and blast exposure) to the brain.

A Methodology to Map Clinical Assessments With Biomechanical Simulations

Most, if not all, analyses of traumatic brain injury to date have been approached through three major disciplines: pre-clinical, clinical, and computational studies. The pre-clinical studies have been conducted to understand the pathogenesis through molecular, biochemical, imaging, and behavioral studies by replicating real-world injury scenarios using animal subjects. The clinical studies have used Warfighter and civilian clinical cases of TBI with several techniques, such as imaging data and post-mortem histopathology/biochemical analyses. The computational modeling and simulation approaches have attempted to quantify biomechanical responses at multiple scales to predict the observed injury in pre-clinical and clinical scenarios, both with and without protective equipment. All three approaches have explored blast overpressure, blunt, and ballistic impact loadings.

The clinical imaging and computational simulation data for the two cases considered in this paper represent two aspects of injury presentation. The key clinical aspect here was the utilization of post-incident T2-FLAIR to establish the type and location of injury, and ADC maps derived from DWI modality to obtain quantitative data for clinical quantification of injury. Several multi-parametric MRI data sets were acquired such as MPAGE, DWI, SWI, FLAIR, and ADC. Of these data sets, ADC was deemed to be quantitatively the most discriminatory for the injury types assessed clinically, and utilized for the comparison between computational simulation and clinical MRI. The ADC allowed representing the changes in the state of the tissues due to the insult by parameterizing and representing the degree of diffusion of water molecules to identify multiple forms of brain injury (Sener, 2001; Hagmann et al., 2006; Nelson et al., 2008; Tong et al., 2008). ADC also identified transition of a volume in the brain occupied by CSF (with higher diffusion values due to large water content) to a mixture of blood (with lower diffusion values due to less water content) or other fluids and CSF, and quantified such changes. ADC is limited because it provides an average value over a plurality of layers (i.e., thicker slices of brain) from T1 and T2 MRI slices. This reduces the resolution and sensitivity to an extent in a given plane when compared with the sensitivity in T1 and T2 data (The details in T2 shown in **Supplementary Materials** apply for T1 data; not shown here).

Computational biomechanical analyses of these cases primarily address the energy distribution and absorption from blunt impact to the head and the brain, and the biomechanical

parameters that correlate with clinical imaging of such insults. For blunt impact insults, the energy is transferred from the skull into the brain. Positive (compressive) and negative (tensile) pressure waves as well as shear stress waves could be generated in the brain tissue. In most biological tissues, tensile stress is more injurious than the compression mostly because the interstitial fluid cannot resist the tension in supporting tissue structural components. Compared with pressure waves, shear waves propagate within the brain at a much slower speed, last longer, and cause larger deformations of tissues and tearing of adjacent structures. Strain rate represents how fast the shear is happening with respect to time. For the viscoelastic brain tissue, material shearing behaves differently with the increase in strain rates. **Figure 7** showed our consideration of a multitude of biomechanical measures to identify the best mapping parameters with ADC maps and clinical assessment of the injury for both the cases.

Hydrostatic pressure is used here because it includes stresses in multiple directions by considering the mean of normal stress components in the tissue. Gradual increase in pressure, as in deep sea diving, where the pressures are excessive, does not adversely affect a diver while diving deeper. However, it is well known that if the diver comes up to the sea level quickly, this rapid ascent creates a pressure difference between the inside of the body and the outside, and can subject the diver's organs to tensile loading, which is injurious to the tissues. The same phenomenon is possible in brain tissue due to large negative pressures when the head is subjected to impacts or shock fronts.

For the two cases studied here, strain rate and tensile pressure show correspondence with quantifiable changes in ADC values in the tissue and clinical diagnosis from evaluation of MRI images. It is conceivable that in case 1, with the high strain rate in the coup region (but not in the contrecoup region), the impact yields very localized deformation patterns, as supported by high ADC values in this region. Likewise, in case 2 with the head impacting a larger object at a lower velocity, the momentum distribution is over a larger area showing no localized deformation. In this case, the tensile pressure shows a closer correspondence with the ADC values in both coup and contrecoup regions.

Based on the above correspondence, we develop a methodology that can map clinical diagnosis, clinical information, and quantitative data, with biomechanical simulation data. The key is creating a biomechanical analogy of quantitative measurements from clinical assessment, e.g., ADC, and establishing how these biomechanical measures can be used as mapping or equivalent corresponding parameters. As more clinical cases are collected and quantified, biomechanical simulation data can be generated by model reconstruction of incidents using the approach as presented in this paper. With more cases analyzed, the aggregated knowledge of correlating biomechanics and clinical outcomes will improve the understanding for various injury classifications. Artificial intelligence tools and machine learning algorithm utilizing such knowledge can then be created to predict the nature of the insults and injury modalities of brain (Raj et al., 2019).

Future research can cross-validate these findings using a large dataset to relate biomechanical assessment of TBI with image-based assessment and analysis. Other avenues are to explore possible correspondence between biomechanical prediction and other MRI data such as fractional anisotropy (FA) values representing demyelination due to oligodendrocyte ischemia and subsequent apoptosis, as well as explore injury modalities due to blast overpressure and ballistic impact loadings.

Assumptions and Limitations

There are several limitations in this study: (1) We recognize the differences in head sizes in our design of experiments (shown in **Supplementary Table 1**). Although the differences due to head size variations are small, they may affect the simulation results. Morphing the computational head model to reflect the dimensions of the actual head geometry could improve simulation accuracy and mapping with clinical image-based data. Advanced morphing techniques such as the ones developed in Refs. (Jolivet et al., 2015; Zhang et al., 2017; Hu, 2018) could be utilized and extended to develop a subject-specific head model based on the current head model. Incorporating such modeling nuances to quantify errors introduced by using a 50th percentile human head computational model has not been addressed in this paper. (2) We have used simplified material models for different tissues. For example, we modeled the cortical and trabecular skull bones as isotropic elastoplastic materials, as found in the literature, although the skull bone is recognized to be anisotropic in nature and has been known to exhibit viscoelastic strain-rate sensitive behavior under dynamic loading. Another material model aspect that we did not consider is person-to-person variability of human tissue properties. We did not consider such uncertainties treating them as higher-order factors. (3) We treated the CSF in the head as a highly incompressible elastic solid. Treating the CSF as a fluid and applying a fluid–tissue interface to solve the fluid–structure interaction between the CSF and surrounding tissues by a sophisticated coupled fluid–solid solver might refine the approach but would add significant complexity and computational challenge. (4) The accidents in both cases were reconstructed based on information from the hospital where emergency care was provided to the patients, eyewitness reports, clinical assessment reports, and imaging data by the clinicians. Unlike the blunt impact data obtained from a controlled scientific experiment, the reconstruction of uncontrolled real-world incidents such as the two cases may not be unique. We assumed that the impactor is a stone with a spherical shape with a radius that is varied for different cases. Using a non-smooth surface or object with multiple edges will increase the complexity of computational simulation, but may not be consequential to refining the methodology. (5) Due to logistical constraints, we recognize that there is inevitably a time delay between the accident and the MRI scan at the hospital. During this period, the level of interstitial edema may increase slowly following the injury. However, the region of ADC abnormality caused by hemorrhage is unlikely to change significantly within this time frame (Gasparetto et al., 2011). (6) Longer simulation times combined with the proper simulation of large brain rotation can predict other outcomes that may

be necessary for lower speed impact loading conditions. In the future, applying the techniques in this paper to other head trauma cases, together with proper pattern match and statistical analyses, will result in more objective correlative metrics, which enhance biomechanical simulations in predicting the injury risk and patterns and can inform additional diagnosis considerations to the attending physicians.

CONCLUSION

We showed a methodology to map computational biomechanical simulation results for blunt impact loading with clinical brain imaging data for two cases. Biomechanical parameters such as pressure, shear stress, principal strain, strain rate, product of strain and strain rate, and strain energy were considered to quantitatively compare biomechanical simulations with clinical assessments. Based on the simulation result analysis, we found different biomechanical measures to explain different blunt impact injury modalities. The minimum pressure (i.e., maximum tensile pressure) and maximum strain rate in brain tissue were seen to best represent tissue damage/injury identified by *in vivo* ADC values from MRI analysis. Specifically, for case 1, a blunt impact with a small solid object resulting in an indented skull, the ADC contours of contusion corresponded well with those for effective strain rates higher than 250 s^{-1} . For case 2, a blunt impact with a larger solid object producing a coup–contrecoup injury and no noticeable skull indentation, the ADC contours showing contusion and edema mapped well with a negative pressure of -90 kPa or more. The methodology comparing biomechanical simulations with ADC from image-based clinical analysis presented here can lead to a future roadmap to understand and interpret injury criteria, and to improve accuracy in biomechanical prediction.

DATA AVAILABILITY STATEMENT

The original contributions presented in the study are included in the article/**Supplementary Material**, further inquiries can be directed to the corresponding author/s.

ETHICS STATEMENT

The studies involving human participants were reviewed and approved by the written, informed consent was obtained from the individuals for the publication of any potentially identifiable images or data included in this article. The institutional Ethics Committee for Institute of Nuclear Medicine and Allied Sciences (INMAS) approved the study. The patients/participants provided their written informed consent to participate in this study.

AUTHOR CONTRIBUTIONS

Methodology and data processing were conceptualized by XT, VS, and AB. XT conducted the modeling and simulation and led the data analysis and documentation. VS analyzed the imaging data,

contributed to the data analysis and documentation. MD's collected the imaging and patient case history data, analyzed the clinical data, and contributed to the documentation. RG, JL, and AS helped with the technical discussions and technical editing. AB contributed to the data analysis, documentation, discussions, and interfacing between the four organizations contributing to this manuscript. All authors contributed to the article and approved the submitted version.

FUNDING

Partial funding was provided by the Office of Naval Research (ONR) through NRL's Basic Research Program. It was also funded in part by the US Department of Defense (DOD) and the Indian MOD/DRDO through the collaborative US–India Research Program PA #US-IN-A-16-0002. This work was supported in part by a grant of computer time from the DOD High Performance Computing Modernization Program at the Army Research Laboratory, Air Force Research Laboratory, and Army Engineer Research Laboratory DOD Supercomputing Resource Centers.

ACKNOWLEDGMENTS

We acknowledge the US–India #US-IN-A-16-0002 team, Dr. Thomas O'Shaughnessy and Dr. Y. C. Chen for technical

discussions. We also acknowledge technical discussions on medical image with Dr. Subash Khushu at INMAS.

SUPPLEMENTARY MATERIAL

The Supplementary Material for this article can be found online at: <https://www.frontiersin.org/articles/10.3389/fbioe.2021.654677/full#supplementary-material>

Supplementary Figure 1 | Case 1 of skull indentation: medical images (FLAIR, CSF in dark) on axial/transverse planes.

Supplementary Figure 2 | Case 2 of coup-contrecoup injury: medical images (FLAIR, CSF in dark) on axial/transverse planes.

Supplementary Figure 3 | Contours of different strain rate measures showing similar patterns but with different magnitudes.

Supplementary Figure 4 | Correspondence between ADC values and maximum effective strain rate at coup location in transverse plane of case 1. Values are plotted along horizontal line through the coup between points C and A. 1, 2, and 3 mark the location filled with fluid, C stands for coup region. The dotted line represents approximate mean ADC value of brain tissue.

Supplementary Figure 5 | Correspondence between ADC values and minimum pressure at showing coup location in transverse plane at the coup of case 2. Values are plotted along for the line through the contrecoup between points A and CC. 1, 2, and 3 mark the location filled with fluid, CC stands for contrecoup regions. The dotted line represents approximate mean ADC value of brain tissue.

Supplementary Table 1 | Comparison of heads of case 1 and case 2 with computational head model.

REFERENCES

- Ahrens, J., Geveci, B., and Law, C. (2005). *ParaView: An End-User Tool for Large Data Visualization*. Los Alamos, NM: Los Alamos National Laboratory. .
- Amyot, F., Arciniegas, D. B., Brazaitis, M. P., Curley, K. C., Diaz-Arrastia, R., Gandjbakhche, A., et al. (2015). A review of the effectiveness of neuroimaging modalities for the detection of traumatic brain injury. *J. Neurotrauma* 32, 1693–1721. doi: 10.1089/neu.2013.3306
- Bar-Kochba, E., Scimone, M. T., Estrada, J. B., and Franck, C. (2016). Strain and rate-dependent neuronal injury in a 3D in vitro compression model of traumatic brain injury. *Sci. Rep.* 6:30550. doi: 10.1038/srep30550
- Bonet, J., Marriotti, H., and Hassan, O. (2001). Stability and comparison of different linear tetrahedral formulation for nearly incompressible explicit dynamic applications. *Int. J. Numer. Methods Eng.* 50, 119–133. doi: 10.1002/1097-0207(20010110)50:1<119::aid-nme24>3.0.co;2-c
- Brewick, P., Saunders, R., and Bagchi, A. (2017). *Biomechanical Modeling of Human Head, NRL Report, Distribution A, NRL/FR/6350-17-10, 304*. Available online at: <http://www.dtic.mil/dtic/tr/fulltext/u2/1040988.pdf>
- Budday, S., Ovaert, T. C., Holzapfel, G. A., Steinmann, P., and Kuhl, E. (2020). Fifty shades of brain: a review on the mechanical testing and modeling of brain tissue. *Arch. Computat. Methods Eng.* 27, 1187–1230. doi: 10.1007/s11831-019-09352-w
- CDC (2020). *United States Centers for Disease Control and Prevention: Traumatic Brain Injury and Concussion –Get the Facts*. Available online at: https://www.cdc.gov/traumaticbraininjury/get_the_facts.html, (accessed March 3, 2020). doi: 10.1007/s11831-019-09352-w
- Cernak, I., Stein, D. G., Elder, G. A., Ahlers, S., Curley, K., DePalma, R. G., et al. (2017). Preclinical modelling of militarily relevant traumatic brain injuries: challenges and recommendations for future directions. *Brain Injury* 31, 1168–1176. doi: 10.1080/02699052.2016.1274779
- Cotton, R. T., Pearce, C. W., Young, P. G., Kota, N., Leung, A. C., Bagchi, A., et al. (2015). Development of a geometrically accurate and adaptable finite element head model for impact simulation: the naval research laboratory-simpleware head model. *Comput. Meth. Biomech. Biomed. Eng.* 19, 101–113. doi: 10.1080/10255842.2014.994118
- Fernandes, F. A. O., and Alves de Sousa, R. J. (2015). Head injury predictors in sports trauma – a state-of-the-art review. *Proc. Inst. Mech. Eng. H* 229, 592–608. doi: 10.1177/0954411915592906
- Florence, C. S., Bergen, G., Atherly, A., Burns, E. R., Stevens, J. A., and Drake, C. (2018). Medical costs of fatal and nonfatal falls in older adults. *J. Am. Geriatr. Soc.* 66, 693–698. doi: 10.1111/jgs.15304
- Gasparetto, E. L., Rueda Lopes, F. C., Domingues, R. C., and Domingues, R. C. (2011). Diffusion imaging in traumatic brain injury. *Neuroimaging Clin. N. Am.* 21, 115–125. doi: 10.1016/j.nic.2011.02.003
- Giudice, J. S., Zeng, W., Wu, T., Alshareef, A., Shedd, D. F., and Panzer, M. B. (2019). An analytical review of the numerical methods used for finite element modeling of traumatic brain injury. *Ann. Bio. Eng.* 47, 1855–1872. doi: 10.1007/s10439-018-02161-5
- Goetz, P., Blamire, A., Rajagopalan, B., Cadoux-Hudson, T., Young, D., and Styles, P. (2004). Increase in apparent diffusion coefficient in normal appearing white matter following human traumatic brain injury correlates with injury severity. *J. Neurotrauma* 21, 645–654. doi: 10.1089/0897715041269731
- Goldsmith, W. (2001). The state of head injury biomechanics: past, present, and future. Part 1. *Crit. Rev. Biomed. Eng.* 29, 441–600. doi: 10.1615/critrevbiomedeng.v29.i56.10
- Hagmann, P., Jonasson, L., Maeder, P., Thiran, J. P., Wedeen, V. J., and Meuli, R. (2006). Understanding diffusion MR imaging techniques: from scalar diffusion-weighted imaging to diffusion tensor imaging and beyond. *Radiographics* 26 Suppl_1, S205–S223.
- Hardy, W. N., Mason, M. J., Foster, C. D., Shah, C. S., Kopacz, J. M., Yang, K. H., et al. (2007). A study of the response of the human cadaver head to impact. *Stapp. Car. Crash J.* 51, 17–80.
- Holdgate, A., Ching, N., and Angonese, L. (2006). Variability in agreement between physicians and nurses when measuring the glasgow coma scale in the

- emergency department limits its clinical usefulness. *Emerg. Med. Australas.* 18, 379–384. doi: 10.1111/j.1742-6723.2006.00867.x
- Hu, J. (2018). *Parametric Human Modeling, Basic Finite Element Method as Applied to Injury Biomechanics*. Cambridge, MA: Academic Press, 417–445.
- Hunter, J. V., Wilde, E. A., Tong, K. A., and Holshouser, B. A. (2012). Emerging imaging tools for use with traumatic brain injury research. *J. Neurotrauma* 29, 654–671. doi: 10.1089/neu.2011.1906
- Ji, S., Ghadyani, H., Bolander, R. P., Beckwith, J. G., Ford, J. C., McAllister, T. W., et al. (2014). Parametric comparisons of intracranial mechanical responses from three validated finite element models of the human head. *Ann. Biomed. Eng.* 42, 11–24. doi: 10.1007/s10439-013-0907-2
- Jolivet, E., Lafon, Y., Petit, P., and Beillas, P. (2015). Comparison of kriging and moving least square methods to change the geometry of human body models. *Stapp. Car. Crash J.* 59, 337–357.
- Kang, B. K., Na, D. G., Ryoo, J. W., Byun, H. S., Roh, H. G., and Pyeon, Y. S. (2001). Diffusion-weighted MR imaging of intracerebral hemorrhage. *Korean J. Radiol.* 2, 183–191. doi: 10.3348/kjr.2001.2.4.183
- Kang, W., and Raphael, M. (2018). Acceleration-induced pressure gradients and cavitation in soft biomaterials. *Sci. Rep.* 8:15840. doi: 10.1038/s41598-018-34085-4
- Kazam, J. J., and Tsiouris, A. J. (2015). Brain magnetic resonance imaging for traumatic brain injury: why, when, and how? *Top. Magn. Reson. Imaging* 24, 225–239. doi: 10.1097/rmr.0000000000000061
- Li, X., Zhou, Z., and Kleiven, S. (2020). An anatomically detailed and personalizable head injury model: significance of brain and white matter tract morphological variability on strain. *Biomech. Model. Mechanobiol.* 20, 403–431. doi: 10.1007/s10237-020-01391-8
- Lu, L., Wei, X., Li, M., Li, Y., and Li, W. (2014). Emerging MRI and metabolic neuroimaging techniques in mild traumatic brain injury. *Neurol. India* 62, 487–491. doi: 10.4103/0028-3886.144434
- Mangrum, W., Christianson, K., Duncan, S., Maxfield, C., and Merkle, E. (2012). *Duke Review of MRI Principles: Case Review Series*. Maryland Heights, MO: Mosby.
- Mao, H., Zhang, L., Jiang, B., Genthikatti, V. V., Jin, X., Zhu, F., et al. (2013). Development of a finite element human head model partially validated with thirty five experimental cases. *J. Biomech. Eng.* 135:111002. doi: 10.1115/1.4025101
- McEntire, B. J., and Whitley, P. (2005). *Blunt Impact Performance Characteristics of The Advanced Combat Helmet and Paratrooper and Infantry Personal Armor System for Ground Troop Helmet, USAARL Report No 2005-12 DTIC No ADA437530*. Fort Belvoir, VA: Defense Technical Information Center.
- Moen, K. G., Haberg, A. K., Skandsen, T., Finnanger, T. G., and Vik, A. (2014). A longitudinal magnetic resonance imaging study of the apparent diffusion coefficient values in corpus callosum during the first year after traumatic brain injury. *J. Neurotrauma* 31, 56–63. doi: 10.1089/neu.2013.3000
- Nahum, A., Smith, R., and Ward, C. (1977). *Intracranial Pressure Dynamics During Head Impact*. SAE Tech Pap No 770922. San Diego: Department of Surgery University of California.
- Nelson, F., Poonawalla, A., Hou, P., Wolinsky, J. S., and Narayana, P. A. (2008). 3D MPRAGE improves classification of cortical lesions in multiple sclerosis. *Mult. Scler.* 14, 1214–1219. doi: 10.1177/1352458508094644
- Post, A., Hoshizaki, T. B., Gilchrist, M. D., Brien, S., Cusimano, M., and Marshall, S. (2015). The dynamic response characteristics of traumatic brain injury. *Accid. Anal. Prev.* 79, 33–40. doi: 10.1016/j.aap.2015.03.017
- Prabhu, R. K., Begonia, M. T., Whittington, W. R., Murphy, M. A., Mao, Y., Liao, J., et al. (2019). Compressive mechanical properties of porcine brain: experimentation and modeling of the tissue hydration effects. *Bioengineering* 6:40. doi: 10.3390/bioengineering6020040
- Raj, R., Luostarinen, T., Pursiainen, E., Posti, J. P., Takala, R. S. K., Bendel, S., et al. (2019). Machine learning-based dynamic mortality prediction after traumatic brain injury. *Sci. Rep.* 9:17672. doi: 10.1038/s41598-019-53889-6
- Saunders, R. N., Kota, N., Bagchi, A., and Qidwai, S. (2018). *On Challenges in Developing a High-Fidelity Model of the Human Head for Traumatic Brain Injury Prediction*. Distribution A, NRL/MR/63 50-9807. Fort Belvoir, VA: Defense Technical Information Center.
- Saunders, R. N., Tan, X. G., Qidwai, S. M., and Bagchi, A. (2019). Towards identification of correspondence rules to relate traumatic brain injury in different species. *Ann. Bio. Eng.* 47, 2005–2018. doi: 10.1007/s10439-018-02157-1
- Schneider, C. A., Rasband, W. S., and Eliceiri, K. W. (2012). NIH image to ImageJ: 25 years of image analysis. *Nat. Methods* 9, 671–675. doi: 10.1038/nmeth.2089
- Sener, R. N. (2001). Diffusion MRI: apparent diffusion coefficient (ADC) values in the normal brain and a classification of brain disorders based on ADC values. *Comput. Med. Imaging Graph.* 25, 299–326. doi: 10.1016/s0895-6111(00)00083-5
- Shah, N., Reichel, T., and Fleckenstein, J. L. (2004). Diffusion findings in blood clot: the last word? *AJNR Am. J. Neuroradiol.* 25:157. doi: 10.1007/978-3-642-67644-4_15
- Tan, X. G., D'Souza, M. M., Khushu, S., Gupta, R. K., DeGiorgi, V. G., Singh, A. K., et al. (2020). Computational modeling of blunt impact to head and correlation of biomechanical measures with medical images. *J. Eng. Sci. Med. Diagn. Ther.* 3:011007.
- Tan, X. G., and Matic, P. (2020). Simulation of cumulative exposure statistics for blast pressure transmission into the brain. *Mil. Med.* 185:214. doi: 10.1093/milmed/usz308
- Tan, X. G., and Przekwas, A. J. (2011). A computational model for articulated human body dynamics. *Int. J. Human Factors Model. Simul.* 2, 85–110. doi: 10.1504/ijhfm.2011.041639
- Tan, X. G., Przekwas, A. J., and Gupta, R. K. (2017). Computational modeling of blast wave interaction with a human body and assessment of traumatic brain injury. *Shock Waves* 27, 889–904. doi: 10.1007/s00193-017-0740-x
- Teferri, K., Tan, X. G., Iliopoulos, A., Michopoulos, J., and Qidwai, S. (2018). Effect of human head morphological variability on the mechanical response of blast overpressure loading. *Int. J. Numer. Method Biomed. Eng.* 34:e3109. doi: 10.1002/cnm.3109
- Tong, K. A., Ashwal, S., Obenaus, A., Nickerson, J. P., Kido, D., Haacke, E. M., et al. (2008). Susceptibility-weighted MR imaging: a review of clinical applications in children. *AJNR Am. J. Neuroradiol.* 29, 9–17. doi: 10.3174/ajnr.A0786
- Trosseille, X., Tarriere, C., Lavaste, F., Guillon, F., and Domont, A. (1992). “Development of a FEM of the human head according to a specific test protocol,” in *Proceedings of the 46th Stapp Car Conference* (San Diego, SAE), 235–253.
- Van Boven, R. W., Harrington, G. S., Hackney, D. B., Ebel, A., Gauger, G., Bremner, J. D., et al. (2009). Advances in neuroimaging of traumatic brain injury and posttraumatic stress disorder. *J. Rehabil. Res. Dev.* 46, 717–757.
- Vaswani, A. K., Nizamani, W. M., Ali, M., Aneel, G., Shahani, B. K., and Hussain, S. (2014). Diagnostic accuracy of contrast-enhanced FLAIR magnetic resonance imaging in diagnosis of meningitis correlated with CSF analysis. *ISRN Radiol.* 2014:578986. doi: 10.1155/2014/578986
- Wu, X., Kirov, I. I., Gonen, O., Ge, Y., Grossman, R. I., and Lui, Y. W. (2016). MR imaging applications in mild traumatic brain injury: an imaging update. *Radiology* 279, 693–707. doi: 10.1148/radiol.16142535
- Yang, X., and Zhang, B. (2019). Material embrittlement in high strain-rate loading. *Int. J. Extrem. Manuf.* 1:022003. doi: 10.1088/2631-7990/ab263f
- Zhang, K., Cao, L., Fanta, A., Reed, M. P., Neal, M., Wang, J. T., et al. (2017). An automated method to morph finite element whole-body human models with a wide range of stature and body shape for both men and women. *J. Biomech.* 60, 253–260. doi: 10.1016/j.jbiomech.2017.06.015
- Zhang, L., Yang, K. H., and King, A. I. (2004). A proposed injury threshold for mild traumatic brain injury. *J. Biomech. Eng.* 126, 226–236. doi: 10.1115/1.1691446
- Zhang, L., Yang, K. H., King, A. I., and Viano, D. C. (2003). “A new biomechanical predictor for mild traumatic brain injury – a preliminary finding,” in *Proceedings of the ASME Bioengineering Conference*, Key Biscayne, FL.
- Zhou, Z., Li, X., and Kleiven, S. (2019). Fluid–structure interaction simulation of the brain–skull interface for acute subdural haematoma prediction. *Biomech. Model. Mechanobiol.* 18, 155–173. doi: 10.1007/s10237-018-1074-z

Conflict of Interest: The authors declare that the research was conducted in the absence of any commercial or financial relationships that could be construed as a potential conflict of interest.

Copyright © 2021 Tan, Sajja, D'Souza, Gupta, Long, Singh and Bagchi. This is an open-access article distributed under the terms of the Creative Commons Attribution License (CC BY). The use, distribution or reproduction in other forums is permitted, provided the original author(s) and the copyright owner(s) are credited and that the original publication in this journal is cited, in accordance with accepted academic practice. No use, distribution or reproduction is permitted which does not comply with these terms.



Brain Shape Changes Associated With Cerebral Atrophy in Healthy Aging and Alzheimer's Disease

Yana Blinkouskaya and Johannes Weickenmeier*

Department of Mechanical Engineering, Stevens Institute of Technology, Hoboken, NJ, United States

OPEN ACCESS

Edited by:

Mohsen Asadnia,
Macquarie University, Australia

Reviewed by:

Zhen Qiu,
Michigan State University,
United States
Bowen Ji,
Northwestern Polytechnical
University, China

*Correspondence:

Johannes Weickenmeier
johannes.weickenmeier@
stevens.edu

Specialty section:

This article was submitted to
Micro- and Nanoelectromechanical
Systems,
a section of the journal
Frontiers in Mechanical Engineering

Received: 05 May 2021

Accepted: 22 June 2021

Published: 19 July 2021

Citation:

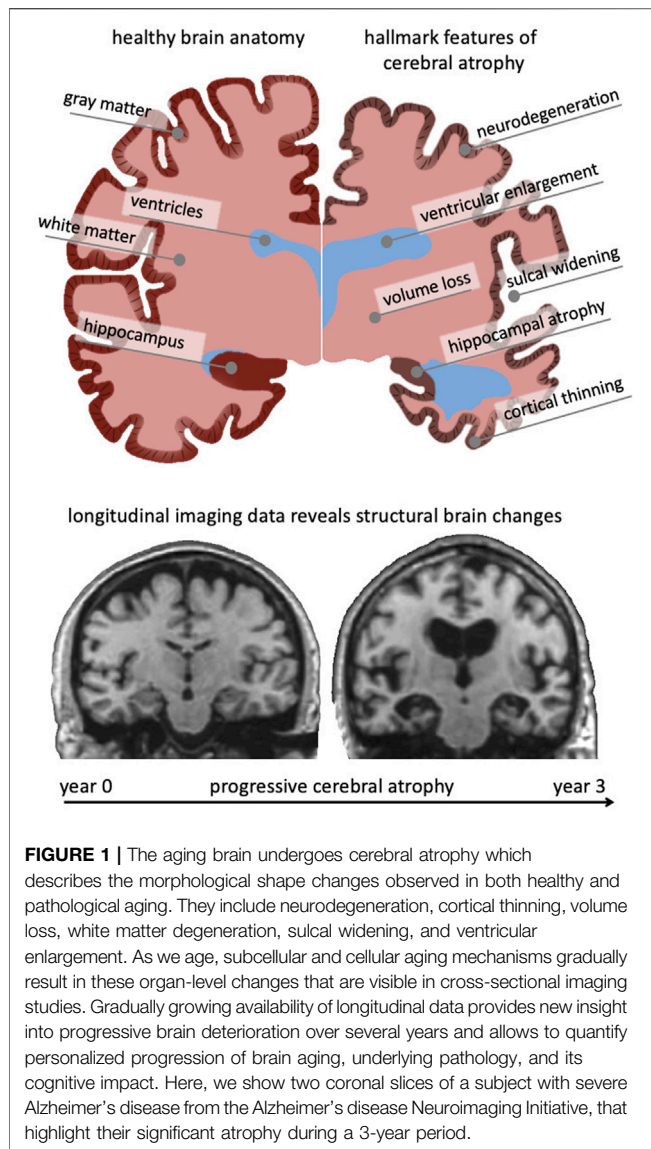
Blinkouskaya Y and Weickenmeier J
(2021) Brain Shape Changes
Associated With Cerebral Atrophy in
Healthy Aging and
Alzheimer's Disease.
Front. Mech. Eng 7:705653.
doi: 10.3389/fmech.2021.705653

Both healthy and pathological brain aging are characterized by various degrees of cognitive decline that strongly correlate with morphological changes referred to as cerebral atrophy. These hallmark morphological changes include cortical thinning, white and gray matter volume loss, ventricular enlargement, and loss of gyrification all caused by a myriad of subcellular and cellular aging processes. While the biology of brain aging has been investigated extensively, the mechanics of brain aging remains vastly understudied. Here, we propose a multiphysics model that couples tissue atrophy and Alzheimer's disease biomarker progression. We adopt the multiplicative split of the deformation gradient into a shrinking and an elastic part. We model atrophy as region-specific isotropic shrinking and differentiate between a constant, tissue-dependent atrophy rate in healthy aging, and an atrophy rate in Alzheimer's disease that is proportional to the local biomarker concentration. Our finite element modeling approach delivers a computational framework to systematically study the spatiotemporal progression of cerebral atrophy and its regional effect on brain shape. We verify our results *via* comparison with cross-sectional medical imaging studies that reveal persistent age-related atrophy patterns. Our long-term goal is to develop a diagnostic tool able to differentiate between healthy and accelerated aging, typically observed in Alzheimer's disease and related dementias, in order to allow for earlier and more effective interventions.

Keywords: cerebral atrophy, brain aging, Alzheimer's disease, multiphysics modeling, finite element modeling, brain shape changes

1 INTRODUCTION

Brain aging is characterized by a myriad of biological, chemical, and mechanical hallmark features. While biological and chemical aging processes have been studied for decades, the mechanical aspects of brain aging remain understudied (Raz and Rodrigue, 2006; Hall et al., 2020). The brain undergoes several key morphological changes referred to as cerebral atrophy which manifests primarily as gray and white matter volume loss, ventricular enlargement, and sulcal widening (Fjell and Walhovd, 2010). While healthy brain aging is characterized by these changes, neurodegenerative diseases, such as Alzheimer's disease (AD) and related dementias, exhibit a significant acceleration of brain aging mechanisms that cause a noticeable divergence from the healthy atrophy trajectory observed in cross-sectional studies (Coupé et al., 2019). **Figure 1** shows a qualitative comparison between a healthy brain (left hemisphere) and a brain exhibiting severe age-related atrophy features (right hemisphere). Strikingly, the changes in the aging brain become so pervasive that they are clearly



visible in medical images (Lockhart and DeCarli, 2014). Despite each person's brain looking differently, cross-sectional imaging studies reveal significant trends in volume loss, ventricular enlargement, cortical thinning, and the emergence of white matter lesions (Walhovd et al., 2011; Suzuki et al., 2019).

Brain aging is a highly heterogeneous process that is strongly linked to local cellular composition as well as the gradual aggregation of neurotoxic proteins and waste products that fail to drain into the glymphatic system (Boland et al., 2018). The superposition of metabolic slowing and decreased cellular regeneration in most of the brain, leads to structural and functional degeneration that drives cognitive decline (Ownby, 2010; Mattson and Arumugam, 2018). AD is characterized by the accumulation of neurotoxic amyloid beta plaques that interfere with normal synaptic transmission (Reddy and Beal, 2008; Milà-Alomà et al., 2020) and neurofibrillary tangles that disrupt axonal

transport causing loss of signal transmission and axon death (Malpetti et al., 2020). Both proteins exhibit a prion-like behavior in that they recruit healthy protein, trigger their misfolding, and gradually form growing plaques and tangles (Jack and Holtzman, 2013). This leads to their systematic spread throughout the brain (Jack et al., 2013). While plaques spread extracellularly, tangles spread primarily along the structural axonal network and are able to eventually reach distant brain regions (Kim et al., 2019). This systemic infiltration of the brain has major implications for brain function such as memory, motor control, behavior, and ultimately death (Mattson, 2004).

From a mechanics perspective, brain aging is drastically understudied as it may provide new avenues to broaden our understanding of the relationship between cell- and tissue-level neurodegeneration and their aggregated effect on organ level morphological shape changes (Hall et al., 2020). Only a few studies have presented a mechanistic model of cerebral atrophy and are based on either non-rigid registration of two medical images (Karaçali and Davatzikos, 2006; Khanal et al., 2017) or the finite element method (Camara et al., 2006; Weickenmeier et al., 2018; Harris et al., 2019; Schäfer et al., 2019). Registration methods aim at minimizing intensity differences between two images by iteratively distorting a moving image to match the reference image. This minimization process may be subject to elasticity constraints derived from mechanics (Hamamci and Unal, 2013; Garcia et al., 2018). Finite element-based approaches are based on a constitutive model of volume loss that is implemented for two or three dimensional simulations (Budday and Kuhl, 2020). Harris et al. developed a two dimensional sagittal and coronal brain model to simulate volume loss representative for the brain's response following a traumatic brain injury (Harris et al., 2019). The model is calibrated such that gray matter (GM) and white matter (WM) undergo different atrophy rates and shows an overall contraction of the cross-sectional brain image. The model does not capture aging-related ventricular enlargement, most likely due to the boundary conditions imposed on the model at the inferior edge of the brainstem. In a similar approach, Schäfer et al. presented a multiphysics model that couples protein spread in AD and volume loss (Schäfer et al., 2019). The model incorporates anisotropic diffusion of intracellular tau protein along the axon network. The two dimensional finite element (FE) model is characterized by an overall uniform area shrinking, although ventricular area marginally increases and cortical folds remain close together. In order to use computational modeling as a diagnostic tool to differentiate between healthy and pathological aging, simulation accuracy has to be improved.

Here, we expand on a multiphysics model of cerebral atrophy which allows to differentiate between healthy and pathological aging (Weickenmeier et al., 2018; Schäfer et al., 2019). We employ classical continuum theory and model cerebral atrophy as negative growth *via* a multiplicative split of the deformation gradient into an atrophy part and an elastic part (Schäfer et al., 2019). Accelerated aging is driven by the gradual accumulation of an AD biomarker. We assume the atrophy factor to increase proportional to the biomarker concentration which we diffuse in the brain *via* a reaction-diffusion model, see **Section 2**. Using a

subject specific FE model, we simulate healthy and AD-related brain aging and compare our model's response to cross-sectional data reported in literature. Our comparison focuses on the hallmark features of cerebral atrophy and shows good qualitative agreement with the persistent trends observed in large-scale imaging studies.

2 METHODS

2.1 Multiphysics Model of Cerebral Atrophy

Our goal is to identify differences in spatiotemporal atrophy patterns characteristic for healthy and AD-related brain aging. Therefore, we formulate a multiphysics approach that couples mechanics-driven volume loss and the biology-driven spreading of toxic proteins (Weickenmeier et al., 2018). In our constitutive model, we pose that healthy aging is linked to a steady volume loss in gray and white matter tissues, while AD accelerates atrophy proportional to the local toxic protein level (Schäfer et al., 2019). We solve our continuum problem on an anatomically accurate finite element (FE) brain model and quantify hallmark features of cerebral atrophy including volume loss, cortical thinning, ventricular enlargement, and sulcal widening.

2.1.1 Continuum Model for Protein Spread

AD is characterized by the accumulation and spreading of misfolded, neurotoxic proteins (Jucker and Walker, 2018). Post-mortem studies on AD patients have shown that protein spread follows a characteristic spatial pattern that is characterized by consistent onset locations and spreading pathways (Jack et al., 2013). Mathematically, these progression patterns are well approximated by a reaction-diffusion model known as the Fisher-Kolmogorov equation (Fisher, 1937; Kolmogorov et al., 1937). We define the concentration of misfolded protein, c , that spreads *via* linear diffusion.

$$\frac{\partial c}{\partial t} = d \Delta c + \alpha c [1 - c], \quad (1)$$

where d is the isotropic diffusion constant, Δc denotes the Laplacian of the protein concentration c , and α controls the growth rate of the concentration. For a derivation of the kinetic equations governing the prion-like behavior of proteins linked to AD, we refer the reader to our previous works (Schäfer et al., 2019; Weickenmeier et al., 2019). In brief, we derive a kinetic model that accounts for two configurations of the protein, a healthy state and a misfolded state. We then derive a kinetic equation that balances the total amount of healthy protein p and misfolded protein \tilde{p} , as a function of production rate of healthy protein k_0 , clearance rate of healthy and misfolded proteins k_1 k_1 , and conversion of healthy to misfolded protein k_{12} .

$$\frac{\partial p}{\partial t} = k_0 - k_1 p - k_{12} p \tilde{p} \quad \text{and} \quad \frac{\partial \tilde{p}}{\partial t} = -\tilde{k}_1 \tilde{p} + k_{12} p \tilde{p}. \quad (2)$$

Through introduction of the misfolded protein concentration c , which may vary between 0 and 1, equilibrium considerations,

and re-parameterization of the governing Eq. 2, we arrive at the partial differential Eq. 1, with

$$\alpha = k_{12} \frac{k_0}{k_1} - \tilde{k}_1. \quad (3)$$

Model parameters d and α allow to adjust for the amount of spread and progression speed of misfolded proteins observed in individual subjects affected by varying AD severity.

2.1.2 Continuum Model for Cerebral Atrophy

To model the mechanical behavior of the brain, we use the nonlinear equations of continuum theory and introduce the mapping $\boldsymbol{\varphi}$ from the undeformed, unloaded configuration \mathcal{B}_0 at time t_0 to the deformed, loaded configuration \mathcal{B}_t at time t . We adopt the conventional notation, $\mathbf{x} = \boldsymbol{\varphi}(\mathbf{X}, t)$, where $\mathbf{x} \in \mathcal{B}_t$ denotes the position vector in the deformed configuration at time t and $\mathbf{X} \in \mathcal{B}_0$ denotes the position vector of the initial configuration at time t_0 . We characterize local deformations by introducing the deformation gradient, $\mathbf{F}(\mathbf{X}, t) = \nabla_{\mathbf{X}} \boldsymbol{\varphi}(\mathbf{X}, t)$, and local volume changes by its determinant, $J = \det(\mathbf{F})$. Following previous work, we model cerebral atrophy as volumetric shrinking and use the classical approach of splitting the deformation gradient into an elastic part \mathbf{F}^e and an atrophy part \mathbf{F}^a (Schäfer et al., 2019). The multiplicative decomposition of the deformation gradient, $\mathbf{F} = \nabla_{\mathbf{X}} \boldsymbol{\varphi}$, yields

$$\mathbf{F} = \mathbf{F}^e \cdot \mathbf{F}^a \quad \text{with} \quad J = J^e J^a. \quad (4)$$

The multiplicative split extends to the Jacobian J which breaks down into an elastic volume change $J^e = \det(\mathbf{F}^e)$ and volume loss by cerebral atrophy $J^a = \det(\mathbf{F}^a)$. To characterize the hyperelastic material behavior of brain tissue, we adopt the neo-Hookean strain energy density function Ψ_0 as the atrophy-weighted elastic stored energy Ψ , which depends exclusively on the elastic part of the deformation gradient,

$$\Psi_0 = J^a \Psi, \quad \text{with} \quad \Psi = \frac{1}{2} \mu [\mathbf{F}^e : \mathbf{F}^e - 3 - 2 \ln(J^e)] + \frac{1}{2} \lambda \ln^2(J^e). \quad (5)$$

Parameters μ and λ are the standard Lamé coefficients which can be expressed *via* Young's modulus E and the Poisson's ratio ν in the elastic limit as $\lambda = E\nu/[1 + \nu][1 - 2\nu]$ and $\mu = E/[2(1 + \nu)]$. Following arguments of thermodynamics, we can derive the first Piola-Kirchhoff stress tensor \mathbf{P} ,

$$\mathbf{P} = \frac{d\psi_0}{d\mathbf{F}} = J^a \frac{d\psi}{d\mathbf{F}^e} = J^a [\mu \mathbf{F}^e + [\lambda \ln(J^e) - \mu] \mathbf{F}^{eT}]. \quad (6)$$

The Piola-Kirchhoff stress tensor is governed by the quasistatic balance of linear momentum,

$$0 = \text{Div}(\mathbf{P}) + \mathbf{F}^a \text{in } \Omega, \quad (7)$$

where Ω denotes the domain which is the brain. We assume that we can neglect external body forces $\mathbf{F}^b = 0$. In our multiphysics framework here, the atrophy problem is coupled to the protein spreading problem through the atrophy part of the deformation gradient \mathbf{F}^a , which is considered to be a function of age and biomarker concentration c . More specifically, we assume that gray and white matter atrophy is purely isotropic,

$$\mathbf{F}^a = \sqrt[3]{\vartheta} \mathbf{I} \text{ and } \mathbf{F}^e = \frac{\mathbf{F}}{\sqrt[3]{\vartheta}}, \quad (8)$$

where we introduced a measure for volume loss ϑ which is related to cerebral atrophy J^a ,

$$\vartheta = J^a \text{ and } J^e = \frac{J}{\vartheta}. \quad (9)$$

We propose a constitutive model for the evolution of the atrophy measure ϑ that allows to differentiate between healthy brain aging and accelerated aging observed in many neurodegenerative diseases such as AD (Weickenmeier et al., 2018; Schäfer et al., 2019). As such, we introduce a health atrophy rate, G_h , as well as a biomarker concentration, c , dependent atrophy rate, G_c , which allows us to capture accelerated cerebral atrophy due to the progressive accumulation of misfolded, neurotoxic protein. Our model is formulated such that natural atrophy is accelerated if the biomarker concentration, c , exceeds a critical threshold, c^{crit} , such that the evolution equation reads.

$$\dot{\vartheta} = [1 + \gamma(c)] G_h = \begin{cases} G_h & \text{if } c < c^{\text{crit}} \\ G_h + G_c & \text{if } c \geq c^{\text{crit}} \end{cases}, \quad (10)$$

where $\gamma(c) = \frac{G_c}{G_h} \mathcal{H}(c - c^{\text{crit}})$.

Here, $\mathcal{H}(c - c^{\text{crit}})$ denotes the Heaviside step function and marks the transition from healthy to accelerated, or diseased, atrophy at c^{crit} . Healthy and diseased atrophy rates, G_h and G_c , may be treated as subject-specific aging parameters that can be tuned to capture their specific progression behavior.

2.2 Finite Element Implementation

We implemented our continuum model in the finite element software Abaqus (Simulia, Providence RI) and solved our coupled problem as a thermo-mechanical analysis. We add the nonlinear source term of the protein spreading equation (Raz and Rodrigue, 2006) to the standard heat transfer problem using the subroutine HETVAL which requires the flux, $f^c = \alpha c [1 - c]$ and rate of change of heat flux per temperature, $df^c/dc = \alpha[1 - 2c]$. Similarly, we incorporate our constitutive material model using the user subroutine UMAT which requires Cauchy stress and its Jaumann rate. To determine Cauchy stress at the integration point level, we calculate the atrophy factor *via* a finite difference scheme,

$$\dot{\vartheta} = \frac{\vartheta - \vartheta_n}{\Delta t}, \text{ such that } \vartheta = \vartheta_n + [1 + \gamma(c)] G_h \Delta t, \quad (11)$$

where (\circ) and $(\circ)_n$ denote the unknown quantity at $t = t_{n+1}$ and the converged quantity at the previous time step $t = t_n$, respectively, and $\Delta t = t - t_n > 0$ is the current time increment. Here, we approximate the Heaviside step function \mathcal{H} in $\gamma(c)$ (Eq. 10) as a smooth function,

$$\mathcal{H}(c - c^{\text{crit}}) = \frac{1}{1 + \exp(\beta(c - c^{\text{crit}}))}, \quad (12)$$

where β controls the transition between the two states. We store the converged atrophy factor as a state variable for post-processing,

then calculate the atrophy part and the elastic part of the deformation gradient \mathbf{F}^a and \mathbf{F}^e (Eq. 4). We then calculate Cauchy stress, $\sigma = J^{-1} \mathbf{P} \mathbf{F}^T$, and its Jaumann rate,

$$\dot{\mathbf{c}}^{\text{abaqus}} = \dot{\mathbf{c}} + \frac{1}{2} [\dot{\sigma} \otimes \mathbf{I} + \mathbf{I} \otimes \dot{\sigma} + \dot{\sigma} \otimes \mathbf{I} + \mathbf{I} \otimes \dot{\sigma}], \quad (13)$$

with the consistently linearized tangent stiffness matrix, \mathbf{c} ,

$$\mathbf{c} = \frac{1}{J^e} [\mathbf{I} \otimes \mathbf{F}^e] : \frac{\partial^2 \psi}{\partial \mathbf{F}^e \otimes \partial \mathbf{F}^e} : [\mathbf{I} \otimes \mathbf{F}^{eT}], \quad (14)$$

where we used the tensor operators $\{\bullet \otimes \bullet\}_{ijkl} = \{\bullet\}_{ik} \otimes \{\bullet\}_{jl}$ and $\{\bullet \otimes \bullet\}_{ijkl} = \{\bullet\}_{il} \otimes \{\bullet\}_{jk}$.

2.3 Finite Element Model Generation

We created an anatomically accurate FE brain model from T1-weighted magnetic resonance images of a healthy adult male brain. We used ScanIp from Simpleware (Synopsis Inc., Mountain View CA) to semi-automatically segment the regions of interest and generate the FE mesh. Our model differentiates between gray matter (GM), white matter (WM), the hippocampus, ventricles, and cerebrospinal fluid (CSF). **Figure 2A** shows representative sagittal, axial, and coronal MRI slices of the subject's brain, as well as the volumetric reconstructions of the respective substructures. We built our model sequentially and began segmentation with reconstruction of the ventricles, followed by WM, GM, and finally CSF. We avoided reconstructing the skull by defining zero-displacement Dirichlet boundary conditions on the peripheral surface of CSF. Here, we merged the lateral ventricles, third ventricle, and fourth ventricle into a single volume in order to quantify ventricular enlargement, one of the hallmark features of brain aging. We paid close attention to the segmentation of WM tissue to accurately capture individual sulci and gyri across all lobes. To realistically simulate cortical thinning and sulcal widening, we must prevent self-contact of the cortical layer. Therefore, we inflated the WM segmentation by a constant thickness of 3 mm to obtain the GM layer. We then manually modified the GM layer to remove self-contact between lobes and folds in each slice. Ultimately, we aimed for a balance between agreement of segmentation and MRI on the one hand, and obtaining a FE mesh that may realistically predict structural shape changes of the brain on the other. Following WM and GM segmentation, we isolated the hippocampus as a separate substructure, given its relevance in AD as one of the first brain structures to markedly shrink. Finally, we inflated the GM layer by 5 mm and applied smoothing to obtain the CSF layer. This layer allows us to anchor the brain in our atrophy simulations while minimizing external forces on the GM layer.

Model Properties: Our model consists of 1,361,277 tetrahedral elements: 7,925 elements for the ventricles, 2,898 elements for the hippocampus, 121,904 elements for WM, 172,238 elements for GM, and 98,755 elements for CSF. We restricted element edge length to vary from 2.0 to 2.3 mm to minimize element distortion and obtain similarly sized elements.

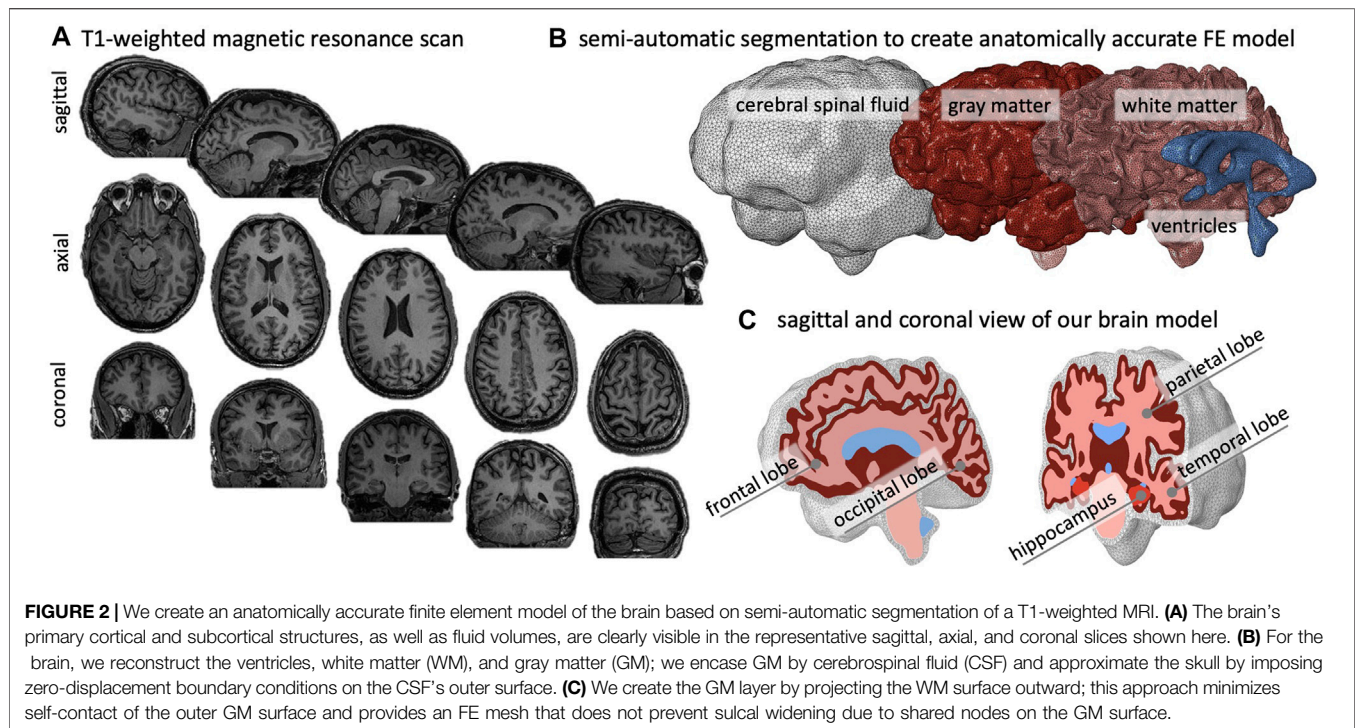


TABLE 1 | Multiphysics atrophy model parameters which include Lamé constants, healthy and pathological atrophy rates, critical biomarker concentration, and biomarker spreading parameters for white matter, gray matter, the hippocampus, ventricles, and cerebrospinal fluid.

	Lamé constants		Atrophy model parameters			Biomarker model parameters	
	λ [kPa]	μ [kPa]	G_h [-]	G_c [-]	c^{crit} [-]	d [W/kg m ³]	α [-]
White matter	64.67	2	0.0015	0.0035	0.5	15	0.09
Gray matter	32.33	1	0.001	0.002	0.5	15	0.09
Hippocampus	32.33	1	0.001	0.002	0.5	15	0.09
Ventricles	29.77	15.34	—	—	—	0	0.09
CSF	7.22	14.43	—	—	—	0	0.09

We imported the mesh into Abaqus for analysis. Specifically, we use linear tetrahedral elements C3D4 and define two simulation cases. We simulate healthy aging by simply solving the atrophy problem and simulate accelerated aging by running a thermo-mechanical analysis. In both cases, we only prescribe zero-displacement Dirichlet boundary conditions to the outer surface of the CSF layer to fix the model in space. In the AD case, we additionally prescribe an initial concentration of $c_0 = 0.3$ in the hippocampus. We used model parameters from our previous experimental and computational studies (Schaer et al., 2008; Weickenmeier et al., 2018; Weickenmeier et al., 2016) and summarize the model parameters for the atrophy and protein problem (Eq. 1, Eq. 5, Eq. 10) in Table 1. To assess long-term brain shape changes we simulate an age range of 40 years. Literature provides a myriad of large cohort studies that assess volumetric changes across this age-range (Apostolova et al., 2012; Coupé et al., 2019). Moreover, this allows us to review the impact of AD-onset time by varying the critical prion load necessary to trigger accelerated aging.

2.4 Data Analysis

We wrote custom python codes for post-processing of our simulations in order to determine volume ratios, anterior-posterior variations of the gyrification index, sulcal widening, and cortical thinning.

To calculate relative volume ratios of WM, GM, hippocampus, and ventricles, we sum the volume of all elements belonging to one of these subregions and divide by the total brain volume; we repeat this step for each time increment to obtain longitudinal changes as shown in Figure 7.

The gyrification index (GI) is determined by slicing our 3D model into 160 coronal slices (1 mm spacing between slices) and creating a binary image showing the domain associated with brain tissues, i.e., GM, WM, hippocampus, and ventricles wherever present. The subsequent steps are based on functions in the scikit-image processing package. Specifically, we determine the convex hull that fully encapsulates the brain domain to obtain the smoothed outer circumference and

extract the contour tightly lining the pial surface. We repeat this process for each slice and determine the gyrification index as the local ratio between exact pial surface length and smooth outer circumference, as shown in **Figure 11**.

Our cortical thickness measurement is based on the approach used in FreeSurfer (<http://surfer.nmr.mgh.harvard.edu>) (Han et al., 2006). We create triangulated surfaces of the outer GM surface and the outer WM surface and define cortical thickness t_c as the average of two distance measures, d_{ij} and d_{jk} . We iterate over every node of the GM surface, n_i , identify the closest node on the WM surface, n_j , and save the Euclidian distance between these two nodes as d_{ij} . We repeat this search for that particular WM node, n_j , and save the Euclidian distance between n_j and GM node n_k as distance d_{jk} . We ultimately obtain a cortical thickness measure at each GM surface node as $t_c = 0.5[d_{ij} + d_{jk}]$ and plot the result as a surface plot, as shown in **Figure 8**. We export nodal coordinates of our surfaces in the undeformed and the deformed configuration in order to determine cortical thickness at a young and an old age.

We introduce sulcal widening as the volume increase in the fluid-filled cavity of five prominent sulci, i.e., the intra-parietal sulcus, the superior temporal sulcus, the central sulcus, the sylvian fissure, and the superior frontal sulcus, as shown in **Figure 10**. Similar to determining the relative volume fractions, we sum the volume of all elements of a particular sulcal fold for each time increment of our simulation.

3 RESULTS

We evaluate our simulations with respect to hallmark features of cerebral atrophy and aim at identifying key differences between healthy brain aging and accelerated aging associated with AD.

3.1 Spatiotemporal Progression of Toxic Proteins in Alzheimer's Disease

We simulate the spreading of neurofibrillary tangles (NFT) consisting of misfolded tau protein based on the toxic protein spreading model described in §2.1. Pathological studies have shown that NFTs first appear in the entorhinal cortex and subsequently spread throughout the brain. **Figure 3** shows the spatiotemporal propagation of the NFT concentration through the brain. We observe that the hippocampus is affected first, then infiltrates the temporal lobe next, followed by the parietal lobe, occipital lobe, and in the late stages reaches the frontal lobe. Our observations are in line with cadaver studies that show a similar progression pattern of NFTs (Jucker and Walker, 2018). The coronal view shows a highly symmetric protein spread in the left and right hemisphere; from the axial and coronal cross-sections, it can be seen that deep gray matter structures tend to saturate with NFTs first. Early deep gray matter involvement, such as putamen and thalamus (de Jong et al., 2008), is linked to well-known early symptoms of AD, including short-term memory loss, difficulty performing daily tasks, and mood changes. The delay between onset and cortical layer involvement is part of the long pre-symptomatic phase of AD (Hanseeuw et al., 2019) and consistent with imaging studies that observed spatially heterogeneous atrophy patterns (Anderson et al., 2012).

3.2 Spatiotemporal Distribution of the Atrophy Factor in Healthy Brain Aging and Alzheimer's Disease

The atrophy model allows us to differentiate between healthy and AD aging. On top of an age-proportional atrophy factor in healthy aging, we added additional toxic protein concentration-related atrophy to simulate AD. **Figure 4** shows the spatiotemporal distribution of the atrophy factor, i.e. the

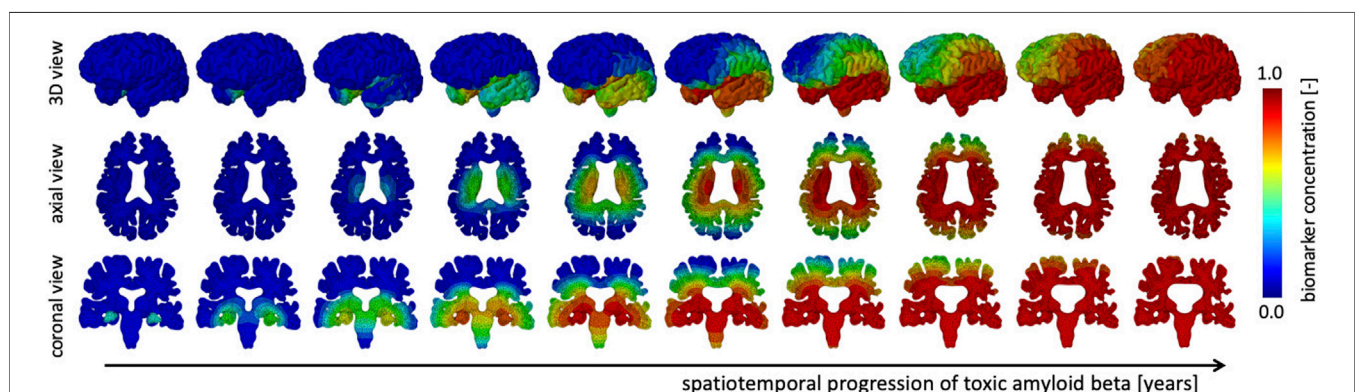
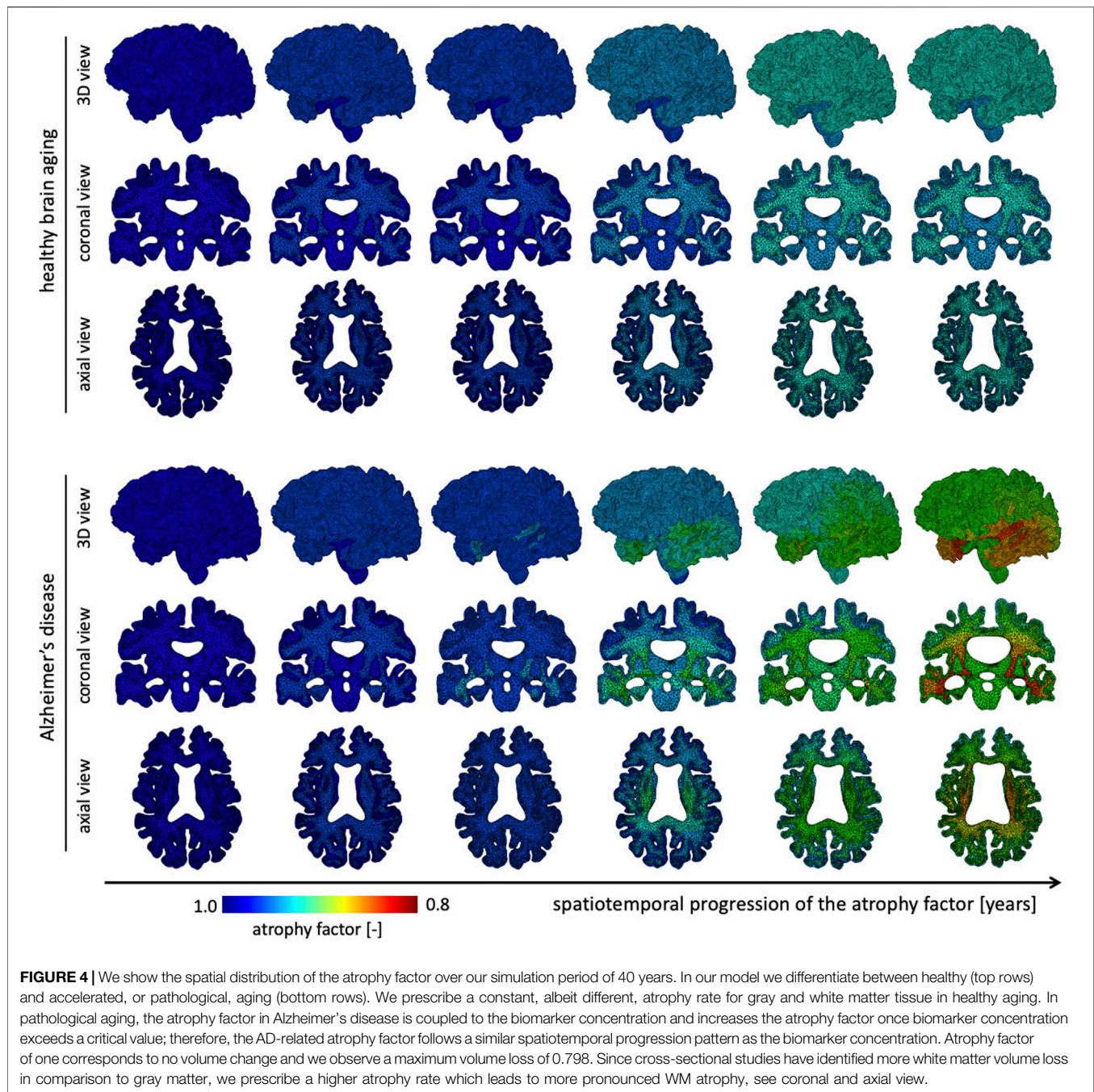


FIGURE 3 | The spatiotemporal spreading behavior of our biomarker for neurodegenerative disease is governed by a reaction-diffusion equation. We seed the biomarker in the hippocampus and observe a gradual infiltration of the whole brain. The temporal lobe is affected first, followed by the occipital, then parietal, and finally the frontal lobes, see 3D view. Moreover, we observe an early affect on deep gray and white matter structures before diffusing outward into the cortical layer, see axial view. In our current version of the model, we prescribe equal diffusion in gray and white matter tissue, which is reflected in the diffuse spreading of the biomarker concentration.



volume shrinking fraction, which ranges from 1 (no shrinking) to 0.8 (maximum volume loss). We differentiate between WM and GM atrophy rates due to tissue specific neurodegenerative processes. Therefore, GM and WM have the same atrophy factors in healthy aging, respectively. In AD, we see a spatially heterogeneous distribution with maximum atrophy in deep WM and GM structures and in the frontal lobe. The coronal view shows that the cortex exhibits an atrophy gradient that ranges from the temporal lobe to the frontal lobe; in WM we observe a

gradient ranging from the temporal lobe to the parietal lobe. Both are consistent with imaging studies investigating regional atrophy rates in the cortex (McDonald et al., 2009).

3.3 Brain Deformations in Healthy Brain Aging and Alzheimer's Disease

Figure 5 shows the temporal progression of the predicted deformation field and corresponding equivalent structural

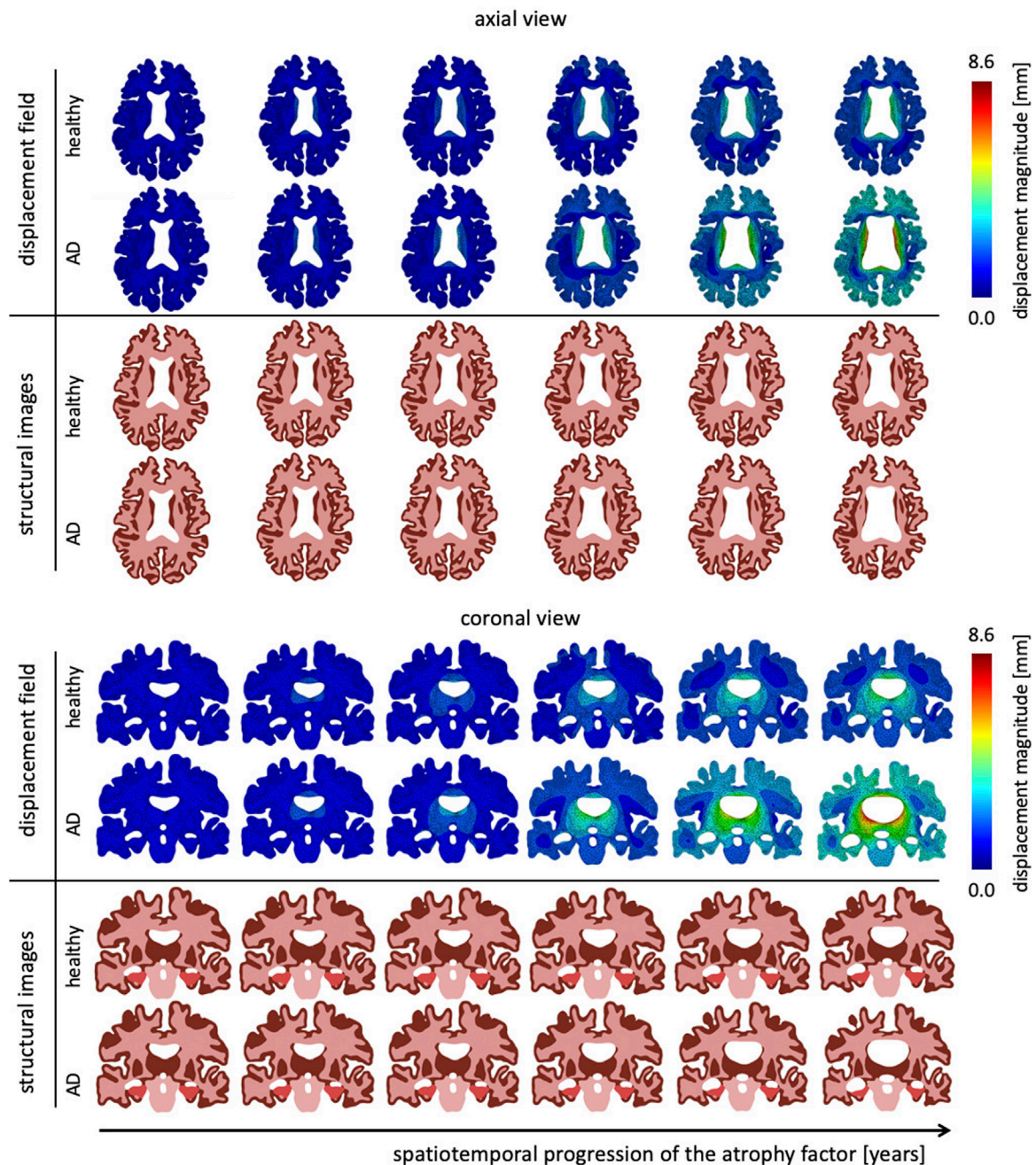


FIGURE 5 | Representative axial and coronal views of the displacement magnitude and structural images at six time points during the aging process. We show healthy aging and Alzheimer's disease-related aging in the top and bottom rows, respectively. Brain deformation is higher in Alzheimer's disease than healthy aging, and is largest around the ventricles. Moreover, we observe significant enlargement of the ventricular horns in the vicinity of the hippocampus, see coronal view. The fourth time point clearly shows a distinct separation of the displacement trajectories.

image for healthy aging and AD for representative axial and coronal sections. We observe maximum displacement magnitudes of 7.17 mm for healthy aging and 8.58 mm in AD. Maximum displacements concentrate around the lateral ventricles which undergo significant enlargement, especially in

the AD brain. In comparison to the atrophy factor, which affects the hippocampus first, ventricles, and the surrounding white and gray matter regions, appear to deform early, followed by cortical deformations. For late stages we observe higher displacement magnitudes for the GM layer in comparison to deep white matter

structures. The structural scans reveal hallmark features of cerebral atrophy: hippocampal shrinking, early onset of deep GM shrinking, cortical thinning, and ventricular enlargement. We generally observe that these features are exacerbated in AD in comparison to healthy aging. These observations are strongly correlated with medical imaging based studies that observe hippocampal shrinking, cortical thinning, and ventricular enlargement as early predictors for AD (Apostolova et al., 2012). Previous computational studies typically prescribe a zero-boundary condition on nodes of the brainstem in order to fix the model in space (Harris et al., 2019; Schäfer et al., 2019). These boundary conditions significantly impact the simulated deformation field and limit these models' abilities to resolve temporospatial patterns or critical features such as ventricular enlargement. Here, the cerebrum is loosely tethered to the skull *via* the ultrasoft CSF layer which allows for physical features to emerge naturally. Strikingly, we observe global brain involvement despite scattered atrophy features.

3.4 Ventricular Enlargement in Healthy Brain Aging and Alzheimer's Disease

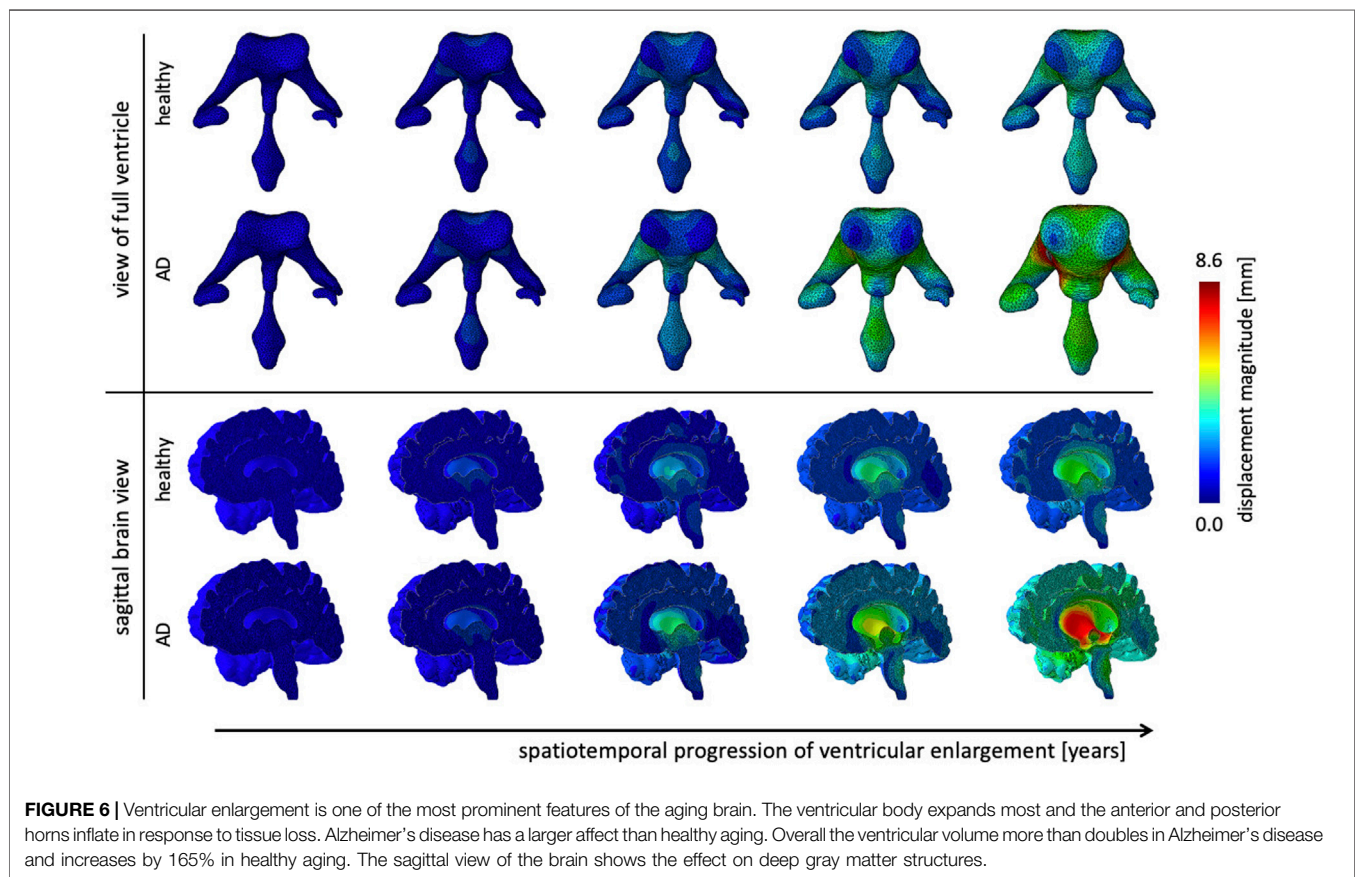
Figure 6 shows the gradual expansion of the lateral ventricles for healthy aging and AD. We observe significantly larger

ventricles in AD, which increase by a factor 2.66, in comparison to healthy aging, where ventricles increase by a factor 1.76. The simulation predicts a predominantly uniform inflation of the entire ventricular cavity in healthy brain aging at a moderate expansion rate. In AD, we observe consistent overall ventricular dilation, but notice a significant concentration of maximum expansion in the body of the ventricles and the posterior horns. This observation is consistent with a medical imaging study that reported a temporal pattern that starts in the occipital horn, then affects the body, and ultimately reaches the frontal horns (Apostolova et al., 2012). The sagittal view of the brain shows the corresponding white and gray matter loss. As the ventricles expand, we observe a smoothing of the superior horn, temporal horn, and occipital horns with an overall decrease in curvature of the ventricular surface.

4 DISCUSSION

4.1 The Origin of Brain Volume Loss

Cerebral atrophy is caused by diverse tissue damage mechanisms that culminate in brain volume loss (Oschwald et al., 2020; Blinkouskaya et al.). While healthy aging and AD share some of the gray and white matter damage mechanisms there is a



distinct point during the lifespan where the atrophy trajectory in AD diverges from the healthy model due to accelerated neurodegeneration (Callaghan et al., 2014; Coupé et al., 2019). Most common damage mechanisms are neurodegeneration in GM (Farokhian et al., 2017), demyelination in WM (Vernooij et al., 2008), activation of microglia cells (Von Bernhardi et al., 2015), and cerebral small vessel disease which is associated with microbleads, lacunes, and perivascular spaces (Cuadrado-Godia et al., 2018).

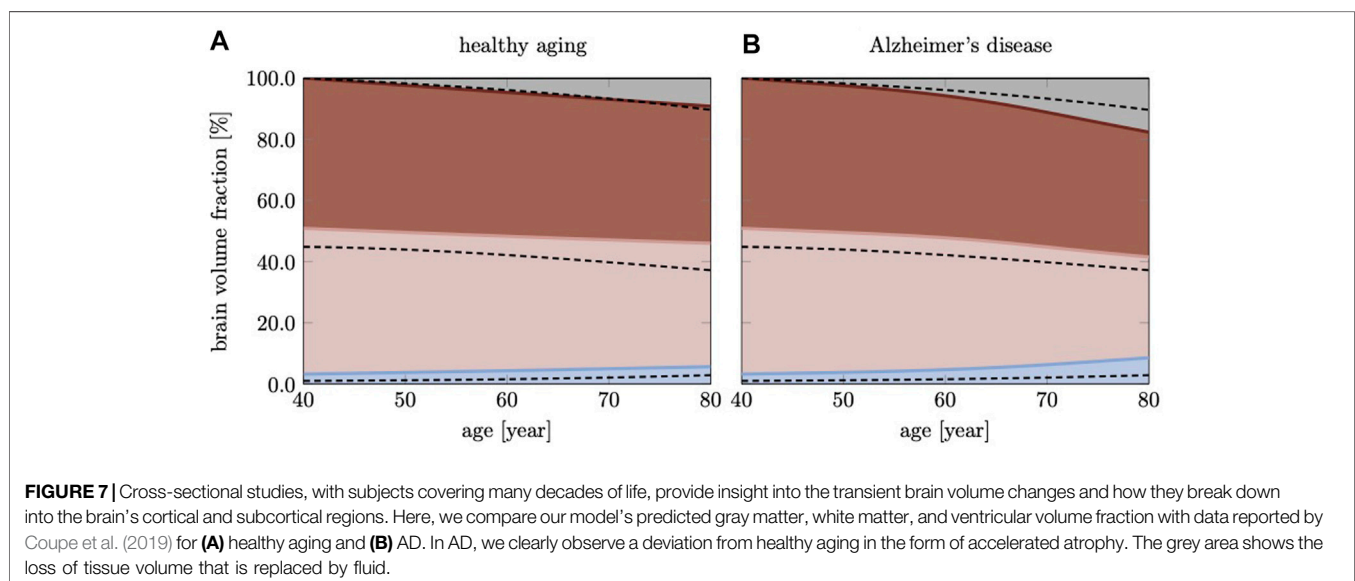
In gray matter, neurons undergo morphological changes linked to a reduction in the complexity of dendrite arborization (Dickstein et al., 2007). The underlying dendritic shortening and loss of dendritic spines leads to a progressive decrease in synaptic density and synaptic transmission with major implications on cognitive decline (Dickstein et al., 2013). Unlike healthy aging, AD is accompanied by neuron death due to the ever-increasing presence of neurotoxic proteins such as amyloid beta plaques and neurofibrillary tangles (Serrano-Pozo et al., 2011). GM volume loss is therefore exacerbated in AD and manifests in accelerated atrophy rates (Anderson et al., 2012) and increased cortical thinning (Du et al., 2007). It is well established today that the very first morphological changes associated with AD appear in the entorhinal cortex and hippocampus at least 10 years before the diagnosis (Dickstein et al., 2007).

In WM the most prevalent tissue changes are characterized by partial loss of myelin, axons, and oligodendroglial cells (Xiong and Mok, 2011); mild reactive astrocytic gliosis linked to WM lesions (Rodríguez-Arellano et al., 2016); arteriolosclerosis of small vessels resulting in incomplete ischemia and cell death (Pantoni, 2002); and the emergence of perivascular spaces that interfere with the glymphatic drainage of the brain's waste products (Rasmussen et al., 2018; Wardlaw et al., 2020).

During normal aging, amyloid beta plaques can be found in the frontal lobe, hippocampus, and entorhinal cortex of healthy elderly. In addition, neurofibrillary tangles, although much rarer than plaques, are commonly found in the medial temporal areas after 50 years of age (Dickstein et al., 2007). In AD, however, the progressive aggregation of plaques and NFTs has detrimental effects on neuronal morphology and synapses. Unlike in normal aging when neurons shrink, AD triggers sustained neuronal loss in neocortical and entorhinal regions of up to about 30% (Mattson, 2004).

4.2 Atrophy Dynamics During Aging

Figure 7 shows brain volume fractions of GM, WM, and ventricles representative of a brain aged 40 years and older. We extracted atrophy data from Coupé et al. who identified volume changes from a cross-sectional study with 4,329 subjects (2,944 healthy subjects and 3,262 subjects with AD and mild cognitive impairment) (Coupé et al., 2019), see dashed lines. We focus on brain aging and calibrate our model parameters such that our model provides good qualitative agreement for healthy brain aging, (Figure 7A). Our model successfully reproduces GM and WM volume loss and ventricular enlargement. The offset between GM, WM, and ventricular volume fractions is due to comparison of a personalized brain model with cross-sectional data. More importantly, the numerically observed atrophy trajectories paint a representative picture that demonstrates the ability of our modeling approach to predict shape changes associated with brain aging. Our model predicts GM volume fraction to drop from 52.36% at age 40 years to 50.49% at age 80 years in healthy aging and 49.34% in AD; WM volume fraction to drop from 47.63% at age 40 years to 40.29% at age 80 years in healthy aging and 32.95% in AD; ventricular volume fraction increases from 3.22% at age 40 years to 5.66% at age 80 years in healthy aging and 8.57% in AD. AD clearly



exacerbates tissue loss and exhibits an accelerating atrophy rate with increasing age, (**Figure 7B**). Tissue lost due to atrophy is replaced by fluid (volume fraction shown in grey) linked in one part to ventricular enlargement and in another part to sulcal widening and loss of gyrification (Scahill et al., 2003).

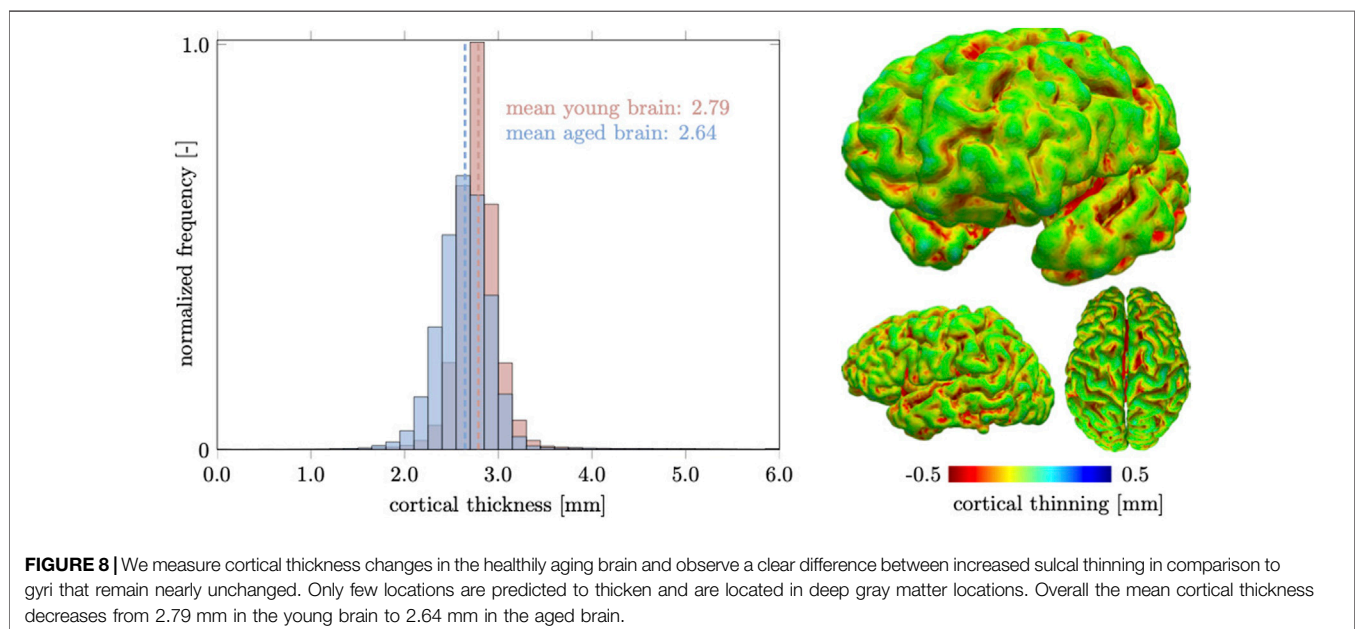
4.3 Cortical Thinning

The cortical layer is subject to spatially heterogeneous age-related cortical thinning. The deterioration of dendritic connections and the loss of GM neurons cause volume loss that can be broken down into cortical thickness and surface area. These two properties do not necessarily follow each other chronologically (Dickerson et al., 2009). The differentiation between both measures has proven useful, however, because of increased sensitivity with respect to age-related changes (Storsve et al., 2014; Dotson et al., 2016). In our computer model, we observe a mean cortical thickness of 2.79 mm in the young brain and 2.64 mm in the aged brain. In **Figure 8**, we report our model's brain thickness which ranges from 1.5 to 4.3 mm in the young brain and decreases to a range from 1.3 to 3.9 mm in the aged brain. These values compare well to results presented by Fjell et al. who observed a progressive decline in overall cortical thickness in their three subject groups aged < 40, 40–60, and > 60 (Fjell et al., 2001; Fjell and Walhovd, 2010). They report that sulci undergo more pronounced thinning than gyri and that thinning is unevenly distributed across the cortex. Based on data extracted from Fjell et al., the cortex appears to thin by roughly 0.1% per year, or 0.00745 mm, which corresponds to an overall thickness decrease of about 0.3 mm over the course of 4 decades for subjects aged > 40 (Fjell et al., 2015). The linearly decreasing relationship between cortical thickness and age across several datasets provides strong support for our modeling approach which

assumes a constant atrophy rate for all ages (Fjell et al., 2001; Du et al., 2006). Despite significant efforts to identify common thinning trajectories in the human brain, cortical thinning is driven by molecular and cellular processes that are not limited to individual regions. Cross-sectional studies report that the frontal cortices are most strongly affected and that the medial-temporal cortices, i.e., parahippocampal and entorhinal cortex, are moderately affected. Lateral inferior parts of the temporal lobes show least thinning and the superior parts of the lateral temporal lobes exhibits more pronounced thinning than the inferior parts (Fjell et al., 2001; Fjell and Walhovd, 2010). In our model, we observe slightly higher thinning in the frontal and temporal region, while the occipital lobe thins less. In aging research the temporal lobes play a significant role because they are functionally related to the hippocampus and other GM structures that are associated with memory loss and cognitive decline (Dickerson et al., 2009; Dhikav et al., 2014). In the end, our model leads to fairly similar cortical thinning across the entire brain due to the prescribed constant GM atrophy rate. Coupling to the spreading of neurotoxic proteins may lead to a stronger heterogeneity in terms of thinning.

4.4 Hippocampal Shrinking and Ventricular Enlargement

The hippocampus is one of the, if not, the earliest cortical substructures to undergo detectable atrophy in Alzheimer's disease and related dementias (Henneman et al., 2009). Hippocampal changes can be detected as early as 10 years prior to the onset of symptoms and is therefore considered to be a strong indicator for abnormal aging processes (Ritchie et al., 2016; Kinnunen et al., 2018). Hippocampal shrinking precedes most cortical changes by up to 5 years and is reported



to shrink by 5.2% per year based on data from cross-sectional brain imaging studies (Thompson et al., 2004; Henneman et al., 2009). It is primarily linked to de-arborization of subcortical GM neurons (Esiri, 2007; Dickstein et al., 2013). In comparison to healthy aging, Alzheimer's disease accelerates neuronal degeneration due to accumulation of neurotoxic amyloid beta plaques and neurofibrillary tangles (Bobinski et al., 1999). **Figure 9** shows our model's predicted volumetric shrinking for healthy aging and AD. We observe a decrease of the hippocampal brain volume fraction by 8.87% for healthy aging and by 24.1% for AD. The direct comparison illustrates the distinct difference in the atrophy trajectory in accelerated aging in AD observed in cross-sectional studies (Coupé et al., 2019).

The brain tissue volume lost due to cerebral atrophy, is replaced by fluid. Structurally, this manifests in significant ventricular enlargement (Pagani et al., 2008; Apostolova et al., 2012) and an increase in the space between folds, i.e., sulcal widening (Liu et al., 2013; Jin et al., 2018). Ventricular enlargement is one of the most prominent features in longitudinal medical images and represents a major change in brain topology (Sengoku, 2020). Mechanically, the extent of ventricular enlargement is significant and will lead to high loads on the membrane separating ventricle and cerebrum.

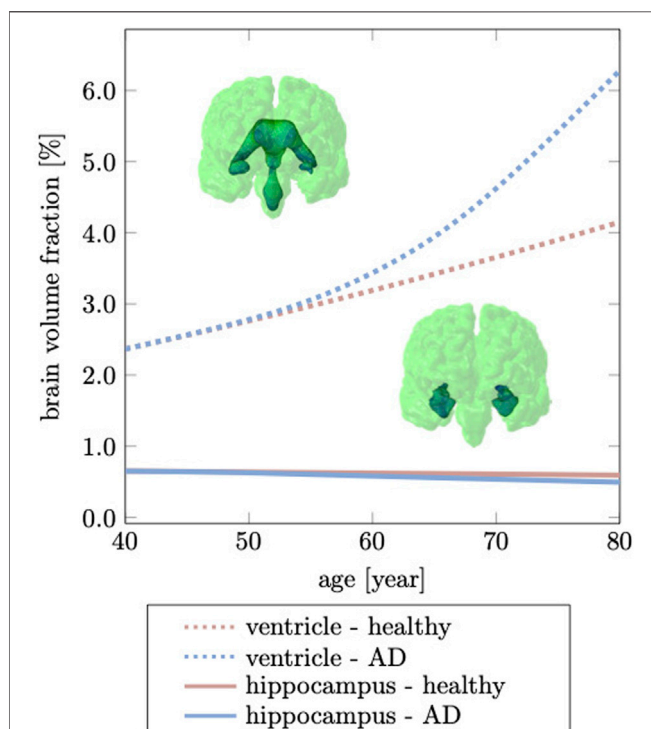
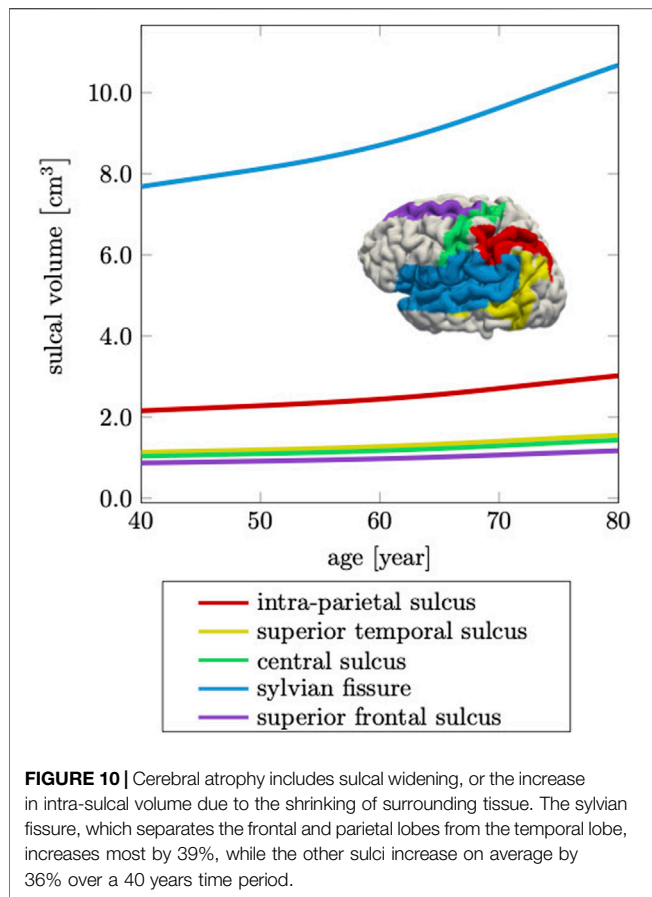


FIGURE 9 | Hippocampal shrinking and ventricular enlargement differ for healthy aging and Alzheimer's disease. The initial overlap between healthy aging and Alzheimer's disease is due to the gradual spread of our biomarker through the brain which ultimately accelerates brain changes passed the age of 60 years. This deviation from the healthy trajectory is used as a biomarker for detecting Alzheimer's disease (Apostolova et al., 2012).

The ependymal cells lining the ventricular wall are likely to be fatigued with age, leading to CSF leakage into white matter and causing tissue degeneration, such as leukoariosis in the vicinity of ventricular horns (Milhorat et al., 1970; Todd et al., 2018). Our model predicts a uniform volumetric expansion of the entire ventricles which is reflective of findings from imaging studies (Salat et al., 2009; Coupé et al., 2019). Our simulation is able to reproduce this deformation mode due to our physically motivated boundary conditions on the FE model. Instead of constraining individual nodes in the brainstem (Harris et al., 2019; Schäfer et al., 2019), here, we *suspend* the brain inside the skull by mimicking CSF as an ultrasoft, highly compressible solid. The suspension of the shrinking cerebrum allows for the ventricles to expand. This leads to a fairly symmetric displacement field with respect to the left and right hemisphere. In our model, the initial ventricular volume corresponds to 2.37% of the total intracranial volume. In our simulation, we observe an increase to 4.15% of total intracranial volume, or a 75.03% volume increase in healthy aging; In AD, ventricular volume fraction increases to 6.28%, or an overall volume increase by 164.98%. Our data aligns well with data reported by Coupé et al. that observe significant acceleration of ventricular expansion at age 40 (Coupé et al., 2019). Microstructurally, ventricular expansion is accompanied by a progressive deterioration of the ventricular wall which is composed of ciliated ependymal cells that undergo significant cellular stretch during each pulsation cycle. Over the course of a lifetime, these cells accumulate significant mechanical fatigue and cause membrane failure (Milhorat et al., 1970; Jiménez et al., 2014). The subsequent leakage of CSF into white matter tissue causes leukoariosis and white matter deterioration.

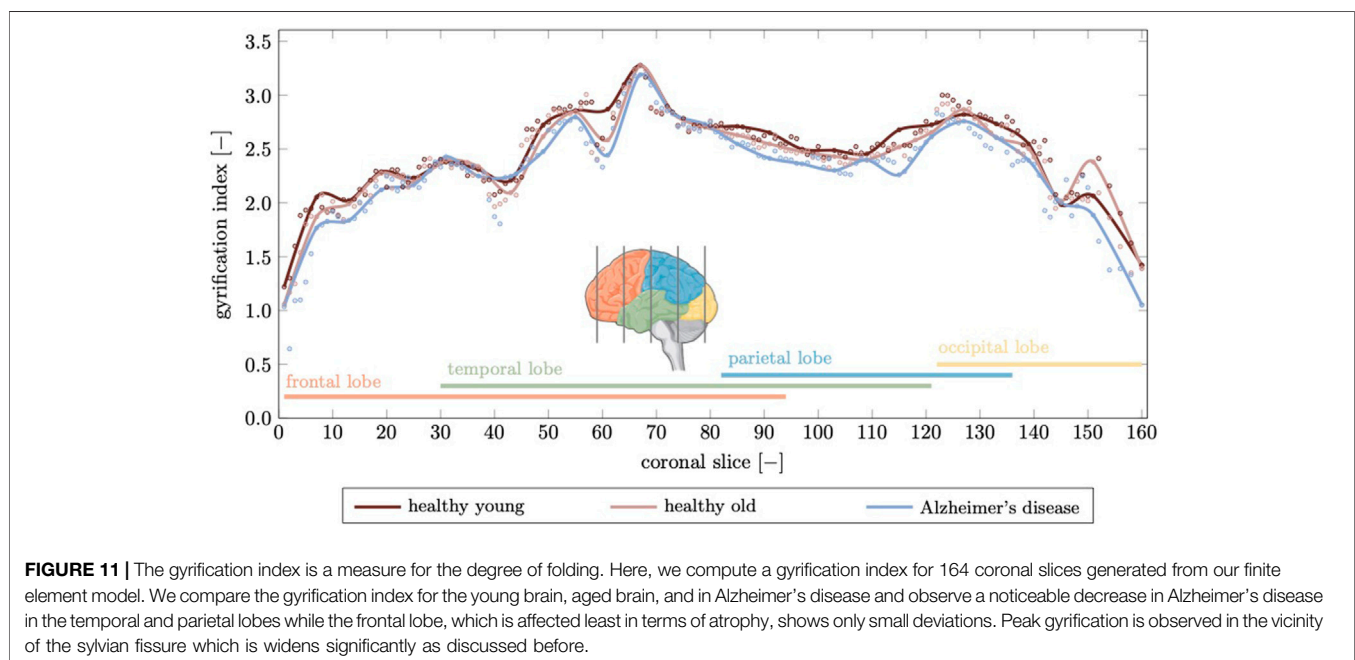
4.5 Sulcal Widening and Loss of Gyrfication

Ventricular enlargement is accompanied by an increase in the space between folds and loss of gyrfication (Hamelin et al., 2015; Aso et al., 2020). This feature is less prominent on medical images, but is another indicator for the significant topological changes of the brain (Plochanski et al., 2016; Shen et al., 2018). From a FE modeling perspective, creating an anatomically accurate mesh that properly capture sulcal widening represents a major challenge. Most folds touch each other such that the segmentation process typically does not produce a GM surface without self-contact. This leads to node sharing of elements that belong to different folds and ultimately, prevents models to allow for separation of the GM surface upon tissue atrophy. Here, we specifically address this issue and produced a FE mesh that has minimal node sharing between neighboring folds. Therefore, our model exhibits this hallmark feature of cerebral atrophy and allows us to compare model response with imaging data. Jin et al., for example, report that the mean sulcal width between primary sulci increases by $\sim 17.3\%$ from 1.27 ± 0.17 mm in middle-aged persons to 1.49 ± 0.20 mm in older adults (71). In **Figure 10** we report sulcal widening, a measure of the volume increase of the fluid between folds. We segment these volumes for five prominent



sulci, the intra-parietal sulcus, the superior temporal sulcus, the central sulcus, the sylvian fissure, and the superior frontal sulcus (Kochunov et al., 2005; Liu et al., 2013). We observe that the overall volume change of all sulci follow a similar trend and increase by up to 40%. Similar to previous work, the sylvian fissure exhibits the largest increase in width and is noticeably larger in individuals with AD in comparison to cognitively normal subjects (Park et al., 2013; Cai et al., 2017). Overall, we observed that the technical challenges associated with detailed geometric interpretation of sulcal changes, such as sulcal widening and changes in sulcal depth, represent a barrier to serving as a reliable biomarker for morphological changes in the aging brain. Especially, subject-specificity will limit absolute comparisons with any healthy or diseased cohort (Shen et al., 2018).

The gyrification index (GI), defined as the ratio between actual GM surface divided by the smooth surface surrounding the cortex, is another parameter that is closely linked to the topology of brain folds (Madan, 2021). In **Figure 11** we show the gyrification index for 164 coronal slices calculated for the healthy young brain, healthy aged brain, and the brain affected by Alzheimer's disease. The GI is highest across the brain for the young brain. With aging or AD, the GI decreases due to decreased folding. We observe the highest GI in the temporal lobe with 3.28 for young, 3.27 for aged, and 3.19 for the AD brain; minimum GI is observed in the frontal lobe with 1.22 in young, 1.06 in aged, and 0.64 in the AD brain. We observe a mean GI of 2.48 ± 0.38 in the young, 2.42 ± 0.4 in the aged, and 2.32 ± 0.44 in the AD brain. The most prominent and persistent drop in GI is observed in the temporal and parietal lobes which are heavily affected by early infiltration of our neurotoxic biomarker and corresponding accelerated atrophy.



Our reported values compare well with cross-sectional studies reported in literature (Jockwitz et al., 2017; Madan, 2021). In a cross-sectional study by Cao et al., the GI drops from 3.4 at age 10 to 2.6 at age 85, following the curve $GI = a + b \ln(A + c)$, with age A and parameters $a = 3.4$, $b = -0.175$, and $c = -2.9991$ (Cao et al., 2017). According to this formula, GI drops from 2.8 at age 40 to 2.6 at age 80, or by 4.5% between ages 40 and 80. Our model predicts a 2.7% change for the most folded coronal slice.

4.6 Limitations

Our computational model is based on several assumptions and thus not without limitations. For example, when creating the FE mesh, we uniformly inflate the WM surface to create a GM layer which results in a fairly homogeneous GM thickness across the brain. In reality, the gray matter layer is characterized by thickness differences between sulci and gyri (Lin et al., 2021) and varies across the brain (Fischl and Dale, 2000). We chose this approach due to the necessity to avoid self-contact between GM folds in order to capture sulcal widening during atrophy. Furthermore, our current constitutive model differentiates between GM and WM atrophy rates, but assumes a uniform parameter across the brain. Cross-sectional studies have demonstrated significant regional variation in brain shrinking rates in healthy aging and AD (Fox and Schott, 2004; Fjell et al., 2014). The coupling of biomarker concentration and atrophy rate in our model introduces, however, a degree of heterogeneity that exacerbates spatiotemporal differences between healthy aging and AD. Our model shows good agreement with cross-sectionally observed image-based atrophy patterns. Going forward, there is a need to develop a validation approach that allows to calibrate model parameters against longitudinal imaging data of individual subjects (Rusinek et al., 2003). To that end, we will develop a non-rigid registration technique that delivers the full-field displacements of the brain between two images (Wang et al., 2021). And lastly, AD is characterized by two different protein spreading mechanisms: connectivity-based spread *via* intracellular diffusion of neurofibrillary tangles along the axon network and proximity-based spread of amyloid beta *via* extracellular aggregation of plaques (Jack and Holtzman, 2013). Here, we only consider isotropic diffusion through the bulk tissue. As a next step, we will integrate the diffusion tensor imaging-based tractome to more accurately represent intracellular spreading of tau which has shown to better correlate with neurocognitive decline (Raj et al., 2015).

REFERENCES

- Anderson, V. M., Schott, J. M., Bartlett, J. W., Leung, K. K., Miller, D. H., and Fox, N. C. (2012). Gray Matter Atrophy Rate as a Marker of Disease Progression in Ad. *Neurobiol. Aging* 33, 1194–1202. doi:10.1016/j.neurobiolaging.2010.11.001
- Apostolova, L. G., Green, A. E., Babakchian, S., Hwang, K. S., Chou, Y.-Y., Toga, A. W., et al. (2012). Hippocampal Atrophy and Ventricular Enlargement in Normal Aging, Mild Cognitive Impairment (MCI), and Alzheimer Disease. *Alzheimer Dis. Associated Disord.* 26, 17–27. doi:10.1097/wad.0b013e3182163b62
- Aso, T., Sugihara, G., Murai, T., Ubukata, S., Urayama, S.-i., Ueno, T., et al. (2020). A Venous Mechanism of Ventriculomegaly Shared between Traumatic Brain Injury and normal Ageing. *Brain* 143, 1843–1856. doi:10.1093/brain/awaa125
- Blinkouskaya, Y., Caçoilo, A., Gollamudi, T., Jalalian Sedaghati, S., and Weickenmeier, J. j. v. y., “Brain Aging Mechanisms with Mechanical Manifestations (Under Review).”
- Bobinski, M., De Leon, M. J., Wegiel, J., Desanti, S., Convit, A., Saint Louis, L. A., et al. (1999). The Histological Validation of post Mortem Magnetic Resonance Imaging-Determined Hippocampal Volume in Alzheimer’s Disease. *Neuroscience* 95, 721–725. doi:10.1016/s0306-4522(99)00476-5

5 CONCLUSION

Brain shape undergoes many changes throughout life. Advanced aging is characterized by progressive atrophy which appears as brain volume loss, cortical thinning, sulcal widening, and ventricular enlargement. These morphological changes are part of healthy brain aging and it remains unclear how these changes relate to cognitive decline. In case of accelerated aging, such as in neurodegenerative diseases like AD, these structural changes are exacerbated due to the presence of neurotoxic proteins that spread through the brain. Here, we developed a constitutive framework for the simulation of three-dimensional morphological changes of the brain in healthy aging and AD. Our anatomically accurate FE model nicely captures volume loss, GM thinning, ventricular enlargement, and loss of gyrification. We compare our numerical results to commonly studied structural properties extracted from medical images and demonstrate that our generalized model shows good agreement with cross-sectional aging data. As a next step, we will utilize our modeling approach to create subject-specific FE models and validate our simulations against their longitudinal imaging data. This work has the potential to systematically investigate the impact of gray and white matter aging mechanisms, such as cerebral small vessel disease, leukoaraiosis, lacunes, and the dearborization of neurons, on the evolving morphology of the healthily and pathologically aging brain.

DATA AVAILABILITY STATEMENT

The raw data supporting the conclusion of this article will be made available by the authors, without undue reservation.

AUTHOR CONTRIBUTIONS

YB and JW designed the study, YB performed the numerical analysis and evaluated the data, YB and JW wrote the manuscript. All authors contributed to manuscript revision, read, and approved the submitted version.

FUNDING

This work was supported by the National Institute on Aging of the National Institutes of Health under award R21AG067442 to JW.

- Boland, B., Yu, W. H., Corti, O., Mollereau, B., Henriques, A., Bezaud, E., et al. and others, "Promoting the Clearance of Neurotoxic Proteins in Neurodegenerative Disorders of Ageing," *Nat. Rev. Drug Discov.* 17, 660–688. 2018. doi:10.1038/nrd.2018.109
- Budday, S., and Kuhl, E. (2020). Modeling the Life Cycle of the Human Brain. *Curr. Opin. Biomed. Eng.* 15, 16–25. doi:10.1016/j.cobme.2019.12.009
- Cai, K., Xu, H., Guan, H., Zhu, W., Jiang, J., Cui, Y., et al. (2017). Identification of Early-Stage Alzheimer's Disease Using Sulcal Morphology and Other Common Neuroimaging Indices. *PLoS One* 12, e0170875. doi:10.1371/journal.pone.0170875
- Callaghan, M. F., Freund, P., Draganski, B., Anderson, E., Cappelletti, M., Chowdhury, R., et al. and others, "Widespread Age-Related Differences in the Human Brain Microstructure Revealed by Quantitative Magnetic Resonance Imaging," *Neurobiol. Aging* 35, 1862–1872. 2014. doi:10.1016/j.neurobiolaging.2014.02.008
- Camara, O., Schweiger, M., Scallan, R. I., Crum, W. R., Sneller, B. I., Schnabel, J. A., et al. (2006). Phenomenological Model of Diffuse Global and Regional Atrophy Using Finite-Element Methods. *IEEE Trans. Med. Imaging* 25, 1417–1430. doi:10.1109/tmi.2006.880588
- Cao, B., Mwangi, B., Passos, I. C., Wu, M.-J., Keser, Z., Zunta-Soares, G. B., et al. (2017). Lifespan Gyrfication Trajectories of Human Brain in Healthy Individuals and Patients with Major Psychiatric Disorders. *Scientific Rep.* 7, 1–8. doi:10.1038/s41598-017-00582-1
- Coupé, P., Manjón, J. V., Lanuza, E., and Catheline, G. (2019). "Lifespan Changes of the Human Brain in Alzheimer's Disease. *Scientific Rep.* 9 (1–12). doi:10.1038/s41598-019-39809-8
- Cuadrado-Godia, E., Dwivedi, P., Sharma, S., Ois Santiago, A., Roquer Gonzalez, J., Balcells, M., et al. (2018). Cerebral Small Vessel Disease: A Review Focusing on Pathophysiology, Biomarkers, and Machine Learning Strategies. *J. Stroke* 20, 302–320. doi:10.5853/jos.2017.02922
- de Jong, L. W., van der Hiele, K., Veer, I. M., Houwing, J. J., Westendorp, R. G. J., Bollen, E. L. E. M., et al. (2008). Strongly Reduced Volumes of Putamen and Thalamus in Alzheimer's Disease: an MRI Study. *Brain* 131, 3277–3285. doi:10.1093/brain/awn278
- Dhikav, V., Sethi, M., and Anand, K. S. (2014). Medial Temporal Lobe Atrophy in Alzheimer's Disease/mild Cognitive Impairment with Depression. *Bjr* 87, 20140150. doi:10.1259/bjr.20140150
- Dickerson, B. C., Feczko, E., Augustinack, J. C., Pacheco, J., Morris, J. C., Fischl, B., et al. (2009). Differential Effects of Aging and Alzheimer's Disease on Medial Temporal Lobe Cortical Thickness and Surface Area. *Neurobiol. Aging* 30, 432–440. doi:10.1016/j.neurobiolaging.2007.07.022
- Dickstein, D. L., Kabaso, D., Rocher, A. B., Luebke, J. I., Wearne, S. L., and Hof, P. R. (2007). Changes in the Structural Complexity of the Aged Brain. *Aging Cell* 6, 275–284. doi:10.1111/j.1474-9726.2007.00289.x
- Dickstein, D. L., Weaver, C. M., Luebke, J. I., and Hof, P. R. (2013). Dendritic Spine Changes Associated with normal Aging. *Neuroscience* 251, 21–32. doi:10.1016/j.neuroscience.2012.09.077
- Dotson, V. M., Szymkowicz, S. M., Sozda, C. N., Kirtan, J. W., Green, M. L., O'Shea, A., et al. (2016). Age Differences in Prefrontal Surface Area and Thickness in Middle Aged to Older Adults. *Front. Aging Neurosci.* 7, 250. doi:10.3389/fnagi.2015.00250
- Du, A.-T., Schuff, N., Chao, L. L., Kornak, J., Jagust, W. J., Kramer, J. H., et al. and others, "Age Effects on Atrophy Rates of Entorhinal Cortex and hippocampus," *Neurobiol. Aging* 27, 733–740. 2006. doi:10.1016/j.neurobiolaging.2005.03.021
- Du, A. T., Schuff, N., Kramer, J. H., Rosen, H. J., Gorno-Tempini, M. L., Rankin, K., et al. (2007). Different Regional Patterns of Cortical Thinning in Alzheimer's Disease and Frontotemporal Dementia. *Brain* 130, 1159–1166. doi:10.1093/brain/awn016
- Esiri, M. M. (2007). Ageing and the Brain. *The J. Pathol. A J. Pathological Soc. Great Britain Ireland* 211, 181–187.
- Farokhian, F., Yang, C., Beheshti, I., Matsuda, H., and Wu, S. (2017). Age-related gray and white Matter Changes in normal Adult Brains. *Aging Dis.* 8, 899. doi:10.14336/ad.2017.0502
- Fischl, B., and Dale, A. M. (2000). Measuring the Thickness of the Human Cerebral Cortex from Magnetic Resonance Images. *Proc. Natl. Acad. Sci.* 97, 11050–11055. doi:10.1073/pnas.200033797
- Fisher, R. A. (1937). The Wave of advance of Advantageous Genes. *Ann. eugenics* 7, 355–369. doi:10.1111/j.1469-1809.1937.tb02153.x
- Fjell, A. M., Grydeland, H., Krogstad, S. K., Amlie, I., Rohani, D. A., Ferschmann, L., et al. (2015). Development and Aging of Cortical Thickness Correspond to Genetic Organization Patterns. *Proc. Natl. Acad. Sci. USA* 112, 15462–15467. doi:10.1073/pnas.1508831112
- Fjell, A. M., and Walhovd, K. B. (2010). Structural Brain Changes in Aging: Courses, Causes and Cognitive Consequences. *Rev. Neurosci.* 21, 187–221. doi:10.1515/revneuro.2010.21.3.187
- Fjell, A. M., Westlye, L. T., Amlie, I., Espeseth, T., Reinvang, I., Raz, N., et al. (2001–2012/2009). Fischl, B., and Others, "High Consistency of Regional Cortical Thinning in Aging across Multiple Samples. *Cereb. Cortex* 19.
- Fjell, A. M., Westlye, L. T., Grydeland, H., Amlie, I., Espeseth, T., Reinvang, I., et al. (2014). Accelerating Cortical Thinning: Unique to Dementia or Universal in Aging? *Cereb. Cortex* 24, 919–934. doi:10.1093/cercor/bhs379
- Fox, N. C., and Schott, J. M. (2004). Imaging Cerebral Atrophy: normal Ageing to Alzheimer's Disease. *The Lancet* 363, 392–394. doi:10.1016/s0140-6736(04)15441-x
- Garcia, K. E., Robinson, E. C., Alexopoulos, D., Dierker, D. L., Glasser, M. F., Coalson, T. S., et al. and others, "Dynamic Patterns of Cortical Expansion during Folding of the Preterm Human Brain," *Proc. Natl. Acad. Sci. USA*, 115, 3156–3161. 2018. doi:10.1073/pnas.1715451115
- Hall, C. M., Moenendary, E., and Sheridan, G. K. (2020). "Mechanobiology of the Brain in Ageing and Alzheimer's Disease. *Eur. J. Neurosci.* doi:10.1111/ejn.14766
- Hamami, A., and Unal, G. (2013). Registration of Brain Tumor Images Using Hyper-Elastic Regularization. *Computational Biomechanics for Medicine*. New York, NY: Springer, 101–114.
- Hamelin, L., Bertoux, M., Bottlaender, M., Corne, H., Lagarde, J., Hahn, V., et al. and others, "Sulcal Morphology as a New Imaging Marker for the Diagnosis of Early Onset Alzheimer's Disease," *Neurobiol. Aging*, 36, 2932–2939. 2015. doi:10.1016/j.neurobiolaging.2015.04.019
- Han, X., Jovicich, J., Salat, D., van der Kouwe, A., Quinn, B., Czanner, S., et al. and others, "Reliability of Mri-Derived Measurements of Human Cerebral Cortical Thickness: the Effects of Field Strength, Scanner Upgrade and Manufacturer," *Neuroimage* 32, 180–194. 2006. doi:10.1016/j.neuroimage.2006.02.051
- Hanseeuw, B. J., Betensky, R. A., Jacobs, H. I. L., Schultz, A. P., Sepulcre, J., Becker, J. A., et al. and others, "Association of Amyloid and Tau with Cognition in Preclinical Alzheimer Disease," *JAMA Neurol.* 76, 915–924. 2019. doi:10.1001/jamaneurol.2019.1424
- Harris, T. C., de Rooij, R., and Kuhl, E. (2019). The Shrinking Brain: Cerebral Atrophy Following Traumatic Brain Injury. *Ann. Biomed. Eng.* 47, 1941–1959. doi:10.1007/s10439-018-02148-2
- Henneman, W. J. P., Sluiter, J. D., Barnes, J., Van Der Flier, W. M., Sluiter, I. C., Fox, N. C., et al. (2009). Hippocampal Atrophy Rates in Alzheimer Disease: Added Value over Whole Brain Volume Measures. *Neurology* 72, 999–1007. doi:10.1212/01.wnl.0000344568.09360.31
- Jack, C. R., Jr, and Holtzman, D. M. (2013). Biomarker Modeling of Alzheimer's Disease. *Neuron* 80, 1347–1358. doi:10.1016/j.neuron.2013.12.003
- Jack, C. R., Jr, Knopman, D. S., Jagust, W. J., Petersen, R. C., Weiner, M. W., Aisen, P. S., et al. "Tracking Pathophysiological Processes in Alzheimer's Disease: an Updated Hypothetical Model of Dynamic Biomarkers," *Lancet Neurol.* 12, 207–216. 2013.
- Jiménez, A. J., Domínguez-Pinos, M.-D., Guerra, M. M., Fernández-Llebrez, P., and Pérez-Figares, J.-M. (2014). Structure and Function of the Ependymal Barrier and Diseases Associated with Ependyma Disruption. *Tissue Barriers* 2, e28426. doi:10.4161/tisb.28426
- Jin, K., Zhang, T., Shaw, M., Sachdev, P., and Cherbuin, N. (2018). Relationship between Sulcal Characteristics and Brain Aging. *Front. Aging Neurosci.* 10, 339. doi:10.3389/fnagi.2018.00339
- Jockwitz, C., Caspers, S., Lux, S., Jütten, K., Schleicher, A., Eickhoff, S. B., et al. (2017). Age- and Function-Related Regional Changes in Cortical Folding of the Default Mode Network in Older Adults. *Brain Struct. Funct.* 222, 83–99. doi:10.1007/s00429-016-1202-4
- Jucker, M., and Walker, L. C. (2018). Propagation and Spread of Pathogenic Protein Assemblies in Neurodegenerative Diseases. *Nat. Neurosci.* 21, 1341–1349. doi:10.1038/s41593-018-0238-6
- Karaçali, B., and Davatzikos, C. (2006). Simulation of Tissue Atrophy Using a Topology Preserving Transformation Model. *IEEE Trans. Med. Imaging* 25, 649–652. doi:10.1109/tmi.2006.873221
- Khanal, B., Ayache, N., and Pennec, X. (2017). Simulating Longitudinal Brain Maps with Known Volume Changes and Realistic Variations in Image Intensity. *Front. Neurosci.* 11, 132. doi:10.3389/fnins.2017.00132

- Kim, H.-R., Lee, P., Seo, S. W., Roh, J. H., Oh, M., Oh, J. S., et al. (2019). Comparison of Amyloid β and Tau Spread Models in Alzheimer's Disease. *Cereb. Cortex* 29, 4291–4302. doi:10.1093/cercor/bhy311
- Kinnunen, K. M., Cash, D. M., Poole, T., Frost, C., Benzinger, T. L. S., Ahsan, R. L., et al. and others., Presymptomatic Atrophy in Autosomal Dominant Alzheimer's Disease: A Serial Magnetic Resonance Imaging Study," *Alzheimer's Dement.*, 14, 43–53. 2018. doi:10.1016/j.jalz.2017.06.2268
- Kochunov, P., Mangin, J.-F., Coyle, T., Lancaster, J., Thompson, P., Rivière, D., et al. and others., "Age-related Morphology Trends of Cortical Sulci," *Hum. Brain Mapp.* 26, 210–220. 2005. doi:10.1002/hbm.20198
- Kolmogorov, A., Petrovsky, I., and Piskunov, N. (1937). Investigation of the Equation of Diffusion Combined with Increasing of the Substance and its Application to a Biology Problem. *Bull. Mosc. State. Univ. Ser. A: Math. Mech* 1, 1–25.
- Lin, H. Y., Huang, C. C., Chou, K. H., Yang, A. C., Lo, C. Z., Tsai, S. J., et al. (2021). Differential Patterns of Gyral and Sulcal Morphological Changes during normal Aging Process. *Front. Aging Neurosci.* 13 (15), 625931. doi:10.3389/fnagi.2021.625931
- Liu, T., Sachdev, P. S., Lipnicki, D. M., Jiang, J., Cui, Y., Kochan, N. A., et al. (2013). Longitudinal Changes in Sulcal Morphology Associated with Late-Life Aging and Mci. *Neuroimage* 74, 337–342. doi:10.1016/j.neuroimage.2013.02.047
- Lockhart, S. N., and DeCarli, C. (2014). Structural Imaging Measures of Brain Aging. *Neuropsychol. Rev.* 24, 271–289. doi:10.1007/s11065-014-9268-3
- Madan, C. R. (2021). Age-related Decrements in Cortical Gyrfication: Evidence from an Accelerated Longitudinal Dataset. *Eur. J. Neurosci.* 53, 1661–1671. doi:10.1111/ejn.15039
- Malpetti, M., Kievit, R. A., Passamonti, L., Jones, P. S., Tsvetanov, K. A., Rittman, T., et al. and others., Microglial Activation and Tau burden Predict Cognitive Decline in Alzheimer's Disease," *Brain*, 143, 1588–1602. 2020. doi:10.1093/brain/awaa088
- Mattson, M. P., and Arumugam, T. V. (2018). Hallmarks of Brain Aging: Adaptive and Pathological Modification by Metabolic States. *Cel. Metab.* 27, 1176–1199. doi:10.1016/j.cmet.2018.05.011
- Mattson, M. P. (2004). Pathways towards and Away from Alzheimer's Disease. *Nature* 430, 631–639. doi:10.1038/nature02621
- McDonald, C. R., McEvoy, L. K., Gharapetian, L., Fennema-Notestine, C., Hagler, D. J., Holland, D., et al. "Regional Rates of Neocortical Atrophy from normal Aging to Early Alzheimer Disease," *Neurology* 73, 457–465. 2009. doi:10.1212/wnl.0b013e3181b16431
- Milà-Alomà, M., Salvadó, G., Gispert, J. D., Vilor-Tejedor, N., Grau-Rivera, O., Sala-Vila, A., et al. "Amyloid Beta, Tau, Synaptic, Neurodegeneration, and Glial Biomarkers in the Preclinical Stage of the Alzheimer's Continuum," *Alzheimer's Dement.* 16, 1358–1371. 2020.
- Milhorat, T. H., Clark, R. G., Hammock, M. K., and McGrath, P. P. (1970). Structural, Ultrastructural, and Permeability Changes in the Ependyma and Surrounding Brain Favoring Equilibration in Progressive Hydrocephalus. *Arch. Neurol.* 22, 397–407. doi:10.1001/archneur.1970.00480230015002
- Oschwald, J., Guye, S., Liem, F., Rast, P., Willis, S., Röcke, C., et al. (2020). Brain Structure and Cognitive Ability in Healthy Aging: a Review on Longitudinal Correlated Change. *Rev. Neurosciences* 31, 1–57.
- Owby, R. L. (2010). Neuroinflammation and Cognitive Aging. *Curr. Psychiatry Rep.* 12, 39–45. doi:10.1007/s11920-009-0082-1
- Pagani, E., Agosta, F., Rocca, M. A., Caputo, D., and Filippi, M. (2008). Voxel-based Analysis Derived from Fractional Anisotropy Images of white Matter Volume Changes with Aging. *Neuroimage* 41, 657–667. doi:10.1016/j.neuroimage.2008.03.021
- Pantoni, L. (2002). Pathophysiology of Age-Related Cerebral white Matter Changes. *Cerebrovasc. Dis.* 13, 7–10. doi:10.1159/000049143
- Park, H., Yang, J. J., Seo, J., and Lee, J. M., and others., Dimensionality Reduced Cortical Features and Their Use in Predicting Longitudinal Changes in Alzheimer's Disease," *Neurosci. Lett.*, 550, 17, 22. 2013. doi:10.1016/j.neulet.2013.06.042
- Plocharski, M., Østergaard, L. R., and Initiative, A. D. N., and others., Extraction of Sulcal Medial Surface and Classification of Alzheimer's Disease Using Sulcal Features," *Comput. Methods Programs Biomed.* 133, 35–44. 2016. doi:10.1016/j.cmpb.2016.05.009
- Raj, A., LoCastro, E., Kuceyeski, A., Tosun, D., Relkin, N., Weiner, M., and Adni, A. D. N. I., and others., Network Diffusion Model of Progression Predicts Longitudinal Patterns of Atrophy and Metabolism in Alzheimer's Disease," *Cel. Rep.* 10, 359–369. 2015. doi:10.1016/j.celrep.2014.12.034
- Rasmussen, M. K., Mestre, H., and Nedergaard, M. (2018). The Glymphatic Pathway in Neurological Disorders. *Lancet Neurol.* 17, 1016–1024. doi:10.1016/s1474-4422(18)30318-1
- Raz, N., and Rodrigue, K. M. (2006). Differential Aging of the Brain: Patterns, Cognitive Correlates and Modifiers. *Neurosci. Biobehavioral Rev.* 30, 730–748. doi:10.1016/j.neubiorev.2006.07.001
- Reddy, P. H., and Beal, M. F. (2008). Amyloid Beta, Mitochondrial Dysfunction and Synaptic Damage: Implications for Cognitive Decline in Aging and Alzheimer's Disease. *Trends Molecular Medicine* 14, 45–53. doi:10.1016/j.molmed.2007.12.002
- Ritchie, K., Carrière, I., Berr, C., Amieva, H., Dartigues, J.-F., Ancelin, M.-L., et al. (2016). "The Clinical Picture of Alzheimer's Disease in the Decade before Diagnosis: Clinical and Biomarker Trajectories. *J. Clin. Psychiatry* 77, 305–311. doi:10.4088/jcp.15m09989
- Rodríguez-Arellano, J. J., Parpura, V., Zorec, R., and Verkhatsky, A. (2016). Astrocytes in Physiological Aging and Alzheimer's Disease. *Neuroscience* 323, 170–182. doi:10.1016/j.neuroscience.2015.01.007
- Rusinek, H., De Santi, S., Frid, D., Tsui, W.-H., Tarshish, C. Y., Convit, A., et al. (2003). Regional Brain Atrophy Rate Predicts Future Cognitive Decline: 6-year Longitudinal Mr Imaging Study of normal Aging. *Radiology* 229, 691–696. doi:10.1148/radiol.2293021299
- Salat, D., Greve, D., Pacheco, J., Quinn, B., Helmer, K., Buckner, R., et al. (2009). Regional white Matter Volume Differences in Nondemented Aging and Alzheimer's Disease. *Neuroimage* 44, 1247–1258. doi:10.1016/j.neuroimage.2008.10.030
- Scahill, R. I., Frost, C., Jenkins, R., Whitwell, J. L., Rossor, M. N., and Fox, N. C. (2003). A Longitudinal Study of Brain Volume Changes in normal Aging Using Serial Registered Magnetic Resonance Imaging. *Arch. Neurol.* 60, 989–994. doi:10.1001/archneur.60.7.989
- Schaer, M., Cuadra, M. B., Tamarit, L., Lazeyras, F., Eliez, S., and Thiran, J.-P. (2008). A Surface-Based Approach to Quantify Local Cortical Gyrfication. *IEEE Trans. Med. Imaging* 27, 161–170. doi:10.1109/tmi.2007.903576
- Schäfer, A., Weickenmeier, J., and Kuhl, E. (2019). The Interplay of Biochemical and Biomechanical Degeneration in Alzheimer's Disease. *Comput. Methods Appl. Mech. Eng.* 352, 369–388. doi:10.1016/j.cma.2019.04.028
- Sengoku, R. (2020). Aging and Alzheimer's Disease Pathology. *Neuropathology* 40, 22–29. doi:10.1111/neup.12626
- Serrano-Pozo, A., Frosch, M. P., Masliah, E., and Hyman, B. T. (2011). Neuropathological Alterations in Alzheimer Disease. *Cold Spring Harbor Perspect. Med.* 1, a006189. doi:10.1101/cshperspect.a006189
- Shen, X., Liu, T., Tao, D., Fan, Y., Zhang, J., Li, S., et al. "Variation in Longitudinal Trajectories of Cortical Sulci in normal Elderly," *Neuroimage* 166, 1–9. 2018.
- Storsve, A. B., Fjell, A. M., Tamnes, C. K., Westlye, L. T., Overbye, K., Aasland, H. W., et al. (2014). Differential Longitudinal Changes in Cortical Thickness, Surface Area and Volume across the Adult Life Span: Regions of Accelerating and Decelerating Change. *J. Neurosci.* 34, 8488–8498. doi:10.1523/jneurosci.0391-14.2014
- Suzuki, H., Venkataraman, A. V., Bai, W., Guitton, F., Guo, Y., Dehghan, A., et al. (2019). Associations of Regional Brain Structural Differences with Aging, Modifiable Risk Factors for Dementia, and Cognitive Performance. *JAMA Netw. Open* 2, e1917257. doi:10.1001/jamanetworkopen.2019.17257
- Thompson, P. M., Hayashi, K. M., De Zubicaray, G. I., Janke, A. L., Rose, S. E., Semple, J., et al. and others., "Mapping Hippocampal and Ventricular Change in Alzheimer Disease," *Neuroimage* 22, 1754–1766. 2004. doi:10.1016/j.neuroimage.2004.03.040
- Todd, K. L., Brighton, T., Norton, E. S., Schick, S., Elkins, W., Pletnikova, O., et al. and others., "Ventricular and Periventricular Anomalies in the Aging and Cognitively Impaired Brain," *Front. Aging Neurosci.* 9, pp. 445, 2018. doi:10.3389/fnagi.2017.00445
- Vernooij, M. W., de Groot, M., van der Lugt, A., Ikram, M. A., Krestin, G. P., Hofman, A., et al. (2008). White Matter Atrophy and Lesion Formation Explain the Loss of Structural Integrity of white Matter in Aging. *Neuroimage* 43, 470–477. doi:10.1016/j.neuroimage.2008.07.052
- Von Bernhardi, R., Eugenin-von Bernhardi, L., and Eugenin, J. (2015). Microglial Cell Dysregulation in Brain Aging and Neurodegeneration. *Front. Aging Neurosci.* 7, 124. doi:10.3389/fnagi.2015.00124

- Walhovd, K. B., Westlye, L. T., Amlien, I., Espeseth, T., Reinvang, I., Raz, N., et al. (2011/2011). Consistent Neuroanatomical Age-Related Volume Differences across Multiple Samples. *Neurobiol. Aging* 32, 916–932. doi:10.1016/j.neurobiolaging.2009.05.013
- Wang, Z., Martin, B., Weickenmeier, J., and Garikipati, K. (2021). “2, 100023. doi:10.1016/j.brain.2021.100023 An Inverse Modelling Study on the Local Volume Changes during Early Morphoelastic Growth of the Fetal Human Brain *Brain Multiphysics*
- Wardlaw, J. M., Benveniste, H., Benveniste, H., Nedergaard, M., Zlokovic, B. V., Mestre, H., et al. and others, “Perivascular Spaces in the Brain: Anatomy, Physiology and Pathology,” *Nat. Rev. Neurol.* 16, 137–153. 2020. doi:10.1038/s41582-020-0312-z
- Weickenmeier, J., de Rooij, R., Budday, S., Steinmann, P., Ovaert, T. C., and Kuhl, E. (2016). Brain Stiffness Increases with Myelin Content. *Acta Biomater.* 42, 265–272. doi:10.1016/j.actbio.2016.07.040
- Weickenmeier, J., Jucker, M., Goriely, A., and Kuhl, E. (2019). A Physics-Based Model Explains the Prion-like Features of Neurodegeneration in Alzheimer’s Disease, Parkinson’s Disease, and Amyotrophic Lateral Sclerosis. *J. Mech. Phys. Sol.* 124, 264–281. doi:10.1016/j.jmps.2018.10.013
- Weickenmeier, J., Kuhl, E., and Goriely, A. (2018). Multiphysics of Prionlike Diseases: Progression and Atrophy. *Phys. Rev. Lett.* 121, 158101. doi:10.1103/physrevlett.121.158101
- Xiong, Y. Y., and Mok, V. (2011). Age-related white Matter Changes. *J. Aging Res.* 2011, 617927. doi:10.4061/2011/617927

Conflict of Interest: The authors declare that the research was conducted in the absence of any commercial or financial relationships that could be construed as a potential conflict of interest.

Copyright © 2021 Blinkouskaya and Weickenmeier. This is an open-access article distributed under the terms of the Creative Commons Attribution License (CC BY). The use, distribution or reproduction in other forums is permitted, provided the original author(s) and the copyright owner(s) are credited and that the original publication in this journal is cited, in accordance with accepted academic practice. No use, distribution or reproduction is permitted which does not comply with these terms.



Poroviscoelastic Effects During Biomechanical Testing of Human Brain Tissue

Alexander Greiner¹, Nina Reiter¹, Friedrich Paulsen^{2,3}, Gerhard A. Holzapfel^{4,5}, Paul Steinmann^{1,6}, Ester Comellas^{7*} and Silvia Budday^{1*}

¹Department Mechanical Engineering, Institute of Applied Mechanics, Friedrich-Alexander-University Erlangen-Nürnberg, Erlangen, Germany, ²Institute of Functional and Clinical Anatomy, Friedrich-Alexander-University Erlangen-Nürnberg, Erlangen, Germany, ³Department of Operative Surgery and Topographic Anatomy, Sechenov University, Moscow, Russia, ⁴Institute of Biomechanics, Graz University of Technology, Graz, Austria, ⁵Department of Structural Engineering, Norwegian University of Science and Technology (NTNU), Trondheim, Norway, ⁶Glasgow Computational Engineering Centre, University of Glasgow, Glasgow, United Kingdom, ⁷Serra Hünter Fellow, Department of Physics, Laboratori de Càlcul Numèric (LaCàN), Universitat Politècnica de Catalunya (UPC), Barcelona, Spain

OPEN ACCESS

Edited by:

Hanxing Zhu,
Cardiff University, United Kingdom

Reviewed by:

Ralph Sinkus,
INSERM U1148 Laboratoire de
Recherche Vasculaire Translationnelle,
France
Alessio Gizzi,
Campus Bio-Medico University, Italy
Shan Tang,
Dalian University of Technology, China

*Correspondence:

Ester Comellas,
ester.comellas@upc.edu
Silvia Budday
silvia.budday@fau.de

Specialty section:

This article was submitted to
Biomechanical Engineering,
a section of the journal
Frontiers in Mechanical Engineering

Received: 11 May 2021

Accepted: 03 August 2021

Published: 17 August 2021

Citation:

Greiner A, Reiter N, Paulsen F,
Holzapfel GA, Steinmann P,
Comellas E and Budday S (2021)
Poroviscoelastic Effects During
Biomechanical Testing of Human
Brain Tissue.
Front. Mech. Eng 7:708350.
doi: 10.3389/fmech.2021.708350

Brain tissue is one of the softest tissues in the human body and the quantification of its mechanical properties has challenged scientists over the past decades. Associated experimental results in the literature have been contradictory as characterizing the mechanical response of brain tissue not only requires well-designed experimental setups that can record the ultrasoft response, but also appropriate approaches to analyze the corresponding data. Due to the extreme complexity of brain tissue behavior, nonlinear continuum mechanics has proven an expedient tool to analyze testing data and predict the mechanical response using a combination of hyper-, visco-, or poro-elastic models. Such models can not only allow for personalized predictions through finite element simulations, but also help to comprehensively understand the physical mechanisms underlying the tissue response. Here, we use a nonlinear poro-viscoelastic computational model to evaluate the effect of different intrinsic material properties (permeability, shear moduli, nonlinearity, viscosity) on the tissue response during different quasi-static biomechanical measurements, i.e., large-strain compression and tension as well as indentation experiments. We show that not only the permeability but also the properties of the viscoelastic solid largely control the fluid flow within and out of the sample. This reveals the close coupling between viscous and porous effects in brain tissue behavior. Strikingly, our simulations can explain why indentation experiments yield that white matter tissue in the human brain is stiffer than gray matter, while large-strain compression experiments show the opposite trend. These observations can be attributed to different experimental loading and boundary conditions as well as assumptions made during data analysis. The present study provides an important step to better understand experimental data previously published in the literature and can help to improve experimental setups and data analysis for biomechanical testing of brain tissue in the future.

Keywords: human brain, viscoelasticity, poroelasticity, constitutive modeling, mechanical properties, biomechanical testing, indentation, finite element analysis

1 INTRODUCTION

In recent years, it has increasingly been recognized that mechanical signals play an important role for brain development (Budday et al., 2015b; Koser et al., 2016; Thompson et al., 2019), injury (Meaney et al., 2014; Hemphill et al., 2015; Keating and Cullen, 2021), and disease (Murphy et al., 2016; Barnes et al., 2017; Gerischer et al., 2018; Park et al., 2018). In silico modeling based on the theory of nonlinear continuum mechanics has therefore proven a valuable tool to, on the one hand, computationally test hypotheses that complement experimental studies and provide a predictive understanding of processes in the brain under physiological and pathological conditions (Goriely et al., 2015; Budday et al., 2020). On the other hand, computational modeling can assist diagnosis and treatment of neurological disorders through personalized predictions (Angeli and Stylianopoulos, 2016; Lytton et al., 2017; Weickenmeier et al., 2017).

A major challenge when aiming to explore the role of brain mechanics in health and disease is reliably quantifying the mechanical properties of brain tissue. Brain tissue is ultrasoft—arguably softer than any other tissue in the human body—and deforms noticeably when it is taken out of its physiological environment within the skull, e.g., for *ex vivo* mechanical testing. In addition, it has an exceptionally high water content, 0.83 g/ml in gray matter and 0.71 g/ml in white matter (Whittall et al., 1997). From the total of about 80% water, approximately 20–40% is free-flowing cerebrospinal fluid, while the rest resides inside the cells. The extreme softness and biphasic nature of brain tissue pushes mechanical testing and modeling approaches to their limits. Early studies had therefore significantly overestimated the stiffness of brain tissue (Galford and McElhaney, 1970; Chatelin et al., 2010), but more recent studies indicate that the stiffness lies on the order of 1 kPa (Budday et al., 2020). Still, the exact values have varied notably depending on the testing setup (Chatelin et al., 2010; Budday et al., 2020). It is thus difficult to control specimen geometry, local deformation states, and their relation to the recorded forces (Rashid et al., 2012).

Partially, the observed discrepancies can be attributed to the fact that different testing techniques measure the properties on different length scales (cell, tissue, organ) and different time scales (quasistatic, dynamic). But even on a seemingly similar spatial and temporal resolution, experimental observations may differ, both qualitatively and quantitatively. For instance, gray matter shows a stiffer response than white matter during large-strain compression, tension, and shear experiments (Budday et al., 2017a), while one observes the opposite regional trends during tissue-scale indentation (Van Dommelen et al., 2010; Budday et al., 2015a). Here, we hypothesize that these observations may be attributed to different boundary and drainage conditions in combination with the biphasic, poro-viscoelastic nature of brain tissue (Franceschini et al., 2006; Comellas et al., 2020). Depending on the testing setup, the fluid is trapped within the tissue or free to escape, which may largely affect the recorded reaction forces. Therefore, realistic computational predictions

and the profound understanding of brain tissue behavior require sophisticated mechanical models that capture the complex and unique characteristics of this ultrasoft and biphasic tissue.

Several poroelastic models have been proposed to reproduce the biphasic nature of brain tissue, but with specific applications in mind, e.g., drug delivery (Ehlers and Wagner, 2015), hydrocephalus (Kim et al., 2015), tumor growth and treatment (Angeli and Stylianopoulos, 2016), decompressive craniotomy (Fletcher et al., 2016), or tissue fracture (Terzano et al., 2021). Early numerical studies that specifically focused on elucidating the mechanisms behind the observed mechanical properties of brain tissue studied its nonlinear ultrasoft viscous behavior without incorporating the biphasic nature of the tissue (Bilston et al., 2001; Prevost et al., 2011; Budday et al., 2017b,c).

Initial models incorporating both porous and viscous responses aimed at fitting a single experimental setup (Cheng and Bilston, 2007) or included important analytical simplifications and were tailored to particular applications related to cerebrospinal fluid circulation (Mehrabian and Abolesleiman, 2011; Hasan and Drapaca, 2015; Mehrabian et al., 2015). To our knowledge, the formulation proposed by our group (Comellas et al., 2020) and the model described by Hosseini-Farid et al. (2020) are the only approaches to date with the potential of capturing the wide range of characteristics observed in the response of brain tissue under different biomechanical loading scenarios.

In this study, we use a finite poro-viscoelastic model to evaluate the individual porous and viscous contributions in numerical simulations of quasi-static unconfined compression and tension as well as indentation experiments (with loading frequencies on the order of 0.01 Hz). Through systematic parameter studies, we identify parameter ranges that can explain the phenomenon observed when comparing the mechanical properties of gray and white matter brain tissue, where indentation yields the opposite regional trend than large-strain compression experiments. By exploring the effects of permeability, shear moduli, nonlinearity, and viscosity on the numerical response during the different experimental loading conditions, we discuss their individual physical meaning by closely considering the underlying poro-viscoelastic modeling framework.

2 MATERIALS AND METHODS

2.1 Human Brain Experiments

As a reference and to confirm the validity of seemingly contradictory results in the literature, we performed indentation and large-strain compression and tension experiments on exactly the same sample extracted from human gray and white matter tissue, respectively, as illustrated in **Figure 1**. Human brain tissue was extracted from a body donor (female, age 77) who had given her written consent to donate her body to research. The study was additionally approved by the Ethics Committee of Friedrich-Alexander-University Erlangen-Nürnberg, Germany, with the approval number 405_18 B.

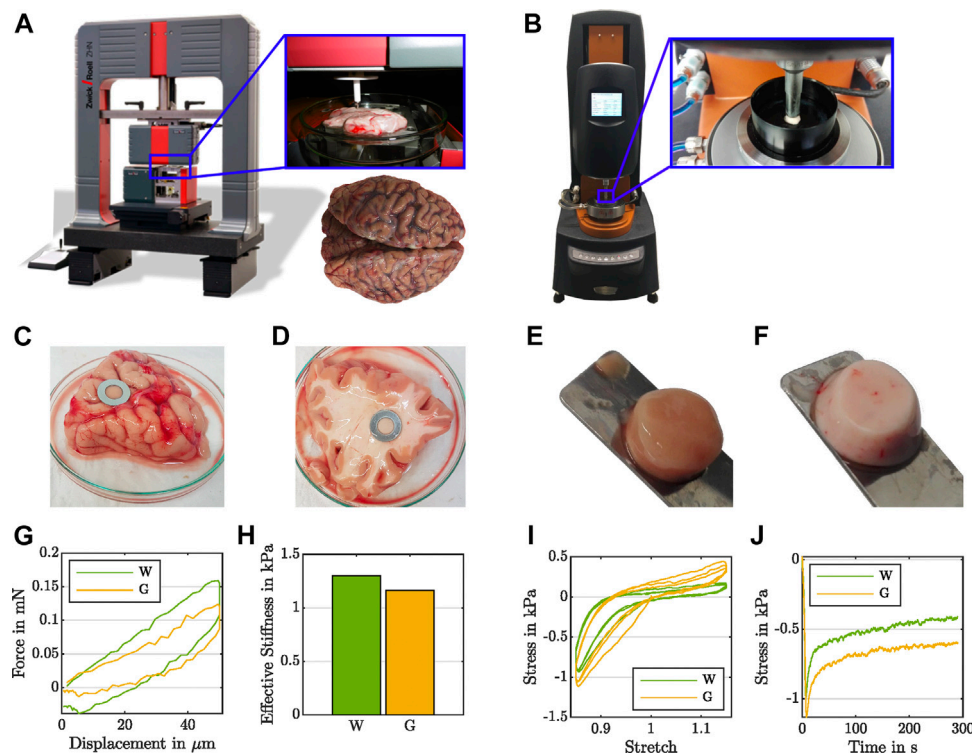


FIGURE 1 | Experimental evidence for the effect of the testing setup on the recorded regional mechanical response of human brain tissue. During indentation measurements (A), white matter (D) shows higher forces (G) and a higher effective modulus (H) than gray matter (C). During rheometer measurements (B) under large-strain cyclic compression and tension (I) as well as compression relaxation (J), white matter (F) yields lower stresses than gray matter (E).

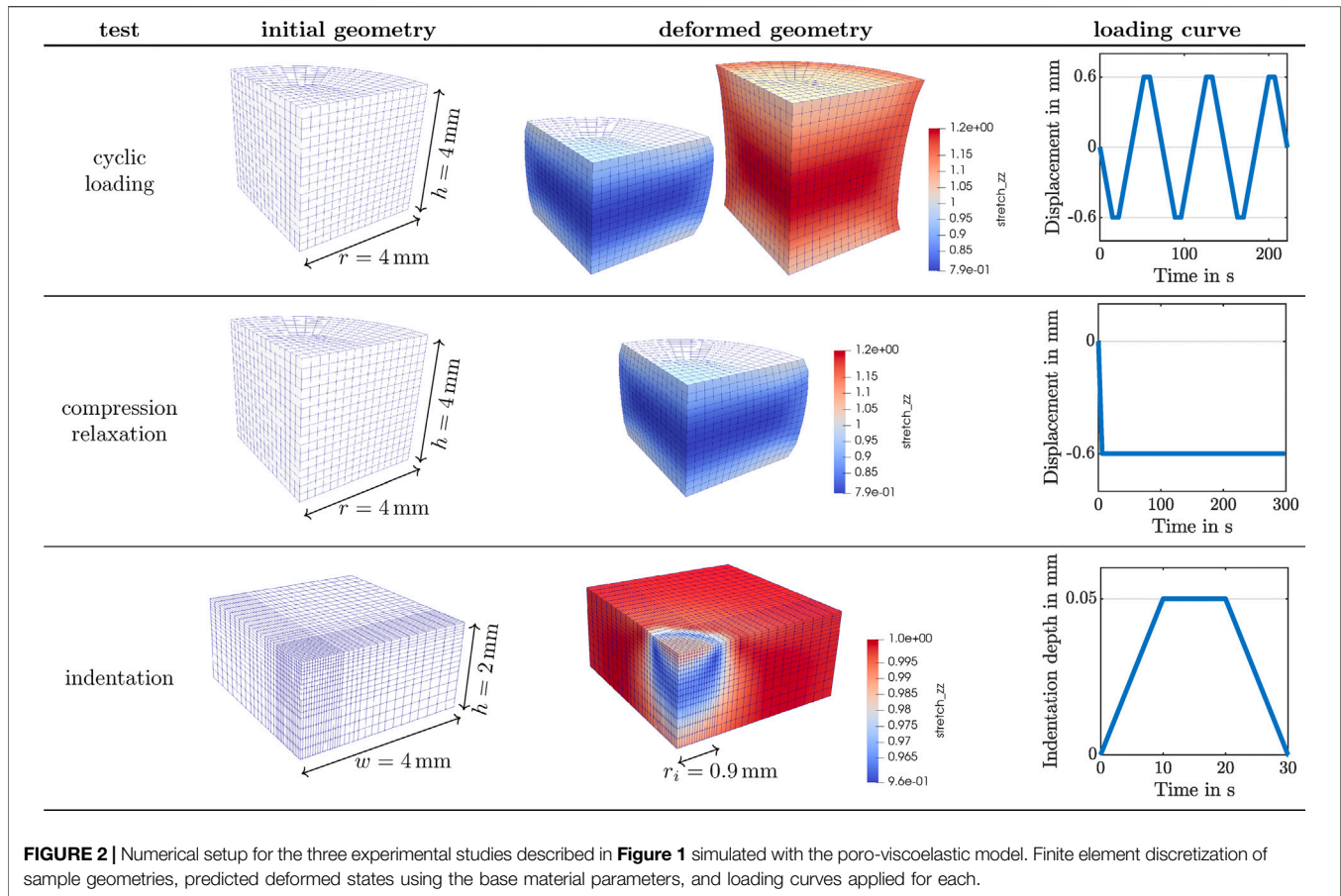
For indentation experiments, we used the ZHN-Nanoindenter by ZwickRoell GmbH and Co. KG (Ulm, Germany), as shown in **Figure 1A**, and closely followed the indentation procedure established in Budday et al. (2015a). We prepared tissue slices in a 120 mm-diameter Petri dish and stabilized the samples using a 10 mm-diameter stainless steel washer (see **Figures 1C,D**). To ensure a homogeneous specimen response, we used a circular flat punch indenter with a diameter of 1.8 mm and a ceramic shaft extension. We conducted all indentation tests at room temperature under displacement control using a trapezoidal loading-holding-unloading profile with a maximum indentation depth of $50 \mu\text{m}$, as illustrated in **Figure 2**, bottom right, and recorded the corresponding force (see **Figure 1G**).

For compression and tension experiments, we extracted cylindrical samples with a radius of $r = 4 \text{ mm}$ (see **Figures 1E,F**) and used a Discovery HR-3 rheometer from TA instruments (New Castle, Delaware, United States), as shown in **Figure 1B**. We fixed the specimens to the upper and lower specimen holder using sandpaper and superglue. After a waiting period of 30–60 s to let the glue dry, we immersed the specimen in PBS to keep it hydrated during the experiment. We conducted all rheometer tests at 37°C . We note that previous studies have indicated that the mechanical response of brain tissue is not significantly affected by temperature in the range between 22°C

and 37°C (Rashid et al., 2012). We first applied three cycles of compression and tension with a loading velocity of $40 \mu\text{m/s}$, and minimum and maximum overall vertical stretches of $\lambda = [h + \Delta z]/h = 0.85$ and $\lambda = 1.15$, where h denotes the initial specimen height and Δz the displacement in the direction of loading (see **Figure 1I**). Subsequently, we performed a compression relaxation test at $\lambda = 0.85$ with a loading velocity of $100 \mu\text{m/s}$ and a holding period of 300 s (see **Figure 1J**). We recorded the corresponding force f_z and determined the nominal stress as $P_{\text{exp}} = f_z/A$, where $A = \pi r^2$ is the undeformed cross-sectional area of the specimen. For more details on the testing procedure, we refer to Linka et al. (2021).

2.2 Nonlinear Poro-Viscoelastic Model

We model brain tissue as a poro-viscoelastic material where the viscoelastic solid represents the network of cells embedded within the extracellular matrix (ECM) and the free-flowing pore fluid is the interstitial fluid bathing the ECM. We use the numerical framework based on the Theory of Porous Media presented in our previous work (Comellas et al., 2020). In this section we summarize the main characteristics of the formulation, which assumes a fully-saturated compressible biphasic material, and that the solid and fluid constituents are separately incompressible. A detailed description of the derivation of all equations presented here can be found in Comellas et al. (2020) and its supplementary material.



2.2.1 Continuum Kinematics

Following the Theory of Porous Media, the same spatial position \mathbf{x} in the current configuration at a given time t is occupied simultaneously by the solid and fluid components. However, the material particles of each component originate from different reference positions at time t_0 . Then, the constituent deformation map is $\mathbf{x} = \chi_S(\mathbf{X}_S, t) = \chi_F(\mathbf{X}_F, t)$, where \mathbf{X}_S and \mathbf{X}_F indicate the reference position of the solid and fluid components, respectively. The displacement of the solid component is, thus,

$$\mathbf{u}_S = \mathbf{x} - \mathbf{X}_S, \quad (1)$$

and

$$\mathbf{F}_S = \partial \mathbf{x} / \partial \mathbf{X}_S \quad (2)$$

is its material deformation gradient.

2.2.2 Governing Equations

The weak form of the governing equations in the reference configuration is

$$\int_{B_0} \nabla(\delta \mathbf{u}) : \boldsymbol{\tau} dV_{0S} = 0 \quad \forall \delta \mathbf{u}, \quad \text{and} \quad (3)$$

$$\int_{B_0} \delta p \dot{J}_S dV_{0S} - \int_{B_0} \nabla(\delta p) \cdot \mathbf{w} J_S dV_{0S} = 0 \quad \forall \delta p. \quad (4)$$

The linear momentum balance **Eq. 3** introduces the viscoelastic solid displacement test function $\delta \mathbf{u}$ while the mass balance **Eq. 4** introduces the fluid pore pressure test function δp . Both equations are defined in the reference configuration B_0 of the biphasic material, where dV_{0S} refers to the volume element of the material in the reference configuration of the solid. The Kirchhoff stress tensor $\boldsymbol{\tau}$ is given by the constitutive equation of the solid component while the constitutive equation of the fluid provides the volume-weighted seepage velocity \mathbf{w} . The Jacobian J_S is the determinant of the material deformation gradient of the solid component $J_S = \det(\mathbf{F}_S) > 0$, and \dot{J}_S indicates its material time derivative. We neglect volumetric forces due to the effect of gravity and do not prescribe any external traction vector in **Eq. 3**. Forced fluid flow across the boundaries in **Eq. 4** is not prescribed either. Note that the time dependencies of the mass balance equation result in a nonstationary nature of the governing equations, even though they are formulated in a quasi-static framework.

2.2.3 Constitutive Equations

The deformation gradient of the solid component is split multiplicatively into elastic and viscous parts, $\mathbf{F}_S = \mathbf{F}_S^e \cdot \mathbf{F}_S^v$, such that the “extra” part of the stress tensor is the sum of the equilibrium (eq) part, the non-equilibrium (neq) part, and a volumetric (vol) contribution,

$$\boldsymbol{\tau} = \boldsymbol{\tau}_E^S - pJ_S \mathbf{I} = \boldsymbol{\tau}_E^{\text{eq}} + \boldsymbol{\tau}_E^{\text{neq}} + \boldsymbol{\tau}_E^{\text{vol}} - pJ_S \mathbf{I}. \quad (5)$$

Based on previous studies (Budday et al., 2017a, Budday et al., 2020), we select a one-term Ogden material model for both the equilibrium and non-equilibrium parts. Then,

$$\begin{aligned} \boldsymbol{\tau}_E^{\text{eq}} &= \sum_{A=1}^3 \beta_{\infty,A} \mathbf{n}_{S,A} \otimes \mathbf{n}_{S,A} \quad \text{with} \quad \beta_{\infty,A} \\ &= \mu_{\infty} \left[\tilde{\lambda}_{S,A}^{\alpha_{\infty}} - \frac{1}{3} [\tilde{\lambda}_{S,1}^{\alpha_{\infty}} + \tilde{\lambda}_{S,2}^{\alpha_{\infty}} + \tilde{\lambda}_{S,3}^{\alpha_{\infty}}] \right], \end{aligned} \quad (6)$$

where α_{∞} and μ_{∞} are the equilibrium Ogden shear and nonlinearity parameters, $\tilde{\lambda}_{S,a}$ for $a \in \{1, 2, 3\}$ are the isochoric principal stretches, and $\mathbf{n}_{S,A}$ are the eigenvectors of the left Cauchy-Green tensor $\mathbf{b}_S = \mathbf{F}_S \cdot \mathbf{F}_S^T$, such that $\mathbf{b}_S = \sum_{A=1}^3 \lambda_{S,A}^2 \mathbf{n}_{S,A} \otimes \mathbf{n}_{S,A}$. Note that the Ogden shear parameter μ_{∞} is related to the classical shear modulus, known from the linear theory, through $\mu_{\infty}^0 = \frac{1}{2} \mu_{\infty} \alpha_{\infty}$.

The non-equilibrium counterpart is

$$\begin{aligned} \boldsymbol{\tau}_E^{\text{neq}} &= \sum_{A=1}^3 \beta_{1,A} \mathbf{n}_{S,A}^e \otimes \mathbf{n}_{S,A}^e \quad \text{with} \quad \beta_{1,A} \\ &= \mu_1 \left[(\tilde{\lambda}_{S,A}^e)^{\alpha_1} - \frac{1}{3} [(\tilde{\lambda}_{S,1}^e)^{\alpha_1} + (\tilde{\lambda}_{S,2}^e)^{\alpha_1} + (\tilde{\lambda}_{S,3}^e)^{\alpha_1}] \right], \end{aligned} \quad (7)$$

where α_1 and μ_1 are the non-equilibrium Ogden shear and nonlinearity constitutive parameters, which again are related to the corresponding classical shear modulus through $\mu_1^0 = \frac{1}{2} \mu_1 \alpha_1$. The terms $\tilde{\lambda}_{S,a}^e$ for $a \in \{1, 2, 3\}$ are the isochoric elastic principal stretches, and $\mathbf{n}_{S,A}^e$ are the eigenvectors of the elastic part of the left Cauchy-Green tensor $\mathbf{b}_S^e = \mathbf{F}_S^e \cdot (\mathbf{F}_S^e)^T$, such that $\mathbf{b}_S^e = \sum_{A=1}^3 [\lambda_{S,A}^e]^2 \mathbf{n}_{S,A}^e \otimes \mathbf{n}_{S,A}^e$.

An evolution equation is required to complete the definition of the viscous solid behavior. To this aim, we introduce

$$-\mathcal{L}_v \mathbf{b}_S^e \cdot (\mathbf{b}_S^e)^{-1} = \frac{1}{\eta} \boldsymbol{\tau}^{\text{neq}}, \quad (8)$$

which assumes isotropy and introduces the viscosity of the solid component, η , such that we *a priori* satisfy a non-negative viscous dissipation term, i.e.,

$$\mathcal{D}_v = \frac{1}{2\eta} \boldsymbol{\tau}^{\text{neq}} : \boldsymbol{\tau}^{\text{neq}} \geq 0 \quad \text{for} \quad \eta > 0. \quad (9)$$

The viscous dissipation density rate \mathcal{D}_v derives from the Clausius–Duhem inequality and represents the dissipation due to internal processes occurring within the viscous solid component.

Finally, the definition of the solid stress tensor 5) is completed with the volumetric contribution,

$$\boldsymbol{\tau}_E^{\text{vol}} = \lambda^* [1 - n_{0S}^S]^2 \left[\frac{J_S}{1 - n_{0S}^S} - \frac{J_S}{J_S - n_{0S}^S} \right] \mathbf{I}, \quad (10)$$

where λ^* is the first Lamé parameter of the solid component and n_{0S}^S is the volume fraction of the solid component with respect to the solid reference configuration at the initial time. The term $\boldsymbol{\tau}_E^{\text{vol}}$ accounts for the compressibility effects of the deforming biphasic material. It ensures the correct modeling of the compaction point,

which occurs when all pores are closed such that no fluid remains in the material. Further volume deformations are not possible at this point due to the incompressibility constraint of the solid component (Ehlers and Eipper, 1999).

The constitutive behavior of the fluid component follows a Darcy-like law,

$$\mathbf{w} = -\frac{1}{\mu^{\text{FR}}} \left[\frac{J_S - n_{0S}^S}{1 - n_{0S}^S} \right] \mathbf{K}_0^S \cdot \nabla p, \quad (11)$$

where μ^{FR} is the effective shear viscosity of the pore fluid and \mathbf{K}_0^S is the initial intrinsic permeability tensor, which is assumed to be isotropic, i.e., $\mathbf{K}_0^S = K_0 \mathbf{I}$. Here, we have neglected the effect of gravity on the fluid behavior.

Like its counterpart \mathcal{D}_v in Eq. 9, the porous dissipation rate density derives from the Clausius–Duhem inequality and represents the dissipation due to the seepage process related to the material porosity. It is defined as

$$\mathcal{D}_p = \mu^{\text{FR}} \left[\frac{1 - n_{0S}^S}{J_S - n_{0S}^S} (K_0 \mathbf{I})^{-1} \cdot \mathbf{w} \right] \cdot \mathbf{w} \geq 0, \quad (12)$$

which will always be non-negative, given that μ^{FR} and K_0 are necessarily positive and $n_{0S}^S \in (0, 1)$.

2.2.4 Finite Element Implementation

We implemented the discretized governing equations using the open source finite element library *deal.ii* (Arndt et al., 2020). A detailed derivation of the constitutive equations and dissipation terms as well as the discretization and numerical implementation details are available in Comellas et al. (2020) and its associated supplementary material.

2.2.5 Numerical Setup

We investigate the behavior of the poro-viscoelastic formulation for three distinct loading scenarios corresponding to the experimental studies in Section 2.1: 1) cyclic compression-tension (see Figure 1I) and 2) compression relaxation (see Figure 1J) of a cylindrical specimen (see Figures 1E,F) using a rheometer (see Figure 1B) as well as 3) indentation with a flat punch (see Figures 1A,C,D,G,H). Figure 2 summarizes the numerical setup for the three test cases. A quarter of the cylindrical specimen is spatially discretized with 384 full integration Q2P1 elements for the cyclic loading and compression relaxation studies. That is, we approximate the solid displacement with quadratic shape functions and the pore pressure with linear ones. A quadrature of order 3 is considered. The degrees of freedom at the bottom of the geometry are fixed in space, while the vertical displacement shown in the right-most column is prescribed to the top surface. Symmetry boundary conditions are applied to the flat lateral surfaces. Solely the cylinder hull is drained, i.e. fluid can only leave the solid through the curved lateral surface. The deformed geometry depicts the local vertical stretch distribution on the fully compressed and extended states of the specimen for the cyclic loading, and the fully compressed state for the compression relaxation test. These states correspond to a

TABLE 1 | Poro-viscoelastic material parameters used in the simulations described in **Figure 2**.

Parameter	Value
Solid component	
n_{0S}^S	0.75
λ^*	1 MPa
μ_{∞}^0	{0.12, 0.32, 0.84} kPa
μ_1^0	{1.2, 3.2, 8.4} kPa
α	{-5, -8, -13}
η	{14, 28, 56} kPa-s
Fluid component	
μ^{FR}	0.89 Pa-s
K_0	{ 10^{-8} , 10^{-10} , 10^{-12} } mm ²

15% overall vertical strain. The spatial discretization to simulate the indentation experiments is composed of 2048 full integration Q2P1 elements. Again, in order to save computational effort, the computations are carried out only on one quarter of the real geometry. The finite element mesh is refined towards the center of the sample to approximate the flat punch indentation as accurately as possible, while maintaining a feasible computational cost. The bottom of the geometry is fixed in space and a vertical load shown in the bottom right of **Figure 2** is applied to the degrees of freedom within the radius of the flat punch. Symmetry boundary conditions are applied to the inner lateral surfaces. All surfaces are undrained, except the unloaded part of the top surface, which is drained.

The material parameters used are given in **Table 1**. The initial solid volume fraction is set to 0.75. The first Lamé parameter λ^* is fixed to a value large enough that the quasi-incompressibility of the solid component is correctly enforced. The effective shear fluid viscosity of the free-flowing fluid in the brain tissue is assumed to be that of water at room temperature. Based on our previous findings (Budday and Steinmann, 2018; Budday et al., 2020), the same nonlinearity Ogden parameter is used for the equilibrium and non-equilibrium parts $\alpha = \alpha_{\infty} = \alpha_1$. Throughout our simulations, we vary the equilibrium shear modulus μ_{∞}^0 , the non-equilibrium shear modulus μ_1^0 , the nonlinearity Ogden parameter α , the solid viscosity η and the initial intrinsic permeability K_0 . The ranges considered are given in **Table 1**.

The numerical implementations of the three new experimental setups in the original code available from the `deal.ii` code gallery website and an exemplary input file for each type are provided in Supplementary Material.

2.3 Data Analysis

We derive a series of useful quantities based on the experiments and our finite element results with the aim of analyzing the effect of different material parameters on computational measures with a direct experimental counterpart or numerical quantities that have a recognizable physical meaning.

The total reaction force on the loaded surfaces is computed at each integration point of the element faces of the loaded boundary $\partial B_{0,l}$, given in the reference configuration, from

$$\mathbf{r} = \int_{\partial B_{0,l}} \boldsymbol{\sigma} \cdot \mathbf{N} \, dA_{0S}. \quad (13)$$

Here, $\boldsymbol{\sigma} = \boldsymbol{\tau}/J_S$ is the total Cauchy stress and \mathbf{N} is the outward unit vector of the loaded surface with area element dA_{0S} , which is defined in the reference configuration of the solid component. Based on the definition of the Kirchhoff stress (5), the reaction force can also be split into a solid and a fluid contribution,

$$\mathbf{r}_S = \int_{\partial B_{0,l}} \boldsymbol{\sigma}_E \cdot \mathbf{N} \, dA_{0S} \quad \text{and} \quad \mathbf{r}_F = \int_{\partial B_{0,l}} -p \mathbf{N} \, dA_{0S}. \quad (14)$$

For the cyclic loading and compression relaxation tests, we calculate the total, solid, and fluid contributions to the nominal stresses as the vertical component of the corresponding reaction force divided by the original cross-section of the sample. The total reaction force and total nominal stress are measures that are comparable to those typically obtained in experimental setups, as shown in **Figure 1**. Our modeling approach allows us to break them into solid and fluid contributions, and, in this way, explore how they respond to different loading scenarios and material parameters.

We compute numerically the values of the viscous and porous total dissipation rates in the whole sample at each time step from the corresponding dissipation density rates defined in **Eq. 9** and **Eq. 12**, respectively. In particular,

$$\mathcal{D}_i^{\text{total}} = \int_{B_0} \mathcal{D}_i \, dV_{0S}, \quad (15)$$

where $i = \{p, v\}$ for the porous and viscous contributions, respectively. Here, B_0 refers to the domain of the biphasic material in the reference configuration and dV_{0S} is the volume element of the material in the reference configuration of the solid component. To obtain the accumulated dissipation over time, we determine the product $\mathcal{D}_i^{\text{total}} \Delta t$ at each time step, and sum over time. These dissipation terms are a measure of the porous and viscous contributions to the overall deformation process simulated in our numerical examples.

The solid volume of the sample is numerically computed as

$$V_S = \int_{B_0} n_{0S}^S J_S \, dV_{0S}, \quad (16)$$

where the term $n_{0S}^S J_S$ is known as the (current) solid volume fraction n_S at a given integration point. As in the previous equation, both B_0 and dV_{0S} correspond to the reference configuration. Ideally, the total solid volume should be constant due to the incompressibility assumption, but we compute it as a means of measuring how well the incompressibility has been enforced in our simulations.

Similarly to the reaction forces, the fluid flow across the drained boundaries $\partial B_{0,d}$, given in the reference configuration, is computed as

$$Q = \int_{\partial B_{0,d}} \mathbf{w} \cdot \mathbf{N} \, dA_{0S}. \quad (17)$$

Here, \mathbf{w} is the volume-weighted seepage velocity as defined in **Eq. 11** and \mathbf{N} is the outward unit vector of the drained surface

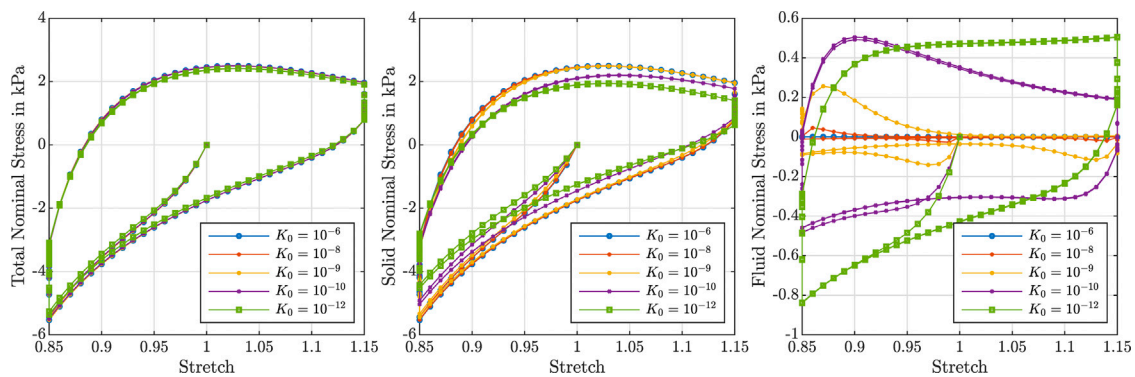


FIGURE 3 | Cyclic compression–tension test up to 15% strain. Total nominal stress (left), solid nominal stress (middle) and fluid nominal stress (right) versus overall stretch for $\mu_{\infty}^0 = 0.32$ kPa, $\mu_i^0 = 8.4$ kPa, $\alpha = -8$, $\eta = 14$ kPa · s and different initial intrinsic permeabilities $K_0 = \{10^{-6}, 10^{-8}, 10^{-9}, 10^{-10}, 10^{-12}\}$ mm².

with area element dA_{0S} , which is defined in the reference configuration of the solid component. The fluid flow predicted in our simulations provides additional insights into the porous behavior of the material and can potentially be related to experimental measures, e.g., fluid collected after confined compression of a sample.

Finally, following the procedure described in Budday et al. (2015a), we compute the effective modulus for the indentation simulations as

$$E_{\text{eff}} = \frac{3}{4} \frac{k}{2r_i} \quad (18)$$

from the contact stiffness k and the punch radius r_i . The contact stiffness k is defined as the average slope of the upper 50% of the reaction force curve during loading, as commonly used for the analysis of indentation experiments (Oliver and Pharr, 2004; Gupta et al., 2007; Budday et al., 2015a).

3 RESULTS

To evaluate the influence of different material properties on the response of human brain tissue during different quasi-static biomechanical experiments, we perform parameter studies in the following and systematically vary the intrinsic permeability, equilibrium and non-equilibrium shear moduli, nonlinearity, and viscosity. We simulate the tissue behavior during cyclic compression–tension experiments, stress relaxation in compression, and indentation measurements, and analyze the corresponding behavior. The parameter ranges are chosen to represent different brain regions, e.g., cortex and corona radiata, with the aim to explain the contradictory results between large-strain compression and indentation experiments illustrated in Figure 1 based on the complex poro-viscoelastic model introduced in Section 2.2 with the setup-dependent boundary conditions introduced in Section 2.2.5.

3.1 The Effect of the Intrinsic Permeability

Figure 3 illustrates the effect of varying initial intrinsic permeabilities K_0 on the response during cyclic compression–tension experiments. The total nominal stress is

plotted on the left, the solid contribution in the middle and the fluid contribution on the right. While the total stress is only marginally affected by the intrinsic permeability, the individual contributions of the solid and fluid component change significantly. The solid nominal stress decreases with decreasing permeabilities, while the fluid nominal stress increases: A lower permeability results in a higher fluid contribution to the total nominal stress. For intrinsic permeabilities of $K_0 \geq 10^{-6}$ mm², the contribution of the fluid is negligible, while it makes up about one sixth of the total nominal stress under compressive loading and about one fourth under tensile loading for smaller permeabilities.

Depending on the intrinsic permeability, the stress–stretch curves for the fluid nominal stress change notably. This can be directly related to the fluid’s ability to move through the solid faster or slower, which may generate inertial-like effects due to a delayed response or resistance to change of the fluid flow. For high permeabilities, the fluid moves easily through the solid structure such that, after overcoming inertia effects when the loading rate or direction changes, the fluid stress decreases rapidly. In contrast, for low permeabilities, the fluid moves slower through the solid experiencing more resistance. For the case with the smallest permeability, the fluid stress increases throughout the entire loading time before a delayed response to the change of loading direction takes place, resulting in stress–stretch curves more similar to the viscous solid itself.

Figure 4 shows the accumulated viscous dissipation over the set of three cycles on the left, the accumulated porous dissipation in the middle and the volume change of the solid component on the right. For the present choice of parameters, the viscous dissipation is distinctly larger than the porous dissipation. In addition, changing the intrinsic permeability barely influences the viscous dissipation. Interestingly, for the porous dissipation, we observe a maximum for an intrinsic permeability of $K_0 = 10^{-10}$ mm². This effect is associated with Eq. 12, which indicates that a decreasing initial intrinsic permeability leads to an increase in the porous dissipation but also a decrease in the volume-weighted seepage velocity w , which results in the observed maximum.

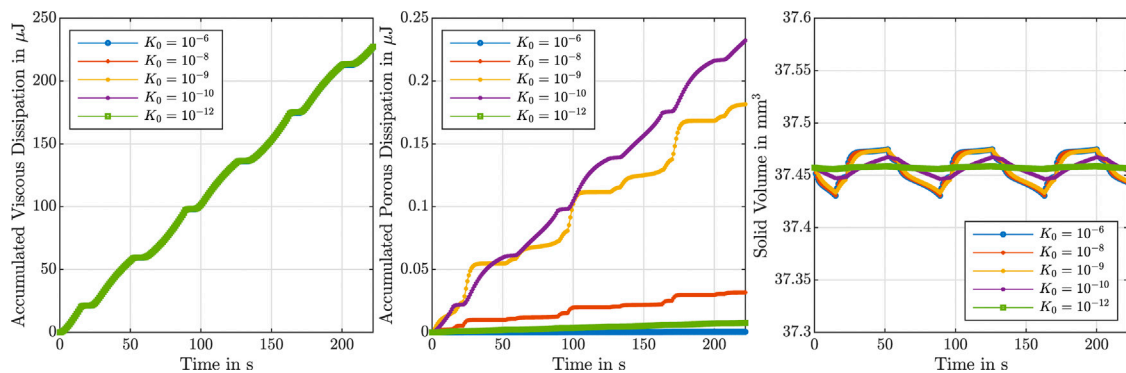


FIGURE 4 | Cyclic compression–tension test up to 15% strain. Accumulated viscous dissipation (**left**), accumulated porous dissipation (**middle**) and solid volume (**right**) over time for $\mu_{\infty}^0 = 0.32$ kPa, $\mu_1^0 = 8.4$ kPa, $\alpha = -8$, $\eta = 14$ kPa · s and different initial intrinsic permeabilities $K_0 = \{10^{-6}, 10^{-8}, 10^{-9}, 10^{-10}, 10^{-12}\}$ mm².

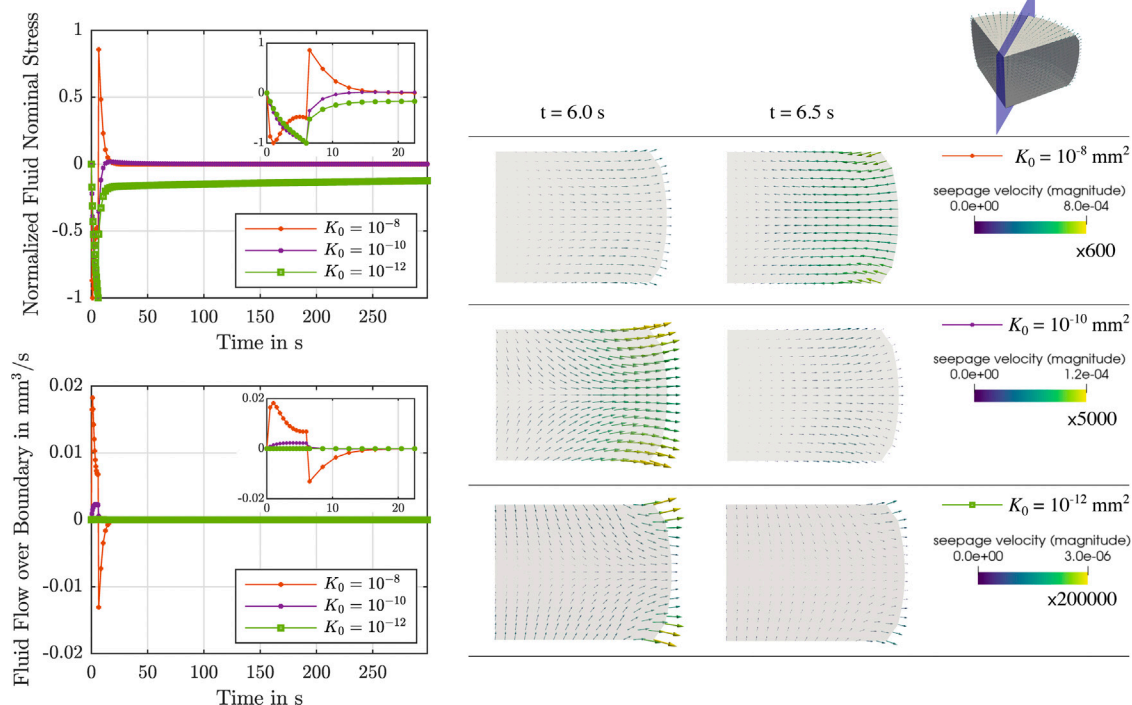


FIGURE 5 | Compression relaxation test up to 15% strain. Left: Normalized fluid nominal stress (**top left**) and fluid flow over the boundary (**bottom left**) over time for $\mu_{\infty}^0 = 0.32$ kPa, $\mu_1^0 = 8.4$ kPa, $\alpha = -8$, $\eta = 14$ kPa · s and different initial intrinsic permeabilities $K_0 = \{10^{-8}, 10^{-10}, 10^{-12}\}$ mm². Right: Corresponding finite element results of the seepage velocity at the end of loading ($t = 6$ s) and for the subsequent time step ($t = 6.5$ s). The depicted arrows on the selected vertical plane of the sample are sized proportional to the magnitude of the seepage velocity, given in mm/s, scaled by the factor indicated below each colorbar legend. Corresponding videos with the full simulation results are available in Supplementary Material.

The slight variations in the solid volume in **Figure 4**, right, show that the intrinsic permeability affects how strictly the incompressibility is enforced. As the formulation has a volumetric stress defined in terms of the first Lamé parameter λ^* (see **Eq. 10**), we have selected a constant λ^* instead of a constant Poisson's ratio ν in our parameter study. Enforcing a constant ν when exploring variations of the shear modulus and

nonlinearity parameter in the Ogden model would result in different λ^* values for each combination of parameters, given that $\lambda^* = 2\mu^0\nu/(1-2\nu)$, where μ^0 is the classical shear modulus. By selecting a constant λ^* , we ensure that the volumetric part of the stress is independent of these parameters and, hence, avoid unwanted interference in the sensitivity study. In addition, initial attempts to explore the effect of the Poisson's ratio on

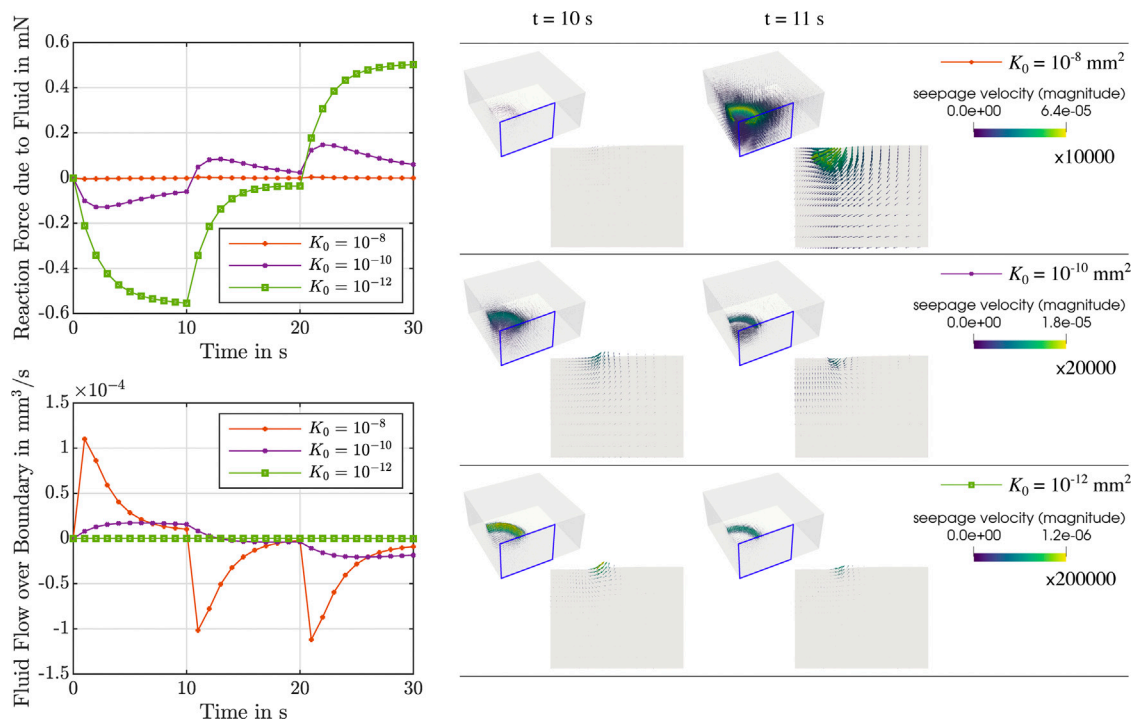


FIGURE 6 | Indentation test with an indentation depth of 50 μm . Left: Reaction force due to the fluid (**top left**) and fluid flow over the boundary (**bottom left**) over time for $\mu_\infty = 0.32$ kPa, $\mu_1 = 8.4$ kPa, $\alpha = -8$, $\eta = 14$ kPa \cdot s and different initial intrinsic permeabilities $K_0 = \{10^{-8}, 10^{-10}, 10^{-12}\}$ mm². Right: Corresponding finite element results of the seepage velocity at the end of loading ($t = 10$ s) and for the subsequent time step ($t = 11$ s). Results are shown for the whole sample and for the indicated vertical cross-section. The depicted arrows are sized proportional to the magnitude of the seepage velocity, given in mm/s, scaled by the factor indicated below each colorbar legend. Corresponding videos with the full simulation results on the vertical cross-section are available in Supplementary Material.

the predicted material response resulted in numerical instabilities around peak loading times for the compression relaxation tests, even with values above 0.49. In these simulations we converted the Poisson's ratio to λ^* using the equilibrium shear modulus, i.e., with $\mu^0 = \frac{1}{2}\mu_\infty\alpha$. Upon closer inspection we realized that the sum of the equilibrium and non-equilibrium shear moduli should be used instead, $\mu^0 = \frac{1}{2}(\mu_\infty + \mu_1)\alpha$, to avoid the instabilities. We realized conversion from ν to λ^* is not straightforward for the viscoelastic case, supporting our decision of selecting a constant λ^* to remove any unsought effect of changes in the parameter used to enforce the quasi-incompressibility. Yet, even with a constant λ^* , we note that a lower permeability results in a better quasi-incompressibility of the solid component. This could be attributed to the fact that a lower permeability results in more fluid “trapped” in the pores of the biphasic material, which then exerts a larger hydrostatic pressure on the solid component.

During stress relaxation and indentation experiments, trends in fluid flow over the boundary can directly be tied to the behavior over time of the fluid nominal stresses, as illustrated in **Figures 5, 6**. For high permeabilities, we observe that the fluid stresses adopt positive values as soon as the loading rate is zero (holding period). This can be attributed to the fact that fluid immediately starts to flow back into the sample. For lower permeabilities, in contrast, fluid continues to flow out, but at smaller rates. Therefore, we suppose that there is a longer period of inertial-like effects. It is interesting to note that we may observe a negative fluid flow over

the boundary, i.e., overall fluid is entering the sample, but locally have fluid flowing outwards. This can, for instance, be seen during indentation experiments in **Supplementary Figure S1**. Another interesting effect we observe is that when the biphasic material deforms and occupies new volume in space, it can potentially incorporate new fluid. This occurs when the loading inertia forcing fluid outwards is negligible or does not offer enough resistance to the potential inward flow. In summary, as the sample is immersed in fluid during the experiments to avoid dehydration, small and slow displacements may result in fluid flow into the sample across drained boundaries.

In the sequel, we will evaluate the effects of the equilibrium and non-equilibrium shear moduli, nonlinearity, and viscosity on the tissue response for different initial intrinsic permeabilities $K_0 = \{10^{-8}, 10^{-10}, 10^{-12}\}$ mm².

3.2 The Effect of the Shear Modulus

Figure 7, first column, shows the effect of varying shear moduli μ_∞^0 and intrinsic permeabilities K_0 on the maximum overall nominal stress with individual solid and fluid contributions during cyclic compression (A1) and tension (A2), the corresponding accumulated viscous (A3) and porous (A4) dissipation, the maximum stress during stress relaxation (A5), and the effective modulus during indentation experiments (A6). Under compressive loading, the maximum overall nominal stress increases for increasing shear modulus and also increases slightly

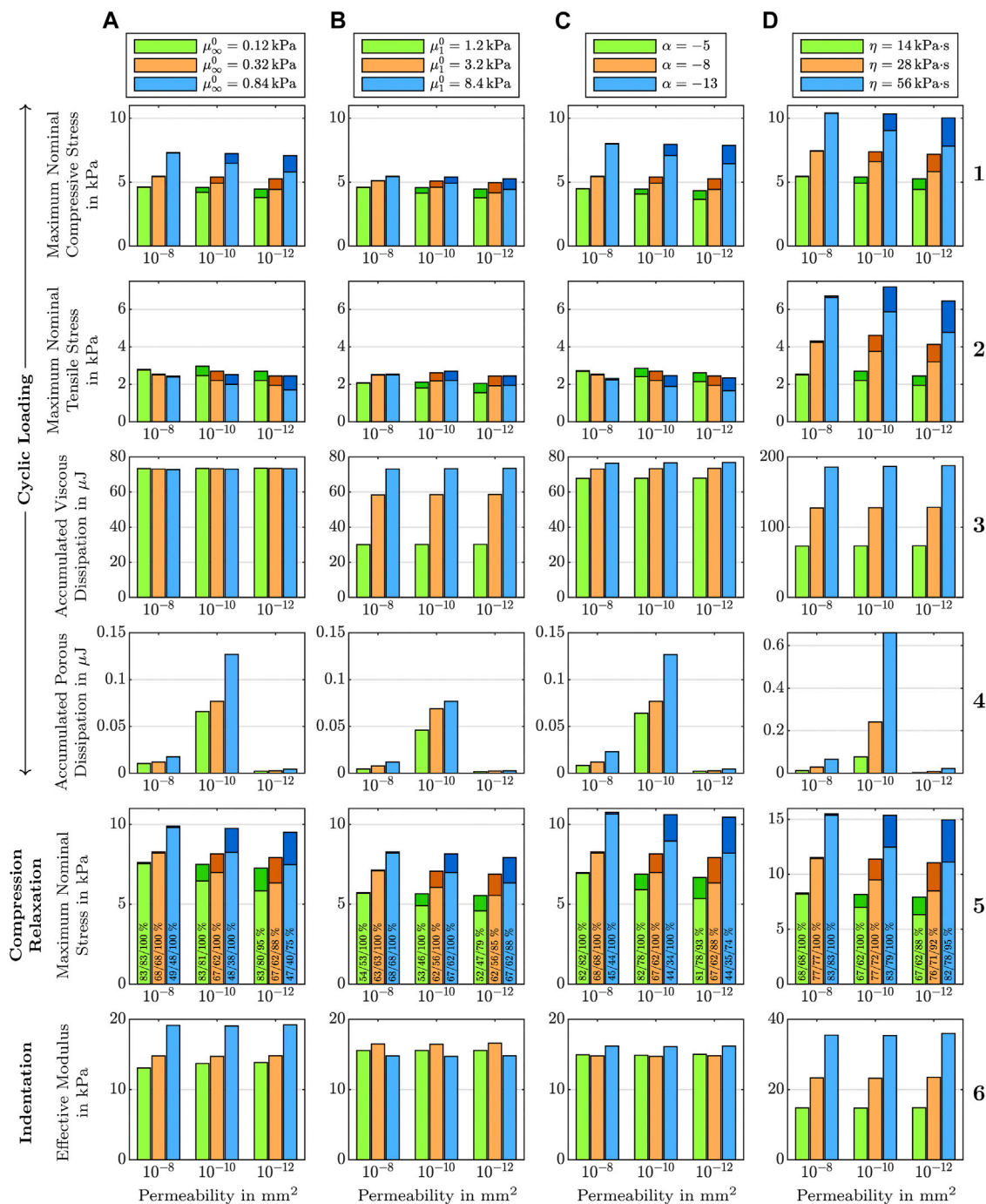


FIGURE 7 | Effect of (A) the equilibrium shear modulus μ_{∞}^0 , (B) the non-equilibrium shear modulus μ_1^0 , (C) the nonlinearity Ogden parameter α , and (D) the solid viscosity η for different initial intrinsic permeabilities $K_0 = \{10^{-8}, 10^{-10}, 10^{-12}\} \text{ mm}^2$ on the maximum stresses, and viscous and porous dissipations during cyclic compression–tension (rows 1–4), maximum stresses and the total/solid/fluid contributions to stress relaxation after 300 s in percent for compression relaxation (row 5), and the effective modulus from indentation (row 6). For nominal stress plots, the fluid contribution to the total stress is indicated in a darker shade.

for increasing permeability (see **Figure 7 A1** and **A5**). The effective modulus from indentation also increases for increasing μ_{∞}^0 , but is only marginally affected by a change in the permeability (see **Figure 7 A6**). Under tensile loading, the maximum nominal stress shows the opposite trend and decreases

for increasing equilibrium shear modulus (see **Figure 7 A2**). It reaches a maximum for $K_0 = 10^{-10} \text{ mm}^2$, which can be attributed to the significant increase in the fluid contribution between $K_0 = 10^{-8} \text{ mm}^2$ and $K_0 = 10^{-10} \text{ mm}^2$. In general, the fluid contribution is higher in tension than in compression.

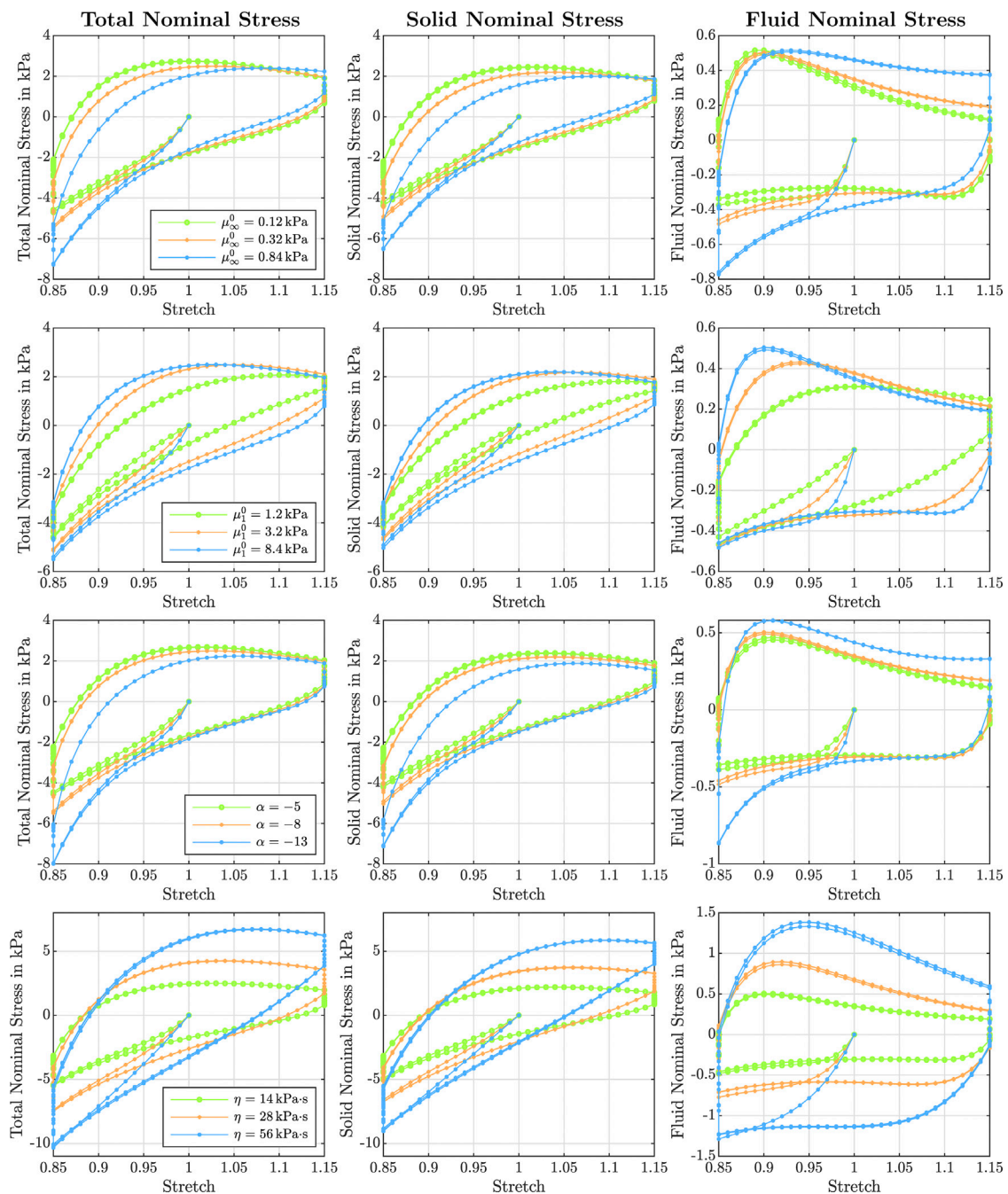


FIGURE 8 | Effect of the equilibrium shear modulus μ_{∞}^0 (first row), the non-equilibrium shear modulus μ_1^0 (second row), the nonlinearity Ogden parameter α (third row), and the solid viscosity η (fourth row) on the stress-stretch response during cyclic compression-tension for an initial intrinsic permeability $K_0 = 10^{-10} \text{ mm}^2$.

The viscous dissipation remains almost constant for different shear moduli and permeabilities (see **Figure 7 A3**). The porous dissipation, in contrast, shows a coupled dependency on the shear modulus and the intrinsic permeability (see **Figure 7 A4**). It increases with increasing shear modulus and again shows its maximum for an intrinsic permeability of $K_0 = 10^{-10} \text{ mm}^2$. These results demonstrate that the stiffness of the solid has a strong influence on the fluid response. Varying the shear modulus also

noticeably affects the stress-stretch curves for the fluid nominal stress, as illustrated in **Figure 8**, first row. We note that, depending on the shear modulus, the maximum tensile stress is not necessarily reached for the maximum stretch.

The stress relaxation experiments in **Figure 7 A5** reveal that the stress relaxed after 300 s of holding time decreases with increasing shear modulus. Independent of the shear modulus and permeability, the fluid stress relaxes faster than the solid stress.

While for higher permeabilities, the fluid stress has fully relaxed after five minutes, it still contributes to the total stress for the lowest intrinsic permeability of $K_0 = 10^{-12} \text{ mm}^2$ as only between 75 % and 95% of the fluid nominal stress have relaxed. Still, the overall stress relaxation remains almost constant, as the increasing fluid contribution takes over some part of the solid relaxation.

Figure 7, second column, shows the effect of the non-equilibrium shear modulus μ_1^0 on cyclic compression–tension, compression stress relaxation, and indentation experiments. The maximum nominal compressive stress increases with increasing shear modulus (see **Figure 7 B1** and **B5**), but this effect is less pronounced than for the equilibrium shear modulus. In contrast to the influence of μ_{∞}^0 , the maximum nominal tensile stress also increases with increasing μ_1^0 (see **Figure 7 B2**). The opposite effect on the total tensile stresses is also well visible in the stress–stretch curves in **Figure 8**. When comparing the first and second row, the trends are similar in compression, but differ in tension. Both viscous and porous dissipation strongly depend on the non-equilibrium shear modulus (see **Figure 7 B3** and **B4**): the dissipation increases with increasing μ_1^0 . Consequently, while the effect of a varying non-equilibrium shear modulus on the maximum stress during the stress relaxation experiments is similar to the effect of the equilibrium shear modulus (see **Figure 7 B5**), the total stress relaxed after 5 min holding time increases instead of decreasing. In addition, the effective modulus from indentation simulations shows significantly different trends (see **Figure 7 B6**). Here, the effective modulus reaches a maximum for an intermediate non-equilibrium shear modulus but decreases again, when the shear modulus is further increased.

3.3 The Effect of the Nonlinearity

Figure 7, third column, shows the effect of the nonlinearity parameter α on cyclic compression–tension, compression stress relaxation, and indentation experiments. We chose negative values for α to capture the stiffer response under compression than under tension, which is an important feature of brain tissue behavior, as shown in **Figure 11**. Under compressive loading, increasing α values result in an increase of the maximum nominal stress, both in cyclic loading and stress relaxation (**Figure 7 C1** and **C5**). Under tensile loading, we observe the opposite trend (**Figure 7 C2**), similar to the effect of μ_{∞}^0 . This can be attributed to similar stress–stretch curves during cyclic loading in **Figure 8** for α (third row) and μ_{∞}^0 (first row). We further observe increased fluid nominal stresses under both compressive and tensile loading, showing that the fluid response also depends on the nonlinearity of the viscous solid. The accumulated viscous dissipation increases with increasing nonlinearity (see **Figure 7 C3**) and this effect is even more pronounced for the porous dissipation (see **Figure 7 C4**). This clearly shows that the nonlinearity not only affects the viscous response but also the behavior of the fluid. A high nonlinearity of $\alpha = -13$ not only produces larger stresses associated to the solid part (“extra” Cauchy stress τ_b^s in **Eq. 5**, see **Figure 9**, bottom left), but also largely affects the pore fluid values and distributions (see **Figure 9**, bottom right). Higher nonlinearities result in a longer porous relaxation (the pore pressure takes much longer to relax to

zero). These individual components add up to the total Cauchy stress shown in **Figure 9**, top left. We observe that higher nonlinearities yield higher stresses during loading and, additionally, stress relaxation progresses more slowly. The total stress relaxed after 5 minutes decreases for increasing α (see **Figure 7 C5**). Larger “extra” stresses can be associated with the larger solid volume fraction values (see **Figure 10**, top left), which in turn are linked to the fluid flowing out of the sample (see seepage velocities in **Figure 10**, top right). This is another example of how the behavior of the solid and fluid components is linked and, thus, the coupling of porous and viscous contributions. For larger α values the viscous (see **Figure 10**, bottom left) and porous (see **Figure 10**, bottom right) dissipation rates are slightly higher at the end of loading. However, the viscous dissipation reduces faster for $\alpha = -13$ than for lower nonlinearities, while we observe the opposite trend for the porous dissipation. We note that the finite element results in **Figures 9, 10** also demonstrate that all values are inhomogeneously distributed in the vertical cross-section of the sample due to the loading conditions not being purely uniaxial.

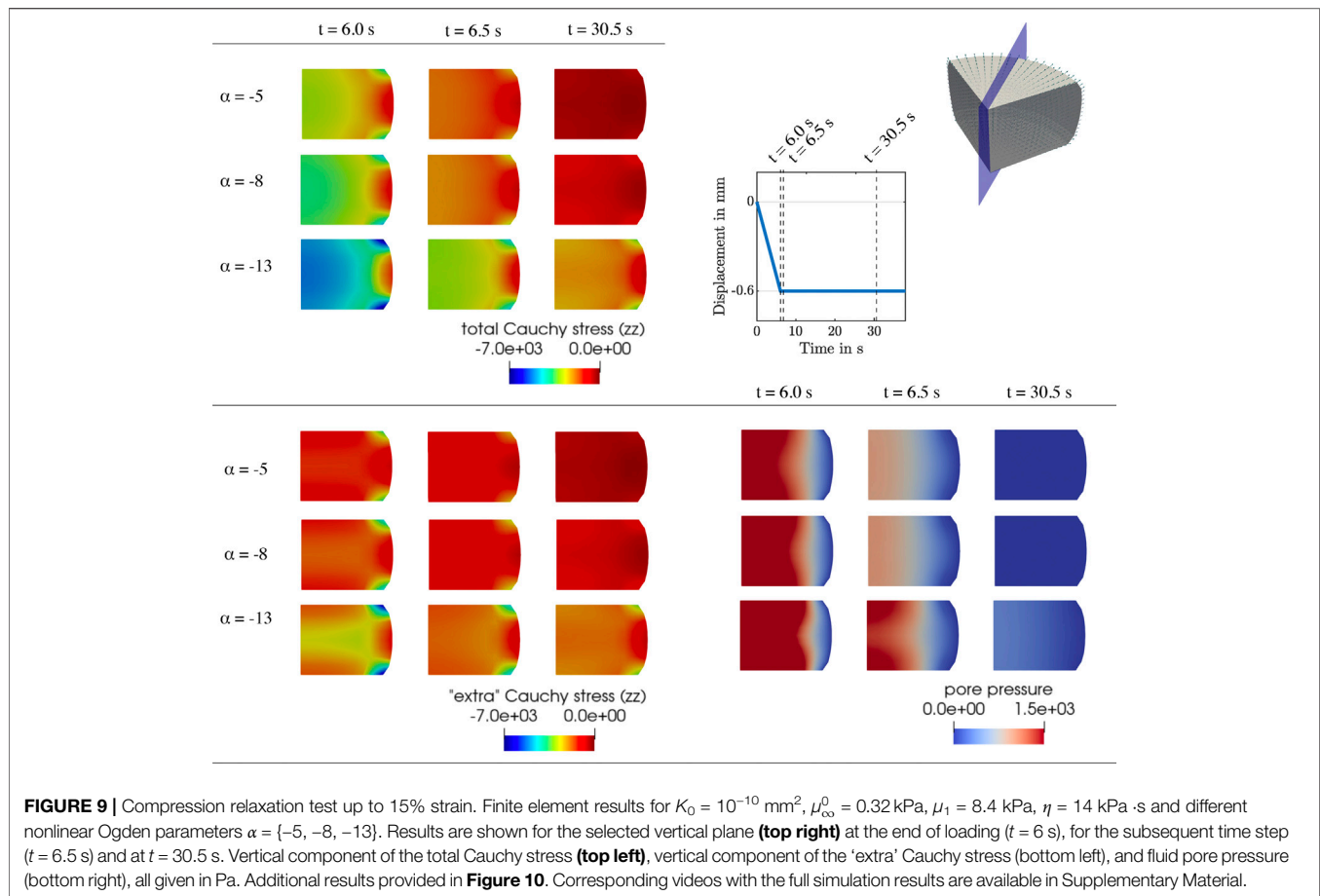
Since the nonlinearity parameter has an exponential character, its influence becomes more pronounced for larger deformations. Therefore, the indentation results (see **Figure 7 C6**), which are associated with smaller strains than the compression and tension experiments, are only marginally affected by changes in α . Interestingly, the effective modulus is lowest for the intermediate α , and increases for higher or smaller values. This shows that the relation between α and the indentation modulus is not linear.

3.4 The Effect of the Viscosity

Figure 7, fourth column, shows the effect of the viscosity η on cyclic compression–tension, compression stress relaxation, and indentation experiments. Increasing the viscosity leads to a significant increase in the maximum nominal stress during both compression and especially tension (see **Figure 7 D1**, **D2**, and **D5**). Interestingly, increasing the viscosity leads to a less nonlinear and less compression–tension asymmetric response (see **Figure 8**, bottom left). In addition, the fluid contribution to the total nominal stress increases notably. The effect of the viscosity on the fluid nominal stress can also be seen in the corresponding stress–stretch curves in **Figure 8**, bottom right. Depending on η , the amount of stretch at which the maximum fluid stress is reached shifts. In addition, both viscous and porous dissipation increase significantly for increasing viscosity (see **Figure 7 D3** and **D4**). As expected, also the stress relaxed after 5 min during stress relaxation experiments increases with increasing η (see **Figure 7 D5**). Finally, the viscosity largely affects the effective modulus from indentation simulations (see **Figure 7 D6**)—more than any other material parameter.

4 DISCUSSION

In this work, we have used a poro-viscoelastic computational model for brain tissue behavior to systematically analyze the



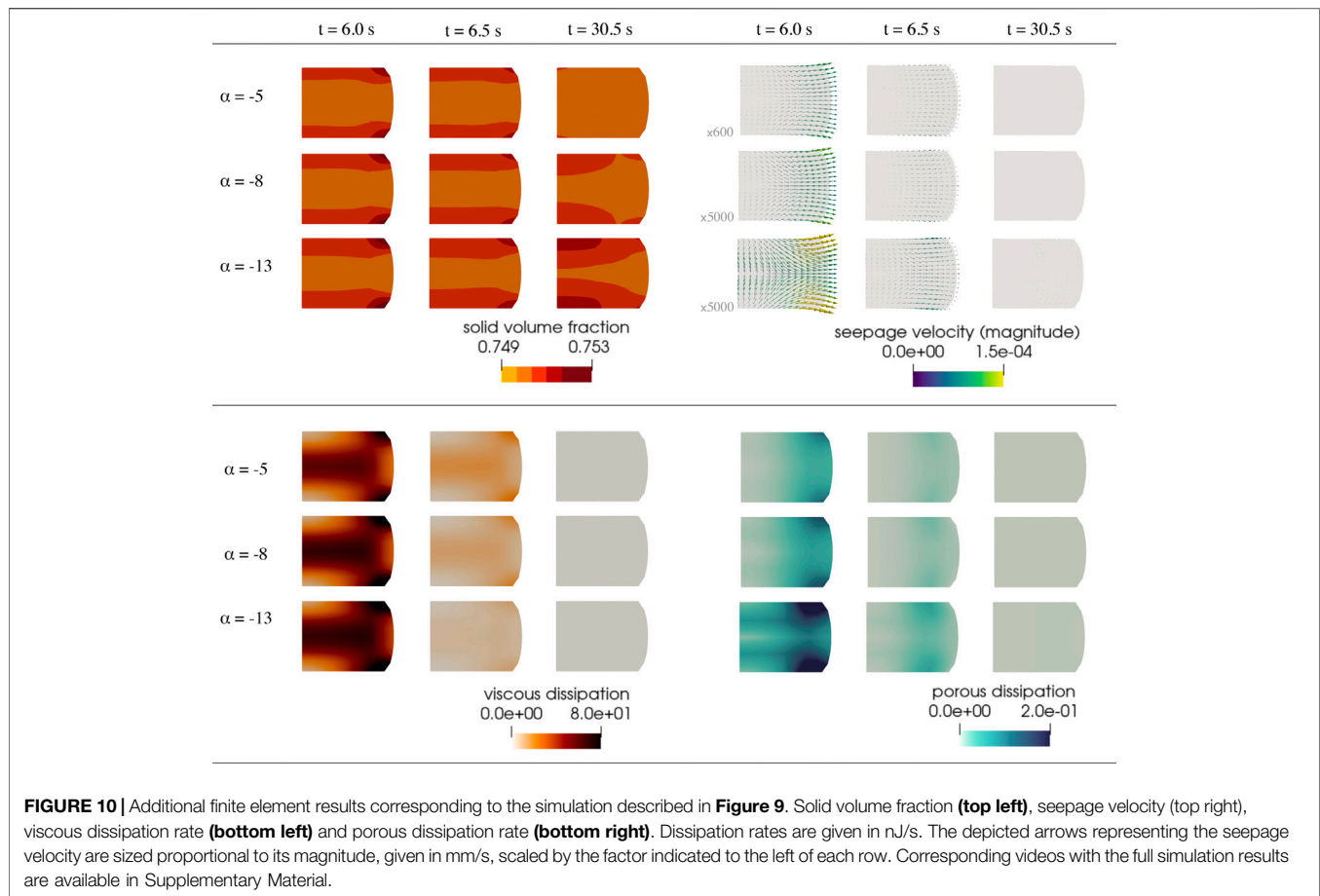
viscous and porous contributions to the quasi-static response recorded during common biomechanical testing setups, i.e., large-strain compression and tension as well as indentation experiments. Through systematic parameter studies, we have demonstrated the effects of the initial intrinsic permeability, shear moduli, nonlinearity, and viscosity on the test-setup-dependent recorded mechanical response and associated read-outs. Our analyses allow us to evaluate and explain differences in the reported data on human brain tissue mechanics that stem from poro-viscoelastic effects in combination with different drainage and loading conditions that differ greatly depending on the experimental procedure.

4.1 The Poro-Viscoelastic Nature of Brain Tissue Explains Discrepancies Between Indentation and Compression Experiments

Common biomechanical testing techniques to quantify the quasi-static, continuum scale, region-dependent mechanics of brain tissue include indentation experiments (Van Dommelen et al., 2010; Chen et al., 2015; Budday et al., 2015a; MacManus et al., 2017, 2018) and large-strain measurements under multiple loading modes, i.e., compression (Galford and McElhaney, 1970; Miller and Chinzei, 1997), tension (Miller and Chinzei,

2002), shear (Donnelly and Medige, 1997; Prange and Margulies, 2002; Chatelin et al., 2012), or combinations thereof (Jin et al., 2013; Budday et al., 2017a). Strikingly, while white matter tissue shows a “stiffer” response than gray matter during indentation measurements, we observe the opposite trend during large-strain compression, tension, and shear. To confirm this trend, we have tested one and the same human brain tissue specimens with both indentation and large-strain compression–tension experiments, as illustrated in **Figure 1**. While the effective modulus from indentation is higher for white matter (see **Figures 1G,H**), the maximum stresses reached during cyclic compression–tension and compression relaxation are higher for gray matter tissue (see **Figures 1I,J**).

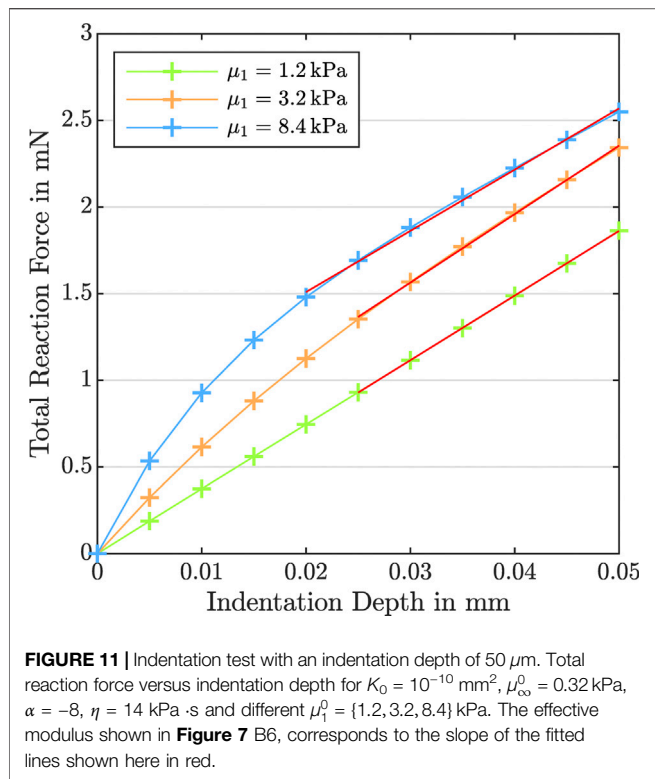
In this study, we have made an effort to trace this observation to the poro-viscoelastic nature of brain tissue—and the differences in the permeability, shear moduli, nonlinearity, and viscosity in different regions—through systematic numerical simulations. Our results show the tight coupling between the properties of the viscoelastic solid and the fluid behavior; the porous dissipation is highest for intermediate permeabilities and largely depends on the shear moduli, nonlinearity, and viscosity of the solid. Naturally, these complex and nonlinear dependencies cannot be captured by a single effective modulus determined from indentation experiments at relatively low strains or



maximum stresses during large-strain loading. Such values may change depending on the loading and boundary conditions and do not necessarily represent the actual stiffness of the material. Since the nonlinearity parameter α has an exponential character, for instance, its influence becomes more pronounced for larger deformations during compression and tension experiments than during indentation measurements. Therefore, certain material properties may affect the maximum stresses during large-strain compression differently than the effective modulus from indentation. Our results demonstrate that increasing μ_1^0 from 3.2 to 8.4 kPa leads to an increase in maximum compressive and tensile stresses, while—for the same sets of parameters—it leads to a decrease in the effective modulus from indentation. We observe a similar but less pronounced effect when increasing the nonlinearity from $\alpha = -5$ to $\alpha = -8$. These computationally-observed phenomena can explain the experimental results in **Figure 1**, which might seem contradictory at first sight. Interestingly, our previous results indeed suggest that the non-equilibrium shear modulus is higher for cortical gray matter than for white matter (Budday et al., 2017b; Budday and Steinmann, 2018) in agreement with the results in **Figure 7B**. In summary, the different trends for compression and indentation experiments can, on the one hand, be attributed to the complex coupling between porous and viscous effects and the material nonlinearity.

On the other hand, these trends can result from different methods used to analyze experimental data. Here, we determined the effective modulus from the averaged contact stiffness over the region between 50 and 100% of the maximum indentation force (as introduced in **Section 2.3**), similar to previous approaches in the literature (Oliver and Pharr, 2004; Budday et al., 2015a). This ensures to minimize the influence of adhesion (Gupta et al., 2007), but can significantly affect the results for highly nonlinear materials. **Figure 11** illustrates that the numerically-predicted indentation curve changes with varying non-equilibrium shear modulus and that it might make a difference to use a different portion of the curve to determine the effective modulus.

These considerations emphasize that when testing ultrasoft and biphasic materials such as brain tissue, one needs to be particularly careful when post-processing recorded experimental data. Our simulations further show that the fluid flow within and across the boundaries of the sample is key to the overall response of the tissue (as measured by traditional methods). Therefore, also experimental setups should be carefully designed in the future to avoid unwanted effects and measure the particular property relevant for a certain application. In this respect, finite element modeling provides a useful tool to explore the complex behavior under different loading conditions and better understand the role of individual material properties, such as permeability, stiffness,



nonlinearity, and viscosity, on the measured response, as discussed in detail in the following.

4.2 The Role of the Intrinsic Permeability on the Tissue Response

Although the initial intrinsic permeability K_0 barely affects the total nominal stress and effective modulus (see **Figures 3, 7**), the individual fluid and solid contributions change noticeably. The permeability regulates how “fast” the fluid flow reacts to loading. In addition, our results demonstrate that there are significant local variations in the fluid flow within the sample for the different testing setups investigated here (e.g., see **Figures 5, 6**). We consistently observe that the amount of fluid “trapped” in the viscoelastic solid network is proportional to the contribution of the fluid part to the biphasic tissue response: Lower intrinsic permeabilities result in a larger fluid contribution to the total nominal stresses (see rows 1,2 and 5 in **Figure 7**). From a physical perspective, one can explain these trends considering that lower intrinsic permeabilities result in smaller relative movement between solid and fluid phases and, hence, less overall fluid flowing out of the loaded sample. Therefore, the incompressible fluid is “trapped” inside the sample and notably contributes to the stress response. For higher permeabilities, in contrast, there is a smaller proportion of fluid component in the biphasic material, so that the solid part must take on a larger part of the load.

Interestingly, our simulations further show that variations in the intrinsic permeability can result in extreme differences in the temporal course of the response, as observed in **Figures 5, 6**.

Here, we see for both compression relaxation and indentation loading that abrupt changes in loading rate, e.g., from loading to the holding period, can completely reverse the fluid flow and increase its magnitude ($K_0 = 10^{-8} \text{ mm}^2$) or only reduce the magnitude without changing the flow direction ($K_0 = 10^{-10} \text{ mm}^2$ and $K_0 = 10^{-12} \text{ mm}^2$). As the fluid flow has a direct impact on the global material response, reliably and accurately assessing the permeability of tissue samples in experiments is key to thoroughly understand how brain tissue deforms under different loading scenarios. This becomes an imperative under “real-life” loading conditions that are not homogeneous, where we see complex local interactions of the biphasic tissue deformation, seepage velocity and resulting fluid flow directions.

Our results demonstrate that for the testing setups considered here, unconfined large-strain compression and tension as well as indentation experiments, the fluid flow within the sample and across the boundary is not well controlled. Therefore, it may be important to redesign experimental setups in the future in order to avoid unwanted effects of the fluid flow on the measured response, especially when comparing different regions of brain tissue where there seem to be local differences in permeability. This becomes even more relevant as we observed that the fluid flow also depends on the viscoelastic properties (as discussed in detail in the next section) and such coupling effects can lead to additional effects during experiments that are rather related to different boundary conditions than the actual material properties.

4.3 Coupling Between Viscous and Porous Effects

The thorough exploration of the poro-viscoelastic parameters in our computational model confirms that the viscous and porous responses to loading are highly interrelated. Typically, we associate the fluid constituent behavior to the porous response, while the solid component is linked to the viscous one. Yet, changes in a single parameter, either linked to the viscoelastic solid ($\mu_{\infty}^0, \mu_1^0, \alpha, \eta$) or the pore fluid (K_0) have considerable effects on both porous and viscous features of the tissue behavior (see rows 3 and 4 in **Figure 7**). For all loading cases studied here, the fluid response depends on the stiffness and nonlinearity of the viscoelastic solid in addition to the initial intrinsic permeability. While the latter is evidently the main determinant in the fluid part of the biphasic response, (**Figures 5, 6**), interestingly, also different combinations of the solid parameters $\mu_{\infty}^0, \mu_1^0, \alpha$, and η have a noticeable effect (see fluid nominal stress in **Figure 8**, pore pressure in **Figure 9** and seepage velocity in **Figure 10**). These observations agree well with our previous findings (Reiter et al., 2021), showing that cells inside brain tissue still keep moving in the direction of loading during the holding period of compression relaxation experiments—only with decreasing velocity. This further supports the idea that the porous and viscous contributions to the response of brain tissue are strongly coupled, i.e., the moving fluid might exert a drag force on cell bodies and thereby displace them.

Porous dissipation results, surprisingly, are not directly proportional to the initial intrinsic permeability (see **Figure 4**

center and **Figure 7**, row 4), but rather peak for intermediate values of K_0 . This hints at complex interactions between the deforming viscoelastic solid and the fluid flow behavior under loading. From a numerical perspective, and considering the definitions (11) and (12), the unexpected response can be attributed to the coupling between the pressure and displacement variables. Solid deformation and stresses are affected by a hydrostatic component due to the fluid constituent exerting pressure on the solid. At the same time, seepage velocity incorporates the effect of the deformations in the changing intrinsic permeability value to account for the “closing” of the pores under loading. However, for different values of the solid parameters and loading conditions, we observe important variations in local pressure distributions and, hence, in the gradients of pressure, which determine seepage velocity together with the intrinsic permeability. Consequently, from a computational perspective, the pressure variable is the key—and its effects are nuanced as we have repeatedly observed in our simulations.

Our results indicate that the viscoelastic solid influences the porous response to a much larger extent than the fluid constituent affects the viscous response. While the solid nominal stress shows a slight dependence on the intrinsic permeability (**Figure 3** center), the accumulated viscous dissipation remains unaltered by the change in K_0 (see **Figure 4**, left, and **Figure 7**, row 3). These observations are highly relevant when aiming to design experimental procedures and protocols to reliably determine poro- and viscoelastic material parameters for brain tissue. We could previously show that a combination of cyclic and stress relaxation experiments under multiple loading modes are well suited to calibrate viscoelastic material parameters (Budday et al., 2017b; Budday and Steinmann, 2018). By considering multiple loading modes simultaneously, one can avoid that the optimization problem is ill-posed. To reliably calibrate poro-viscoelastic models for brain tissue, however, experimental designs need to be adopted to test the unique property of interest. Ideally, experimental setups are optimized under close consideration of the modeling framework and with the help of computational simulations. This has the advantage that the effects we have observed in the current study can be taken into account.

4.4 Perspectives and Future Directions

In this study, we have performed computational parameter studies to systematically understand the individual viscous and porous contributions to brain tissue behavior under different biomechanical testing conditions, but have not aimed at calibrating material parameters through an inverse parameter identification scheme. The reason for that is that current experimental setups and data available in the literature are not sufficient to reliably determine the model parameters. For the setups investigated here, for instance, which have previously been successfully used to calibrate viscoelastic material parameters (Budday et al., 2017b; Budday and Steinmann, 2018), porous and viscous effects are strongly coupled. This makes it difficult to

uniquely identify poro-viscoelastic parameter sets. Also, previously reported viscoelastic parameters are not readily transferable. As an example, the first Lamé parameter in our poro-viscoelastic model is not equivalent to the first Lamé parameter in a single-phase viscoelastic material because ours only represents the solid component behavior, while the latter implicitly incorporates the whole tissue behavior, including the fluid contribution to the material bulk behavior. Therefore, in the future we plan to design new experimental setups and protocols, e.g., to determine the intrinsic permeability of brain tissue, under close consideration of the continuum mechanics modeling framework and systematic predictions from finite element simulations. The latter are a valuable tool to evaluate the sensitivity of certain parameters towards specific loading conditions and, like this, optimize experiments. This will eventually allow us to develop more realistic simulations for personalized medicine.

We note that we only focused on quasi-static experiments in the current work, which are relevant for applications on intermediate time scales, such as the well-known phenomenon of brain shift: When the skull is open during a neurosurgery, brain tissue immediately undergoes large deformations and “shifts” compared to the situation on preoperative images. This is a major issue in neuronavigation (Gerard et al., 2017). In the future, the model can also be adopted to study effects during further experimental setups, for instance magnetic resonance elastography (MRE) and ultrasound elastography (USE), where the brain is loaded under small strains at high frequencies. Importantly, these techniques allow for *in vivo* measurements. Therefore, it will be interesting to investigate, on the one hand, the capability of the model to capture the tissue behavior in this small-strain high-frequency regime, and, on the other hand, to evaluate the suitability of *in vivo* measurements for the calibration of biphasic, large-strain mechanical models as the one presented here. Expanding our numerical inquiries to additional experimental setups will also provide a more comprehensive set of data to analyze the general sensitivity of the model parameters.

From a purely modeling perspective, it would be interesting to challenge certain assumptions made in the current form of the formulation. In particular, an alternative to Darcy’s law for the fluid behavior would likely have a significant impact on the results, especially the effect of the intrinsic permeability. For example, one could introduce a direct solid-dependence in the definition of the volume-weighted seepage velocity (11) to model stress-assisted diffusion. Regarding the well-known regional differences in brain tissue, these could be numerically investigated in several ways, e.g., with a non-isotropic permeability tensor and/or viscous evolution equation that better reflect the local microstructure of the tissue. In addition, adhesion effects could be introduced. Finally, for certain applications, it may be necessary to incorporate the effects of gravity as well as an osmotic pressure to predict swelling in the brain. The computational approach presented in this study provides a robust numerical framework on which to build increasingly sophisticated models tailored to specific applications.

DATA AVAILABILITY STATEMENT

The raw data supporting the conclusions of this article will be made available by the authors, without undue reservation.

ETHICS STATEMENT

The studies involving human participants were reviewed and approved by Ethics Committee of Friedrich-Alexander-University Erlangen-Nürnberg, Germany, with approval number 405 18 B. The patients/participants provided their written informed consent to participate in this study.

AUTHOR CONTRIBUTIONS

EC and SB conceptualized the study. PS, GAH, EC, and SB developed the model. EC implemented the initial computational code. AG implemented the numerical setups and performed the simulations. AG analyzed the computational data and prepared the figures with the help of EC. FP provided human brain tissue. NR performed the mechanical experiments and analyzed the corresponding data. AG, EC, and SB wrote the first draft. GAH, PS, EC and SB acquired funding. SB supervised the project. All authors have discussed the results, reviewed and edited the final manuscript.

REFERENCES

- Angeli, S., and Stylianopoulos, T. (2016). Biphasic Modeling of Brain Tumor Biomechanics and Response to Radiation Treatment. *J. Biomech.* 49, 1524–1531. doi:10.1016/j.jbiomech.2016.03.029
- Arndt, D., Bangerth, W., Blais, B., Clevenger, T. C., Fehling, M., Grayver, A. V., et al. (2020). The deal.II Library, Version 9.2. *J. Numer. Maths.* 0 28 (3), 131–146. doi:10.1515/jnma-2020-0043
- Barnes, J. M., Przybyla, L., and Weaver, V. M. (2017). Tissue Mechanics Regulate Brain Development, Homeostasis and Disease. *J. Cell. Sci.* 130, 71–82. doi:10.1242/jcs.191742
- Bilston, L. E., Liu, Z., and Phan-Thien, N. (2001). Large Strain Behaviour of Brain Tissue in Shear: Some Experimental Data and Differential Constitutive Model. *Biorheology* 38, 335–345.
- Budday, S., Nay, R., de Rooij, R., Steinmann, P., Wyrobek, T., Ovaert, T. C., et al. (2015a). Mechanical Properties of gray and white Matter Brain Tissue by Indentation. *J. Mech. Behav. Biomed. Mater.* 46, 318–330. doi:10.1016/j.jmbbm.2015.02.024
- Budday, S., Ovaert, T. C., Holzapfel, G. A., Steinmann, P., and Kuhl, E. (2020). Fifty Shades of Brain: A Review on the Mechanical Testing and Modeling of Brain Tissue. *Arch. Comput. Methods Eng.* 27, 1187–1230. doi:10.1007/s11831-019-09352-w
- Budday, S., Sommer, G., Birk, C., Langkammer, C., Haybaeck, J., Kohnert, J., et al. (2017a). Mechanical Characterization of Human Brain Tissue. *Acta Biomater.* 48, 319–340. doi:10.1016/j.actbio.2016.10.036
- Budday, S., Sommer, G., Haybaeck, J., Steinmann, P., Holzapfel, G. A., and Kuhl, E. (2017b). Rheological Characterization of Human Brain Tissue. *Acta Biomater.* 60, 315–329. doi:10.1016/j.actbio.2017.06.024
- Budday, S., Sommer, G., Steinmann, P., Holzapfel, G. A., and Kuhl, E. (2017c). Viscoelastic Parameter Identification of Human Brain Tissue. *J. Mech. Behav. Biomed. Mater.* 74, 463–476. doi:10.1016/j.jmbbm.2017.07.014
- Budday, S., Steinmann, P., and Kuhl, E. (2015b). Physical Biology of Human Brain Development. *Front. Cell. Neurosci.* 9, 257. doi:10.3389/fncel.2015.00257
- Budday, S., and Steinmann, P. (2018). On the Influence of Inhomogeneous Stiffness and Growth on Mechanical Instabilities in the Developing Brain. *Int. J. Sol. Structures* 132–133, 31–41. doi:10.1016/j.ijsolstr.2017.08.010

FUNDING

We gratefully acknowledge the funding by the Deutsche Forschungsgemeinschaft (DFG, German Research Foundation) through the grants BU 3728/1-1 to SB, BU 3728/3-1—STE 544/70-1 to SB, PS and GH, as well as PA 738/15-1 to FP. This project has received funding from the European Union's Horizon 2020 research and innovation programme under the Marie Skłodowska-Curie grant agreement No 841047 to EC.

ACKNOWLEDGMENTS

We cordially thank Sarah Nistler for her valuable help in performing the indentation experiments as well as Lars Bräuer and Lisa Stache for preparing the human brain.

SUPPLEMENTARY MATERIAL

The Supplementary Material for this article can be found online at: <https://www.frontiersin.org/articles/10.3389/fmech.2021.708350/full#supplementary-material>

- Chatelin, S., Constantinesco, A., and Willinger, R. (2010). Fifty Years of Brain Tissue Mechanical Testing: from *In Vitro* to *In Vivo* Investigations. *Biorheology* 47, 255–276. doi:10.3233/bir-2010-0576
- Chatelin, S., Vappou, J., Roth, S., Raul, J.-S., and Willinger, R. (2012). Towards Child versus Adult Brain Mechanical Properties. *J. Mech. Behav. Biomed. Mater.* 6, 166–173. doi:10.1016/j.jmbbm.2011.09.013
- Chen, F., Zhou, J., Li, Y., Wang, Y., Li, L., and Yue, H. (2015). Mechanical Properties of Porcine Brain Tissue in the Coronal Plane: Interregional Variations of the corona Radiata. *Ann. Biomed. Eng.* 43, 2903–2910. doi:10.1007/s10439-015-1350-3
- Cheng, S., and Bilston, L. E. (2007). Unconfined Compression of white Matter. *J. Biomech.* 40, 117–124. doi:10.1016/j.jbiomech.2005.11.004
- Comellas, E., Budday, S., Pelteret, J.-P., Holzapfel, G. A., and Steinmann, P. (2020). Modeling the Porous and Viscous Responses of Human Brain Tissue Behavior. *Comput. Methods Appl. Mech. Eng.* 369, 113128. doi:10.1016/j.cma.2020.113128
- Donnelly, B., and Medige, J. (1997). Shear Properties of Human Brain Tissue. *J. Biomech. Eng.* 119, 423–432. doi:10.1115/1.2798289
- Ehlers, W., and Eipper, G. (1999). Finite Elastic Deformations in Liquid-Saturated and Empty Porous Solids. *Transp. Porous Media* 34, 179–191. doi:10.1023/A:1006565509095
- Ehlers, W., and Wagner, A. (2015). Multi-component Modelling of Human Brain Tissue: a Contribution to the Constitutive and Computational Description of Deformation, Flow and Diffusion Processes with Application to the Invasive Drug-Delivery Problem. *Comput. Methods Biomech. Biomed. Engin.* 18, 861–879. doi:10.1080/10255842.2013.853754
- Fletcher, T. L., Wirthl, B., Kolas, A. G., Adams, H., Hutchinson, P. J. A., and Sutcliffe, M. P. F. (2016). Modelling of Brain Deformation after Decompressive Craniectomy. *Ann. Biomed. Eng.* 44, 3495–3509. doi:10.1007/s10439-016-1666-7
- Franceschini, G., Bigoni, D., Regitnig, P., and Holzapfel, G. A. (2006). Brain Tissue Deforms Similarly to Filled Elastomers and Follows Consolidation Theory. *J. Mech. Phys. Sol.* 54, 2592–2620. doi:10.1016/j.jmps.2006.05.004
- Galford, J. E., and McElhaney, J. H. (1970). A Viscoelastic Study of Scalp, Brain, and Dura. *J. Biomech.* 3, 211–221. doi:10.1016/0021-9290(70)90007-2

- Gerard, I. J., Kersten-Oertel, M., Petrecca, K., Sirhan, D., Hall, J. A., and Collins, D. L. (2017). Brain Shift in Neuronavigation of Brain Tumors: A Review. *Med. Image Anal.* 35, 403–420. doi:10.1016/j.media.2016.08.007
- Gerischer, L. M., Fehlnner, A., Köbe, T., Prehn, K., Antonenko, D., Grittner, U., et al. (2018). Combining Viscoelasticity, Diffusivity and Volume of the hippocampus for the Diagnosis of Alzheimer's Disease Based on Magnetic Resonance Imaging. *NeuroImage: Clin.* 18, 485–493. doi:10.1016/j.nicl.2017.12.023
- Goriely, A., Geers, M. G., Holzapfel, G. A., Jayamohan, J., Jérusalem, A., Sivaloganathan, S., et al. (2015). Mechanics of the Brain: Perspectives, Challenges, and Opportunities. *Biomech. Model. Mechanobiol.* 14, 931–965. doi:10.1007/s10237-015-0662-4
- Gupta, S., Carrillo, F., Li, C., Pruitt, L., and Puttlitz, C. (2007). Adhesive Forces Significantly Affect Elastic Modulus Determination of Soft Polymeric Materials in Nanoindentation. *Mater. Lett.* 61, 448–451. doi:10.1016/j.matlet.2006.04.078
- Hasan, M. M., and Drapaca, C. S. (2015). A Poroelastic-Viscoelastic Limit for Modeling Brain Biomechanics. *Mater. Res. Soc. Symp. Proc.* 1753, 53–59. doi:10.1557/opl.2015.111
- Hemphill, M. A., Dauth, S., Yu, C. J., Dabiri, B. E., and Parker, K. K. (2015). Traumatic Brain Injury and the Neuronal Microenvironment: A Potential Role for Neuropathological Mechanotransduction. *Neuron* 85, 1177–1192. doi:10.1016/j.neuron.2015.02.041
- Hosseini-Farid, M., Ramzanpour, M., McLean, J., Ziejewski, M., and Karami, G. (2020). A Poro-Hyper-Viscoelastic Rate-dependent Constitutive Modeling for the Analysis of Brain Tissues. *J. Mech. Behav. Biomed. Mater.* 102, 103475. doi:10.1016/j.jmbbm.2019.103475
- Jin, X., Zhu, F., Mao, H., Shen, M., and Yang, K. H. (2013). A Comprehensive Experimental Study on Material Properties of Human Brain Tissue. *J. Biomech.* 46, 2795–2801. doi:10.1016/j.jbiomech.2013.09.001
- Keating, C. E., and Cullen, D. K. (2021). Mechanosensation in Traumatic Brain Injury. *Neurobiol. Dis.* 148, 105210. doi:10.1016/j.nbd.2020.105210
- Kim, H., Min, B.-K., Park, D.-H., Hawi, S., Kim, B.-J., Czosnyka, Z., et al. (2015). Poroelastohyperelastic Anatomical Models for Hydrocephalus and Idiopathic Intracranial Hypertension. *J. Neurosurg.* 122, 1–11. doi:10.3171/2014.12.JNS14516
- Koser, D. E., Thompson, A. J., Foster, S. K., Dwivedy, A., Pillai, E. K., Sheridan, G. K., et al. (2016). Mechanosensing Is Critical for Axon Growth in the Developing Brain. *Nat. Neurosci.* 19, 1592–1598. doi:10.1038/nn.4394
- Linka, K., Reiter, N., Würges, J., Schicht, M., Bräuer, L., Cyron, C. J., et al. (2021). Unraveling the Local Relation between Tissue Composition and Human Brain Mechanics through Machine Learning. *Front. Bioeng. Biotechnol. Submitted* 9, 704738. doi:10.3389/fbioe.2021.704738
- Lytton, W. W., Arle, J., Bobashev, G., Ji, S., Klassen, T. L., Marmarelis, V. Z., et al. (2017). Multiscale Modeling in the Clinic: Diseases of the Brain and Nervous System. *Brain Inform.* 4, 219–230. doi:10.1007/s40708-017-0067-5
- MacManus, D. B., Murphy, J. G., and Gilchrist, M. D. (2018). Mechanical Characterisation of Brain Tissue up to 35% Strain at 1, 10, and 100/s Using a Custom-Built Micro-indentation Apparatus. *J. Mech. Behav. Biomed. Mater.* 87, 256–266. doi:10.1016/j.jmbbm.2018.07.025
- MacManus, D. B., Pierrat, B., Murphy, J. G., and Gilchrist, M. D. (2017). Region and Species Dependent Mechanical Properties of Adolescent and Young Adult Brain Tissue. *Sci. Rep.* 7, 13729. doi:10.1038/s41598-017-13727-z
- Meaney, D. F., Morrison, B., and Bass, C. D. (2014). The Mechanics of Traumatic Brain Injury: a Review of what We Know and what We Need to Know for Reducing its Societal burden. *J. Biomech. Eng.* 136, 021008. doi:10.1115/1.4026364
- Mehrabian, A., and Abousleiman, Y. (2011). General Solutions to Poroelastic Model of Hydrocephalic Human Brain Tissue. *J. Theor. Biol.* 291, 105–118. doi:10.1016/j.jtbi.2011.09.011
- Mehrabian, A., Abousleiman, Y. N., Mapstone, T. B., and El-Amm, C. A. (2015). Dual-porosity Poroelasticity and Quantitative Hydromechanical Characterization of the Brain Tissue with Experimental Hydrocephalus Data. *J. Theor. Biol.* 384, 19–32. doi:10.1016/j.jtbi.2015.08.001
- Miller, K., and Chinzei, K. (1997). Constitutive Modelling of Brain Tissue: experiment and Theory. *J. Biomech.* 30, 1115–1121. doi:10.1016/s0021-9290(97)00092-4
- Miller, K., and Chinzei, K. (2002). Mechanical Properties of Brain Tissue in Tension. *J. Biomech.* 35, 483–490. doi:10.1016/s0021-9290(01)00234-2
- Murphy, M. C., Jones, D. T., Jack, C. R., Jr, Glaser, K. J., Senjem, M. L., Manduca, A., et al. (2016). Regional Brain Stiffness Changes across the Alzheimer's Disease Spectrum. *NeuroImage: Clin.* 10, 283–290. doi:10.1016/j.nicl.2015.12.007
- Oliver, W. C., and Pharr, G. M. (2004). Measurement of Hardness and Elastic Modulus by Instrumented Indentation: Advances in Understanding and Refinements to Methodology. *J. Mater. Res.* 19, 3–20. doi:10.1557/jmr.2004.19.1.3
- Park, K., Lonsberry, G. E., Gearing, M., Levey, A. I., and Desai, J. P. (2018). Viscoelastic Properties of Human Autopsy Brain Tissues as Biomarkers for Alzheimer's Diseases. *IEEE Trans. Biomed. Eng.* 66, 1705–1713. doi:10.1109/TBME.2018.2878555
- Prange, M. T., and Margulies, S. S. (2002). Regional, Directional, and Age-dependent Properties of the Brain Undergoing Large Deformation. *J. Biomech. Eng.* 124, 244–252. doi:10.1115/1.1449907
- Prevost, T. P., Balakrishnan, A., Suresh, S., and Socrate, S. (2011). Biomechanics of Brain Tissue. *Acta Biomater.* 7, 83–95. doi:10.1016/j.actbio.2010.06.035
- Rashid, B., Destrade, M., and Gilchrist, M. D. (2012). Temperature Effects on Brain Tissue in Compression. *J. Mech. Behav. Biomed. Mater.* 14, 113–118. doi:10.1016/j.jmbbm.2012.04.005
- Reiter, N., Roy, B., Paulsen, F., and Budday, S. (2021). Insights into the Microstructural Origin of Brain Viscoelasticity. *J. Elasticity.* doi:10.1007/s10659-021-09814-y
- Terzano, M., Spagnoli, A., Dini, D., and Forte, A. E. (2021). Fluid-solid Interaction in the Rate-dependent Failure of Brain Tissue and Biomimicking Gels. *J. Mech. Behav. Biomed. Mater.* 104530. doi:10.1016/j.jmbbm.2021.104530
- Thompson, A. J., Pillai, E. K., Dimov, I. B., Foster, S. K., Holt, C. E., and Franze, K. (2019). Rapid Changes in Tissue Mechanics Regulate Cell Behaviour in the Developing Embryonic Brain. *eLife* 8, e39356. doi:10.7554/eLife.39356
- Van Dommelen, J., Van der Sande, T., Hrapko, M., and Peters, G. (2010). Mechanical Properties of Brain Tissue by Indentation: Interregional Variation. *J. Mech. Behav. Biomed. Mater.* 3, 158–166. doi:10.1016/j.jmbbm.2009.09.001
- Weickenmeier, J., Butler, C., Young, P., Goriely, A., and Kuhl, E. (2017). The Mechanics of Decompressive Craniectomy: Personalized Simulations. *Comp. Methods Appl. Mech. Eng.* 314, 180–195. doi:10.1016/j.cma.2016.08.011
- Whittall, K. P., Mackay, A. L., Graeb, D. A., Nugent, R. A., Li, D. K., and Paty, D. W. (1997). In Vivo measurement of T2 Distributions and Water Contents in normal Human Brain. *Magn. Reson. Med.* 37, 34–43. doi:10.1002/mrm.1910370107

Conflict of Interest: The authors declare that the research was conducted in the absence of any commercial or financial relationships that could be construed as a potential conflict of interest.

Publisher's Note: All claims expressed in this article are solely those of the authors and do not necessarily represent those of their affiliated organizations, or those of the publisher, the editors and the reviewers. Any product that may be evaluated in this article, or claim that may be made by its manufacturer, is not guaranteed or endorsed by the publisher.

Copyright © 2021 Greiner, Reiter, Paulsen, Holzapfel, Steinmann, Comellas and Budday. This is an open-access article distributed under the terms of the Creative Commons Attribution License (CC BY). The use, distribution or reproduction in other forums is permitted, provided the original author(s) and the copyright owner(s) are credited and that the original publication in this journal is cited, in accordance with accepted academic practice. No use, distribution or reproduction is permitted which does not comply with these terms.



Unraveling the Local Relation Between Tissue Composition and Human Brain Mechanics Through Machine Learning

Kevin Linka¹, Nina Reiter², Jasmin Würges², Martin Schicht³, Lars Bräuer³, Christian J. Cyron^{1,4}, Friedrich Paulsen^{3,5} and Silvia Budday^{2*}

¹Institute of Continuum and Material Mechanics, Hamburg University of Technology, Hamburg, Germany, ²Institute of Applied Mechanics, Department Mechanical Engineering, Friedrich-Alexander-University Erlangen-Nürnberg, Erlangen, Germany, ³Institute of Functional and Clinical Anatomy, Faculty of Medicine, Friedrich-Alexander-University Erlangen-Nürnberg, Erlangen, Germany, ⁴Institute of Material Systems Modeling, Helmholtz-Zentrum Hereon, Geesthacht, Germany, ⁵Department of Operative Surgery and Topographic Anatomy, Sechenov University, Moscow, Russia

OPEN ACCESS

Edited by:

Georges Limbert,
University of Southampton,
United Kingdom

Reviewed by:

Olga Barrera,
Oxford Brookes University,
United Kingdom
Maria Jose Gomez-Benito,
University of Zaragoza, Spain

*Correspondence:

Silvia Budday
Silvia.Budday@fau.de

Specialty section:

This article was submitted to
Biomechanics,
a section of the journal
Frontiers in Bioengineering and
Biotechnology

Received: 03 May 2021

Accepted: 28 July 2021

Published: 17 August 2021

Citation:

Linka K, Reiter N, Würges J, Schicht M, Bräuer L, Cyron CJ, Paulsen F and Budday S (2021) Unraveling the Local Relation Between Tissue Composition and Human Brain Mechanics Through Machine Learning. *Front. Bioeng. Biotechnol.* 9:704738. doi: 10.3389/fbioe.2021.704738

The regional mechanical properties of brain tissue are not only key in the context of brain injury and its vulnerability towards mechanical loads, but also affect the behavior and functionality of brain cells. Due to the extremely soft nature of brain tissue, its mechanical characterization is challenging. The response to loading depends on length and time scales and is characterized by nonlinearity, compression-tension asymmetry, conditioning, and stress relaxation. In addition, the regional heterogeneity—both in mechanics and microstructure—complicates the comprehensive understanding of local tissue properties and its relation to the underlying microstructure. Here, we combine large-strain biomechanical tests with enzyme-linked immunosorbent assays (ELISA) and develop an extended type of constitutive artificial neural networks (CANNs) that can account for viscoelastic effects. We show that our viscoelastic constitutive artificial neural network is able to describe the tissue response in different brain regions and quantify the relevance of different cellular and extracellular components for time-independent (nonlinearity, compression-tension-asymmetry) and time-dependent (hysteresis, conditioning, stress relaxation) tissue mechanics, respectively. Our results suggest that the content of the extracellular matrix protein fibronectin is highly relevant for both the quasi-elastic behavior and viscoelastic effects of brain tissue. While the quasi-elastic response seems to be largely controlled by extracellular matrix proteins from the basement membrane, cellular components have a higher relevance for the viscoelastic response. Our findings advance our understanding of microstructure - mechanics relations in human brain tissue and are valuable to further advance predictive material models for finite element simulations or to design biomaterials for tissue engineering and 3D printing applications.

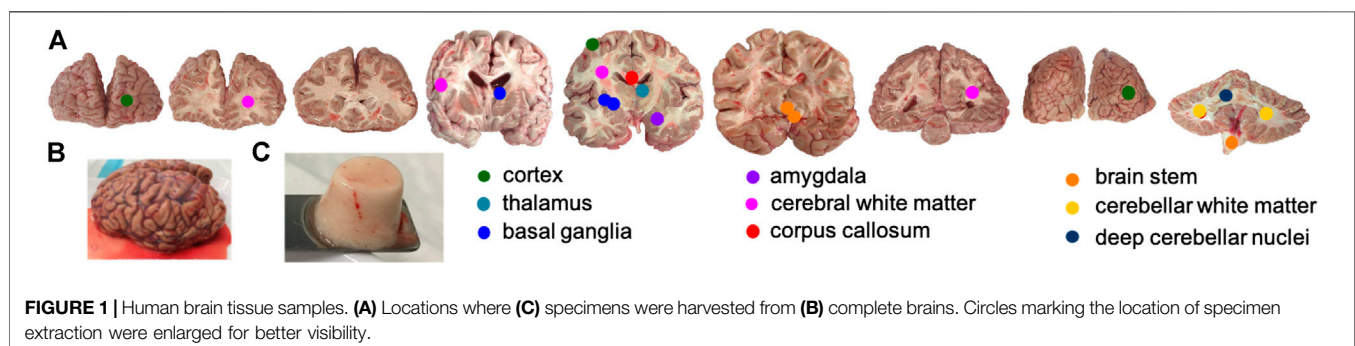
Keywords: human brain, viscoelasticity, constitutive modeling, microstructure, mechanical properties, artificial neural network, extracellular matrix

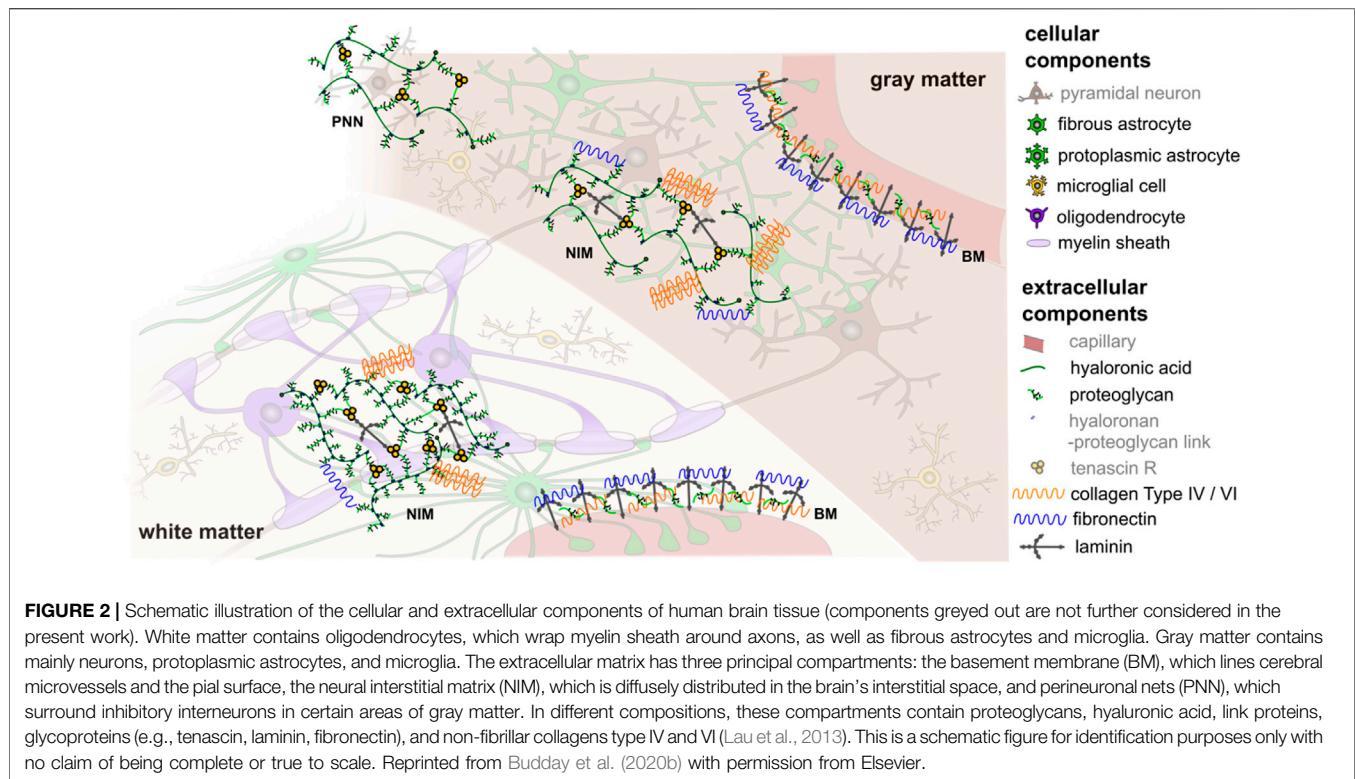
1 INTRODUCTION

The human brain is a fascinating organ, which has been studied intensively by researchers from various fields but still remains incompletely understood. Recent studies have highlighted the important role of mechanical properties and forces for certain processes during brain development (Budday et al., 2015b; Koser et al., 2016; Thompson et al., 2019; injury Meaney et al., 2014; Hemphill et al., 2015; Keating and Cullen, 2021), and disease (Murphy et al., 2016; Barnes et al., 2017; Gerischer et al., 2018; Park et al., 2018). Mechanical instabilities seem to underlie cortical folding during brain development (Budday et al., 2015b; Garcia et al., 2018), and brain cells react to their mechanical environment by converting mechanical stimuli into neural signals through mechanotransduction, which again triggers cellular or extracellular reactions (Moshayedi et al., 2010, 2014; Tyler, 2012; Franze et al., 2013; Blumenthal et al., 2014; Humphrey et al., 2014; Irianto et al., 2016; Koser et al., 2016; Urbanski et al., 2016; Barriga et al., 2018). Consequently, the human brain continuously changes its microstructure, mechanical properties, and shape during its lifetime (Budday and Kuhl, 2020), which makes it one of the most complex organs in the human body. For many pathological conditions, such as degenerative diseases, microstructural changes have been investigated by neuropathologists (Alafuzoff, 2018). However, the link between changes in microstructural components, the corresponding tissue mechanics, and the effect induced through the mechanosensing of cells remains to be clarified (Begonia et al., 2010). Better understanding whether and how microstructural components contribute to the macroscopic mechanical behavior of brain tissue is key to gain further insights into the mechanisms underlying mechanics-related injury and disease. In addition, computational models based on nonlinear continuum mechanics can be a valuable tool to predictively understand the processes in the human brain (Goriely et al., 2015; Budday et al., 2020a). Eventually, they could even be used to assist diagnosis and treatment of neurological disorders or the detailed planning of surgical procedures (Weickenmeier et al., 2017a; Zarzor et al., 2021). In this respect, understanding the link between microstructure and mechanics of brain tissue can help to develop more realistic material models that capture local variations in tissue properties (Budday et al., 2020b; Reiter et al., 2021).

One challenge when modeling the behavior of brain tissue is the exceptional heterogeneity in mechanical properties resulting from regional differences in the microstructure due to local functional demands. While we can clearly distinguish two tissue types on the macroscopic scale, gray and white matter (see **Figure 1**), the microstructure will locally vary significantly—even within those regions. Previous research on the microstructural composition of brain tissue has largely focused on the brain's cellular components with an emphasis on neurons. However, also support cells called neuroglia as well as the extracellular matrix highly contribute to normal and abnormal brain functioning (Lau et al., 2013). In general, the neuroglia can be divided into macroglia and microglia. The macroglia originate from the neural tube, i.e., are of ectodermal origin, the microglia originate from the mesoderm. The most important types of macroglia are astrocytes with mechanical and metabolic tasks such as maintaining the blood-brain barrier, oligodendrocytes, which support transduction through myelin sheath formation, and ependymal cells, which line the inner cerebrospinal fluid spaces (the latter, however, do not play a role for the investigations made in this work). The microglial cells are the macrophages of the central nervous system. All the glial cells mentioned (except ependym) have numerous cell processes. Unlike nerve cells, glial cells can proliferate. They support neurons and contribute to tissue homeostasis, and thereby influence the mechanical properties of the tissue. The majority of brain tumors originate from glial cells, which further highlights their importance for pathological processes. Furthermore, extracellular matrix components, such as proteoglycans, hyaluronic acid, and non-fibrillar collagens surround the cells, as illustrated in **Figure 2** (Novak and Kaye, 2000; Lau et al., 2013; Budday et al., 2020b). They embody approximately 40% of the brain's volume during development (Rauch, 2004) and 20% during adulthood (Bellail et al., 2004; Rauch, 2004; Ohashi et al., 2015) and might thus also play an important role in brain tissue mechanics.

An important challenge associated with the aim to define the relations between mechanics and microstructure is to reliably and consistently quantify these features. In terms of mechanics, the exceptionally complex mechanical response—characterized by nonlinearity, compression-tension-asymmetry, conditioning effects, and stress relaxation—makes it impossible to describe the mechanical properties through a single stiffness value. The





measured modulus highly depends on the loading mode, strain regime, strain rate, drainage conditions, and length scale (Chatelin et al., 2010; Budday et al., 2020a). Therefore, to account for nonlinear and time-dependent effects, it is important to, on the one hand, perform large-strain biomechanical tests combining cyclic and stress relaxation experiments, and, on the other hand, analyze the corresponding experimental data based on the theory of nonlinear continuum mechanics (Miller and Chinzei, 1997; Bilston et al., 2001; Miller and Chinzei, 2002; Prevost et al., 2011; Rashid et al., 2012; Budday et al., 2017a, 2020a).

In terms of microstructure, previously used techniques to investigate tissue components include histological and immunohistochemical stains or western blots (Yang and Mahmood, 2012; Alafuzoff, 2018), which can provide information about the presence, morphology, local distribution, or molecular weight of certain tissue components. In neuropathology, they are frequently used to distinguish the diseased from the healthy state. Yet, these methods only show a small section of the tissue and fail to provide trustworthy quantitative values on the amount of specific molecules (Taylor and Levenson, 2006; Yang and Mahmood, 2012; Dabbs, 2014). An alternative enabling a more reliable quantitative assessment is another immunological method called enzyme-linked immunosorbent assay (ELISA). It is an extremely sensitive colorimetric method to quantify biological molecules by using antibody-antigen complexes (Gan and Patel, 2013). As ELISA is an accurate, cost-effective, and quick technique, it has become a widely used method for the qualitative or quantitative analysis of molecules in versatile

fields. Still, it has to the best of the authors' knowledge not been used in the context of microstructure - mechanics relations in brain tissue yet.

Previous studies relating microstructure and mechanics of brain tissue have indicated that tissue stiffness increases with myelination during development in white matter (Weickenmeier et al., 2016; Weickenmeier et al., 2017b), negatively correlates with the fractional anisotropy (a structural parameter from magnetic resonance imaging and diffusion tensor imaging) (Budday et al., 2017a), and negatively correlates with the density of cell nuclei (Antonovaite et al., 2018; Budday et al., 2020b). However, these studies were based on the evaluation of imaging data which quantify the tissue composition much less accurately than ELISAs. In addition, they evaluated only the correlation between composition and individual mechanical parameters, such as the shear modulus, nonlinearity, or stress relaxation, but did not consider the entire loading history.

While first studies have successfully incorporated distinct microstructural parameters into analytic constitutive laws for brain tissue (Budday et al., 2020b; Reiter et al., 2021), data-driven approaches such as machine learning bear the potential to open up a much more comprehensive view. First attempts to use machine learning for relating tissue microstructure to macroscopic mechanical properties used simple end-to-end model architectures (Liang et al., 2017). To overcome the large amount of data required by such approaches, (Linka et al., 2021) recently introduced constitutive artificial neural networks (CANNs) as a novel machine learning architecture that incorporates substantial prior knowledge from materials theory. Thereby, it can learn to describe and in fact also

TABLE 1 | Human brains.

Brain	Sex	Age	Cause of death
1	Male	92	dotage
2	Female	62	liver and kidney failure
3	Male	68	metastasizing bronchial carcinoma
4	Male	75	cardiac insufficiency
5	Male	75	metastasizing bronchial carcinoma

predict the nonlinear behavior of soft biological tissue from information about its microstructure and composition based on a much smaller amount of training data than previous methods.

In this paper, we generalize the concept of CANNs to viscoelasticity and apply it to experimental data from human brain tissue. These data include results from large-strain mechanical tests and compositional analysis using ELISAs. Using relevance propagation, a concept of explainable artificial intelligence (Samek et al., 2021), we identify the importance of the different tissue constituents for the mechanical response of human brain tissue, where quasi-elastic and viscous effects show distinct regional trends.

2 MATERIALS AND METHODS

2.1 Human Brain Tissue

We obtained five whole human brains including the cerebrum, cerebellum, and brainstem (see **Figure 1B**) from one female and four male body donors who had given their written consent to donate their body to research. The body donors were aged between 62 and 92 years and none of them had suffered from any neurological disease known to affect the microstructure of the brain (see **Table 1**). We note that for subjects 3 and 5, we could not find metastases in the brain. The brains 1–3 and 5 were immersed in cerebrospinal fluid surrogate (CSFS) during transport. Brain 4 was kept in phosphate buffered saline solution (PBS). We received the brains between 9 and 24 h *post mortem* and directly cut them into 1 cm thick coronal slices. After that, we kept the slices refrigerated at 4 °C in CSFS or PBS until mechanical testing. We completed the mechanical experiments within 72 h *post mortem*. The study was approved by the Ethics Committee of Friedrich-Alexander University Erlangen-Nürnberg, Germany, with the approval number 405_18 B.

2.1.1 Specimen Preparation

The samples for the ELISAs of brain 3–5 were extracted directly after cutting the brains into slices to minimize the *post mortem* degradation of proteins before the samples were frozen and stored at –20°C. **Figure 1A** shows the anatomical brain regions that we included in our study. For brains 1 and 2, we extracted the ELISA samples simultaneously with the respective mechanical sample. Therefore, the ELISA samples of those two brains were frozen at different *post mortem* times.

The specimens for the mechanical characterization were extracted directly next to the locations of the ELISA specimens and were prepared right before testing. We used a biopsy punch to extract cylindrical samples of 8 mm diameter, as shown in **Figure 1C**. We punched the specimens out of the coronal slices while they were immersed in CSFS so that the cylindrical specimens could slide out of the biopsy punch without adhering to it. Like this, we could ensure that our samples only experienced small deformations before they were probed mechanically. If the small cylinders had a height of more than 6 mm, we carefully shortened them with a surgical scalpel. The specimen height ranged between 3.5 and 6 mm. For most regions, it was possible to extract homogeneous specimens of this size. The only exception were the deep cerebellar nuclei: The corresponding samples contained a certain amount of cerebellar white matter, which might affect the results.

We included a total number of $n = 86$ samples for mechanical experiments and $n = 78$ samples for the ELISAs, as, for eight of the ELISA samples, we were able to extract two corresponding mechanical specimens. **Table 2** summarizes the samples extracted from each brain region.

2.1.2 Mechanical Testing

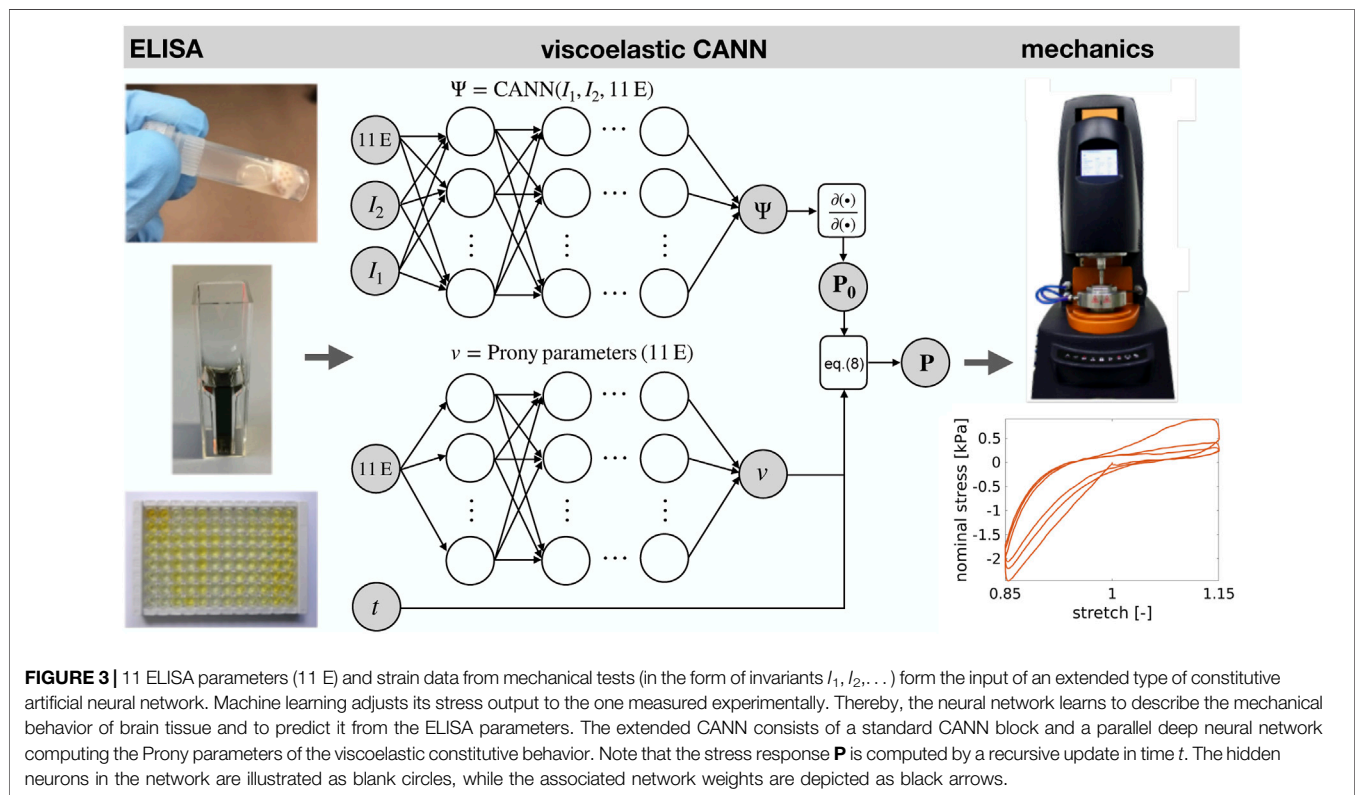
We used a Discovery HR-3 rheometer from TA instruments (New Castle, Delaware, United States) to measure the tissue response under compression and tension (see **Figure 3B**). After calibration, we fixed the specimens to the upper and lower specimen holder using sandpaper and superglue. We waited 30–60 s to let the glue dry before immersing the specimen in PBS to keep it hydrated during the experiment. We conducted all tests at 37°C. We first applied three cycles of compression and tension with a loading velocity of 40 $\mu\text{m/s}$ and minimum and maximum stretches of $\lambda = [H + \Delta z]/H = 0.85$ and $\lambda = 1.15$, where H denotes the initial specimen height and Δz the displacement in the direction of loading. Subsequently, we performed a compression relaxation test at $\lambda = 0.85$ with a loading velocity of 100 $\mu\text{m/s}$ and a holding period of 300 s, and a tension relaxation test at $\lambda = 1.15$, with the same loading velocity and holding period. We recorded the corresponding force f_z and determined the nominal stress as $P_{\text{exp}} = f_z/A$, where A is the cross-sectional area of the specimen in the undeformed configuration.

2.1.3 ELISA

We used commercially available enzyme-linked immunosorbent assay kits (ELISAs from Cloud-Clone and Cusabio, Wuhan, China) to quantify the amount of GFAP, MBP, Iba1, Col I, Col IV, CS, LAM, FN, HA, Col VI, and LUM (see **Table 3**) in samples of protein extracts from human brain tissue (see **Figure 3B**). We isolated protein out of the brain samples using 300 μl Triton buffer containing 0.2% protease and 0.2% phosphatase inhibitors. The brain solutions were incubated on ice for 30 min. After centrifuging at 13,000 rpm and 4°C for 5 min, we diluted the solutions to 1 ml with Triton buffer to ensure that we could perform all ELISAs. Subsequently, we decanted the supernatant and measured the protein concentration with a Bradford assay. The analysis was performed using a microplate

TABLE 2 | Samples for mechanical testing and ELISA.

Anatomical region		Number of mechanical samples	Number of ELISA samples
Cortex	C	15	15
Thalamus	TH	4	4
Basal ganglia	BG	14	14
Amygdala	AMY	3	3
Corona radiata	CR	19	19
Corpus callosum	CC	10	5
Brainstem	BS	15	12
Cerebellar white matter	cWM	5	5
Deep cerebellar nuclei	cNC	1	1



spectrophotometer (ELISA-reader) at a wavelength of 450 and 405 nm for measuring the absorbance. The received optical density results for the standard dilutions were then utilized to create standard curves using the software MARS Data Analysis from BMG Labtech and the 4- or 5-parameter best fit. By comparing with the standard series and the determined values for antigen concentration (protein concentration), we calculated the content of the protein in ng/total protein in mg in each sample.

2.2 Viscoelastic Constitutive Artificial Neural Network

Constitutive artificial neural networks (CANNs) have recently been introduced as a novel machine learning architecture and

shown to be a powerful tool for using machine learning for mechanical constitutive modeling (Linka et al., 2021). To empower them to deal with brain tissue, we use herein an extension that combines a standard CANN for the quasi-elastic response to loading (i.e., on very short time scales) with an additional, parallel deep neural network computing so-called Prony parameters accounting for the time-dependent stress relaxation observed in viscoelastic materials. In the following, we discuss the technical details of this architecture under the assumption that brain tissue can be modeled as a quasi-linear viscoelastic incompressible isotropic material.

2.2.1 Constitutive Artificial Neural Networks

To reduce the amount of training data required to learn the mechanical constitutive behavior of materials, CANNs exploit the

role of symmetries in materials theory. For the simple special case of incompressible isotropic materials, on which we focus herein, this means that CANNs capture the constitutive behavior of materials via a deep neural network mapping the first (I_1) and second (I_2) principal invariants

$$I_1 = \text{tr}(\mathbf{C}), \quad I_2 = \frac{1}{2} [(\text{tr} \mathbf{C})^2 - \text{tr} \mathbf{C}^2], \quad (1)$$

of the right Cauchy-Green deformation tensor $\mathbf{C} = \mathbf{F}^T \mathbf{F}$ on the strain energy

$$\Psi(\mathbf{C}) = \Psi(I_1, I_2). \quad (2)$$

Here, \mathbf{F} denotes the deformation gradient. The first and second Piola-Kirchhoff stress tensors \mathbf{P}_0 and \mathbf{S}_0 can be obtained in this setting simply by symbol-to-symbol automatic differentiation of the output Ψ of the neural network. We note that the first Piola-Kirchhoff stress tensor \mathbf{P}_0 corresponds to the nominal stress recorded during the experiments described in section 2.1.2. An important feature of CANNs is that their input is formed not only by invariants of the deformation state but also by any kind of additional quantities potentially carrying information about the constitutive behavior of the material of interest. In our case, these additional quantities are the 11 parameters measured in our experiments by ELISAs (see **Figure 3** and section 2.1.3). This architecture enables CANNs to learn not only how to resemble stress-strain curves of brain tissue but also to predict such curves from ELISAs, as discussed in more detail in Linka et al. (2021).

2.2.2 History Dependence

The response to loading of viscoelastic materials is in general governed not only by the current loading but also by the loading history. Skipping herein the complex theory of general nonlinear viscoelastic materials, we adopt the theory of quasi-linear viscoelasticity as introduced by Y. C. Fung in particular for biological tissues (Fung, 2013). This theory allows stress to depend nonlinearly both on strain and time. However, it assumes that the role of strain and time can be separated by a multiplicative split. While this limits the generality of the theory, it has been found that many biological materials of interest can be modeled at least in very good approximation as quasi-linear viscoelastic

materials. Within this setting, the history-dependent stress can be expressed by the convolution integral

$$\mathbf{P} = \int_0^t g(t-s) \frac{\partial \mathbf{P}_0}{\partial s} ds, \quad (3)$$

where \mathbf{P}_0 denotes the quasi-elastic stress response (i.e., on very short time scales) of a material under a Heaviside strain as approximated by a CANN, and g is a kernel function characterizing stress relaxation over time t . In this work, we assume a Prony-type kernel function (Taylor et al., 2009)

$$g(t) = g_0 + \sum_{i=1}^p g_i \exp\left[-\frac{t}{\tau_i}\right] \quad (4)$$

with scalar weighting coefficients g_i with a partition of unity property

$$g_0 + \sum_{i=1}^p g_i = 1 \quad (5)$$

and relaxation time constants τ_i . The set of Prony parameters is denoted herein by

$$\nu = \{g_0, g_1, \tau_1, g_2, \tau_2, \dots\}. \quad (6)$$

The stress response \mathbf{P} can be split into a long-term elastic and a transient viscoelastic contribution as

$$\mathbf{P} = g_0 \mathbf{P}_0 + \underbrace{\sum_{i=1}^p \int_0^t g_i \exp\left[-\frac{t}{\tau_i}\right] \frac{d\mathbf{P}_0}{ds} ds}_{h_i} \quad (7)$$

with the i -th history integral $h_i(t)$. Following Goh et al. (2004), this formula can be used to evaluate the current stress \mathbf{P} over time t efficiently in a time-discrete setting with time points t^n by the pair of recursive formulae

$$\begin{aligned} \mathbf{P}(t^{n+1}) &= g_0 \mathbf{P}_0(t^{n+1}) + \sum_{i=1}^p h_i(t^{n+1}), \\ h_i(t^{n+1}) &= \exp(-\Delta t/\tau_i) h_i(t^n) + g_i \frac{1 - \exp(-\Delta t/\tau_i)}{\Delta t/\tau_i} \\ &\quad [\mathbf{P}_0(t^{n+1}) - \mathbf{P}_0(t^n)]. \end{aligned} \quad (8)$$

TABLE 3 | Proteins investigated by ELISA.

Investigated protein		Manufacturer	Cat. nr	ELISA type	Detection range [ng/ml]
Glial fibrillary acidic protein	GFAP	Cloud-Clone	SEA068Hu	sandwich	0.156–10
Ionized calcium-binding adapter molecule 1	Iba1	Cloud-Clone	SEC288Hu	sandwich	0.0312–2
Myelin basic protein	MBP	Cloud-Clone	SEA539Hu	sandwich	0.156–10
Hyaluronic acid	HA	Cusabio	CSB-E04805h	sandwich	0.156–10
Chondroitin sulfate	CS	Cloud-Clone	CEA723Ge	competitive	0.03906–10
Lumican	LUM	Cloud-Clone	SEB496Hu	sandwich	0.312–20
Collagen I	Col I	Cloud-Clone	SEA571Hu	sandwich	0.156–10
Collagen IV	Col IV	Cloud-Clone	SEA180Hu	sandwich	7.8–500
Collagen VI	Col VI	Cloud-Clone	SED123Hu	sandwich	0.78–50
Fibronectin	FN	Cloud-Clone	SEA037Hu	sandwich	1.56–100
Laminin	LA	Cloud-Clone	SEA082Hu	sandwich	7.8–500

Altogether, the extended type of CANN used herein computes the quasi-elastic stress response P_0 of the materials and its Prony parameters by two separate, parallel deep neural networks. Subsequently, it computes the time-dependent current stress using Eq. (8), as illustrated in Figure 3. Note that the dependence of the stress response on the 11 ELISA values is learned by the viscoelastic CANN. In agreement with previous studies (Prange and Margulies, 2002; Budday et al., 2015a; Budday et al., 2017b), we used $p = 2$ Prony terms in our machine learning architecture.

2.2.3 Model Training and Hyperparameter Tuning

To train our viscoelastic CANNs, we used Adam optimization Kinga and Adam, (2015) for minimizing the mean-squared-error (MSE) loss function

$$\text{MSE} = \sum_i |P_{zz}^i - P_{\text{exp}}^i|^2. \quad (9)$$

Here, P_{zz}^i is the stress component in loading direction as computed by our viscoelastic CANN and P_{exp}^i is the corresponding experimentally observed value. The index i loops through all experimentally collected stretch-stress tuples included in the training process. Our whole framework was implemented using Keras with TensorFlow backend (Chollet, 2015; Abadi et al., 2020). We used Glorot weight initialization (Glorot and Bengio, 2010) at the beginning of the training and fixed the learning rate at 0.001 during the training of different layers. Training was performed with 250 data pairs in each iteration (also referred to as batch size), which was chosen corresponding to the amount of cyclic stress-stretch data points of a single tissue specimen. Before starting the actual training, we performed a hyperparameter tuning for the network topology, dropout rate, L2-regularization and the activation functions using a Bayesian optimization with a Gaussian process model (Mockus, 1994; Chollet, 2015). This tuning was performed on cyclic loading data of one representative tissue specimen. It led to a CANN architecture with three hidden layers with (32, 32, 48) computational units (neurons) with hyperbolic tangent activation functions, an elu activation function (Clevert et al., 2015) for the output, and a dropout layer after the first hidden layer with a rate of 0.5. For the network computing the Prony parameters, hyperparameter tuning resulted in a single hidden layer with 12 computational units and a sigmoid activation function.

Leave-one-out cross validation (LOO-CV) was used to train the model on the full range of available cyclic loading data. Here, the number of evaluation folds is equal to the number of samples in the data set ($N = 86$). Accordingly, each model was first trained based on $N - 1$ data sets, and then the trained model was applied to the single left out validation sample to evaluate the ability of the trained neural network to generalize (predict). In this way, each individual sample was used for one particular model training as validation sample. Each model instance was trained for 4,000 epochs, and the epoch with the best validation set accuracy was chosen for evaluation purposes to prevent overfitting that might occur after too many epochs. More details on training and

validation are provided in the supplementary materials *Model Training and Validation*.

For validation of our trained machine-learning model, we computed for the validation sample the coefficient of determination

$$R^2 = 1 - (S_{\text{res}}/S_{\text{tot}}), \quad \text{with} \quad S_{\text{res}} = \sum_i (P_{\text{exp}}^i - P_{11}^i)^2, \\ S_{\text{tot}} = \sum_i \left(P_{\text{exp}}^i - \bar{P}_{\text{exp}} \right)^2, \quad (10)$$

where \bar{P}_{exp} is the mean of the experimental data points.

2.2.4 Layer-wise Relevance Propagation

A primary goal of this work is the evaluation of the impact of the different compositional parameters measured by the ELISAs on the mechanical properties. To this end, we use the concept of layer-wise relevance propagation. It is a method from the research area of explainable artificial intelligence and particularly suitable for deep neural networks, which map some input through a series of layers to an output layer. The l th layer consists of computational units (neurons) passing the values x_i^l to the next layer, where i is the index of the neuron within layer l . The propagation of values from layer $l - 1$ to layer l can in general be described by

$$z_{ij}^l = w_{ij}^l x_i^{l-1}, \quad z_j^l = \sum_i z_{ij}^l + b_j^l, \quad x_j^l = n_j^l(z_j^l). \quad (11)$$

Here w_{ij}^l is the weight connecting the neuron i in layer $l - 1$ with neuron j in layer l ; z_j^l is the input neuron j in layer l receives from all neurons of the previous layer plus the bias b_j^l of this neuron; x_j^l is the output this neuron passes to the neurons on the subsequent layer after application of its in general nonlinear activation function n_j^l .

Within this general setting, layer-wise relevance propagation aims at tracing back a given output to individual components of the input layer of the deep neural network. To this end, it starts at the output layer. Then it recursively computes the relevance score R_i^{l-1} of all neurons i in layer $l - 1$ from known relevance scores R_j^l of the neurons j in layer l , see also Figure 4. In this procedure, the relevance R_j^l is propagated backwards from layer l to layer $l - 1$ by dividing it into relevance contributions $R_{i \leftarrow j}^{l-1, l}$ for each neuron i in layer $l - 1$, observing the conservation property

$$\sum_i R_{i \leftarrow j}^{l-1, l} = R_j^l. \quad (12)$$

The relevance of neuron i in layer $l - 1$ is then generally computed as

$$R_i^{l-1} = \sum_j R_{i \leftarrow j}^{l-1, l}. \quad (13)$$

The key of such relevance propagation schemes is the formula by which the relevance contributions $R_{i \leftarrow j}^{l-1, l}$ propagated from layer l back to layer $l - 1$ are computed. Herein, we follow Bach et al. (2015) and define

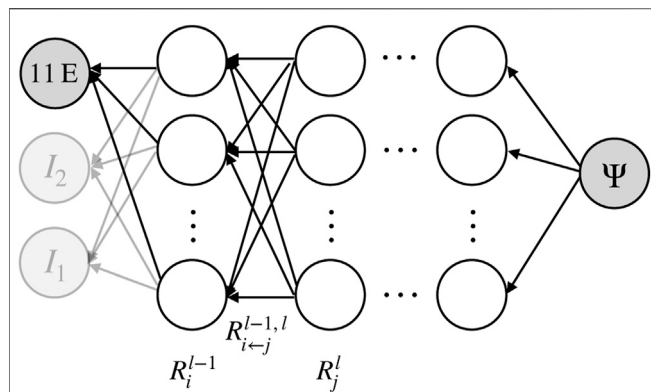


FIGURE 4 | Illustration of layer-wise (backwards) relevance propagation in a CANN. In a trained neural network, recursive application of this scheme from the output layer to the input layer can quantify the relevance of the individual input parameters such as the ELISA values for the output. Neurons are illustrated as empty circles, weights as black arrows.

$$R_{i \leftarrow j}^{l-1, l} = R_j^l \left[\alpha \frac{z_{ij}^{l+}}{z_j^{l+}} + \beta \frac{z_{ij}^{l-}}{z_j^{l-}} \right] \quad (14)$$

where the superscripts $-$ and $+$ denote the negative and positive parts of z_{ij}^l and b_j^l . For example, if $z_j^l \geq 0$, then $z_j^{l+} = z_j^l$ and $z_j^{l-} = 0$. By contrast, if $z_j^l < 0$, then $z_j^{l+} = 0$ and $z_j^{l-} = z_j^l$. α and β are coefficients partitioning unity and weighting the positive and negative parts.

In our relevance analysis we included only the training samples of training folds where $R^2 \geq 0.7$ was reached for the validation sample to guarantee a high model accuracy and, thus, a high reliability of the relevance analysis itself. Our machine learning architecture consists of a standard CANN block and an additional deep neural network block for the computation of the Prony parameters. We performed our relevance analysis separately for both blocks. In both cases, we quantified the relevance of the 11 ELISA values. For the entire relevance analysis we used $\alpha = 2$ and $\beta = -1$ in (14).

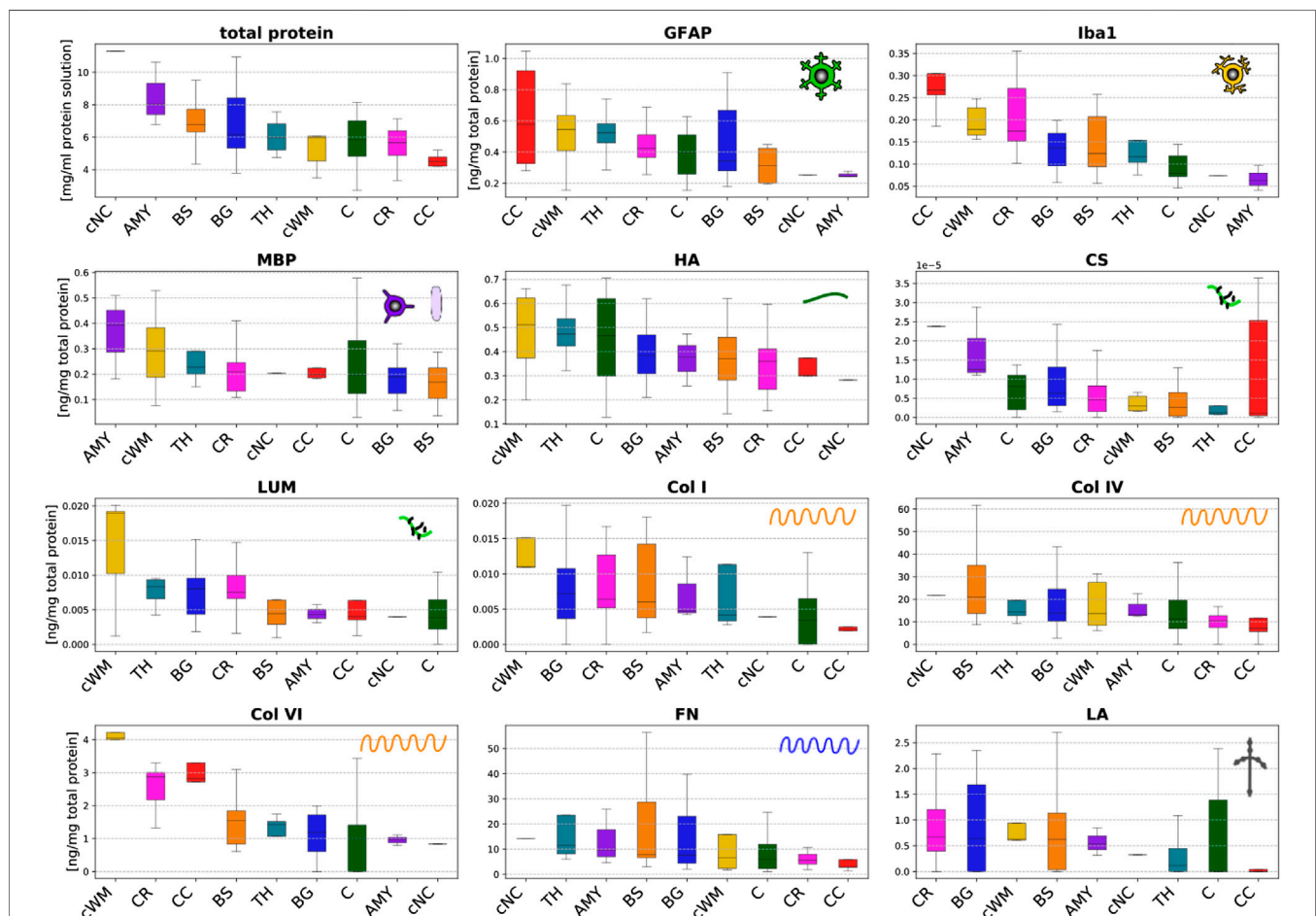
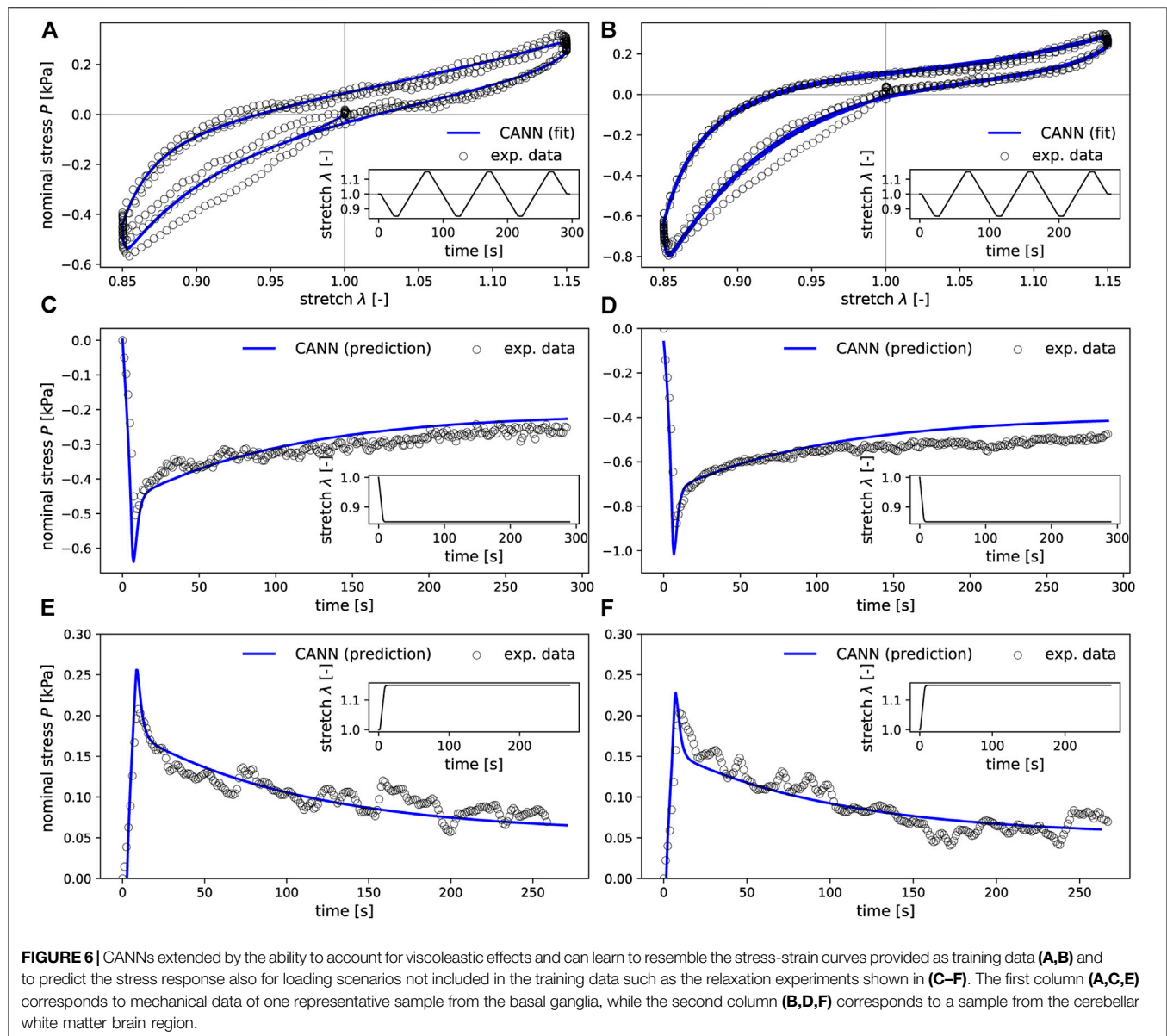


FIGURE 5 | Total protein content (upper left) and protein mass fractions of 11 species (glial fibrillary acidic protein (GFAP), microglia- and macrophage-specific protein Iba1 (Iba1), myelin basic protein (MBP), hyaluronic acid (HA), chondroitin sulfate (CS), lumican (LUM), collagen I (Col I), collagen IV (Col IV), collagen VI (Col VI), fibronectin (FN), and laminin (LA)) evaluated by ELISAs in 9 different brain regions (cortex (C), thalamus (TH), basal ganglia (BG), amygdala (AMY), cerebellar white matter (CWM), corpus callosum (CC), brainstem (BS), cerebellar white matter (cWM), and deep cerebellar nuclei (cNC)).



3 RESULTS

3.1 Regional Microstructural Components Quantified Through ELISA

Figure 5 summarizes the total protein content (per millimeter solution) and the results of the ELISAs reported in nanogram per microgram total protein for the different brain regions specified in **Figure 1A**. The total protein content quantifies the amount of proteins per milliliter solution. It ranges from 1 to 11.5 mg/ml solution. We note that these absolute values do not necessarily refer to how much proteins are present in different brain regions as they represent the protein content per milliliter solution but not the protein content per milligram tissue.

The ELISA results vary significantly for the different microstructural components introduced in **Figure 2**, and range

from extremely small values on the order of 10^{-5} ng/mg total protein for chondroitin sulfate to values of up to 60 ng/mg total protein for collagen IV and fibronectin. Interestingly, the content of cellular proteins (GFAP, MBP, Iba1) is rather small compared to specific extracellular proteins (FN, Col IV).

The glial fibrillary acidic protein (GFAP) values quantifying the amount of the hallmark intermediate filament protein in astrocytes lie in the range of 0.1–1.1 ng/mg total protein. The GFAP concentration is highest in the corpus callosum, thalamus and cerebellar white matter, while it is lowest in the amygdala and deep cerebellar nuclei. The amount of GFAP in the brainstem is relatively low compared to all other white matter regions. The values for the microglia- and macrophage-specific protein Iba1 range from 0.04 to 0.35 ng/mg total protein. The amount of Iba1 is generally higher in white matter than in gray matter

regions. The brainstem shows a lower content than other white matter regions, while the corpus callosum has the highest content of Iba1. The myelin basic protein (MBP) concentration lies in the range of 0.02–0.54 ng/mg total protein. It is highest in the amygdala and lowest in the brainstem. Most regions, including both gray and white matter, show a value of approximately 0.2 ng/mg total protein.

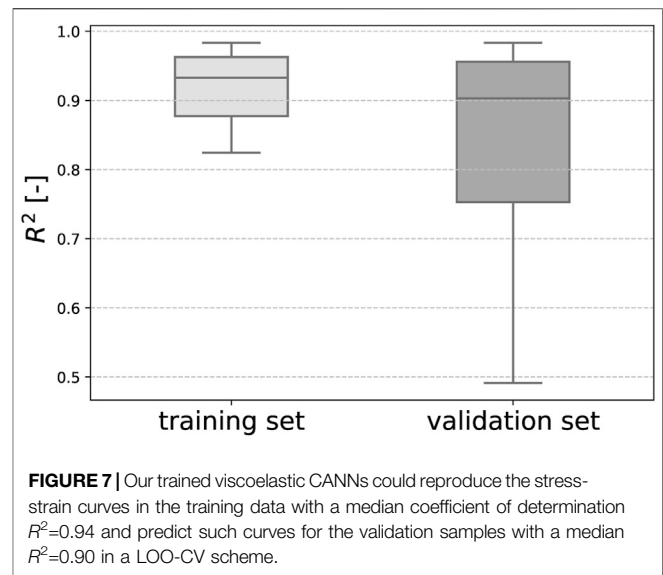
The hyaluronic acid (HA) content ranges from 0.13 to 0.71 ng/mg total protein. In the cerebrum, gray matter regions (TH, C, BG, AMY) have a higher amount of HA than white matter regions (BS, CR, CC). In the cerebellum, we observe the opposite trend with a higher HA value for the cerebellar white matter than the deep cerebellar nuclei. The amount of the proteoglycan chondroitin sulfate is at least two orders of magnitude lower than for all other proteins. Despite the exception of the thalamus with a relatively low value, gray matter regions have a higher content of chondroitin sulfate than white matter regions. The concentration of the proteoglycan lumican ranging from 0.002 to 0.032 ng/mg total protein is higher than for chondroitin sulfate but still low. Collagen I was the only fibrillar collagen we analyzed in the current work. Its content varies between 0 and 0.015 ng/mg total protein with highest values in the cerebellar white matter and lowest in the corpus callosum. Our results show that the most abundant collagen type in brain tissue is the non-fibrillar collagen IV with concentrations ranging from 0 to 62 ng/mg total protein. The collagen IV concentrations are higher in deep gray matter, the brainstem and the cerebellum than in the cortex, corona radiata, and corpus callosum. Collagen VI, another non-fibrillar collagen type, shows concentrations ranging from 0 to 4.3 ng/mg total protein. The collagen VI content is consistently higher in white than in gray matter regions. The fibronectin content ranges from 1 to 58 ng/mg total protein, similar to collagen IV. It also shows a similar regional distribution as collagen IV with lowest values for the cortex, corona radiata, and corpus callosum. The concentration of laminin lies between 0 and 2.7 ng/mg total protein.

3.2 Performance of Viscoelastic CANNs

In the training process, the neural networks employed in our study learned to resemble the stress-stretch curves provided as training data. Representative examples are depicted in **Figures 6A, B**. Moreover, the trained networks were able to predict the stress response of relaxation experiments not included in the training data, as shown in **Figures 6C–F**. Once trained for each fold in the LOO-CV scheme, the neural networks could reproduce the stress-stretch curves of the training data with a median coefficient of determination $R^2 = 0.94$ (standard deviation 0.24) and predict such curves for the validation samples with $R^2 = 0.90$ (standard deviation of ± 0.51), see **Figure 7**.

3.3 Relevance Analysis Revealing the Link Between Mechanics and Microstructure

Figure 8 illustrates the relevance (quantified through the backward pass in the viscoelastic CANN) of different



microstructural components (quantified through ELISAs) for the quasi-elastic (**Figure 8A**) and viscoelastic (**Figure 8B**) contributions of the complex mechanical response of brain tissue. Fibronectin has the highest relevance for both the quasi-elastic response and viscoelastic effects. Concerning the quasi-elastic response, fibronectin is—with a certain distance—followed by Iba1 associated with microglia, the extracellular matrix proteins laminin and hyaluronic acid, as well as MBP associated with myelination of nerve fibers. Our results further suggest that collagen IV and GFAP slightly affect the quasi-elastic tissue response, while the influence of collagen VI, collagen I, lumican, and chondroitin sulfate seems to be negligible.

Concerning viscoelastic effects, interestingly all cellular components, quantified through GFAP (astrocytes), MBP (myelin, oligodendrocytes), and Iba1 (microglia), have the highest relevance after fibronectin. In addition, the extracellular matrix components collagen VI and hyaluronic acid seem to affect the viscoelastic behavior of brain tissue. We note that we find the lowest relevance for collagen IV, which is actually the protein with the highest amount per total protein, as illustrated in **Figure 5**. But, it appears to be irrelevant for the viscoelastic response of the tissue.

3.3.1 Regional Trends for the Quasi-Elastic Stress Response

Figure 9 displays the relevance of the different ELISA values for the quasi-elastic stress response in each brain region. The cortex and thalamus show a similar sequence. In the basal ganglia, laminin has a higher relevance than in all other gray matter regions, but the general trends are the same. In general, the relevance of Iba1 is higher for white matter than for gray matter regions. Furthermore, in all white matter regions (CR, CC, cWM) with the exception of the brainstem, GFAP shows a higher relevance than in gray matter regions. We observe that laminin has a relatively high relevance of approximately 1.2 in

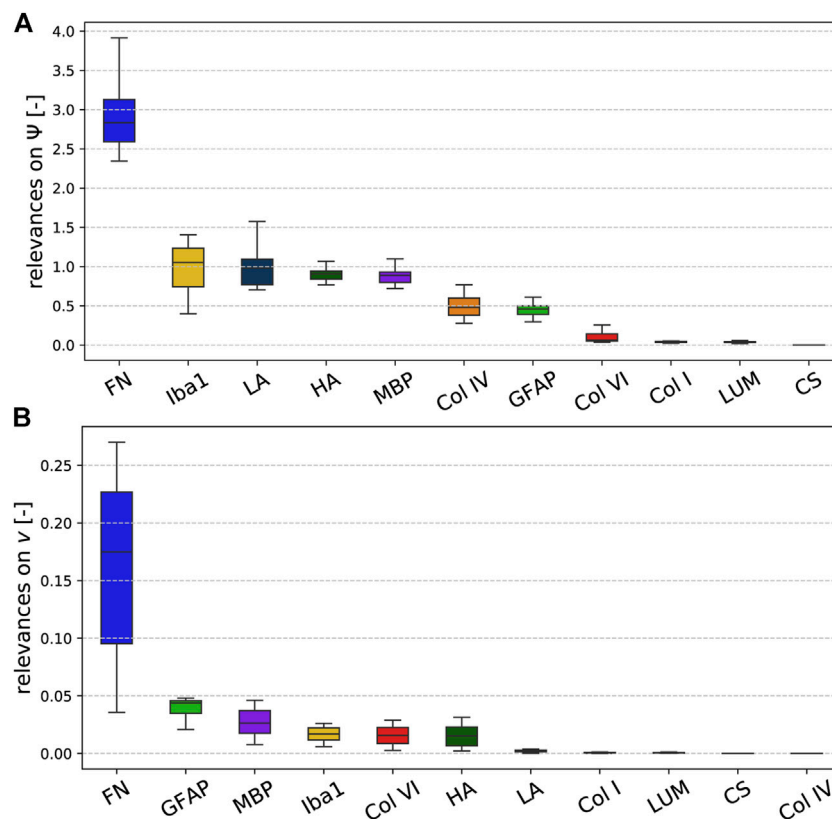


FIGURE 8 | Relevance of the ELISA values for the (A) quasi-elastic stress response on very short time scales (governed by Ψ) and (B) viscoelastic effects (governed by the Prony series parameters collected in the set v).

the corona radiata and cerebellar white matter. The relevance of hyaluronic acid lies on the order of 1 for the cerebral gray matter regions and cerebellar white matter, and around 0.5 for cerebral white matter regions and deep cerebellar nuclei. Interestingly, the only region, where fibronectin does not have the highest relevance, is the corpus callosum; here, Iba1 seems to control the quasi-elastic tissue response.

3.3.2 Regional Trends for Viscoelastic Effects

Figure 10 displays the relevance of the different ELISA values for the viscoelastic behavior in each brain region. The regional trends are more diverse than for the quasi-elastic stress response in Figure 9. In different orders, MBP, hyaluronic acid, GFAP, Iba1, and fibronectin are most relevant for viscoelastic effects in gray matter regions. In cerebral white matter regions (CR, CC, BS), especially GFAP and Iba1 appear to play an important role. In addition, MBP, hyaluronic acid, and collagen VI show a certain relevance.

4 DISCUSSION

In this study, we have combined mechanical large-strain compression and tension experiments (cyclic loading and stress relaxation) with microstructural investigations using

enzyme-linked immunosorbent assays (ELISA) and an extended type of constitutive artificial neural network (CANN) that can account for viscoelastic effects to identify the link between the microstructural composition and complex mechanical response of human brain tissue.

4.1 Insights Into the Regional Microstructural Composition of Brain Tissue

To quantify the tissue composition in different regions of the human brain (see Figure 1), we have used ELISAs for selected cellular (GFAP - astrocytes, Iba1 - microglia, MBP - oligodendrocytes/myelin sheaths) and extracellular (hyaluronic acid, chondroitin sulfate, lumican, collagen I/IV/VI, fibronectin, laminin) proteins. The amount of cellular proteins was relatively low compared to certain extracellular components, which can be attributed to the fact that the investigated proteins only represent part of the cell. For instance, the myelin basic protein (MBP) represents 25–30% of all myelin proteins (Deber and Reynolds, 1991), and quantifies only part of the oligodendrocytes and myelin sheaths. We found MBP to be present in both gray and white matter regions. Interestingly, the MBP concentration was lowest in the brainstem. The microglia- and macrophage-specific protein Iba1 was more abundant in white

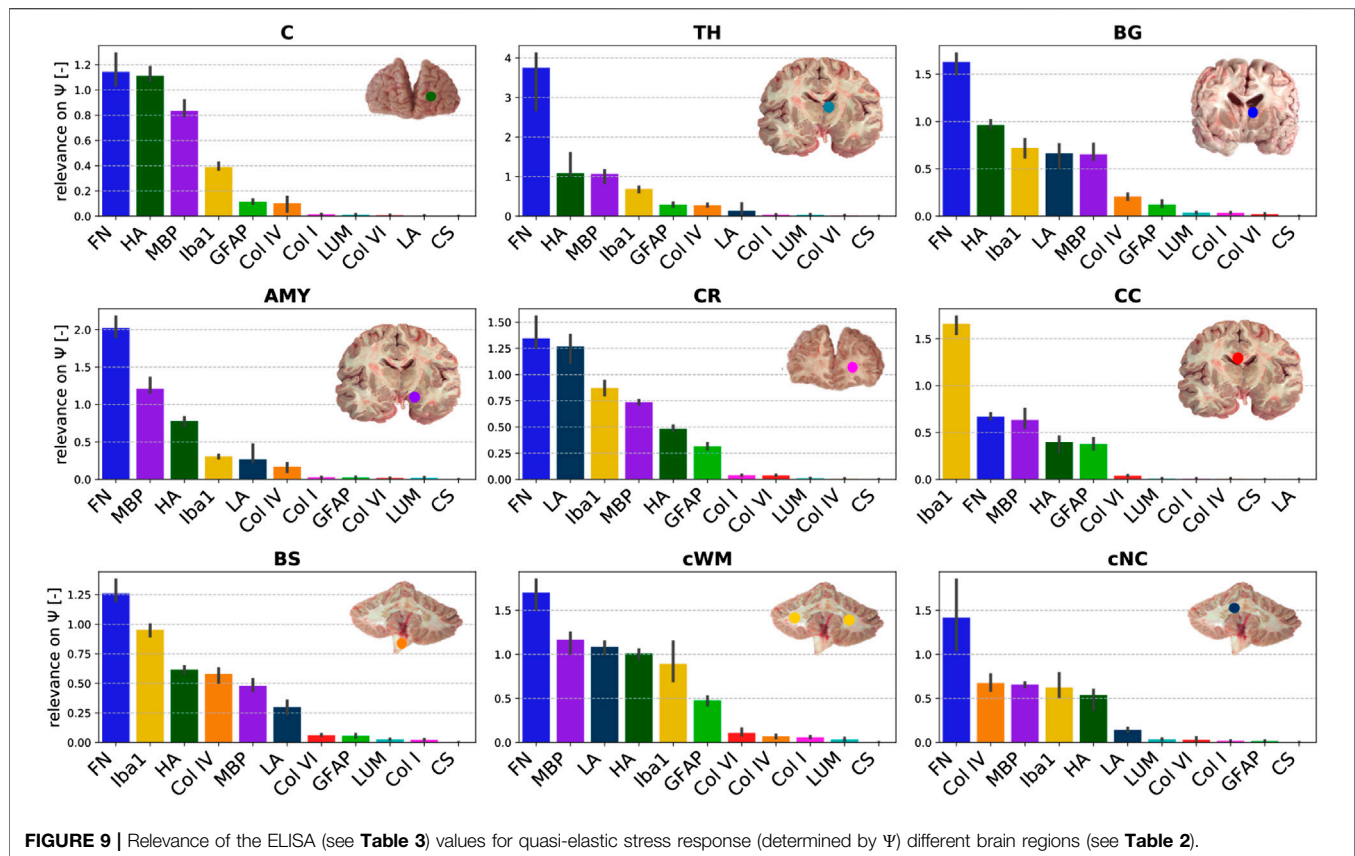


FIGURE 9 | Relevance of the ELISA (see Table 3) values for quasi-elastic stress response (determined by Ψ) different brain regions (see Table 2).

matter than gray matter regions. This agrees well with a previous study reporting slightly higher densities of microglia in white matter tissue of different mammals (Dos Santos et al., 2020). Similar to Iba1, the astrocyte-specific protein GFAP was highest in the corpus callosum and the cerebellar white matter and lowest in the amygdala and cerebellar nuclei. The brainstem showed a significantly lower concentration of GFAP than all other white matter regions but was in the same range as the analyzed gray matter regions. This may be related to the fact that our brainstem samples included various small gray matter regions, such as the red nucleus and the substantia nigra in the midbrain, the pontine nuclei in the pons, and the medullary reticular formation and inferior olive in the medulla.

Overall, the most abundant proteins were fibronectin and collagen IV—both extracellular matrix components. Fibronectin is produced by endothelial cells, pericytes, and macrophages, and is predominant in perineural nets (Wang et al., 2011), as schematically illustrated in Figure 2. The high content of collagen IV agrees with findings in the literature reporting that collagen IV takes up about 50% of the basement membrane (Kim et al., 2018). Interestingly, the variation in the fibronectin and collagen IV content between different brain regions was relatively low, both having the lowest concentrations for tissue from the corpus callosum. Collagen VI was more abundant in white matter than gray matter regions with the highest content in the cerebellar white matter, closely followed by corona radiata and corpus callosum. For tissue from the cerebrum, hyaluronic acid (HA)

showed the opposite trend with higher concentrations in gray matter than in white matter regions. This may be attributed to the fact that HA is an important component of perineuronal nets (see also Figure 2) that help regulate neuronal activity. In white matter, HA is more diffusely distributed around astrocytes and oligodendrocytes (Sherman et al., 2015).

The proteoglycan chondroitin sulfate appeared to be more abundant in the amygdala and the cerebellar nuclei than in all other brain regions—although its content was generally extremely low. In the amygdala, chondroitin sulfate is an important component of perineuronal nets (Pantazopoulos et al., 2008), and abnormalities in the chondroitin sulfate content are related to disorders like schizophrenia (Pantazopoulos et al., 2015). Similar to the proteoglycans, the concentration of fibrillar collagen I is particularly low in all brain regions, which is related to the ultrasoft mechanical response of brain tissue (Barnes et al., 2017).

4.2 Link Between Microstructural Composition and Macromechanical Properties

To quantify the mechanical properties of human brain tissue, we have introduced an extended type of CANN that incorporates substantial prior knowledge from materials theory and viscoelastic effects. It was able to learn the complex mechanical response of human brain tissue with a high accuracy over a large range of stress-stretch states. Moreover,

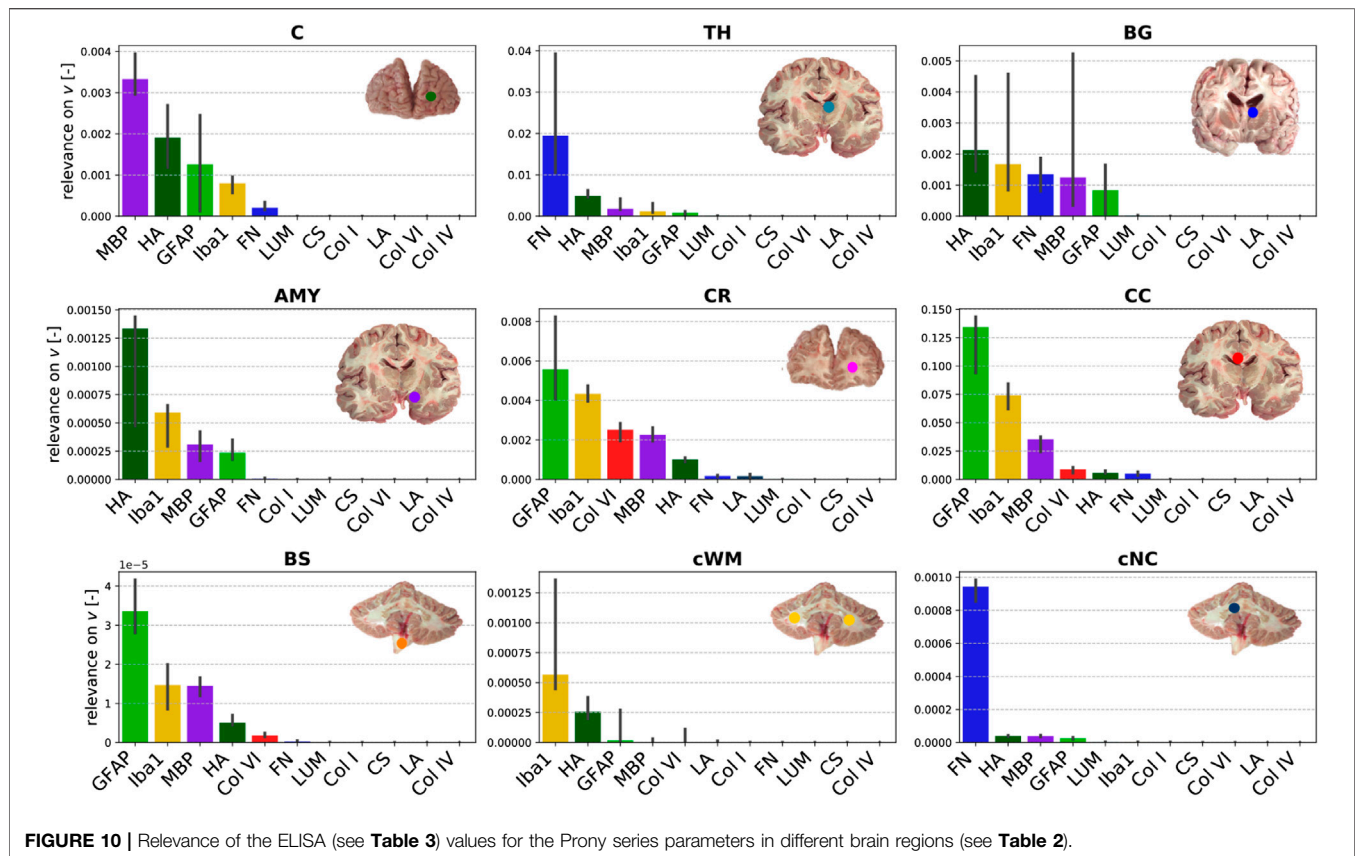


FIGURE 10 | Relevance of the ELISA (see **Table 3**) values for the Prony series parameters in different brain regions (see **Table 2**).

it learned to predict the mechanical behavior of brain tissue from the 11 constituent concentrations measured through ELISAs. A layer-wise relevance propagation analysis allowed us to quantify the importance of the 11 individual constituent concentrations for the complex mechanical response.

The results of this analysis suggest that the content of fibronectin is by far the most relevant of the examined features for both the quasi-elastic stress response to loading and viscoelastic effects. This may be attributed to the fact that fibronectin forms fibrillar networks, which provide mechanical support. Interestingly, in a recent study on somite formation during embryogenesis, the fibronectin matrix was specifically perturbed to tune tissue mechanics (de Almeida et al., 2019). It has further been shown that the amount of fibronectin decreases in the aging brain (Syková et al., 1998; Wang et al., 2011), which may thus crucially contribute to the observed softening of brain tissue with age (Sack et al., 2009). Our results further indicate that the elastic tissue response is especially controlled by extracellular matrix proteins that are part of the basement membrane (Eriksdotter-Nilsson et al., 1986; Abhijit and Yao, 2019), i.e., fibronectin, laminin and collagen IV. Therefore, we suppose that the degree of vascularization plays an important role for brain stiffness, not least because we expect a higher stiffness for blood vessels compared to the brain parenchyma. It has been shown that both fibronectin and laminin are upregulated after traumatic brain injury (George and Geller, 2018). In addition, increased collagen IV and

fibronectin signals were observed during ischemia (Michalski et al., 2020). This motivates the hypothesis that, in the future, altered mechanical properties could serve as a potential biomarker for such disorders. In addition to basement membrane proteins, hyaluronic acid (HA) appears to be relevant for the quasi-elastic tissue response. This agrees well with the general notion that HA plays the main structural role in the formation of the brain extracellular matrix (Bignami et al., 1993). Interestingly, HA appeared to be even more relevant for the elastic than for the viscoelastic response of brain tissue, which is surprising considering its hydrophilic nature.

The most relevant cellular protein for the quasi-elastic response is Iba1, which is specific to microglia and macrophages. Interestingly, microglia have been shown to preferably migrate towards stiffer regions (Bollmann et al., 2015). This could explain why the presence of microglia correlates with local mechanical tissue properties. The additional relevance of the cellular protein MBP also agrees well with previous findings showing that brain tissue stiffness correlates with myelin content (Weickenmeier et al., 2016; Weickenmeier et al. 2017b).

Viscoelastic effects seem to depend in particular on all cellular proteins, GFAP, MBP and Iba1, even though the absolute quantities of these proteins were rather low in all samples. This observation also agrees with our previous findings (Reiter et al., 2021), where we could show that the network of intercellular connections behaves viscoelastically. Interestingly,

GFAP showed a higher relevance for the viscoelastic than for the quasi-elastic response of the tissue, which further supports the importance of the cellular network for brain viscoelasticity. In addition to fibronectin and cellular proteins, collagen VI showed a certain relevance, which we attribute to its ability to interact with fibrils and cells suggesting that it takes part in the viscoelastic network.

Despite the relatively high content of collagen IV in brain tissue, it is only moderately relevant for the quasi-elastic response and has the lowest relevance of all investigated proteins for the viscoelastic response. This demonstrates the effectiveness of the chosen approach using the backward pass through the viscoelastic CANN to evaluate the relevance of different microstructural components for complex brain tissue mechanics. The proteoglycans lumican and chondroitin sulfate and the fibrillar collagen I generally have only a very low influence on the mechanical properties of the tissue. They also exhibit the lowest concentrations.

4.3 Regional Differences in the Relevance of Constituents for Tissue Mechanics

When comparing the relation between composition and mechanical response of the tissue in different brain regions, we observe that relevances for the quasi-elastic tissue response are relatively insensitive towards the brain region. The only region that deviates from the highest relevance of fibronectin is the corpus callosum. Here, Iba1 seems to largely control the quasi-elastic tissue response. This might be related to the regional heterogeneity of microglia in the brain, where a different gene expression pattern was observed for the corpus callosum than for all other brain regions (Tan et al., 2020). Interestingly, GFAP is especially relevant in the corona radiata and corpus callosum—for the viscoelastic relaxation additionally in the brainstem—indicating that reactive astrocytes may significantly contribute to the mechanical response in these regions. Laminin was only relevant for the quasi-elastic response of the corona radiata, cerebellar white matter, basal ganglia, amygdala, and brainstem. In these regions, it was also most abundant. While fibronectin had a high relevance for the quasi-elastic response in all regions, it was also relevant for viscoelastic effects in gray matter regions. In general, we found that the regional trends were much more diverse for viscoelastic effects than for the quasi-elastic response. For instance, MBP was identified as most relevant in the cortex, fibronectin in the thalamus and cerebellar nuclei, HA in basal ganglia and amygdala, GFAP in cerebral white matter and the brainstem, and Iba1 in cerebellar white matter.

4.4 Implications for Microstructure-informed Constitutive Modeling

Independent of the brain region, fibronectin, HA, MBP, and Iba1 have a notable relevance for the quasi-elastic tissue response. Therefore, these constituents should be considered when developing refined microstructure-based material models for brain tissue in the future. We note, however, that ELISAs can

only be performed *post mortem* or when tissue is surgically resected. Consequently, one may consider other techniques, potentially also *in vivo* imaging, to quantify the distribution of the constituents relevant for brain mechanics. Despite the relatively high content of collagen IV, our results indicate that its relevance for tissue mechanics is negligible. This could be attributed to the fact that collagen IV is a non-fibrillar collagen type. Also, fibrillar collagen I, which has previously been incorporated in material models for arteries (Gasser et al., 2006) or cartilage (Linka and Itskov, 2016), plays a negligible role for brain tissue mechanics as its concentration is very low.

With regard to viscoelastic effects, the most relevant constituents of the tissue seem to be Iba1, HA, MBP, and GFAP. As the relevance of the different proteins varied notably between different brain regions, it may be necessary to introduce region-specific constitutive models. According to our results, it might even be expedient to introduce different regional classifications for the quasi-elastic and viscoelastic contributions.

4.5 Limitations

As the samples for the ELISA analyses were extracted between 12 and 72 (brains 1 and 2) or 12 and 26 (brains 3–5) hours *post mortem*, some of the investigated proteins could already have degraded (Fountoulakis et al., 2001) and the mechanical response of the tissue could differ from the *in vivo* situation. When comparing the samples taken from the five human brains investigated here, which all reached our lab after different *post mortem* times, we did not detect noticeable differences in the protein content or mechanical response. Therefore, we anticipate that at least the comparison of the different brains and brain regions is reasonable. Here we focused on the relevance of different components on tissue mechanics and the comparison of different brain regions rather than only on determining the content of the individual proteins in the human brain.

4.6 Future Directions

In the future, we will further evaluate the predictive capabilities of the extended CANN framework. Potentially, it could be used to predict disease- or injury-related changes in tissue properties based on ELISA results performed on tissue extracted during a biopsy. In addition, it will be interesting to use a similar approach to predict the complex mechanical response of human brain tissue based on *in vivo* imaging data. In terms of the relation between microstructure and mechanics in the human brain, the next step is to not only consider the total amount of microstructural components, but also their morphology and three-dimensional arrangement. Concerning cellular components, it may be more reliable to quantify the number of nuclei instead of the concentration of GFAP and Iba1, which only represent part of the cell. In addition, we will consider the contribution of neurons and their connectivity.

5 CONCLUSION

In this study, we have followed a new paradigm by combining large-strain mechanical testing, enzyme-linked immunosorbent assays (ELISA), continuum mechanics theory and machine

learning techniques to reveal the relation between human brain tissue composition and its mechanical properties. We introduced a viscoelastic constitutive artificial neural network model and were able to capture the mechanical response of the tissue during cyclic compression - tension experiments, and to predict the response during stress relaxation in compression and tension. By including the specimen-specific ELISA results into the network to model the mechanical response, and subsequently evaluating the backward pass through the viscoelastic CANN, we were able to reveal the relevance of the local tissue composition on the corresponding nonlinear and viscoelastic mechanical response. We have assessed the individual contribution of several cellular (GFAP, Iba1, MBP) and extracellular (hyaluronic acid, chondroitin sulfate, lumican, collagen I/IV/VI, fibronectin, laminin) proteins and evaluated region-dependent trends. Our results suggest that the extracellular matrix protein fibronectin has the highest overall relevance for both the elastic and viscous behavior of human brain tissue. While the quasi-elastic response seems to be largely controlled by extracellular matrix proteins from the basement membrane, cellular components have a higher importance for the viscoelastic effects. The tissue components relevant for the quasi-elastic response (fibronectin, hyaluronic acid, MBP, Iba1) are relatively insensitive towards the brain region. In contrast, regional trends for viscoelastic effects are more diverse. GFAP has a high relevance for white matter regions in the cerebrum and brainstem, and hyaluronic acid for most gray matter regions. Our results can have important implications for the development of microstructure-informed constitutive models to predict the regional behavior of brain tissue in finite element simulations. The latter promise to become a useful tool in assisting diagnosis and treatment of diseases or preventing injury. In addition, the relation between human brain tissue composition and mechanical properties facilitates the design of biomaterials for neural tissue engineering and 3D printing applications, where the investigated extracellular components could be valuable to enhance the biocompatibility and properties of matrix materials.

DATA AVAILABILITY STATEMENT

The ELISA results and mechanical data presented in the study are included in the article/**Supplementary Material**, further inquiries can be directed to the corresponding author.

REFERENCES

- Abadi, M., Agarwal, A., Barham, P., Brevdo, E., Chen, Z., Citro, C., et al. (2020). TensorFlow: Large-Scale Machine Learning on Heterogeneous Systems. Available at: tensorflow.org.
- Alafuzoff, I. (2018). "Techniques in Neuropathology," in *Handbook of Clinical Neurology* (Elsevier), 3–7. doi:10.1016/b978-0-12-802395-2.00001-8
- Antonovaite, N., Beekmans, S. V., Hol, E. M., Wadman, W. J., and Iannuzzi, D. (2018). Regional Variations in Stiffness in Live Mouse Brain Tissue Determined by Depth-Controlled Indentation Mapping. *Sci. Rep.* 8, 12517. doi:10.1038/s41598-018-31035-y
- Bach, S., Binder, A., Montavon, G., Klauschen, F., Müller, K.-R., and Samek, W. (2015). On Pixel-wise Explanations for Non-linear Classifier Decisions by Layer-wise Relevance Propagation. *PloS one* 10, e0130140. doi:10.1371/journal.pone.0130140
- Barnes, J. M., Przybyla, L., and Weaver, V. M. (2017). Tissue Mechanics Regulate Brain Development, Homeostasis and Disease. *J. Cel. Sci.* 130, 71–82. doi:10.1242/jcs.191742
- Barriga, E. H., Franze, K., Charras, G., and Mayor, R. (2018). Tissue Stiffening Coordinates Morphogenesis by Triggering Collective Cell Migration *In Vivo*. *Nature* 554, 523–527. doi:10.1038/nature25742

ETHICS STATEMENT

The studies involving human participants were reviewed and approved by the Ethics Committee of the Friedrich-Alexander University Erlangen-Nürnberg, Germany, approval number 405_18 B. The participants provided their written informed consent to donate their body to research.

AUTHOR CONTRIBUTIONS

KL and SB conceptualized the study. FP, LB, and MS provided human brain tissue, supervised the microstructural analyses and contributed to the interpretation of the results. JW together with MS performed the ELISAs and analyzed the corresponding data. NR performed the mechanical measurements and analyzed the corresponding data. KL designed, implemented and analyzed the viscoelastic CANNs used herein. CJC contributed to their development. NR and SB interpreted the results. KL and SB prepared the Figures. KL, NR, and SB wrote the first draft. SB supervised the project and acquired funding. All authors discussed the results and contributed to the final manuscript.

FUNDING

We gratefully acknowledge the funding by the Deutsche Forschungsgemeinschaft (DFG, German Research Foundation) through the grant BU 3728/1-1 to SB and the Emerging Fields Initiative by the Friedrich-Alexander University Erlangen-Nürnberg to SB and FP.

ACKNOWLEDGMENTS

We cordially thank Anke Fischer-Gößwein und Maike Hemmerlein for their valuable help with the ELISAs as well as Lisa Stache for preparing the human brains.

SUPPLEMENTARY MATERIAL

The Supplementary Material for this article can be found online at: <https://www.frontiersin.org/articles/10.3389/fbioe.2021.704738/full#supplementary-material>

- Begonia, M. T., Prabhu, R., Liao, J., Horstemeyer, M. F., and Williams, L. N. (2010). The Influence of Strain Rate Dependency on the Structure-Property Relations of Porcine Brain. *Ann. Biomed. Eng.* 38, 3043–3057. doi:10.1007/s10439-010-0072-9
- Bellail, A. C., Hunter, S. B., Brat, D. J., Tan, C., and Van Meir, E. G. (2004). Microregional Extracellular Matrix Heterogeneity in Brain Modulates Glioma Cell Invasion. *Int. J. Biochem. Cel Biol.* 36, 1046–1069. doi:10.1016/j.biocel.2004.01.013
- Bignami, A., Hosley, M., and Dahl, D. (1993). Hyaluronic Acid and Hyaluronic Acid-Binding Proteins in Brain Extracellular Matrix. *Anat. Embryol.* 188, 419–433. doi:10.1007/bf00190136
- Bilston, L. E., Liu, Z., and Phan-Thien, N. (2001). Large Strain Behaviour of Brain Tissue in Shear: Some Experimental Data and Differential Constitutive Model. *Biorheol.* 38, 335–345.
- Blumenthal, N. R., Hermanson, O., Heimrich, B., and Shastri, V. P. (2014). Stochastic Nanoroughness Modulates Neuron-Astrocyte Interactions and Function via Mechanosensing Cation Channels. *Proc. Natl. Acad. Sci. USA* 111, 16124–16129. doi:10.1073/pnas.1412740111
- Bollmann, L., Koser, D. E., Shahapure, R., Gautier, H. O. B., Holzapfel, G. A., Scarcelli, G., et al. (2015). Microglia Mechanics: Immune Activation Alters Traction Forces and Durotaxis. *Front. Cel. Neurosci.* 9, 363. doi:10.3389/fncel.2015.00363
- Budday, S., and Kuhl, E. (2020). Modeling the Life Cycle of the Human Brain. *Curr. Opin. Biomed. Eng.* 15, 16–25. doi:10.1016/j.cobme.2019.12.009
- Budday, S., Nay, R., de Rooij, R., Steinmann, P., Wyrobek, T., Ovaert, T. C., et al. (2015a). Mechanical Properties of gray and white Matter Brain Tissue by Indentation. *J. Mech. Behav. Biomed. Mater.* 46, 318–330. doi:10.1016/j.jmbbm.2015.02.024
- Budday, S., Ovaert, T. C., Holzapfel, G. A., Steinmann, P., and Kuhl, E. (2020a). Fifty Shades of Brain: A Review on the Mechanical Testing and Modeling of Brain Tissue. *Arch. Computat Methods Eng.* 27, 1187–1230. doi:10.1007/s11831-019-09352-w
- Budday, S., Sarem, M., Starck, L., Sommer, G., Pfeifferle, J., Phunchago, N., et al. (2020b). Towards Microstructure-Informed Material Models for Human Brain Tissue. *Acta Biomater.* 104, 53–65. doi:10.1016/j.actbio.2019.12.030
- Budday, S., Sommer, G., Birkel, C., Langkammer, C., Haybaeck, J., Kohnert, J., et al. (2017a). Mechanical Characterization of Human Brain Tissue. *Acta Biomater.* 48, 319–340. doi:10.1016/j.actbio.2016.10.036
- Budday, S., Sommer, G., Haybaeck, J., Steinmann, P., Holzapfel, G. A., and Kuhl, E. (2017b). Rheological Characterization of Human Brain Tissue. *Acta Biomater.* 60, 315–329. doi:10.1016/j.actbio.2017.06.024
- Budday, S., Steinmann, P., and Kuhl, E. (2015b). Physical Biology of Human Brain Development. *Front. Cel. Neurosci.* 9, 257. doi:10.3389/fncel.2015.00257
- Chatelin, S., Constantinesco, A., and Willinger, R. (2010). Fifty Years of Brain Tissue Mechanical Testing: from *In Vitro* to *In Vivo* Investigations. *Biorheol.* 47, 255–276. doi:10.3233/bir-2010-0576
- Chollet, F. (2015). Keras. <https://github.com/fchollet/keras>.
- Clevert, D.-A., Unterthiner, T., and Hochreiter, S. (2015). Fast and Accurate Deep Network Learning by Exponential Linear Units (Elus). *arXiv preprint*, arXiv:1511.07289.
- Dabbs, D. (2014). *Diagnostic Immunohistochemistry: Theranostic and Genomic Applications*. Philadelphia, PA: Elsevier/Saunders.
- Deber, C. M., and Reynolds, S. J. (1991). Central Nervous System Myelin: Structure, Function, and Pathology. *Clin. Biochem.* 24, 113–134. doi:10.1016/0009-9120(91)90421-a
- Dos Santos, S. E., Medeiros, M., Porfirio, J., Tavares, W., Pessôa, L., Grinberg, L., et al. (2020). Similar Microglial Cell Densities across Brain Structures and Mammalian Species: Implications for Brain Tissue Function. *J. Neurosci.* 40, 4622–4643. doi:10.1523/jneurosci.2339-19.2020
- Eriksson-Nilsson, M., Björklund, H., and Olson, L. (1986). Laminin Immunohistochemistry: a Simple Method to Visualize and Quantitate Vascular Structures in the Mammalian Brain. *J. Neurosci. Methods* 17, 275–286. doi:10.1016/0165-0270(86)90128-7
- Fountoulakis, M., Hardmeier, R., Höger, H., and Lubec, G. (2001). Postmortem Changes in the Level of Brain Proteins. *Exp. Neurol.* 167, 86–94. doi:10.1006/exnr.2000.7529
- Franze, K., Janmey, P. A., and Guck, J. (2013). Mechanics in Neuronal Development and Repair. *Annu. Rev. Biomed. Eng.* 15, 227–251. doi:10.1146/annurev-bioeng-071811-150045
- Fung, Y. C. (2013). *Biomechanics: Mechanical Properties of Living Tissues*. Springer Science & Business Media.
- Gan, S. D., and Patel, K. R. (2013). Enzyme Immunoassay and Enzyme-Linked Immunosorbent Assay. *J. Invest. Dermatol.* 133, e12. doi:10.1038/jid.2013.287
- Garcia, K. E., Kroenke, C. D., and Bayly, P. V. (2018). Mechanics of Cortical Folding: Stress, Growth and Stability. *Phil. Trans. R. Soc. B* 373, 20170321. doi:10.1098/rstb.2017.0321
- Gasser, T. C., Ogden, R. W., and Holzapfel, G. A. (2006). Hyperelastic Modelling of Arterial Layers with Distributed Collagen Fibre Orientations. *J. R. Soc. Interf.* 3, 15–35. doi:10.1098/rsif.2005.0073
- George, N., and Geller, H. M. (2018). Extracellular Matrix and Traumatic Brain Injury. *J. Neuro Res.* 96, 573–588. doi:10.1002/jnr.24151
- Gerischer, L. M., Fehlner, A., Köbe, T., Prehn, K., Antonenko, D., Grittner, U., et al. (2018). Combining Viscoelasticity, Diffusivity and Volume of the hippocampus for the Diagnosis of Alzheimer's Disease Based on Magnetic Resonance Imaging. *NeuroImage: Clin.* 18, 485–493. doi:10.1016/j.nicl.2017.12.023
- Glorot, X., and Bengio, Y. (2010). “Understanding the Difficulty of Training Deep Feedforward Neural Networks,” in *Proceedings of the Thirteenth International Conference on Artificial Intelligence and Statistics*, 249–256.
- Goh, S. M., Charalambides, M. N., and Williams, J. G. (2004). Determination of the Constitutive Constants of Non-linear Viscoelastic Materials. *Mech. Time-Dependent Mater.* 8, 255–268. doi:10.1023/b:mtmd.0000046750.65395.fe
- Gomes de Almeida, P., Rifes, P., Martins-Jesus, A. P., Pinheiro, G. G., Andrade, R. P., and Thorsteinsdóttir, S. (2019). Fibronectin-dependent Tissue Mechanics Regulate the Translation of Segmentation Clock Oscillations into Periodic Somite 1790 Formation. *bioRxiv preprint*. doi:10.1101/808121
- Goriely, A., Geers, M. G. D., Holzapfel, G. A., Jayamohan, J., Jérusalem, A., Sivaloganathan, S., et al. (2015). Mechanics of the Brain: Perspectives, Challenges, and Opportunities. *Biomech. Model. Mechanobiol.* 14, 931–965. doi:10.1007/s10237-015-0662-4
- Hemphill, M. A., Dauth, S., Yu, C. J., Dabiri, B. E., and Parker, K. K. (2015). Traumatic Brain Injury and the Neuronal Microenvironment: A Potential Role for Neuropathological Mechanotransduction. *Neuron* 85, 1177–1192. doi:10.1016/j.neuron.2015.02.041
- Humphrey, J. D., Dufresne, E. R., and Schwartz, M. A. (2014). Mechanotransduction and Extracellular Matrix Homeostasis. *Nat. Rev. Mol. Cel Biol.* 15, 802–812. doi:10.1038/nrm3896
- Irianto, J., Pfeifer, C. R., Xia, Y., and Discher, D. E. (2016). Snapshot: Mechanosensing Matrix. *Cell* 165, 1820. doi:10.1016/j.cell.2016.06.002
- Keating, C. E., and Cullen, D. K. (2021). Mechanosensation in Traumatic Brain Injury. *Neurobiol. Dis.* 148, 105210. doi:10.1016/j.nbd.2020.105210
- Kihan Park, K., Lonsberry, G. E., Gearing, M., Levey, A. I., and Desai, J. P. (2018). Viscoelastic Properties of Human Autopsy Brain Tissues as Biomarkers for Alzheimer's Diseases. *IEEE Trans. Biomed. Eng.* 66, 1705–1713. doi:10.1109/TBME.2018.2878555
- Kim, Y., Meade, S. M., Chen, K., Feng, H., Rayyan, J., Hess-Dunning, A., et al. (2018). Nano-architectural Approaches for Improved Intracortical Interface Technologies. *Front. Neurosci.* 12, 456. doi:10.3389/fnins.2018.00456
- Kinga, D. P., and Ba, J. (2014). Adam: A method for Stochastic Optimization. *arXiv preprint*, arXiv:1412.6980.
- Koser, D. E., Thompson, A. J., Foster, S. K., Dwivedy, A., Pillai, E. K., Sheridan, G. K., et al. (2016). Mechanosensing Is Critical for Axon Growth in the Developing Brain. *Nat. Neurosci.* 19, 1592–1598. doi:10.1038/nn.4394
- Lau, L. W., Cua, R., Keough, M. B., Haylock-Jacobs, S., and Yong, V. W. (2013). Pathophysiology of the Brain Extracellular Matrix: a New Target for Remyelination. *Nat. Rev. Neurosci.* 14, 722–729. doi:10.1038/nrn3550
- Liang, L., Liu, M., and Sun, W. (2017). A Deep Learning Approach to Estimate Chemically-Treated Collagenous Tissue Nonlinear Anisotropic Stress-Strain Responses from Microscopy Images. *Acta Biomater.* 63, 227–235. doi:10.1016/j.actbio.2017.09.025
- Linka, K., Hillgärtner, M., Abdolazizi, K. P., Aydin, R. C., Itskov, M., and Cyron, C. J. (2021). Constitutive Artificial Neural Networks: A Fast and General Approach to Predictive Data-Driven Constitutive Modeling by Deep Learning. *J. Comput. Phys.* 429, 110010. doi:10.1016/j.jcp.2020.110010

- Linka, K., and Itskov, M. (2016). Mechanics of Collagen Fibrils: A Two-Scale Discrete Damage Model. *J. Mech. Behav. Biomed. Mater.* 58, 163–172. doi:10.1016/j.jmbbm.2015.08.045
- Meaney, D. F., Morrison, B., and Dale Bass, C. (2014). The Mechanics of Traumatic Brain Injury: a Review of what We Know and what We Need to Know for Reducing its Societal burden. *J. Biomech. Eng.* 136, 021008. doi:10.1115/1.4026364
- Michalski, D., Spielvogel, E., Puchta, J., Reimann, W., Barthel, H., Nitzsche, B., et al. (2020). Increased Immunoreactions of Collagen IV and Fibronectin Indicate Ischemic Consequences for the Neurovascular Matrix Adhesion Zone in Various Animal Models and Human Stroke Tissue. *Front. Physiol.* 11, 575598. doi:10.3389/fphys.2020.575598
- Miller, K., and Chinzei, K. (1997). Constitutive Modelling of Brain Tissue: experiment and Theory. *J. Biomech.* 30, 1115–1121. doi:10.1016/s0021-9290(97)00092-4
- Miller, K., and Chinzei, K. (2002). Mechanical Properties of Brain Tissue in Tension. *J. Biomech.* 35, 483–490. doi:10.1016/s0021-9290(01)00234-2
- Mockus, J. (1994). Application of Bayesian Approach to Numerical Methods of Global and Stochastic Optimization. *J. Glob. Optim.* 4, 347–365. doi:10.1007/bf01099263
- Moshayedi, P., da F Costa, L., Christ, A., Lacour, S. P., Fawcett, J., Guck, J., et al. (2010). Mechanosensitivity of Astrocytes on Optimized Polyacrylamide Gels Analyzed by Quantitative Morphometry. *J. Phys. Condens. Matter* 22, 194114. doi:10.1088/0953-8984/22/19/194114
- Moshayedi, P., Ng, G., Kwok, J. C. F., Yeo, G. S. H., Bryant, C. E., Fawcett, J. W., et al. (2014). The Relationship between Glial Cell Mechanosensitivity and Foreign Body Reactions in the central Nervous System. *Biomaterials* 35, 3919–3925. doi:10.1016/j.biomaterials.2014.01.038
- Murphy, M. C., Jones, D. T., Jack, C. R., Jr, Glaser, K. J., Senjem, M. L., Manduca, A., et al. (2016). Regional Brain Stiffness Changes across the Alzheimer's Disease Spectrum. *NeuroImage: Clin.* 10, 283–290. doi:10.1016/j.nicl.2015.12.007
- Nirwane, A., and Yao, Y. (2019). Laminins and Their Receptors in the Cns. *Biol. Rev.* 94, 283–306. doi:10.1111/brv.12454
- Novak, U., and Kaye, A. H. (2000). Extracellular Matrix and the Brain: Components and Function. *J. Clin. Neurosci.* 7, 280–290. doi:10.1054/jocn.1999.0212
- Oohashi, T., Edamatsu, M., Bekku, Y., and Carulli, D. (2015). The Hyaluronan and Proteoglycan Link Proteins: Organizers of the Brain Extracellular Matrix and Key Molecules for Neuronal Function and Plasticity. *Exp. Neurol.* 274, 134–144. doi:10.1016/j.expneurol.2015.09.010
- Pantazopoulos, H., Markota, M., Jaquet, F., Ghosh, D., Wallin, A., Santos, A., et al. (2015). Aggrecan and Chondroitin-6-Sulfate Abnormalities in Schizophrenia and Bipolar Disorder: a Postmortem Study on the Amygdala. *Transl. Psychiatry* 5, e496. doi:10.1038/tp.2014.128
- Pantazopoulos, H., Murray, E. A., and Berretta, S. (2008). Total Number, Distribution, and Phenotype of Cells Expressing Chondroitin Sulfate Proteoglycans in the normal Human Amygdala. *Brain Res.* 1207, 84–95. doi:10.1016/j.brainres.2008.02.036
- Prange, M. T., and Margulies, S. S. (2002). Regional, Directional, and Age-dependent Properties of the Brain Undergoing Large Deformation. *J. Biomech. Eng.* 124, 244–252. doi:10.1115/1.1449907
- Prevost, T. P., Balakrishnan, A., Suresh, S., and Socrate, S. (2011). Biomechanics of Brain Tissue. *Acta Biomater.* 7, 83–95. doi:10.1016/j.actbio.2010.06.035
- Rashid, B., Destrade, M., and Gilchrist, M. D. (2012). Mechanical Characterization of Brain Tissue in Compression at Dynamic Strain Rates. *J. Mech. Behav. Biomed. Mater.* 10, 23–38. doi:10.1016/j.jmbbm.2012.01.022
- Rauch, U. (2004). Extracellular Matrix Components Associated with Remodeling Processes in Brain. *Cmls, Cel. Mol. Life Sci.* 61, 2031–2045. doi:10.1007/s00018-004-4043-x
- Reiter, N., Roy, B., Paulsen, F., and Budday, S. (2021). Insights into the Microstructural Origin of Brain Viscoelasticity. *J. Elasticity* 2021, 979. doi:10.1007/s10659-021-09814-y
- Sack, I., Beierbach, B., Wuerfel, J., Klatt, D., Hamhaber, U., Papazoglou, S., et al. (2009). The Impact of Aging and Gender on Brain Viscoelasticity. *Neuroimage* 46, 652–657. doi:10.1016/j.neuroimage.2009.02.040
- Samek, W., Montavon, G., Lapuschkin, S., Anders, C. J., and Müller, K.-R. (2021). Explaining Deep Neural Networks and beyond: A Review of Methods and Applications. *Proc. IEEE* 109, 247–278. doi:10.1109/JPROC.2021.3060483
- Sherman, L. S., Matsumoto, S., Su, W., Srivastava, T., and Back, S. A. (2015). Hyaluronan Synthesis, Catabolism, and Signaling in Neurodegenerative Diseases. *Int. J. Cel Biol.* 2015, 1–10. doi:10.1155/2015/368584
- Syková, E., Mazel, T., and Šimonová, Z. (1998). Diffusion Constraints and Neuron-Glia Interaction during Aging. *Exp. Gerontol.* 33, 837–851. doi:10.1016/s0531-5565(98)00038-2
- Tan, Y.-L., Yuan, Y., and Tian, L. (2020). Microglial Regional Heterogeneity and its Role in the Brain. *Mol. Psychiatry* 25, 351–367. doi:10.1038/s41380-019-0609-8
- Taylor, C. R., and Levenson, R. M. (2006). Quantification of Immunohistochemistry?issues Concerning Methods, Utility and Semiquantitative Assessment II. *Histopathol.* 49, 411–424. doi:10.1111/j.1365-2559.2006.02513.x
- Taylor, Z. A., Comas, O., Cheng, M., Passenger, J., Hawkes, D. J., Atkinson, D., et al. (2009). On Modelling of Anisotropic Viscoelasticity for Soft Tissue Simulation: Numerical Solution and Gpu Execution. *Med. image Anal.* 13, 234–244. doi:10.1016/j.media.2008.10.001
- Thompson, A. J., Pillai, E. K., Dimov, I. B., Foster, S. K., Holt, C. E., and Franze, K. (2019). Rapid Changes in Tissue Mechanics Regulate Cell Behaviour in the Developing Embryonic Brain. *eLife* 8, e39356. doi:10.7554/eLife.39356
- Tyler, W. J. (2012). The Mechanobiology of Brain Function. *Nat. Rev. Neurosci.* 13, 867–878. doi:10.1038/nrn3383
- Urbanski, M. M., Kingsbury, L., Moussouros, D., Kassim, I., Mehjabeen, S., Paknejad, N., et al. (2016). Myelinating Glia Differentiation Is Regulated by Extracellular Matrix Elasticity. *Sci. Rep.* 6, 33751. doi:10.1038/srep33751
- Wang, J., Yin, L., and Chen, Z. (2011). New Insights into the Altered Fibronectin Matrix and Extrasynaptic Transmission in the Aging Brain. *J. Clin. Gerontol. Geriatr.* 2, 35–41. doi:10.1016/j.jcgg.2010.12.002
- Weickenmeier, J., Butler, C. A. M., Young, P. G., Goriely, A., and Kuhl, E. (2017a). The Mechanics of Decompressive Craniectomy: Personalized Simulations. *Comp. Methods Appl. Mech. Eng.* 314, 180–195. doi:10.1016/j.cma.2016.08.011
- Weickenmeier, J., de Rooij, R., Budday, S., Ovaert, T. C., and Kuhl, E. (2017b). The Mechanical Importance of Myelination in the central Nervous System. *J. Mech. Behav. Biomed. Mater.* 76, 119–124. doi:10.1016/j.jmbbm.2017.04.017
- Weickenmeier, J., de Rooij, R., Budday, S., Steinmann, P., Ovaert, T. C., and Kuhl, E. (2016). Brain Stiffness Increases with Myelin Content. *Acta Biomater.* 42, 265–272. doi:10.1016/j.actbio.2016.07.040
- Yang, P.-C., and Mahmood, T. (2012). Western Blot: Technique, Theory, and Trouble Shooting. *North. Am. J. Med. Sci.* 4, 429. doi:10.4103/1947-2714.100998
- Zarzor, M. S., Kaessmair, S., Steinmann, P., Blümcke, I., and Budday, S. (2021). A Two-Field Computational Model Couples Cellular Brain Development with Cortical Folding. *Brain Multiphysics* 2, 100025. doi:10.1016/j.brain.2021.100025

Conflict of Interest: The authors declare that the research was conducted in the absence of any commercial or financial relationships that could be construed as a potential conflict of interest.

Publisher's Note: All claims expressed in this article are solely those of the authors and do not necessarily represent those of their affiliated organizations, or those of the publisher, the editors and the reviewers. Any product that may be evaluated in this article, or claim that may be made by its manufacturer, is not guaranteed or endorsed by the publisher.

Copyright © 2021 Linka, Reiter, Würges, Schicht, Bräuer, Cyron, Paulsen and Budday. This is an open-access article distributed under the terms of the Creative Commons Attribution License (CC BY). The use, distribution or reproduction in other forums is permitted, provided the original author(s) and the copyright owner(s) are credited and that the original publication in this journal is cited, in accordance with accepted academic practice. No use, distribution or reproduction is permitted which does not comply with these terms.



An Overview of the Effectiveness of Bicycle Helmet Designs in Impact Testing

Javid Abderezaei^{1†}, Fargol Rezayaraghi^{1†}, Brigit Kain^{2†}, Andrea Menichetti³ and Mehmet Kurt^{1,4*}

¹Department of Mechanical Engineering, Stevens Institute of Technology, Hoboken, NJ, United States, ²Department of Biomedical Engineering, Stevens Institute of Technology, Hoboken, NJ, United States, ³Biomechanics Section, Mechanical Engineering Department, KU Leuven, Leuven, Belgium, ⁴BioMedical Engineering and Imaging Institute, Icahn School of Medicine at Mount Sinai, New York, NY, United States

OPEN ACCESS

Edited by:

Silvia Budday,
University of Erlangen Nuremberg,
Germany

Reviewed by:

Madelen Fahlstedt,
Royal Institute of Technology, Sweden
Fady Abayazid,
Imperial College London,
United Kingdom

*Correspondence:

Mehmet Kurt
mkurt@stevens.edu

[†]These authors have contributed
equally to this work

Specialty section:

This article was submitted to
Biomechanics,
a section of the journal
Frontiers in Bioengineering and
Biotechnology

Received: 31 May 2021

Accepted: 18 August 2021

Published: 27 September 2021

Citation:

Abderezaei J, Rezayaraghi F, Kain B,
Menichetti A and Kurt M (2021) An
Overview of the Effectiveness of
Bicycle Helmet Designs in
Impact Testing.
Front. Bioeng. Biotechnol. 9:718407.
doi: 10.3389/fbioe.2021.718407

Cycling accidents are the leading cause of sports-related head injuries in the US. Conventional bicycle helmets typically consist of polycarbonate shell over Expanded Polystyrene (EPS) foam and are tested with drop tests to evaluate a helmet's ability to reduce head kinematics. Within the last decade, novel helmet technologies have been proposed to mitigate brain injuries during bicycle accidents, which necessitates the evaluation of their effectiveness in impact testing as compared to conventional helmets. In this paper, we reviewed the literature to collect and analyze the kinematic data of drop test experiments carried out on helmets with different technologies. In order to provide a fair comparison across different types of tests, we clustered the datasets with respect to their normal impact velocities, impact angular momentum, and the type of neck apparatus. When we analyzed the data based on impact velocity and angular momentum clusters, we found that the bicycle helmets that used rotation damping based technology, namely MIPS, had significantly lower peak rotational acceleration (PRA) and Generalized Acceleration Model for Brain Injury Threshold (GAMBIT) as compared to the conventional EPS liner helmets ($p < 0.01$). SPIN helmets had a superior performance in PRA compared to conventional helmets ($p < 0.05$) in the impact angular momentum clustered group, but not in the impact-velocity clustered comparisons. We also analyzed other recently developed helmets that primarily use collapsible structures in their liners, such as WaveCel and Koroyd. In both of the impact velocity and angular momentum groups, helmets based on the WaveCel technology had significantly lower peak linear acceleration (PLA), PRA, and GAMBIT at low impact velocities as compared to the conventional helmets, respectively ($p < 0.05$). The protective gear with the airbag technology, namely Hövding, also performed significantly better compared to the conventional helmets in the analyzed kinematic-based injury metrics ($p < 0.001$), possibly due to its advantage in helmet size and stiffness. We also observed that the differences in the kinematic datasets strongly depend on the type of neck apparatus. Our findings highlight the importance and benefits of developing new technologies and impact testing

standards for bicycle helmet designs for better prevention of traumatic brain injury (TBI).

Keywords: bicycle helmets, concussion, traumatic brain injury, TBI, brain injury risk, mitigation system, impact biomechanics, drop test

1 INTRODUCTION

Traumatic brain injury (TBI) is a major cause of death and disability, affecting millions of people every year in the U.S. (Taylor et al., 2017). Sport-related TBIs which annually affects about 300,000 to 3.8 million people in the U.S. makes up a large portion of these TBI cases (Winkler et al., 2016; Taylor et al., 2017).

Even though contact sports such as football have amassed extensive attention from the public and media due to frequent reports of career-ending head injuries (Bland et al., 2020), cycling has contributed the highest number of sports-related head injuries (Coronado et al., 2015). The popularity of cycling has been increasing and the number of bicycle-related injuries (Sanford et al., 2015) and fatalities are growing, correspondingly (Fischer, 2017). According to the American Association of Neurological Surgeons, cycling injuries estimated 85,389 of the 446,788 sports-related head injuries reported in the emergency rooms in 2009 (Healy, 2015; AANS, 2018). Besides being a regular form of exercise or an enjoyable pastime for all age groups, cycling is often used as a daily means of transportation in dangerously crowded cities for many individuals which has made cycling-related head injuries a growing cause of concern nationwide.

In the U.S., a recent study found that only 22% of cyclists who sustained head and neck injuries were wearing helmets during the accident; an overwhelming 78% of cyclists were not wearing proper safety equipment for injury prevention (Scott et al., 2019). As of yet, bicycle helmets are the best strategy to protect the head against severe head and brain injuries (Crompton et al., 2014; Joseph et al., 2017; Olivier and Creighton, 2017; Høye, 2018). According to the Fatality Analysis Reporting System, 62% of cyclists killed in 2019 were not wearing a helmet, 15% were helmeted, and 23% were unknown (FARS, 2019). Therefore, substantial attention has been given to the design of protective equipment for cyclists (Sacks et al., 1991; Karkhanavaz et al., 2006). Over the years, bicycle helmet designs have employed similar approaches to combating TBIs and have consistently utilized similar, if not the same, materials. These helmets are usually made up of an external shell and a soft polymeric foam liner (Andena et al., 2016). Expanded Polystyrene (EPS) or Polypropylene (EPP) are common material that have been used in the inner liner (Andena et al., 2016). Traditional EPS liners are primarily designed and manufactured to dampen the impacts and reduce the head impact force (Stigson et al., 2017). conventional bicycle helmets have been shown to mitigate linear acceleration which is a requirement by bicycle helmet safety standards such as U.S. Consumer Product Safety Commission (CPSC), Australian and New Zealand Standard (AS/NZS 2063), EN 1078, Snell Memorial Foundation (e.g.

B95) and American Society for Testing and Materials (ASTM F1447) (Commission, 1998; Hansen et al., 2013; McIntosh et al., 2013). In these tests, helmets are placed on a headform and dropped onto a steel anvil coated with adhesive-backed 80-grit paper (Commission, 1998; Hansen et al., 2013; McIntosh et al., 2013; Bland, 2019; Bliven et al., 2019; Petersen et al., 2020). The head kinematics during the drop tests are then measured using accelerometers and gyroscopes, which are attached at the center of gravity of the headforms. As outlined in these mandatory safety standards, the linear acceleration of the headform should not exceed a certain threshold (i.e., 300 g outlined in CPSC, 1998, Snell B95 Cheung et al., 2004, and ASTM F1447 Chang, 2003, as well as 250 g outlined in AS/NZS 2512.1, 2009, and Sandberg et al., 2018, EN, 1078, 1997). However, cyclists often fall off their bicycles and impact their heads at angles that are not always direct and usually varies between 30° and 60° (Bourdet et al., 2012; Bourdet et al., 2014). These impacts not only can cause linear acceleration but can also result in rotational acceleration due to the tangential forces to the head (McIntosh et al., 2013; Willinger et al., 2019). Many studies have shown that the rotational acceleration or rotational velocity rather than the linear acceleration are responsible for causing large shear strains in the brain tissue, which could lead to strain concentration (Laksari et al., 2015; Laksari et al., 2018; Abderezaei et al., 2019; Laksari et al., 2020; Mojahed et al., 2020), and potentially result in mild TBI (Holbourn, 1943; Holbourn, 1944; Hardy et al., 2007; Post and Blaine Hoshizaki, 2015; Deck et al., 2019).

Recently, new technologies that are aimed towards mitigating the head's kinematics through rotation-damping systems have been introduced. These mitigation systems either include spherical slip interfaces (Bliven et al., 2019), and collapsible structures (Hansen et al., 2013; Stigson et al., 2017) in the liner structure, or use a new form of protective gear based on airbag technology (Kurt et al., 2017). Multi-directional Impact Protection System (MIPS) is a relatively new concept that introduces a slip liner inside the helmet; MIPS aims to mitigate rotational impact forces by allowing the head to slide relative to the helmet during the impact (Bottlang et al., 2020). Other technologies, such as WaveCel and Koroyd, utilize a collapsible cellular structure that absorbs the force of impact and minimizes the energy transferred to the cyclist's head (Hansen et al., 2013; Bliven et al., 2019). Although these advancements are opening the door to the future of cycling safety and TBI prevention, a robust and thorough evaluation of the effectiveness of these novel helmets in mitigating impacts is still incomplete. The aim of this paper is to perform a literature review in PubMed and SCOPUS databases and collect the kinematics of drop test experiments performed on bicycle helmets. We will investigate the kinematic-based injury metrics including peak linear acceleration (PLA), peak

TABLE 1 | Overview of the literature with relevant kinematic information of the bicycle helmet drop test experiments.

Study	Mitigation type	Headform model	Anvil angle (°)	Impact location	Impact velocity (m/s)	Number of side impact locations(s) ^b	Number of front impact locations(s) ^b
Mills and Gilchrist (2008)	Conventional	Ogle headform w/o the neck ^a	0	Side	4.5	1	1
Hansen et al. (2013)	Conventional, AIM	Magnesium ISO headform on the HIII neck	0, 30	Front	4.8	0	2
Cripton et al. (2014)	Conventional	HIII headform on the ball arm neck	0	Front	5.4, 6.3, 7.7	1	1
Stigson et al. (2017)	Conventional, MIPS, Hövding, Koroyd	HIII headform w/o the neck	45	Side, Front	6	1	1
Kurt et al. (2017)	Conventional, Hövding	NOCSAE headform on the rigid neck	0	Side	6	1	0
Bland et al. (2018a)	Conventional	NOCSAE or HIII headform with and w/o the HIII neck	45	Side, Front	6	1	1
Bland et al. (2018b)	Conventional, MIPS, Koroyd	NOCSAE headform on the HIII neck	30	Side	5.1, 6.6	1	0
Bland et al. (2018c)	Conventional, MIPS, Koroyd	Magnesium ISO headform on the ball arm neck	0	Side	3.4, 6.2	1	0
Bliven et al. (2019)	Conventional, MIPS, WaveCel	HIII headform on the HIII neck	30, 45, 60	Front	4.8, 6.2	0	3
Petersen et al. (2020)	Conventional	NOCSAE headform on the HIII neck	45	Side, Front	6.5	1	1
Bottlang et al. (2020)	Conventional, MIPS, SPIN, ODS	HIII headform on the HIII neck	45	Front	6.19	0	1
Abayazid et al. (2021)	Hövding, SPIN, WaveCel	HIII headform w/o the neck	45	Side, Front	6.3	2	1

^aThe Ogle headform in Mills and Gilchrist (2008) was connected to a partial neck which was considered in the no-neck group in our analysis.

^bShows the variation of impact locations on the side and front of the helmet.

rotational acceleration (PRA), and Generalized Acceleration Model for Brain Injury Threshold (GAMBIT) of each new mitigation technology as compared to the conventional helmets. Additionally, the effect of different drop test protocols such as anvil angle, headform position, presence or absence of the neck will be considered in the above analysis.

2 METHODS

2.1 Searching Methodologies and Data Collection

The articles retrieved from the electronic databases PubMed and SCOPUS were selected in a multi-step process. The following key terms were used for PubMed and SCOPUS respectively: 1- (helmet* AND (cycl* OR bicycle*) AND (drop test* OR impact test* OR impact pendulum test*)), 2- helmet* AND (cycl* OR bicycle*) AND ((drop test*) OR (impact test*) OR (impact pendulum test*)). After inputting the key terms into each database, the titles and abstracts of each article were manually screened to determine the relevance to the topic of bicycle helmet testing. After excluding irrelevant articles, the full text of each article was reviewed for the following exclusion criteria: 1) Does not perform bicycle helmet drop tests, 2) Does not specify the helmet model, 3) Does not test adult bicycle helmets, 4) Does not test side or front impact performance of the bicycle helmets (since these are the most common impact locations in real-life cycling accidents (Larsen, 1991)), 5) Does not have quantitative information about impact velocity of the drop test, 6) Does not provide quantitative information on kinematic parameters including PLA, and PRA.

The date of the last search was May 13, 2021, and the search was restricted to the English language. The inclusion criteria and data extraction of the papers were cross-checked by three independent reviewers.

Having identified all the relevant articles in the two databases, we retrieved the following information for each of the helmet tests from each paper: 1) Type of mitigation technology in the bicycle helmet, 2) PLA, PRA, and PRV, 3) Drop test impact velocity, 4) Anvil angle, 5) Headform model, 6) Presence or absence of the neck surrogate in the headform, 7) Impact location.

2.2 Types of Impact Mitigation Technologies in Bicycle Helmets

The helmets collected and analyzed in this paper were mainly organized into two different categories: 1) Conventional helmets, which only use one layer of EPS or Expanded Polypropylene (EPP) as a liner (**Table 1; Supplementary Table S1**). 2) Helmets with a mitigation system that use one of the following materials or technologies in the liner or the overall design: MIPS, *Shear Pad Inside* (SPIN), *Omni-Directional Suspension* (ODS), *WaveCel*, *Angular Impact Mitigation* (AIM), *Koroyd* and *Hövding* (**Table 1; Supplementary Table S1**).

Conventional bicycle helmets consist of three layers: an ABS plastic outer shell, an EPS or EPP foam liner, and an inner layer of soft foam padding. MIPS seeks to reduce rotational kinematics of the head by permitting sliding between the helmet and head during the impact (Halldin et al., 2003; Bliven et al., 2019; Bottlang et al., 2020). In these helmets, the slip liner that is

attached underneath the EPS layer allows for relative motion in all directions and aims to reduce the amount of energy transferred to an individual's head (Bottlang et al., 2020). SPIN is a technology that replaces comfort padding with silicone padding (Bottlang et al., 2020). These specially developed pads are placed in critical locations in the helmet under the EPS layer and can shear in any direction to produce the same effect as a moving slip liner (Bliven et al., 2019; Abayazid et al., 2021). ODS utilizes two EPS liners that are connected by an array of elastomeric dampers (Bottlang et al., 2020). The array of dampers is designed to support the EPS liners to isolate impact energy from the brain and deflect angular impacts (Bottlang et al., 2020). The collapsible structure mitigation systems we considered in this paper are WaveCel and Koroyd technologies. WaveCel is made from a cellular copolymer material that flexes and glides to absorb energy from impacts and redirect energy away from the head (Bliven et al., 2019; Abayazid et al., 2021). The V-shaped collapsible cellular structure is recessed within the helmet liners and provides rotational suspension (Bliven et al., 2019). Koroyd utilizes thousands of copolymer extruded tubes that are thermally welded together to create thermo-formed sheets of the helmet liner (Gokhale, 2016). The large compression volumes of the structures create a crumple zone that allows for minimal energy transfer to the head (Gokhale, 2016). AIM is another helmet that uses collapsible structure mitigation system. The AIM system is a non-commercially available cellular structure technology developed by (Hansen et al., 2013). The AIM system replaces EPS by an elastically suspended aluminum honeycomb liner between an inner and outer shell that absorbs linear and angular acceleration (Hansen et al., 2013; Bliven et al., 2019). The honeycomb structure creates a crumple zone that dissipates impact energy through in-plane deformation (Hansen et al., 2013). Additionally, we also considered Hövding, an expandable helmet that uses high-rate micro-electrical-mechanical sensors that can detect a collision and expand to protect the rider's head before impact (Kurt et al., 2017). Unlike most helmets, Hövding protective gear (all versions including 1, 2, and 3) employs air pressure as a means of protection rather than a typical foam padding (Kurt et al., 2017).

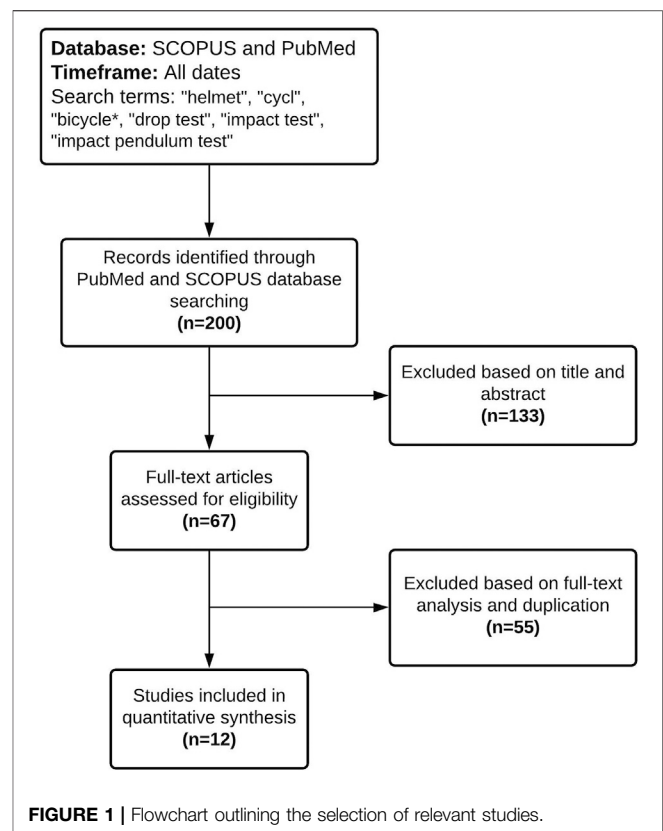
2.3 Post Processing of the Extracted Data

In order to provide a fair comparison across different types of tests, we clustered the datasets with respect to their normal impact velocities and impact angular momentums. In the first part, to be able to compare all the extracted headform kinematics whose drop tests were performed at anvil angles ranging from 0° to 60°, an impact velocity clustering step was performed so that the velocity vector would be perpendicular to the anvil:

$$V_N = V \cos \theta \quad (1)$$

where V_N is the impact velocity perpendicular to the anvil plate with angle θ .

In the second part, to investigate the effect of headform position and presence or absence of the neck on the rotational acceleration, we clustered the data according to the impact angular momentum H_{Impact} . For more information regarding the calculation of H_{Impact} please see **Supplemental Material**.

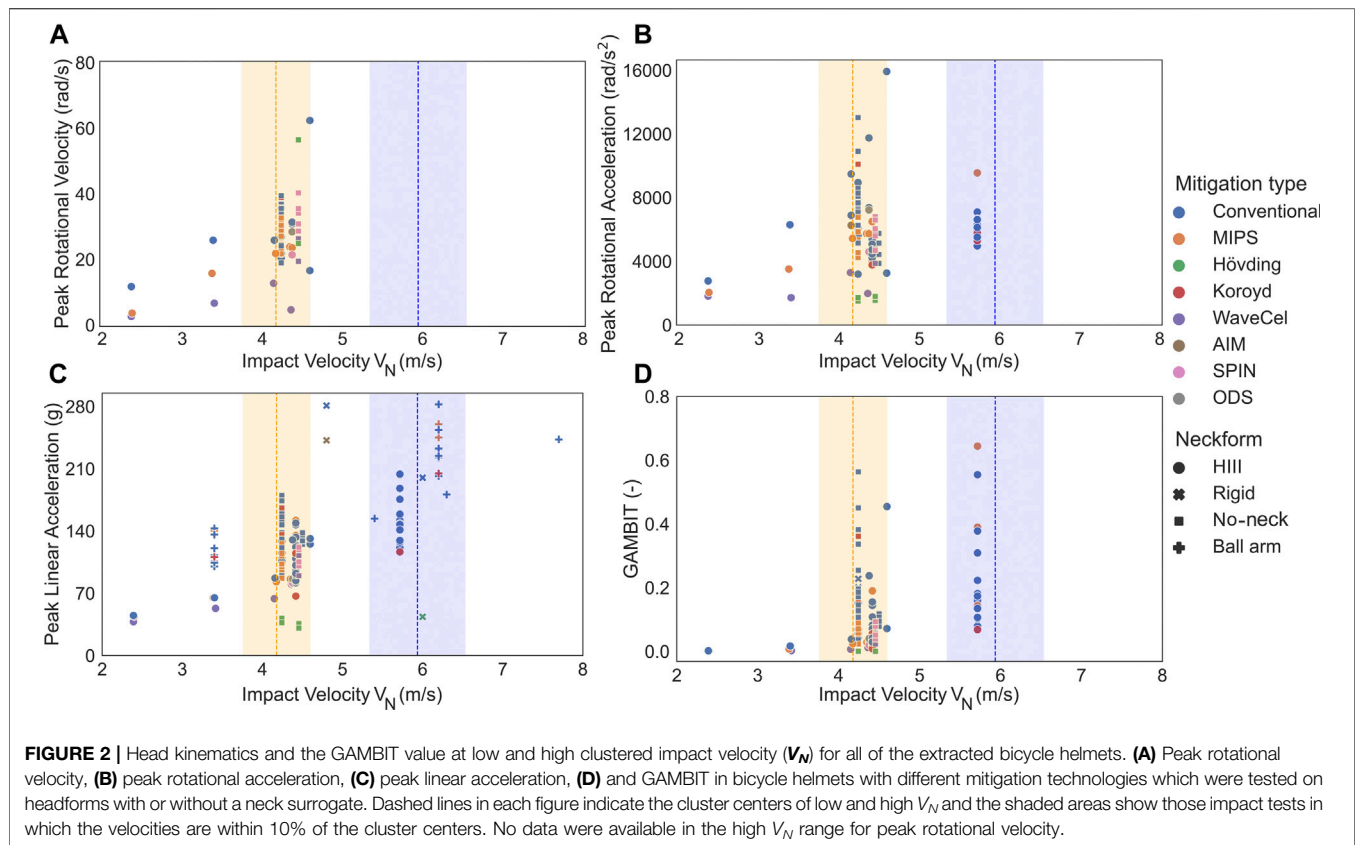


Next, the K-means algorithm from Python's machine learning library Scikit-learn (Pedregosa et al., 2011) was used to cluster the data according to V_N and H_{Impact} . For V_N , two cluster centers were calculated by using K-means algorithm for low and high V_N and the impact tests with V_N within $\pm 10\%$ of the cluster centers were retained for each group. For H_{Impact} , after removing outliers with $H_{Impact} > 5.2$, we calculated one cluster center and the impact tests with H_{Impact} within $\pm 15\%$ of the cluster center were retained.

The kinematic-based injury metrics including PLA, PRA, and GAMBIT were then compared between the helmets within each group of low and high V_N as well as H_{Impact} . Here, we used GAMBIT since it can be directly calculated from the available kinematics data, and can be used as injury criteria investigating the combined effect of linear and rotational impulses (Newman, 1986; Newman and Shewchenko, 2000; Klug et al., 2015). The GAMBIT value in its general form can be written as:

$$G = \max \left(\left[\left(\frac{a(t)}{a_c} \right)^n + \left(\frac{\alpha(t)}{\alpha_c} \right)^m \right]^{1/s} \right) \quad (2)$$

where $a(t)$ and $\alpha(t)$ are translational and rotational accelerations at time t , respectively. n , m , and s are empirically derived constant parameters that were fitted to experimental data (Newman and Shewchenko, 2000). a_c and α_c are thresholds derived for a pure translational and rotational acceleration, respectively. Here, we selected $n = m = s = 2$, $a_c = 250$ g, and $\alpha_c = 25,000$ rad/s² as was



suggested by (Newman and Shewchenko, 2000). It should be noted that when analyzing GAMBIT, $G = 1$ correspond to a 50% probability of Abbreviated Injury Scale (AIS) > 3 which corresponds to serious injury (Newman and Shewchenko, 2000).

2.4 Statistical Analysis

In the next step, we investigated the collected drop test results for the following parameters: 1) Presence or absence of the mitigation system, 2) Effect of mitigation type, and 3) Presence or absence of the neck surrogate. To analyze the effect of the presence of the mitigation system, PLA, PRA, and GAMBIT at low and high V_N were compared between the conventional helmets and helmets that used a mitigation system. We then restricted our data to tests that had either included or excluded the neck surrogate in their experiments and performed the same analysis. Finally, the data was clustered according to H_{Impact} and the effect of mitigation systems and neckform on PRA was analyzed.

Before performing the statistical analysis, we used Shapiro-Wilk's test to verify the normality of the distribution of the data within each group (Shapiro and Wilk, 1965). We then tested the equal variance of every couple of sample groups considered for the comparisons via Levene's test (Olkin et al., 1960). We carried out the two-sample t-test if both of the compared groups were normally distributed, otherwise we performed the two-sided Kolmogorov-Smirnov test (Hodges, 1958).

3 RESULTS

A flowchart is used to show the procedure of the literature review and the articles that were excluded and included (Figure 1). The PubMed database search resulted in 53 articles pertaining to bicycle helmet testing and the SCOPUS search resulted in 147 articles. Each resulting article was screened and excluded if the title and abstract were not deemed relevant, which resulted in the removal of 133 studies from the data pool. The remaining 67 articles were screened for the necessary inclusion criteria, such as PLA, PRV, PRA (Section 2.1), as well as duplicates. In the end, 12 articles were eligible for inclusion in this review paper (Figure 1; Table 1; Supplementary Table S1).

A total of 148 bicycle helmet drop tests were collected from the selected papers (It should be mentioned that those data in the studied papers that didn't pass our criteria, were not included in this review paper). 88 of these helmet drop tests were carried out on the conventional helmets which only used one layer of EPS or EPP as a liner in their design (Figure 2; Table 1; Supplementary Table S1). The remaining 60 of the drop tests were performed on MIPS, SPIN, ODS, WaveCel, AIM, and Koroyd helmets and Hövding protective gear (Figure 2; Table 1; Supplementary Table S1). The impact velocities of the tests varied between 3.4 m/s and 7.7 m/s. After applying the k-mean clustering algorithm (Pedregosa et al., 2011), we found $V_N = 4.2$ m/s and $V_N = 5.9$ m/s to be the cluster centers of low and high impact

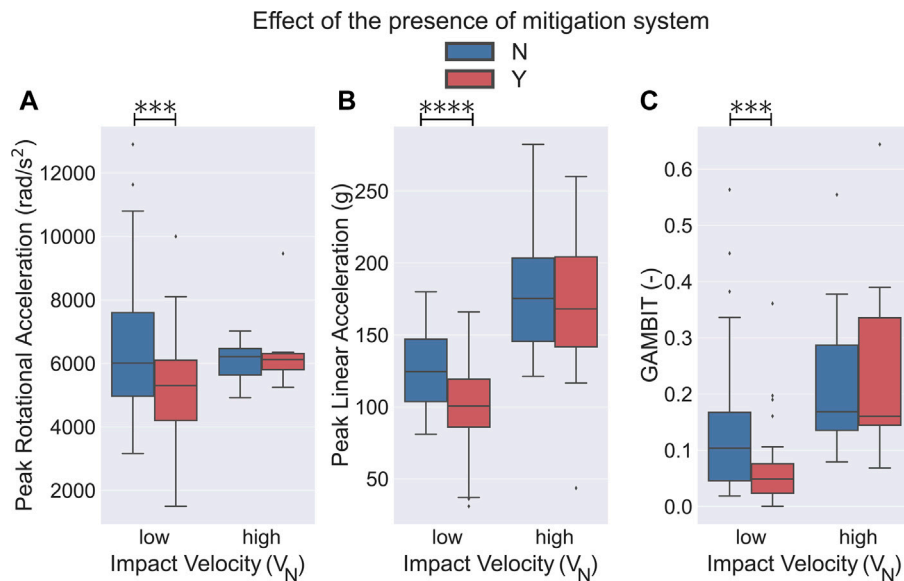


FIGURE 3 | Effect of the presence or absence of the mitigation system on bicycle helmet performance in impact tests. Helmets using a mitigation technology had a significantly lower **(A)** PRA, **(B)** PLA, and **(C)** low V_N as compared to the conventional helmets ($p < 0.001$). No statistical significance was observed in high V_N (5.9 ± 0.6 m/s) drop tests between the two different helmet types. ♦ shows the outlier data.

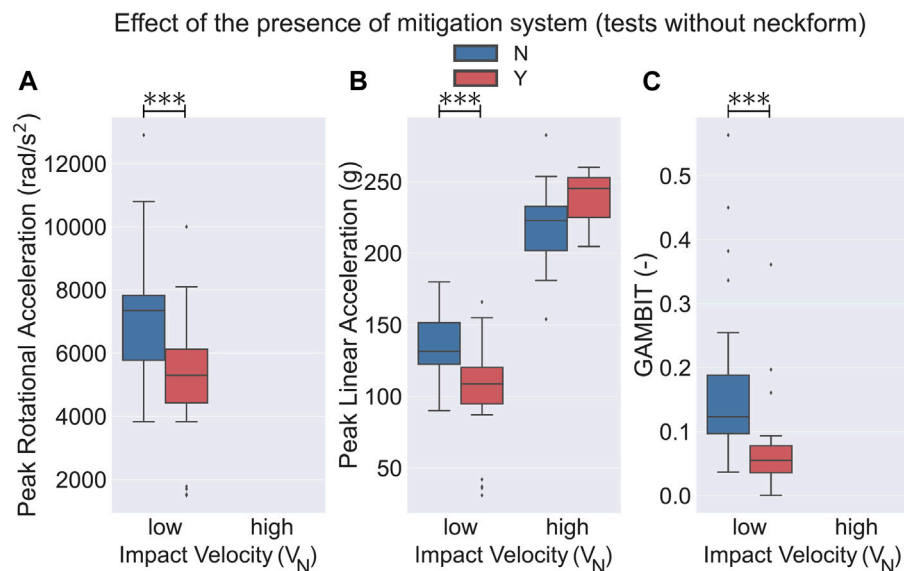


FIGURE 4 | Effect of the presence of the mitigation system on bicycle helmets that were tested on headforms without a neck surrogate. Helmets with a mitigation technology had a significantly lower **(A)** PRA ($p < 0.001$), **(B)** PLA ($p < 0.001$), and **(C)** GAMBIT ($p < 0.001$) in drop tests at low V_N (4.2 ± 0.4 m/s). No statistical significance was observed in PLA at high V_N (5.9 ± 0.6 m/s) drop tests. In high V_N drop tests, no data were available for PRA and GAMBIT. ♦ depicts the outlier data.

velocities, respectively (Figure 2; Table 1; Supplementary Table S1). Impact tests outside the 10% of the cluster centers were then removed, resulting in 75 conventional and 51 mitigation type helmet drop tests. Among the studied literature for this paper, four different types of neck-headform attachments were observed: 1- No neckform was attached to the head (N in Figure 2), 2- The headform was attached to a ball-arm neck

(Ball arm in Figure 2), 3- The headform was attached to a rigid neck (Rigid in Figure 2), and 4- The headform was attached to a Hybrid III 50th-percentile male neck (Y in Figure 2).

Having collected all the existing bicycle helmet drop test results from the literature survey, we first analyzed the effect of the presence or absence of the impact mitigation systems on the resultant kinematics and the associated injury metrics during

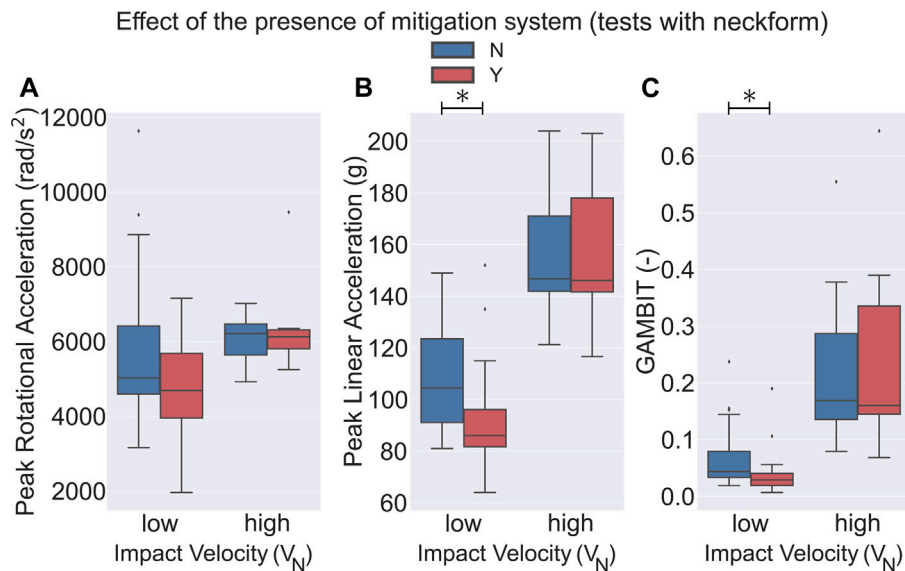


FIGURE 5 | Effect of the presence of the mitigation system on bicycle helmets that were tested on headforms with a neck surrogate. **(A)** No statistical significance was observed in PRA between the two groups at both low and high V_N (5.9 ± 0.6 m/s) drop tests of neck included groups. Helmets with a mitigation system had a significantly lower **(B)** PLA and **(C)** GAMBIT at low V_N as compared to the conventional helmets ($p < 0.05$). No statistical significance was observed for PLA and GAMBIT at high V_N (5.9 ± 0.6 m/s). ♦ depicts the outlier data.

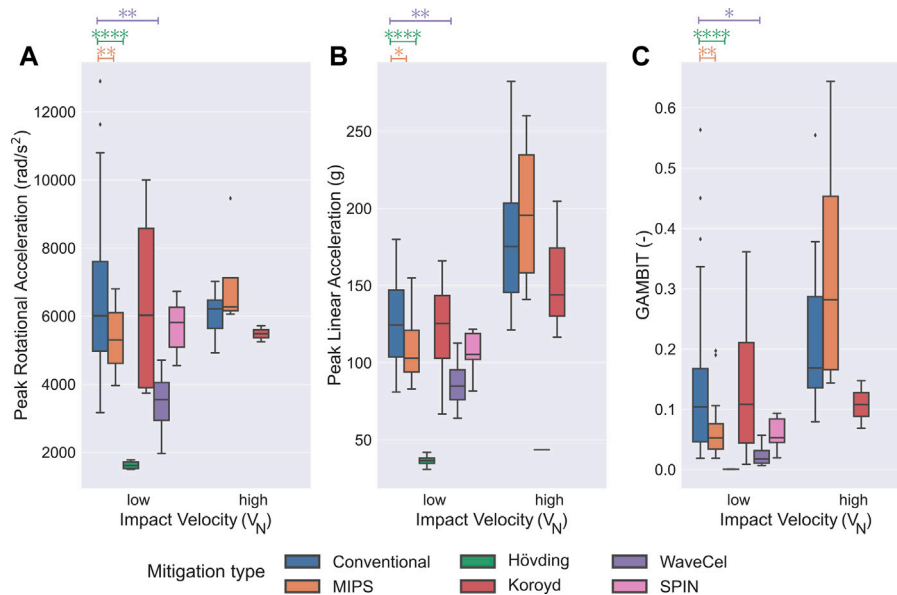


FIGURE 6 | Effect of different mitigation systems in drop tests at low and high V_N s. **(A)** Compared to the conventional bicycle helmets, PRA was significantly less in WaveCel ($p < 0.0001$), SPIN ($p < 0.05$), Hövding ($p < 0.001$) and MIPS ($p < 0.05$) at low V_N (4.2 ± 0.4 m/s) drop tests. **(B)** Compared to the conventional bicycle helmets, PLA was significantly less in Hövding ($p < 0.0001$) and WaveCel ($p < 0.05$) in drop tests at low V_N (4.2 ± 0.4 m/s). **(C)** GAMBIT was significantly less in Hövding ($p < 0.001$), WaveCel ($p < 0.05$) and SPIN ($p < 0.05$) compared to the conventional ones in low V_N (4.2 ± 0.4 m/s) drop tests. No statistically significant differences were observed at high V_N (5.9 ± 0.6 m/s) drop tests between the conventional helmets and other technologies. In this figure, only technologies with at least 4 data points were included. ♦ depicts the outlier data.

drop tests (Figure 3). We observed that at low V_N (4.2 ± 0.4 m/s) drop tests, the bicycle helmets with a mitigation system, on average, had significantly lower PLA, PRA, and GAMBIT values

compared to conventional helmets (approximately 20.2, 21.8, and 52.6% lower respectively, Figures 3A–C, $p < 0.01$). Here, the low V_N (4.2 ± 0.4 m/s) drop test experiments of the bicycle helmets with a

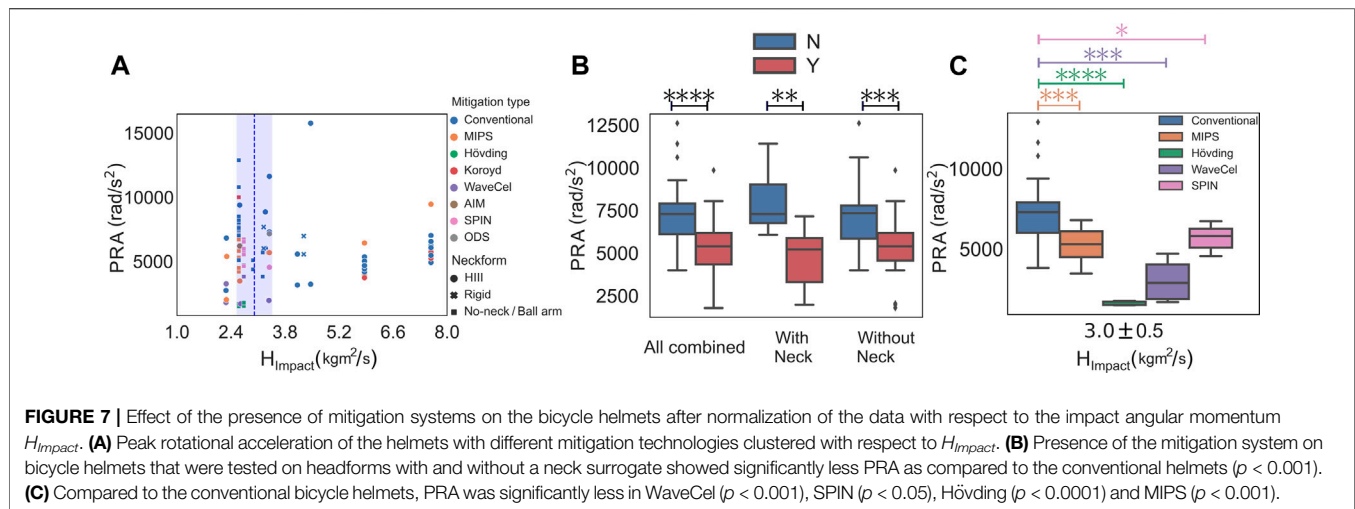
mitigation system resulted in average PLA, PRA, and GAMBIT of 100.1 ± 30.4 m/s, $5,043.6 \pm 1740.8$ rad/s², and 0.062 ± 0.066 , respectively. The conventional bicycle helmets, on the other hand, experienced an average PLA, PRA and GAMBIT of 125.5 ± 26.9 m/s, $6,448.8 \pm 1985.6$ rad/s², and 0.131 ± 0.111 , respectively. In the drop tests at high V_N (5.9 ± 0.6 m/s), we did not observe any statistically significant differences between the kinematics of the bicycle helmets with and without the mitigation systems (**Figures 3A–C**). For these experiments, we observed average PLA, PRA, and GAMBIT values of 169.5 ± 61.0 m/s, $6,504.7 \pm 1,370.0$ rad/s², and 0.261 ± 0.198 , for the helmets with a mitigation system, respectively. The experiments on the conventional helmets resulted in average PLA, PRA, and GAMBIT values of 179.6 ± 41.6 m/s, $6,075.7 \pm 548.9$ rad/s², and 0.215 ± 0.126 , respectively.

One crucial difference in the different drop tests we considered for this paper was the presence or absence of the neck surrogate. We found that 65 experiments were performed on headforms with an attached neck surrogate and the remaining 52 were tested on headforms without a neck component. 8 helmets were tested with a rigid neck attached to the headform and 23 were tested while being attached to a ball arm. In our analysis, we considered the headforms attached to a ball arm in the no-neck group since in both of these groups the headform could rotate without resistance at the time of the impact. Our first finding was that in almost all of the categories, tests without a neck component experienced a higher PLA, PRA, and GAMBIT on average as compared to the group with an attached neck component (**Figures 4, 5**). Here, in the low V_N (4.2 ± 0.4 m/s) drop tests, PLA, PRA, and GAMBIT, on average, were approximately 10.3, 7.3, and 59.3% higher in the no-neck group, respectively. At high V_N (5.9 ± 0.6 m/s) drop tests, PLA was on average 51.0% higher in the no-neck group. It should be noted that no PRA values were available at high V_N (5.9 ± 0.6 m/s) drop tests for the no-neck group. Next, we analyzed the effect of the presence of an impact mitigation system in each of the neck and no-neck groups. We observed that for the low V_N (4.2 ± 0.4 m/s) tests, in the no-neck group the bicycle helmets with a mitigation system had a significantly lower PLA (24.7%), PRA (27.5%), and GAMBIT (59.7%) as compared to the conventional bicycle helmets (**Figure 4**, $p < 0.001$). Whereas, in the neck-included group, only PLA (13%) and GAMBIT (36.2%) were significantly lower in the helmets with a mitigation system (**Figure 5**, $p < 0.05$). Additionally, we did not observe any statistically significant differences of PLA between the helmet models at high V_N (5.9 ± 0.6 m/s) drop tests. No data points were available for PRA and GAMBIT in the no-neck group at high V_N (**Figures 4A–C**).

In the next step, we investigated the efficacy of the different mitigation technologies by comparing PRA, PLA, and GAMBIT of each specific mitigation technology with conventional bicycle helmets (**Figure 6**). Here, we only considered helmet types with at least 4 data points for the comparison. We found that among the helmets that used rotation-damping based technologies, only MIPS had approximately 16.8 and 49.3% lower PRA and GAMBIT at low V_N (4.2 ± 0.4 m/s) as compared to the conventional helmets, respectively (**Figures 6A,C**, $p < 0.05$). While SPIN helmets had on average lower PLA, PRA, and

GAMBIT of about 14.5, 11.9, and 53.8%, respectively, we did not find any statistically significant differences in these helmets as compared to the conventional ones. Next, we analyzed the effectiveness of helmets that used collapsible structures in their liner. In this category, helmets based on the WaveCel technology had a significantly lower PLA, PRA, and GAMBIT of approximately 31.0, 46.6, and 81.1% at low V_N (4.2 ± 0.4 m/s) as compared to the conventional helmets, respectively (**Figures 6A–C**), $p < 0.05$). Whereas, Koroyd which is another helmet based on collapsible structures did not show any statistical differences compared to the conventional ones (**Figure 6A–C**), $p < 0.05$). Compared to the investigated helmets in the literature, the Hövding protective gear had the best performance in the analyzed kinematic based injury metrics with PLA, PRA, and GAMBIT of about 70.9, 74.8, and 99.5% lower than the conventional helmets ($p < 0.0001$). At high V_N (5.9 ± 0.6 m/s), we observed no statistical significance when we compared PRA, PLA, and GAMBIT between the conventional and each of the other helmet types (**Figure 6A–C**). It should also be noted that, for high V_N (5.9 ± 0.6 m/s) we did not have data points for PRA, and GAMBIT values of SPIN, WaveCel, and Hövding protective gears. Moreover, the Koroyd helmets only had two data points at high V_N (5.9 ± 0.6 m/s) experiments for PRA, and GAMBIT, therefore, were not compared with the conventional helmets in this category.

To take into account the effect of headform orientation at the time of impact, as well as the presence or absence of the neckform, we clustered the data according to the impact angular momentum (H_{Impact}) and checked the rotational acceleration of the helmets (**Figure 7**). After removing the outlier data ($H_{Impact} > 5.2$ kgm²/s) we found $H_{Impact} = 3.0 \pm 0.5$ kgm²/s to be the cluster center. This narrowed the data from the literature to 79 tested helmets within the range of $H_{Impact} = 3.0 \pm 0.5$ kgm²/s (**Figure 7A**). In the next step, we analyzed the effect of the mitigation system on PRA of the headforms. We observed that within $H_{Impact} = 3.0 \pm 0.5$ kgm²/s, the PRA of the helmets that used a mitigation system was approximately 31.0% lower compared to the conventional helmets ($p < 0.0001$; **Figure 7B**). Next, we separately analyzed the PRA of the groups with and without the neckform. We observed in both of these two groups that the PRA of the helmets with a mitigation system was significantly lower compared to the conventional helmets ($p < 0.01$; **Figure 7B**). Finally, within the range of $H_{Impact} = 3.0 \pm 0.5$ kgm²/s, we analyzed the performance of each of these individual mitigation technologies against the conventional helmets. For this analysis, we only considered mitigation technologies with at least 4 data points. We observed that within this H_{Impact} range, Hövding protective gear had the best performance, with a lower PRA of approximately 78% in comparison to the conventional helmets ($p < 0.0001$; **Figure 7C**). WaveCel with a lower PRA of about 58% as compared to the conventional helmets was the next best performing technology in PRA that followed Hövding ($p < 0.001$; **Figure 7C**). Helmets with a dedicated rotation-damping technologies including MIPS and SPIN also had a significantly lower PRA of approximately 27% ($p < 0.001$) and 22% ($p < 0.05$) as compared to the conventional helmets, respectively (**Figure 7C**).



4 DISCUSSION

The recent developments in bicycle helmet design technologies have been promising for the future of cycling safety and TBI prevention. In this paper, we performed a literature review on the recent advancements and improvements of these new bicycle helmets and analyzed their performance in reducing the head kinematics compared to the conventional designs. To do so, we extracted kinematic datasets of more than 140 helmet drop tests from the retrieved articles and investigated several kinematics-based injury metrics including PLA, PRA, and GAMBIT.

Overall, we observed that the new protective gear technologies including MIPS, WaveCel, and Hövding significantly decreased PLA, PRA, and the GAMBIT value of the headform at low V_N (4.2 ± 0.4 m/s) drop tests. While the bicycle helmets based on MIPS had a significantly lower PRA, PLA and GAMBIT as compared to the conventional helmets, no statistical differences was observed for the SPIN helmets. The significantly lower PRA values of the MIPS helmets could be due to the dedicated rotation-damping systems in these helmets. In these helmets, the rotational damping mechanism works by adding slip liners underneath the main EPS liner, which allows sliding between the head and the helmet during the impact (Halldin et al., 2003; Bland et al., 2018b; Bottlang et al., 2020). Additionally, the improved PLA response of the MIPS helmets might be due to the improved design and manufacturing quality of these helmets such as the changes in the thickness of EPS padding and the helmets weight. These encouraging findings, highlight the benefit of including rotation damping technologies in helmets in order to reduce the TBI risk during cycling accidents. It should be noted that the lack of statistical differences for the PRA values of the SPIN helmets could be due to grouping the data only according to their impact velocity, which might cause some errors and will be discussed further below.

Next, we investigated the kinematics of other recently developed bicycle helmets based on collapsible structure mitigation systems including WaveCel and Koroyd (Stigson

et al., 2017; Bland et al., 2018b; Bland et al., 2018c), our analyses were inconclusive. While the WaveCel helmets performed significantly better than the conventional helmets in linear and rotational kinematics, and the consequential brain injury risk at low V_N (4.2 ± 0.4 m/s) drop tests, the Koroyd based helmets did not show any statistical differences. One of the reasons for the observed kinematics of the Koroyd helmets is potentially due to the low number of available data points. Only 6 drop test results from 3 different Koroyd helmets were available in the literature. When we investigated the performance of each of these helmets, we observed that one of the Koroyd helmets had a significantly better performance than the conventional ones, whereas, the other two had either the same level or much worse performance in the metrics considered. This shows that in addition to incorporating the new technologies in a helmet, it could be important to optimize the conventional helmet design parameters such as weight and liner thickness. The WaveCel helmets, on the other hand, performed consistently better than all others except for Hövding. The significant reduction of PLA as compared to the conventional helmets suggests that the buckling of WaveCel's organized cellular structure might attenuate radial forces better than the commonly used EPS material (Bland et al., 2018b; Bliven et al., 2019). The significant mitigation of PRA by these helmets could be due to the folding properties of its cellular structure (Bliven et al., 2019). First, each cell can deform tangentially which allows absorption of the shear force between the head and the helmet (Bliven et al., 2019). Second, these cells can also have an elastic in-plane deformation allowing a rotational suspension that decouple the head from the helmet (Bliven et al., 2019). Overall, in addition to the impact performance of WaveCel helmets in the mitigation of kinematic based injury metrics, advantages such as its light weight, high heat transfer rate, and airflow permeability, make such honeycomb based helmets potentially a good candidate to replace the conventional EPS/EPP helmets (Caserta et al., 2011; Caccese et al., 2013; Hansen et al., 2013; Bliven et al., 2019).

The Hövding protective gear had a lower PLA, PRA, and GAMBIT as compared to the other helmets. The reasons for this performance stem from the helmet's large size and low stiffness (Kurt et al., 2017; Abayazid et al., 2021). Such properties result in an increased duration of the impact and significantly lower peak acceleration values (Kurt et al., 2017; Abayazid et al., 2021). Despite the substantial mitigation of PLA and PRA, it should be noted that the prolonged duration of the impact could potentially result in a high PRV, which could carry increased injury risks (Ommaya and Hirsch, 1971; Margulies and Thibault, 1992; Rowson et al., 2012; Hernandez et al., 2015a; Abayazid et al., 2021). Additionally, the Hövding's large size and its increased duration of the impact, could mean increased coupling of the neck and shoulder during real-life impacts (Abayazid et al., 2021). Therefore, further tests regarding the potential neck injuries (as with any newly developed technology that might introduce such injuries), and other relevant TBI metrics are a necessary step before the widespread use of this type of helmet (Kurt et al., 2017). For instance, due to the lack of standard testing procedures, this type of helmet cannot be sold in the U.S. market (Kurt et al., 2017). However, regardless of these factors, the existing kinematic data highlight the potential of these airbag type bicycle helmets in mitigating the risks of TBI.

Having analyzed the effect of the mitigation systems after grouping the data with respect to the normal impact velocity V_N , we also analyzed the effect of headform positioning at the time of the impact. In the experiments gathered from the literature, the helmets have been dropped at various angles of 0–90° on anvils with varying angles of 0–60°. The differences in the impact location of the headform could result in increased or decreased PRA. To analyze this effect, the data was also clustered with respect to the impact angular momentum H_{Impact} . Similar to our previous observations, we found that the helmets with the mitigation technologies still had a significantly lower PRA as compared to the conventional ones (Figure 7). Interestingly, we observed that while the SPIN helmets did not have statistically different PRA compared to the conventional helmets in the normal low V_N group, in the new H_{Impact} group, they had a significantly lower PRA. This suggests that in the initial grouping according to the low V_N , some of the drop tests might have been performed at an angle that caused high angular momentum and high PRA values.

Our analyses of the kinematics data from the literature demonstrate the necessity of taking new steps toward the standardization of bicycle helmet testing procedures. We observed that the presence or absence of the neckform in the drop test experiment affected the recorded kinematics. Initially we grouped the data according to their impact velocity V_N (Figures 4, 5). We observed that at low V_N for the no-neck group, the bicycle helmets with the mitigation system showed a significant reduction of the PLA, PRA, and GAMBIT. Whereas, in the neck included group, there were only statistical differences in the PLA, and GAMBIT values (Figures 4, 5). Additionally, the PRA, PLA, and GAMBIT were substantially larger in the no-neck group. The observed lack of statistical significance of PRA in the neck included group could be due to the absorption of part of the rotational kinematics by the stiff neck (Hernandez et al., 2015b).

It has been shown in laboratory testing that the Hybrid III neck surrogate (the most commonly used neck model in the analyzed studies, Table 1; Supplementary Tables S1, S2) produces impact dynamics with a higher damping factor and lower natural frequency as compared to real-world impacts (Gwin et al., 2010; Hernandez et al., 2015b). Due to this slowing of the dynamics (Gwin et al., 2010), the mitigation systems might become less engaged in decreasing the head kinematics. Others have also reported similar findings, where the presence or absence of the neck surrogate could result in markedly different kinematics (Hering and Derler, 2000; Bartsch et al., 2012; Camarillo et al., 2013; Bland et al., 2018a), with significantly larger PLA, PRV, and PRA in the no-neck tests of the same helmets (Bland et al., 2018a). Another interesting observation we had was with regards to the presence of the neckform in the impact velocity (V_N) and impact angular momentum H_{Impact} cluster analyses. While the PRA comparisons in the V_N cluster analysis strongly depended on the presence of the neckform (Figures 4, 5), this dependence was not observed in the H_{Impact} cluster analysis (Figure 7B). These findings, further highlight the importance of standardized testing and analysis of helmet drop tests.

Our results are subject to several limitations. The experimental drop tests in the literature are performed at various heights which result in different impact velocities across the studies. To address this issue, we applied k-mean clustering algorithm to the extracted data and selected two cluster centers and 10% of their surrounding as the impact velocities of interest. This allowed removing outlier data which might have affected the findings because of their high or low impact velocities. To correct for the effect of impact location on the headform which might affect PRA, we also created another group according to the impact angular momentum with one cluster center and 15% standard deviation. Another limitation of our study is the lack of enough data points for some of the compared categories. This was more evident in the lack of PRA values of the drop tests at high V_N (5.9 ± 0.6 m/s) performed without a neck surrogate, as well as, lack of sufficient kinematic data for some of the newly developed helmet technologies. In our results, we observed no statistical significance in the effect of mitigation system for high V_N (5.9 ± 0.6 m/s) tests, which could mainly be due to the lack of enough data points in that testing category. Moreover, in the literature we observed that the drop tests were carried out at various configurations such that the headform and anvil had relative angles in the range of 0–90°. These differences in the experimental procedures could lead to increased or decreased PLA and PRA between similar helmets that were tested in different configurations. To address this limitation we clustered the data according to normal impact velocity (V_N) and impact angular momentum (H_{Impact}), which allowed comparison of these helmets with each other. Additionally, it should be noted that, here, we analyzed different mitigation technologies across various helmets. A more accurate analysis would be to do this investigation on the same helmets under the same impact conditions, with or without the specific technologies. As such, other parameters such as the liner thickness, helmet mass, presence or absence of the neck surrogate (Fahlstedt et al., 2016; Bland, 2019; Fahlstedt et al.,

2021), as well as the headform model (Kendall et al., 2012; Cobb et al., 2016; Bland, 2019) might also confound the interpretation of these results significantly.

5 CONCLUSION

With the introduction of various new bicycle helmet technologies in the last decade, there is a dire need to compare their efficacy in reducing head kinematics with respect to the commonly used conventional bicycle helmets. In this work, we reviewed the literature to collect and analyze various bicycle helmet technologies, by investigating their resultant kinematic-based head injury data from drop test experiments. We observed that the helmets that used new technologies such as rotation damping systems, collapsible cellular structures, and expandable models, performed significantly better than the conventional helmets for kinematics-based metrics at low impact velocities and low impact angular momentum. Additionally, we observed that presence or absence of the neck surrogate in the experimental procedure could result in different kinematics. These findings

highlight the importance of rethinking conventional helmet designs, consideration of novel technologies for better prevention of cycling-related TBIs, and the need for more thorough evaluation and impact testing of bicycle helmets.

AUTHOR CONTRIBUTIONS

All authors contributed to the conception and design of the study. JA, FR, and BK organized the database. AM performed the statistical analysis. All authors contributed to the data analysis. JA, FR, and BK wrote the first draft of the manuscript. AM wrote sections of the manuscript. All authors contributed to manuscript revision, read, and approved the submitted version.

SUPPLEMENTARY MATERIAL

The Supplementary Material for this article can be found online at: <https://www.frontiersin.org/articles/10.3389/fbioe.2021.718407/full#supplementary-material>

REFERENCES

- Abderezaei, J., Zhao, W., Grijalva, C. L., Fabris, G., Ji, S., Laksari, K., and Kurt, M. (2019). Nonlinear Dynamical Behavior of the Deep White Matter During Head Impact. *Phys. Rev. Appl.* 12, 014058.
- AANS (2018). *Sports-related Head Injury*, American Association of Neurological Surgeons (Aans). American Association of Neurological Surgeons. Available at: <https://www.aans.org/patients/neurosurgical-conditions-and-treatments/sports-related-head-injury>.
- Abayazid, F., Ding, K., Zimmerman, K., Stigson, H., and Ghajari, M. (2021). A New Assessment of Bicycle Helmets: the Brain Injury Mitigation Effects of New Technologies in Oblique Impacts. *Ann. Biomed. Eng.* 2021, 1–18. doi:10.1007/s10439-021-02785-0
- Andena, L., Caimmi, F., Leonardi, L., Ghisi, A., Mariani, S., and Braghin, F. (2016). Towards Safer Helmets: Characterisation, Modelling and Monitoring. *Proced. Eng.* 147, 478–483. doi:10.1016/j.proeng.2016.06.224
- AS/NZS 2512.1 (2009). "Definitions and Headforms," in *Methods of Testing Protective Helmets* (Sydney, New Zealand: Standards Australia/Standards New Zealand).
- B. EN, 1078 (1997). *Helmets for Pedal Cyclists and for Users of Skateboards and Roller Skates*. London: British Standards Institution.
- Bartsch, A., Benzel, E., Miele, V., and Prakash, V. (2012). Impact Test Comparisons of 20th and 21st century American Football Helmets. *Jns* 116, 222–233. doi:10.3171/2011.9.jns111059
- Bland, M. L., McNally, C., and Rowson, S. (2018b). Differences in Impact Performance of Bicycle Helmets during Oblique Impacts. *J. Biomech. Eng.* 140, 1. doi:10.1115/1.4040019
- Bland, M. L. (2019). *Assessing the Efficacy of Bicycle Helmets in Reducing Risk of Head Injury*. Virginia: Virginia Tech. Ph.D. thesis.
- Bland, M. L., McNally, C., and Rowson, S. (2018a). "Headform and Neck Effects on Dynamic Response in Bicycle Helmet Oblique Impact Testing," in *Proceedings of the IRCOBI Conference* (Athens, Greece: International Research Council on Biomechanics of Injury), 413–423.
- Bland, M. L., McNally, C., Zubly, D. S., Mueller, B. C., and Rowson, S. (2020). Development of the star Evaluation System for Assessing Bicycle Helmet Protective Performance. *Ann. Biomed. Eng.* 48, 47–57. doi:10.1007/s10439-019-02330-0
- Bland, M. L., Zubly, D. S., Mueller, B. C., and Rowson, S. (2018c). Differences in the Protective Capabilities of Bicycle Helmets in Real-World and Standard-Specified Impact Scenarios. *Traffic Inj. Prev.* 19, S158–S163. doi:10.1080/15389588.2017.1388915
- Bliven, E., Rouhier, A., Tsai, S., Willinger, R., Bourdet, N., Deck, C., et al. (2019). Evaluation of a Novel Bicycle Helmet Concept in Oblique Impact Testing. *Accid. Anal. Prev.* 124, 58–65. doi:10.1016/j.aap.2018.12.017
- Bottlang, M., Rouhier, A., Tsai, S., Gregoire, J., and Madey, S. M. (2020). Impact Performance Comparison of Advanced Bicycle Helmets with Dedicated Rotation-Damping Systems. *Ann. Biomed. Eng.* 48, 68–78. doi:10.1007/s10439-019-02328-8
- Bourdet, N., Deck, C., Carreira, R. P., and Willinger, R. (2012). Head Impact Conditions in the Case of Cyclist Falls. *Proc. Inst. Mech. Eng. P: J. Sports Eng. Tech.* 226, 282–289. doi:10.1177/1754337112442326
- Bourdet, N., Deck, C., Serre, T., Perrin, C., Llari, M., and Willinger, R. (2014). In-depth Real-World Bicycle Accident Reconstructions. *Int. J. Crashworthiness* 19, 222–232. doi:10.1080/13588265.2013.805293
- Caccese, V., Ferguson, J. R., and Edgecomb, M. A. (2013). Optimal Design of Honeycomb Material Used to Mitigate Head Impact. *Compos. Structures* 100, 404–412. doi:10.1016/j.compstruct.2012.12.034
- Camarillo, D. B., Shull, P. B., Mattson, J., Shultz, R., and Garza, D. (2013). An Instrumented Mouthguard for Measuring Linear and Angular Head Impact Kinematics in American Football. *Ann. Biomed. Eng.* 41, 1939–1949. doi:10.1007/s10439-013-0801-y
- Caserta, G. D., Iannucci, L., and Galvanetto, U. (2011). Shock Absorption Performance of a Motorbike Helmet with Honeycomb Reinforced Liner. *Compos. Structures* 93, 2748–2759. doi:10.1016/j.compstruct.2011.05.029
- Chang, C.-Y., Ho, C.-H., and Chang, S.-Y. (2003). Design of a Helmet, ME 499, 599.
- Cheung, A., and Gibson, T. (2004). Assessing the Level of Safety Provided by the Snell B95 Standard for Bicycle Helmets, CR 220.
- Cobb, B. R., Zadnik, A. M., and Rowson, S. (2016). Comparative Analysis of Helmeted Impact Response of Hybrid Iii and National Operating Committee on Standards for Athletic Equipment Headforms. *Proc. Inst. Mech. Eng. Part P: J. Sports Eng. Tech.* 230, 50–60. doi:10.1177/1754337115599133
- Commission, C. P. S. (1998). Cpsc 16 Cfr Part 1203-safety Standard for Bicycle Helmets. *Fed. Registry* 63, 11711–11747.
- Coronado, V. G., Haileyesus, T., Cheng, T. A., Bell, J. M., Haarbauer-Krupa, J., Lionbarger, M. R., et al. (2015). Trends in Sports- and Recreation-Related Traumatic Brain Injuries Treated in US Emergency Departments. *J. head Trauma Rehabil.* 30, 185–197. doi:10.1097/htr.0000000000000156
- CPSC (1998). *Safety Standard for Bicycle Helmets Final Rule (16 CFR Part 1203)*. United States: Standard, United States Consumer Product Safety Commission.
- Cripton, P. A., Dressler, D. M., Stuart, C. A., Dennison, C. R., and Richards, D. (2014). Bicycle Helmets Are Highly Effective at Preventing Head Injury during Head Impact: Head-form Accelerations and Injury Criteria for Helmeted and Unhelmeted Impacts. *Accid. Anal. Prev.* 70, 1–7. doi:10.1016/j.aap.2014.02.016
- Deck, C., Bourdet, N., Meyer, F., and Willinger, R. (2019). Protection Performance of Bicycle Helmets. *J. Saf. Res.* 71, 67–77. doi:10.1016/j.jsr.2019.09.003

- Fahlstedt, M., Abayazid, F., Panzer, M. B., Trotta, A., Zhao, W., Ghajari, M., et al. (2021). Ranking and Rating Bicycle Helmet Safety Performance in Oblique Impacts Using Eight Different Brain Injury Models. *Ann. Biomed. Eng.* 49, 1097–1109. doi:10.1007/s10439-020-02703-w
- Fahlstedt, M., Halldin, P., S Alvarez, V., and Kleiven, S. (2016). "Influence of the Body and Neck on Head Kinematics and Brain Injury Risk in Bicycle Accident Situations," in *IRCOBI 2016* (Malaga, Spain International Research Council on the Biomechanics of Injury), 459–478.
- FARS (2019). *National Highway Traffic Safety Administration, Fatality Analysis Reporting System (Fars), National Highway Traffic Safety Administration*. Washington: National Highway Traffic Safety Administration. Available at: <https://www-fars.nhtsa.dot.gov/main/index.aspx>.
- Fischer, P. (2017). *A Right to the Road: Understanding and Addressing Bicyclist Safety*. Governors Highway Safety Association.
- Gokhale, V. V. (2016). *Design of a Helmet with an Advanced Layered Composite for Energy Dissipation Using a Multi-Material Compliant Mechanism Synthesis*. United States: Purdue University. Ph.D. thesis.
- Gwin, J. T., Chu, J. J., Diamond, S. G., Halstead, P. D., Crisco, J. J., and Greenwald, R. M. (2010). An Investigation of the Nocsae Linear Impactor Test Method Based on *In Vivo* Measures of Head Impact Acceleration in American Football. *J. Biomech. Eng.* 132, 011006. doi:10.1115/1.4000249
- Halldin, P., Aare, M., Kleiven, S., and von Holst, H. (2003). "Improved Helmet Design and Test Methods to Reduce Rotational Induced Brain Injuries," in *RTO Specialist Meeting, The NATO's Research and Technology Organization (RTO)*.
- Hansen, K., Dau, N., Feist, F., Deck, C., Willinger, R., Madey, S. M., et al. (2013). Angular Impact Mitigation System for Bicycle Helmets to Reduce Head Acceleration and Risk of Traumatic Brain Injury. *Accid. Anal. Prev.* 59, 109–117. doi:10.1016/j.aap.2013.05.019
- Hardy, W. N., Mason, M. J., Foster, C. D., Shah, C. S., Kopacz, J. M., Yang, K. H., et al. (2007). A Study of the Response of the Human Cadaver Head to Impact. *Stapp Car Crash J.* 51, 17. doi:10.4271/2007-22-0002
- Healy, D. G. (2015). *Head Injuries in Sport. ABC of Sports and Exercise Medicine*. United States: Blackwell Publishing Ltd, 10.
- Hering, A., and Derler, S. (2000). "Motorcycle Helmet Drop Tests Using a Hybrid Iii Dummy," in *IRCOBI Conf* (Montpellier, France: International Research Council on the Biomechanics of Injury), 307–320.
- Hernandez, F., Shull, P. B., and Camarillo, D. B. (2015b). Evaluation of a Laboratory Model of Human Head Impact Biomechanics. *J. Biomech.* 48, 3469–3477. doi:10.1016/j.jbiomech.2015.05.034
- Hernandez, F., Wu, L. C., Yip, M. C., Laksari, K., Hoffman, A. R., Lopez, J. R., et al. (2015a). Six Degree-Of-freedom Measurements of Human Mild Traumatic Brain Injury. *Ann. Biomed. Eng.* 43, 1918–1934. doi:10.1007/s10439-014-1212-4
- Hodges, J. L. (1958). The Significance Probability of the Smirnov Two-Sample Test. *Ark. Mat.* 3, 469–486. doi:10.1007/bf02589501
- Holbourn, A. H. S. (1943). Mechanics of Head Injuries. *The Lancet* 242, 438–441. doi:10.1016/s0140-6736(00)87453-x
- Holbourn, A. H. S. (1944). The Mechanics of Trauma with Special Reference to Herniation of Cerebral Tissue. *J. Neurosurg.* 1, 190–200. doi:10.3171/jns.1944.1.3.0190
- Høy, A. (2018). Bicycle Helmets—To Wear or Not to Wear? a Meta-Analyses of the Effects of Bicycle Helmets on Injuries. *Accid. Anal. Prev.* 117, 85–97.
- Joseph, B., Azim, A., Haider, A. A., Kulvatunyou, N., O'Keeffe, T., Hassan, A., et al. (2017). Bicycle Helmets Work when it Matters the Most. *Am. J. Surg.* 213, 413–417. doi:10.1016/j.amjsurg.2016.05.021
- Karkhanavh, M., Kalenga, J.-C., Hagel, B. E., and Rowe, B. (2006). Effectiveness of Bicycle Helmet Legislation to Increase Helmet Use: a Systematic Review. *Inj. Prev.* 12, 76–82. doi:10.1136/ip.2005.010942
- Kendall, M., Walsh, E. S., and Hoshizaki, T. B. (2012). Comparison between Hybrid III and Hodgson-WSU Headforms by Linear and Angular Dynamic Impact Response. *Proc. Inst. Mech. Eng. Part P: J. Sports Eng. Tech.* 226, 260–265. doi:10.1177/1754337112436901
- Klug, C., Feist, F., and Tomasch, E. (2015). *Testing of Bicycle Helmets for Preadolescents*. Lyon, France: International Research Council on the Biomechanics of Injury (IRCOBI), 136–155.
- Kurt, M., Laksari, K., Kuo, C., Grant, G. A., and Camarillo, D. B. (2017). Modeling and Optimization of Airbag Helmets for Preventing Head Injuries in Bicycling. *Ann. Biomed. Eng.* 45, 1148–1160. doi:10.1007/s10439-016-1732-1
- Laksari, K., Kurt, M., Babaee, H., Kleiven, S., and Camarillo, D. (2018). Mechanistic Insights into Human Brain Impact Dynamics Through Modal Analysis. *Physical Rev. Lett.* 120, 138101.
- Laksari, K., Wu, L. C., Kurt, M., Kuo, C., and Camarillo, D. C. (2015). Resonance of Human Brain Under Head Acceleration. *J. R. Soc. Interface* 12, 20150331.
- Laksari, K., Fanton, M., Wu, L. C., Nguyen, T. H., Kurt, M., Giordano, C., et al. (2020). Multi-Directional Dynamic Model for Traumatic Brain Injury Detection. *J. Neurotrauma* 37, 982–993.
- Larsen, L. (1991). "Epidemiology of Bicyclist's Injuries," in *1991 International IRCOBI Conference on the Biomechanics of Impacts* (Berlin: International Research Council on the Biomechanics of Injury), 217–230.
- Margulies, S. S., and Thibault, L. E. (1992). A Proposed Tolerance Criterion for Diffuse Axonal Injury in Man. *J. Biomech.* 25, 917–923. doi:10.1016/0021-9290(92)90231-o
- McIntosh, A. S., Lai, A., and Schilter, E. (2013). Bicycle Helmets: Head Impact Dynamics in Helmeted and Unhelmeted Oblique Impact Tests. *Traffic Inj. Prev.* 14, 501–508. doi:10.1080/15389588.2012.727217
- Mills, N. J., and Gilchrist, A. (2008). Oblique Impact Testing of Bicycle Helmets. *Int. J. Impact Eng.* 35, 1075–1086. doi:10.1016/j.ijimpeng.2007.05.005
- Mojahed, A., Abderezaei, J., Kurt, M., Bergman, L. A., and Vakakis, A. F. (2020). A Nonlinear Reduced-Order Model of the Corpus Callosum Under Planar Coronal Excitation. *J. Biomech. Eng.* 142.
- Newman, J. A. (1986). "A Generalized Acceleration Model for Brain Injury Threshold (Gambit)," in *Proceedings of International IRCOBI Conference* (Zurich: International Research Council on Biomechanics of Injury).
- Newman, J. A., and Shewchenko, N. (2000). "A Proposed New Biomechanical Head Injury Assessment Function-The Maximum Power index," in *Proceedings of the 44th STAPP Car Crash Conference*, Atlanta, Georgia, November 6–8, 2000 SAE paper no. 2000-01-SC16.
- Olivier, J., and Creighton, P. (2017). Bicycle Injuries and Helmet Use: a Systematic Review and Meta-Analysis. *Int. J. Epidemiol.* 46, 278–292. doi:10.1093/ije/dyw153
- Olkin, I., Ghurye, S. G., Hoeffding, W., Madow, W. G., and Mann, H. B. (1960). *Contributions to Probability and Statistics: Essays in Honor of harold Hotelling*. Stanford University Press, 278–292.
- Ommaya, A. K., and Hirsch, A. E. (1971). Tolerances for Cerebral Concussion from Head Impact and Whiplash in Primates. *J. Biomech.* 4, 13–21. doi:10.1016/0021-9290(71)90011-x
- Pedregosa, F., Varoquaux, G., Gramfort, A., Michel, V., Thirion, B., Grisel, O., et al. (2011). Scikit-learn: Machine Learning in Python. *J. Machine Learn. Res.* 12, 2825–2830.
- Petersen, P. G., Smith, L. V., and Nevins, D. (2020). The Effect of Surface Roughness on Oblique Bicycle Helmet Impact Tests. *Proc. Inst. Mech. Eng. Part P: J. Sports Eng. Tech.* 234, 320–327. doi:10.1177/1754337120917809
- Post, A., and Blaine Hoshizaki, T. (2015). Rotational Acceleration, Brain Tissue Strain, and the Relationship to Concussion. *J. Biomech. Eng.* 137, 1. doi:10.1115/1.4028983
- Rowson, S., Duma, S. M., Beckwith, J. G., Chu, J. J., Greenwald, R. M., Crisco, J. J., et al. (2012). Rotational Head Kinematics in Football Impacts: an Injury Risk Function for Concussion. *Ann. Biomed. Eng.* 40, 1–13. doi:10.1007/s10439-011-0392-4
- Sacks, J. J., Holmgren, P., Smith, S. M., and Sosin, D. M. (1991). Bicycle-associated Head Injuries and Deaths in the United States from 1984 through 1988. How many Are Preventable? *Jama* 266, 3016–3018. doi:10.1001/jama.266.21.3016
- Sanford, T., McCulloch, C. E., Callcut, R. A., Carroll, P. R., and Breyer, B. N. (2015). Bicycle Trauma Injuries and Hospital Admissions in the united states, 1998–2013. *Jama* 314, 947–949. doi:10.1001/jama.2015.8295
- Sandberg, M., Tse, K. M., Tan, L. B., and Lee, H. P. (2018). A Computational Study of the en 1078 Impact Test for Bicycle Helmets Using a Realistic Subject-Specific Finite Element Head Model. *Comput. Methods Biomech. Biomed. Eng.* 21, 684–692.
- Scott, L. R., Bazargan-Hejazi, S., Shirazi, A., Pan, D., Lee, S., Teruya, S. A., et al. (2019). Helmet Use and Bicycle-Related Trauma Injury Outcomes. *Brain Inj.* 33, 1597–1601. doi:10.1080/02699052.2019.1650201
- Shapiro, S. S., and Wilk, M. B. (1965). An Analysis of Variance Test for Normality (Complete Samples). *Biometrika* 52, 591–611. doi:10.1093/biomet/52.3-4.591
- Stigson, H., Rizzi, M., Ydenius, A., Engström, E., and Kullgren, A. (2017). "Consumer Testing of Bicycle Helmets," in *International Research Council on the Biomechanics of Injury Conference (IRCOBI Conference)* (Antwerp, Belgium, Sept: International Research Council on Biomechanics of Injury), 13–15.
- Taylor, C. A., Bell, J. M., Breiding, M. J., and Xu, L. (2017). Traumatic Brain Injury-Related Emergency Department Visits, Hospitalizations, and Deaths -

- United States, 2007 and 2013. *MMWR Surveill. Summ.* 66, 1–16. doi:10.15585/mmwr.ss6609a1
- Willinger, R., Deck, C., Halldin, P., and Otte, D. (2019). “Towards Advanced Bicycle Helmet Test Methods,” in *International Cycling Safety Conference* (Brisbane, Australia: The Centre for Accident Research and Road Safety-Queensland), 18–19.
- Winkler, E. A., Yue, J. K., Burke, J. F., Chan, A. K., Dhall, S. S., Berger, M. S., et al. (2016). Adult Sports-Related Traumatic Brain Injury in United States Trauma Centers. *Foc* 40, E4. doi:10.3171/2016.1.focus15613

Conflict of Interest: The authors declare that the research was conducted in the absence of any commercial or financial relationships that could be construed as a potential conflict of interest.

Publisher’s Note: All claims expressed in this article are solely those of the authors and do not necessarily represent those of their affiliated organizations, or those of the publisher, the editors and the reviewers. Any product that may be evaluated in this article, or claim that may be made by its manufacturer, is not guaranteed or endorsed by the publisher.

Copyright © 2021 Abderezaei, Rezayaraghi, Kain, Menichetti and Kurt. This is an open-access article distributed under the terms of the Creative Commons Attribution License (CC BY). The use, distribution or reproduction in other forums is permitted, provided the original author(s) and the copyright owner(s) are credited and that the original publication in this journal is cited, in accordance with accepted academic practice. No use, distribution or reproduction is permitted which does not comply with these terms.



A Machine Learning Approach to Investigate the Uncertainty of Tissue-Level Injury Metrics for Cerebral Contusion

Andrea Menichetti^{1*}, Laura Bartsoen¹, Bart Depreitere², Jos Vander Sloten¹ and Nele Famaey¹

¹Biomechanics Section, Department of Mechanical Engineering, KU Leuven, Leuven, Belgium, ²Neurosurgery, University Hospitals Leuven, Leuven, Belgium

OPEN ACCESS

Edited by:

Silvia Budday,
University of Erlangen Nuremberg,
Germany

Reviewed by:

Songbai Ji,
Worcester Polytechnic Institute,
United States
Zhou Zhou,
Royal Institute of Technology, Sweden
Kenneth L. Monson,
the University of Utah, United States

*Correspondence:

Andrea Menichetti
andrea.menichetti@kuleuven.be

Specialty section:

This article was submitted to
Biomechanics,
a section of the journal
Frontiers in Bioengineering and
Biotechnology

Received: 24 May 2021

Accepted: 10 August 2021

Published: 08 October 2021

Citation:

Menichetti A, Bartsoen L, Depreitere B,
Vander Sloten J and Famaey N (2021)
A Machine Learning Approach to
Investigate the Uncertainty of Tissue-
Level Injury Metrics for
Cerebral Contusion.
Front. Bioeng. Biotechnol. 9:714128.
doi: 10.3389/fbioe.2021.714128

Controlled cortical impact (CCI) on porcine brain is often utilized to investigate the pathophysiology and functional outcome of focal traumatic brain injury (TBI), such as cerebral contusion (CC). Using a finite element (FE) model of the porcine brain, the localized brain strain and strain rate resulting from CCI can be computed and compared to the experimentally assessed cortical lesion. This way, tissue-level injury metrics and corresponding thresholds specific for CC can be established. However, the variability and uncertainty associated with the CCI experimental parameters contribute to the uncertainty of the provoked cortical lesion and, in turn, of the predicted injury metrics. Uncertainty quantification via probabilistic methods (Monte Carlo simulation, MCS) requires a large number of FE simulations, which results in a time-consuming process. Following the recent success of machine learning (ML) in TBI biomechanical modeling, we developed an artificial neural network as surrogate of the FE porcine brain model to predict the brain strain and the strain rate in a computationally efficient way. We assessed the effect of several experimental and modeling parameters on four FE-derived CC injury metrics (maximum principal strain, maximum principal strain rate, product of maximum principal strain and strain rate, and maximum shear strain). Next, we compared the *in silico* brain mechanical response with cortical damage data from *in vivo* CCI experiments on pig brains to evaluate the predictive performance of the CC injury metrics. Our ML surrogate was capable of rapidly predicting the outcome of the FE porcine brain undergoing CCI. The now computationally efficient MCS showed that depth and velocity of indentation were the most influential parameters for the strain and the strain rate-based injury metrics, respectively. The sensitivity analysis and comparison with the cortical damage experimental data indicate a better performance of maximum principal strain and maximum shear strain as tissue-level injury metrics for CC. These results provide guidelines to optimize the design of CCI tests and bring new insights to the understanding of the mechanical response of brain tissue to focal traumatic brain injury. Our findings also highlight the potential of using ML for computationally efficient TBI biomechanics investigations.

Keywords: brain biomechanics, cerebral contusion, finite element modeling, tissue-level injury criteria, machine learning, controlled cortical impact, traumatic brain injury

INTRODUCTION

Cerebral contusion (CC) is a common type of traumatic brain injury (TBI) found across all age groups, which is often associated with lifelong disability and mortality (Alahmadi et al., 2010; Kirkman et al., 2013; Melvin and Yoganandan, 2015). CC is a focal TBI occurring from direct impacts and consisting of a bruise on the brain's surface (Hardman and Manoukian, 2002). CC is pathologically characterized by hemorrhagic lesions accompanied by necrosis and edema that generate within the cortex. In severe cases, CC can develop in the subcortical white matter, which may require immediate surgical intervention (McGinn and Povlishock, 2016). Besides falls and assaults, accidents on public roads are a major cause of CC (Ratnaike et al., 2011). Depreitere et al. (2004) found that 73% of the victims of bicycle-related casualties were diagnosed with CC. There is still no consensus on the mechanism causing CC, although a few theories have been proposed; these include the cavitation arising from the negative pressures generated at the opposite side with respect to the impact location (Gross, 1958) and the shear strain at bony protuberances consequent to the relative motion between skull and brain tissue (Holbourn, 1943), which could explain why the majority of CC are observed in the frontal and temporal lobes (Ommaya and Ommaya, 1995; Depreitere et al., 2004; Ratnaike et al., 2011).

Controlled cortical impact (CCI) is commonly used as a model of brain trauma to investigate the mechanopathology of CC *in vivo* on different animal species, including ferret, rodent, swine, and nonhuman primates (Xiong et al., 2013; Osier and Dixon, 2017; Kinder et al., 2019). In CCI experiments, a pneumatically or electromagnetically driven piston delivers the impact on the animal's exposed brain with a preestablished velocity and depth of indentation, therefore inducing a reproducible and localized injury. The swine model has been largely used because of the similarities with humans in terms of pathological features (Kinder et al., 2019) and brain tissue's mechanical properties (MacManus et al., 2020). However, a large span of values has been reported in the literature for experimental parameters, including but not limited to, the geometrical characteristics of the impactor or the depth and velocity of impact (Duhaime et al., 2000; Alessandri et al., 2003; Manley et al., 2006; Meissner et al., 2011; Sindelar et al., 2017; De Kegel et al., 2021). The variability and the uncertainty of the experimental parameters all contribute to the uncertainty in the injury outcome provoked by CCI.

Computational models of the head have been extensively used to quantify in mechanical terms the intracranial response to TBI by analyzing the relationship between the functional/structural damage and the brain tissue's stress and strain fields (Chen et al., 2014). In particular, finite element (FE) models have been regarded as valuable tools to determine tissue-level local injury thresholds for specific types of TBI (Kleiven, 2007; Scott et al., 2016; Giordano et al., 2017; Zhao et al., 2017; Horstemeyer et al.,

2019; Zhou et al., 2019; Hajiaghameh et al., 2020; Trotta et al., 2020; Wu et al., 2021). Regarding CC, several injury metrics have been proposed based on different quantities, with lack of agreement on which criterion outperforms the others. These metrics include maximum principal strain (Shreiber et al., 1997; Miller et al., 1998; Viano and Lövsund, 1999; Mao et al., 2010b; Mao and Yang, 2011), shear strain (Mao and Yang, 2011), strain rate (Viano and Lövsund, 1999; King et al., 2003), product of strain and strain rate (Viano and Lövsund, 1999; King et al., 2003), strain energy density (Shreiber et al., 1997; Mao and Yang, 2011), von Mises stress (Shreiber et al., 1997; Miller et al., 1998), maximum principal stress (Shreiber et al., 1997), shear stress (Huang et al., 2000), and intracranial pressure (Miller et al., 1998; Huang et al., 2000; Takhounts et al., 2003; Mao and Yang, 2011; Mao et al., 2013). In the case of focal injury patterns resulting from, for example, CCI or dynamic vacuum pressure tests, the use of strain and strain rate injury criteria is preferred over other metrics assessed in the literature, such as those based on stress, intracranial pressure, or strain energy (Shreiber et al., 1997; Mao and Yang, 2011). While several FE models of the pig brain have been developed to investigate different diffuse TBI scenarios (Coats et al., 2012; Zhu et al., 2013; Yates and Untaroiu, 2016; Hajiaghameh and Margulies, 2021; Wu et al., 2021), no computational model has specifically targeted the localized brain response to CCI experiments.

A recognized disadvantage of FE head models that have a high degree of geometrical complexity and biofidelity is the significant simulation runtime (Takhounts et al., 2008; Wu et al., 2020; Ghazi et al., 2021; Zhan et al., 2021) even when using high-performance computing platforms. This hampers the feasibility of studies that require repeated simulations, such as design optimization workflows, parameter estimation, or uncertainty quantification analyses. For the latter category, probabilistic methods are commonly used in biomechanics (Pal et al., 2008; Laz and Browne, 2010; Strickland et al., 2010; Bartsoen et al., 2021). Among them, the Monte Carlo simulation (MCS) is regarded as the gold standard technique because of its robustness and ability to converge to the correct uncertainty distribution solution (Laz and Browne, 2010). However, MCS is a time-consuming technique since it involves random sampling of the complex model, for example, the FE porcine brain model, depending on the statistical distribution of the input parameters. The accuracy of the solution (i.e., the uncertainty of the outcome of the model) depends on the number of samples considered, which can lead to computationally costly analyses. A time-efficient alternative is to use surrogates of the computationally expensive FE models. The development and implementation of supervised machine learning (ML)-based surrogates of complex biomechanics models is relatively recent. Promising applications of the ML surrogates include parameter estimation and uncertainty quantification

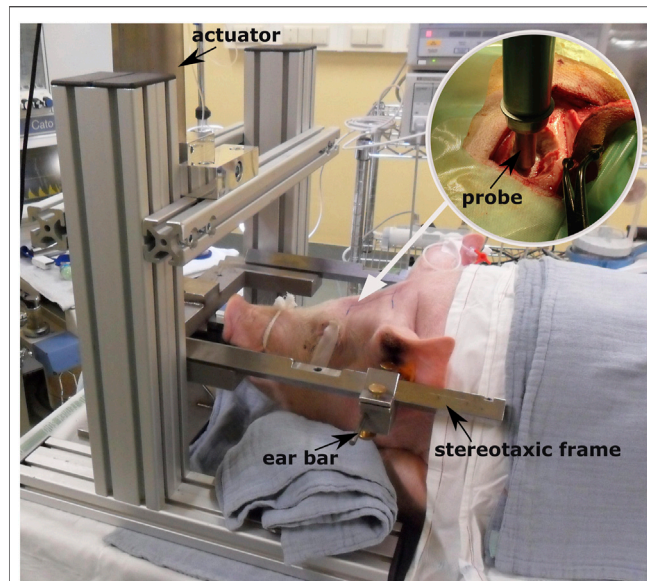


FIGURE 1 | Controlled cortical impact setup [adapted from De Kegel (2018)] and positioning of the animal prior to testing. The white arrow indicates the point where the craniotomy is performed after sedating the animal. The circular image on the top right corner illustrates how the probe is mounted on the electromagnetically driven actuator and is placed over the closed dura mater before the impact.

problems across several fields, such as TBI (Cai et al., 2018; Wu et al., 2019; Ghazi et al., 2021; Schroder et al., 2021; Zhan et al., 2021), cardiovascular (Davies et al., 2019; Cai et al., 2021) and musculoskeletal biomechanics (Pal et al., 2008; Strickland et al., 2010; Bartsoen et al., 2021). Regarding the research on head impact biomechanics, Wu et al. (2019), Ghazi et al. (2021), Zhan et al. (2021) employed machine learning algorithms to predict the brain strain response of computationally expensive FE models of the human head in an accurate and time-efficient way. Once trained and tested, the ML surrogates can estimate the outcome of the complex model in a conveniently short time frame. In the case of uncertainty quantification problems, an MCS can be directly performed on the ML surrogate outcome with the advantage of reducing dramatically the computational cost, albeit accepting a degree of approximation (Laz and Browne, 2010).

This study has four main outcomes. First, we present the FE model of an atlas-based porcine brain undergoing CCI, which predicts the mechanical response of the brain tissue to the impact. Second, we develop an artificial neural network as a computationally efficient ML surrogate of the FE pig brain model. Third, by means of the ML surrogate model, we evaluate the effect of different experimental and modeling parameters on four potential CC injury metrics, that is, maximum principal strain, maximum principal strain rate, product of maximum principal strain and strain rate, and maximum shear strain. Finally, we compare the experimental cortical injury data from *in vivo* CCI tests on pig brain with the *in silico* results in order to evaluate the prediction performance of the tissue-level injury metrics specific for CC.

MATERIALS AND METHODS

Controlled Cortical Impact Tests

The experimental data on the assessment of CC damage were retrieved from a previous study within our research group, where 34 Landrace male domestic pigs, aged 4–5 months, and weighing on average 60.7 ± 10.9 kg underwent controlled cortical impacts *in vivo* (Figure 1). The full description of the experimental protocol can be found in De Kegel et al. (2021) and it is briefly summarized here. General anesthesia was induced to the animals prior to performing craniotomy, which was done unilaterally on the left hemisphere and was located immediately parasagittal and posterior to the coronal suture. Afterward, the impact was delivered directly on the exposed dura mater by means of an electromagnetically controlled cortical impactor (PinPoint PCI3000, Hatteras Instrument Inc.), which regulated the impact depth (range between 1.1–12.6 mm), velocity (range between 0.4–2.2 m/s), and dwell time (= 200 ms) of an hemispherical stainless steel tip (diameter = 10 mm). A brain magnetic resonance (MR) scan (Prisma Fit 3T scanner, Siemens) was performed under general anesthesia 48 h after the impact to ensure full development of CC. The presence of cortical damage and underlying white matter edema were evaluated on the MR scans by a senior neuroradiologist and a senior neurosurgeon. The volume of white matter edema was quantified using image segmentation (Mimics, Materialise). After the scans, the animals were euthanized and the brain was extracted for histology processing with the aim of confirming the presence of cortical necrosis, an indicator of the provoked CC. Table 1 summarizes the combination of impact parameters chosen and the cortical damage evaluation in the 14 cases of the cohort for which full CC assessment was possible.

Development and Validation of the FE Model of the Porcine Brain Undergoing CCI

The FE model mimics the experimental loading conditions that the porcine brains underwent during CCI testing. The model

TABLE 1 | Experimental impact parameters and results of the CCI performed *in vivo* on the pig brain (De Kegel et al., 2021) for which medical imaging and histological assessment of CC were available. In case of detectable disruption of the cortical layer the “Cortical damage” is marked as “+,” otherwise as “–.” The animal number in parentheses refers to the numbering used in De Kegel et al. (2021).

Animal #	Peak depth (mm)	Velocity (m/s)	Cortical damage
I (12)	11.2	2.1	+
II (13)	8.9	2.2	–
III (14)	9.1	1.8	+
IV (15)	10.8	1.8	+
V (16)	10.8	1.8	+
VI (17)	12.6	1.7	+
VII (18)	8.9	2.2	+
VIII (19)	6.9	2.2	+
IX (20)	5.5	2.0	+
X (21)	4.3	1.5	–
XI (22)	2.3	0.8	–
XII (31)	2.0	0.4	–
XIII (33)	1.1	0.4	–
XIV (34)	2.8	0.4	+

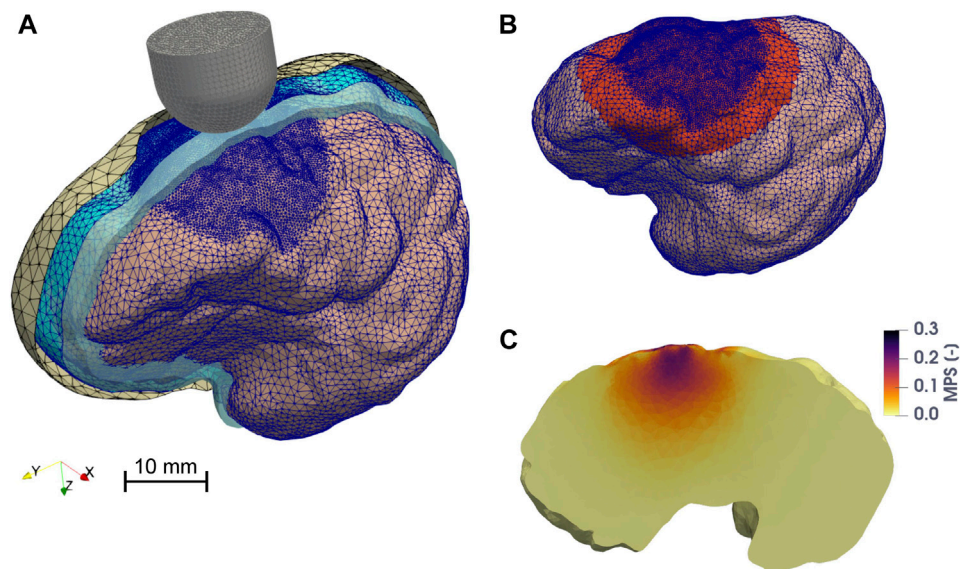


FIGURE 2 | Finite element model of the porcine brain undergoing CCI. **(A)** Overview of the assembly of the model. The skull, the DAM, and the CSF are represented with parallel sectioned views. The mesh of the discrete rigid parts (skull = yellow and probe = gray) is depicted in black, while the mesh of the deformable bodies (brain hemisphere = pink, DAM = cyan), which is finer in the vicinity of the impact point, is colored in blue. The cavity filled by CSF is represented in light blue. **(B)** The zone highlighted in red represents the elements of the brain (in the undeformed configuration) belonging to the region of interest (ROI), considered for the computation of the 95th percentile of MPS, MPSR, MPSXSR, and MSS. **(C)** Maximum principal strain distribution on a parasagittal cross section of the brain when the probe reaches maximum depth. The image is taken from one of the FE CCI simulations used to train the ANN. The input parameters were: a hemispherical probe (diameter = 15 mm), velocity of indentation = 1.8 m/s, depth of indentation = 5.4 mm, angle of inclination = 3°, DAM-probe friction coefficient = 0.24, and thickness of the meninges = 0.655 mm. The highest MPS values are concentrated around the impact point, within the ROI.

consists of the impacting probe, the skull, the meningeal complex, the cerebrospinal fluid, and the brain. The geometry of the brain was generated in 3-Matic (Materialise) after segmentation in Mimics (Materialise) using a high voxel resolution ($100\ \mu\text{m} \times 150\ \mu\text{m} \times 100\ \mu\text{m}$) MR image-based 3D atlas of the domestic pig's brain (Saikali et al., 2010). The obtained mask was smoothed while preserving the gyral pattern. The 3D atlas-based geometry was rescaled by a factor of 1.27 to match the average brain size of the pigs of the experimental cohort, calculated by measuring the anteroposterior length of the corpus callosum in the sagittal plane of every post-CCI MR scan. Since the standard deviation of the scaling factors was relatively low ($= 0.07$), we used a single brain size for all CCI cases. In order to reduce the computational cost, only the left hemisphere was considered for the model. This is a fair approximation, justified by the fact that unilateral CCI has a negligible effect on the unimpacted hemisphere (Elliott et al., 2008; Mao and Yang, 2011). The two outermost meningeal membranes (i.e., the dura-arachnoid mater (DAM)) were modeled as a unique part, while the third and innermost layer (the pia mater) was integrated into the brain part, in a similar fashion as MacManus et al. (2017). The DAM geometry was generated in 3-Matic by offsetting the cortical surface of the brain outwards and subsequently wrapping and smoothing the brain convolutions. Similar to Coats et al. (2012), an average gap of 1 mm was maintained between the surface of the brain and the inner surface of the DAM to account for the subarachnoid space in which the cerebrospinal fluid (CSF) flows.

The skull was generated by extending the DAM geometry outwards. A circular hole (diameter = 23 mm) on the superior part of the skull was created in 3-Matic to mimic the unilateral craniotomy and to virtually expose the dura mater. Here, the discrete rigid skull surface is acting as a geometrical boundary to constrain unrealistic deformations of the DAM and the brain, rather than being a strict anatomical representation of the porcine cranial bones (Figure 2).

All the porcine geometrical parts were imported into ANSA (BETA CAE Systems) for mesh generation, which was performed using quality control criteria that included an aspect ratio < 3 , skewness > 0.7 , Jacobian > 0.7 , minimum angle for triangles and tetrahedrons $> 30^\circ$, and maximum angle for triangles and tetrahedrons $< 120^\circ$. The meshes of the brain and DAM were refined in the vicinity of the impact point of the probe. A convergence analysis was carried out on the brain mesh to ensure stability and sufficient resolution of the mesh while minimizing the computational runtime. The optimal brain mesh resulting from the convergence analysis findings counted 203,167 quadratic tetrahedral elements of type C3D10M from the Abaqus/Explicit v.2019 (Dassault Systèmes) library. This was preferred over the regular second-order tetrahedrons of type C3D10 due to its superior performance in minimizing volumetric locking for nearly incompressible materials. The skull mesh consists of 3,090 linear triangular discrete rigid elements, while the DAM consists of 20,590 linear triangular shell elements (type S3R) with thickness that varies between 0.413

TABLE 2 | Material properties used in the FE model of the porcine brain FE.

Part	Density	Material model	Material parameters
Brain	1,060 kg/m ³	Neo-Hookean-based quasi-linear viscoelastic MacManus et al. (2017)	$\mu = 6.97$ kPa $\nu = 0.49995$ $g_1 = 0.451$ $g_2 = 0.301$ $\tau_1 = 0.021$ s $\tau_2 = 0.199$ s
Dura-arachnoid mater (DAM)	1,000 kg/m ³	Neo-Hookean-based quasi-linear viscoelastic MacManus et al. (2017)	$\mu = 19.10$ kPa $\nu = 0.4$ $g_1 = 0.568$ $g_2 = 0.240$ $\tau_1 = 0.034$ s $\tau_2 = 0.336$ s
Cerebrospinal fluid (CSF)	1,000 kg/m ³	Homogeneous fluid-filled cavity	$K = 2.1$ GPa

μ , shear modulus; ν , Poisson's ratio; g_1 and g_2 , first and second term of the relaxation function of the Prony series that describes the viscoelastic behavior; τ_1 and τ_2 , first and second term of the time constant of the Prony series that describes the viscoelastic behavior; K , bulk modulus.

and 1.058 mm (see *Input and Output Parameters of the FE Model*) to cover the range of values reported by Vanmol (2017) and Walsh et al. (2018). Linear triangular discrete rigid elements were used to mesh the probe, with the number of elements varying between 498 and 5,324 depending on the diameter size.

Both the brain and the DAM were considered to be homogeneous and isotropic materials, using neo-Hookean-based quasi-linear viscoelastic models. The material properties were retrieved from MacManus et al. (2017), who characterized the mechanical behavior of the porcine brain and the DAM under large deformation by means of dynamic indentation *in situ*. Specifically, the viscoelastic parameters were obtained by fitting the results of an inverse finite element model of the indentation experiments with simulated loading conditions representative for the CCI.

The presence of CSF was included by using the fluid-filled cavity definition available in Abaqus to model liquid-filled structures enclosed by surfaces. The density and bulk modulus of water were used to approximate the CSF (Kleiven, 2007). **Table 2** provides a summary of all the material parameters used in the FE model of the porcine brain.

The “general contact” definition was used to govern the interactions between parts, with a penalty friction formulation to model the interaction between the probe and the outer surface of the DAM. The friction coefficient varied between 0.07 and 0.26 (see *Input and Output Parameters of the FE Model*) or the range of values reported by Rashid et al. (2012), who estimated the friction between the porcine brain and metal platens with unconfined compression tests. Here, we assumed that the porcine brain and DAM have the same frictional behavior against metal. Only one hemisphere was considered in the FE model; therefore, we constrained the out-of-sagittal plane linear and rotational motion of the medial side of the DAM to mimic the presence and mechanical role of the falx (Walsh et al., 2021). In a similar way, given the distance from the area of influence to the impacting probe, we simplified the presence of the diencephalon, the brainstem, and the cerebellum by constraining any translation of the inferior part of the DAM. The simulated time was varied as a

function of the assigned probe's displacement-time profile to include 50 ms of dwell time after the probe reached the maximum indentation depth. The simulations were run using the explicit solver of Abaqus v. 2019, which accounted for geometric nonlinearities throughout the whole computation. Element mass scaling was introduced if the stable time increment decreased below 1.2×10^{-6} s. We verified that the total percent change in mass of the model resulting from mass scaling was <4% for all simulations.

With the aim of collecting data to validate the assumptions made in the FE model, we performed an additional test *in vivo* on a pig (from an unrelated experiment) to measure the reaction force exerted by the brain on the probe during a CCI, since De Kegel et al. (2021) reported no quantitative assessment of the mechanical response of the pigs' brains to the impacts. To this extent, a dynamic load cell (PCB 208B, load capacity = ± 45 N, resolution = 0.0009 N) was mounted on the CCI device using a custom-made nylon support. The hemispherical probe was connected to the load cell by means of a lightweight, aluminum threaded support. The pig underwent the same testing protocol as described in De Kegel et al. (2021), with the same velocity and depth of indentation of case III (**Table 1**), that is, 1.8 m/s and 9.1 mm. During the impact, the force in the direction of the axis of the probe was measured with a sampling rate of 5,000 Hz. Subsequently, the CCI was simulated with the porcine brain FE model, and the force exerted by the brain on the probe in the direction of its axis was computed. The computational and experimental force-time signals were compared and their correlation was quantified using the software CORA (Correlation and Analysis, Version 3.6.1) (Gehre et al., 2009) to verify that the brain impact mechanics was correctly modeled. The CORA software combines two independent rating techniques (the cross-correlation and the corridor method) to express the level of similarity between the experimental and computational curves with a score between 0 and 1, with 1 meaning perfect correlation. The two ratings had equal weight on the overall rating ($G1 = G2 = 0.5$). Regarding the cross-correlation-based score, we set equal weights ($= 1/3$) to amplitude, shape, and phase errors. A linear transition between ratings was chosen ($k_V = k_P = k_G = 1$).

TABLE 3 | Range of values and statistical distribution of the input parameters of the porcine brain FE model considered for the uncertainty and sensitivity analyses. For the DAM-probe friction and DAM thickness parameters normal distributions are used, since their values are measured experimentally. The parameters that are selected upon designing the CCI experiments have either a discrete or uniform distribution.

Input parameter	Lower bound	Upper bound	Statistical Distribution
Diameter probe	5 mm	20 mm	Discrete
Shape of the tip of the probe	0 (=cylindrical)	1 (=hemispherical)	Discrete
Velocity of indentation	0.4 m/s	4 m/s	Uniform
Depth of indentation	1.1 mm	12.6 mm	Uniform
Inclination of the probe	−15°	15°	Uniform
DAM-probe friction	0.07	0.26	Normal
Thickness DAM	0.413 mm	1.058 mm	Normal

Input and Output Parameters of the FE Model

Seven parameters of the FE model were considered for the uncertainty and sensitivity analyses due to the relatively large spread of values reported in the literature. The list included the probe's diameter and shape (hemispherical or cylindrical), the velocity and the depth of indentation, the friction between the DAM and the probe, the inclination angle between the axis of the probe and the normal of the DAM surface, and the thickness of the DAM. Each of these input parameters varied between a lower and upper bound with specific statistical distributions (Table 3). The lower and upper bounds for the probe geometrical and kinematics parameters (i.e., diameter, shape, angle of inclination, and velocity and depth of indentation) were chosen to comprise the values reported in the literature for CCI tests on pig brain (Madsen and Reske-Nielsen, 1987; Duhaime et al., 2000; Alessandri et al., 2003; Manley et al., 2006; Meissner et al., 2011; Sindelar et al., 2017; De Kegel et al., 2021). For the friction between the probe and the DAM, the coefficients obtained experimentally by Rashid et al. (2012) were used. Finally, the measures on the porcine meninges performed by Vanmol (2017) and Walsh et al. (2018) were used to determine the lower and upper bound of the DAM thickness.

The FE porcine brain model was used to compute the mechanical response of the brain to the CCI. We considered four different tissue-level injury metrics: the logarithmic maximum principal strain (MPS), the logarithmic maximum principal strain rate (MPSR), the product of logarithmic maximum principal strain and strain rate (MPSXSR), and the logarithmic maximum shear strain (MSS). As estimators of CC, we computed the 95th percentile of the peak MPS, MPSR, MPSXSR, and MSS of the brain elements belonging to the region of interest (ROI) in the brain that is directly affected by the CCI, namely, where the primary focal traumatic brain injury can arise (Figure 2). The elements were considered as a part of the ROI if their centroid was within a 40 mm distance from the impact point on the brain surface. We did not consider the 100th percentile of the peaks in order to discard any unrealistically high values due to computational artifacts (Panzer et al., 2012).

Machine Learning-Based Surrogate Model

To perform the uncertainty quantification in a computationally efficient way, we developed a surrogate of the FE porcine brain model. An artificial neural network (ANN) was employed as the surrogate modeling technique, which was implemented in

TensorFlow 2.0.2 (Abadi et al., 2016). The ANN algorithm was adapted from Bartsoen et al. (2021), who demonstrated the superior accuracy performance of ANN with respect to other probabilistic modeling techniques based on the response surface method, such as 2nd order polynomial, Gaussian process regression, or support vector regression (Laz and Browne, 2010). To train and validate the ANN, we generated a total of n samples, where each sample consisted of a set of seven input values (one per input parameter) selected with the Sobol sequence among the ranges indicated in Table 3, and four outputs (the 95th percentile of MPS, MPSR, MPSXSR, and MSS) computed with the FE porcine brain model. The amount of training and validation samples were $0.9n$ and $0.1n$, respectively.

The architecture of the network consisted of fully connected layers (7:256:128:64:32:16:4) with the Softplus activation function $a(x) = \ln(1 + \exp(x))$, where x is the input to a neuron. The output layer had the ReLU activation function $a(x) = x^+ = \max(0, x)$ to exclude negative outputs. As our loss function, we used the Huber loss function, as given below:

$$\begin{cases} \frac{1}{2} e^2 & \text{if } |e| \leq d \\ \frac{1}{2} d^2 + d(|e| - d) & \text{if } |e| > d \end{cases}, \quad (1)$$

where e represents the residuals, that is, the difference between the observed (y) and predicted values (\hat{y}): $e = y - \hat{y}$, while d is a parameter set equal to 0.1. The Huber loss computed using Eq. 1 has a similar behavior as the mean squared error (MSE) for small errors but the mean absolute error (MAE) for large errors so that it is less affected by outliers. The network was trained using an Adam optimizer with a learning rate = 0.001 that decays upon convergence of the loss. To prevent overtraining, L2 kernel regularization was applied. The ANN accuracy was further improved with ensemble averaging, in which we considered a weighted average of six networks trained on the same training and validation data. The weights were optimized by minimization of the validation MSE. The normalized mean absolute error (nMAE), normalized root mean squared error (nRMSE), and 95% absolute error (95% AE) were evaluated. The nMAE and nRMSE were computed after normalizing the output range to [0;1], while the 95% AE gives the 95th percentile of the AE. The optimal number of samples used to train and validate the ANN was selected after carrying out a 5-fold cross-validation.

The ANN performance was evaluated considering the nMAE, nRMSE, and 95% AE on the validation and training samples for each of the four outputs, considering a total of 10, 20, 40, and 80 samples. The minimum number of samples that yielded nMAE, nRMSE, and 95% AE < 4% was 80 (training samples = 72, validation samples = 8).

With the ML surrogate model, we achieved a considerable increase in computational efficiency compared to a typical FE model simulation. The average computational time to simulate a CCI with the FE porcine brain model was approximately 2 h when parallelizing the execution between 144 domains (Xeon Gold 6140, CPUs at 2.3 GHz) using the high-performance computing centrum (VSC—Flemish Supercomputer Center). On the contrary, generating 80 FE samples took ~160 h, while the training of the ANN was completed in about 7 min. Predicting the values of the CC injury estimators with the trained ANN was immediate (<0.01s); therefore, the advantage of utilizing a surrogate model for uncertainty and sensitivity analyses is clear, especially when considering the large number of simulations necessary for the sensitivity analysis (see *Sensitivity Analysis*).

Sensitivity Analysis

Once the ANN was trained and tested, we utilized the surrogate model as basis for the Monte Carlo simulations because of its very low computational cost in generating a large number of samples (Laz and Browne, 2010). Knowing the statistical distributions of the input parameters (Table 3), we performed the uncertainty analysis using the MCS with 10,000 samples. In each MCS, one parameter was kept constant and equal to a value inside the bounds according to its statistical distribution. In particular, the shape had two possible levels (0 = cylindrical probe and 1 = hemispherical probe), the diameter of the probe had four (5–10–15–20 mm), and all the other parameters had ten each (ten values equally spaced between the lower and the upper bound, shown in Table 3). Therefore, we repeated the MCS 56 times in order to assess the effect of each individual input on the injury metrics.

To rank the importance of the influence of the input uncertainty on the output distribution, we computed two global indicators using the open source Python's library SALib. The first one is the δ moment-independent measure (Borgonovo, 2007)

$$\delta_i = \frac{1}{2} E_{X_i} [s(X_i)],$$

where δ_i is the moment-independent indicator of the sensitivity of the output, Y , to the input parameter X_i , and $E_{X_i}[s(X_i)]$ represents the expected shift in the distribution of Y provoked by X_i .

The second indicator considered here is the first-order sensitivity index $S1_i$ (Sobol, 2001),

$$S1_i = \frac{V_i}{V[Y]},$$

where $S1_i$ is the first-order sensitivity index specific to the input parameter X_i , which represents the expected reduction in the

variance of the output $V[Y]$ in a hypothetical case in which the uncertainty relative to the input parameter, X_i , would be excluded.

One common mathematical property for both indicators is that given an input parameter, X_i , for a fixed output, Y , the closer δ_i or $S1_i$ are to 1, the more important the parameter X_i is for Y . In the extreme case, if δ_i or $S1_i = 1$, then Y only depends on X_i ; conversely if δ_i or $S1_i = 0$, then X_i has no influence on Y . The seven δ_i 's and seven $S1_i$'s were estimated after generating 10,000 sets of input parameters by means of Latin Hypercube sampling, which were used in the ML surrogate model to predict the 95th percentile of MPS, MPSR, MPSXS, and MSS.

Performance Evaluation of the CC Injury Metrics

The case-specific 95th percentile MPS, MPSR, MPSXS, and MSS were predicted by the trained ANN using the known experimental parameters of each CCI test as input. For all the CCI cases we used diameter of the probe = 10 mm, inclination of the probe = 0°, and shape of the tip = 1 (hemispherical). We assumed friction of the DAM-probe = 0.163 mm and thickness of the DAM = 0.736 mm, that is, the mean values of the corresponding normal distributions (Table 3). The velocity and depth of indentation were chosen depending on the values specific for each test (Table 1). In order to use binary values to express the presence or absence of visible disruption of the cortical layer (Table 1), we used the dummy variable "1" when CC was confirmed and "0" when no injury was detected.

A Wilcoxon Rank-Sum test (significance level = 0.05) was carried out to assess the effectiveness of each injury estimator in distinguishing between CCI cases with cortical damage and without cortical damage.

The injury risk curves that express the likelihood of sustaining CC depending on the different FE-derived injury predictors were obtained by performing univariate logistic regression, a technique that has been broadly used to determine injury tolerances based on experimental data and predict the outcome of TBI (Shreiber et al., 1997; Takhounts et al., 2003; Kleiven, 2007; Steyerberg et al., 2008; Cai et al., 2018; Anderson et al., 2020; Hajiaghmemar et al., 2020). We selected a logistic regression classifying method due to the binary nature (CC or no CC) of the outcome of the CCI data, obtained by means of the post-injury MR scans and histology assessments (De Kegel et al., 2021). In the logistic regression model the probability p of sustaining CC as function of an injury predictor X is described by the relationship

$$p(X) = \frac{1}{1 + \exp(-b_0 + b_1 \cdot X)},$$

where b_0 and b_1 are the regression coefficients.

The accuracy of the injury metric-specific prediction of CC likelihood was evaluated using a leave-one-out cross-validation (LOOCV). We selected a LOOCV framework because of its low bias and the limited size of our dataset (14 samples) (Beleites et al., 2005; Cai et al., 2018; Anderson et al., 2020). In order to perform an objective comparison between the performances of the

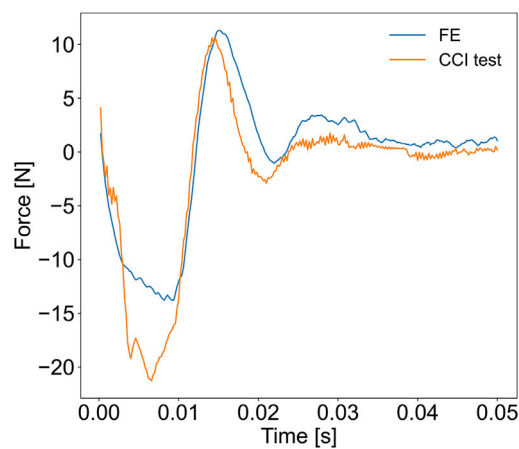


FIGURE 3 | Results of the validation of the FE porcine brain model. The reaction force exerted by the impacted brain on the probe during the CCI was measured experimentally and compared with the force-time history simulated with the FE model.

univariate logistic regression classifiers, we computed the LOOCV accuracy, sensitivity, and specificity. We also reported the AUC, that is, the area under the receiver operating characteristic (ROC) curve, for both the training and the testing datasets, similar to Cai et al. (2018) and Anderson et al. (2020). In particular, the metric-specific AUC value for the training dataset was calculated as the average of the AUCs of 14 independent injury predictions and each one obtained considering 13 simulated CCI cases, conforming to the LOOCV framework. The metric-specific AUC value for the testing dataset was determined taking into account the 14 independent injury predictions. The implementation of the LOOCV framework and the performance evaluation of the injury estimators were carried out using Python's machine learning library scikit-learn.

RESULTS

To validate the FE model of the porcine brain undergoing CCI, we calculated the CORA score by comparing the experimentally measured and the simulated force-time curves of the probe. The overall CORA rating was equal to 0.827 (the cross-correlation method = 0.880 and the corridor method = 0.773), which corresponds with the “good biofidelity” category. Therefore, the FE model yielded a sufficiently accurate prediction of the localized force-time response of the pig's brain to CCI (**Figure 3**).

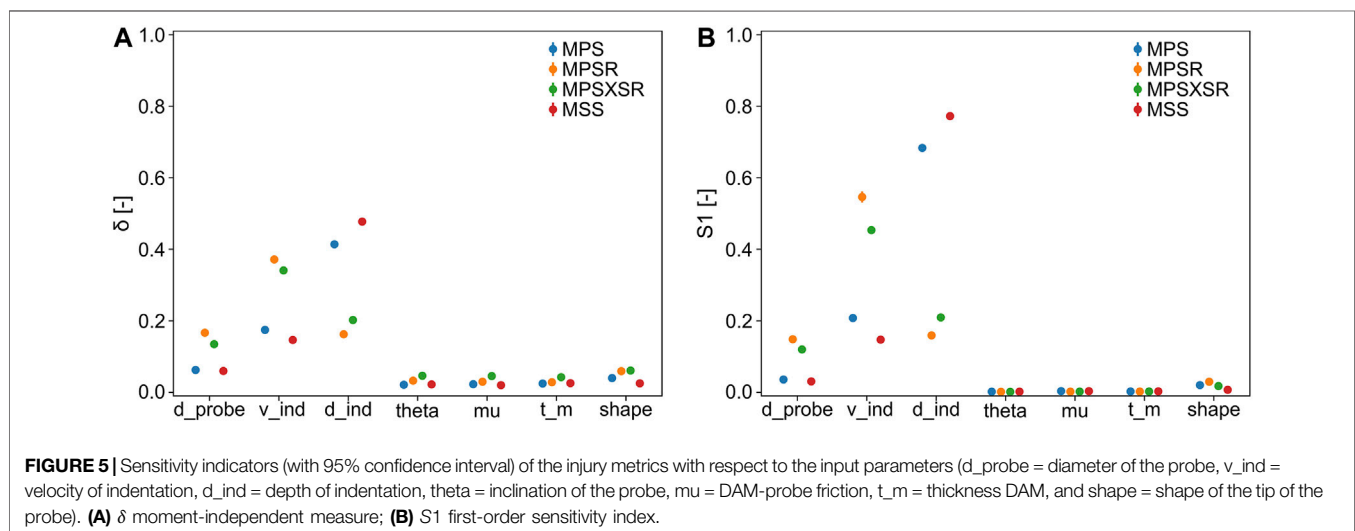
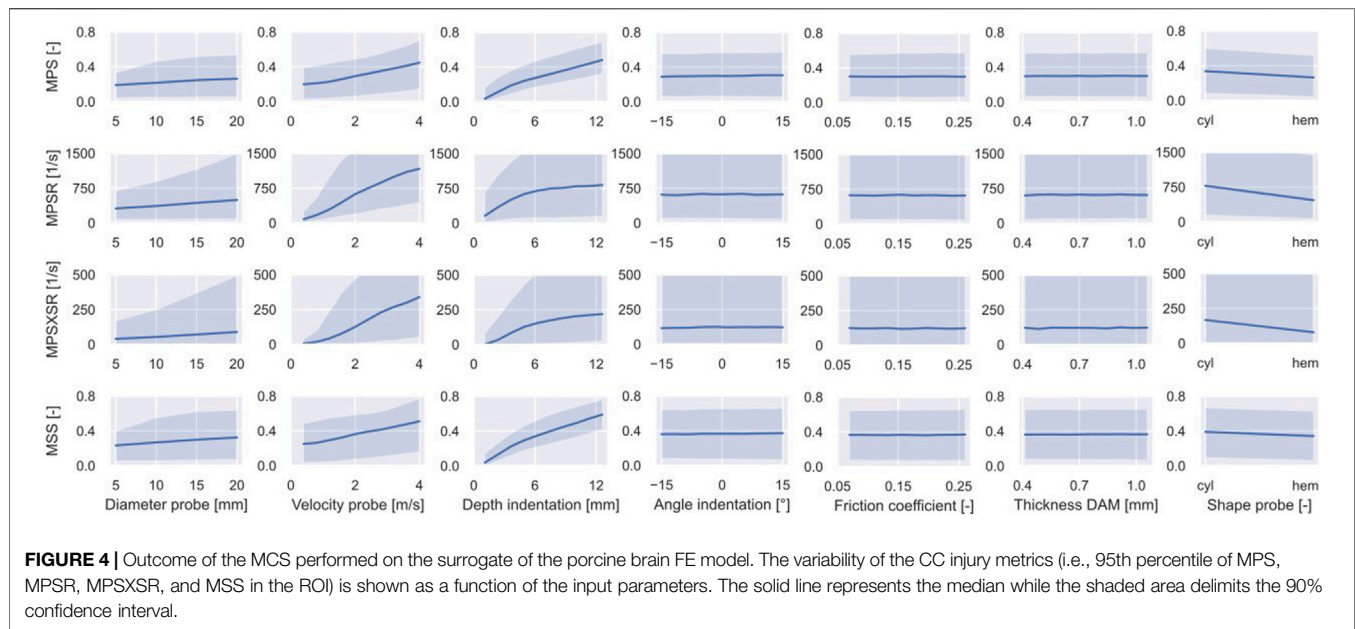
The 95th percentiles of the MPS, MPSR, MPSXSR, and MSS of 10,000 simulations were predicted using the ML-based surrogate of the porcine brain's FE model. The results of the MCS are shown in **Figure 4**, which displays the effect (indicated by the slope of the curves representing the median response) that each individual input parameter has on the predicted injury metrics, as well as on their variability. Interestingly, the angle of inclination, the DAM-probe friction, and the thickness of the DAM have minimal or no influence

on the four injury metrics. The difference in shape of the probe's tip has little effect on MSS and MPS, while it produces more pronounced discrepancies in terms of MPSR and MPSXSR. In particular, a hemispherical probe yields both lower strain and strain rates. The median of all four injury metrics increases quasi-linearly with the diameter of the probe; however, their variability (i.e., the 95% confidence interval bound) increases nonlinearly when considering larger diameters. Although all injury metrics increase with the velocity of indentation, the quasi-linear relationship observed with MPS and MSS is not apparent for MPSR and MPSXSR where large variability for higher speeds is visible. Large variability at higher values and nonlinearity of the median are also noticeable for MPSR and MPSXSR as a function of the depth of indentation. MPS and MSS exhibit quasi-linear and monotonically increasing relations with the depth of indentation. The variability of MPS and MSS as a function of the depth of indentation is the lowest of all, suggesting that the depth of indentation has a prominent role in the definition of the brain strain field.

The results of the sensitivity analysis with 10,000 samples are displayed in **Figure 5**. Both sensitivity indicators show a very similar trend in terms of ranking the importance of the input parameters despite showing different absolute values. In particular, the most important parameter for MPS and MSS is the depth of indentation (MPS: $\delta = 0.414 \pm 0.008$, $S1 = 0.683 \pm 0.008$; MSS: $\delta = 0.477 \pm 0.007$, $S1 = 0.772 \pm 0.004$), while the parameter with the biggest influence on MPSR and MPSXSR is the velocity of impact (MPSR: $\delta = 0.372 \pm 0.008$, $S1 = 0.546 \pm 0.015$; MPSXSR: $\delta = 0.341 \pm 0.007$, $S1 = 0.453 \pm 0.011$). On the contrary, the angle of inclination, the DAM-probe friction, and the thickness of the DAM exhibited little or no influence on any of the four injury metrics, which was demonstrated by both δ (<0.05 for all injury metrics) and $S1$ (<0.005 for all injury metrics). The diameter of the probe ranked as the third most influential parameter on all injury metrics (MPS: $\delta = 0.063 \pm 0.003$, $S1 = 0.036 \pm 0.007$; MPSR: $\delta = 0.167 \pm 0.004$, $S1 = 0.148 \pm 0.010$; MPSXSR: $\delta = 0.135 \pm 0.008$, $S1 = 0.120 \pm 0.011$; MSS: $\delta = 0.060 \pm 0.003$, $S1 = 0.031 \pm 0.007$). The shape of the probe exhibited limited influence on the outcome of the simulations, with slightly higher δ in case of MPSR and MPSXSR (0.059 ± 0.005 and 0.061 ± 0.003 , respectively) and slightly higher $S1$ when considering MPSR ($= 0.030 \pm 0.005$). The complete table with δ moment-independent measures and first order sensitivity indices $S1$ of the injury metrics as a function of the input variables is available in the **Supplementary Material**.

The effectiveness of each scalar injury metric in separating between cases with CC and without CC based on the magnitude of the estimator was assessed *via* the Wilcoxon Rank-Sum test. The statistical analysis (**Figure 6**) confirmed that the 95th percentiles of MPS and MSS were significantly different between the simulated cortical damage and no damage cases (p -value = 0.0234 in both cases). Conversely, within the considered dataset, the 95th percentile of MPSR and MPSXSR of the injury and no injury groups were not significantly different (p -values = 0.110 and 0.083, respectively).

The LOOCV procedure was implemented to test the robustness and compare the performance of the metric-specific univariate logistic regressions. Within the LOOCV framework, the accuracy, sensitivity, specificity, and AUC on the testing dataset scores were



equivalent for all the FE-based injury predictors (Table 4). However, the AUC score calculated on the training datasets revealed that MPS and MSS (both average AUC = 0.878) outperformed MPSR (0.767) and MPSXSR (0.789). The ROC curves for both the testing and training datasets are available in the **Supplementary Material**.

Figure 7 illustrates the injury risk curves representing the probability of sustaining CC as a function of the 95th percentile of MPS, MPSR, MPSXSR, and MSS predicted with the porcine brain ML surrogate model and based on the *in vivo* CCI data. We determined the metric-specific injury thresholds by computing the value of the predictors that corresponds to a 50% probability of sustaining CC, estimated using the univariate logistic regression curve of the whole dataset. The obtained thresholds were MPS = 0.16, MPSR = 245 s^{-1} , MPSXSR = 45 s^{-1} , and MSS = 0.22.

DISCUSSION

FE Porcine Brain Model

The FE model simulated the intracranial response of the porcine brain undergoing CCI to explore the relationship between the deformation and rate of deformation of the cerebral tissue and the risk of sustaining CC. Besides the reduced simulation runtime resulting from using a simplified geometry, the rationale behind the development of a single brain hemisphere model was the focal nature of CC induced by CCI tests, which are designed to damage only the ipsilateral side of impact (Alessandri et al., 2003; Elliott et al., 2008). Contrary to other porcine head FE models that cope with loading conditions involving the kinematics of the whole head (Coats et al., 2012; Yates and Untaroiu, 2016; Hajiaghameh and Margulies, 2021), the current model is

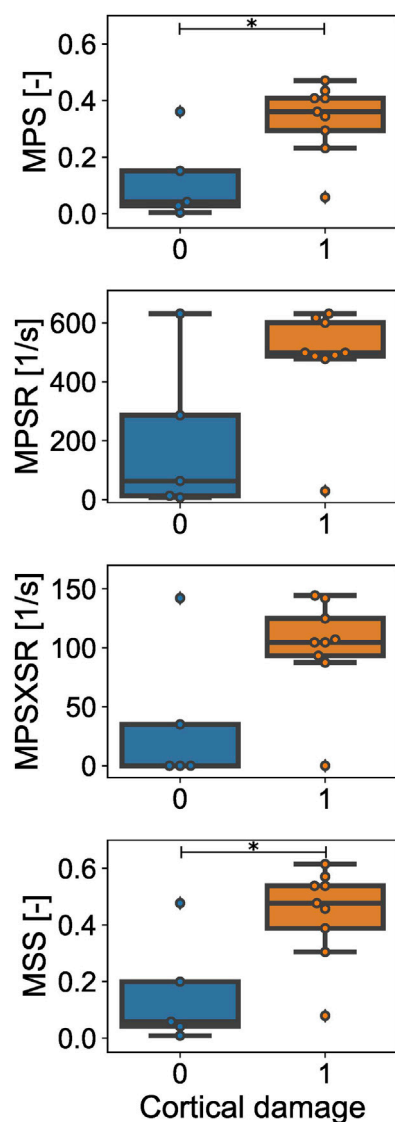


FIGURE 6 | Estimated values of the injury metrics for the CCI injury (orange) vs. no injury (blue) cases. Maximum principal strain (MPS) and maximum shear strain (MSS) are different for cases with observed cortical damage vs. no damage. No statistical difference is observed in terms of maximum principal strain rate (MPSR) and maximum principal strain x strain rate (MPSXSR) between injury and no injury cases. * = p -value < 0.05.

conceived to simulate localized impacts only, therefore the geometrical simplification adopted is sufficient. The validation carried out by comparing the impact forces supported the suitability of the FE model and its boundary conditions. However, no experimental measurement of the brain tissue deformation was available for further validation, which, therefore, represents a limitation. *In vivo* measurements of the deformation of the brain tissue during CCI are practically very challenging, given the very limited visibility of the cortex and accessibility between the probe and the craniotomy burr hole. Future validation efforts could consider measuring dynamic cortical deformation *in vivo* by applying vacuum pulses on the

exposed parenchyma, as reported by Schreiber et al. (1997) and Mao et al. (2006) using rat brains. The stability of the model was ensured for all the simulations, where no excessive distortion of the deformable parts (i.e., brain and DAM) was observed.

The assumptions of homogeneity and isotropy of both the brain-pia mater and DAM complexes could represent a matter of debate for the present FE model. Indeed, various studies have reported that porcine gray and white matter might display different stiffness, although these differences seem to depend on the testing conditions (Prange and Margulies, 2002; Gefen and Margulies, 2004; van Dommelen et al., 2010; Elkin et al., 2011; Kaster et al., 2011; Li Z. et al., 2020). Moreover, integrating the pia mater with the underlying brain tissue might underestimate the protective role of the innermost meningeal layer, which exhibits a higher elastic modulus than the brain (Li Y. et al., 2020; Walsh et al., 2021). While it is generally agreed upon that gray matter shows an isotropic behavior, it has been reported that white matter exhibits a degree of anisotropy in regions with significant axonal fiber alignment such as the corpus callosum (Prange and Margulies, 2002; van Dommelen et al., 2010; Feng et al., 2017). On the other hand, the homogeneity and isotropy of the mechanical behavior of the cerebral dura mater, in spite of the presence of collagen fibers, has been confirmed in different studies (De Kegel et al., 2018; Pierrat et al., 2020). Nevertheless, there is no constitutive law capable of capturing the mechanical behavior of the cerebral and meningeal tissues under any arbitrary loading condition, which necessitates that the selected material models be calibrated under testing conditions similar to the problem considered (de Rooij and Kuhl, 2016). Therefore, the neo-Hookean quasi-linear viscoelastic models for the brain-pia mater and DAM complexes obtained by MacManus et al. (2017) were a reasonable choice, as they were calibrated with dynamic indentations of the brain surface.

Several approaches have been adopted in the literature to model the presence of CSF in FE head models, such as the use of linear elastic solid elements for the CSF (Kleiven, 2007; Coats et al., 2012; Trotta et al., 2020), or fluid-structure interaction (Zhou et al., 2019). Other studies incorporated the cerebral vasculature in the FE head models and found that it reduces the brain strains resulting from blast exposures (Unnikrishnan et al., 2019) and head collisions (Zhao and Ji, 2020b). Coats et al. (2012) explored the possibility of modeling the brain-skull interface by replacing the pia-arachnoid mater complex, CSF, and blood vasculature with spring connector elements with assigned stiffness of cortical veins. This suggests that the vascular structure is an important constituent that is affected by nonimpact large head rotations. These rotations, however, do not reflect the mechanical loading scenario of a CCI. Therefore, we hypothesize that the fluid-filled cavity approach used here is sufficient to model the presence of an incompressible material between the impacted DAM and the brain. Future developments of the porcine brain FE model should explore the load-bearing behavior of the structural interaction between the CSF and the cortical vasculature during direct impacts.

Machine Learning Model

A surrogate of the porcine brain FE model was fitted using an artificial neural network with the aim of performing uncertainty

TABLE 4 | Summary of the performance scores of the four different injury predictors. The scores were obtained using the leave-one-out cross-validation framework. The AUC-training values are presented as the average (standard deviation) of the testing datasets. The best and worst AUC-training measures are also reported.

Injury metric	Accuracy	Sensitivity	Specificity	AUC-testing	AUC-training	Best AUC-Training	Worst AUC-Training
95th MPS	0.784	0.8	0.75	0.711	0.878 (0.032)	0.972	0.847
95th MPSR	0.784	0.8	0.75	0.711	0.767 (0.055)	0.944	0.708
95th MPSXSR	0.784	0.8	0.75	0.711	0.789 (0.049)	0.944	0.736
95th MSS	0.784	0.8	0.75	0.711	0.878 (0.032)	0.972	0.847

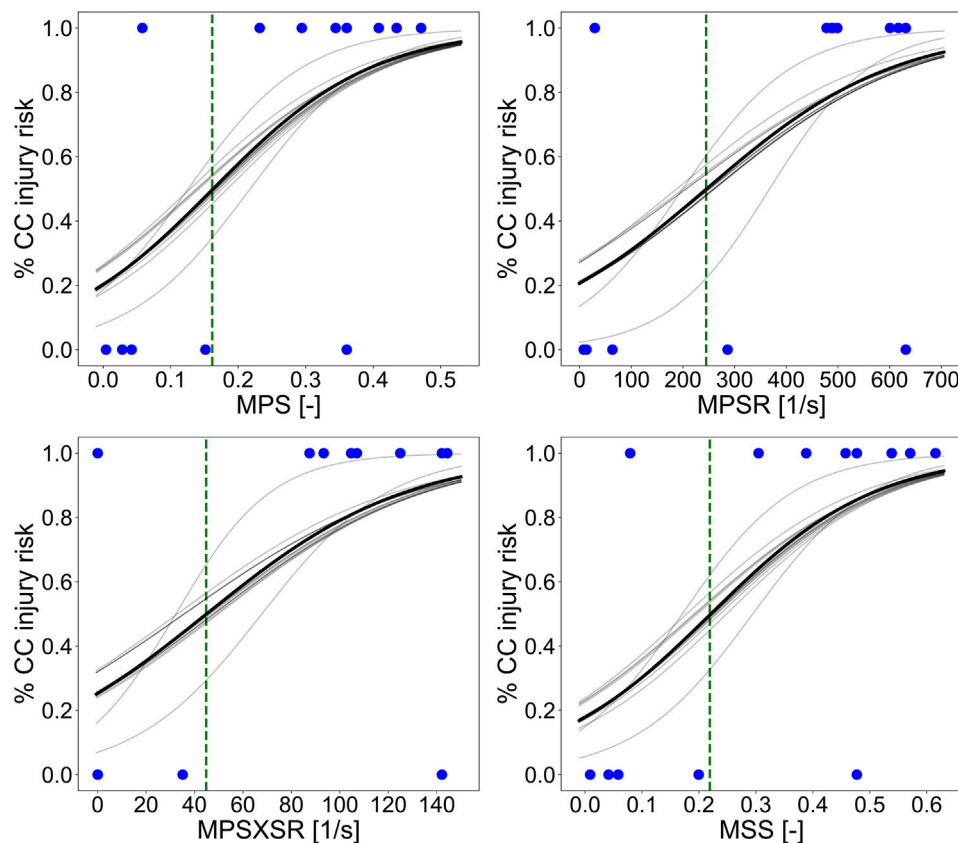


FIGURE 7 | Injury risk curves representing the probability of sustaining CC as a function of the 95th percentile of MPS, MPSR, MPSXSR, and MSS predicted with the porcine brain ML surrogate. The solid black line represents the logistic regression curve performed on the whole dataset. The light gray lines represent the logistic regression curves of each training dataset of the leave-one-out cross-validation procedure. The green vertical dashed lines indicate the thresholds corresponding to the 50% chance of CC (MPS = 0.16, MPSR = 245 s⁻¹, MPSXSR = 45 s⁻¹, and MSS = 0.22), while the blue dots represent the experimental data (cortical damage = 1 and no damage = 0) collected by means of the MR and histology assessments post-CCI.

and sensitivity analyses with reduced simulation runtime and computing resources. The trained and tested ANN was able to predict the 95th percentile MPS, MPSR, MPSXSR, and MSS of the porcine brain undergoing CCI in <0.01s using a low-end laptop, contrarily to the ~2 h runtime required to simulate a single impact with the “traditional” FE porcine brain model using a high-performance computing platform. Considering the large number of samples required by the MCS (56 times 10,000), the computational time saved by performing the uncertainty analysis on the ML surrogate model is evident.

We reached the desired accuracy for uncertainty quantification by using only 80 samples in the training and

testing process for the ANN. Most machine learning-based models would require more samples to be able to achieve errors <4%; however, since only three out of the seven input parameters were proved to be highly influential, this relatively low number of training and validation samples is plausible.

The fully connected seven-layers ANN architecture used in this study is relatively simple and only considers a one-dimensional array as input. There exist more complex deep learning-based surrogates of FE head models in the literature, such as convolutional neural networks (CNN) (Wu et al., 2019; Ghazi et al., 2021). Improving the outcomes from Wu et al. (2019), Ghazi et al. (2021) combined the head impact rotational

velocity and acceleration temporal profiles into a two-dimensional input to train a CNN architecture composed of convolutional, pooling, flattening, and fully connected layers. The CNN was trained to predict the MPS distribution across the whole brain of the anisotropic Worcester Head Injury Model (Zhao and Ji, 2020a). With a conceptually similar workflow, Zhan et al. (2021) utilized features describing the characteristics of rotational kinematics of football and mixed martial arts' head impacts as input of a five-layer deep neural network to predict the MPS map of the brain elements of the KTH head model (Ho and Kleiven, 2007).

The remarkable advantage of these approaches is the preservation of the information about the nonlinear impact-whole brain deformation relationship, which is otherwise inevitably lost when considering discrete inputs and single-value metrics outputs as in our study. Nevertheless, the focal nature of the cortical damage induced by the CCI reduces the relevance of predicting the brain mechanical response outside the ROI that is directly affected by the impacting probe. The ANN was, therefore, sufficient to achieve the goal of estimating the effect of the experimental and modeling parameters on the localized strain and strain rate of the impacted pig brain. Future studies should investigate the use of more sophisticated deep learning networks that include the nonlinear temporal profile of input parameters such as depth and velocity of indentation, which, due to the dynamic nature of the brain tissue properties, might influence the predicted intracranial mechanical response.

Sensitivity to the CCI Model Parameters

The uncertainty and sensitivity analyses demonstrated that the selected input parameters have different degrees of influence on the deformation and rate of deformation of the porcine cerebral tissue undergoing CCI. Both sensitivity indices, S_1 and δ , highlighted the predominant effect of the depth of indentation on strain-based injury metrics. The crucial effect that increasing the depth of indentation has in terms of both functional responses and tissue structural injury pattern is well reported in the literature of CCI on rodent (Goodman et al., 1994; Saatman et al., 2006; Elliott et al., 2008; Mao et al., 2010a) and pig brains (Manley et al., 2006; Baker et al., 2019). The evaluation of the uncertainty propagation showed that by eliminating the uncertainty on the depth of indentation in a CCI experiment, one could dramatically reduce the variability of MPS and MSS. This demonstrates that this input parameter should be carefully selected and measured when performing a CCI experiment. Interestingly, MPSR and MPSXSR seem to reach a plateau for depths of indentation approaching 12 mm, which suggests that it may not be crucial for the impactor to reach depths larger than 12 mm in order to produce further damage. This is in agreement with Manley et al. (2006) and Baker et al. (2019), who both observed that CCI carried out on pig brain with a depth of indentation greater or equal than 12 mm produces largely extended areas with neuroparenchymal damage and loss and intraparenchymal hematoma, which overshadows the mere cortical contusion.

The other critical parameter is the velocity of impact, which unsurprisingly ranked first in order of importance with the strain rate injury metrics, MPSR and MPSXSR. This is a logical consequence of the viscoelastic nature of the brain tissue. The strain rate dependence introduced by the brain tissue viscoelastic material model could also explain why large asymmetry in the uncertainty distribution are observed for MPSR and MPSXSR, especially for higher values of velocity and depth of indentation. Indeed, it is known that brain tissue shows more viscous behavior and its shear modulus exhibits a more rapid decay with increasing strain rates (Qian et al., 2018).

The effect of the interaction between the depth and velocity of indentation was not investigated in our study. However, CCI experiments on pig brain by Baker et al. (2019) showed that the interaction between these two parameters influence the cortical lesion size and the observable functional deficit. The combined effect of depth and velocity of indentation on brain tissue deformation and deformation rate should be object of future research.

The trends of the median of all four injury predictors observable in **Figure 4** reveal that the geometrical properties of the probe influence the brain's response to the CCI, although less than the depth or the velocity of impact. Unsurprisingly, a larger diameter of the probe results into larger strains and strain rates. Moreover, hemispherical probes are associated with lower MPS, MPSR, MPSXSR, and MSS than cylindrical flat tips, which is explained by the higher concentration of stresses due to smaller radii. This is confirmed by the CCI experiments on mice by Pleasant et al. (2011), who observed a greater acute cortical hemorrhage and neural loss with a flat probe when compared to a hemispherical one.

The uncertainty of the angle of indentation, the friction coefficient between the DAM and the probe, and the thickness of the DAM show no meaningful effect on the propagation of the uncertainties of all the injury metrics. This demonstrates that committing an error in positioning the axis of the probe with an angle relative to the surface of the brain parenchyma in the range $[-15^\circ; 15^\circ]$ is tolerable in terms of achieving the desired localized cortical damage in a CCI experiment. A similar consideration holds for the assessed ranges of the two modeling parameters, namely the thickness of the DAM shell elements and the friction between the DAM and the probe.

The choice of a neo-Hookean material model was dictated by the similarity of the loading scenario between the material calibration tests (MacManus et al., 2017) and the CCI experiments considered here. Nevertheless, there exist other more refined hyperelastic material model definitions (e.g., Mooney-Rivlin, Ogden) which might better capture the asymmetry in the tension-compression response of the tissues (de Rooij and Kuhl, 2016; Zhao et al., 2018; Budday et al., 2019). Provided that these constitutive laws are calibrated with experimental loading conditions that are similar to a CCI, future studies should include the material model as an input variable for the sensitivity analysis and assess the effect of the uncertainty of the hyper-viscoelastic parameters on the injury metrics. Another possible extension of this study should regard the assessment of the effect of the location of the point of impact

on the DAM surface on the brain's mechanical response. However, in order to assess the influence of the impact location, the limitation of the current FE model in considering a scaled average brain must be first overcome. These analyses could be repeated using subject-specific FE brain models with geometry obtained from high-resolution images, which were not available for this study. This could bring more insight, since these models could then capture the accurate morphology of the superficial gyral pattern, as it can alter the strain and the strain rate pattern (Ho and Kleiven, 2009). Finally, it is worth mentioning that the importance ranking of the input parameters refers to the brain's response localized around the area that is directly affected by the CCI. The influence of the parameters on the spatial distribution of the whole brain strains and strain rates might differ; however, this was outside of the scope of our study.

CC Tissue-Level Injury Metrics

The use of FE head models to investigate the mechanical tolerances associated with specific traumatic brain injuries is regarded as a promising area of brain biomechanics research with potential applications in the engineering and optimization of protective devices such as helmets, as well as in forensics. With the current investigation, we assessed the injury prediction performance of four strain and strain rate-based injury metrics for cerebral contusion using *in silico* porcine brain models.

Given the very localized injury pattern resulting from CCI, the use of strain and strain rate injury criteria has been preferred over other metrics assessed in the literature, such as those based on stress, intracranial pressure, or strain energy. Interestingly, the uncertainty analysis highlights that MPS exhibits, indeed, the least variability in comparison with the other injury metrics (Figure 4). Mao and Yang (2011) developed a FE model of the rat brain undergoing a CCI and confirmed the predictive capability of maximum principal strain and maximum shear strain as injury thresholds, finding no correlation between CC and the intracranial pressure. This can be ascribed to the fact that CCI affects only a limited area in proximity of the brain surface, and it is different than the coup-countercoup contusions that result from impacts where the global head kinematics are involved.

Among the injury metrics considered, only the strain-based indicators were tested as being statistically significantly effective in distinguishing between injury and no injury cases. The LOOCV model evaluation confirmed the superior robustness and performance of MPS and MSS compared to MPSR and MPSXSR in terms of predicting CC. This suggests that the mechanical deformation pattern of the brain tissue—rather than its rate of deformation—shows potential in predicting focal TBI. Despite the small size of the CC injury dataset, the 50% injury risk thresholds are in line with the values reported in the literature, even though from different animal models. Our estimates of the MPS and MSS-based thresholds (0.16 and 0.22, respectively) are close to the 0.265 MPS and 0.281 MSS reported by Mao and Yang (2011) who performed CCI on rat brains. An engineering strain of 0.19 was suggested by Viano and Lövsund (1999) for 50% risk of contusion, after analyzing the results of CCI tests on ferrets.

They also determined the threshold for the product of strain and strain rate as equal to 30.7 s^{-1} , which is in the neighborhood of the value estimated here ($\text{MPSXSR} = 45 \text{ s}^{-1}$). Nevertheless, the interpretation of the comparison across species needs to be done with caution, given the considerable anatomical and structural brain differences. To the best of the authors' knowledge, no other studies reported CC injury thresholds obtained by analyzing data from CCI experiments *in vivo* on pig brains.

An evident limitation of this study is the small size of the experimental dataset, which yields broad confidence intervals for the estimated CC injury thresholds, thus discouraging the use of these values as ultimate CC criteria. It is nevertheless unrealistic to presume the existence of a single injury metric capable of predicting with absolute certainty the risk of CC resulting from any loading scenario. Indeed, the use of injury metrics based on FE-derived mechanical quantities hypothesizes a direct relationship between the outcome of a TBI and the biomechanical response of brain tissue. Even in a well-controlled testing scenario as a CCI, this inevitably excludes all the complex pathophysiological mechanisms typical of secondary injury responses, which can arise during the 48 h considered by De Kegel et al. (2021) for the postimpact contusion evaluation. These biological processes are not pathognomonic to CC and depend on the genetic variability between animals. It is also unknown how they influence the targeted injury outcome, which complicates the establishment of an injury threshold and therefore represents a shortcoming. Nevertheless, a scan taken immediately following the impact could be interpreted as falsely negative. Therefore, the only objective way to determine the actual cerebral contusion damage was a binary assessment of disruption vs. no disruption of the thin cortical layers 48 h post-CCI.

Machine learning-based algorithms (e.g., deep neural networks, support vector machine, and random forest classifiers) have been regarded as promising tools to predict TBI in a more accurate and effective way (Hernandez et al., 2015; Cai et al., 2018; Wu et al., 2018; Wu et al., 2020). The advantage of these techniques is that the injury classification is performed utilizing multiple features such as elementwise brain strain. On the contrary, the FE-based scalar metrics considered here *via* the predictor-specific LOOCV suffer from information loss, since they basically reduce the complex mechanical response of the brain to a single value. Provided that a larger injury vs. no injury dataset is available, future studies should consider the evaluation of machine learning feature-based CC predictors, which can overcome the limitation of the use of single value injury metrics.

CONCLUSION

We investigated the effect of common experimental and computational variables on the mechanical response of the porcine brain undergoing CCI. We successfully developed a machine learning surrogate of the finite element porcine brain model to perform the uncertainty and sensitivity analyses in a computationally efficient way. We observed that the depth and velocity of indentation should be chosen carefully when designing

CCI experiments as they produce the largest influence on the brain tissue's deformation and rate of deformation. Four strain and strain rate-based criteria have been evaluated as injury metrics to predict cerebral contusion. The maximum principal strain and maximum shear strain were found to be good candidates as tissue-level metrics specific for cerebral contusion. We demonstrated that the proposed blended *in vivo-in silico* methodology shows potential in predicting CC, although the reliability depends on the size of the animal experimental injury vs. no injury dataset. Accurate CC injury classification methods and tolerances will find practical application in the development of safer protective headgear and in forensics.

DATA AVAILABILITY STATEMENT

The original contributions presented in the study are included in the article/**Supplementary Material**; further inquiries can be directed to the corresponding author.

ETHICS STATEMENT

The animal study was reviewed and approved by the Ethical Committee for Animal Experiments, KU Leuven, Belgium. The animal experiments were carried out at the Animal Research Center, KU Leuven, Belgium.

AUTHOR CONTRIBUTIONS

AM wrote the manuscript with the help of LB. AM processed the computational data, performed the analyses, and designed the figures. LB developed the machine learning framework. BD

provided the experimental data. JVS, BD, and NF supervised the conception and design of the work. NF and LB critically reviewed the article. All authors contributed to the article and approved the submitted version.

FUNDING

This research was made possible through a predoctoral fellowship of the Research Foundation Flanders (FWO) (Project no. 1S25920N).

ACKNOWLEDGMENTS

The authors would like to thank Ann Belmans and Bavo Kempen for the advice and help in the statistical analyses. The authors would also like to acknowledge Sofie Dietvorst and Veerle De Sloovere for the help in performing the validation CCI experiment. The authors thank Gabriele Nasello for the contribution in realizing the FE model illustrations. The authors would like to thank Em Triolo, Manon Laporte and Dries De Kegel for proofreading the manuscript. Laura Bartsoen acknowledges the support of the Materialise chair for image based, patient-specific biomechanics.

SUPPLEMENTARY MATERIAL

The Supplementary Material for this article can be found online at: <https://www.frontiersin.org/articles/10.3389/fbioe.2021.714128/full#supplementary-material>

REFERENCES

- Abadi, M., Barham, P., Chen, J., Chen, Z., Davis, A., Dean, J., et al. (2016). "TensorFlow: A System for Large-Scale Machine Learning," in Proceedings of the 12th USENIX Symposium on Operating Systems Design and Implementation (OSDI '16), Savannah, GA, USA, November 2–4, 2016. doi:10.1016/0076-6879(83)01039-3
- Alahmadi, H., Vachhrajani, S., and Cusimano, M. D. (2010). The Natural History of Brain Contusion: an Analysis of Radiological and Clinical Progression. *Jns* 112, 1139–1145. doi:10.3171/2009.5.JNS081369
- Alessandri, B., Heimann, A., Filippi, R., Kopacz, L., and Kempfski, O. (2003). Moderate Controlled Cortical Contusion in Pigs: Effects on Multi-Parametric Neuromonitoring and Clinical Relevance. *J. Neurotrauma* 20, 1293–1305. doi:10.1089/089771503322686094
- Anderson, E. D., Giudice, J. S., Wu, T., Panzer, M. B., and Meaney, D. F. (2020). Predicting Concussion Outcome by Integrating Finite Element Modeling and Network Analysis. *Front. Bioeng. Biotechnol.* 8, 309. doi:10.3389/fbioe.2020.00309
- Baker, E. W., Kinder, H. A., Hutcheson, J. M., Duberstein, K. J. J., Platt, S. R., Howerth, E. W., et al. (2019). Controlled Cortical Impact Severity Results in Graded Cellular, Tissue, and Functional Responses in a Piglet Traumatic Brain Injury Model. *J. Neurotrauma* 36, 61–73. doi:10.1089/neu.2017.5551
- Bartsoen, L., Faes, M. G. R., Wesseling, M., Wirix-Speetjens, R., Moens, D., Jonkers, L., et al. (2021). Computationally Efficient Optimization Method to Quantify the Required Surgical Accuracy for a Ligament Balanced TKA. *IEEE Trans. Biomed. Eng.* 1, 1. doi:10.1109/TBME.2021.3069330
- Beleites, C., Baumgartner, R., Bowman, C., Somorjai, R., Steiner, G., Salzer, R., et al. (2005). Variance Reduction in Estimating Classification Error Using Sparse Datasets. *Chemom. Intell. Lab. Syst.* 79, 91–100. doi:10.1016/j.chemolab.2005.04.008
- Borgonovo, E. (2007). A New Uncertainty Importance Measure. *Reliab. Eng. Syst. Saf.* 92, 771–784. doi:10.1016/j.res.2006.04.015
- Budday, S., Ovaert, T. C., Holzapfel, G. A., Steinmann, P., and Kuhl, E. (2019). Fifty Shades of Brain: A Review on the Mechanical Testing and Modeling of Brain Tissue. *Arch. Computat Methods Eng.* 27, 1187–1230. doi:10.1007/s11831-019-09352-w
- Cai, Y., Wu, S., Zhao, W., Li, Z., Wu, Z., and Ji, S. (2018). Concussion Classification via Deep Learning Using Whole-Brain white Matter Fiber Strains. *PLoS One* 13, e0197992–21. doi:10.1371/journal.pone.0197992
- Cai, Z., Xia, Y., Bao, Z., Mao, H., Campbell, J. Q., Malone, D., et al. (2019). Creating a Human Head Finite Element Model Using a Multi-Block Approach for Predicting Skull Response and Brain Pressure. *Comput. Methods Biomech. Biomed. Eng.* 22, 169–179. doi:10.1080/10255842.2018.1541983
- Cai, L., Ren, L., Wang, Y., Xie, W., Zhu, G., and Gao, H. (2021). Surrogate Models Based on Machine Learning Methods for Parameter Estimation of Left Ventricular Myocardium. *R. Soc. Open Sci.* 8, 201121. doi:10.1098/rsos.201121
- Chen, Y., Mao, H., Yang, K. H., Abel, T., and Meaney, D. F. (2014). A Modified Controlled Cortical Impact Technique to Model Mild Traumatic Brain Injury Mechanics in Mice. *Front. Neurol.* 5, 1–14. doi:10.3389/fneur.2014.00100

- Coats, B., Eucker, S. A., Sullivan, S., and Margulies, S. S. (2012). Finite Element Model Predictions of Intracranial Hemorrhage from Non-impact, Rapid Head Rotations in the Piglet. *Int. J. Dev. Neurosci.* 30, 191–200. doi:10.1016/j.jdevneu.2011.12.009
- Davies, V., Noè, U., Lazarus, A., Gao, H., Macdonald, B., Berry, C., et al. (2019). Fast Parameter Inference in a Biomechanical Model of the Left Ventricle by Using Statistical Emulation. *J. R. Stat. Soc. C* 68, 1555–1576. doi:10.1111/rssc.12374
- De Kegel, D., Vastmans, J., Fehervary, H., Depreitere, B., Vander Sloten, J., and Famaey, N. (2018). Biomechanical Characterization of Human Dura Mater. *J. Mech. Behav. Biomed. Mater.* 79, 122–134. doi:10.1016/j.jmbbm.2017.12.023
- De Kegel, D., Musigazi, G. U., Menichetti, A., Hellings, P.-W., Sciort, R., Demaerel, P., et al. (2021). Investigation of Tissue Level Tolerance for Cerebral Contusion in a Controlled Cortical Impact Porcine Model. *Traffic Inj. Prev.*, 1–7. doi:10.1080/15389588.2021.1957856
- De Kegel, D. (2018). *Tissue-Level Tolerance Criteria for Crash-Related Head Injuries*. Leuven (Belgium): KU Leuven. [PhD dissertation].
- de Rooij, R., and Kuhl, E. (2016). Constitutive Modeling of Brain Tissue: Current Perspectives. *Appl. Mech. Rev.* 68, 010801. doi:10.1115/1.4032436
- Depreitere, B., Van Lierde, C., Maene, S., Plets, C., Vander Sloten, J., Van Audekercke, R., et al. (2004). Bicycle-related Head Injury: a Study of 86 Cases. *Accid. Anal. Prev.* 36, 561–567. doi:10.1016/S0001-4575(03)00062-9
- Duhaime, A.-C., Margulies, S. S., Durham, S. R., O'Rourke, M. M., Golden, J. A., Marwaha, S., et al. (2000). Maturation-dependent Response of the Piglet Brain to Scaled Cortical Impact. *J. Neurosurg.* 93, 455–462. doi:10.3171/jns.2000.93.3.0455
- Elkin, B. S., Ilankova, A., and Morrison, B. (2011). Dynamic, Regional Mechanical Properties of the Porcine Brain: Indentation in the Coronal Plane. *J. Biomech. Eng.* 133, 071009. doi:10.1115/1.4004494
- Elliott, M. B., Jallo, J. J., and Tuma, R. F. (2008). An Investigation of Cerebral Edema and Injury Volume Assessments for Controlled Cortical Impact Injury. *J. Neurosci. Methods* 168, 320–324. doi:10.1016/j.jneumeth.2007.10.019
- Feng, Y., Lee, C.-H., Sun, L., Ji, S., and Zhao, X. (2017). Characterizing white Matter Tissue in Large Strain via Asymmetric Indentation and Inverse Finite Element Modeling. *J. Mech. Behav. Biomed. Mater.* 65, 490–501. doi:10.1016/j.jmbbm.2016.09.020
- Gefen, A., and Margulies, S. S. (2004). Are *In Vivo* and *In Situ* Brain Tissues Mechanically Similar? *J. Biomech.* 37, 1339–1352. doi:10.1016/j.jbiomech.2003.12.032
- Gehre, C., Gades, H., and Wernicke, P. (2009). “Objective Rating of Signals Using Test and Simulation Responses,” in Proceedings of the 21st International Technical Conference on the enhanced Safety of Vehicles ESV, Stuttgart (Germany), June 15–18, 2009. (Paper 09-0407).
- Ghazi, K., Wu, S., Zhao, W., and Ji, S. (2021). Instantaneous Whole-Brain Strain Estimation in Dynamic Head Impact. *J. Neurotrauma* 38, 1023–1035. doi:10.1089/neu.2020.7281
- Giordano, C., Zappalà, S., Kleiven, S., Chiara, B., and Se, G. C. (2017). Anisotropic Finite Element Models for Brain Injury Prediction: the Sensitivity of Axonal Strain to white Matter Tract Inter-subject Variability. *Biomech. Model. Mechanobiol.* 16, 1269–1293. doi:10.1007/s10237-017-0887-5
- Goodman, J. C., Cherian, L., Bryan, R. M., and Robertson, C. S. (1994). Lateral Cortical Impact Injury in Rats: Pathologic Effects of Varying Cortical Compression and Impact Velocity. *J. Neurotrauma* 11, 587–597. doi:10.1089/neu.1994.11.587
- Gross, A. G. (1958). A New Theory on the Dynamics of Brain Concussion and Brain Injury. *J. Neurosurg.* 15, 548–561. doi:10.3171/jns.1958.15.5.0548
- Hajiaghdammar, M., and Margulies, S. S. (2021). Multi-Scale White Matter Tract Embedded Brain Finite Element Model Predicts the Location of Traumatic Diffuse Axonal Injury. *J. Neurotrauma* 38, 144–157. doi:10.1089/neu.2019.6791
- Hajiaghdammar, M., Wu, T., Panzer, M. B., and Margulies, S. S. (2020). Embedded Axonal Fiber Tracts Improve Finite Element Model Predictions of Traumatic Brain Injury. *Biomech. Model. Mechanobiol.* 19, 1109–1130. doi:10.1007/s10237-019-01273-8
- Hardman, J. M., and Manoukian, A. (2002). Pathology of Head Trauma. *Neuroimaging Clin. North Am.* Elsevier, 12, 175–187. doi:10.1016/s1052-5149(02)00009-6
- Hernandez, F., Wu, L. C., Yip, M. C., Laksari, K., Hoffman, A. R., Lopez, J. R., et al. (2015). Six Degree-Of-Freedom Measurements of Human Mild Traumatic Brain Injury. *Ann. Biomed. Eng.* 43, 1918–1934. doi:10.1007/s10439-014-1212-4
- Ho, J., and Kleiven, S. (2007). Dynamic Response of the Brain with Vasculature: A Three-Dimensional Computational Study. *J. Biomech.* 40, 3006–3012. doi:10.1016/j.jbiomech.2007.02.011
- Ho, J., and Kleiven, S. (2009). Can Sulci Protect the Brain from Traumatic Injury? *J. Biomech.* 42, 2074–2080. doi:10.1016/j.jbiomech.2009.06.051
- Holbourn, A. H. S. (1943). Mechanics of Head Injuries. *Lancet* 242, 438–441. doi:10.1016/s0140-6736(00)87453-x
- Horstemeyer, M. F., Panzer, M. B., and Prabhu, R. K. (2019). State-of-the-Art Modeling and Simulation of the Brain's Response to Mechanical Loads. *Ann. Biomed. Eng.* 47, 1829–1831. doi:10.1007/s10439-019-02351-9
- Huang, H. M., Lee, M. C., Lee, S. Y., Chiu, W. T., Pan, L. C., and Chen, C. T. (2000). Finite Element Analysis of Brain Contusion: An Indirect Impact Study. *Med. Biol. Eng. Comput.* 38, 253–259. doi:10.1007/BF02347044
- Kaster, T., Sack, I., and Samani, A. (2011). Measurement of the Hyperelastic Properties of *Ex Vivo* Brain Tissue Slices. *J. Biomech.* 44, 1158–1163. doi:10.1016/j.jbiomech.2011.01.019
- King, A. I., Yang, K. H., Zhang, L., and Hardy, W. (2003). “Is Head Injury Caused by Linear or Angular Acceleration?” in IRCOBI Conference 2003, Lisbon (Portugal), September 25–26, 2003.
- Kirkman, M. A., Jenks, T., Bouamra, O., Edwards, A., Yates, D., and Wilson, M. H. (2013). Increased Mortality Associated with Cerebral Contusions Following Trauma in the Elderly: Bad Patients or Bad Management? *J. Neurotrauma* 30, 1385–1390. doi:10.1089/neu.2013.2881
- Kleiven, S. (2007). Predictors for Traumatic Brain Injuries Evaluated through Accident Reconstructions. *Stapp Car Crash J.* 51. doi:10.4271/2007-22-0003
- Laz, P. J., and Browne, M. (2010). A Review of Probabilistic Analysis in Orthopaedic Biomechanics. *Proc. Inst. Mech. Eng. H* 224, 927–943. doi:10.1243/09544119JIM739
- Li, Y., Zhang, W., Lu, Y.-C., and Wu, C. W. (2020a). Hyper-viscoelastic Mechanical Behavior of Cranial Pia Mater in Tension. *Clin. Biomech.* 80, 105108. doi:10.1016/j.clinbiomech.2020.105108
- Li, Z., Ji, C., Li, D., Luo, R., Wang, G., and Jiang, J. (2020b). A Comprehensive Study on the Mechanical Properties of Different Regions of 8-Week-Old Pediatric Porcine Brain under Tension, Shear, and Compression at Various Strain Rates. *J. Biomech.* 98, 109380. doi:10.1016/j.jbiomech.2019.109380
- MacManus, D. B., Pierrat, B., Murphy, J. G., and Gilchrist, M. D. (2017). Protection of Cortex by Overlying Meninges Tissue during Dynamic Indentation of the Adolescent Brain. *Acta Biomater.* 57, 384–394. doi:10.1016/j.actbio.2017.05.022
- MacManus, D. B., Menichetti, A., Depreitere, B., Famaey, N., Vander Sloten, J., and Gilchrist, M. (2020). Towards Animal Surrogates for Characterising Large Strain Dynamic Mechanical Properties of Human Brain Tissue. *Brain Multiphys.* 1, 100018. doi:10.1016/j.brain.2020.100018
- Madsen, F. F., and Reske-Nielsen, E. (1987). A Simple Mechanical Model Using a Piston to Produce Localized Cerebral Contusions in Pigs. *Acta neurochir* 88, 65–72. doi:10.1007/BF01400517
- Manley, G. T., Rosenthal, G., Lam, M., Morabito, D., Yan, D., Derugin, N., et al. (2006). Controlled Cortical Impact in Swine: Pathophysiology and Biomechanics. *J. Neurotrauma* 23, 128–139. doi:10.1089/neu.2006.23.128
- Mao, H., and Yang, K. H. (2011). Investigation of Brain Contusion Mechanism and Threshold by Combining Finite Element Analysis with *In Vivo* Histology Data. *Int. J. Numer. Meth. Biomed. Engng.* 27, 357–366. doi:10.1002/cnm.1403
- Mao, H., Zhang, L., Yang, K. H., and King, A. I. (2006). Application of a Finite Element Model of the Brain to Study Traumatic Brain Injury Mechanisms in the Rat. *Stapp Car Crash J.*, 583–600. doi:10.4271/2006-22-0022
- Mao, H., Jin, X., Zhang, L., Yang, K. H., Igarashi, T., Noble-Haeusslein, L. J., et al. (2010a). Finite Element Analysis of Controlled Cortical Impact-Induced Cell Loss. *J. Neurotrauma* 27, 877–888. doi:10.1089/neu.2008.0616
- Mao, H., Yang, K. H., King, A. I., and Yang, K. (2010b). Computational Neurotrauma-Design, Simulation, and Analysis of Controlled Cortical Impact Model. *Biomech. Model. Mechanobiol.* 9, 763–772. doi:10.1007/s10237-010-0212-z
- Mao, H., Zhang, L., Jiang, B., Genthikatti, V. V., Jin, X., Zhu, F., et al. (2013). Development of a Finite Element Human Head Model Partially Validated with

- Thirty Five Experimental Cases. *J. Biomech. Eng.* 135, 111002. doi:10.1115/1.4025101
- McGinn, M. J., and Povlishock, J. T. (2016). Pathophysiology of Traumatic Brain Injury. *Neurosurg. Clin. North Am.* 27, 397–407. doi:10.1016/j.nec.2016.06.002
- Meissner, A., Timaru-Kast, R., Heimann, A., Hoelper, B., Kempfski, O., and Alessandri, B. (2011). Effects of a Small Acute Subdural Hematoma Following Traumatic Brain Injury on Neuromonitoring, Brain Swelling and Histology in Pigs. *Eur. Surg. Res.* 47, 141–153. doi:10.1159/000330756
- Melvin, J. W., and Yoganandan, N. (2015). Biomechanics of Brain Injury: A Historical Perspective,” in *Biomechanics of Brain Injury: A Historical Perspective BT - Accidental Injury: Biomechanics and Prevention*, in, Editors N. Yoganandan, A. M. Nahum, and J. W. Melvin (New York, NY: Springer New York), 221–245. doi:10.1007/978-1-4939-1732-7_9
- Miller, R. T., Margulies, S. S., Leoni, M., Nonaka, M., Chen, X., Smith, D. H., and Meaney, D. F. (1998). “Finite Element Modeling Approaches for Predicting Injury in an Experimental Model of Severe Diffuse Axonal Injury,” in Stapp Car Crash Conference (SAE International). doi:10.4271/983154
- Ommaya, A. K., and Ommaya, A. K. (1995). Head Injury Mechanisms and the Concept of Preventive Management: A Review and Critical Synthesis. *J. Neurotrauma* 12, 527–546. doi:10.1089/neu.1995.12.527
- Osier, N., and Dixon, C. E. (2017). The Controlled Cortical Impact Model of Experimental Brain Trauma: Overview, Research Applications, and Protocol. *Methods Mol. Biol.* 1462, 177–192. doi:10.1007/978-1-4939-3816-2_11
- Pal, S., Haider, H., Laz, P. J., Knight, L. A., and Rullkoetter, P. J. (2008). Probabilistic Computational Modeling of Total Knee Replacement Wear. *Wear* 264, 701–707. doi:10.1016/j.wear.2007.06.010
- Panzer, M. B., Myers, B. S., Capehart, B. P., and Bass, C. R. (2012). Development of a Finite Element Model for Blast Brain Injury and the Effects of CSF Cavitation. *Ann. Biomed. Eng.* 40, 1530–1544. doi:10.1007/s10439-012-0519-2
- Pierrat, B., Carroll, L., Merle, F., MacManus, D. B., Gaul, R., Lally, C., et al. (2020). Mechanical Characterization and Modeling of the Porcine Cerebral Meninges. *Front. Bioeng. Biotechnol.* 8, 1–16. doi:10.3389/fbioe.2020.00801
- Pleasant, J. M., Carlson, S. W., Mao, H., Scheff, S. W., Yang, K. H., and Saatman, K. E. (2011). Rate of Neurodegeneration in the Mouse Controlled Cortical Impact Model Is Influenced by Impactor Tip Shape: Implications for Mechanistic and Therapeutic Studies. *J. Neurotrauma* 28, 2245–2262. doi:10.1089/neu.2010.1499
- Prange, M. T., and Margulies, S. S. (2002). Regional, Directional, and Age-dependent Properties of the Brain Undergoing Large Deformation. *J. Biomech. Eng.* 124, 244–252. doi:10.1115/1.1449907
- Qian, L., Zhao, H., Guo, Y., Li, Y., Zhou, M., Yang, L., et al. (2018). Influence of Strain Rate on Indentation Response of Porcine Brain. *J. Mech. Behav. Biomed. Mater.* 82, 210–217. doi:10.1016/j.jmbbm.2018.03.031
- Rashid, B., Destrade, M., and Gilchrist, M. D. (2012). Determination of Friction Coefficient in Unconfined Compression of Brain Tissue. *J. Mech. Behav. Biomed. Mater.* 14, 163–171. doi:10.1016/j.jmbbm.2012.05.001
- Ratnaike, T. E., Hastie, H., Gregson, B., and Mitchell, P. (2011). The Geometry of Brain Contusion: Relationship between Site of Contusion and Direction of Injury. *Br. J. Neurosurg.* 25, 410–413. doi:10.3109/02688697.2010.548879
- Saatman, K. E., Feeko, K. J., Pape, R. L., and Raghupathi, R. (2006). Differential Behavioral and Histopathological Responses to Graded Cortical Impact Injury in Mice. *J. Neurotrauma* 23, 1241–1253. doi:10.1089/neu.2006.23.1241
- Saikali, S., Meurice, P., Sauleau, P., Eliat, P.-A., Bellaud, P., Randuineau, G., et al. (2010). A Three-Dimensional Digital Segmented and Deformable Brain Atlas of the Domestic Pig. *J. Neurosci. Methods* 192, 102–109. doi:10.1016/j.jneumeth.2010.07.041
- Shreiber, D. I., Bain, A. C., and Meaney, D. F. (1997). “In Vivo thresholds for Mechanical Injury to the Blood-Brain Barrier,” in Proc. of the 41th Stapp Car Crash Conference, Lake Buena Vista, FL, USA, November 13–14, 1997, 277–291.
- Schroder, A., Lawrence, T., Voets, N., Garcia-Gonzalez, D., Jones, M., Peña, J.-M., et al. (2021). A Machine Learning Enhanced Mechanistic Simulation Framework for Functional Deficit Prediction in TBI. *Front. Bioeng. Biotechnol.* 9, 587082. doi:10.3389/fbioe.2021.587082
- Scott, G. G., Margulies, S. S., and Coats, B. (2016). Utilizing Multiple Scale Models to Improve Predictions of Extra-axial Hemorrhage in the Immature Piglet. *Biomech. Model. Mechanobiol.* 15, 1101–1119. doi:10.1007/s10237-015-0747-0
- Sindelar, B., Bailes, J., Sherman, S., Finan, J., Stone, J., Lee, J., et al. (2017). Effect of Internal Jugular Vein Compression on Intracranial Hemorrhage in a Porcine Controlled Cortical Impact Model. *J. Neurotrauma* 34, 1703–1709. doi:10.1089/neu.2016.4648
- Sobol', I. M. (2001). Global Sensitivity Indices for Nonlinear Mathematical Models and Their Monte Carlo Estimates. *Mathematics Comput. Simul.* 55, 271–280. doi:10.1016/S0378-4754(00)00270-6
- Steyerberg, E. W., Mushkudiani, N., Perel, P., Butcher, I., Lu, J., McHugh, G. S., et al. (2008). Predicting Outcome after Traumatic Brain Injury: Development and International Validation of Prognostic Scores Based on Admission Characteristics. *Plos Med.* 5, e165, 2008. discussion e165. doi:10.1371/journal.pmed.0050165
- Strickland, M. A., Arsene, C. T. C., Pal, S., Laz, P. J., and Taylor, M. (2010). A Multi-Platform Comparison of Efficient Probabilistic Methods in the Prediction of Total Knee Replacement Mechanics. *Comput. Methods Biomech. Biomed. Eng.* 13, 701–709. doi:10.1080/10255840903476463
- Takhounts, E. G., Eppinger, R. H., Campbell, J. Q., Tannous, R. E., Power, E. D., and Shook, L. S. (2003). On the Development of the SIMon Finite Element Head Model. *Stapp Car Crash J.* 47, 107–133. Available at: <http://www.ncbi.nlm.nih.gov/pubmed/17096247>. doi:10.4271/2003-22-0007
- Trotta, A., Clark, J. M., McGoldrick, A., Gilchrist, M. D., and Annaidh, A. N. (2020). Biofidelic Finite Element Modelling of Brain Trauma: Importance of the Scalp in Simulating Head Impact. *Int. J. Mech. Sci.* 173, 105448. doi:10.1016/j.jimecsci.2020.105448
- Unnikrishnan, G., Mao, H., Sundaramurthy, A., Bell, E. D., Yeoh, S., Monson, K., et al. (2019). A 3-D Rat Brain Model for Blast-Wave Exposure: Effects of Brain Vasculature and Material Properties. *Ann. Biomed. Eng.* 47, 2033–2044. doi:10.1007/s10439-019-02277-2
- van Dommelen, J. A. W., van der Sande, T. P. J., Hrapko, M., and Peters, G. W. M. (2010). Mechanical Properties of Brain Tissue by Indentation: Interregional Variation. *J. Mech. Behav. Biomed. Mater.* 3, 158–166. doi:10.1016/j.jmbbm.2009.09.001
- Vanmol, L. (2017). *Biomechanical Characterization of Human and Porcine Dura Mater*. Leuven (Belgium): KU Leuven. [Master's thesis].
- Viano, D. C., and Lövsund, P. (1999). Biomechanics of Brain and Spinal-Cord Injury: Analysis of Neuropathologic and Neurophysiology Experiments. *J. Crash Prev. Inj. Control.* 1, 35–43. doi:10.1080/10286589908915739
- Walsh, D. R., Ross, A. M., Malijauskaite, S., Flanagan, B. D., Newport, D. T., McGourty, K. D., et al. (2018). Regional Mechanical and Biochemical Properties of the Porcine Cortical Meninges. *Acta Biomater.* 80, 237–246. doi:10.1016/j.actbio.2018.09.004
- Walsh, D. R., Zhou, Z., Li, X., Kearns, J., Newport, D. T., and Mulvihill, J. J. E. (2021). Mechanical Properties of the Cranial Meninges: A Systematic Review. *J. Neurotrauma* 38, 1748–1761. doi:10.1089/neu.2020.7288
- West, F., Kinder, H., and Baker, E. (2019). The Pig as a Preclinical Traumatic Brain Injury Model: Current Models, Functional Outcome Measures, and Translational Detection Strategies. *Neural Regen. Res.* 14, 413–424. doi:10.4103/1673-5374.245334
- Wu, L. C., Kuo, C., Loza, J., Kurt, M., Laksari, K., Yanez, L. Z., et al. (2018). Detection of American Football Head Impacts Using Biomechanical Features and Support Vector Machine Classification. *Sci. Rep.* 8, doi:10.1038/s41598-017-17864-3
- Wu, S., Zhao, W., Ghazi, K., and Ji, S. (2019). Convolutional Neural Network for Efficient Estimation of Regional Brain Strains. *Sci. Rep.* 9, 17326. doi:10.1038/s41598-019-53551-1
- Wu, S., Zhao, W., Rowson, B., Rowson, S., and Ji, S. (2020). A Network-Based Response Feature Matrix as a Brain Injury Metric. *Biomech. Model. Mechanobiol.* 19, 927–942. doi:10.1007/s10237-019-01261-y
- Wu, T., Hajiaghdammar, M., Giudice, J. S., Alshareef, A., Margulies, S. S., and Panzer, M. B. (2021). Evaluation of Tissue-Level Brain Injury Metrics Using Species-specific Simulations. *J. Neurotrauma* 38, 1879–1888. doi:10.1089/neu.2020.7445
- Xiong, Y., Mahmood, A., and Chopp, M. (2013). Animal Models of Traumatic Brain Injury. *Nat. Rev. Neurosci.* 14, 128–142. doi:10.1038/nrn3407
- Yates, K., and Untaroiu, C. (2016). “Identifying Traumatic Brain Injury (TBI) Thresholds Using Animal and Human Finite Element Models Based on In-Vivo Impact Test Data,” in Proc. 14th Int. LS-DYNA Users Conf, Detroit, MI, USA, June 12–14, 2016. 1–10.

- Zhan, X., Liu, Y., Raymond, S. J., Vahid Alizadeh, H., Domel, A., Gevaert, O., et al. (2021). Rapid Estimation of Entire Brain Strain Using Deep Learning Models. *IEEE Trans. Biomed. Eng.* 9294, 1. doi:10.1109/TBME.2021.3073380
- Zhao, W., and Ji, S. (2020a). Displacement- and Strain-Based Discrimination of Head Injury Models across a Wide Range of Blunt Conditions. *Ann. Biomed. Eng.* 48, 1661–1677. doi:10.1007/s10439-020-02496-y
- Zhao, W., and Ji, S. (2020b). Incorporation of Vasculature in a Head Injury Model Lowers Local Mechanical Strains in Dynamic Impact. *J. Biomech.* 104, 109732. doi:10.1016/j.jbiomech.2020.109732
- Zhao, W., Cai, Y., Li, Z., and Ji, S. (2017). Injury Prediction and Vulnerability Assessment Using Strain and Susceptibility Measures of the Deep white Matter. *Biomech. Model. Mechanobiol.* 16, 1709–1727. doi:10.1007/s10237-017-0915-5
- Zhao, W., Choate, B., and Ji, S. (2018). Material Properties of the Brain in Injury-Relevant Conditions - Experiments and Computational Modeling. *J. Mech. Behav. Biomed. Mater.* 80, 222–234. doi:10.1016/j.jmbbm.2018.02.005
- Zhou, Z., Li, X., and Kleiven, S. (2019). Fluid-structure Interaction Simulation of the Brain-Skull Interface for Acute Subdural Haematoma Prediction. *Biomech. Model. Mechanobiol.* 18, 155–173. doi:10.1007/s10237-018-1074-z
- Zhu, F., Skelton, P., Chou, C. C., Mao, H., Yang, K. H., and King, A. I. (2013). Biomechanical Responses of a Pig Head under Blast Loading: A Computational Simulation. *Int. J. Numer. Meth. Biomed. Engng.* 29, 392–407. doi:10.1002/cnm.2518
- Conflict of Interest:** The authors declare that the research was conducted in the absence of any commercial or financial relationships that could be construed as a potential conflict of interest.
- Publisher's Note:** All claims expressed in this article are solely those of the authors and do not necessarily represent those of their affiliated organizations, or those of the publisher, the editors, and the reviewers. Any product that may be evaluated in this article, or claim that may be made by its manufacturer, is not guaranteed or endorsed by the publisher.

Copyright © 2021 Menichetti, Bartsoen, Depreitere, Vander Sloten and Famaey. This is an open-access article distributed under the terms of the Creative Commons Attribution License (CC BY). The use, distribution or reproduction in other forums is permitted, provided the original author(s) and the copyright owner(s) are credited and that the original publication in this journal is cited, in accordance with accepted academic practice. No use, distribution or reproduction is permitted which does not comply with these terms.



A Nitric Oxide–Modulated Variable-Order Fractional Maxwell Viscoelastic Model of Cerebral Vascular Walls

Corina S. Drapaca*

Department of Engineering Science and Mechanics, Pennsylvania State University, University Park, PA, United States

OPEN ACCESS

Edited by:

Silvia Budday,
University of Erlangen Nuremberg,
Germany

Reviewed by:

João Laranjinha,
University of Coimbra, Portugal
Justyna Niestrawska,
Medical University of Graz, Austria

*Correspondence:

Corina S. Drapaca
csd12@psu.edu

Specialty section:

This article was submitted to
Micro- and Nanoelectromechanical
Systems,
a section of the journal
Frontiers in Mechanical Engineering

Received: 02 March 2021

Accepted: 10 September 2021

Published: 18 October 2021

Citation:

Drapaca CS (2021) A Nitric
Oxide–Modulated Variable-Order
Fractional Maxwell Viscoelastic Model
of Cerebral Vascular Walls.
Front. Mech. Eng 7:674860.
doi: 10.3389/fmech.2021.674860

It is well known that the mechanical behavior of arterial walls plays an important role in the pathogenesis of vascular diseases. Most studies existing in the literature focus on the mechanical interactions between the blood flow and wall's deformations. However, in the brain, the smaller vessels experience not only oscillatory forces due to the pulsatile blood flow but also structural and morphological changes controlled by the surrounding brain cells. In this study, the mechanical deformation of the cerebral arterial wall caused by the pulsatile blood flow and the dynamics of the neuronal nitric oxide (NO) is investigated. NO is a small diffusive gaseous molecule produced by the endothelial cells and neurons, which is involved in the regulation of cerebral blood flow and pressure. The cerebral vessel is assumed to be a hollow axial symmetric cylinder whose wall thickness is much smaller than the cylinder's radius and longitudinal length is much less than the propagating wavelength. The wall is an isotropic, homogeneous linear viscoelastic material described by an NO-modulated variable-order fractional Maxwell model. A fractional telegraph equation is obtained for the axial component of the displacement. Patterns of wall's deformation are investigated through numerical simulations. The results suggest that a significantly decreased inactivation of the neuronal NO may cause a reduction in the shear stress at the blood-vessel interface, which could lead to a decrease in the production of shear-induced endothelial NO and neurovascular disease.

Keywords: variable-order fractional Maxwell viscoelastic model, cerebral nitric oxide dynamics, vascular wall deformation, variable-order fractional telegraph equation, separation of variables method

INTRODUCTION

Cerebral vasculature plays a critical role in brain's metabolism and neurovascular conditions. The literature abounds with studies of cerebral blood flow and its interactions with the vasculature and brain cells [reviews of models and computer simulations can be found in chapter 4 of Drapaca and Sivaloganathan (2019)]. Recent advancements in technology have allowed researchers to gain invaluable knowledge about the intricate chemo-mechanical connections among neurons, glial, vascular, and blood cells. It is now acknowledged that the neurons and glial cells control the cerebral blood flow through the chemo-mechanical activation of the cells within the vascular wall (Attwell et al., 2010).

One of the many particles that facilitate the chemo-mechanical communications among the brain cells, blood, and the vascular wall is the nitric oxide (NO). A small diffusive gaseous molecule, the

cerebral NO is mainly produced by shear-induced mechanotransduction at the blood-vessel interface (Sriram et al., 2016) and by synthesis reactions within the endothelial cells of the blood vessels and neurons (Forstermann and Sessa, 2012). NO diffuses and is removed from brain through some specialized chemical processes (Palacios-Callender et al., 2007; Unitt et al., 2010; Santos et al., 2011; Santos et al., 2012; Helms et al., 2016). In its role as a neuro-glial-vascular messenger, NO controls the cerebral blood flow and the release of neurotransmitters (Huang, 1999; Iadecola, 2004; Attwell et al., 2010; Contestabile et al., 2012; Iadecola, 2017). The regulation of the blood flow in brain is achieved through vasomotor mechanisms in which both the neuronal and endothelial NO are involved (Cockcroft, 2005; Metea and Newman, 2006; Attwell et al., 2010; Atochin and Huang, 2011; Petzold and Murthy, 2011; Contestabile et al., 2012; Lourenco et al., 2014; Haselden et al., 2020). However, throughout the entire cardiovascular system, the endothelial NO usually acts as a vasodilator (Attwell et al., 2010; Schuler et al., 2014). While the cerebral NO activity causes the local vasodilatation of downstream cerebral vessels at the neuro-glial-vascular unit site, the NO diffusion within the vascular wall relaxes the smooth muscle cells leading to the so-called remote vasodilation due to the propagation of muscle's relaxation to the upstream arteries via the intercellular communications among endothelial and smooth muscle cells (Freed and Guterman, 2017) facilitated by vascular gap junctions (Iadecola, 2004; Iadecola, 2017). Impaired cerebral NO production and/or decay can signal the presence of a neurovascular disease (Parker and Parks, 1995; Maurer et al., 2000; Wilkinson et al., 2004; Unitt et al., 2010; Santos et al., 2011; Haselden et al., 2020).

Although the NO-modulated vasodilation contributes to the mechanical deformation of the vascular walls of intracerebral vessels, existing mathematical models and corresponding numerical simulations of blood flow interacting with the deformable vascular wall do not account for it since their focus is the mechanics of big arteries in the presence of the pulsatile blood flow. The arteries are usually modeled as anisotropic, incompressible, nonlinear elastic materials whose constitutive stress-strain relationships may also incorporate collagen fibers' orientations and waviness, and/or the activation of smooth muscle cells (see Ebrahimi, 2009; Holzapfel and Ogden, 2010; Kim and Wagenseil, 2014; Espinosa et al., 2018 and references within). For instance, muscle activation has been modeled using 1) the (original or modified) Hill model (Hill, 1938), 2) an elastic strain-energy function dependent on the concentration of free intracellular calcium (Rachev and Hayashi, 1999), 3) a strain-energy function dependent on the chemical kinetics of the smooth muscle (Stalhand et al., 2008), and 4) a lumped Hodgkin-Huxley-like electrical circuit of the smooth muscle cell membrane coupled with a fluid compartment model describing the mass balances of considered ions and a contractile kinematics model regulated by intracellular calcium (Yang et al., 2003). Given the viscoelastic behavior of constituent cells (Kasza et al., 2007) of the blood vessels (and biological tissues, in general), the vascular wall has also been modeled as a viscoelastic material (Toth et al., 1998; Orosz et al., 1999; Holzapfel et al., 2002; Hodis and Zamir, 2008;

Ebrahimi, 2009). Since these models do not incorporate the NO influence on the vascular wall, they are not able to predict neurovascular pathologies in which NO plays a critical role. Furthermore, the coupling of most of the above models with the cerebral NO dynamics will probably increase the already large number of model parameters that are practically impossible to find in a living brain with minimally invasive procedures using present-day technologies.

The aim of this study is to propose a novel mechanical model for cerebral arterioles that accounts for changes in the wall's mechanical behavior due to the NO-activated vascular cells and has few parameters. Orosz et al. (1999) used stress-relaxation measurements in cerebral arteries of human cadavers to show that four- and five-element generalized Maxwell viscoelastic models provide more accurate descriptions of the vascular wall mechanics than the two-element Maxwell viscoelastic model. One way to obtain a linear viscoelastic constitutive law with fewer parameters that perform as well as (or better) a spring-dashpot model with many elements is to use an integral formulation instead of the differential operator representation commonly associated with rheological (spring-dashpot) models. Integral constitutive laws admit equivalent differential formulations only for certain expressions of their relaxation functions (Gurtin and Sternberg, 1965; Drapaca et al., 2007). It was observed experimentally that relaxation functions represented as power functions of negative fractional exponents accurately describe the fading memory of many viscoelastic materials, including polymers and soft biological tissues (Nutting, 1921; Gemant, 1935; Gemant, 1936; Scott Blair and Coppen, 1939; Scott Blair and Coppen, 1942; Nutting, 1943; Guttinger, 1966; Caputo and Mainardi, 1971; Bagley and Torvik, 1983a; Bagley and Torvik, 1983b; Koeller, 1984; Torvik and Bagley, 1984; Suki et al., 1994; Mainardi, 2010). Integral constitutive laws with decaying fraction power-law relaxation functions have equivalent differential representations like those used in classic rheological models where integer-order derivatives were replaced by fractional-order derivatives (convolutions between decaying fraction power functions and integer-order derivatives). These fractional viscoelastic models are causal at zero time (Bagley and Torvik, 1983b; Torvik and Bagley, 1984) and can be derived from molecular theories that incorporate the molecular complexity of various polymers (Bagley and Torvik, 1983b; Suki et al., 1994). In this context, the fractional order of the strain history models the "contribution of the long-chain molecules to the macroscopic stress" (Suki et al., 1994). Also, Suki et al. (1994) noticed the structural similarities between the lung tissue and some polymers and showed that a fractional viscoelastic model can successfully predict the viscoelastic behavior of lung tissue. Given that lungs are highly vascularized, it is reasonable to assume that a fractional viscoelastic model could be employed in studies of blood vessels mechanics.

Therefore, this study proposes a new NO-modulated variable-order fractional Maxwell viscoelastic model for the cerebral vascular wall and investigates its predictions through numerical simulations. The suggested constitutive equation is

a generalization of the (constant order) fractional Maxwell viscoelastic model (see, for instance, Mainardi, 2010). The classic (first-order) Maxwell viscoelastic model has been previously used in the literature to model vascular walls (see, for instance, Hodis and Zamir, 2008), and therefore, this is the model which was chosen to be generalized here. According to Lorenzo and Hartley (2002), variable-order fractional operators are suitable in modeling, for instance, the *fading memory* characteristic of viscoelastic materials and the *order memory* which records the order in which memories are recalled [a recent review of applications of variable-order fractional operators can be found in Patnaik et al. (2020)]. In the model proposed here, the neuronal NO dynamics controls the order memory. With only three parameters, the proposed model can account for vessel's mechanics and the fact that the order memory of chemo-mechanical events is essential to the proper functionality of the constituent cells of the vascular wall. Lastly, the vascular wall is assumed to be isotropic and homogeneous.

As in Hodis and Zamir (2008), it is further assumed that the cerebral vessel is a hollow axial symmetric cylinder whose wall thickness is much smaller than the cylinder's radius, and longitudinal length is much less than the propagating wavelength. These assumptions together with the new constitutive equation led to a variable-order fractional telegraph equation for the unknown axial displacement of the vessel's wall. By assuming that the blood-vessel interface was exposed to the pulsatile blood flow and the vessel-tissue interface was tethered (Hodis and Zamir, 2008), an initial-boundary value problem was obtained and solved using the separation of variables method and finite difference schemes. The assumption of a tethered vessel-tissue interface is supported by experiments performed using high-resolution ultrasonic scanning that shows significantly larger longitudinal displacements of the wall's middle layers than the corresponding displacements of the wall's outer layers (Persson et al., 2003; Cinthio et al., 2006). Lastly, the variable fractional order was taken to be proportional to the concentration of neuronal NO. Two cases of neuronal NO synthesis (NOS) were considered: 1) a stepwise activation of NO with drastically decreased NO inactivation and 2) a dynamic activation of NO (Hall and Garthwaite, 2006). Case 1 may not be physiological because the main neuronal NOS activation matches the short pulsatile Ca^{2+} -calmodulin binding activation in dendritic spines (Hall and Garthwaite, 2006), and thus, this case may model impaired neuronal NO dynamics. Indeed, the temporal variation of NO resembles a stepwise function when the NO inactivation is drastically reduced by either brain ischemia (Santos et al., 2011) or the inhibition of cytochrome c oxidase (COX) (Palacios-Callender et al., 2007; Unitt et al., 2010). Brains of Alzheimer disease (AD) patients may suffer from a COX inhibition and thus an accumulation of NO (primarily in the temporal cortex and hippocampus) because a selective defect of COX causing a significant reduction in COX activity was found in AD brains (Parker and Parks, 1995; Maurer et al., 2000). Numerical simulations generated in MATLAB show smaller

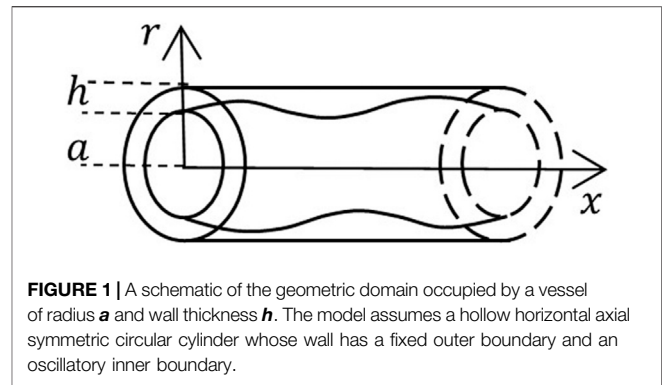


FIGURE 1 | A schematic of the geometric domain occupied by a vessel of radius a and wall thickness h . The model assumes a hollow horizontal axial symmetric circular cylinder whose wall has a fixed outer boundary and an oscillatory inner boundary.

displacements within the vascular wall in the case of stepwise NOS than in the case of dynamic NOS. Also, the shear stress at the bloodvessel interface is smaller in the case of stepwise neuronal NOS. Since the production of shear-induced endothelial NO is proportional to the shear stress at the inner boundary of the vessel's wall (Sriram et al., 2016), it follows that less endothelial NO will be produced in this case which could ultimately lead to neurovascular disease. Thus, the model could be used as a complementary clinical tool for early detection of disease and intervention (Alzheimer, for instance).

The study is structured as follows. The proposed mathematical model and the initial-boundary value problem under investigation are presented in *Mathematical Model*. The corresponding semi-analytic solution is given in *Semi-Analytic Solution*. Numerical simulations are shown in *Results*, which is followed by the last section containing a discussion of the results and final conclusions.

MATHEMATICAL MODEL

The vessel is modeled as a hollow horizontal axial symmetric circular cylinder of radius a and thickness h (Figure 1). As in Hodis and Zamir (2008), it is assumed that the vessel's wall is made of a homogeneous, linear viscoelastic material that is tethered at the outer boundary (the wall-tissue interface) and exposed to oscillations caused by the heart pulsations at its inner boundary (the blood-wall interface). In addition, it is assumed that the spatial variations of the oscillations can be neglected in a first approximation because they are of the same order of magnitude as the propagating wavelength (which is approximately 10 m at a frequency of 1 Hz in the systemic circulation) while the vessel's length is much smaller than the wavelength. Thus, only the time variations of the oscillations at the inner boundary of the vessel's wall will contribute to the wall's deformation. If (r, θ, x) are the cylindrical coordinates, then the modeling assumptions made so far reduce the equation of motion which is relevant to the work presented here to the following equation (Hodis and Zamir, 2008):

$$\rho \frac{\partial^2 \xi}{\partial t^2} = \frac{\partial \sigma_{rx}}{\partial r} + \frac{\sigma_{rx}}{r}, \quad (1)$$

for $(\mathbf{r}, t) \in (\mathbf{a}, \mathbf{a} + \mathbf{h}) \times [0, T]$. In Eq. 1, ρ is the mass density, $\xi(\mathbf{r}, t)$ is the axial displacement of a material point of the vessel's wall, and $\sigma_{rx}(\mathbf{r}, t)$ is the shear stress of a wall's point. Lastly, because the wall thickness h is usually much smaller than the radius a , the curvature term σ_{rx}/r is smaller than the other terms of Eq. 1, and thus, it can be neglected. Therefore, Eq. 1 reduces to (Hodis and Zamir, 2008):

$$\rho \frac{\partial^2 \xi}{\partial t^2} = \frac{\partial \sigma_{rx}}{\partial r}. \quad (2)$$

In this study, it is assumed that the mechanical behavior of the vessel's wall is described by the constitutive equation of a *variable-order fractional Maxwell linear viscoelastic material*:

$$\partial_t^{\alpha(t)} \sigma_{rx} = E \left(\partial_t^{\alpha(t)} \epsilon_{rx} - \frac{\sigma_{rx}}{\mu_\alpha} \right), \quad (3)$$

where, based on the model's assumptions, the infinitesimal strain ϵ_{rx} reduces to:

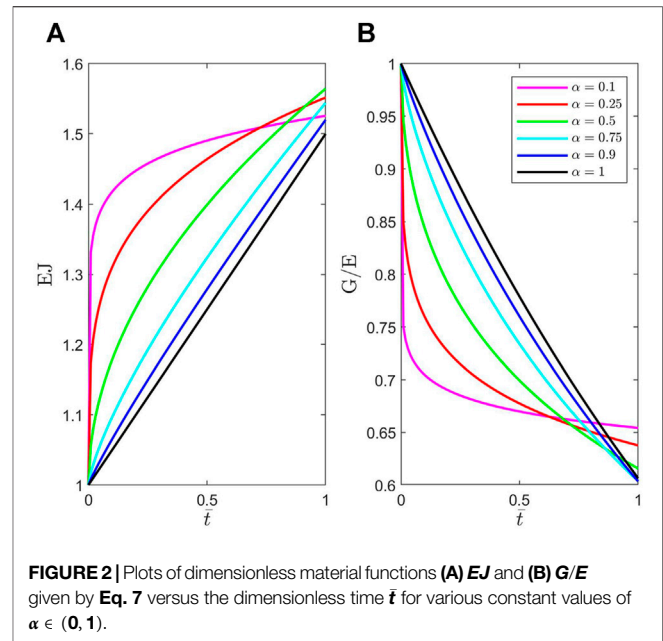
$$\epsilon_{rx} = \frac{\partial \xi}{\partial r}. \quad (4)$$

The constitutive Eq. 3 has three physical parameters: E , the modulus of elasticity, μ_α , and $\alpha(t)$, $0 < \alpha(t) \leq 1$. Without loss of generality, it is assumed further that $\epsilon_{rx}(\mathbf{r}, 0+) = 0$ and $\sigma_{rx}(\mathbf{r}, 0+) = 0$ (Bazhlekova and Bazhlekova, 2017). Lastly, the variable-order fractional derivative used in Eq. 3 is as follows (see for instance Ramirez and Coimbra, 2010; Moghaddam and Machado, 2017):

$$\partial_t^{\alpha(t)} \varphi(t) = \begin{cases} \frac{1}{\Gamma(1-\alpha(t))} \int_0^t \frac{\varphi^{(m)}(s) ds}{(t-s)^{\alpha(t)}}, & \text{if } m-1 < \alpha(t) < m, \forall t > 0 \\ \varphi^{(m)}(t), & \text{if } \alpha(t) = m, \forall t > 0 \\ \frac{1}{\Gamma(-\alpha(t))} \int_0^t \frac{\varphi(s) ds}{(t-s)^{1+\alpha(t)}}, & \text{if } \alpha(t) < 0, \forall t > 0 \end{cases}, \quad (5)$$

where $m \in \{1, 2, 3, \dots\}$, $\varphi(t)$ is an arbitrary, continuously m^{th} -order differentiable function whose m^{th} -order derivative is denoted by $\varphi^{(m)}(t)$ such that $\varphi^{(k)}(0+) = 0$, $k \in \{0, 1, \dots, m-1\}$, $\alpha(t)$ is a continuously differentiable function, and $\Gamma(z) = \int_0^\infty y^{z-1} \exp(-y) dy$ ($\text{Re}(z) > 0$) is the gamma function. For $\alpha(t)$ constant, the fractional derivative given by Eq. 5 reduces to the Caputo fractional derivative (see, for instance, Caputo and Mainardi, 1971).

According to Ramirez and Coimbra (2010), Eq. 5 is desirable in modeling of physical processes since a physical interpretation of the variable fractional order $\alpha(t) \in (0, 1)$ can be provided in this case: the order of a variable-order model describing the dynamics of a viscoelastic oscillator in stationary motion is a normalized phase shift. Since Eq. 5 preserves the well-known formula of calculating the integer-order derivative of a monomial (Samko and Ross, 1993), the following property holds for nonconstant analytic functions satisfying the zero initial



conditions mentioned above (Theorem 1, pg. 82 in West et al., 2003):

$$\partial_t^{\alpha(t)} \partial_t^{\beta(t)} \varphi(t) = \partial_t^{\beta(t)} \partial_t^{\alpha(t)} \varphi(t) = \partial_t^{\alpha(t)+\beta(t)} \varphi(t), \quad (6)$$

Equation 6 yields $\partial_t^{\alpha(t)} \partial_t^{-\alpha(t)} \varphi(t) = \varphi(t)$.

From Eq. 5 and the zero initial conditions satisfied by ϵ_{rx} and σ_{rx} , it follows that Eq. 3 becomes the fractional Maxwell model for $\alpha(t)$ a constant in the interval $(0, 1)$ and reduces to the classic Maxwell model for $\alpha(t) = 1, \forall t > 0$. Note that in the classic Maxwell model parameter μ_α becomes the viscosity denoted by μ . When the fractional order is a constant $\alpha \in (0, 1)$, properties of the (Caputo) fractional derivative Eq. 5 and the Laplace transform can be combined to obtain the following expressions for the creep compliance J and relaxation modulus G (Mainardi, 2010; Bazhlekova and Bazhlekova, 2017):

$$J(t) = \frac{1}{E} \left(\frac{g}{\Gamma(1+\alpha)} t^\alpha + 1 \right), G(t) = EE_\alpha(-gt^\alpha), \quad (7)$$

where $g = E/\mu_\alpha$ and the Mittag-Leffler function is, by definition, $E_\alpha(z) = \sum_{k=0}^\infty \frac{z^k}{\Gamma(\alpha k + 1)}$. Figure 2 shows plots of dimensionless material functions EJ and G/E given by Eq. 7 versus the dimensionless time $\bar{t} = t/T$ for various values of α . Thus, the material functions for a variable order $\alpha(t) \in (0, 1)$ will combine the behavior of multiple material functions shown in Figure 2.

Replacing Eq. 4 in Eq. 3, applying operator $\partial_t^{-\alpha(t)}$ to Eq. 3, and using Eq. 6 give:

$$\sigma_{rx} = E \left(\frac{\partial \xi}{\partial r} - \frac{1}{\mu_\alpha} \partial_t^{-\alpha(t)} \sigma_{rx} \right). \quad (8)$$

TABLE 1 | List of parameters with corresponding values and units. Due to a lack of experimental data, the value of T was fixed first, and then, the values of f and g were chosen such that a semi-analytic solution could be found for the initial boundary value problem **Eqs 15–17**. The normalized value of the wall's density was chosen for mathematical simplicity.

Considerations	Parameters	Values and units [reference]
Geometry and Viscoelasticity	ρ	1 Kg/m ³
	ω	1 Hz [Hodis and Zamir, 2008]
	f	0.1 s ⁻²
	g	0.5 s ^{-α}
	T	10 s
NO synthesis and inactivation (Hall and Garthwaite, 2006; Mehala and Rajendran, 2014)	v_1	1 nM/s
	k_1	2 s ⁻¹
	k_2	1.5 s ⁻¹
	V_{max}	2 × 10 ³ nM/s
	K_m	10 nM

Differentiating **Eq. 8** with respect to the spatial variable r and using **Eq. 2** yield:

$$\frac{\partial \sigma_{rx}}{\partial r} = E \left(\frac{\partial^2 \xi}{\partial r^2} - \frac{\rho}{\mu_\alpha} \partial_t^{2-\alpha(t)} \xi \right). \quad (9)$$

Lastly, by replacing **Eq. 9** in **Eq. 2** the following equation is obtained:

$$\frac{\partial^2 \xi}{\partial t^2} + g \partial_t^{2-\alpha(t)} \xi = \frac{E}{\rho} \frac{\partial^2 \xi}{\partial r^2}, \quad (10)$$

Eq. 10 is a *variable-order fractional telegraph equation* (or *two-term time-variable fractional diffusion-wave equation*).

The initial and boundary conditions are as follows:

$$\xi(r, 0) = 0, \quad \frac{\partial \xi}{\partial t}(r, 0) = \xi_0 \omega, \quad (11)$$

$$\xi(a, t) = \xi_0 \sin \omega t, \quad \xi(a + h, t) = 0. \quad (12)$$

It is assumed that the variable fractional order $\alpha(t) \in (0, 1)$ models the temporal effects of the neuronal NO on the vessel's wall. At this incipient stage, the shape of $\alpha(t)$ is considered to look like the temporal profile of the concentration of neuronal NO. Hall and Garthwaite (2006) proposed two models of neuronal NO dynamics: 1) stepwise activation of NO and 2) dynamic activation of NO. Both models include the NO inactivation. The equation of the first model is as follows:

$$\frac{d[NO]}{dt} = v_1 - \frac{V_{max}[NO]}{K_m + [NO]},$$

whose approximate analytic solution for zero initial condition is (Mehala and Rajendran, 2014) as follows:

$$[NO](t) = \frac{v_1}{\kappa} (1 - \exp(-\kappa t)). \quad (13)$$

The equation of the second model is as follows:

$$\frac{d[NO]}{dt} = v_1 (1 - \exp(-k_1 t)) \exp(-k_2 t) - \frac{V_{max}[NO]}{K_m + [NO]}$$

whose approximate analytic solution for zero initial condition is (Mehala and Rajendran, 2014) as follows:

$$[NO](t) = v_1 \left(\frac{-\exp(-k_2 t)}{k_2 - \kappa} + \frac{-\exp(-(k_1 + k_2)t)}{k_1 + k_2 - \kappa} + \exp(-\kappa t) \left(\frac{1}{k_2 - \kappa} - \frac{1}{k_1 + k_2 - \kappa} \right) \right). \quad (14)$$

Here, $[NO]$ is the concentration of NO, v_1 is the constant rate of NOS, V_{max} is the maximum rate at saturating concentration of NO, K_m is the concentration of NO at which the reaction rate is $\frac{V_{max}}{2}$, k_1 and k_2 are constant kinetic parameters, and $\kappa = V_{max}/K_m$. The values in **Table 1** were chosen such that the numerical solutions to the above differential equations for $[NO]$ and the corresponding approximate analytic solutions agree (Mehala and Rajendran, 2014). **Figures 3A,B** show plots of the NO concentrations given by **Eqs 13, 14**, respectively, while **Figures 3C,D** show two proposed profiles for the variable order $\alpha(t) \in (0, 1)$ which are obtained by simply multiplying the NO concentrations shown in **Figures 3A,B** by a factor of 10^2 . The scaling factor was chosen as follows. As seen in **Figures 3A,B**, the maximum concentrations of NO are in the low picomolar range, while physiological values are in the low nanomolar range (Hall and Garthwaite, 2006). A mere multiplication of the NO concentrations by 10^2 brings the maximum values within the physiological range for the NO concentrations. Since these scaled concentrations are still less than 1 nM , they can be used as expressions for $\alpha(t)$. Another advantage of this scaling factor is that significant differences are observed between the displacements and the shear stresses at the blood-vessel interface corresponding to the two profiles of $\alpha(t)$ shown in **Figures 3C,D** (see later).

The aim of the study is to find a semi-analytic solution to the initial-boundary value problem (10–12) for two variable orders given by scaled **Eqs 13, 14**. The first step is to formulate a corresponding non-dimensional problem. By introducing the dimensionless quantities:

$$\bar{r} = \frac{r-a}{h}, \quad \bar{t} = \frac{t}{T}, \quad \bar{\xi} = \frac{\xi}{\xi_0},$$

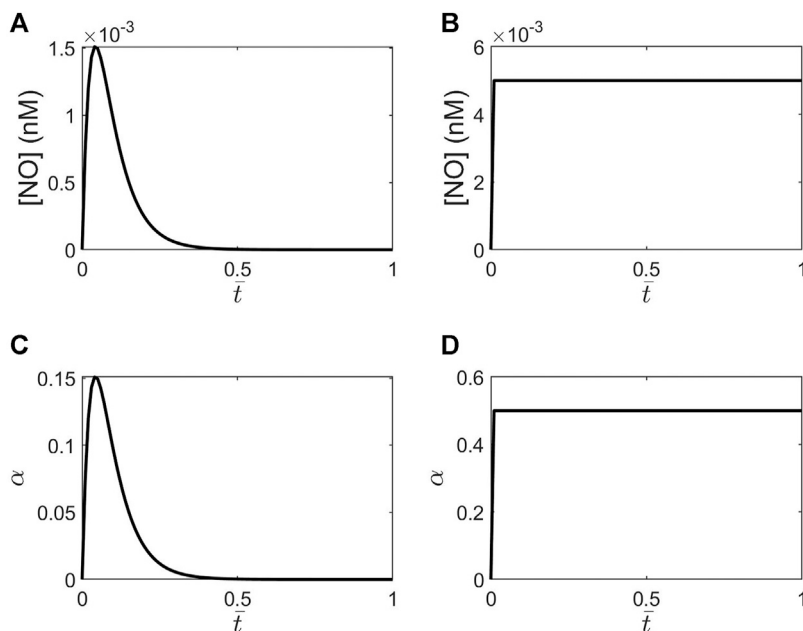


FIGURE 3 | Plots of NO concentrations versus the dimensionless time \bar{t} for (A) the dynamic synthesis of NO (Eq. 14) and (B) the stepwise synthesis of NO (Eq. 13). The proposed shapes for the variable order $\alpha(\bar{t})$ corresponding to the two cases of NOS (A) and (B) are shown in plots (C) and (D), respectively.

the initial-boundary value problem (10–12) transforms into the following dimensionless form:

$$\frac{\partial^2 \bar{\xi}}{\partial \bar{r}^2} + gT^{\alpha(\bar{t})} \partial_{\bar{t}}^{2-\alpha(\bar{t})} \bar{\xi} = fT^2 \frac{\partial^2 \bar{\xi}}{\partial \bar{r}^2}, \quad (\bar{r}, \bar{t}) \in (0, 1)^2, \quad (15)$$

$$\bar{\xi}(\bar{r}, 0) = 0, \quad \frac{\partial \bar{\xi}}{\partial \bar{t}}(\bar{r}, 0) = \omega T, \quad (16)$$

$$\bar{\xi}(0, \bar{t}) = \sin(\omega T \bar{t}), \quad \bar{\xi}(1, \bar{t}) = 0. \quad (17)$$

In Eq. 15, $f = E/(\rho h^2)$. The solution for problem (15–17) is presented in the next section.

SEMI-ANALYTIC SOLUTION

A classic approach of solving initial-boundary value problems for partial differential equations is used. Look for a solution to problem (15–17) of the form:

$$\bar{\xi}(\bar{r}, \bar{t}) = V(\bar{r}, \bar{t}) + W(\bar{r}, \bar{t}), \quad (18)$$

such that $V(0, \bar{t}) = \bar{\xi}(0, \bar{t}) = \sin(\omega T \bar{t})$, $V(1, \bar{t}) = \bar{\xi}(1, \bar{t}) = 0$ and $\frac{\partial^2 V}{\partial \bar{r}^2} = 0$. It is straightforward to solve for $V(\bar{r}, \bar{t})$ and find that:

$$V(\bar{r}, \bar{t}) = (1 - \bar{r}) \sin(\omega T \bar{t}). \quad (19)$$

Combining Eqs 18, 19 yields:

$$\bar{\xi}(\bar{r}, \bar{t}) = (1 - \bar{r}) \sin(\omega T \bar{t}) + W(\bar{r}, \bar{t}). \quad (20)$$

By substituting Eq. 20 in problem (15–17), the following initial-boundary value problem for $W(\bar{r}, \bar{t})$ is obtained:

$$\frac{\partial^2 W}{\partial \bar{r}^2} + gT^{\alpha(\bar{t})} \partial_{\bar{t}}^{2-\alpha(\bar{t})} W = fT^2 \frac{\partial^2 W}{\partial \bar{r}^2} + (1 - \bar{r}) \left[(\omega T)^2 \sin(\omega T \bar{t}) - gT^{\alpha(\bar{t})} \partial_{\bar{t}}^{2-\alpha(\bar{t})} (\sin(\omega T \bar{t})) \right], \quad (21)$$

$$W(\bar{r}, 0) = 0, \quad \frac{\partial W}{\partial \bar{t}}(\bar{r}, 0) = \omega T \bar{r}, \quad (22)$$

$$W(0, \bar{t}) = 0, \quad W(1, \bar{t}) = 0. \quad (23)$$

The first step in solving problem (21–23) is to look for a solution to the corresponding homogeneous equation:

$$\frac{\partial^2 W}{\partial \bar{r}^2} + gT^{\alpha(\bar{t})} \partial_{\bar{t}}^{2-\alpha(\bar{t})} W = fT^2 \frac{\partial^2 W}{\partial \bar{r}^2}. \quad (24)$$

The method of separation of variables suggests looking for a solution of the form $W(\bar{r}, \bar{t}) = F(\bar{t})G(\bar{r})$. Then, Eq. 24 and the boundary conditions (Eq. 23) yield the following Sturm-Liouville problem for $G(\bar{r})$:

$$fT^2 \frac{d^2 G}{d\bar{r}^2} - \lambda G = 0, \quad G(0) = G(1) = 0 \quad (25)$$

Thus, the eigenfunctions satisfying problem (25) are $G_n(\bar{r}) = \sin(n\pi\bar{r})$, $n \in \{1, 2, 3, \dots\}$, and the corresponding eigenvalues are $\lambda_n = -(n\pi T)^2 f$, $n \in \{1, 2, 3, \dots\}$. The solution to problem (21, 22) is thus of the form:

$$W(\bar{r}, \bar{t}) = \sum_{n=1}^{\infty} A_n(\bar{t}) \sin(n\pi\bar{r}). \quad (26)$$

Substituting Eq. 26 in problem (21, 22) and using the half-range Fourier sine series expansions of the functions $1 - \bar{r}$ and \bar{r} yield the following initial value problem for $A_n(\bar{t})$, $n \in \{1, 2, 3 \dots\}$:

$$\frac{d^2 A_n}{d\bar{t}^2} + g T^{\alpha(\bar{t})} \partial_{\bar{t}}^{2-\alpha(\bar{t})} A_n = -f(n\pi T)^2 A_n + \frac{2}{n\pi} \left[(\omega T)^2 \sin(\omega T \bar{t}) - g T^{\alpha(\bar{t})} \partial_{\bar{t}}^{2-\alpha(\bar{t})} (\sin(\omega T \bar{t})) \right], \quad (27)$$

$$A_n(0) = 0, \quad \frac{dA_n}{d\bar{t}}(0) = 2\omega T \frac{(-1)^{n+1}}{n\pi}. \quad (28)$$

Let

$$Z_n(\bar{t}) = A_n(\bar{t}) + \frac{2}{n\pi} \sin(\omega T \bar{t}), \quad n \in \{1, 2, 3 \dots\}. \quad (29)$$

By replacing expression (29) in problem (27, 28), the following problem for the unknown function $Z_n(\bar{t})$, $n \in \{1, 2, 3 \dots\}$ is obtained:

$$\frac{d^2 Z_n}{d\bar{t}^2} + B \partial_{\bar{t}}^{2-\alpha(\bar{t})} Z_n + C_n Z_n = D_n \sin(\omega T \bar{t}), \quad (30)$$

$$Z_n(0) = 0, \quad \frac{dZ_n}{d\bar{t}}(0) = F_n, \quad (31)$$

where $B = g T^{\alpha(\bar{t})}$, $C_n = (n\pi T)^2 f$, $D_n = 2n\pi T^2 f$, and $F_n = 2\omega T \frac{(-1)^{n+1}}{n\pi}$. Once the solution to the initial value problem (30, 31) is found, Eqs 20, 26, and 29 can be combined to find the solution to the original problem (15–17):

$$\bar{\xi}(\bar{r}, \bar{t}) = (1 - \bar{r}) \sin(\omega T \bar{t}) + \sum_{n=1}^{\infty} \left[Z_n(\bar{t}) - \frac{2}{n\pi} \sin(\omega T \bar{t}) \right] \sin(n\pi \bar{r}), \quad (32)$$

Thus, the last step is finding a solution to problem (30, 31). If the fractional order is a constant $\alpha \in (0, 1)$, then a closed-form solution of problem (30, 31) can be obtained by using either the Laplace transform method (Gorenflo et al., 2014) or an operational method proposed by Luchko and Gorenflo (1999) (it is worth noticing here that the Laplace transform method belongs to the class of operational methods). Not only that this analytic solution is cumbersome and difficult to implement in a computer program but also may not be generalizable to the case of variable fractional order. Therefore, looking for a numerical solution to problem (Eqs 30, 31) is a better approach. Eq. 30 is a linear multi-term fractional differential equation which for a constant fractional order $\alpha \in (0, 1)$, can be solved numerically using the elegant explicit, implicit, and predictor-corrector methods involving product-integration rules proposed by Garrappa (2018). For the variable-order fractional differential Eq. 30, the finite difference schemes given by Moghaddam and Machado (2017) can be used. Thus, in this study, the second-order derivative of Eq. 20 will be approximated by a center difference scheme, and the variable-order fractional derivative will be approximated by the forward difference

scheme proposed in theorem 3.1 of Moghaddam and Machado (2017). For the sake of completeness, the numerical discretization of Eq. 30 is presented further.

Let $0 = \bar{t}_0 < \bar{t}_1 < \dots < \bar{t}_N = 1$ be an equally spaced discretization of the interval $[0, 1]$ of constant step size $\Delta \bar{t} = 1/N$. Denoting by $Z_n^k = Z_n(\bar{t}_k)$, $k \in \{0, 1, \dots, N\}$, n fixed, and $\alpha^k = \alpha(\bar{t}_k)$, $k \in \{0, 1, \dots, N\}$, the numerical approximations of the derivatives in Eq. 30 can be written as:

$$\frac{d^2 Z_n}{d\bar{t}^2}(\bar{t}_{k+1}) \approx \frac{Z_n^{k+2} - 2Z_n^{k+1} + Z_n^k}{\Delta \bar{t}^2}, \quad (33)$$

$$\partial_{\bar{t}}^{2-\alpha(\bar{t}_{k+1})} Z_n(\bar{t}_{k+1}) \approx \frac{\Delta \bar{t}^{-2+\alpha^{k+1}}}{\Gamma(1+\alpha^{k+1})} \sum_{j=0}^k \psi_{2,k,j} (Z_n^{k-j+2} - 2Z_n^{k-j+1} + Z_n^{k-j}), \quad (34)$$

where $\psi_{2,k,j} = (j+1)^{\alpha^{k+1}} - j^{\alpha^{k+1}}$ (Moghaddam and Machado, 2017). The truncation error of scheme Eq. 33 is of order $O(\Delta \bar{t}^2)$, while for scheme Eq. 34, it is of order $O(\Delta \bar{t})$. By replacing approximations Eqs 33, 34 in problem (30, 31), the following explicit scheme is obtained:

$$\begin{aligned} Z_n^0 &= 0, \quad Z_n^1 = F_n \Delta \bar{t} \\ Z_n^{k+2} - 2Z_n^{k+1} + Z_n^k + B \frac{\Delta \bar{t}^{\alpha^{k+1}}}{\Gamma(1+\alpha^{k+1})} \sum_{j=0}^k \psi_{2,k,j} (Z_n^{k-j+2} - 2Z_n^{k-j+1} \\ &+ Z_n^{k-j}) + C_n \Delta \bar{t}^2 Z_n^{k+1} \\ &= D_n \Delta \bar{t}^2 \sin(\omega T \bar{t}_{k+1}), \quad k \in \{0, 1, \dots, N-2\}. \end{aligned} \quad (35)$$

The semi-analytic solution to problem (15–17) is then obtained by replacing the discrete solution (35) for $n \in \{1, 2, \dots\}$ in Eq. 32.

The shear stress distribution within the vessel's wall is obtained from the dimensionless form of Eq. 2 by integration (Hodis and Zamir, 2008):

$$\bar{\sigma}_{rx}(\bar{r}, \bar{t}) = \frac{1}{f T^2} \int_0^{\bar{r}} \frac{\partial^2 \bar{\xi}(\bar{r}, \bar{t})}{\partial \bar{t}^2} d\bar{r} + \bar{\sigma}_{rx}(0, \bar{t}), \quad (36)$$

where the following non-dimensionalization was used for the shear stress: $\bar{\sigma}_{rx}(\bar{r}, \bar{t}) = \sigma_{rx}(r, t) / (\frac{E_0 a}{h})$. By replacing Eq. 32 in Eq. 36, the following expression for the shear stress at the blood-vessel interface is obtained:

$$\tau_w \equiv \bar{\sigma}_{rx}(0, \bar{t}) = \sum_{n=1}^{\infty} \frac{-1}{n\pi f T^2} \left[\frac{d^2 Z_n(\bar{t})}{d\bar{t}^2} - \frac{2\omega^2 T^2}{n\pi} \sin(\omega T \bar{t}) \right] \quad (37)$$

RESULTS

Numerical scheme Eq. 35 was implemented in MATLAB, and plots of the distributions of dimensionless displacements within the vessel's wall (Eq. 32) and the dimensionless shear stress at the blood-vessel interface (Eq. 37) were generated for two expressions of the variable fractional order: the stepwise NOS and the dynamic NOS. The values of the parameters used in the

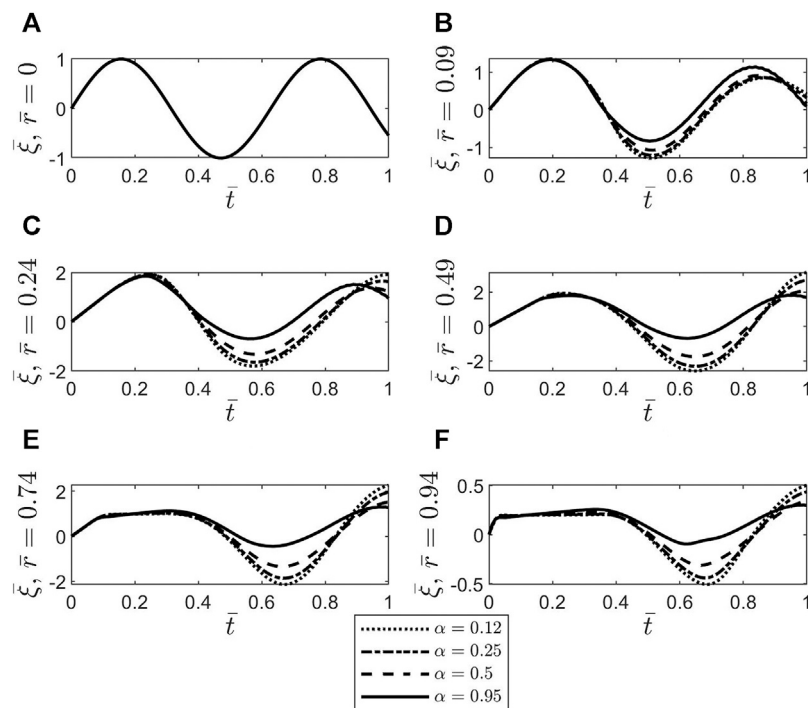


FIGURE 4 | Plots of the dimensionless axial displacement ξ versus the dimensionless time \bar{t} at various dimensionless radial locations \bar{r} within the vascular wall (A) $\bar{r}=0$, (B) $\bar{r}=0.09$, (C) $\bar{r}=0.24$, (D) $\bar{r}=0.49$, (E) $\bar{r}=0.74$, and (F) $\bar{r}=0.94$ and for various constant values of $\alpha \in (0, 1)$.

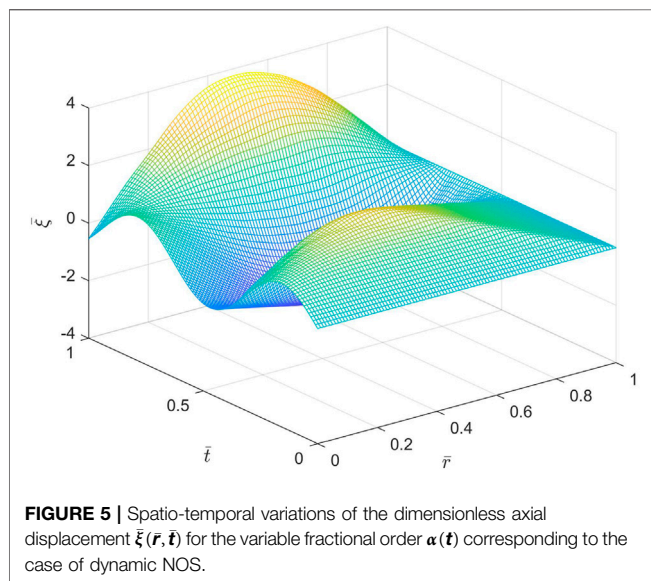


FIGURE 5 | Spatio-temporal variations of the dimensionless axial displacement $\xi(\bar{r}, \bar{t})$ for the variable fractional order $\alpha(\bar{t})$ corresponding to the case of dynamic NOS.

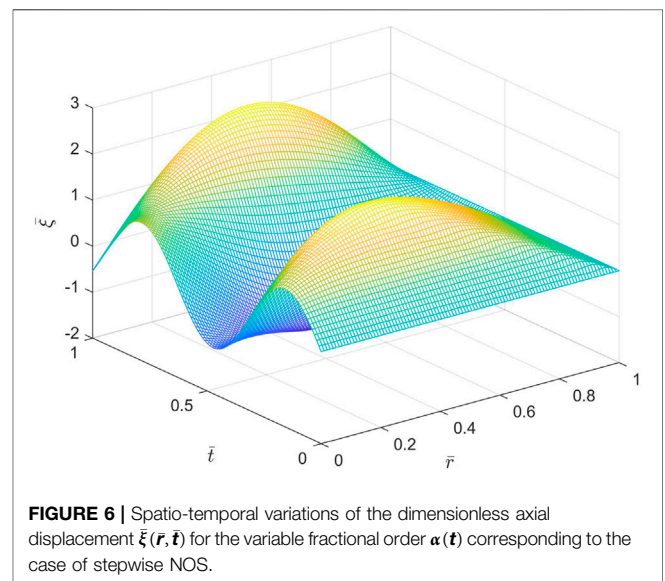


FIGURE 6 | Spatio-temporal variations of the dimensionless axial displacement $\xi(\bar{r}, \bar{t})$ for the variable fractional order $\alpha(\bar{t})$ corresponding to the case of stepwise NOS.

numerical simulations are given in **Table 1**. Numerical simulations used a step size $\Delta \bar{t} = 0.00025$ and 20 terms of the Fourier series in **Eq. 32**.

Figure 4 shows temporal profiles of the dimensionless axial displacement $\xi(\bar{r}, \bar{t})$ at various radial locations inside the vascular wall and for constant fractional orders. These plots were generated using MATLAB's function

MT_FDE_PI12_PC developed by Garrappa which is an implementation of the predictor-corrector scheme proposed by Garrappa (2018). The same results are obtained with the forward scheme **Eq. 35** when α is constant. This agreement of numerical solutions validates scheme **Eq. 35**. The plots of **Figure 4** show that while the amplitudes of the oscillations are approaching zero as $\bar{r} \rightarrow 1$ for all values of α , the decaying in

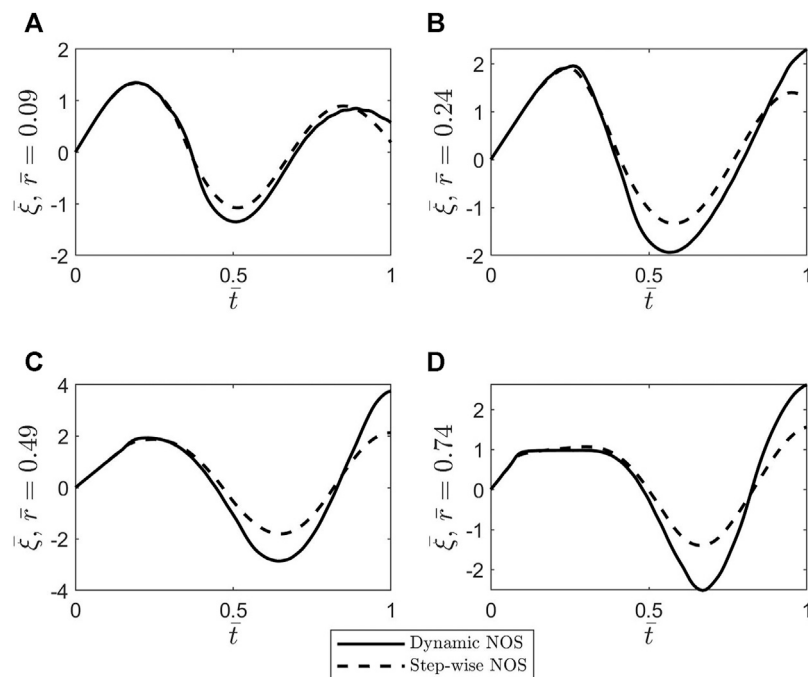


FIGURE 7 | Plots of the dimensionless axial displacement ξ versus the dimensionless time \bar{t} at various dimensionless radial locations \bar{r} within the vascular wall (A) $\bar{r}=0.09$, (B) $\bar{r}=0.24$, (C) $\bar{r}=0.49$, and (D) $\bar{r}=0.74$ for the variable fractional order $\alpha(\bar{t})$ corresponding to the case of dynamic NOS (solid line) and to the case of stepwise NOS (dashed line).

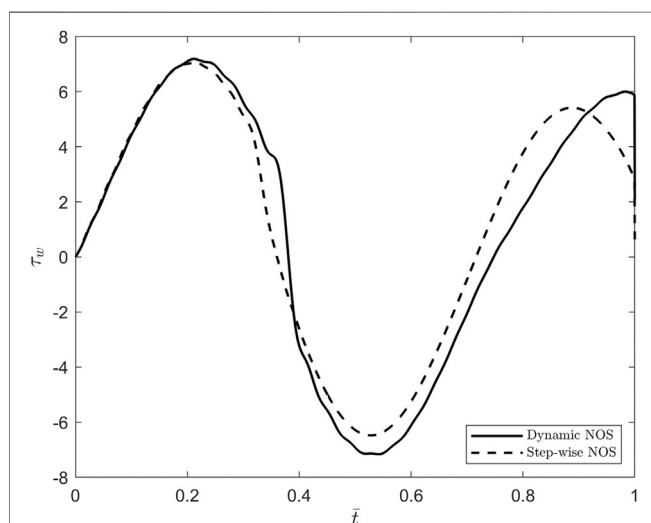


FIGURE 8 | Plots of the dimensionless shear stress at the bloodvessel interface τ_w versus the dimensionless time \bar{t} for the variable fractional order $\alpha(\bar{t})$ corresponding to the case of dynamic NOS (solid line) and to the case of stepwise NOS (dashed line).

amplitude decreases faster as α increases. The solutions for constant fractional orders provide a first glimpse into the shapes of the displacements for variable fractional orders since these are expected to be a combination of the behaviors of the solutions for constant α .

Figures 5, 6 show spatio-temporal variations of the dimensionless axial displacement $\xi(\bar{r}, \bar{t})$ for the variable fractional order $\alpha(\bar{t})$ corresponding to the case of decaying dynamic NOS (Figure 5) and to the case of stepwise NOS (Figure 6). The amplitude of the oscillations appears to be bigger in the dynamic NOS case than in the stepwise NOS case. This is confirmed in Figure 7 which shows temporal profiles of the dimensionless axial displacement at various radial locations inside the vascular wall which was extracted from the surfaces presented in Figures 5, 6. Since the results in Figure 7 resemble those in Figure 4, it can be concluded that the solutions for variable fractional orders are plausible. According to Figures 3C,D, the maximum value of $\alpha(\bar{t})$ for the case of dynamic NOS is 0.15 which is smaller than the almost constant value of 0.5 that $\alpha(\bar{t})$ in the case of stepwise NOS. The results in Figure 7 confirmed what was already known from Figure 4, namely that the amplitude of oscillations corresponding to the higher values of $\alpha(\bar{t})$ is smaller than the one corresponding to lower values of $\alpha(\bar{t})$.

To better understand the differences noticed between the oscillatory patterns corresponding to the two cases of stepwise NOS and dynamic NOS, the dimensionless shear stress at the blood-vessel interface was calculated using Eq. 37 and MATLAB's built-in function gradient. The results of this comparison are shown in Figure 8. The amplitude of the shear stress is bigger in the case of dynamic NOS which was expected given that the amplitude of the axial displacement is also bigger in this case. By varying the scaling factor of order $\alpha(\bar{t})$ corresponding to the case of stepwise neuronal NOS, the

difference between the shear stresses at the inner boundary of the vessel wall corresponding to the two cases 1) vanishes when the fractional order of the stepwise neuronal NOS gets smaller and 2) is almost unchanged when the fractional order of the stepwise neuronal NOS approaches 1. The possible implications of this finding will be discussed in the next section.

DISCUSSION

The main contribution of this study is modeling the wall of a cerebral blood vessel using an NO-modulated variable-order fractional Maxwell viscoelastic model. The variable fractional order is assumed to be proportional to the neuronal NO dynamics, and thus, the order memory introduced by this choice guides the pattern of the fading memory of this viscoelastic material. Two cases of NOS are considered: a stepwise activation of NO and a dynamic activation of NO. Following the approach of Hodis and Zamir (2008), a variable-order fractional telegraph equation for the axial displacement of the wall was obtained which was solved under the assumptions that the outer boundary of the vascular wall was tethered, and the inner boundary of the wall was exposed to the pulsatile blood flow. Numerical simulations were created in MATLAB using numerical scheme (Eq. 35) and Garrappa's function MT_FDE_PI12_PC (Garrappa, 2018) for constant fractional orders. The function MT_FDE_PI12_PC was used to validate scheme (Eq. 35) in the case of constant fractional orders. The main finding of these simulations is that a significantly decreased inactivation of the neuronal NO causes a reduction in the shear stress at the blood-vessel interface which could lead to a decrease in the production of shear-induced endothelial NO and ultimately to neurovascular disease.

Testing the computer code for various values of the parameters f , g , and T which are present in the coefficients of Eq. 15 showed that both approaches, scheme (Eq. 35) and MT_FDE_PI12_PC, were sensitive to these parameters for variable and constant fractional orders. These numerical schemes are stable only for narrow ranges of f , g , and T . These parameters couple mechanical parameters E , μ_α , wall thickness h , and the characteristic time T . Thus, if these narrow ranges of f , g , and T are subsets of their corresponding physiological ranges, this stability issue could be disregarded. However, for $E = 6 \times 10^5 \text{ N/m}^2$, $\mu_\alpha = 1.5 \times 10^5 \text{ Kg}/(\text{m} \times \text{s}^{2-\alpha})$ derived from Hodis and Zamir (2008) for arteries and ($\alpha = 1$), a wall thickness $h = 10^{-3} \text{ m}$ measured in human intracranial arteries *in vivo* (Yuan et al., 2021), and a more accurate value of the wall density $\rho \approx 1.1 \times 10^3 \frac{\text{Kg}}{\text{m}^3}$ (IT'IS Foundation, 2021), the following values are obtained: $f = 5.45 \times 10^8 \text{ s}^{-2}$ and $g = 4 \text{ s}^{-\alpha}$. These values, together with the chosen $T = 10 \text{ s}$, make Eq. 15 stiff since the order of magnitude of the coefficient of the right-hand side term is much bigger than the magnitudes of the coefficients of the left-hand-side terms. For a smaller wall thickness which is more appropriate for an intracerebral arteriole which experiences NO-modulated vasodilation, the order of magnitude of the coefficient of the right-hand-side term of Eq. 15 becomes even bigger. The proposed numerical

schemes are unstable for a stiff Eq. 15, and a mere decrease of the step size Δt does not resolve this issue. Finding algorithms for stiff variable-order fractional differential equations is an open problem in numerical analysis. Nevertheless, for a characteristic time T of order of ms which may be more suitable for NO dynamics *in vivo* (Hall and Garthwaite, 2006), a possibly lower value of E corresponding to cerebral arterioles (Medical Physiology, 2021), and a more realistic value of the wall density, the numerical stiffness can be avoided, and thus, the presented results will hold.

Emerging imaging techniques could help validate the proposed model in animal models and thus make the model relevant to clinical applications. For instance, a multimodal *in vivo* magnetic resonance (MR)/electron paramagnetic resonance (EPR) spectroscopy/fluorometry could be used to visualize NO production and spatio-temporal distribution (Sharma et al., 2014). Also, intravascular optical coherence tomography could be used for the *in vivo* real-time estimation of the vascular stiffness (Potlov et al., 2020). By combining these imaging techniques and the high-resolution ultrasonic scanning of Persson et al. (2003) and Cinthio et al. (2006) for the visualization of wall's longitudinal displacements, the cerebral NO dynamics and vascular wall mechanics may be investigated simultaneously. This approach can be used to estimate $\alpha(t)$, f , g , and T and validate the mathematical model proposed here. If a significant decrease in the neuronal NO inactivation is observed, then the model's prediction could suggest the use of a preventive therapy [such as NO inhalation proposed by Terpolilli et al. (2016)] to reduce imminent brain damage.

Until the above-mentioned imaging techniques are adapted and approved for clinical applications, animal models can be used to find healthy physiological ranges for the model's parameters and investigate the potential of using these parameters as biomarkers. For example, animal models of cerebral ischemia have shown that the decreasing amount of endothelial NO will act as a protective agent for a few minutes after the injury, while the amount of neuronal NO will increase causing neuronal injury (Huang, 1999; Wei et al., 1999). If the production of shear-induced endothelial NO mediated by the blood flow ceases to happen following ischemia, then the stepwise concentration of neuronal NO is a consequence of the significantly decreased NO inactivation caused by ischemia (Santos et al., 2011) and thus, according to the prediction made by the proposed model, may contribute to the reduction of the localized endothelial NO produced by the lower shear stress in the vessel wall at its inner boundary. Thus, the model's prediction may explain the interplay between the endothelial and neuronal NO seen in cerebral ischemia. Lastly, model's parameters estimated using the multimodal *in vivo* imaging techniques mentioned above could suggest the presence of cerebral ischemia and thus be used as a complementary diagnostic tool.

Improving the mathematical model may provide more sensitive biomarkers and helps avoiding the numerical stiffness issue mentioned earlier. According to Iadecola (2004), the NO-modulated local vasodilation of the intracerebral arterioles and capillaries propagates upstream in the vascular network which causes an increase of blood flow in the upstream arteries that leads to increased shear stress at the blood-vessel interface and

thus an increase in the amount of shear-induced endothelial NO and a further flow-mediated vasodilation. The proposed model represents the blood flow as an inner boundary condition, and thus, this mechanism of global production of shear-induced endothelial NO is not accounted for. Thus, the decrease in the local production of the shear-induced endothelial NO due to a stepwise neuronal NOS predicted by the model proposed in this study might not be significant enough to cause adverse effects if the cerebral blood flow is intact. Coupling the deformation of the vessel's wall and the blood flow and incorporating in the model the mechanism described above should provide a better prediction of the amount of shear-induced endothelial NO and the possible role that the neuronal NO dynamics may play in this process. Introducing more detailed information about the complex, multi-layered structure of the vascular wall could also enhance the accuracy of model's predictions. Lastly, the full three-dimensional fluid-structure interaction problem should be formulated and solved since the simplifying assumptions made by Hodis and Zamir (2008) and implemented here that reduced the model to a one-dimensional problem might not be valid for cerebral arterioles given the overly complex geometry of the cerebral vascular network (Reina-De La Torre et al., 1998). The parameters of this enhanced mathematical model could be found either from *in vitro/in situ* measurements or from *in vivo*, real-time observations using medical imaging techniques.

REFERENCES

- Atwell, D., Buchan, A. M., Charpak, S., Lauritzen, M., MacVicar, B. A., and Newman, E. A. (2010). Glial and Neuronal Control of Brain Blood Flow. *Nature* 468, 232–243. doi:10.1038/nature09613
- Bagley, R. L., and Torvik, P. J. (1983b). A Theoretical Basis for the Application of Fractional Calculus to Viscoelasticity. *J. Rheology* 27, 201–210. doi:10.1122/1.549724
- Bagley, R. L., and Torvik, P. J. (1983a). Fractional Calculus - A Different Approach to the Analysis of Viscoelastically Damped Structures. *AIAA J.* 21, 741–748. doi:10.2514/3.8142
- Bazhlekova, E., and Bazhlev, I. (2017). Stokes' First Problem for Viscoelastic Fluids with a Fractional Maxwell Model. *Fractal Fract* 1, 7. doi:10.3390/fractalfract1010007
- Blair, G. W. S., and Caffyn, J. (1942). The Classification of the Rheological Properties of Industrial Materials in the Light of Power-Law Relations between Stress, Strain and Time. *J. Sci. Instrum.* 19, 88–93. doi:10.1088/0950-7671/19/6/303
- Caputo, M., and Mainardi, F. (1971). A New Dissipation Model Based on Memory Mechanism. *Pageoph* 91, 134–147. doi:10.1007/bf00879562
- Cinthio, M., Ahlgren, Å. R., Bergkvist, J., Jansson, T., Persson, H. W., and Lindström, K. (2006). Longitudinal Movements and Resulting Shear Strain of the Arterial wall. *Am. J. Physiology-Heart Circulatory Physiol.* 291 (1), H394–H402. doi:10.1152/ajpheart.00988.2005
- Cockcroft, J. (2005). Exploring Vascular Benefits of Endothelium-Derived Nitric Oxide. *Am. J. Hypertens.* 18, 177–183. doi:10.1016/j.amjhyper.2005.09.001
- Contestabile, A., Monti, B., and Polazzi, E. (2012). Neuronal-glial Interactions Define the Role of Nitric Oxide in Neural Functional Processes, *Curr. Neuropharmacology* 10, no. 4, 303–310. doi:10.2174/157015912804143522
- Drapaca, C. S., and Sivaloganathan, S. (2019). *Mathematical Modelling and Biomechanics of the Brain*. New York, USA: Fields Institute Monographs, Springer Science+Business Media, LLC. doi:10.1007/978-1-4939-9810-4
- In conclusion, the study proposes a novel NO-modulated variable-order fractional Maxwell viscoelastic model of the cerebral arterioles and investigates the effects of the neuronal NOS on the mechanical behavior of the vessel's wall. Numerical simulations show how neuronal NO dynamics influence the deformation and shear stress within the vascular wall. A generalization of this model to a three-dimensional geometry and the incorporation of the blood flow into the model should provide a better understanding of the coupling between NO dynamics and mechanical damage and their combined role in neurovascular diseases.
- ## DATA AVAILABILITY STATEMENT
- The original contributions presented in the study are included in the article/supplementary material; further inquiries can be directed to the corresponding author.
- ## AUTHOR CONTRIBUTIONS
- CD stated the problem under investigation, proposed the mathematical model and its semi-analytic solution, implemented code in MATLAB, generated results, and wrote the paper.
- Drapaca, C. S., Sivaloganathan, S., and Tenti, G. (2007). Nonlinear Constitutive Laws in Viscoelasticity. *Maths. Mech. Sol.* 12, 475–501. doi:10.1177/1081286506062450
- Ebrahimi, A. P. (2009). Mechanical Properties of normal and Diseased Cerebrovascular System. *J. Vasc. Interv. Neurol.* 2 (2), 155–162.
- Forstermann, U., and Sessa, W. C. (2012). Nitric Oxide Synthases: Regulation and Function. *Eur. Heart J.* 33, 829–837. doi:10.1093/eurheartj/ehs304
- Freed, J. K., and Gutterman, D. D. (2017). Communication Is Key: Mechanisms of Intercellular Signaling in Vasodilation. *J. Cardiovasc. Pharmacol.* 69 (5), 264–272. doi:10.1097/FJC.0000000000000463
- Gabriela Espinosa, M., Catalin Staiculescu, M., Kim, J., Marin, E., and Wagenseil, J. E. (2018). Elastic Fibers and Large Artery Mechanics in Animal Models of Development and Disease. *J. Biomech. Eng.* 140 (2), 0208031–02080313. doi:10.1115/1.4038704
- Garrappa, R. (2018). Numerical Solution of Fractional Differential Equations: A Survey and a Software Tutorial. *Mathematics* 6, 16. doi:10.3390/math6020016
- Gemant, A. (1936). A Method of Analyzing Experimental Results Obtained from Elasto-Viscous Bodies. *Physics* 7, 311–317. doi:10.1063/1.1745400
- Gemant, A. (1935). Compression Waves in media with Complex Viscosity. *Physics* 6, 363–365. doi:10.1063/1.1745278
- Gorenflo, R., Kilbas, A. A., Mainardi, F., and Rogosin, S. V. (2014). *Mittag-Leffler Functions, Related Topics and Applications*. New York, USA: Springer-Verlag. doi:10.1007/978-3-662-43930-2_6
- Gurtin, M., and Sternberg, E. (1965). On the Linear Theory of Viscoelasticity. *Archive Rational Mech. Anal.* 11, 291–356.
- Guttinger, W. Generalized Functions and Dispersion Relations in Physics. *Fortschritte der Physik* 14, 483–602. doi:10.1002/prop.19660140114
- Hall, C. N., and Garthwaite, J. (2006). Inactivation of Nitric Oxide by Rat Cerebellar Slices. *J. Physiol.* 577 (2), 549–567. doi:10.1113/jphysiol.2006.118380
- Haselden, W. D., Kedarasetti, R. T., and Drew, P. J. (2020). Spatial and Temporal Patterns of Nitric Oxide Diffusion and Degradation Drive Emergent Cerebrovascular Dynamics. *Plos Comput. Biol.* 16 (7), e1008069. doi:10.1371/journal.pcbi.1008069

- Helms, C. C., Liu, X., and Kim-Shapiro, D. B. (2017). Recent Insights into Nitrite Signaling Processes in Blood. *Biol. Chem.* 398, 319–329. doi:10.1515/hsz-2016-0263
- Hill, A. V. (1938). The Heat of Shortening and the Dynamic Constants of Muscle. *Proc. R. Soc. Lond. B* 126, 136–195. doi:10.1098/rspb.1938.0050
- Hodis, S., and Zamir, M. (2008). Solutions of the Maxwell Viscoelastic Equations for Displacement and Stress Distributions within the Arterial wall. *Phys. Rev. E Stat. Nonlin Soft Matter Phys.* 78, 021914. doi:10.1103/PhysRevE.78.021914
- Holzapfel, G. A., Gasser, T. C., and Stadler, M. (2002). A Structural Model for the Viscoelastic Behavior of Arterial walls: Continuum Formulation and Finite Element Analysis. *Eur. J. Mech. - A/Solids* 21, 441–463. doi:10.1016/s0997-7538(01)01206-2
- Holzapfel, G. A., and Ogden, R. W. (2010). Constitutive Modelling of Arteries. *Proc. R. Soc. A* 466, 1551–1597. doi:10.1098/rspa.2010.0058
- Huang, P. L. (1999). Neuronal and Endothelial Nitric Oxide Synthase Gene Knockout Mice. *Braz. J. Med. Biol. Res.* 32, 1353–1359. doi:10.1590/s0100-879x1999001100005
- Iadecola, C. (2004). Neurovascular Regulation in the normal Brain and in Alzheimer's Disease. *Nat. Rev. Neurosci.* 5, 347–360. doi:10.1038/nrn1387
- Iadecola, C. (2017). The Neurovascular Unit Coming of Age: a Journey through Neurovascular Coupling in Health and Disease. *Neuron* 96, 17–42. doi:10.1016/j.neuron.2017.07.030
- IT'S Foundation (2021). Tissue Properties Database: Density. Available at: <https://itis.swiss/virtual-population/tissue-properties/database/density/>. Zurich: Zurich43.
- Kasza, K. E., Rowat, A. C., Liu, J., Angelini, T. E., Brangwynne, C. P., Koenderink, G. H., et al. (2007). The Cell as a Material. *Curr. Opin. Cell Biol.* 19, 101–107. doi:10.1016/j.ceb.2006.12.002
- Kim, J., and Wagenseil, J. E. (2014). Bio-chemo-mechanical Models of Vascular Mechanics. *Ann. Biomed. Eng.* 43, 1477–1487. doi:10.1007/s10439-014-1201-7
- Koeller, R. C. (1984). Applications of Fractional Calculus to the Theory of Viscoelasticity. *ASME J. Appl. Mech.* 51, 299–307. doi:10.1115/1.3167616
- Lorenzo, C. F., and Hartley, T. T. (2002). *Variable Order and Distributed Order Fractional Operators*. NASA/TM-2002-211376, New York, USA: Springer Link. doi:10.1023/A:1016586905654
- Lourenço, C. F., Santos, R. M., Barbosa, R. M., Cadenas, E., Radi, R., and Laranjinha, J. (2014). Neurovascular Coupling in hippocampus Is Mediated via Diffusion by Neuronal-Derived Nitric Oxide. *Free Radic. Biol. Med.* 73, 421–429. doi:10.1016/j.freeradbiomed.2014.05.021
- Luchko, Y., and Gorenflo, R. (1999). An Operational Method for Solving Fractional Differential Equations with the Caputo Derivatives. *Acta Mathematica Vietnamica* 24 (2), 207–233.
- Mainardi, F. (2010). *Fractional Calculus and Waves in Linear Viscoelasticity*. London, UK: Imperial College Press.
- Maurer, I., Zierz, S., and Moller, H.-J. (2000). A Selective Defect of Cytochrome C Oxidase Is Present in Brain of Alzheimer Disease Patients. *Neurobiol. Aging* 21, 455–462. doi:10.1016/s0197-4580(00)00112-3
- Medical Physiology, 3rd Edition: *Elastic Properties of Blood Vessels* (2021). <https://doctorlib.info/physiology/medical/104.html>. Chicago: Doctorlib.
- Mehala, N., and Rajendran, L. (2014). Analytical Solutions of Nonlinear Differential Equations in the Mathematical Model for Inactivation of Nitric Oxide by Rat Cerebellar Slices. *Ajag* 05, 908–919. doi:10.4236/ajag.2014.514099
- Metea, M. R., and Newman, E. A. (2006). Glial Cells Dilate and Constrict Blood Vessels: A Mechanism of Neurovascular Coupling. *J. Neurosci.* 26 (11), 2862–2870. doi:10.1523/jneurosci.4048-05.2006
- Moghaddam, B. P., and Machado, J. A. T. (2017). Extended Algorithms for Approximating Variable Order Fractional Derivatives with Applications. *J. Sci. Comput.* 71, 1351–1374. doi:10.1007/s10915-016-0343-1
- N. Atochin, D., and L. Huang, P. (2011). Role of Endothelial Nitric Oxide in Cerebrovascular Regulation. *Cpb* 12 (9), 1334–1342. doi:10.2174/13892011798280974
- Nutting, P. G. (1921). A Study of Elastic Viscous Deformation. *Proc. Amer. Soc. Test. Mater.* 21, 1162–1171. doi:10.2307/3407697
- Nutting, P. G. (1943). A General Stress-Strain-Time Formula. *J. Franklin Inst.* 235, 513–524. doi:10.1016/s0016-0032(43)91483-8
- Orosz, M., Molnárka, G., Toth, M., Nadasy, G. L., and Monos, E. (1999). Viscoelastic Behavior of Vascular wall Simulated by Generalized Maxwell Models – a Comparative Study. *Med. Sci. Monit.* 5 (3), 549–555.
- Palacios-Callender, M., Hollis, V., Mitchison, M., Frakich, N., Unitt, D., and Moncada, S. (2007). Cytochrome C Oxidase Regulates Endogenous Nitric Oxide Availability in Respiring Cells: a Possible Explanation for Hypoxic Vasodilation. *Proc. Natl. Acad. Sci.* 104 (47), 18508–18513. doi:10.1073/pnas.0709440104
- Parker, W. D., and Parks, J. K. (1995). Cytochrome C Oxidase in Alzheimer's Disease Brain. *Neurology* 45, 482–486. doi:10.1212/wnl.45.3.482
- Patnaik, S., Holkamp, J. P., and Semperlotti, F. (2020). Applications of Variable-Order Fractional Operators: a Review. *Proc. R. Soc. A* 476, 20190498. doi:10.1098/rspa.2019.0498
- Persson, M., Rydén Ahlgren, Å., Jansson, T., Eriksson, A., Persson, H. W., and Lindström, K. (2003). A New Non-invasive Ultrasonic Method for Simultaneous Measurements of Longitudinal and Radial Arterial wall Movements: First In Vivo Trial. *Clin. Physiol. Funct. Imaging* 23 (5), 247–251. doi:10.1046/j.1475-097x.2003.00504.x
- Petzold, G. C., and Murthy, V. N. (2011). Role of Astrocytes in Neurovascular Coupling. *Neuron* 71, 782–797. doi:10.1016/j.neuron.2011.08.009
- Potlov, A. Y., Proskurin, S. G., and Frolov, S. V. (2020). Young's Modulus Evaluation for the Blood Vessel walls Using Intravascular Optical Coherence Tomography, 2020 International Conference on e-Health and Bioengineering (EHB), Iasi, Romania, Oct. 2020 1–4. doi:10.1109/EHB50910.2020.9280242
- Rachev, A., and Hayashi, K. (1999). Theoretical Study of the Effects of Vascular Smooth Muscle Contraction on Strain and Stress Distributions in Arteries. *Ann. Biomed. Eng.* 27, 459–468. doi:10.1114/1.191
- Ramirez, L. E. S., and Coimbra, C. F. M. (2010). On the Selection and Meaning of Variable Order Operators for Dynamic Modeling. *Int. J. Differential Equations* 2010, 1–16. doi:10.1155/2010/846107
- Reina-De La Torre, F., Rodriguez-Baeza, A., and Sahuquillo-Barris, J. (1998). Morphological Characteristics and Distribution Pattern of the Arterial Vessels in Human Cerebral Cortex: a Scanning Electron Microscope Study. *Anat. Rec.* 251, 87–96. doi:10.1002/(sici)1097-0185(199805)251:1<87::aid-ar14>3.0.co;2-7
- Samko, S. G., and Ross, B. (1993). Integration and Differentiation to a Variable Fractional Order. *Integral Transforms Spec. Functions* 1 (4), 277–300. doi:10.1080/10652469308819027
- Santos, R. M., Lourenço, C. F., Ledo, A., Barbosa, R. M., and Laranjinha, J. (2012). Nitric Oxide Inactivation Mechanisms in the Brain: Role in Bioenergetics and Neurodegeneration. *Int. J. Cell Biol.* 2012, 1, 13. doi:10.1155/2012/391914
- Santos, R. M., Lourenço, C. F., Pomerleau, F., Huettl, P., Gerhardt, G. A., Laranjinha, J., et al. (2011). Brain Nitric Oxide Inactivation Is Governed by the Vasculature. *Antioxid. Redox Signaling* 14 (6), 1011–1021. doi:10.1089/ars.2010.3297
- Schuler, D., Sansone, R., Freudenberger, T., Rodriguez-Mateos, A., Weber, G., Momma, T. Y., et al. (2014). Measurement of Endothelium-dependent Vasodilation in Mice-Brief Report. *Atvb* 34, no. 12, 2651–2657. doi:10.1161/ATVBAHA.114.304699
- Scott Blair, G. M., and Coppen, F. M. V. (1939). The Subjective Judgement of the Elastic and Plastic Properties of Soft Bodies; the "differential Thresholds" for Viscosities and Compression Moduli. *Proc. R. Soc. Lond. B* 128, 109–125. doi:10.1098/rspb.1939.0046
- Sharma, R., Seo, J.-W., and Kwon, S. (2014). In Vivo Imaging of Nitric Oxide by Magnetic Resonance Imaging Techniques. *J. Nanomater.* 2014, 1–13. doi:10.1155/2014/523646
- Sriram, K., Laughlin, J. G., Rangamani, P., and Tartakovsky, D. M. (2016). Shear-induced Nitric Oxide Production by Endothelial Cells. *Biophysical J.* 111, 208–221. doi:10.1016/j.bpj.2016.05.034
- Stålhand, J., Klarbring, A., and Holzapfel, G. A. (2008). Smooth Muscle Contraction: Mechanochemical Formulation for Homogeneous Finite Strains. *Prog. Biophys. Mol. Biol.* 96, 465–481. doi:10.1016/j.pbiomolbio.2007.07.025
- Suki, B., Barabasi, A. L., and Lutchen, K. R. (1994). Lung Tissue Viscoelasticity: a Mathematical Framework and its Molecular Basis. *J. Appl. Physiol.* 76 (6), 2749–2759. doi:10.1152/jappl.1994.76.6.2749
- Terpolilli, N. A., Feiler, S., Dienel, A., Müller, F., Heumos, N., Friedrich, B., et al. (2016). Nitric Oxide Inhalation Reduces Brain Damage, Prevents Mortality, and Improves Neurological Outcome after Subarachnoid Hemorrhage by Resolving Early Pial Microvasospasms. *J. Cereb. Blood Flow Metab.* 36 (12), 2096–2107. doi:10.1177/0271678X15605848

- Torvik, P. J., and Bagley, R. L. (1984). On the Appearance of the Fractional Derivative in the Behavior of Real Materials. *ASME J. Appl. Mech.* 51, 294–298. doi:10.1115/1.3167615
- Tóth, M., Nádasy, G. L., Nyáry, I., Kerényi, T., Orosz, M., Molnárka, G., et al. (1998). Sterically Inhomogenous Viscoelastic Behavior of Human Saccular Cerebral Aneurysms. *J. Vasc. Res.* 35 (5), 345–355. doi:10.1159/000025604
- Unitt, D. C., Hollis, V. S., Palacios-Callender, M., Frakich, N., and Moncada, S. (2010). Inactivation of Nitric Oxide by Cytochrome C Oxidase under Steady-State Oxygen Conditions. *Biochim. Biophys. Acta (Bba) - Bioenerg.* 1797, 371–377. doi:10.1016/j.bbabo.2009.12.002
- Wei, G., Dawson, V. L., and Zweier, J. L. (1999). Role of Neuronal and Endothelial Nitric Oxide Synthase in Nitric Oxide Generation in the Brain Following Cerebral Ischemia. *Biochim. Biophys. Acta (Bba) - Mol. Basis Dis.* 1455, 23–34. doi:10.1016/s0925-4439(99)00051-4
- West, B. J., Bologna, M., and Grigolini, P. (2003). *Physics of Fractal Operators*. USA: Springer-Verlag New York.
- Wilkinson, I. B., Franklin, S. S., and Cockcroft, J. R. (2004). Nitric Oxide and the Regulation of Large Artery Stiffness. *Hypertension* 44, 112–116. doi:10.1161/01.HYP.0000138068.03893.40
- Yang, J., Clark, J. W., Jr., Bryan, R. M., and Robertson, C. (2003). The Myogenic Response in Isolated Rat Cerebrovascular Arteries: Smooth Muscle Cell Model. *Med. Eng. Phys.* 25, 691–709. doi:10.1016/S1350-4533(03)00100-0
- Yuan, S., Jordan, L. C., Davis, L. T., Cogswell, P. M., Lee, C. A., Patel, N. J., et al. (2021). A Cross-sectional, Case-control Study of Intracranial Arterial wall Thickness and Complete Blood Count Measures in Sickle Cell Disease. *Br. J. Haematol.* 192 (4), 769–777. doi:10.1111/bjh.17262

Conflict of Interest: The authors declare that the research was conducted in the absence of any commercial or financial relationships that could be construed as a potential conflict of interest.

Publisher's Note: All claims expressed in this article are solely those of the authors and do not necessarily represent those of their affiliated organizations, or those of the publisher, the editors and the reviewers. Any product that may be evaluated in this article, or claim that may be made by its manufacturer, is not guaranteed or endorsed by the publisher.

Copyright © 2021 Drapaca. This is an open-access article distributed under the terms of the Creative Commons Attribution License (CC BY). The use, distribution or reproduction in other forums is permitted, provided the original author(s) and the copyright owner(s) are credited and that the original publication in this journal is cited, in accordance with accepted academic practice. No use, distribution or reproduction is permitted which does not comply with these terms.



Subject-Specific Head Model Generation by Mesh Morphing: A Personalization Framework and Its Applications

Xiaogai Li*

Division of Neuronic Engineering, Department of Biomedical Engineering and Health Systems, KTH Royal Institute of Technology, Stockholm, Sweden

OPEN ACCESS

Edited by:

Silvia Budday,
University of Erlangen Nuremberg,
Germany

Reviewed by:

Haojie Mao,
Western University, Canada
J. Sebastian Giudice,
University of Virginia, United States

*Correspondence:

Xiaogai Li
xiaogai@kth.se

Specialty section:

This article was submitted to
Biomechanics,
a section of the journal
Frontiers in Bioengineering and
Biotechnology

Received: 07 May 2021

Accepted: 03 September 2021

Published: 18 October 2021

Citation:

Li X (2021) Subject-Specific Head
Model Generation by Mesh Morphing:
A Personalization Framework and
Its Applications.
Front. Bioeng. Biotechnol. 9:706566.
doi: 10.3389/fbioe.2021.706566

Finite element (FE) head models have become powerful tools in many fields within neuroscience, especially for studying the biomechanics of traumatic brain injury (TBI). Subject-specific head models accounting for geometric variations among subjects are needed for more reliable predictions. However, the generation of such models suitable for studying TBIs remains a significant challenge and has been a bottleneck hindering personalized simulations. This study presents a personalization framework for generating subject-specific models across the lifespan and for pathological brains with significant anatomical changes by morphing a baseline model. The framework consists of hierarchical multiple feature and multimodality imaging registrations, mesh morphing, and mesh grouping, which is shown to be efficient with a heterogeneous dataset including a newborn, 1-year-old (1Y), 2Y, adult, 92Y, and a hydrocephalus brain. The generated models of the six subjects show competitive personalization accuracy, demonstrating the capacity of the framework for generating subject-specific models with significant anatomical differences. The family of the generated head models allows studying age-dependent and groupwise brain injury mechanisms. The framework for efficient generation of subject-specific FE head models helps to facilitate personalized simulations in many fields of neuroscience.

Keywords: finite element modeling, personalized simulation, traumatic brain injury, brain stimulation, neuroimage registration, biomechanics

INTRODUCTION

Finite element (FE) head models have become powerful tools to simulate brain stimulations with direct current (tDCS) (Datta et al., 2009; Datta et al., 2012; Huang et al., 2013; Windhoff et al., 2013; Opitz et al., 2015; Alekseichuk et al., 2019; Li et al., 2020; Wang et al., 2020), magnetic (TMS) (Opitz et al., 2013), and ultrasound (TUS) (Legon et al., 2014). Such models are also being used to study the development of neurodegenerative diseases (Fornari et al., 2019; Noël and Kuhl, 2019; Weickenmeier et al., 2019) and biomechanical consequences of neurosurgery (Weickenmeier et al., 2017; von Holst and Li, 2014; Li et al., 2015; Ji et al., 2009; Hu et al., 2007; Miller et al., 2010). In particular, FE head models have been tremendously used to study traumatic brain injuries (TBIs) in the last decades (see reviews (Giudice et al., 2019; Horstemeyer et al., 2019; Madhukar and Ostojic-Starzewski, 2019)). Meshing is a first step in generating FE models by discretizing a continuous domain into a finite

number of elements, e.g., tetrahedral or hexahedral elements. Generation of FE head models is often time-consuming and challenging due to its complex geometry, though tetrahedral elements are relatively easier to generate, e.g., automatic pipelines have been reported to efficiently generate tetrahedral head models for simulating brain stimulations (Huang et al., 2013; Windhoff et al., 2013). Such efficiency is partially attributed to the well-developed automatic tetrahedral meshing algorithms within mathematics and computer science (Baker, 2005); it is also because the involved partial differential equations (PDEs) are less computationally demanding, permitting a huge number of tetrahedral elements (up to >10 million (Datta et al., 2009)) to capture anatomical details of the brain. Thus, personalized simulations with anatomically detailed subject-specific head models are largely facilitated in these brain stimulation fields.

In contrast to tetrahedrons, hexahedral elements are much more challenging to generate (Baker, 2005; Shepherd and Johnson, 2008) but are preferred in FE head models intended for studying TBIs (hereafter called head injury models) due to their higher efficiency for simulating the incompressible brain under impact (Li et al., 2021). Furthermore, the involved PDEs in head impacts consist of geometrical, material nonlinearity, and complex contacting algorithms, which are more computationally demanding. As a result, many state-of-the-art head injury models (Zhang et al., 2001; Horgan and Gilchrist, 2003; Kleiven, 2007; Takhoumts et al., 2008; Mao et al., 2013a; Sahoo et al., 2014; Ji et al., 2015a; Atsumi et al., 2016) use hexahedrons despite the meshing challenges and have simplified brains to reduce the number of elements for computational efficiency. For example, these models have smoothed out brain surfaces and do not have sulci, and gyri, resulting in fewer elements (often <1 million). While a simplified representation of the brain is a reasonable trade-off for computational efficiency, it's also partially due to the challenges for meshing techniques (e.g., the blocking technique (Mao et al., 2013b)) to capture the anatomical details. It is worth mentioning that the voxel approach is efficient in generating hexahedrons by converting image voxels to hexahedral elements, either directly or with smoothing algorithms. However, a known concern is a less accurate peak strain/stress predicted from such models, especially on the surfaces due to jaggedness. Nevertheless, careful choice of sufficiently refined mesh and result analysis allow such models to provide valuable insights due to their anatomical accuracy (see discussion in (Li et al., 2021)). Besides the much less developed automatic algorithms for generating hexahedrons (Baker, 2005; Shepherd and Johnson, 2008), a necessity to include falx and tentorium to account for their important structural influence on brain mechanical responses during impact (Ho et al., 2017) poses an additional challenge for subject-specific head injury model generation while both structures are often neglected in head models for simulating tDCS, TMS, and TUS. A detailed analysis of the current meshing challenge for head injury models is found in a previous study (Li et al., 2021).

Therefore, the generation of FE head injury models with anatomical details remains a challenge and has become a bottleneck hindering personalized simulations. FE head models without anatomical details such as sulci and gyri also hinder

studying detailed mechanisms at areas of interest, such as chronic traumatic encephalopathy (CTE) with pathologies observed at sulcal depth (McKee et al., 2015). Studies have also shown that the brain size/shape influences brain mechanical responses significantly under impact (Kleiven and von Holst, 2002; Li et al., 2021), suggesting the importance of using personalized models to study the onset of TBI in real life. Along with the many existing adult healthy FE head models, there are only a few elderly, children, and infant models (e.g., (Li et al., 2011; Giordano et al., 2017; Li et al., 2017; Li and Kleiven, 2018; Hajiaghamemar et al., 2019; Li et al., 2019; Zhou et al., 2019; Zhou et al., 2020)). TBIs are influencing all age groups, especially infants and the elderly are overrepresented (Pedersen et al., 2015). Thus, it is imperative to investigate efficient approaches for generating detailed subject-specific head injury models across the lifespan and for pathological brains to understand the injury mechanisms and develop preventions.

This study addresses the challenge of generating subject-specific head injury models with hexahedrons, especially concerns about mesh morphing, which is an efficient approach for generating subject-specific models. The approach has been used in many biomechanics fields on different organs (Couteau et al., 2000; Castellano-Smith et al., 2001; Fernandez et al., 2004; Sigal et al., 2008; Bucki et al., 2010; Bijar et al., 2016; Park et al., 2017), full-body models (Davis et al., 2016; Beillas and Berthet, 2017; Liu et al., 2020), as well as for detailed (Giudice et al., 2020; Giudice et al., 2021; Li et al., 2021; Montanino et al., 2021) and simplified brain models (Hu et al., 2007; Ji et al., 2011; Ji et al., 2015b; Wu et al., 2019). A typical procedure involves image registration (rigid or affine and followed by nonlinear registrations), from which a displacement field representing the geometrical difference between the subject and baseline model is obtained. The displacement field is then applied to morph the baseline model, resulting in a personalized model with updated nodal coordinates while preserving element connections. The displacement field derived from image registrations should generally comply with continuum mechanics conditions on motion, requiring diffeomorphic, non-folding, and one-to-one correspondence to avoid excessive element distortions (Bucki et al., 2010).

In particular, deformable image registration-based mesh morphing has been applied to personalize detailed brain models of healthy subjects (Giudice et al., 2020; Giudice et al., 2021; Li et al., 2021; Montanino et al., 2021). However, despite intensive efforts, inter-subject registration between brains with significant anatomical differences is still challenging within neuroimaging field with limited registration accuracy (Kim et al., 2015). Moreover, when applying image registration for mesh morphing, there is a higher requirement on the smoothness of the obtained displacement field to ensure acceptable element quality in the morphed mesh. Therefore, one major challenge for using mesh morphing to generate subject-specific FE head models is how to design an image registration pipeline that leads to high registration accuracy, meanwhile, not causes excessive element distortions. In a previous study (Li et al., 2021), we proposed a hierarchical image registration pipeline that allows efficient generation of subject-specific head models for

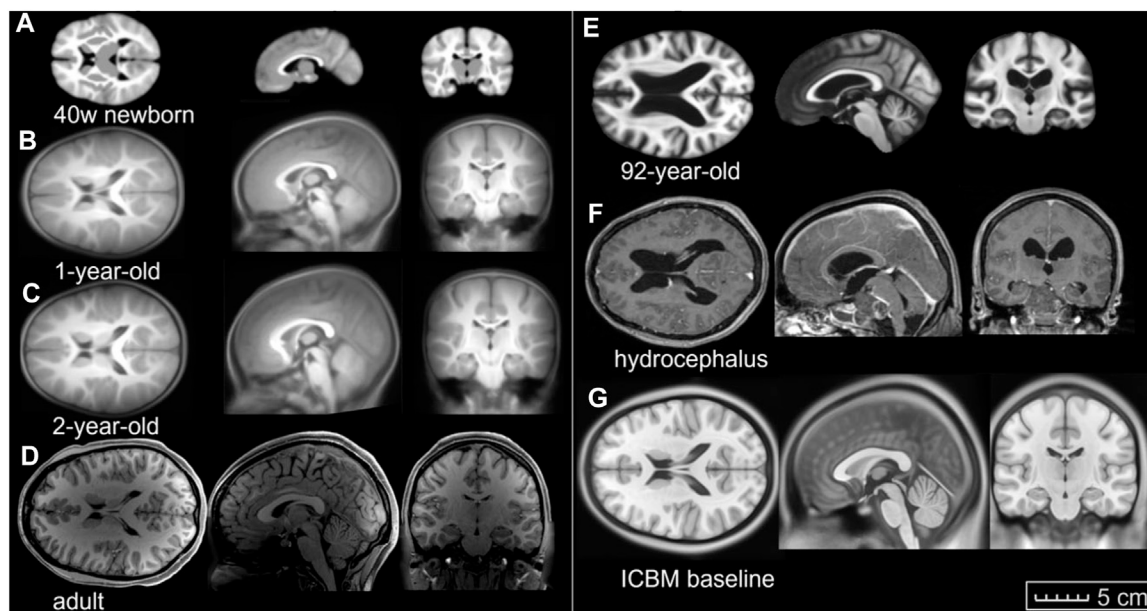


FIGURE 1 | Image data used in this study. Axial, coronal, and sagittal views of (A) 40-week-old newborn, (B) 1-year-old, (C) 2-year-old, (D) an adult, (E) an elderly of 92-year-old, (F) hydrocephalus brain, and (G) the ICBM baseline (the same length scale applies).

healthy adult subjects. But a pipeline that allows morphing a baseline model to subjects with significant anatomical differences is yet to be developed.

Thus, this study aims at developing a personalization framework capable of generating subject-specific head models across the lifespan and for pathological brains with significant anatomical changes. The framework consists of hierarchical multiple feature and multimodality image registration pipelines, mesh morphing, and mesh grouping. Six subject-specific head models are generated to demonstrate its capacity, including a newborn, 1Y, 2Y, adult, 92Y, and a hydrocephalus brain. The results show that the framework is robust to generate subject-specific models across the lifespan and for pathological brains with significant anatomical changes by morphing a baseline model. This framework helps to facilitate personalized simulations in many fields within neurosciences, especially for studying TBIs in which personalized simulations are hindered due to the meshing challenge.

MATERIALS AND METHODS

Subjects

Images of the six subjects (Figures 1A–F) are acquired from previously published open-access datasets, except the hydrocephalus brain is from the author's previous study. The baseline ICBM image (Figure 1G) corresponds to the baseline head model. For detailed preprocessing steps for these images, the readers are referred to the original studies. A brief description is found below and summarized in Table 1.

- Images of a newborn (denoted as 0Y afterward), 1Y, and 2Y are obtained from the UNC Infant 0-1-2 atlases

(Shi et al., 2011) constructed based on 95 subjects with complete 0-1-2Y longitudinal scans of T1W and T2W images acquired with a 3T MRI scanner. Each atlas consists of T1W images, tissue probability maps, and anatomical parcellation maps.

- Image of a single subject from the WU-Minn HCP database in the 26–30 age group, including T1W and T2W images, was acquired with a 3T MRI scanner (Van Essen et al., 2013).
- Image of an elderly (92Y) from the Brain Imaging of Normal Subjects (BRAINS) atlas was created from 48 healthy elderly subjects within age group 9193Y as detailed by Dickie et al. (2016). The atlas contains T1W and tissue probability maps.
- Image of a hydrocephalus subject with a mass lesion at the brain stem front is reused from a previous study (Li and von Holst, 2013).
- The 1-mm isotropic ICBM 2009c Nonlinear Symmetric template (Fonov et al., 2009; Fonov et al., 2011) was constructed based on T1W images from 152 subjects between 18.5–43.5Y acquired on a 1.5 T MRI scanner.

Baseline FE Head Model

A previously developed FE head injury model (the ADAPT model) (Li et al., 2021) serves as a baseline in this study, which is morphed to obtain subject-specific head models. The ADAPT model has been generated based on and has the same geometry as the ICBM template. The model includes the brain, skull, meninges, CSF, and superior sagittal sinus (SSS) (Figure 2). The brain is divided into primary structures of cerebral gray matter (GM) (i.e., cerebral cortex), cerebral white matter (WM), corpus callosum (CC), brain stem (BS), cerebellum GM and WM, thalamus, and hippocampus. The cerebrum is further divided into frontal, frontal, parietal, temporal, and occipital lobes; CSF is

TABLE 1 | Subjects involved in this study.

Subject	ICV (ml)	Imaging modality used for registration	Image sources
0-year-old ^a	463	T1W (atlas)	Shi et al. (2011)
1-year-old	1,015		
2-year-old	1,274		
adult	1,480	T1W, T2W (single subject in age group "26–30")	Van Essen et al. (2013)
92-year-old ^b	1,323	T1W (atlas)	Dickie et al. (2016)
Hydrocephalus	1,255	T1W (single subject)	Li and von Holst, (2013)
ICBM baseline	1,885	T1W, T2W (atlas)	(Fonov et al., 2009; Fonov et al., 2011)

^aThe cerebellum in the T1W atlas was stripped in the original database. The available T2W atlas has a cerebellum but is not chosen in this study as per the requirement of the pipeline.

^bAtlas of age group 91–93Y denoted as 92Ys throughout this study for simplicity.

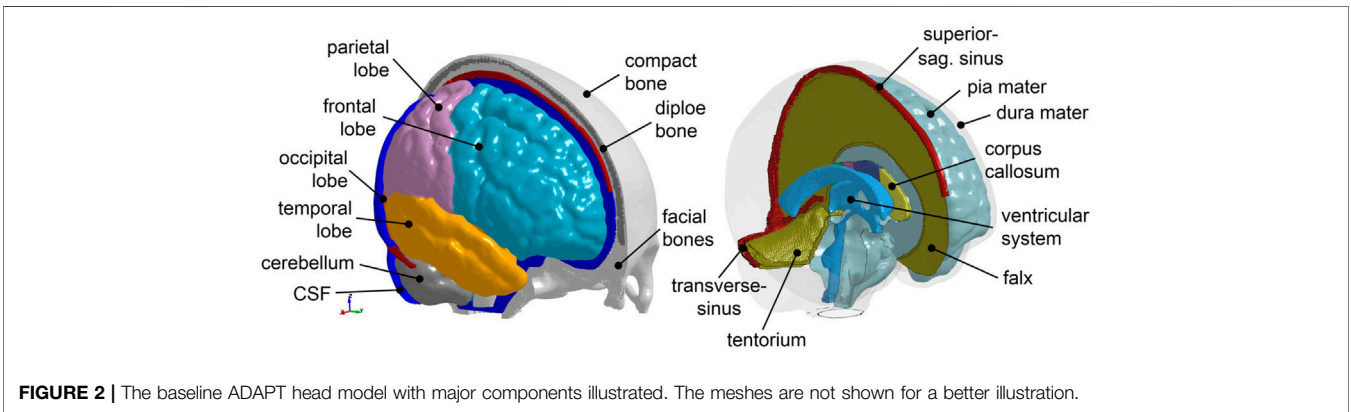


FIGURE 2 | The baseline ADAPT head model with major components illustrated. The meshes are not shown for a better illustration.

divided into outer CSF and ventricular system including lateral ventricles and 3rd and 4th ventricles connected by the cerebral aqueduct. Continuous mesh is used between brain components throughout the model. The total number of elements in the head model is 4.4 million hexahedral and 0.54 million quad elements. The minimum Jacobian in the brain is 0.45. The brain is modeled as hyper-viscoelastic material to account for large deformations and strain rate dependence of the tissue. Pia, dura/falx/tentorium are modeled with nonlinear hyperelastic material using simplified rubber/foam based on the average stress-strain experimental data (van Noort et al., 1981; Aimedieu and Grebe, 2004). The model has been validated against experimental data of close to or injury level brain-skull relative motion, brain strain, and intracranial pressure. Details of the model development, validation, and capacity to study brain responses under impact are presented earlier (Li et al., 2021).

Personalization Framework for Subject-specific Head Model Generation

The personalization framework consists of image registration pipelines, mesh morphing, and mesh grouping (Figure 3). Image registration is an essential part of the framework. A complete registration pipeline involves hierarchical registrations with multiple features and multimodality images shown at the lower row of Figure 3. The sum of dense displacement fields

obtained from each registration step is used to morph the baseline head model to obtain subject-specific models. Afterward, the WM of the morphed brain is regrouped according to the segmented WM image mask of the subject, resulting in the final subject-specific model. Details of each component of the framework are presented in the following subsections.

Registration Pipeline With Multiple Features and Multimodality Imaging

A complete registration pipeline contains five steps (Figure 3 lower row). First, Demons registration is performed between the segmented cranial masks of the baseline ICBM (corresponding to the baseline ADAPT head model) and the subject after being rigidly aligned, resulting in a transformation, i.e., dense displacement field g_{demo} . Second, Demons registration of features is performed, obtaining $g_{f1}, g_{f2} \dots$. Third, Dramms registration is performed on T1W images inherited from Demons steps, obtaining g_{dram} . Next, Dramms registration is performed with multimodality images, obtaining $g_{m1}, g_{m2} \dots$. Finally, brain lesions are handled by more Demons feature registration steps, obtaining $g_{fn} \dots$. In all registration steps, the subject's image serves as *moving* image, and the baseline ICBM image serves as *fixed* image. Note that *features* in this study refer to the segmented binary images of anatomical regions such as lateral ventricles, corpus callosum, or lesion. The input images to Demons registration steps are segmented binary masks. Thus,

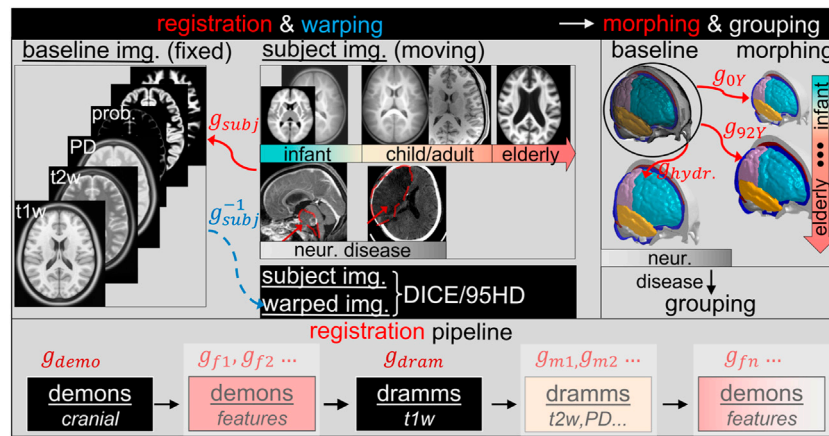


FIGURE 3 | Overview of the personalization framework.

these steps capture local anatomical changes between the *moving* and *fixed* images only in size and shape, while subsequent Dramms registrations capture the internal anatomical differences within the volumes of the binary image masks. The practical usage of the registration pipeline is demonstrated in *Application of the Framework for Subject-specific Model Generation* with six subjects.

In particular, for all Demons steps described above, the diffeomorphic Demons registration algorithm (Vercauteren et al., 2009) implemented in the open-source software *Slicer 3D* is used. Dramms registration algorithm (Ou et al., 2011) implemented as open-source code by the authors (Dramms version 1.5.1, 2018) is used on MRI images of different modalities. Note that for all the six subjects, a smoothness weight, i.e., the *-g* option (see DRAMMS Software Manual), is always set to 1.0 in Dramms registration to ensure a smooth displacement field.

Morphing

The sum of dense displacement fields from all registration steps (Eq. 1) represents the anatomical differences between the subject and the baseline ICBM images.

$$g_{subj} = g_{demo} + g_{f1} + g_{f2} \dots + g_{dram} \dots + g_{m1} + g_{m2} \dots + g_{fn}. \quad (1)$$

As the baseline, ADAPT model is in the same space as the ICBM image; thus, applying g_{subj} to the baseline head model (Figure 2) leads to a subject-specific head model of the subject. For this, the following step is performed to morph the nodes of the baseline head model to new positions:

$$\mathbf{x}^i = \mathbf{X}^i + \mathbf{u}^i, \quad (2)$$

where \mathbf{X}^i is the nodal coordinate of node i , \mathbf{u}^i is the linearly interpolated displacement vector at node n from g_{subj} , \mathbf{x}^i is the updated nodal coordinate, together with the same element definitions as the baseline, forming a subject-specific head model.

Grouping of WM

To capture the subject's WM, the morphed brain elements are regrouped based on the segmented binary image of the subject's cerebral WM. This is achieved by assigning brain FE elements as WM based on Cartesian coordinates of the segmented WM voxels with the following procedures:

- For each element, all WM voxels inside or intersect to a single element of the brain are identified based on spatial coordinates.
- The eight vertices and one centroid of each voxel (i, j, k) are judged; vertices gain a weight of one if falling inside the element; the centroid gains a weight of two if falling inside the element. Weights of the eight vertices and the centroid of the voxel add up, resulting in a total weighting factor for each voxel $w_{i,j,k}$

$$w_{i,j,k} = \sum_{m=1}^9 w_{i,j,k}^m \quad (3)$$

- Finally, weights of each voxel belong to the same label (e.g., the segmented binary image with label A) added up, obtaining a final weight factor for each label. The element is grouped to the label with the largest weight.

$$w_A = \sum_{(i,j,k) \in A} w_{i,j,k}. \quad (4)$$

Figure 4 shows the regrouped WM elements of the morphed brain enclosed by the reconstructed surface of the segmented WM.

Evaluation of Personalization Accuracy

To evaluate registration accuracy, the baseline ICBM image ($img_{baseline}$), which corresponds to the baseline head model, is warped via the inverse of displacement fields from each

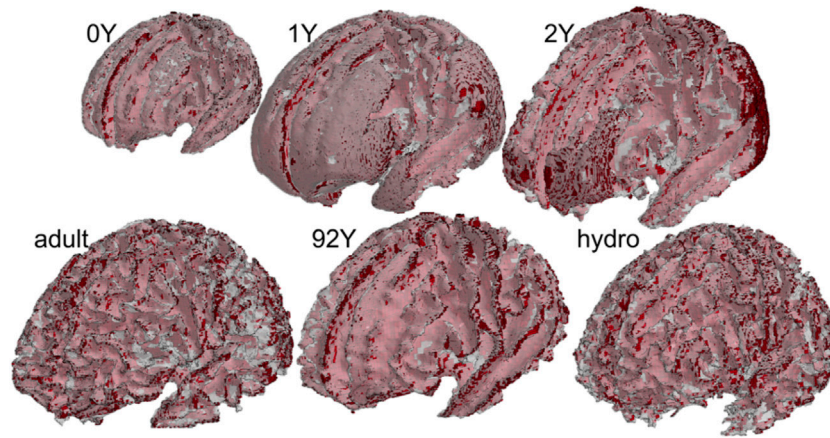


FIGURE 4 | Regrouped WM based on subjects' WM image mask for all the six subjects. The red color shows the WM elements, and the white transparent shows the surfaces reconstructed from the subject's segmented WM image mask.

registration step (g_{subj}^{-1}) (Eq. 5), resulting in a warped image (img_{warped}) (Eq. 6).

$$g_{subj}^{-1} = g_{fn}^{-1}(g_{m2}^{-1}(g_{m1}^{-1}(g_{dram}^{-1}(g_{f2}^{-1}(g_{f1}^{-1}(g_{demo}^{-1})))))), \quad (5)$$

$$img_{warped} = g_{fn}^{-1}(g_{m2}^{-1}(g_{m1}^{-1}(g_{dram}^{-1}(g_{f2}^{-1}(g_{f1}^{-1}(img_{baseline}^{-1})))))). \quad (6)$$

DICE and 95th percentile Hausdorff distance (HD95) between the img_{warped} and subjects' images are then calculated to evaluate registration performance. As img_{warped} corresponds to the personalized subject-specific model, both metrics also reflect the personalization accuracy of the generated subject-specific models.

To calculate DICE and HD95, automated segmentation is performed using the software FreeSurfer (version 7.1.0) with the default brain segmentation pipeline (*recon-all*) for both the warped ICBM and subjects' T1W images. The segmented binary masks for the whole brain and local regions of cerebral GM, WM, CC, BS, hippocampus, thalamus, and cerebellum are used for DICE and HD95 calculation. For the cranial mask, the metrics are calculated based on manually segmented cranial by thresholding followed by noise removal. Similarly, one sagittal slice of CC is manually segmented and used to calculate both matrices. The use of manual segmentation for both regions is due to the insufficient quality (not reflecting the actual anatomy) by *recon-all* for the current dataset. Note that these segmented binary masks are only used for DICE and HD95 calculation, and the quality of the automatic segmentation has no influence on the subject-specific mesh development process.

DICE

DICE is a single metric to measure the spatial overlap between images defined as twice the number of elements common to both sets divided by the sum of the number of elements in each set (Ou et al., 2014):

$$DICE(A, B) = \frac{2|A \cap B|}{|A| + |B|}, \quad (7)$$

where A and B denote the binary segmentation labels, $|A|$ and $|B|$ are the number of voxels in each set, and $|A \cap B|$ is the number of shared voxels by A and B . The DICE value of 0 implies no overlap between both, whereas a DICE coefficient of one indicates perfect overlap between the warped and the target image.

HD95

Hausdorff distance is defined as

$$HD(C, D) = \max(h(C, D), h(D, C)), \quad (8)$$

where C, D are the two sets of vertices from two segmented images

$$h(C, D) = \max_{c \in C} \max_{d \in D} \|c - d\|. \quad (9)$$

The 95th percentile Hausdorff distance (HD95) is used following earlier studies (Ou et al., 2011; Ou et al., 2014). HD95 ranges from 0 to above; a lower value indicates a better registration accuracy between the warped and the target image.

Application of the Framework for Subject-specific Model Generation

A complete registration pipeline is only needed for the most challenging case; fewer registration steps are sufficient for brains with small anatomical differences compared with the baseline. The following three typical subtypes of the pipeline are used to generate subject-specific models for the six subjects.

Type I This is the basic pipeline containing two steps: Demons registration of the cranial mask and Dramms registration of T1W image. This two-step pipeline has been shown to achieve good registration

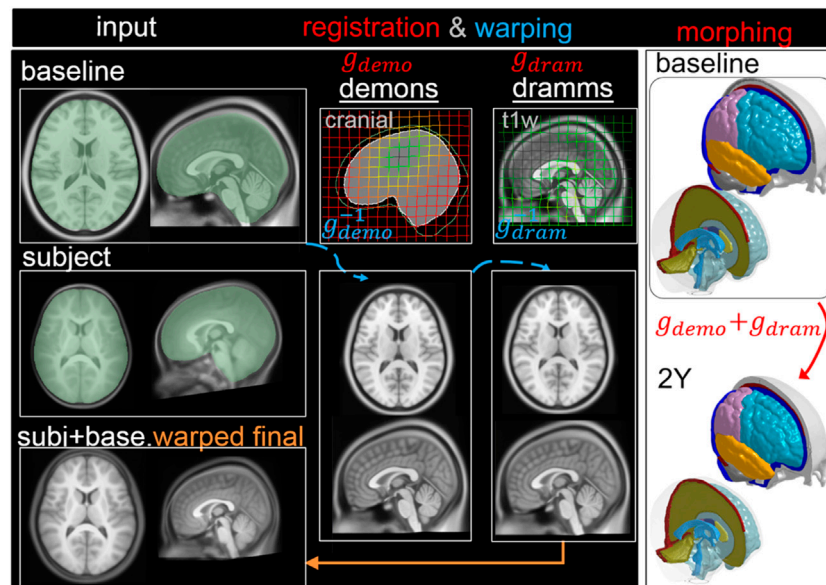


FIGURE 5 | Type I pipeline applied for personalizing the baseline ADAPT model to a subject-specific model of a 2Y. The pipeline consists of two steps: (i) Demons registration with cranial masks; (ii) Dramms registration with T1W image. The displacement field obtained from each step is visualized on the grid together with the warped baseline ICBM images to show its effect. The final warped ICBM is overlaid with the subject's image to visualize registration accuracy.

accuracy for six healthy adult subjects (Li et al., 2021). The capacity of this pipeline is further demonstrated with a 2Y brain.

Type II Multiple feature steps are added to the Type I pipeline, allowing align brains with significant anatomical changes. The capacity of this pipeline is demonstrated with a hydrocephalus brain using three feature steps.

Type III Multi-modality imaging registration steps are added to the Type I pipeline to improve brain alignment as demonstrated with an adult brain.

2YO Model Generation via Pipeline Type I: Two Steps

First, T1W images of ICBM and the 2Y brain are segmented to obtain the cranial masks, which are used as input for Demons registration, from which a dense displacement field g_{demo} is obtained (Figure 5). Next, the baseline ICBM T1W image is warped by g_{demo}^{-1} . The warped ICBM and subject's T1W images are then skull stripped and serve as input for Dramms registration, obtaining g_{dramm} . The two displacement fields add up $g_{subj_2YO} = g_{demo} + g_{dramm}$ which is used to morph the baseline mesh, obtaining the subject-specific head model. Finally, the baseline ICBM image warped to the subject is obtained via $img_{warped_2Y} = (g_{dramm}^{-1}(g_{demo}^{-1}(img_{baseline})))$, which is compared with the T1W image of the 2Y brain to evaluate personalization accuracy.

Hydrocephalus Model via Pipeline Type II: Multiple Features

The workflow is similar to the above, but three additional feature steps are added to capture the enlarged LV, deformed CC, and

brain lesion, resulting in five dense displacement fields that add up as $g_{subj_hydro} = g_{demo} + g_{f1} + g_{f2} + g_{dramm} + g_{f3}$, which is used to morph the baseline mesh and obtain a subject-specific head model (Figure 6). The baseline ICBM image warped to the subject is obtained via $img_{warped_hydro} = (g_{dramm}^{-1}(g_{f2}^{-1}(g_{f1}^{-1}(g_{demo}^{-1}(img_{baseline}))))$, which is compared with the T1W image of the hydrocephalus subject to evaluate personalization accuracy.

Adult Brain Model via Pipeline Type III: Multimodality

The workflow is similar to Type I, but an additional multimodality T2W registration step is performed to further align the LVs resulting in three dense displacement fields added up as $g_{subj_adult} = g_{demo} + g_{dramm} + g_{m1}$, which is used to morph the baseline mesh and obtain the subject-specific head model (Figure 7). The baseline ICBM image warped to the subject is obtained via $img_{warped_adult} = g_{m1}^{-1}(g_{dramm}^{-1}(g_{demo}^{-1}(img_{baseline})))$, which is compared with the T1W image of the hydrocephalus subject to evaluate personalization accuracy.

Pipeline for the 0Y, 1Y, and the 92Y

The 92Y uses Type II pipeline, similar to the hydrocephalus subject, except only one feature step for LV is used, i.e., $g_{subj_92Y} = g_{demo} + g_{f1} + g_{dramm}$. Interestingly, the Dramms registration captures the thinning of CC without the CC feature step as for the hydrocephalus subject. It could be due to the higher quality image of the 92Y than the hydrocephalus brain.

The 1Y could use the same pipeline as the 2Y. However, in this study, an alternative approach is used, using the 2Y as an intermediate step, i.e., align 1Y T1W (as *moving* image) to that of the 2Y (as *fixed* image) by Dramms registration, obtaining

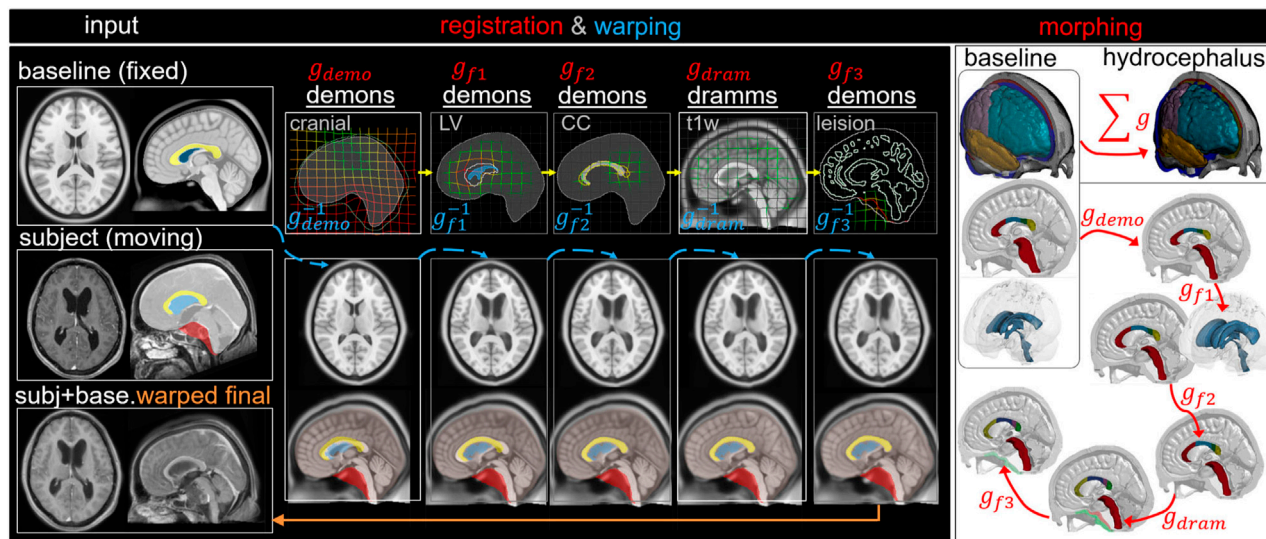


FIGURE 6 | Type II pipeline applied for personalizing the baseline ADAPT model to a subject-specific model of a hydrocephalus brain. The pipeline consists of five steps: (i) Demons registration with cranial masks; (ii) Demons registration with segmented lateral ventricle (LV) mask for capturing the enlarged LV; (iii) Demons registration with segmented CC mask for capturing the CC shape; (iv) Dramms registration with T1W image for capturing local brain anatomy; (v) Demons registration to drag back the skull mesh which is pushed due to the lesion in the cranial mask in step (i). The displacement field obtained from each step is visualized on the grid together with the warped baseline ICBM images and morphed meshes to show its effect. The final warped ICBM is overlaid with the subject's image to visualize registration accuracy.

a displacement field $g_{1Y_to_2Y}$. The final displacement field used for personalizing the baseline model to the 1Y writes: $g_{subj_1Y} = g_{subj_2YO} + g_{1Y_to_2Y}$, and the warped image is obtained via $img_{warped_1Y} = (g_{1Y_to_2Y}^{-1} (g_{subj_2Y}^{-1} (img_{baseline})))$.

The 0Y uses the same pipeline as the 1Y by having 2Y as an intermediate step, i.e., align the 0Y T1W (as *moving* image) to that of the 2Y (as *fixed* image) by Dramms registration. Since the cerebellum for the 0Y was stripped in the original database (**Figure 1A**), a paired T1W image of the 2Y with

cerebellum stripped (readily available in the database) is used for registration, from which a displacement field $g_{0Y_to_2Y}$ is obtained. The remaining steps for personalization and image warping are the same as for the 1Y described above. Note that although the registered images do not have cerebellum, the obtained displacement field $g_{0Y_to_2Y}$ defined in the entire image space does cover the cerebellum region despite values close to zero. The displacement field when used to morph the baseline model that has cerebellum, resulting in

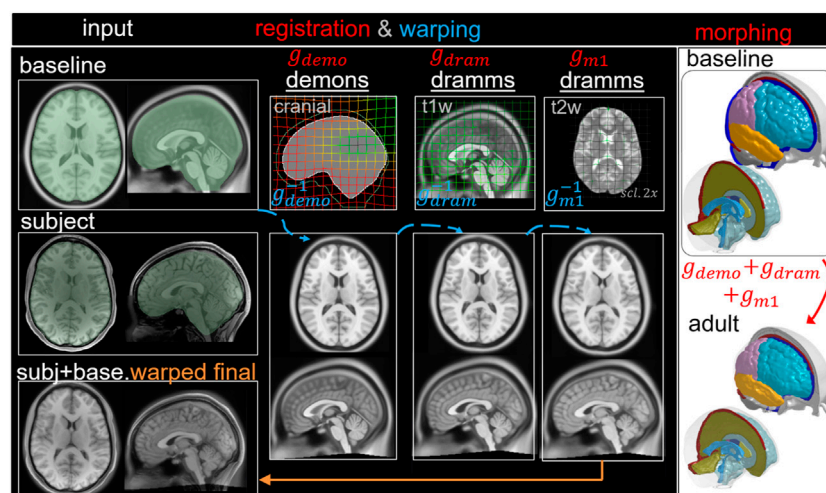


FIGURE 7 | Type III pipeline applied for personalizing the baseline ADAPT model to a subject-specific model of an adult subject. The pipeline consists of three steps: (i) Demons registration with cranial masks; (ii) Dramms registration with T1W image; (iii) Dramms registration with T2W image for further alignment. The displacement field obtained from each step is visualized on the grid together with the warped baseline ICBM images to show its effect. The final warped ICBM is overlaid with the subject's image to visualize registration accuracy.

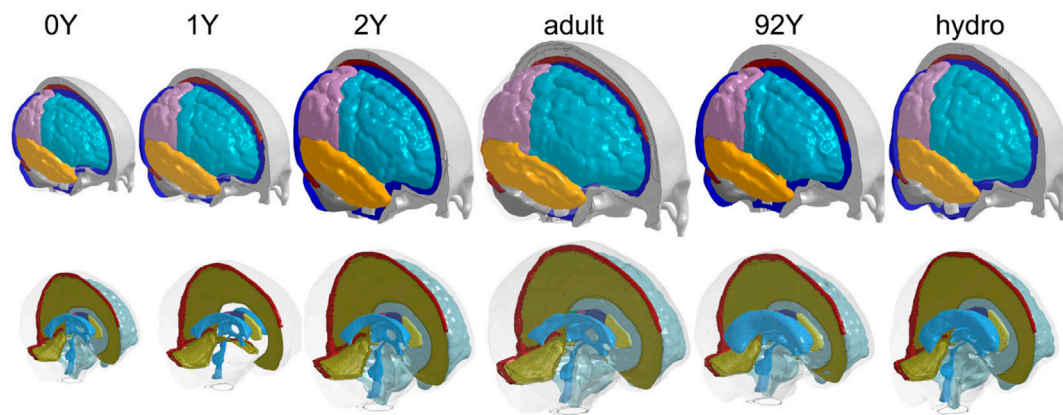


FIGURE 8 | Six subject-specific head models generated including the 0Y, 1Y, 2Y, adult, 92Y, and a hydrocephalus brain (the same length scale applies).

a final subject-specific model of the 0Y with cerebellum included.

RESULTS

Subject-specific Head Models and Element Quality

The generated head models (**Figure 8**) and cross-sections (**Figure 9**) demonstrate the capacity of the framework for generating subject-specific head models with significant anatomical differences; all morphed from a baseline model. Especially, the extensively enlarged LVs and the varying shapes of CC in the hydrocephalus and the elderly 92Y brain are captured (**Figures 10, 11**). The element quality for the models

is listed in **Table 2**, showing that most brain elements ($95.9 \pm 1.5\%$ on average for the six subjects) have a Jacobian over 0.5, and the minimum Jacobian in all the six head models is above 0.13 (in the hydrocephalus brain). In this study, the mesh quality is considered satisfactory when at least 95% of the elements have a Jacobian over 0.5.

Personalization Accuracy

The baseline ICBM image (**Figure 10A**) is warped to the six subjects. The warped images (**Figure 10B**) and subjects' images (**Figure 10C**) are compared to evaluate registration accuracy. The segmented binary masks of the final warped baseline and subjects are overlaid to further visualize personalization accuracy (**Figure 11A**). The evaluated masks include cranial, brain, and six local brain regions. The boxplots of the DICE and HD95 are

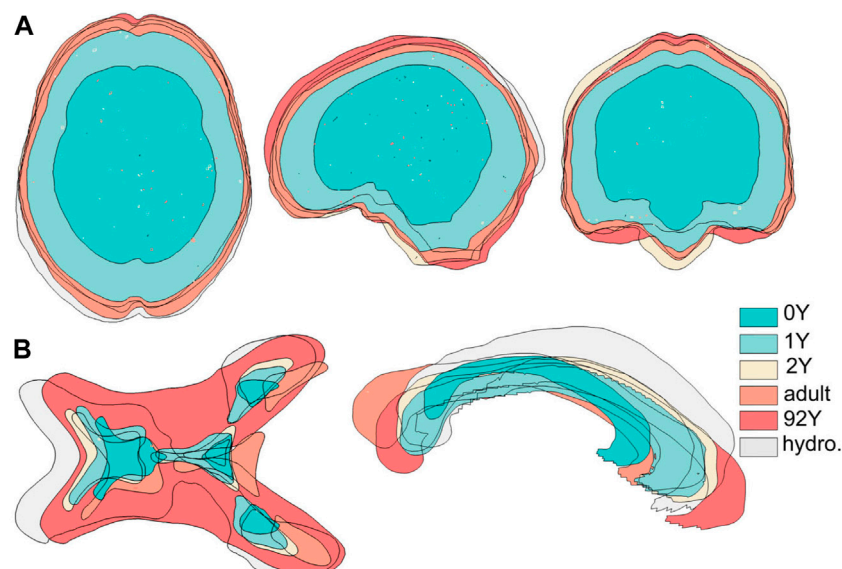


FIGURE 9 | Six subject-specific models are aligned together, showing the generated models have widely varying intracranial volumes (**upper row**) and significant anatomical differences as exemplified with lateral ventricles and corpus callosum (**lower row**).

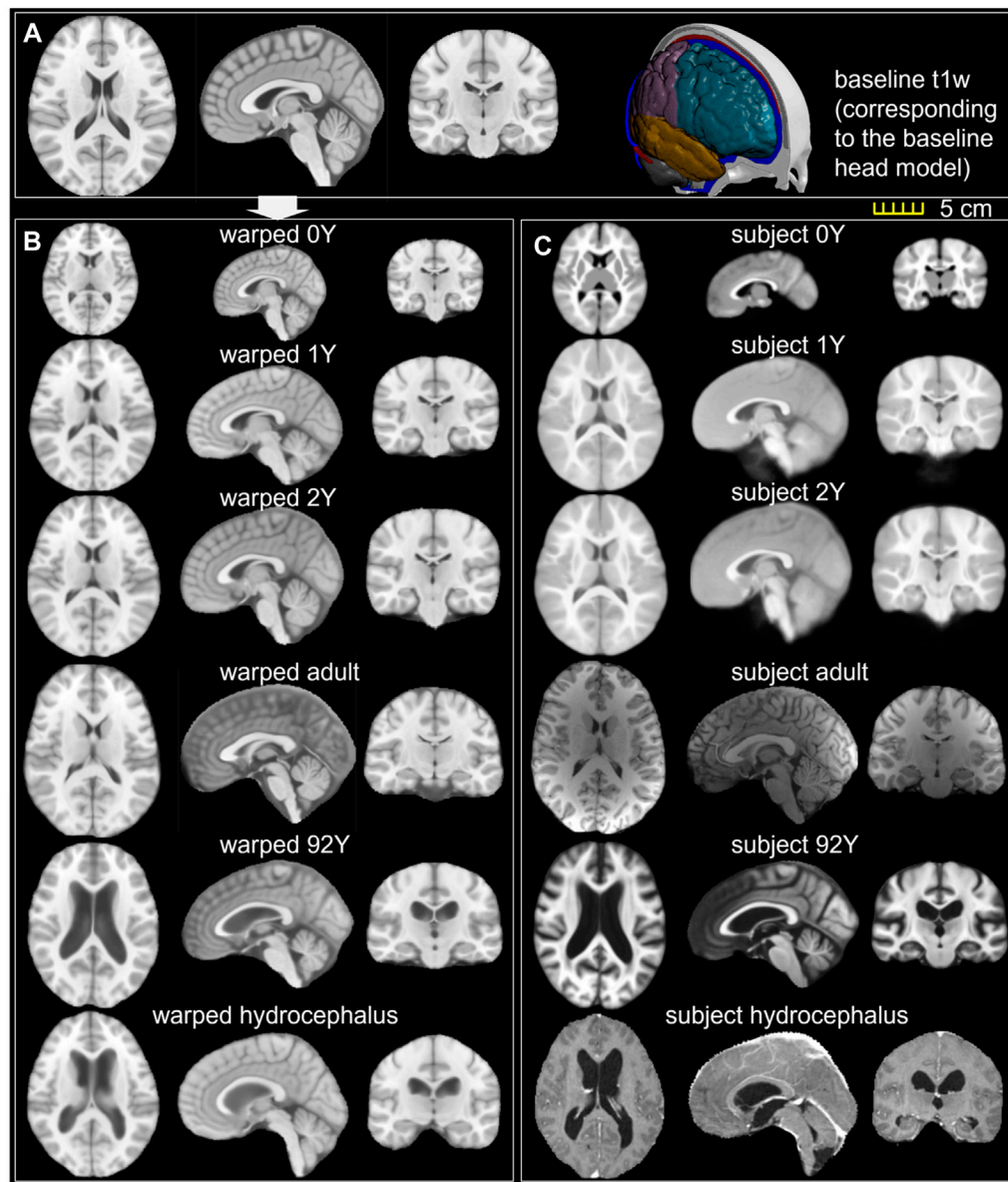


FIGURE 10 | (A) T1W image of the ICBM baseline; **(B)** ICBM baseline warped to the six subjects; **(C)** T1W image of the six subjects. Transverse, sagittal, and coronal cross-sections are captured for each brain.

presented in **Figure 11**, with values listed in **Tables 3, 4**. The average DICE scores are all >0.9 for the cranial mask, the brain, cerebellum, CC, being 0.97, 0.90, 0.89, and 0.94, respectively. Since the cerebellum for the 0Y subject image has been stripped, the evaluation of registration accuracy is without this region. The average DICE score for LV is 0.80. DICE score can be improved by incorporating multimodality step, e.g., with T2W image that has higher contrast for CSF/LVs. For example, the pipeline for the adult subject adding the T2W multimodality step improves personalization accuracy than previously achieved (see **Supplementary Appendix S1**). The DICE values are comparable to that achieved in neuroimaging field (Ou et al.,

2014) despite the higher requirement on the smoothness of displacement field for satisfactory element quality in the personalized head FE models.

Hydrocephalus and the Elderly Brain: Importance of the Feature Step and the Higher Requirement on Displacement Smoothness for Mesh Morphing

The mesh after each morphing step shown in **Figure 12** illustrates the effect of the feature steps, which allow capturing subject's cranial shape (**Figure 12A**), enlarged LVs (**Figure 12B**), CC (**Figure 12C**), as well as pushing back of the skull mesh (**Figure 12E**), while local

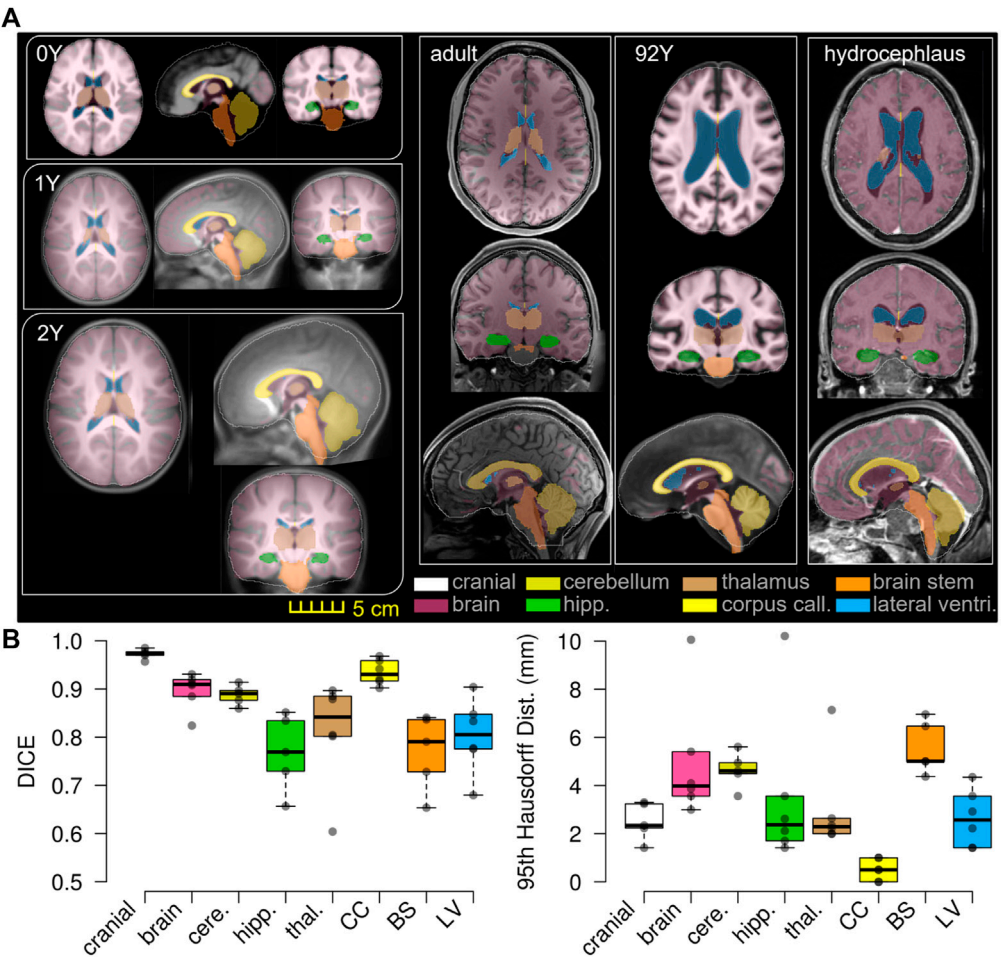


FIGURE 11 | T1W image of the subject is overlaid with the segmented binary masks of the warped baseline, including the cranial mask, the brain, and local brain regions of the cerebellum, hippocampus, thalamus, CC, BS, and lateral ventricles (A). Boxplots of DICE and 95HD. The boxplots show the median, minimum, and maximum values shown (B).

Head model	Element quality index											
	Jacobian ≥ 0.5		Warpage ($^{\circ}$) ≤ 30		Skew ($^{\circ}$) ≤ 60		Aspect ratio ≤ 8		Min. angle ($^{\circ}$) ≥ 30		Max angle ($^{\circ}$) ≤ 150	
	percent	min	percent	max	percent	max	percent	max	percent	min	percent	max
ADAPT	98%	0.45	92%	111.76	99.9%	69.95	99.9%	6.62	99.8%	17.98	99.9%	161.94
Personalized models												
0Y	96%	0.34	92%	112.60	99.9%	70.93	99.9%	7.99	99.9%	14.58	98.0%	168.41
1Y	97%	0.31	92%	111.99	99.9%	69.68	99.9%	8.20	99.9%	16.23	99.0%	167.85
2Y	97%	0.36	92%	110.26	99.9%	67.19	99.9%	6.64	99.9%	16.39	99.0%	166.38
Adult	93%	0.17	90%	139.66	99.9%	74.43	99.9%	10.09	99.0%	8.95	98%	215.91
92Y	96%	0.15	94%	121.81	99.9%	78.53	99.9%	16.09	99.0%	5.56	98%	177.29
Hydrocephalus	95%	0.13	91%	118.31	99.9%	77.71	99.9%	11.07	99.0%	7.80	97%	176.79

TABLE 3 | DICE coefficients for the six subjects.

Subject ID	Cranial	Brain	Cerebellum	Hippocampus	Thalamus	CC	BS	LV
0Y	NaN	0.82	NaN	NaN	0.60	0.92	NaN	0.78
1Y	0.96	0.93	0.89	0.83	0.89	0.96	0.79	0.85
2Y	0.98	0.92	0.90	0.85	0.90	0.94	0.84	0.83
Adult	0.97	0.91	0.88	0.77	0.88	0.90	0.73	0.68
92Y	0.97	0.91	0.91	0.73	0.80	0.97	0.84	0.90
Hydrocephalus	0.99	0.88	0.86	0.66	0.80	0.92	0.65	0.78
Average	0.97	0.90	0.89	0.77	0.81	0.94	0.77	0.80

TABLE 4 | HD95 for the six subjects.

Subject ID	Cranial	Brain	Cerebellum	Hippocampus	Thalamus	CC	BS	LV
0Y	NaN	10.06	NaN	10.21	7.14	1.0	NaN	2.22
1Y	3.24	5.41	4.5	1.71	2.24	0	5.01	1.41
2Y	2.34	4.10	4.61	1.41	2.0	0.5	4.37	1.41
Adult	3.3	3.56	4.95	2.12	2.0	1	5.00	2.92
92Y	2.24	3.0	3.56	2.62	2.34	0	6.96	3.56
Hydrocephalus	1.41	3.87	5.61	3.56	2.64	0.5	6.47	4.35
Average	2.51	5.0	4.65	3.61	3.06	0.50	5.56	2.65

brain structures are captured by Dramms registration (**Figure 12D**). The meshes from these intermediate steps are morphed from the baseline ADAPT head model with displacement fields obtained via the image registration pipeline shown in **Figure 6**.

To further illustrate the importance of the feature registrations, a parametric pipeline without the LV feature step is performed for the 92Y brain, i.e., a complete pipeline writes $g_{subj_92Y} = g_{demo} + g_{dram}$ and $img_{warped_92Y} = g_{dram}^{-1}(g_{demo}^{-1}(img_{baseline}))$ (**Figure 13**). The results show that the Dramms registration, even using the largest allowable smoothness weight ($g = 1$), leads to FE mesh with negative Jacobian in some elements. For example, one FE element at the frontal horn of the LVs with a Jacobian ($J_{FE} = 0.5$) in the baseline mesh (**Figure 13A**, right upper), when morphed by the parametric pipeline resulting in a negative Jacobian ($J_{FE} = -0.05$) (**Figure 13C**, right upper). In contrast, when morphed by the original three-step pipeline, the same element has a positive value ($J_{FE} = 0.31$) (**Figure 13B**, right upper). This parametric pipeline also results in lower registration accuracy than the three-step pipeline (**Figures 13A,B**). This example also demonstrates the higher requirement on the smoothness of displacement than in the neuroimaging field when only Jacobian of the displacement field (J_{img}) is of concern (more detailed analysis presented in **Supplementary Appendix S2**).

DISCUSSIONS

This study presents a personalization framework for the efficient generation of subject-specific head models. The framework consists of hierarchical multiple feature and multimodality imaging registration pipelines, mesh morphing, and mesh grouping. The registration pipeline achieves competitive registration accuracy despite a higher requirement on the smoothness of the displacement field concerning the element

quality of the morphed mesh. The Demons feature registration steps capture significant anatomical differences, allowing a good initialization before applying Dramms registration to further capture the inter-subject anatomical details. The Dramms registration step with multimodality imaging further improves brain alignment. As a final step of the framework, mesh grouping of WM according to the subject's image mask allows incorporating subject-specific WM directly. The framework is successfully applied to subjects across the lifespan and a hydrocephalus brain with significant anatomical changes, achieving competitive personalization accuracy. The results demonstrate that the framework can personalize the baseline head model to brains with significant anatomical differences, resulting in subject-specific models ready for personalized simulations without manual repairing. To the knowledge of the author, this is the first study aligning such a broad scope of brain images suitable for mesh morphing.

The efficiency of the hierarchical two-step pipeline combining Demons and Dramms (Type I) has been previously assessed with six healthy adult subjects that have high-quality T1W images (Li et al., 2021). In this study, an extended pipeline is proposed for obtaining high-quality alignment across heterogeneous data of lifespan and for pathological brains with significant anatomical changes by introducing multiple feature steps as demonstrated with the hydrocephalus (**Figure 12**) and the 92Y brain (**Figure 13**). The registration accuracy for these more challenging cases is comparable with the six healthy adults, with average DICE scores for the cerebellum, CC, and brain all above 0.89. Notably, the average DICE score for LV for the six subjects in this study is 0.80, higher than that of the six adult subjects (0.71) (Li et al., 2021). Note that the same adult subject in an early study (Li et al., 2021) (subject ID 771354) is used here by adding T2W multimodality registration step (Type III). T2W images with higher contrast for CSF/LVs improve personalization

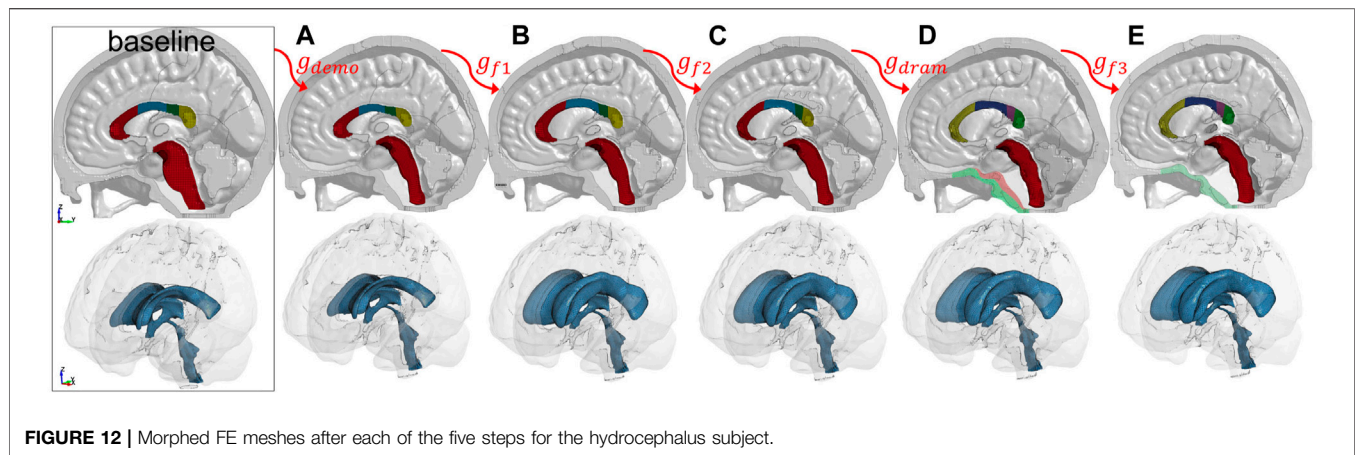


FIGURE 12 | Morphed FE meshes after each of the five steps for the hydrocephalus subject.

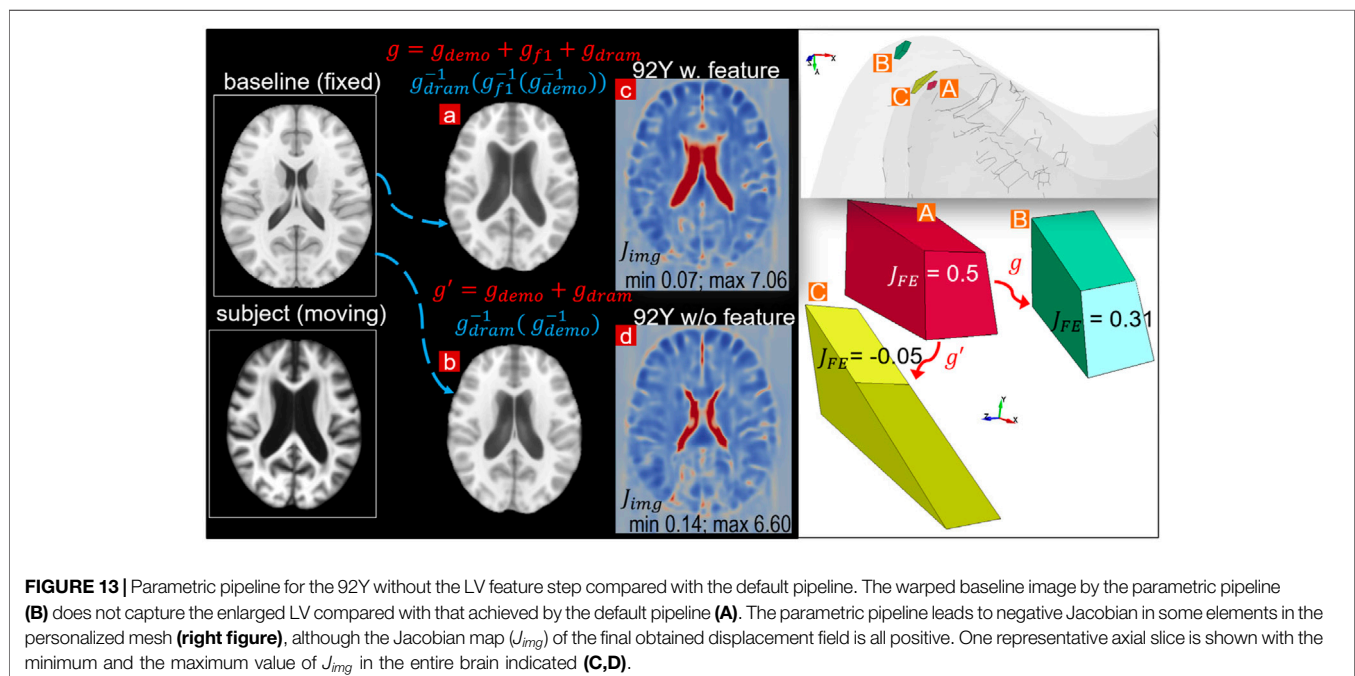


FIGURE 13 | Parametric pipeline for the 92Y without the LV feature step compared with the default pipeline. The warped baseline image by the parametric pipeline (B) does not capture the enlarged LV compared with that achieved by the default pipeline (A). The parametric pipeline leads to negative Jacobian in some elements in the personalized mesh (right figure), although the Jacobian map (J_{img}) of the final obtained displacement field is all positive. One representative axial slice is shown with the minimum and the maximum value of J_{img} in the entire brain indicated (C,D).

accuracy compared with previous results (see **Supplementary Appendix S1**). The mesh grouping step incorporates subject-specific WM directly, which is important for infant models to accurately capture the rapid transition between GM and WM in early infancy. Thus, the promising performance demonstrates the potential of the framework to personalize the baseline model to almost any brains with significant anatomical changes. Besides hydrocephalus, personalized models for brains with other structural changes such as decompressive craniotomy with brain expanded outside the skull (Holst et al., 2012) can also be achieved.

Inter-subject registration between brains with significant anatomical differences is still challenging in neuroimaging field and has limited registration accuracy (Kim et al., 2015); even more challenging is to apply image registration for mesh morphing due to the higher requirement on the smoothness

of the obtained displacement fields concerning element quality of the morphed mesh. There is often a trade-off between registration accuracy and element quality, and higher registration accuracy tends to worsen element quality according to the experience with the six subjects in this study. Especially, FE elements become invalid if their Jacobian become negative, which are not accepted by most FE analysis software. While in neuroimaging field, for physically plausible morphing, only positive Jacobian determinant of displacement field is to be ensured, which is often a looser requirement than FE Jacobian (see detailed analysis in **Supplementary Appendix S1**). Despite the higher requirement, this study achieves competitive registration accuracy compared with that reported in the neuroimaging field (Ou et al., 2014). For example, a previous study reported Jaccard index below 0.6 for all brain regions using popular deformable registration algorithms for inter-subject

registration (Ou et al., 2014), while the average Jaccard index (converted from DICE according to $\text{Jaccard index} = \text{DICE}/(2 - \text{DICE})$ (Ou et al., 2014)) for the six subjects is all above 0.66 for all regions in this study.

The applications of the framework show that different pipelines can be used depending on the anatomical differences between the subject and baseline ICBM, as well as the subject's image quality and available imaging modalities. For brains that are similar to the baseline, Type I pipeline with fewer steps is sufficient, while for brains with significant anatomical differences compared with the baseline, e.g., the hydrocephalus and elderly brain, Type III pipeline is needed to achieve a proper alignment. Furthermore, when T2W images are available, multimodality image allows better alignment of the brain and CSF/LVs. In principle, more multimodality registrations can be performed if available from the subject as the baseline image contains imaging modalities of T1W, T2W, proton density (PD), and tissue probability maps. Besides, more feature steps can be introduced to handle even more challenging cases. Choosing the proper pipeline for a specific case needs trial and error. An overall guideline is to start from Type I then add more registration steps if needed. Note that the multiple feature steps can be combined into one image with multiple binary masks and perform Demons registration at once. However, one feature in each step, as done in this study, tends to be more robust. Furthermore, the framework, though demonstrated with the ADAPT baseline head model, is equally applicable for personalizing other head models as a baseline, e.g., models with tetrahedral elements as commonly used for tDCS, TMS, TUS, as well as smoothed-voxel brain models.

Compared with existing studies registering adult brains, fewer studies align infant brains, which are more challenging partially due to the rapid development of brain anatomy within the first year, especially T1W images are inversed with densities. Not only more challenging for registration algorithms but also the evaluation of performance is also more difficult as most segmentation algorithms are developed based on adult images, such as FreeSurfer. It's worth noting that the lowest registration accuracy in all brains is for the thalamus in the 0Y; a visual check shows FreeSurfer automatically segmented thalamus not accurate enough. Future studies can employ infant FreeSurfer (Zöllei et al., 2020) for more accurate segmentation for infant brain images, thus allows more objective evaluation of personalization accuracy. For adult brain mesh morphing, image registration-based morphing pipelines proposed earlier show promising performance in generating detailed subject-specific head models of healthy adult brains (Giudice et al., 2020; Li et al., 2021) while the framework proposed in this study allows generating models across the lifespan and for brains with significant anatomical changes, which can be used for studying age-specific and groupwise TBIs. Especially, brains with neurological diseases such as hydrocephalus with extensively enlarged LVs mimicking the elderly brain may provide a possible clue for new insights into TBIs. The approach also opens the opportunity for studying how a potentially vulnerable brain, e.g., a hydrocephalus patient, may sustain a TBI injury risk under fall impact, especially hydrocephalus patients who are more prone to

fall. Until today, the biomechanics of TBIs in these groups are much understudied, partially due to the meshing challenge.

Compared with the many existing studies of TBIs for healthy adults, the injury mechanisms of infants and children are understudied. There are few child/infant head models (Li et al., 2011; Giordano et al., 2017; Li et al., 2017). In addition to the meshing challenge for adult models, the development of additional unique features of suture and fontanel plays an essential role in head impact response (Li et al., 2017). Previously, mesh morphing has also been used for morphing a baseline infant head model to different ages using radial basis function (RBF) to interpolate the displacement field obtained from land markers the anatomical features of suture and skull surface (Li et al., 2011). Unlike the image registration-based morphing, the RBF approach needs manual indentation of land markers, which is often tedious (Wu et al., 2019). The RBF approach also does not account for brain anatomies. Comparatively, the morphed detailed infant brain models in this study, when combined with the detailed skull and scalp models (Li et al., 2017; Li et al., 2019), will allow studying brain injury biomechanics under impact for infant head model for abusive head trauma with important legal applications for forensic diagnosis. The newborn infant head models may be used for studying delivery-related neurotrauma and studying new intervention approaches for clinical problems.

Some limitations and future works need to be mentioned here. First, the proposed framework allows efficient generation of subject-specific head models with competitive personalization accuracy and satisfactory element quality without mesh repairing. However, the morphing technique involves manual intervention when selecting which morphing pipeline to use. Thus, there could be user-to-user variability based on which pipelines are chosen and concerns regarding repeatability. For example, selecting improper pipelines could result in reduced morphing accuracy, and certain regions may not be morphed accurately if they are not selected as features by the user. Secondly, this framework requires segmentation for the Demons steps, which may need manual effort to ensure accurate segmentation and would require significant time and effort for large-scale studies. Nevertheless, considering the challenge of generating subject-specific head models, this effort is considered acceptable. Note that this morphing technique generates subject-specific models from a geometric perspective only and does not account for subject-specific material properties. Thirdly, the current framework allows generating head models reflecting the subject's internal brain structures, but the major sulci and gyri lines are not evaluated like most studies in the neuroimaging field. It should also be noted that the framework does not ensure the same characteristic lengths among generated models of different sizes; the infant brains, in general, have smaller elements than that of an adult model. In this regard, the block-based method has an advantage that allows adjusting mesh densities to maintain similar element characteristic lengths (Mao et al., 2013b). Furthermore, Dramms registration algorithm is chosen for registering brain MRI images in this study since it has a clear advantage to align largely different anatomies such as the ventricles in comparison with other popular registration algorithms (Ou et al., 2014). However, other

algorithms, such as implemented in ANTs (Avants et al., 2011) and DARTEL (Vercauteren et al., 2009), when used within the current framework, may achieve similar performance, but it is yet to be investigated. Finally, the framework can be extended to include more registration steps and other advanced nonlinear registration algorithms to handle even more challenging cases.

DATA AVAILABILITY STATEMENT

The original contributions presented in the study are included in the article/**Supplementary Material**; further inquiries can be directed to the corresponding author.

AUTHOR CONTRIBUTIONS

The author confirms being the sole contributor of this work and has approved it for publication.

FUNDING

The present study was supported by research funds from KTH Royal Institute of Technology (Stockholm), and the Swedish Research Council Grants (2016-04203 and 2020-04724).

REFERENCES

- Aimedieu, P., and Grebe, R. (2004). Tensile Strength of Cranial Pia Mater: Preliminary Results. *J. Neurosurg.* 100 (1), 111–114. doi:10.3171/jns.2004.100.1.0111
- Alekseichuk, I., Falchier, A. Y., Linn, G., Xu, T., Milham, M. P., Schroeder, C. E., et al. (2019). Electric Field Dynamics in the Brain during Multi-Electrode Transcranial Electric Stimulation. *Nat. Commun.* 10 (1), 2573. doi:10.1038/s41467-019-10581-7
- Atsumi, N., Nakahira, Y., and Iwamoto, M. (2016). Development and Validation of a Head/brain FE Model and Investigation of Influential Factor on the Brain Response during Head Impact. *Ijvs* 9 (1), 1–23. doi:10.1504/ijvs.2016.077145
- Avants, B. B., Tustison, N. J., Song, G., Cook, P. A., Klein, A., and Gee, J. C. (2011). A Reproducible Evaluation of ANTs Similarity Metric Performance in Brain Image Registration. *Neuroimage* 54 (3), 2033–2044. doi:10.1016/j.neuroimage.2010.09.025
- Baker, T. J. (2005). Mesh Generation: Art or Science? *Prog. Aerospace Sci.* 41 (1), 29–63. doi:10.1016/j.paerosci.2005.02.002
- Beillas, P., and Berthet, F. (2017). An Investigation of Human Body Model Morphing for the Assessment of Abdomen Responses to Impact against a Population of Test Subjects. *Traffic Inj. Prev.* 18 (Suppl. 1), S142–S147. doi:10.1080/15389588.2017.1307971
- Bijar, A., Rohan, P.-Y., Perrier, P., and Payan, Y. (2016). Atlas-Based Automatic Generation of Subject-specific Finite Element Tongue Meshes. *Ann. Biomed. Eng.* 44 (1), 16–34. doi:10.1007/s10439-015-1497-y
- Bucki, M., Lobos, C., and Payan, Y. (2010). A Fast and Robust Patient Specific Finite Element Mesh Registration Technique: Application to 60 Clinical Cases. *Med. Image Anal.* 14 (3), 303–317. doi:10.1016/j.media.2010.02.003
- Castellano-Smith, A. D., Hartkens, T., Schnabel, J., Hose, D. R., Liu, H., Hall, W. A., et al. (2001). “Constructing Patient Specific Models for Correcting Intraoperative Brain Deformation,” in *Medical Image Computing and Computer-Assisted Intervention – MICCAI 2001*. Editors W. J. Niessen and M. A. Viergever (Berlin, Heidelberg 2001: Springer).

ACKNOWLEDGMENTS

Open access funding provided by KTH Royal Institute of Technology. The author thanks the reviewers whose valuable comments and suggestions significantly improved the quality of the manuscript. This work benefits greatly from the open-source imaging dataset and registration algorithms within the neuroimaging field. The WUM HCP data of the adult subject used in this study were provided [in part] by the Human Connectome Project, WU-Minn Consortium (Principal Investigators: David Van Essen and Kamil Ugurbil; 1U54MH091657) funded by the 16 NIH Institutes and Centers that support the NIH Blueprint for Neuroscience Research; and by the McDonnell Center for Systems Neuroscience at Washington University. The data handling was enabled by resources in projects [SNIC 2021/5-406] and [SNIC 2021/5-459] provided by the Swedish National Infrastructure for Computing (SNIC) at PDC, partially funded by the Swedish Research Council through grant agreement no. 2018-05973

SUPPLEMENTARY MATERIAL

The Supplementary Material for this article can be found online at: <https://www.frontiersin.org/articles/10.3389/fbioe.2021.706566/full#supplementary-material>

- Couteau, B., Payan, Y., and Lavallée, S. (2000). The Mesh-Matching Algorithm: an Automatic 3D Mesh Generator for Finite Element Structures. *J. Biomech.* 33 (8), 1005–1009. doi:10.1016/s0021-9290(00)00055-5
- Datta, A., Bansal, V., Diaz, J., Patel, J., Reato, D., and Bikson, M. (2009). Gyri-precise Head Model of Transcranial Direct Current Stimulation: Improved Spatial Focality Using a Ring Electrode versus Conventional Rectangular Pad. *Brain Stimulation* 2 (4), 201–207. 207 e1. doi:10.1016/j.brs.2009.03.005
- Datta, A., Truong, D., Minhas, P., Parra, L. C., and Bikson, M. (2012). Inter-Individual Variation during Transcranial Direct Current Stimulation and Normalization of Dose Using MRI-Derived Computational Models. *Front. Psychiatry* 3, 91. doi:10.3389/fpsy.2012.00091
- Davis, M. L., Koya, B., Schap, J. M., and Gayzik, F. S. (2016). Development and Full Body Validation of a 5th Percentile Female Finite Element Model. *Stapp Car Crash J.* 60, 509–544. doi:10.4271/2016-22-0015
- Dickie, D. A., Job, D. E., Rodriguez, D., Robson, A., Danso, S., Pernet, C., et al. (2016). *Brain Imaging of Normal Subjects (BRAINS) Age-specific MRI Atlases from Young Adults to the Very Elderly (v1.0) [Dataset]*. University of Edinburgh, Edinburgh Imaging, CCBS, BRAINS Imagebank. doi:10.7488/ds/1369
- Fernandez, J. W., Mithraratne, P., Thrupp, S. F., Tawhai, M. H., and Hunter, P. J. (2004). Anatomically Based Geometric Modelling of the Musculo-Skeletal System and Other Organs. *Biomech. Model. Mechanobiology* 2 (3), 139–155. doi:10.1007/s10237-003-0036-1
- Fonov, V., Evans, A. C., Botteron, K., Almli, C. R., McKinstry, R. C., Collins, D. L., et al. (2011). Unbiased Average Age-Appropriate Atlases for Pediatric Studies. *Neuroimage* 54 (1), 313–327. doi:10.1016/j.neuroimage.2010.07.033
- Fonov, V., Evans, A., McKinstry, R., Almli, C., and Collins, D. (2009). Unbiased Nonlinear Average Age-Appropriate Brain Templates from Birth to Adulthood. *Neuroimage* 47, S102. doi:10.1016/s1053-8119(09)70884-5
- Fornari, S., Schäfer, A., Jucker, M., Goriely, A., and Kuhl, E. (2019). Prion-like Spreading of Alzheimer's Disease within the Brain's Connectome. *J. R. Soc. Interf.* 16 (159), 20190356. doi:10.1098/rsif.2019.0356
- Giordano, C., Li, X., and Kleiven, S. (2017). Performances of the PIPER Scalable Child Human Body Model in Accident Reconstruction. *PLoS One* 12 (11), e0187916. doi:10.1371/journal.pone.0187916

- Giudice, J. S., Alshareef, A., Wu, T., Gancayco, C. A., Reynier, K. A., Tustison, N. J., et al. (2020). An Image Registration-Based Morphing Technique for Generating Subject-specific Brain Finite Element Models. *Ann. Biomed. Eng.* 48 (10), 2412–2424. doi:10.1007/s10439-020-02584-z
- Giudice, J. S., Alshareef, A., Wu, T. T., Knutsen, A. K., Hiscox, L. V., Johnson, C. L., et al. (2021). Calibration of a Heterogeneous Brain Model Using a Subject-specific Inverse Finite Element Approach. *Front. Bioeng. Biotechnol.* 9. doi:10.3389/fbioe.2021.664268
- Giudice, J. S., Zeng, W., Wu, T., Alshareef, A., Shedd, D. F., and Panzer, M. B. (2019). An Analytical Review of the Numerical Methods Used for Finite Element Modeling of Traumatic Brain Injury. *Ann. Biomed. Eng.* 47 (9), 1855–1872. doi:10.1007/s10439-018-02161-5
- Hajiaghajammar, M., Lan, I. S., Christian, C. W., Coats, B., and Margulies, S. S. (2019). Infant Skull Fracture Risk for Low Height Falls. *Int. J. Leg. Med.* 133 (3), 847–862. doi:10.1007/s00414-018-1918-1
- Ho, J., Zhou, Z., Li, X., and Kleiven, S. (2017). The peculiar Properties of the Falx and Tentorium in Brain Injury Biomechanics. *J. Biomech.* 60, 243–247. doi:10.1016/j.jbiomech.2017.06.023
- Holst, H., Li, X., and Kleiven, S. (2012). Increased Strain Levels and Water Content in Brain Tissue after Decompressive Craniotomy. *Acta Neurochir* 154 (9), 1583–1593. doi:10.1007/s00701-012-1393-2
- Horgan, T. J., and Gilchrist, M. D. (2003). The Creation of Three-Dimensional Finite Element Models for Simulating Head Impact Biomechanics. *Int. J. Crashworthiness* 8 (4), 353–366. doi:10.1533/ijcr.2003.0243
- Horstemeyer, M. F., Panzer, M. B., and Prabhu, R. K. (2019). State-of-the-Art Modeling and Simulation of the Brain's Response to Mechanical Loads. *Ann. Biomed. Eng.* 47 (9), 1829–1831. doi:10.1007/s10439-019-02351-9
- Hu, J., Jin, X., Lee, J. B., Zhang, L., Chaudhary, V., Guthikonda, M., et al. (2007). Intraoperative Brain Shift Prediction Using a 3D Inhomogeneous Patient-specific Finite Element Model. *Jns* 106 (1), 164–169. doi:10.3171/jns.2007.106.1.164
- Huang, Y., Dmochowski, J. P., Su, Y., Datta, A., Rorden, C., and Parra, L. C. (2013). Automated MRI Segmentation for Individualized Modeling of Current Flow in the Human Head. *J. Neural Eng.* 10 (6), 066004. doi:10.1088/1741-2560/10/6/066004
- Ji, S., Ford, J. C., Greenwald, R. M., Beckwith, J. G., Paulsen, K. D., Flashman, L. A., et al. (2011). Automated Subject-specific, Hexahedral Mesh Generation via Image Registration. *Finite Elem. Anal. Des.* 47 (10), 1178–1185. doi:10.1016/j.finel.2011.05.007
- Ji, S., Roberts, D. W., Hartov, A., and Paulsen, K. D. (2009). Brain-skull Contact Boundary Conditions in an Inverse Computational Deformation Model. *Med. Image Anal.* 13 (4), 659–672. doi:10.1016/j.media.2009.05.007
- Ji, S., Zhao, W., Ford, J. C., Beckwith, J. G., Bolander, R. P., Greenwald, R. M., et al. (2015). Group-wise Evaluation and Comparison of white Matter Fiber Strain and Maximum Principal Strain in Sports-Related Concussion. *J. Neurotrauma* 32 (7), 441–454. doi:10.1089/neu.2013.3268
- Ji, S., Zhao, W., Ford, J. C., Beckwith, J. G., Bolander, R. P., Greenwald, R. M., et al. (2015). Group-Wise Evaluation and Comparison of White Matter Fiber Strain and Maximum Principal Strain in Sports-Related Concussion. *J. Neurotrauma* 32 (7), 441–454. doi:10.1089/neu.2013.3268
- Kim, M., Wu, G., Wang, Q., Lee, S.-W., and Shen, D. (2015). Improved Image Registration by Sparse Patch-Based Deformation Estimation. *Neuroimage* 105, 257–268. doi:10.1016/j.neuroimage.2014.10.019
- Kleiven, S. (2007). Predictors for Traumatic Brain Injuries Evaluated through Accident Reconstructions. *Stapp Car Crash J.* 51, 81–114. doi:10.4271/2007-22-0003
- Kleiven, S., and von Holst, H. (2002). Consequences of Head Size Following Trauma to the Human Head. *J. Biomech.* 35 (2), 153–160. doi:10.1016/s0021-9290(01)00202-0
- Lagon, W., Sato, T. F., Opitz, A., Mueller, J., Barbour, A., Williams, A., et al. (2014). Transcranial Focused Ultrasound Modulates the Activity of Primary Somatosensory Cortex in Humans. *Nat. Neurosci.* 17 (2), 322–329. doi:10.1038/nn.3620
- Li, N., Baldermann, J. C., Kibleur, A., Treu, S., Akram, H., Elias, G. J. B., et al. (2020). A Unified Connectomic Target for Deep Brain Stimulation in Obsessive-Compulsive Disorder. *Nat. Commun.* 11 (1), 3364. doi:10.1038/s41467-020-16734-3
- Li, X. G., and von Holst, H. (2013). Quantification of Stretching in the Ventricular Wall and Corpus Callosum and Corticospinal Tracts in Hydrocephalus before and after Ventriculoperitoneal Shunt Operation. *J. Appl. Maths.* 2013, 350359, 2013. Article ID. doi:10.1155/2013/350359
- Li, X., Holst, H., and Holst, H. (2015). Finite Element Modeling of Decompressive Craniectomy (DC) and its Clinical Validation. *Abse* 2015, 1–9. doi:10.15764/abse.2015.01001
- Li, X., and Kleiven, S. (2018). Improved Safety Standards Are Needed to Better Protect Younger Children at Playgrounds. *Sci. Rep.* 8 (1), 15061. doi:10.1038/s41598-018-33393-z
- Li, X., Sandler, H., and Kleiven, S. (2019). Infant Skull Fractures: Accident or Abuse? *Forensic Sci. Int.* 294, 173–182. doi:10.1016/j.forsciint.2018.11.008
- Li, X., Sandler, H., and Kleiven, S. (2017). The Importance of Nonlinear Tissue Modelling in Finite Element Simulations of Infant Head Impacts. *Biomech. Model. Mechanobiol* 16 (3), 823–840. doi:10.1007/s10237-016-0855-5
- Li, X., Zhou, Z., and Kleiven, S. (2021). An Anatomically Detailed and Personalizable Head Injury Model: Significance of Brain and white Matter Tract Morphological Variability on Strain. *Biomech. Model. Mechanobiol.* 20 (2), 403–431. doi:10.1007/s10237-020-01391-8
- Li, Z., Hu, J., Reed, M. P., Rupp, J. D., Hoff, C. N., Zhang, J., et al. (2011). Development, Validation, and Application of a Parametric Pediatric Head Finite Element Model for Impact Simulations. *Ann. Biomed. Eng.* 39 (12), 2984–2997. doi:10.1007/s10439-011-0409-z
- Liu, S., Beillas, P., Ding, L., and Wang, X. (2020). Morphing an Existing Open Source Human Body Model into a Personalized Model for Seating Discomfort Investigation. *SAE Int.* 2020, 01–0874. doi:10.4271/2020-01-0874
- Madhukar, A., and Ostojic-Starzewski, M. (2019). Finite Element Methods in Human Head Impact Simulations: A Review. *Ann. Biomed. Eng.* 47 (9), 1832–1854. doi:10.1007/s10439-019-02205-4
- Mao, H., Zhang, L., Jiang, B., Genthikatti, V. V., Jin, X., Zhu, F., et al. (2013). Development of a Finite Element Human Head Model Partially Validated with Thirty Five Experimental Cases. *J. Biomech. Eng.* 135 (11), 111002. doi:10.1115/1.4025101
- Mao, H., Gao, H., Cao, L., Genthikatti, V. V., and Yang, K. H. (2013). Development of High-Quality Hexahedral Human Brain Meshes Using Feature-Based Multi-Block Approach. *Comp. Methods Biomech. Biomed. Eng.* 16 (3), 271–279. doi:10.1080/10255842.2011.617005
- McKee, A. C., Stein, T. D., Kiernan, P. T., and Alvarez, V. E. (2015). The Neuropathology of Chronic Traumatic Encephalopathy. *Brain Pathol.* 25 (3), 350–364. doi:10.1111/bpa.12248
- Miller, K., Wittek, A., Joldes, G., Horton, A., Dutta-Roy, T., Berger, J., et al. (2010). Modelling Brain Deformations for Computer-Integrated Neurosurgery. *Int. J. Numer. Meth. Biomed. Engng.* 26 (1), 117–138. doi:10.1002/cnm.1260
- Montanino, A., Li, X., Zhou, Z., Zeineh, M., Camarillo, D., and Kleiven, S. (2021). Subject-specific Multiscale Analysis of Concussion: from Macroscopic Loads to Molecular-Level Damage. *Brain Multiphysics* 2, 100027. doi:10.1016/j.brain.2021.100027
- Noël, L., and Kuhl, E. (2019). Modeling Neurodegeneration in Chronic Traumatic Encephalopathy Using Gradient Damage Models. *Comput. Mech.* 64 (5), 1375–1387. doi:10.1007/s00466-019-01717-z
- Opitz, A., Legon, W., Rowlands, A., Bickel, W. K., Paulus, W., and Tyler, W. J. (2013). Physiological Observations Validate Finite Element Models for Estimating Subject-specific Electric Field Distributions Induced by Transcranial Magnetic Stimulation of the Human Motor Cortex. *Neuroimage* 81, 253–264. doi:10.1016/j.neuroimage.2013.04.067
- Opitz, A., Paulus, W., Will, S., Antunes, A., and Thielscher, A. (2015). Determinants of the Electric Field during Transcranial Direct Current Stimulation. *Neuroimage* 109, 140–150. doi:10.1016/j.neuroimage.2015.01.033
- Ou, Y., Akbari, H., Bilello, M., Da, X., and Davatzikos, C. (2014). Comparative Evaluation of Registration Algorithms in Different Brain Databases with Varying Difficulty: Results and Insights. *IEEE Trans. Med. Imaging* 33 (10), 2039–2065. doi:10.1109/tmi.2014.2330355
- Ou, Y., Sotiras, A., Paragios, N., and Davatzikos, C. (2011). DRAMMS: Deformable Registration via Attribute Matching and Mutual-Saliency Weighting. *Med. Image Anal.* 15 (4), 622–639. doi:10.1016/j.media.2010.07.002
- Park, G., Kim, T., Forman, J., Panzer, M. B., and Crandall, J. R. (2017). Prediction of the Structural Response of the Femoral Shaft under Dynamic Loading Using

- Subject-specific Finite Element Models. *Comp. Methods Biomech. Biomed. Eng.* 20 (11), 1151–1166. doi:10.1080/10255842.2017.1340459
- Pedersen, K., Fahlstedt, M., Jacobsson, A., Kleiven, S., and von Holst, H. (2015). A National Survey of Traumatic Brain Injuries Admitted to Hospitals in Sweden from 1987 to 2010. *Neuroepidemiology* 45 (1), 20–27. doi:10.1159/000381780
- Sahoo, D., Deck, C., and Willinger, R. (2014). Development and Validation of an Advanced Anisotropic Visco-Hyperelastic Human Brain FE Model. *J. Mech. Behav. Biomed. Mater.* 33, 24–42. doi:10.1016/j.jmbbm.2013.08.022
- Shepherd, J. F., and Johnson, C. R. (2008). Hexahedral Mesh Generation Constraints. *Eng. Comput.* 24 (3), 195–213. doi:10.1007/s00366-008-0091-4
- Shi, F., Yap, P.-T., Wu, G., Jia, H., Gilmore, J. H., Lin, W., et al. (2011). Infant Brain Atlases from Neonates to 1- and 2-Year-Olds. *PLoS One* 6 (4), e18746. doi:10.1371/journal.pone.0018746
- Sigal, I. A., Hardisty, M. R., and Whyne, C. M. (2008). Mesh-morphing Algorithms for Specimen-specific Finite Element Modeling. *J. Biomech.* 41 (7), 1381–1389. doi:10.1016/j.jbiomech.2008.02.019
- Takhounts, E. G., Ridella, S. A., Hasija, V., Tannous, R. E., Campbell, J. Q., Malone, D., et al. (2008). Investigation of Traumatic Brain Injuries Using the Next Generation of Simulated Injury Monitor (SIMon) Finite Element Head Model. *Stapp Car Crash J.* 52, 1–31. doi:10.4271/2008-22-0001
- Van Essen, D. C., Smith, S. M., Barch, D. M., Behrens, T. E. J., Yacoub, E., Ugurbil, K., et al. (2013). The Wu-Minn Human Connectome Project: an Overview. *Neuroimage* 80, 62–79. doi:10.1016/j.neuroimage.2013.05.041
- van Noort, R., Black, M. M., Martin, T. R. P., and Meanley, S. (1981). A Study of the Uniaxial Mechanical Properties of Human Dura Mater Preserved in Glycerol. *Biomaterials* 2 (1), 41–45. doi:10.1016/0142-9612(81)90086-7
- Vercauteren, T., Pennec, X., Perchant, A., and Ayache, N. (2009). Diffeomorphic Demons: Efficient Non-parametric Image Registration. *Neuroimage* 45 (1 Suppl. 1), S61–S72. doi:10.1016/j.neuroimage.2008.10.040
- von Holst, H., and Li, X. (2014). Decompressive Craniectomy (DC) at the Non-injured Side of the Brain Has the Potential to Improve Patient Outcome as Measured with Computational Simulation. *Acta Neurochir* 156 (10), 1961–1967. doi:10.1007/s00701-014-2195-5
- Wang, T., Kleiven, S., and Li, X. (2020). *Electroosmosis Based Novel Treatment Approach for Cerebral Edema*. IEEE Trans Biomed Eng. PP.
- Weickenmeier, J., Jucker, M., Goriely, A., and Kuhl, E. (2019). A Physics-Based Model Explains the Prion-like Features of Neurodegeneration in Alzheimer's Disease, Parkinson's Disease, and Amyotrophic Lateral Sclerosis. *J. Mech. Phys. Sol.* 124, 264–281. doi:10.1016/j.jmps.2018.10.013
- Weickenmeier, J., Saez, P., Butler, C. A. M., Young, P. G., Goriely, A., and Kuhl, E. (2017). Bulging Brains. *J. Elast* 129 (1–2), 197–212. doi:10.1007/978-94-024-1220-8_10
- Windhoff, M., Opitz, A., and Thielscher, A. (2013). Electric Field Calculations in Brain Stimulation Based on Finite Elements: An Optimized Processing Pipeline for the Generation and Usage of Accurate Individual Head Models. *Hum. Brain Mapp.* 34 (4), 923–935. doi:10.1002/hbm.21479
- Wu, J., Cai, M., Li, J., Cao, L., Xu, L., Li, N., et al. (2019). Development and Validation of a Semi-automatic Landmark Extraction Method for Mesh Morphing. *Med. Eng. Phys.* 70, 62–71. doi:10.1016/j.medengphy.2019.04.007
- Zhang, L., Yang, K. H., Dwarampudi, R., Omori, K., Li, T., Chang, K., et al. (2001). Recent Advances in Brain Injury Research: a New Human Head Model Development and Validation. *Stapp Car Crash J.* 45, 369–394. doi:10.4271/2001-22-0017
- Zhou, Z., Li, X., and Kleiven, S. (2019). Biomechanics of Acute Subdural Hematoma in the Elderly: A Fluid-Structure Interaction Study. *J. Neurotrauma* 36 (13), 2099–2108. doi:10.1089/neu.2018.6143
- Zhou, Z., Li, X., and Kleiven, S. (2020). Evaluation of Brain-Skull Interface Modelling Approaches on the Prediction of Acute Subdural Hematoma in the Elderly. *J. Biomech.* 105, 109787. doi:10.1016/j.jbiomech.2020.109787
- Zöllei, L., Iglesias, J. E., Ou, Y., Grant, P. E., and Fischl, B. (2020). Infant FreeSurfer: An Automated Segmentation and Surface Extraction Pipeline for T1-Weighted Neuroimaging Data of Infants 0–2 Years. *Neuroimage* 218, 116946. doi:10.1016/j.neuroimage.2020.116946

Conflict of Interest: The author declares that the research was conducted in the absence of any commercial or financial relationships that could be construed as a potential conflict of interest.

Publisher's Note: All claims expressed in this article are solely those of the authors and do not necessarily represent those of their affiliated organizations, or those of the publisher, the editors and the reviewers. Any product that may be evaluated in this article, or claim that may be made by its manufacturer, is not guaranteed or endorsed by the publisher.

Copyright © 2021 Li. This is an open-access article distributed under the terms of the Creative Commons Attribution License (CC BY). The use, distribution or reproduction in other forums is permitted, provided the original author(s) and the copyright owner(s) are credited and that the original publication in this journal is cited, in accordance with accepted academic practice. No use, distribution or reproduction is permitted which does not comply with these terms.

Advantages of publishing in Frontiers



OPEN ACCESS

Articles are free to read
for greatest visibility
and readership



FAST PUBLICATION

Around 90 days
from submission
to decision



HIGH QUALITY PEER-REVIEW

Rigorous, collaborative,
and constructive
peer-review



TRANSPARENT PEER-REVIEW

Editors and reviewers
acknowledged by name
on published articles

Frontiers

Avenue du Tribunal-Fédéral 34
1005 Lausanne | Switzerland

Visit us: www.frontiersin.org

Contact us: frontiersin.org/about/contact



REPRODUCIBILITY OF RESEARCH

Support open data
and methods to enhance
research reproducibility



DIGITAL PUBLISHING

Articles designed
for optimal readership
across devices



FOLLOW US

@frontiersin



IMPACT METRICS

Advanced article metrics
track visibility across
digital media



EXTENSIVE PROMOTION

Marketing
and promotion
of impactful research



LOOP RESEARCH NETWORK

Our network
increases your
article's readership